# Supported Lanthanum Complexes : Grafting and Reactivity

Adrien Bathellier

## To cite this version:

Adrien Bathellier. Supported Lanthanum Complexes : Grafting and Reactivity. Theoretical and/or physical chemistry. INSA de Toulouse, 2020. English. NNT : 2020ISAT0036 . tel-03726315

HAL Id: tel-03726315
https://theses.hal.science/tel-03726315

Submitted on 18 Jul 2022

# THÈSE

En vue de l'obtention du

## DOCTORAT DE L'UNIVERSITÉ DE TOULOUSE

**Délivré par l'Institut National des Sciences Appliquées de Toulouse**

---

**Présentée et soutenue par**

**Adrien BATHELLIER**

Le 17 décembre 2020

# Complexes Supportés de Lanthane: Greffage et Réactivité

---

Ecole doctorale : **SDM - SCIENCES DE LA MATIERE - Toulouse**

Spécialité : **Physico-Chimie Théorique**

Unité de recherche :
**LPCNO-IRSAMC - Laboratoire de Physique et Chimie des Nano-Objets**

Thèse dirigée par
**Iker DEL ROSAL et Chiara DINOI**

Jury
**M. Régis GAUVIN,** Rapporteur
**Mme Fanny BONNET,** Rapporteure
**Mme Blanca MARTIN VACA,** Examinatrice
**Mme Karinne MIQUEU,** Examinatrice
**M. Iker DEL ROSAL,** Directeur de thèse
**Mme Chiara DINOI,** Directrice de thèse

# Remerciement

Tout d'abord je tiens a remercier tous les membres du jury d'avoir accepté de lire et d'évaluer cette these. Je remercie spécialement Blanca Martin Vaca d'avoir présidé ce jury.

Merci à Chiara Dinoi et Iker Del Rosal de m'avoir permis de réaliser cette thèse de doctorat sous leur direction et d'avoir essayé de me transmettre leur savoir scientifique. Je remercie spécialement Chiara pour ses conseils, son investissement et son soutien qui m'ont donné la volonté d'aller au bout de cette aventure.

Je remercie les autres membres permanents de l'équipe Modelisation Physique et Chimique du LPCNO ; en particulier Laurent Maron pour l'aide et le temps précieux qu'il m'a accordés durant ces années.

Ces trois années ont également été l'occasion pour moi d'enseigner, et je voudrais donc remercier les personnes qui m'ont donné l'opportunité de le faire. En particulier, merci à Jérôme Cuny, Romuald Poteau et Sophie Hoyau qui m'ont fait confiance pour enseigner à leurs côtés et m'ont ainsi permis de vivre une expérience enrichissante.

Merci aussi aux non-permanents de l'equipe Modelisation Physique et Chimique, pour la bonne ambiance de travail mais également pour les nombreux bons moments passés ensemble. Entres autres Carlos, Elisa, Roberto, Adrien, Jorge, Ionut et Karl. Un merci particulier à Diego (post-it) qui a apporté sa bonne humeur et a contribué à l'avancement de mes recherches pendant son stage passé dans l'équipe.

Mes remerciements vont également à l'équipe nanotech, mon équipe adoptive pendant ces années, tout particulièrement au microcrew : Simon, Gaëtan et Clyde, merci à eux pour les longues discussions que nous avons partagées et pour tous les bons moments passés ensemble, mais aussi à tous les autres membres du LPCNO, je pense notamment à Romain, François, Nicolas, Alexandre, Pierre, Thibault, Clemence, Arnaud, Mélodie, Louis et tant d'autres.

Je tiens à remercier ma famille et mes amis proches. Ces trois dernières années n'ont pas été de tout repos au niveau personnel. Particulièrement mon frère, Vincent, ma tante, Nathalie, enfin Raphou, Vane, Timtoum et Moumoune, qui ont su m'apporter confiance, écoute et joie pendant les moments difficiles.

Je remercie finalement les dotations d'heures de calculs du CALMIP sans lesquelles les calculs présents dans cette thèse n'auraient pu être réalisés.

# Table des matières

# Part I

# Introduction

## 1 Introduction to catalysis

The chemical challenges facing the planet in terms of energy and environment increase the pressure on the scientific community to find alternative catalytic solutions. In this changing landscape, catalysis remains pivotal since, in principle, it can improve the efficiency, the rate, and the selectivity of any chemical reaction. Heterogeneous catalysis is an important branch of catalysis and is considered as the ideal choice for the chemical industry. Heterogeneous catalysts, indeed, provide the efficient transformation of a wide range of raw and feedstock materials due to their robustness, operational practicability, and their recyclability.[1, 2] Heterogeneous catalysts can be divided into several categories: bulk materials, metal oxides such as $CrO_x$, x = 1-3, $GaO_x$, x = 3/2, 3, $VO_x$, x = 3/2-5/2, etc)[3] or metal sulphides such as $FeS_2$, ZnS, etc[4], zeolites or aluminosilicate, such as $Na_2Al_2Si_3O_{10}{\cdot}2H_2O$, *etc*)[5, 6], supported metal nanoparticles (*eg.* Au nanoparticles supported on $TiO_2$(111), ...),[7] and isolated systems on single sites *i.e.* individual isolated ions, atoms, molecular complexe or bimetallic clusters anchored on high surface area supports.[8] Common to all the industrial heterogeneous catalysts is the difficulty to attain a molecular level understanding of the structure of the active sites and the elementary steps of catalytic processes.[9, 10] This is primarily due to the intrinsic complexity of such catalysts caused by the broad distribution and high diversity of active sites. The characterisation of these catalysts, in addition, may result very complex in some cases, requiring the use of many characterisation techniques. Classical heterogeneous catalysis, mostly based on a 'trial and error approach', could be considered as easier in terms of practical advantages. [11, 12, 13, 14] One of the first examples of heterogeneous catalysis is the ammonia synthesis from $H_2$ and $N_2$, in the Haber Bosch process, whose development required the systematic testing of around 20000 materials as catalyst.[15] Its mechanism and the nature of the active site were elucidated later after decades of research by Ertl and coworkers, thanks to the high development of surface science.[16]

Homogeneous catalysis is currently less common in industry mostly because of their fragility, short lifetime, thermal instability, and the difficulty of the catalyst/product separation after reaction.[14, 11, 12, 13] However, homogeneous catalysts display several competitive advantages over heterogeneous catalysts. Homogeneous catalysts, for example: (*i*) are often active at lower temperatures; (*ii*) have higher selectivities; (*iii*) are chemically better defined; (*iv*) exhibit a reliable structure activity relationship and (*v*) are surrounded by different ligands which provide a very specific steric/electronic environment that could favour a specific product. Changing these ligands allows chemists to tune the catalyst's properties and consequently control their activity and selectivity.[17, 18] The determination and characterisation of their structure, in addition, is easier compared to heterogeneous systems, requiring the use of more common techniques such as elemental analysis,IR spectroscopy, NMR spectroscopy, X-Ray diffraction analysis.[19, 20, 17, 21] Since the 1960s, this structure-activity approach improved numerous catalysts that were adapted for their use in many industrial olefin transformation processes such as olefins epoxidation, olefin hydroformylation, olefin oligomerisation, olefin polymerisation and olefin metathesis.[18, 22] Thus, these two branches of catalysis have followed an independent development offering to the chemical industry different advantages and disavantages. As aforementioned, while homogeneous catalysis is usually more selective, heterogeneous catalysis is more activen allowing the recycling of the catalytic system. based on these findings, a question arise: Can we develop a hybrid system combining the advantages of both these types of catalysis reducing the heterogeneous-homogeneous gap? Starting from an heterogeneous system, attempts to develop hybrid systems have firstly lead to the creation of smaller and more finely dispersed catalysts (such as for example metal nanoparticles) within a porous material. In this case, the improvement of their performance is related to the decrease of the nanoparticle size which leads to a more active catalytic systems. However, the creation of single-atom catalysts (SAC) has become the most active new frontier in heterogeneous catalysis.[23, 24, 25, 26] These isolated atomic sites embedded on a support might mimic a homogeneous catalyst, providing similar reactivity and selectivity. For such catalysts, an environment preventing the single atom surface migration. Thus, a multiple coordination of the single atom with the support is generally occurring, leading to catalysts which can be very robust. The absence of atomic ensemble effects, and the presence of strong electronic effects from the support that modify the electronic structure of a metal atom in SAC, significantly affect the adsorption, finally inducing a different reactivity compared to metallic nanoparticles (NPs). Consequently, SAC exhibit distinctive performances from that of metal NPs for a wide variety of chemical process (such as oxidation, reduction, coupling reaction), finding recent industrial applications.[27, 28] Starting from an homogeneous system, on the other hand, attempts to develop hybrid systems often involves the heterogenisation of homogeneous catalysts which may be covalently bonded onto a porous support material such as silica.[29] Molecular complexes can be therefore either directly chemisorbed or bonded to a hydroxyl group of a linker molecule. This last approach involving the direct coordination of a homogeneous complex on a support will be the one used on this PhD work and consequently developed in the following sections.

## 2 Surface organometallic chemistry

The power of such molecular level structure-activity approach has been recognised early in the development of heterogeneous catalysts.[30, 31, 6, 32, 33] Following the rapid development of homogeneous catalysis, some 50 years ago, attempts to apply the same approaches in heterogeneous catalysis ultimately led to the field known as surface organometallic chemistry (SOMC).[29, 34, 35, 36, 37, 38, 39, 8, 40, 41, 5, 42, 21, 43, 44, 45, 46, 47] Research in this new field has gained much attention in the past 25 years, spurred by the need to improve existing catalysts and the advances in spectroscopic and computational methods, which allow very detailed structural characterisation, an essential step toward catalyst development. The essence of SOMC is to treat the surface of a support, typically a metal oxide, as a bulky rigid ligand onto which molecular precursors, such as organometallic complexes, can be covalently grafted *via* one or more M-O bonds, in order to limit their surface mobility and agglomeration. The grafted molecular complexes can be used directly in catalysis or: (i) transformed after grafting by a thermal post-treatment under vacuum, inert gases; (ii) modified by a post-reaction treatment to incorporate new ancillary ligands. The treatment of the surface before grafting, in addition may regulate the density of the OH functions by which the complexes will be grafted, controlling the site density of the grafted complexes and therefore preventing undesired reactions such as the deactivation processes involving the dimerisation of reactive intermediates.[48] The linkage of the metal complex to the surface oxide OH groups of the support can modify both the electrophilicity of the metal center and its coordination sphere. Each of these effects impacts the activity, selectivity, and stability of these well-defined catalysts leading to different activities and stabilities compared to those observed in closely related homogeneous analogues.[49, 50] In the same way, this approach allows to prepare well-defined surface-grafted species that can be fully characterised by modern solid/surface characterisation techniques (elemental analysis, IR, UV, NMR, EXAFS, etc).[51, 52, 53, 54, 55, 56, 57] The combination of these factors results in stable and highly active and selective supported catalysts for many reactions such as olefin metathesis, polymerisation, hydrogenation, hydrogenolysis, epoxidation, oxidation and deperoxidation reactions.[58, 59, 60, 47, 61, 62, 63, 64, 65] In order to obtain structurally uniform surface sites homogeneously distributed on the surface, the SOMC relies on the molecular-level understanding of the support structure and employs stringent pre-treatment protocols to prepare supports with desired properties. A combination of techniques as IR, SS NMR (Solid-State NMR), EXAFS, UV-vis, EPR spectroscopy (Electron Paramagnetic Resonance spectroscopy) and TEM (transmission electron microscopy) can be used to characterise the bulk structure, the morphology and surface area of the support as well as the structure of the surface oxide OH sites. Today, the best understood and widely used surfaces are silica, alumina and silica-alumina oxide supports.[49] These different supports used in SOMC can be prepared and characterised using similar procedures.

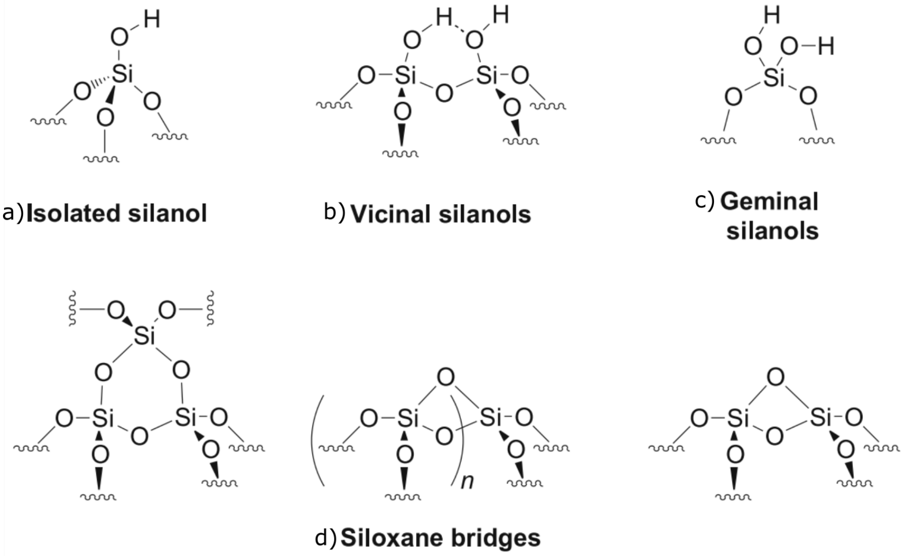

Figure 1: Scheme of the different types of surface hydroxyl groups and siloxane bridges present on the silica surface with a) isolated silanols, b) vicinal silanols, c) geminal silanol, and d) siloxane bridges.

Silica is a highly versatile system: available as a crystalline, mesoporous, and nonporous material.[45, 66, 67, 68, 69] Quartz and cristobalite are crystalline, but the very low surface area of these materials (2.6 $m^2.g^{-1}$ and 2.1 $m^2.g^{-1}$, respectively) limits the number of surface sites per unit mass restricting their applications as supports for heterogeneous catalysts.[68] Ordered mesoporous materials, based for instance on a MCM (Mobile Composition of Matter), SBA (Santa Barbara Amorphous) structure, are silicates obtained by a cooperative self-assembly or a liquid-crystal templating process.[70, 71, 72, 73, 74, 75, 69] Many topologies are also available as ordered 2D (MCM-41, MCM-50, SBA-15, MSU-H, *etc*) or 3D (MCM-48, SBA-6, FDU-12, *etc*) mesostructures but also disordered mesopores (MSU-1, HMS, KIT-1, TUD-1, *etc*). Such materials exhibit remarkable features displaying pores with well-defined sizes and uniform shapes that are ordered to a certain degree over micrometer length scales to yield arrays of non-intersecting channels. The large size of these pores allows to overcome one of the classical problems of traditional microporous materials (such as zeolites, zeotypes and pillar clays) concerning the impossibility of immobilising organometallic complexes due to size restrictions.[76, 77, 78, 79, 80] These materials possess high surface areas of about 1500 $m^2.g^{-1}$ and uniformly arranged mesopores with pore volumes as high as 3 $cm^3.g^{-1}$ as revealed from surface area measurements. Interestingly, in general, these materials can easily withstand dehydroxylation temperatures as high as 500 °C without structural collapse or drastic changes in their specific surface area, pore volume, and pore diameter.[39, 81] However, thermal treatment of mesoporous silica such as MCM-41 can lead to structural collapse, resulting in a sharp loss of specific surface area, if the treatment is performed too fast or at temperatures above 500 - 600 °C. [58, 45] Nonporous amorphous silica, such as AEROSIL® 200, is more widely used due to the relative high specific surface areas of these materials which range between 50 and 500 $m^2.g^{-1}$ depending mainly on the preparation method.[45, 66, 67] These fully amorphous materials are generated from $SiCl_4$ through a flame-based method (high-temperature flame hydrolysis). The formation of $SiO_2$, indeed, can be described by a combination of an oxyhydrogen reaction, in which the formation of water is followed by the hydrolysis of $SiCl_4$ with this same water. Interestingly, on this nonporous amorphous silica surfaces the amount of silanol groups (around 0.9 $mmolOH.g^{-1}$, *i.e.*, a density of 2.7 OH per $nm^2$ for a fumed silica treated at 200 °C) is much smaller than on the surface of ordered mesoporous silicas (1.9-2.2 $mmolOH.g^{-1}$ for MCM-41, 2.5 $mmolOH.g^{-1}$ for MCM-48, 1.8 $mmolOH.g^{-1}$ for SBA-15 and 2.3 $mmolOH.g^{-1}$ for SBA-16 calcinated at 550 °C).[82] The $SiO_2$ materials are often considered as chemically inert and almost inactive relative to other common metal oxides.[83, 84] These materials are also thermally stable and rigid their particle size and shape being controllable. The bulk of silica is composed of tetrahedral $SiO_4$ units connected to each other to siloxane rings of various sizes ranging from flexible 12-membered rings to strained 4-membered rings. As shown in scheme 1, the silica surface provides various reactive sites that have been assigned to different types of silanol ≡Si-OH groups (isolated, vicinal or geminal), and siloxane bridges ≡Si-O-Si≡.[45, 85] The types and density of silanol/ siloxane groups can be modified by thermal treatment under vacuum or in a stream of inert gas or synthetic air, leading to supports referred to as $SiO_2$-T, in which T is the thermal treatment temperature. This process, called dehydroxylation, is routinely carried out in the range 200–1000 °C. For example, at temperatures of 700 °C, mostly isolated silanol groups with a surface of 0.2 $mmolOH.g^{-1}$ (0.7 OH per $nm^2$) remain on the silica surface. As a result, surface complexes grafted on such silica can be considered as isolated complexes and their coordination spheres (and hence reactivities) are usually very similar.[86, 87, 88] As aforementioned, a fumed silica that has been treated at 200 °C, has a hydroxyl concentration of around 0.9 mmolOH.g$^{-1}$, corresponding to a density of 2.7 OH per nm$^2$. Weakly acidic hydroxyl groups are usually inferred to be the most reactive native surface species.[89, 6] The hydroxyl population can be determined by several spectroscopic methods such as solid-state $^1$H NMR and FTIR spectroscopy, mass spectrometry[90, 91, 92, 93, 94, 95, 96, 97] or by titration with different reagents.[96, 98, 99, 100, 101]

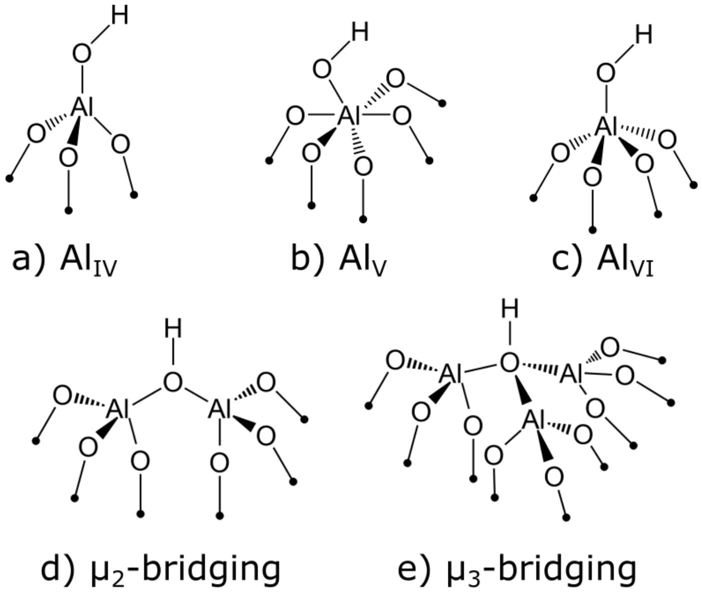
a) $Al_{IV}$ b) $Al_V$ c) $Al_{VI}$

d) $\mu_2$-bridging e) $\mu_3$-bridging

Figure 2: Scheme of the different types of surface hydroxyl groups on alumina with a) $Al_{IV}$, b) $Al_V$, c) $Al_{VI}$, d) $\mu_2$-bridging and e) $\mu_3$-OH bridging Al sites.

Alumina(s) ($Al_2O_3$) has a more complex surface chemistry than silica because of the greater variety of surface functionalities and types of allotropes. Alumina contains a mixture of interconnected tetrahedral $AlO_4$ and octahedral $AlO_6$ units. This oxide exists as pure phases or mixtures of $\alpha$, $\delta$, $\gamma$, $\eta$ and $\theta$ alumina.[102, 103] The amount of tetrahedral aluminium decreases in the order of $\theta$ (50%) to $\delta$ (37%) to $\gamma$ (25%) to $\alpha$ (0%).[104, 105, 106, 107, 108, 109, 110] The $\alpha$-alumina has low surface area (1-10 m$^2$.g$^{-1}$) and is mainly used for the preparation of reforming catalysts because of its stability over 1000 °C. The $\gamma$-alumina can be obtained with relatively large surface areas (200 m$^2$.g$^{-1}$) and is kinetically stable up to 700 °C when treated under vacuum. For this reason, $\gamma$-$Al_2O_3$ is the most widely used phase.[111, 112] Above this temperature, oxygen mobility increases leading to a faster phase transition to $\delta/\theta$-alumina. The presence of two types of Al-sites in the bulk reflects the rich surface chemistry of $\gamma$-alumina surfaces. Surfaces aluminium sites can be hexa- ($Al_{VI}$), penta- ($Al_V$), tetra- ($Al_{IV}$), and tri-coordinate ($Al_{III}$). The surface also contains terminal Al-OH groups bound to $Al_{VI}$, $Al_V$, and $Al_{IV}$ as well as $\mu$2- or $\mu$3-OH bridging between Al sites (scheme 2).[49] Similar to silica, applying a thermal treatment to alumina under vacuum or inert gases leads to a decrease of the Al-OH density. For example, $Al_2O_{3-500}$ and $Al_2O_{3-700}$ has respectively a hydroxyl density of 2.0 and

0.6 OH per nm$^2$. In $\gamma$-alumina treated above 400 °C, in contrast to silica, the dehydroxylation process is also accompanied, by the formation of Lewis acidic Al(III) sites that have been shown to correspond to highly reactive defect sites.[111, 113, 114, 115, 116] Therefore, the grafting of a complex on alumina can take place on surface Al—OH groups or directly on these Lewis acidic Al-sites. The, grafting reaction, thus, involves more than one site on the alumina surface, leading to a mixture of organometallic grafted complexes, which makes the structural determination more complex than on silica.[45] Finally, major differences in reactivity have been found for silica *vs.* alumina supported catalysts. The major differences arise from the fact that while supported systems on silica generate neutral species, supported systems on alumina generate cationic species. For example, strong effects of the support have been shownfor Re-based catalysts in the field of alkene metathesis. While the $Re_2O_7/SiO_2$ system is unreactive, the $Re_2O_7/\gamma$-$Al_2O_3$ species represents one of the best performing systems, which even becomes tolerant to functionalised alkenes such as methyl oleate when $Me_4Sn$ is used as an additive. The origin of the reactivity of $Re_2O_7/\gamma$-$Al_2O_3$ has been linked to the Lewis acidic properties of $\gamma$-alumina.[45] An other exemple concers the alkane metathesis with tungsten systems, the alumina-supported systems outperforming their silica-supported counterparts, which are almost inactive. Here, the difference is mainly due to a higher stability of the active sites. This is particularly evident during the synthesis of silica-supported tungsten hydrides, in which, while on silica only a small fraction of the $(\equiv SiO)W(\equiv C\mathit{t}Bu)(CH_2\mathit{t}Bu)_2$ species is converted into the corresponding hydrides, because of sintering and formation of aggregates, on alumina, on the other hand, rather well-defined tungsten hydrides are generated from the corresponding isostructural alumina supported system, $(Al_sO)W(\equiv C\mathit{t}Bu)(CH_2\mathit{t}Bu)_2$.[98, 117, 118] Such a difference has been explained by the stabilisation of tungsten oxo species by adjacent Lewis acidic sites. In that way, Ballard, Burwell and their collaborators recognised that alumina supports often led to more active and stable single-site catalysts than silica supports.[119, 120, 84]

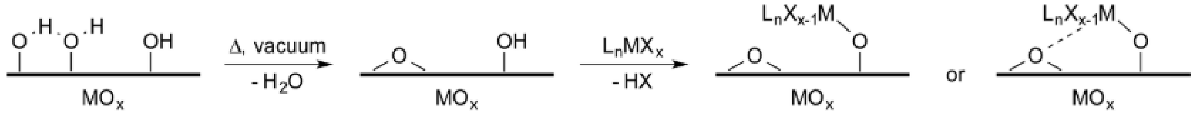

Figure 3: Strategy employed in the direct grafting approach: dehydroxylation of the support surface and grafting of the molecular precursor onto the surface OH groups

Different routes have been developed in the last years for the grafting of inorganic complexes on these kind of supports: (i) direct grafting and (ii) indirect grafting. The direct grafting of a LnMX$_x$ complex (X = R, NR$_2$, OR, Cl) onto a partially dehydroxylated support take places through a protonolysis of at least one M-X bond by surface hydroxyl groups (Surface-OH). This reaction leads to the formation of a monopodal Surface-O-M-LnX$_{x-1}$ species and the release of a HX molecule. Depending on the dehydroxylation temperature bipodal (Surface-O)$_2$-M-LnX$_{x-2}$ or tripodal (Surface-O)$_3$-M-LnX$_{x-3}$ species can also be formed.[121, 122, 123, 124, 125, 126] These grafted species are often referred as well-defined or single-sites. Grafting a metal precursor onto oxide supports requires strict anhydrous and anaerobic conditions. This is due to the general sensitivity of many metal complexes to air and water in solution, surface species supported on a high surfaces area displaying an increased sensitivity.[127, 128, 129] Several supported metal complexes, containing i) early-transition (Zr, V, Ti, Hf, Ta, W, Cr, Mo),[37, 49, 130, 44, 131] ii) late-transition (Ru, Rh, Ir, Pt)[20, 132, 121, 118, 133, 134, 49] and iii) rare-earth (Y, Sc, La-Lu)[135, 136] metals have been described in the literature. The indirect grafting occurs after an initial passivation/consumption of the surface hydroxyl groups by the treatment of the surface with reactive molecules acting as linkers.[39] The subsequent heterogenisation of the catalytically active metal centre by reaction with these linkers produces multifunctional hybrid materials, which are often difficult to characterise. In our case, for the rest of the PhD, we will only consider the direct grafting approach onto different supports.

In numerous Lewis acid-catalysed reactions such as alkene oxidation as well as alkene/alkyne metathesis, silica-grafted species based on lanthanides, group 3 or $d^0$ transition-metal complexes often display higher catalytic performance (activity and stability) than their molecular counterparts.[137] For example, in the case of silica-supported alkylidene complexes, theoretical studies have allowed to delineate the origin of the reactivity in alkene metathesis.[45] It as been shown that the the silica supported rhenium-based catalyst $[(\equiv SiO)(tBuCH_2)Re(=CHtBu)(\equiv CtBu)]$ is more active than its molecular counterpart in olefin metathesis especially in polymerisation of functionalised olefins bearing polar substituents. A simple explanation involves the formation of more electrophilic (more Lewis acidic) centres by including a siloxyligand.[138, 139, 140] This has also been shown in alkene metathesis, the silica supported catalyst has a higher stability compared to their molecular counterpart. The grafting on silica materials, indeed translates into site isolation, which brings higher stability by impeding bimolecular decomposition pathways, including self-aggregation.[141, 142]

In summary, the generation of chemically uniform supports and their subsequent controlled functionalisation towards well-defined active sites has been successfully performed, in particular with silica ($SiO_2$) and alumina ($Al_2O_3$) surfaces. Due to their large surface area and good mechanical and thermal properties, these two supports are good candidates to behave as grafting surfaces.[45, 130] The reaction of the isolated surface−OH groups with the appropriate molecular precursor forms well-defined surface species, which can then be post-treated to modify their environment according to the desired applications.

# 3 Lanthanides in SOMC

Among the metals used in of catalysis, rare-earth systems have been the subject of constant interest due to their high activity in several fields, such as polymerisation[88, 143, 144, 145] and fine chemistry,[146, 87, 147, 148] as well as to their low toxicity and moderate cost. The lanthanide series of chemical elements comprises the 15 metallic chemical elements with atomic numbers 57-71, from lanthanum to lutetium. These elements along with the chemically similar elements scandium and yttrium, are often known as the rare-earth elements, although lanthanides and group III elements differ by ionic radii and electronegativity. All of the lanthanides are f-block elements, corresponding to the filling of the 4f electron shell. Overall, their electronic configuration can be written as: $[Xe]_{54}4f^n5d^16s^2$, with n ranging from 0 to 14. In solution, lanthanides are strongly oxoplilic, forming stable complexes with strongly electron-donnor ligands containing oxygen or fluorine atoms. The most common ions of the lanthanide family are in the oxidation degree +III, although some lanthanides in the oxidation degrees +II and +IV have been described.[149] In this work we will focus on lanthanides at the oxidation degree +III. Due to their +III oxidation degree the complexes considered in the manuscript can be assimilated to $d^0$ compounds. At the oxidation state +III, the lanthanide metal centre has no electrons available to carry out activation mechanisms requiring the modification of its oxidation state, such as for instance oxidative addition reactions. This allows them to react efficiently through mechanisms that operate without changing the oxidation state, such as the bond metathesis processes. There are two types of metathesis: the $\sigma$ bond metathesis and the $\pi$ bond metathesis. The $\sigma$ bond metathesis corresponds to the activation of the $\sigma$ bond of an A-B compound by a metal complex of the type $L_n$M-X leading to the formation of a $L_n$M-A complex and a X-B compound (scheme 4a).[150, 151, 152] This reaction is a concerted process, involving the breaking and the formation of two $\sigma$ bonds, without any change in the oxidation state of the metal. The reaction pattern is divided into two steps: the coordination/activation of the A-B molecule, followed by the formation of a 4c-4e$^-$ transition state. The second metathesis type is a $\pi$ bond metathesis mechanism.[150, 153, 154] The $\pi$ bond metathesis reaction corresponds to the activation of the $\pi$ bond of an A=B compound, leading to the formation of the $L_n$M-A-B-X complex (scheme 4b) This is a concerted process, involving the breaking of one $\sigma$ bond and one $\pi$ bond, with the concomitant formation of two $\sigma$ bonds. The reaction pattern involves the same steps as for the $\sigma$ bond metathesis. Both these reactions involve the formation of a (typically) four-centre transition state involving the break and the formation of two bonds in a concerted process. Figure 4b shows the conventions of the $\alpha$ and $\beta$ attacks sites on the metal complex. It has been shown that the partial charge distribution shown in figure 4b promotes the formation of this kind of transition states.[151] The electro-deficiency of the metal centre favours a negative charge on the centres in $\alpha$ position and a positive charge on the one in $\beta$ position. For example, in the case of a C-H bond's the most favourable orientation from a kinetic point of view is that which places the carbon in $\alpha$ position and the hydrogen in $\beta$ position. This charge relocation thus explains the regioselectivity observed during the activation of heteronuclear bonds, as well as the importance of the polarisability of the bonds to be activated in the kinetics of the reaction. Due to these properties, lanthanide based catalysts are of great interest from an industrial point of view due to their ability to activate C-H,[155, 156, 152] C-Si,[157, 156] N-H[152, 158] and H-H[159, 160] inert bonds and to catalyse many polymerisation reactions.[161, 162, 163, 164, 165, 166] However, among the large variety of reported lanthanide complexes, amido derivatives have been found to be one of the most attractive and versatile family of compounds. The $[Ln[NR_2]_3]$ (R=$SiMe_3$) are synthetically accessible, reasonably sensitive to moisture and oxygen, and known for most of lanthanides.[167, 168, 169] They have been successfully used as catalysts or catalytic precursors in several fields.[170, 171, 172, 173, 174, 175] Thanks to the high reactivity of the Ln-$NR_2$ function, these catalysts can easily be modified : they can afford alkyl derivatives by reaction with alkylating agents,[176] or react with protic reagents as alcohols[177] or cyclopentadienyl derivatives,[178, 179] affording catalytically active species that it would be defficult to generate directly.

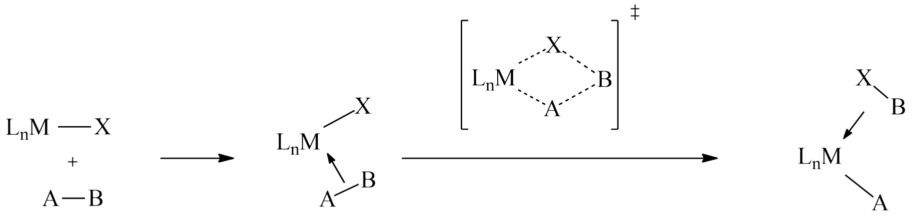

(a) Scheme of $\sigma$ bond metathesis mechanism

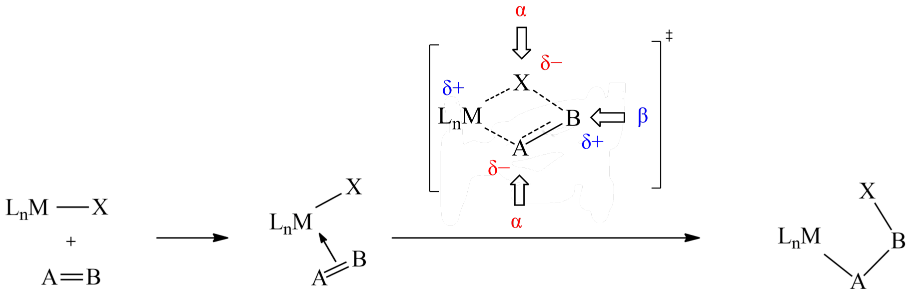

(b) Scheme of $\pi$ bond metathesis mechanism

Figure 4: Scheme of a (a) $\sigma$ and $\pi$ (b) bond metathesis mechanism.

The experimental grafting reaction of homoleptic derivatives of the type [Ln(N(SiMe$_3$)$_2$)$_3$] (Ln = Y, La, Nd, Sm) has already been described by Anwander and coworkers in 1997.[180] These compounds react with hydroxyl groups of silica, leading to the formation of a covalent lanthanide-siloxide bond with the concomitant protonolysis of the lanthanide-amino bond. The nature of the grafting mode of these silica grafted compounds has been characterised by thermogravimetry, IR and NMR spectroscopy. Their reactivity toward, the triphenylphosphine oxide (O=PPh$_3$), used as a probe to measure the acidity of the metal centre, was reported by Gauvin *et al.*[87] As shown by Drago and co-workers, a positive $^{31}$P NMR chemical shift difference ($\Delta\delta$) between physisorbed and chemisorbed OPR$_3$ is indicative of a coordination to an acidic site, the strength of the interaction correlating with the magnitude of the difference.[181] Based on these experimental reports, therefore, different coordination modes of the (SiO$_2$)-[Ln(N(SiMe$_3$)$_2$)$_3$] compound, with SiO$_2$ pre-treated at 200 °C and 700 °C, have been computed and compared with the experimental results.[135, 136] Theses theoretical studies have shown that the formation of a covalent SiO-Ln bond requires the presence of hydroxyl groups on the surface, the nature of the silanol groups at the silica surface influencing the geometry and the stability of the grafted complexes. Different silica-grafted La species have been computed: (i) mono-grafted complexes in the presence of isolated and geminal silanol groups, (ii) bi-grafted complexes in the presence of two vicinal silanols interacting by H-bonding and (iii) tri-grafted complexes obtained by the opening of one or two adjacent siloxane bridges *via* the transfer of a ligand at the metal complex to the silica surface (see Figure 1). The IR vibrational frequencies and the $^{31}$P NMR chemical shifts computed for the corresponding OPPh$_3$ adducts display similar values, indicating a small effect of the grafting mode on the Lewis acidity of the metal centre.

The catalytic properties of the silica-grafted lanthanide complexes were also studied, both theoretically and experimentally, by considering different reactions such as the alkynes dimerisation, the alkenes hydrosilylation, the intramolecular hydroamination/cyclisation of aminoalkenes and the ethylene, $\epsilon$-caprolactone, isoprene, methylmethacrylate and butadiene polymerisation reactions.[182, 144, 183, 184, 166] These studies revealed that the grafting of a molecular complex onto silica surfaces provides a significant modification of its catalytic properties, compared to the molecular analogue.[135, 136, 185] The polymerisation of methylmetacrylate by a silica-supported neodymium catalyst, indeed, leads to the formation of a moderately isotactic polymer whereas the molecular precursor generates a moderately syndiotactic polymer.[161, 184] According to a DFT study, carried out on the same system, the experimental preference for moderately isotactic polymer has been explained by the preferred conformations of the metal enolate–monomer adducts over the first insertions.[166]

# 4 Polymerisation

The development of highly efficient and selective polymerisation catalysts , for the synthesis of high-performance homo- or co-polymers with precisely controlled structures and desired properties, is still nowadays a very challenging topic.[186, 187, 188, 189, 190] Among the several types of polymerisation (step-growth, chain-growth, photo-polymerisation, *etc*), on this PhD work, we will only focus on the chain growth polymerisation reactions. Chain growth polymerisation is a polymerisation technique where unsaturated monomer molecules add onto the active site of a growing polymer chain one at a time. Typically, chain growth polymerisation involves three important steps: i) initiation, leading, by activation of the first monomer, to the formation of the active centre or propagating species, ii) propagation, involving the successive insertion of the monomers, with the increase of the polymer chain and iii) termination, halting the polymer growth process. There are several ways of initiating chain polymerisation which depend not only on the nature of the monomer but also on the nature of the active centre. On this work, two major polymerisation processes will be investigated: coordination insertion polymerisation and ring-opening polymerisation. The termination step may be spontaneous (depending on the nature of the active centres and the mode of polymerisation considered). By definition, a polymer is a substance or material composed by a large number of similar units bonded together while forming a chain. This chain may be decorated with pendant groups, such as methyls, chlorines or phenyls in polypropylene, polyvinyl chloride or polystyrene polymers, respectively. Sometimes, the architecture of a polymer can be more complex than that. For example, low-density polyethylene has branches coming off the main chain, resulting therefore in a branched polymer. Branching sometimes occurs spontaneously during synthesis of polymers, typically by free-radical polymerisation. In some cases, branching is so extensive that the polymer does not resemble a chain at all. Some of these highly-branched polymers are called dendrimers. Dendrimers are tree-like structures that branch out in all directions from a central point. Viewed from a distance, a dendrimer would have an overall shape that is more like a fuzzy ball than like a coiled chain. If the branches on one branched chain connect directly to other chains, then the polymer is said to be a crosslinked polymer. Crosslinked polymers can have extra strength and rigidity because they are less flexible than polymers in which the chains are able to move independently. However, just the right amount of crosslinking can make a polymer more elastic, making it bounce back to its original form after it is flexed. Crosslinking can actually be of two different types: "chemical" or "physical". Chemical crosslinks are permanent covalent bonds between the chains. Physical crosslinks are more temporary.; They are formed by strong intermolecular attractions, such as

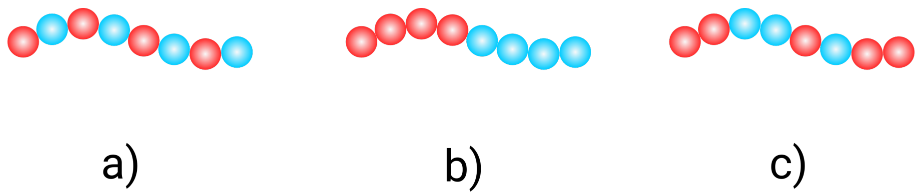

Figure 5: Possible co-polymer chains: a) alternating copolymers, b) block copolymers, c) statistical copolymers.

hydrogen bonds, the between chains. In our case, we focused only on the formation of a linear polymers. If a polymer is made from only one type of monomer or if it has a single repeating unit, it is called a homopolymer. If a polymer is made from more than one type of monomer or has more than a single repeating unit, it is called a copolymer. In this work, we will study homùo- and co-polymerisation reactions. Interestingly, if there are two different monomers, they may be arranged in different ways along the chain: if the two monomers simply alternate, one after the other wa have an an alternating copolymer, if they are distributed at random, we have a random or statistical copolymer, and finally if they are clustered in two separate groups, we have a block copolymer (see figure 5).

Five parametres have to be taken into account when studying a polymerisation reaction: the reaction conditions, the polymerisation activity, the polymer tacticity, the mechanism allowing the stereocontrol of the polymerisation reaction and the degree of polymerisation. A given polymerisation system reported in the literature may report all or just some of the above characteristics.[191]

- The reaction conditions include the polymerisation temperature ($T_p$) and the reaction medium such as the solvent, or the pressure when gaseous monomers are involved.
- The activity of the polymerisation catalyst is given in terms of turnover frequency (TOF: mole of substrate (monomer) consumed per mole of catalyst (initiator) per hour) for meaningful comparisons among the systems. Polymerisation systems with TOF ($h^{-1}$) of $<$10, $>$10, $>$100, $>$1000, and $>$ 10 000 are arbitrarily characterised as exhibiting, *low*, *modest*, *high*, *very high* and *exceedingly high* activities, respectively.
- The polymer tacticity is revealed by the resulting polymer stereomicrostructure (stereoregularity), which is shown by the sequence distribution of the stereogenic centres, *mmmmmmmm*, *rrrrrrrr*, *mrmrmrmr*, and *mmmmrrrr*, corresponding to isotactic (*it*), syndiotactic (*st*), heterotactic (*ht*), and stereoblock (*sb*) stereomicrostructures, respectively (see section 4.1 Tacticity above for more details).
- The mechanism allowing to the of stereocontrol of a given polymeric system is characterised by either i) an enantiomorphic-site control mechanism, *i.e.* the chirality of the active propagating centre dictates the stereochemistry of the monomer enchainment so that the stereoerror (*rr* triads in isospecific polymerization or *mm* triads in syndiospecific polymerisation) is corrected on the next monomer additions, or ii) a chain- end control mechanism,

*i.e.* the stereogenic centre of the last enchained monomer unit dictates the stereochemistry of further the monomer enchainment so that the stereoerror ($r$ dyads in isospecific polymerization or $m$ dyads in syndiospecific polymerisation) is propagated.

- The degree of polymerisation is a common means of expressing the length of a chainand quantifies the number of monomers incorporated into the chain. As with other molecules, a polymer size may also be expressed in terms of molecular weight. Polymer molecular weight is important because it determines many physical properties. If the molecular weight is too low, the transition temperatures and the mechanical properties will generally be too low, affording a polymer material useless for commercial applications. A commercially useful polymer must have transition temperatures to waxes or liquids that are above room temperature (*i.e.*, being a solid at room temperature) and it must have mechanical properties capable of bearing specific weights. Since the synthetic polymerisation techniques typically yield a statistical distribution of chain lengths, the molecular weight is expressed in terms of the weighted averages. The number-average molecular weight ($M_n$) and weight-average molecular weight ($M_w$) are most commonly reported. In a controlled polymerisation the $M_w$, the architecture, and functions of the resulting polymer can be controlled. The ratio of these two values ($M_w$ / $M_n$) is the dispersity $M_W$, which is commonly used to express the width of the molecular weight distribution.

## 4.1 Tacticity

The properties of a polymer are strongly influenced by its molecular microstructure. The variations in the geometric and configurational arrangements of the atoms in the repeat unit, and the distribution of these different spatial arrangements for the repeat units along the chain, are of particular importance. Different molecular microstructures arise from the possible stereochemical modes of propagation. The degree of stereoregularity of a polymer determines its thermal properties, such as melting-transition temperature ($T_m$) and glass-transition temperature ($T_g$). The existence of two isomeric forms of the repeat unit, and in particular their distribution along the polymer chain, are of great significance (see scheme 6). The relative stereochemistry of adjacent chiral centres within a macromolecule is defined as tacticity. Three kinds of polymer stereochemistry are possible: isotactic, syndiotactic and atactic. While in isotactic polymers the substituents are located on the same side of the polymer backbone, in syndiotactic polymers the substituents occupy alternating positions along the chain. In atactic polymers, finally the substituents are placed randomly along the chain.[192]

Tacticity in polymers is frequently determined by NMR spectroscopy. Since diastereisomers have different physical properties, they display different shifts in the $^1$H or $^{13}$C NMR spectra.[192, 193] In a polymer chain, we think about chiral centres in pairs, which we call "diads", because every pair of chiral centres has two possible diastereochemical relationships and therefore two possible chemical shifts. If the methyl groups are on the same side, the chiral centres have a "meso" relationship, whereas if they are on opposite sides, they have a "racemo" relationship. The stereochemistry of macromolecules can be defined even more precisely with the introduction of triads. An isotactic triad (mm) is made up of two adjacent meso diads, a syndiotactic triad (rr) consists of two adjacent racemo diads and a heterotactic triad (rm) is composed of a meso diad adjacent to a racemo diad. The mass fraction of isotactic (mm) triads is a common quantitative measure of tacticity. Triad composition can be calculated from the probability of finding meso diads ($P_m$) (or racemo ($P_r$)). The definition of tetrads and pentads introduce further sophistication and precision to defining tacticity, especially when information on long-range ordering is desirable. Tacticity measurements obtained by $^{13}$C NMR are typically expressed in terms of the relative abundance of various pentads within the polymer molecule, for example: mmmm, mrrm, *etc*

A polymer is classified as atactic (*atactic*), *isotactic*- or *syndiotactic*-biased (rich) atactic, tactic, or highly tactic according to the level of its triad distributions. Hence, polymers with *mr* ∼50, *mm* (*rr*) = 55-69, *mm* (*rr*) = 70-89, and *mm* (*rr*) ≥ 90 are arbitrarily termed *atactic*, *isotactic* (*syndiotactic*)-rich *atactic*, *isotactic* (*syndiotactic*), and highly *isotactic* (*syndiotactic*) polymers, respectively.

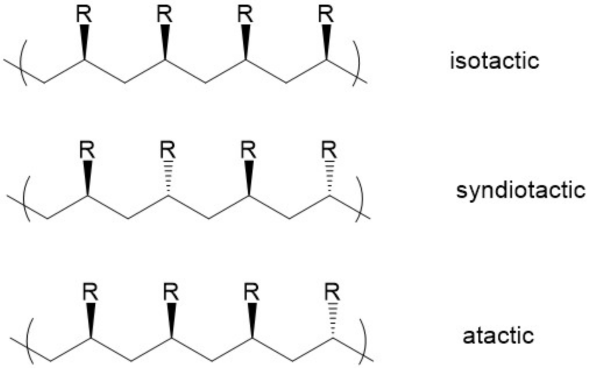

Figure 6: Exemple of isotactic, syndiotactic and atactic polymer.

## 4.2 Olefin coordination-insertion polymerisation

In this section we will present the $\alpha$-olefins and dienes used in this thesis: ethylene, butadiene, styrene and propene. The homopolymerisation of each of these monomers has been explored, as well as the co-polymerisation of ethylene with butadiene or styrene. Polyethylene is the simplest (and cheapest) poly-olefin, having the general formula $(\text{—CH}_2\text{—})_n$. It is typically a semicrystalline material, with mixture of interconnected crystalline and amorphous regions. In terms of microstructure, different polyethylenes are commercially available, with completely dissimilar chemical, physical, and mechanical properties. Polyethylene is conventionally classified as either: (i) high-density polyethylene (HDPE), (ii) low-density polyethylene (LDPE), or (iii) linear low-density polyethylene (LLDPE). HDPE has small amounts of branching (<1 %), with a density of 0.941 g/cm$^3$, LDPE contains a mixture of long (>C6) and short branches (methyl, ethyl, butyl) with a density of about 0.92 g/cm$^3$, while LLDPE has a high content of short branches (<C6) and a density less than 0.925 g/cm$^3$.[193, 192] Polyethylene can be tailored in various applications such as food packaging, carpets that replace natural fibres, biomedical applications, wire and cable insulation, *etc.*

The configurations of polybutadiene are cis- and trans- having a general formula (-$H_2C$-$CH=CH$-$CH_2$-$)_n$. The resulting polymer may have a variety of configurations due to the fact that two types of additions are possible: 1,4- or 1,2-insertion. Therefore, four stereoregular isomers are foreseeable for these polymers: 1,2-istotactic and 1,2-syndiotactic, from the 1,2 addition and cis-1,4 and trans-1,4, from the cis- and trans- 1,4 addition (see figure 7). Thereafter we will focus on the 1,4-insertion. Participation of both double bonds in the polymerisation process gives rise to a 1,4-addition, which can be either cis-1,4- or trans-1,4-, depending upon the disposition of the groups with respect to the polymer double bond. The high cis-l,4-polybutadiene is a soft, easily solubilised elastomer that exhibits excellent dynamic properties, low hysteresis, and good abrasion resistance. A glass-transition temperature of -102 °C is reported for this rubber. The trans-1,4-polybutadiene, in contrast, is a tough elastomer, having a reported glass-transition temperature of -107 °C and -83 °C (94% trans-). In addition to its high hardness and thermoplasticity, it is sparingly soluble in most solvents. The major use of polybutadiene is the manufacture of tyres which represents about 70% of the world production.[194, 195]

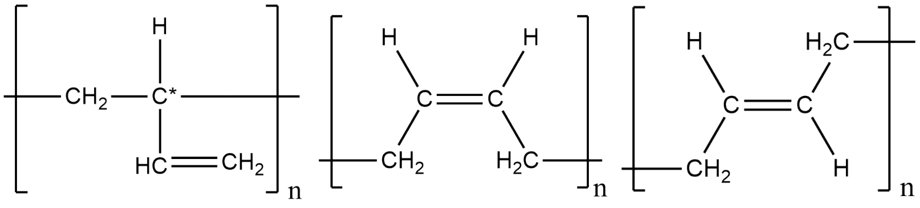
(a) 1,2-addition (b) cis-1,4-addition (c) trans-1,4-addition

Figure 7: Polybutadiene structures.

The copolymerisation of olefins and conjugated dienes is of particular importance since the resulting unsaturated copolymers could have interesting properties (crosslinking efficiency, rubber compatibility, *etc*). This reaction, however, is very difficult to be performed since the two classes of monomers polymerise according to different mechanisms. In most cases, homopolymers are obtained and/or a polymerisation inhibition is observed. Among all the possible applications, the synthesis of tailor-made elastomers for the tyre industry is one of the most prominent. In this field, a leading material is the Ethylene Butadiene Rubber.[196, 197, 198]

Polystyrene, on the other hand, has a general formula (-$CH_2$-CH(Ph)-$)_n$ and is one of the largest volume thermoplastics. It is a versatile polymer whose principal characteristics include transparency, ease of colouring and processing, and low cost. Polystyrene is a linear polymer that, in principle, can be produced in isotactic, syndiotactic, and atactic forms. The commercial product or general-purpose polystyrene is atactic and amorphous (softening temperature around 100 °C, glass transition temperature *ca.* 70±100 °C). Isotactic polystyrene is a partially crystalline polymer (it contains *ca.* 30% crystalline domains). the melting point of the crystalline zones of isotactic polystyrene ranges from *ca.* 230 to 240 °C (glass transition temperature *ca.* 87± 97 °C). The chain conformation of crystalline isotactic polystyrene is a helical conformation with three monomeric units per helix turn. Isotactic polystyrene is still considered as a potentially valuable material because of its high heat resistance and good dielectric properties. However, its low crystallinity its low rate of crystallisation and its high brittleness represent the principal obstacles to its commercial applications as a general-purpose plastic. In contrast to isotactic polystyrene, syndiotactic polystyrene crystallises very rapidly (it contains *ca.* 72% crystalline domains). The chain conformation of crystalline syndiotactic polystyrene is a planar zigzag conformation. Its melting point, however, ranges from *ca.* 270 to 275 °C (glass transition temperature *ca.* 93±96 °C) making the processing of this material problematic. To date, no industrial applications of syndiotactic polystyrene are known. The applications for all grades of polystyrene include packaging, housewares, toys and recreational products, electronics, appliances, furniture, and building and construction insulation. Many of the problems associated with cristalline polystyrene (GP-PS) can be alleviated, or at least minimised, through copolymerisation, blending, or proper formulation.[193, 192]

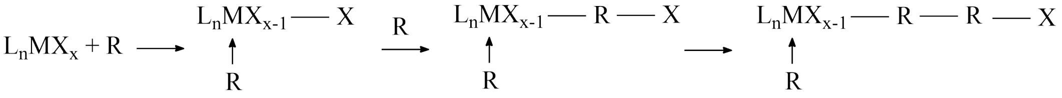

Figure 8: Schematic representation of a coordination-insertion polymerisation mechanism.

Polypropylene, finally, is the third-largest volume polyolefin and one of the major plastics worldwide. Polypropylene can be considered as having a linear polyethylene backbone, but with the H atom on every other carbon atom replaced by a methyl [–$CH_3$] group. Polypropylene can exist in either atactic (noncrystallisable) form or in the crystallisable syndiotactic or isotactic forms. Usually 90% or more of the polymer is in the isotactic form, which displays commercially interesing properties. For the isotactic form, because of the size of the pendant [-$CH_3$] group (relative to the H atom, in polyethylene), the backbone can no longer exist in the planar zigzag form and it must rotate. The lowest energy state is attained by a regular rotation of 120° by each chemical repeating units. This means that there are three chemical repeating units per turn. Isotactic polypropylene is highly crystalline with a melting point of 165 to 171°C, with a density in the range of 0.90 to 0.91 g/cc.[192, 199, 193]

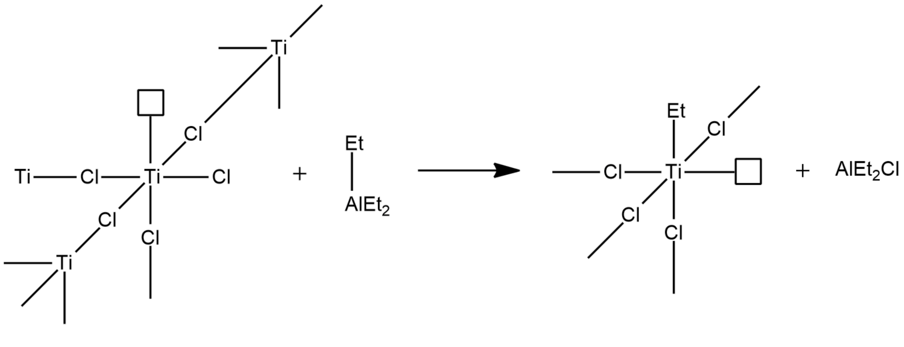

Figure 9: The activation of the Ziegler-Natta $TiCl_4/Et_3Al$ catalytic system.

In the coordination-insertion polymerisation mechanism each incoming monomer inserts into the growing polymer chain according to a particular steric configuration. The global

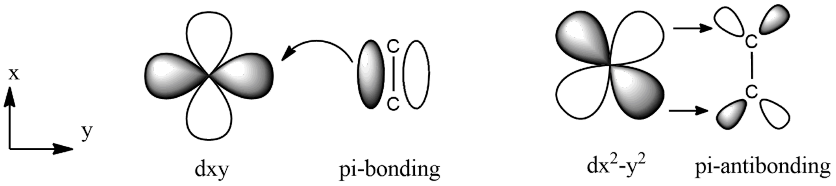

Figure 10: Molecular orbital representation of the monomer coordinating to the metal centre.

coordination-insertion polymerisation mechanism can be described as follows (scheme 8). In the first step a monomer coordinates to the metal centre thanks to the presence of vacant d-orbitals. The preferential orientation of the coordinated monomer is governed by the steric repulsion with the ligands around the metal and by the electronic interactions with the metal atom. In the following step, the coordinated molecule inserts into the metal-X bond (in our case X = carbon), the orientation of the inserted monomer into the metal-carbon bond determining the configuration of the asymmetric carbon atom in the newly-formed unit. The initiation step is therefore completed and the resulting active species may then continue the polymerisation reaction each successive molecule of monomer adopting the preferred orientation during the coordination-insertion process.[192, 193]

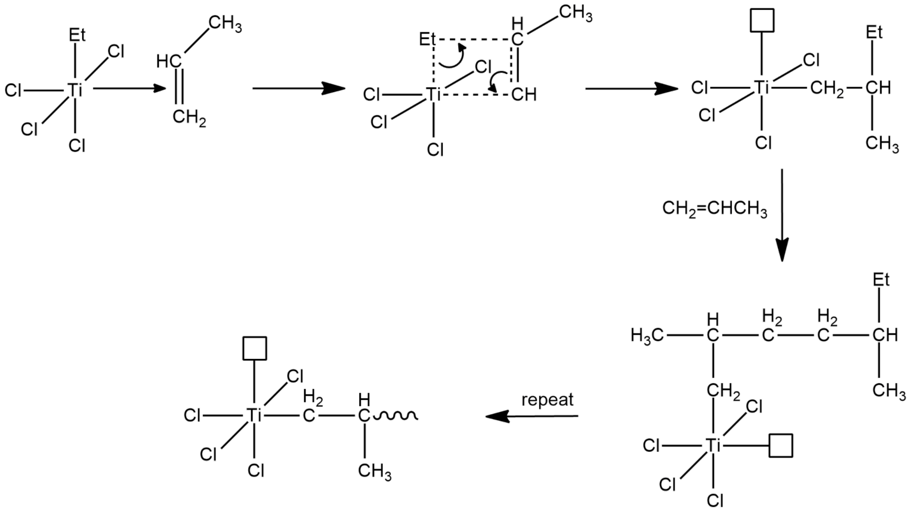

Figure 11: The propagation step in the propene polymerisation catalysed by the $TiCl_4/Et_3Al$ system.

The polymerisation by a coordination-insertion mechanism begins to develop rapidly in the 1950s with the Ziegler-Natta and phillips catalysts.[200, 201, 202, 203] While harsh conditions were required for the synthesis of branched low density polyethylene (LDPE) *via* free radical polymerisation, heterogeneous organometallic catalysts enabled the synthesis of high density PE (HDPE), linear low density PE (LLDPE), and high molecular weight, highly stereospecific polypropylene (PP) at low temperature and pressure. The classical examples of the Ziegler-Natta catalytics systems include the $TiCl_4/Et_3Al$ system (second generation of Ziegler-Natta catalysts).

The titanium chloride compound has a crystal structure in which each Ti atom is coordinated to 6 chlorine atoms. On the crystal surface, a Ti atom is surrounded by 5 chlorine atoms with one empty orbital to be filled. Cossee and coworkers[204] proposed that the catalytic species would form by metathesis reaction of one of the terminal Cl with an alkyl group of the $Et_3Al$ cocatalyst. During this process, the titanium becomes bonded to an ethyl group, transferring one chlorine atom to the Al centre. The catalytic system, therefore, still has an empty *d* orbital which can interact with the olefin monomer, starting the polymerisation process by a coordination-insertion mechanism (Figure 9).

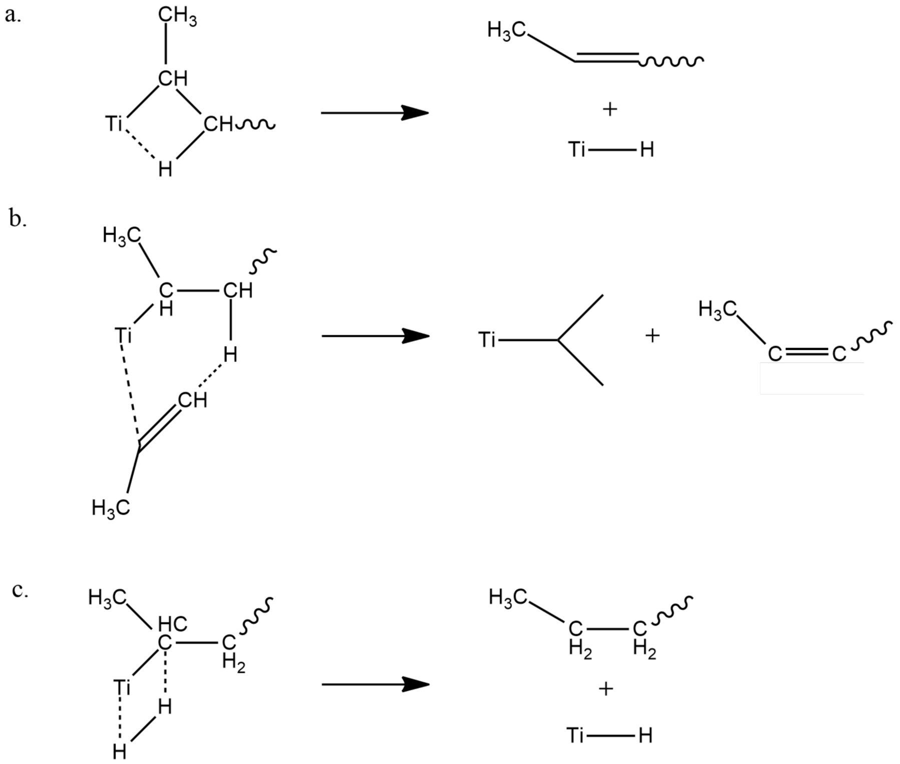

Figure 12: Three termination steps: (a) $\beta$-H-elimination from the polymer chain, with hydrogen transfer to the Ti metal (b) $\beta$-H-elimination from the polymer chain with hydrogen transfer to an incoming monomer; (c) hydrogenation.

The polymerisation reaction is initiated by forming an alkene-metal complex. As shown in Figure 10, there is an empty $d_{xy}$ orbital and a filled $dx^2$-$y^2$ orbital in the Ti outermost shell (the other four orbitals are not shown here). The carbon-carbon double bond of the alkene can be described by a filled $\pi$-bonding orbital and an empty $\pi$-antibonding orbital. While alkene $\pi$-bonding orbital may interact with the Ti $d_{xy}$ orbital,

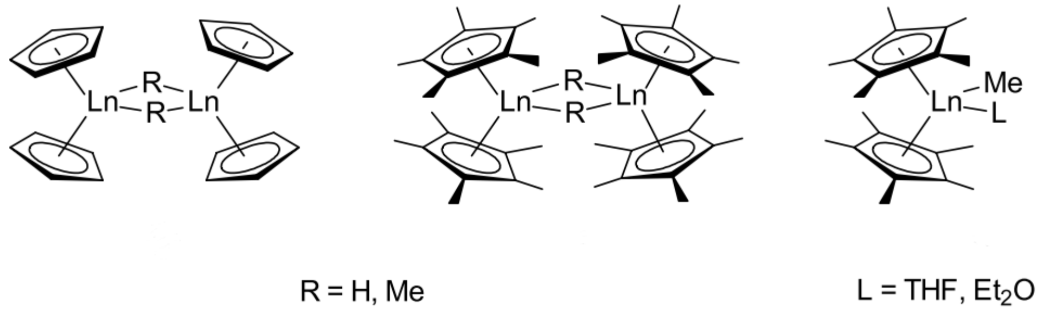

Figure 13: Trivalent lanthanidocene complexes.[199]

After coordination to the active Ti species, the olefin inserts into the metal-alkyl bond *via* a four-centre transition state (Figure 11). When new propene molecules come in, the process keeps going on again and again, giving linear polypropylene. The termination is the final step of a chain-growth polymerisation reaction. Figure 12 illustrates the more common termination approaches. By $\beta$-H elimination, the H in the $\beta$ carbon of the polymer chain can be transferred either to the Ti centre forming the corresponding Ti hydride compound (Figure 12a), or to an incoming monomer, forming the corresponding Ti isopropyl compound (Figure 12b) The addition of hydrogen, finally, may also break the Ti-C bond, provinding the corresponding Ti hydride compound together with polypropylene (Figure 12c).

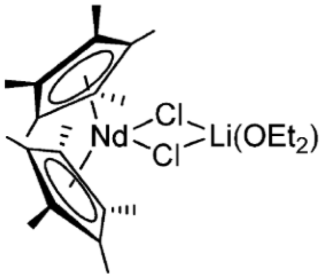

Figure 14: Ansa-chlorolanthanidocenes of Nd.[199]

Another significant breakthrough in the field of polyolefins was the appearance of the homogeneous group 4 metallocene catalysts, followed more recently by the "post-metallocene" catalysts. These molecular catalysts enabled the establishment of a direct correlation between the structure of the catalyst and the polymer microstructure, allowing the synthesis of different kinds of stereoregular polyolefins, some of them with high activities.[192, 195] Although they have been much less studied than their group 4 homologues, the metallocene and post-metallocene complexes of group 3 metals, and lanthanides, have received much attention in the last four decades as ethylene/$\alpha$-olefin polymerisation catalysts.[192, 205, 145, 154] Rare-earth metal complexes, and in particular rare-earth alkyl or hydride derivatives, were reported to show high catalytic activity for the homo and co-polymerisation of a broad range of $\alpha$-olefins, conjugated dienes as well as polar monomers[145, 182, 205, 206, 207, 208]. Early work on rare-earth metal complexes was dominated by the study of differently substituted cyclopentadienyl rare-earth complexes.[207, 192, 209, 208] These ligands, interestingly, allow the stabilisation mononuclear and dinuclear rare earth complexes, with two Cp donors per metal centre. Neutral bis(cyclopentadienyl) alkyl/hydrido lanthanide complexes of the type$[(\eta^5\text{-}C_5R_5)_2MR']_n$ ($R_5$: $H_5$ (Cp), $Me_5$ (Cp$*$); R': H, Me; n = 1, 2) (figure 13) revealed a high intrinsic reactivity towards ethylene without preliminary activation.[199] These complexes were therefore considered a significant economic advantage over the conventional group 4 metallocene catalysts, since their use would have a avoided the use of co-catalysts suach as MAO or trialkylaluminium. Following this economic aspect Ballard and coworkers developed bis(cyclopentadienyl) alkyl complexes of scandium, yttrium and lanthanides with different Cp-type ligands for the ethylene polymerisation.[210] The activity observed was moderate (10-100 kg (PE).mol(Ln)$^{-1}$.bar$^{-1}$.h$^{-1}$) independently of the metal employed. Interestingly, the substituents on the Cp ring had a marked influence on the catalytic activity of the corresponding metal complex as well as on the molecular weight of the final polymers. It was shwon in particular that the higher the steric hindrance around the metal, the higher the catalytic activity and the lower the molecular weight of the polymers. Few years later, Watson *et al.* showed that $[(Cp^*)_2LuMe]_2$ compound, coordinated with one ether molecule,is an active species for the synthesis of HDPE.[211, 154]

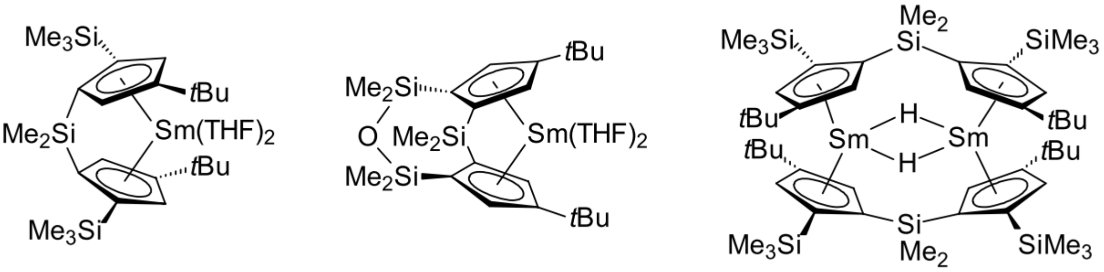

Figure 15: Example of divalent and trivalent lanthanidocenes complexes active in $\alpha$-olefin polymerisation.[199]

As shown by the same group, propene also reacts with the $[(Cp^*)_2LuMe]_2$ compound to produce oligomers, indicating that the transfer and termination reactions are faster than the propagation one. Further studies were carried out with the $[(Cp^*)_2YH]_2$ compound by Casey *et al.*[212, 213] This cyclopentadienyl Y complex, interestingly, efficiently polymerises the ethylene and 1-hexene monomers, resulting, however, inactive for the propene polymerisation. As proposed by the authors, indeed, for ethylene, the insertion into the metal—alkyl bond is very rapid because of the high reactivity of the monomer and the resulting unbranched alkyl chain. The only possible transfer reaction, in addition, is the $\beta$-H elimination reaction, which is very slow compared to the propagation steps. For the propene, on the other hand, the chain growth is slower due to lower monomer reactivity and to the branched nature of the growing alkyl chains that propagate approximately 200 times slower than straight alkyl chains. In addition, the chain termination by abstraction of the allylic sp$^3$ hydrogen from propene to give the corresponding $\eta^3$-allyl yttrium complex is much faster than the $\beta$-H elimination and occurs at the same rate as the propene insertion. The reactivity of the $[(Cp^*)_2YH]_2$ complex towards C-H bonds decreases in the order allylic $CH_3$ >> vinylic C-H >> allylic $CH_2$. Bercaw and coworkers reported a similar reactivity towards propene was observed with scandium analogue complexes by Bercaw and Thompson.[214] The above complexes, especially hydride complexes $[(Cp)_2LnH]_2$, are very sensitive, and their multistep synthesis as their handling remains arduous. An other approach to this difficulty is the in situ formation of alkyl-lanthanide species from readily available precursors, e.g. a chlorolanthanidocene such as $[(Cp^*)_2NdCl_2Li(OEt)_2]$ (figure 14).[199] The reaction of this neodymium complex with a dialkylmagnesium reagent generates an active, stable ethylene polymerisation catalytic system which display, however, lower catalytic activities than those reported for the hydrido complexes above described (8000 $kg(PE).mol(Ln)^{-1}.bar^{-1}.h^{-1}$ at 50°C in cyclohexane). Nevertheless, the much more stable active species in the case of the *in-situ* neodymium system enables a higher productivity. In order to enhance the reactivity of the lanthanidocene species, new sterically demanding ligands were designed. These are based on bridged-Cp ligands possessing narrower Cp–Ln–Cp bite angles (115–117°) in comparison with their non-bridged analogues (135–140°) (see figure 15). The brigdes between the two Cp ligands, indeed, increases the space around the metal on the side where the monomer approaches, favouring the monomer-metal interaction. Effective $\alpha$-olefin polymerisation was observed with the more sterically crowded ligand $Me_2Si(2\text{-}SiMe_3\text{-}4\text{-}tBuC_5H_2)_2$.[215, 216] An yttrium hydrido complex coordinated to this ligand in particular, was shown to catalyse the polymerisation reaction of $\alpha$-olefin, providing highly isotactic polymers (mmmm > 97%).

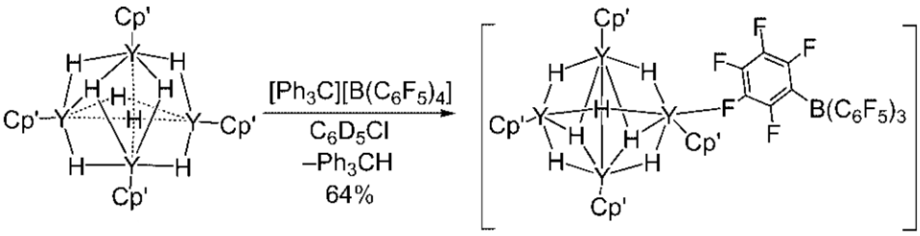

Figure 16: Synthesis of a cationic yttrium polyhydride complex. Cp' = $C_5Me_4SiMe_3$.

Yasuda and co-workers carried out a significant work in this area. By using mono- and bis(silylated)-bridged ligands, they studied the catalytic activity of the corresponding samarium and yttrium alkyls and hydrides compounds in the ethylene and $\alpha$-olefin polymerisation (see figure 17).[207, 217, 208, 218] They showed that the catalytic activity depends on the nature of the metal, the bulkiness of the ligand and the number of THF molecules coordinated to the metal an excess of coordinated THF molecules leading to polymerisation inhibition. Lanthanide calix[n]arene (n = 4, 6, 8; Ln: La, Nd, Sm, Dy, Y) complexes and in the presence of the $Al(iBu)_3$ reagent were found to be effective homogeneous catalysts for ethylene polymerisation.[219] A maximum of activity was noticed at 80 and 120 °C for, respectively, $C_4Nd$ and $C_6Nd$. Cationic rare earth metal alkyls have recently emerged as a new class of catalysts for the polymerisation and copolymerisation of various olefins including cyclic olefins,[220, 189] The active monocationic species $[Ln(L)nR_2]^+$ or $[Ln(L_nX)R]^+$ are usually generated *in situ* by the reaction of

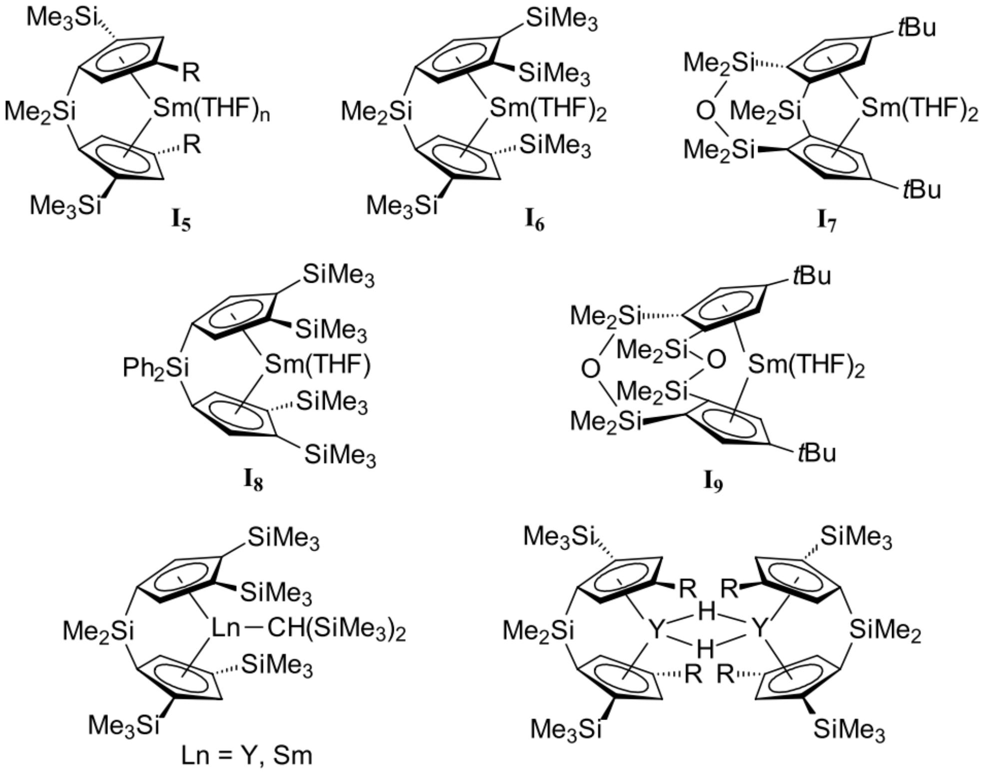

Figure 17: Ansa-lanthanidocene complexes developed by Yasuda and co-workers.[207, 217, 228, 208, 229]

the parent neutral complexes with Lewis acid or Brönsted acid activators. More precisely, the rare earth cationic complexes are generated be mixing the rare earth metal dialkyl precursors with 1 equiv. of cocatalyst such as the borate ($[Ph_3C][B(C_6F_5)_4]$, $[H(OEt_2)_2][B(C_6F_5)_4]$, and $[PhNMe_2H][B(C_6F_5)_4]$) or borane ($B(C_6F_5)_3$) reagents (see figure 16). These complexes exhibited both high activity and high regio-/stereoselectivity in the (co)polymerisation of styrene and conjugated dienes.[221, 222, 220, 223, 224, 225] In 2013, Hou and coworkers reported that the cationic species $[Flu'Sc(CH_2SiMe_3)(THF)][B(C_6F_5)_4]$(figure 18) generated by the reaction of the half-sandwich fluorenyl rare earth dialkyl precursors and 1 equiv. of activator such as $[Ph_3C][B(C_6F_5)_4]$ showed relatively low activities but high syndioselectivities for the styrene polymerisation (syndiotactic selectivity: rrrr>99%).[226, 227]

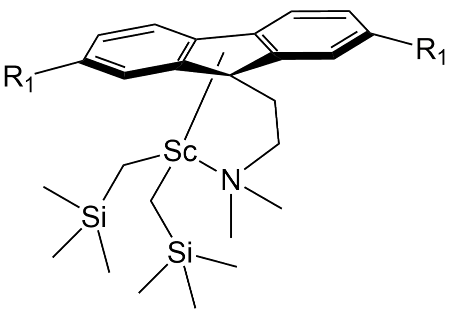

$R_1$ = H
$R_1$ = t-Bu

Figure 18: The [Flu'Sc($CH_2SiMe_3$)(THF)][B($C_6F_5$)$_4$] complex.[165]

The copolymerisation of styrene and ethylene using half-sandwich fluorenyl scandium complexes was then reported, affording styrene-ethylene random copolymers containing syndiotactic styrene-styrene sequences.[226] The activity is up to 9.6 x $10^6$g of copolymer/mol$_{Sc}$.h.atm, and the content of styrene is around 17% to 90%. Copolymerisation of diene with ethylene has been proved to be rather difficult. Boisson *et al.* have shown that the *ansa* bis(fluorenyl) complex such as [($Me_2Si(C_{13}H_8)_2$)-NdCl] in combination with alkylating agents, *e.g.* [HAl($^i$Bu)$_2$($^n$Bu)]$^-$Li$^+$ or Mg(alkyl)$_2$, enables the copolymerisation of ethylene with butadiene at 80 °C and 4 bar to give polymers with low to high molecular weight ($M_n$ = 8000–148,000) and controlled polydispersity ($M_w/M_n$ = 1.2-3.1).[197] The copolymers featured unusual microstructures with high content (53–57%) of 1,2-cyclohexane rings. The activation of the cationic bis(pentamethylcyclopentadienyl) lanthanide complexes [Ln($\eta^5$-$C_5Me_5$)$_2$($\mu$-$C_6F_5$)$_2$B($C_6F_5$)$_2$]$_2$ (Ln = Pr, Nd, Gd, Ce, Sm) with AliBu$_3$ afforded highly cis-1,4-selective initiators for the 1,3-butadiene polymerisation, further supporting the involvement of a cationic active species (figure 19).[230, 231, 232, 233]

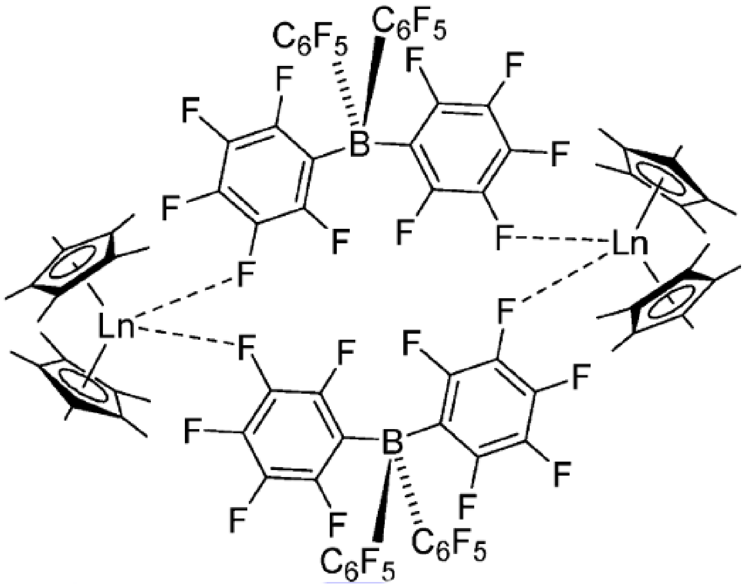

Figure 19: The [Ln($\eta^5$-$C_5Me_5$)$_2$($\mu$-$C_6F_5$)$_2$B($C_6F_5$)$_2$]$_2$ complex (Ln = Pr, Nd, Gd, Ce, Sm).[189]

Alternatively, the [Sm($\eta^5$-$C_5Me_5$)$_2$Me(THF)$_2$], [Ln($\eta^5$-$C_5Me_5$)$_2$($\mu$-Me)$_2$AlMe$_2$]$_2$ (Ln = Gd, Sm, Pr), or [Sm($\eta^5$-$C_5Me_5$)$_2$(THF)$_2$] were used as catalyst precursors to yield cis-1,4-polybutadiene upon activation with either the MMAO or the $[Ph_3C]^+[B(C_6F_5)_4]^-$/AliBu$_3$ cocatalyst.[230, 234, 235] Furthermore, the [Gd($\eta^5$-$C_5Me_4{}^i$Pr)$_2$($\mu$-Me)$_2$AlMe$_2$]$_2$ compound catalysed the cis-1,4-specific polymerisation of isoprene and allowed for butadiene-isoprene copolymerisation.[236] The active species in these systems is probably an alkyl-bridged Ln(III)-Al(III) heterobimetallic cation.[223] Finally, The in situ generated complexes [(Ln($\eta^5$:$\eta^1$,$\mu$-$C_5Me_4SiMe_2PCy$)$_2$($\mu$-$CH_2SiMe_3$)]$^+$[B($C_6F_5$)$_3$R]$^-$ (Cy = cyclohexyl, R = $C_6F_5$, Ln = Y, Lu ; R = $CH_2SiMe_3$, Ln = Y) showed unprecedented isospecific 3,4-polymerisation of isoprene with extremely high stereo- and regio-selectivity (3,4-selectivity 100%; mmmm $>$ 99%).[237] This new, crystalline polymer has a melting temperature of 162 °C. A cationic dinuclear complex with a bridging alkyl group was proposed to be the active species.

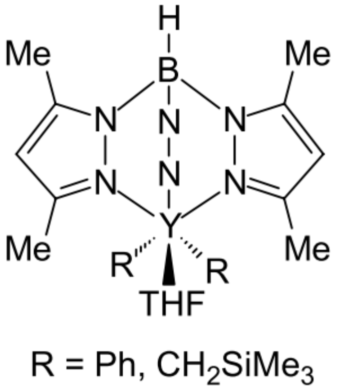

Figure 20: Tris(pyrazolyl)borates as ancillary ligands for ethylene polymerisation.[238]

Because of the permanent search for new-generation polymerisation catalysts, there is considerable interest in developing new rare-earth metal complexes involving solubilising and stabilising ancillary ligands other than the commonly used cyclopentadienyl-type ligands. This new generation of Cp-free catalysts will be referred as post-lanthanidocenes. These complexes will be divided in two categories, based on the nature of the ancillary ligands which can either nitrogen-based or oxygen-based ligands. The use of Trofimenko's tris(pyrazolyl)-based ligands for lanthanide-mediated ethylene polymerisation was reported by Bianconi and Long.[238] Tris(3,5-dimethyl-1-pyrazolyl) borohydride ($Tp^{Me}$) complexes of yttrium of general formula [$Tp^{Me}YR_2(THF)_x$] (R: $C_6H_5$,$CH_2SiMe_3$) and similar ones with variously substituted Tp ligands, as well as analogue lanthanide complexes, were found to be very poorly active in ethylene polymerisation, yielding linear PE with extremely high molecular weight (see Figure 20). In all cases, even for complexes containing large phenyl and trimethylsilylmethyl groups, the polymerisation occurred despite the presence of coordinated THF molecules in the initial complexes. The highest (though still very poor) activity was observed with the $Tp^{Me}YCl_2(THF)/2t$-BuLi catalytic system.

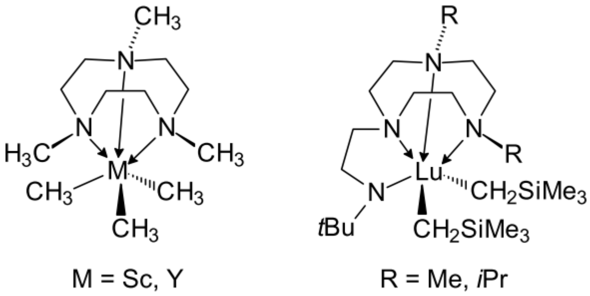

Figure 21: Neutral triazacyclononane based complexes.[199]

The use of tris(3-phenyl-1-pyrazolyl) borohydride ($Tp^{Ph}$) resulted in even smaller quantities of polymers, showing that the steric hindrance at the metal centre affects the extent of polymerisation. Bis(benzamidinato)yttrium alkyl complexes [$(PhC(NSiMe_3)_2)_2YCH_2Ph(THF)$] and [$(PhC(NSiMe_3)_2)Y(\mu\text{-}H)]_2$ were reported to be moderately active in ethylene polymerisation but inactive towards propene and 1-hexene when employed as neutral catalysts.[239] Under rather drastic conditions (55 °C, 70 bar ethylene pressure), the Bis(benzamidinato)yttrium hydride complex exhibited low activity (4 kg (PE).mol $(Y)^{-1}.h^{-1}$), the benzyl derivative displaying an even lower activity . Teuben and co-workers[239] have reported the synthesis of an amido-bis(alkyl) complex [N,N'-$R_2$-1,4,7-triazacyclononane-N"-$(CH_2CH_2)NtBu]Y(CH_2SiMe_3)_2$ (R = iPr or Me) (figure 21), which leads to cationic active species for ethylene polymerisation after reaction with the Brönsted acid activator $[PhNMe_2H][B(C_6F_5)_4]$. The polymerisation was performed under 5 bar of ethylene pressure in toluene solution at various temperatures for 10—15 min. Increasing the reaction temperature enhanced the activity (up to 1800 kg(PE).mol$(Y)^{-1}$.bar$^{-1}$.h$^{-1}$), concomitantly with higher polydispersities. Beside post-lanthanidocene catalysts with nitrogen-based ligands, alkyloxide and aryloxide ligands are also attractive because they offer strong metal oxygen bonds which can stabilise these electropositive metal complexes (see figure 22).

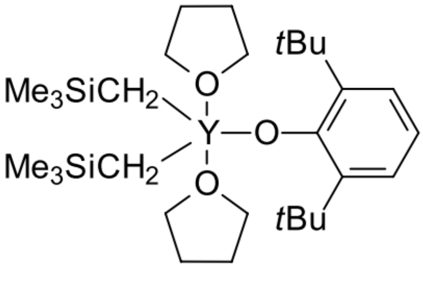

Figure 22: The sole well-defined mixed alkyl-aryloxy complex active in ethylene polymerisation.[199]

To resume, the reactivity of cationic lanthanide complexes in catalytic and stoichiometric reactions has often led to improved activity with respect to their neutral analogues, allowing some cases, to the development of completely new synthetic pathways.

The use of support effects to improve or change the regio- or stereo-chemical result of selective reactions is currently emerging as an area of interest, even though with a limited number of examples available. To name but a few, Bochmann and coworkers in 2005[145] and Gauvin and coworkers in 2006[88] reported the catalytic activity of Ln[N(SiMe$_3$)$_2$]$_3$ (Ln=Sc, Y, La, Nd, Sm, Dg, Dy) complexes grafted onto silica dehydroxylated at 250, 500 or 700 °C (figure 23). These studies showed that, upon mixing the silica-supported catalyst and the alkyl aluminium activator Al($^i$Bu)$_3$ (TIBA), all the different lanthanide compounds are found to be active in the homo-polymerisation of ethylene and 1,3-butadiene.

In particular they showed that all the supported systems display a good catalytic activity for the homopolymerisation of 1,3 butadiene providing high molecular weight polymers with predominately a 1,4-cis stereoselectivity (85-90% by diad analysis). This differs from whereas the lanthanide-based molecular catalysts can also lead to 1,4-trans-polybutadiene.[240, 205, 241] They also showed that the neodymium catalysts are generally more active than the other lanthanide systems, with the exception of the Nd catalyst supported on a silica surface dehydroxylated at 250 °C (in the latter case lanthanum is slightly more efficient than neodymium). They pointed out, finally that while a similar catalytic activity is obtained for the lanthanum compounds grafted onto silica dehydroxylated at 250 or 750 °C, for the neodymium-based systems, on the other hand, the increase of the silica pretreatment temperature significantly increases the global catalytic activity. The silica supported neodymium and dysprosium catalysts were also shown to copolymerise ethylene and 1,3-butadiene, affording multiblock polymers consisting of 1,4-cis, 1,4-trans and ethylene blocks, with molar percentages in the copolymer depending on both the choice of the lanthanide and the feed ratio of the monomers. The aforementioned neodymium catalyst [Nd(N(SiMe$_3$)$_2$)$_3$] was also described by Thomas *et al.* in 2011.[184] They compare the catalytic activity of the complexe grafted onto silica dehydroxylated at 250, 500 or 700 °C with that of its molecular counterpart. This study showed that, in conjunction with an alkyl aluminium activator, all the different neodymium compounds are found to be active in the isoprene polymerisation. They showed that the Nd compound grafted on a silica surface dehydroxylated at 250 °C and 500 °C afforded 95 and 96% of cis-1,4-poly-isoprene, respectively, compared to the 63.5% value obtained for the molecular counterpart. They conclude that the controlled grafting approach represents as a simple and efficient way to enforce selectivity in heterogeneous polymerisation while retaining a fair degree of control just as observed for molecular systems that are accessible through time- and manpower-consuming synthetic procedures.

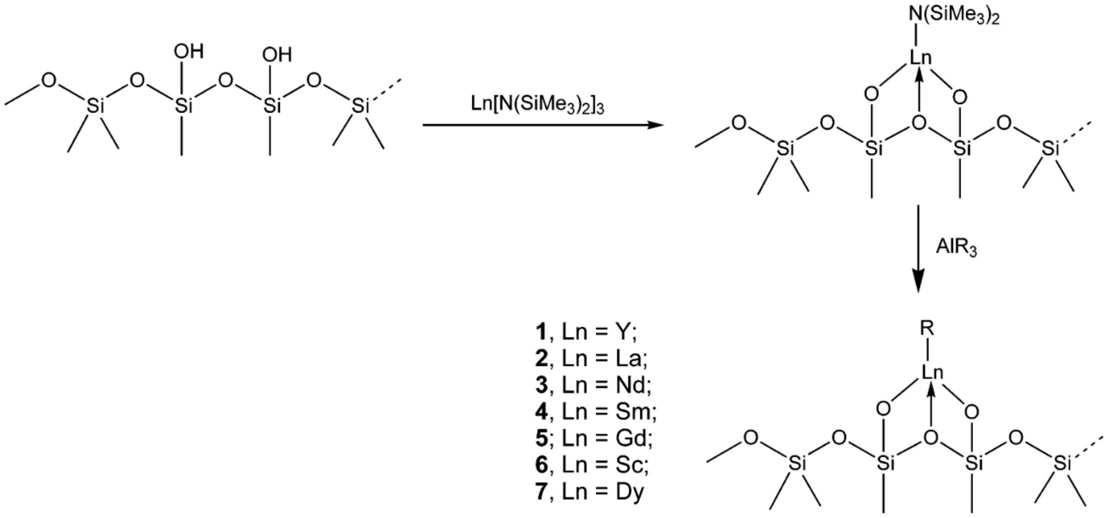

Figure 23: Schematic mechanism of the synthesis of silica-supported alkyl lanthanide complexes.[145]

## 4.3 Ring opening polymerisation

The ring-opening polymerisation (ROP) reaction involves the initial ring-opening of a cyclic monomer followed by different polyaddition steps. This method uses mild reaction conditions, is in general favourable from a thermodynamic point of view and has the advantage of reducing the number of secondary reactions that may occur during the polymerisation. The driving force for the ring-opening of cyclic monomers is the relief of the cycle constraint. The resulting polymers are normally linear. [192, 193]

Depending on the selected catalyst, three main ROP mechanisms can be distinguished, each characterised by different molecular weights, polydispersities, and end groups:[242]

- Cationic ROP: in the cationic ROP, the cyclic monomers are positively charged as a result of the reaction of an initiator molecule to the monomer. CROP can be initiated by Brönsted acids, carbenium ions, onium ions, photoinitiators and covalent initiators. There are essentially two mechanisms that are discussed in the literature for the cationic ROP, both involving the nucleophilic attack of the cyclic monomer on the electrophilic initiator. In one mechanism, the resulting cyclic onium ion undergoes the ring opening when attacked by the nucleophilic atom of another monomer (bimolecular nucleophilic ring-opening). In the second mechanism, alternatively, the activated ring can undergo spontaneous ring-opening resulting in an acyclic cationic species which can then be attacked by a monomer (monomolecular nucleophilic ring-opening).

- Anionic ROP: for the Anionic ROP, a wide variety of nucleophiles can be used as initiators: carbanions, alcoholates, silanoates, carboxylates, thiolates, alkoxides, and tertiary amines. In this case, a nucleophile attacks the less electron-negative atom (X in our case) of a X-Y bond break the bond providing the Y group at the chain end. This newly formed anion attacks another molecule of the monomer, leading to the chain growth of the polymer.

- Coordination-insertion ROP: This is the most common method for chain-growth polymerisation. The metal atom plays the role of the electrophilic catalytic centre that coordinate oxygen of the cyclic ester carbonyl group. This coordination results in the activation of the carbon of the carbonyl group in the cyclic esters or the phosphorus in cyclic phosphates. The initiator group (alkoxy, amino, alkyl *etc*) can be directly bonded or weakly coordinated to the metal centre. Such dual monomer and initiator coordination forms a reaction complex. The first step of the initiation process is the nucleophilic attack with a formation of the tetrahedral carbon (or pentahedral phosphorus) followed by coordination of the exocyclic oxygen to the metal. The second step is the ring-opening process followed by the decoordination of the carbonyl (or phosphate) oxygen atom. This liberates a coordination site for the coordination of a new monomer. At the propagation stage, the alkoxy fragment plays the role of an initiator.

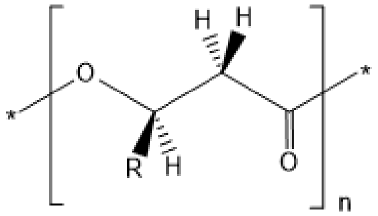

Figure 24: Structure of poly(hydroxyalkanoates)s (PHAs) with R = alkyl and the poly(3-hydroxybutyrate) (PHB) with R = $CH_3$.

Biodegradable and biocompatible polymers are at the forefront of the current polymer material research as they naturally degrade, in the presence of microorganisms, to nontoxic products, preventing the serious environmental pollution caused by undegradable materials such as in particular polyolefins.[243, 244, 245] Of the variety of biodegradable polymers known, linear aliphatic polyesters such as the poly(hydroxyalkanoates)s (PHAs), have a leading position as they may replace petroleum-based undegradable polymers in broad commercial applications, such as i) engineering plastics, including disposable packaging and fiber materials, biomedical implants and drug delivery nanocarriers; ii) fine chemistry, with the production of enantiomerically pure PHA monomers and iii) energy industry, mainly represented by PHA based biofuels.[246, 247] These polyesters are naturally produced by numerous bacteria and algae as an intercellular carbon and energy reserve from renewable bioorganic resources such as starch bearing plants, lignocellulose and fats (Figure 25).[248]

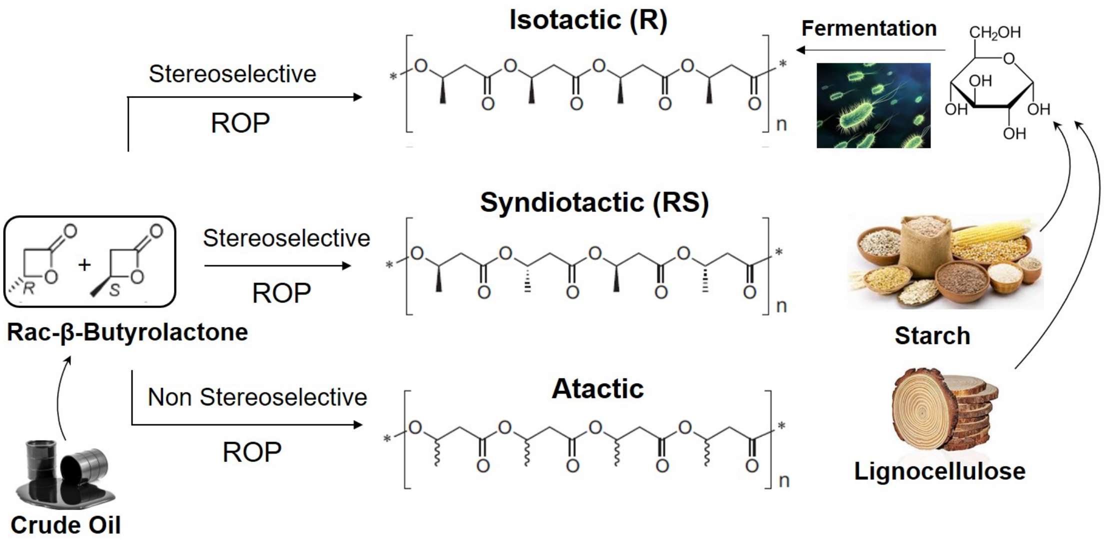

Figure 25: The $\beta$-Butyrolactone stereochemistry and the possible synthetic ways to different PHB microstructures.

In view of its mechanical properties, the poly(3-hydroxybutyrate) (PHB) polymer, consisting of monomeric units of four C atoms, is the most important representative of this PHA class of materials. Natural PHB, obtained by fermentation in numerous microorganisms, is strictly isotactic, featuring exclusively (R)-configuration at the chiral stereocenters of the main chain.[249, 250, 251] Due to its pure isotacticity, natural PHB is a highly crystalline thermoplastic polyester with a high melting temperature (Tm ≈ 175 °C). The isotactic PHB is comparable to the petroleum-based isotactic polypropylene polymer (iPP) regarding a certain number of properties, such as the Young modulus, tensile strength, impact strength, UV resistance and oxygen permeability. The use of pure PHB, however, is very limited and two main drawbacks prevent the replacement of polypropylene by pure PHB: i) its intrinsic brittleness, characterised by a low strain elongation at break[247, 252] and ii) its thermal decomposition at a temperature just above the melting point ($T_{decomposition} \approx 180$ °C), which makes its melting process difficult, limiting its industrial processability.[253, 254] Homopolymer properties strongly depend on intrinsic structural parameters such as molecular weight, polydispersity, tacticity and polymer chain-end.[255, 256] The tacticity of the PHB homopolymer, in particular, strongly influences its mechanical and physical properties: while atactic PHB is an oil, isotactic PHB has a high melting point. Interestingly, it has been shown that decreasing the isotacticity of the PHB polymer to a range between 70 and 80% lowers the melting point to values between 100 and 130 °C.[253, 257] Homopolymers of PHB with different degrees of syndiotacticity were also synthetised, displaying different Young's modulus and elongation to break values depending on the percentage of syndiotacticity.[258] Interestingly it has been further shown that increasing the degree of syndiotacticity, the melting transition increases linearly reaching 183 °C for 94% syndiotacticity.[259, 260] The synthetic production of PHB, therefore, although based on fossil fuel derived monomers, may lead to polymers with variable iso- or syndio-tacticities enabling access to original stereo-controlled PHBs, unlike the fermentative biotechnological synthesis which only afford isotactic PHB. Furthermore, the bacteria-mediated production of PHB on an industrial scale is not so efficient, the time-consuming work-up process preventing cost reduction and hence the extensive use of this kind of biodegradable polyester. Among the possible synthetic ways, the stereoselective ring-opening polymerization (ROP) of racemic $\beta$-butyrolactone (rac-BL), the corresponding four-membered cyclic monomer, proved to be the most efficient manner for preparing PHBs polyesters with controlled structure. A variety of metal-based complexes catalytically initiate the rac-BL ROP and many studies have focused on the development of structurally well-defined homogeneous metal catalysts able to provide a stereochemical control of the polymerisation process, while keeping high molecular weight and narrow molecular weight distributions.

Well-designed homogeneous rare-earth systems, in particular, are among the most reactive species in the ROP of rac-BL: they have shown high catalytic activities under mild conditions as well as a significant degree of control over the polymerisation reaction, allowing the preparation of atactic, isotactic and syndiotactic PHBs.[261, 262, 259, 260, 263, 264, 162, 265, 266, 267, 268] The first rare-earth active complex was the homoleptic yttrium 2-methoxyethoxyde compound, described as "$Y(OCH_2CH_2OCH_3)_3$" by Spassky and co-workers in 1994. Although no stereocontrol was observed during the reaction, the species proved to be highly active with the ROP proceeding readily at room temperature.[262] Later on, Carpentier and co-workers reported new amino-alkoxy-bis(phenolate)yttrium catalysts which displayed high catalytic activity, allowing a living and highly syndiospecific ROP of rac-BL (Pr up to 0.94). A most interesting feature of these catalysts is the possibility to finely tune the stereoselectivity *via* the nature of the substituents of the phenolate ligand. Yttrium, scandium and lanthanum compounds containing the 2,6-bis(naphtholate)pyridine and 2,5-bis(naphtholate)thiophene ligands were also described (figure 26).[263]

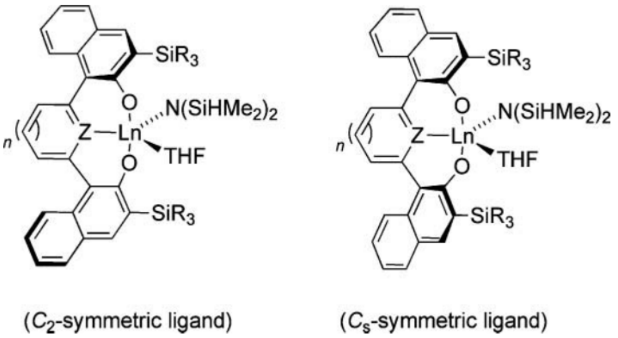

Figure 26: Lanthanide phenolates complexes. Ln = Sc, Y, La. [263]

Interestingly, while the thiophene derivatives afforded low stereoselectivities (Pr = 0.55-0.67), the pyridine derivatives displayed a higher stereocontrol providing syndiotactic-enriched polymers with Pr = 0.76-0.87 for Y and Pr = 0.86 for La. Rare-earth bis(guanidinate) alkoxide complexes were also shown to catalytically initiate the controlled-living ROP of rac-BL with syndiotacticities depending on the metal center. Atactic PHB was obtained with Nd derivatives whereas syndiotactic enriched PHB (Pr = 0.80-0.84) with Y and Lu compounds.[260] By starting from the commercially available $Y(O^iPr)_3$ complex and a tetradentate phenoxyamine (salan-type) ligand, Thomas and coworkers synthetised a mixture of bimetallic complexes which directly initiate the rac-BL ROP without purification, providing highly syndiotactic PHB. It has been proposed that the active species is a mononuclear (salan)$Y(O^iPr)$(BBL) complex formed by cleavage of the dimeric structure by the excess BBL monomer present in solution (figure 27).[264]

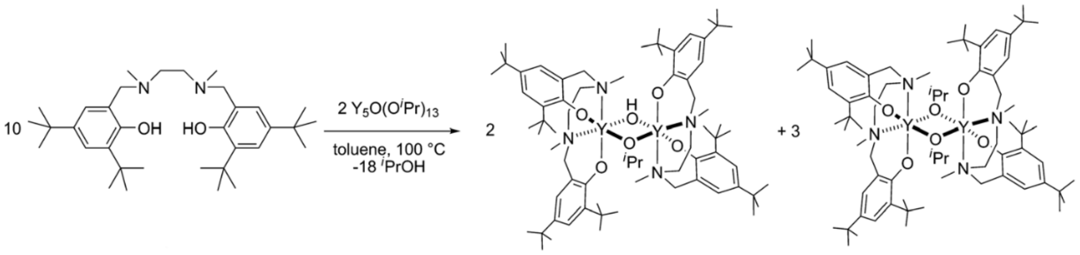

Figure 27: Synthesis of the dimeric $(salan)_2Y_2(O^iPr)(OH)$ structure.[264]

Rare earth borohydrido complexes, such as the $[(DAB)Y(BH_4)_2][Li(DME)_3]$ ($DAB^{2-}$ = $(2,6\text{-}C_6H_3iPr_2)NC(Me){=}C(Me)N(2,6\text{-}C_6H_3iPr_2{}^{2-})$),[269] and the $[Ln(BH_4)_3(THF)_3]$ (Ln = La, Nd,Sm) compounds,[265] have been also shown to initiate the rac-BL ROP efficiently at room temperature (Figure 28).

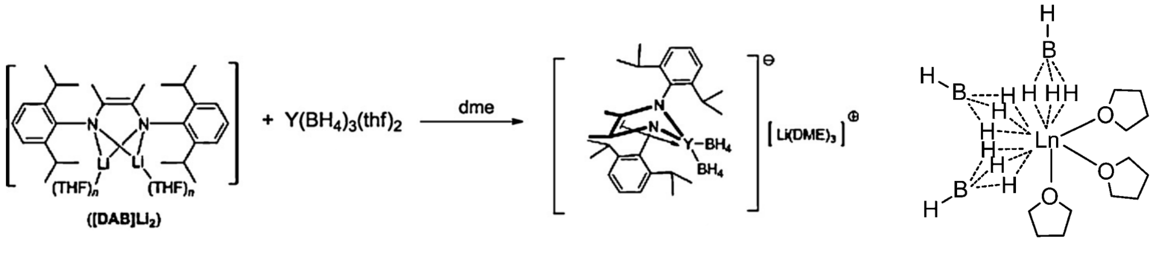

(a) $[(DAB)Y(BH_4)_2][Li(DME)_3]$.

(b) $[Ln(BH_4)_3(THF)_3]$.

Figure 28: Rare earth borohydrido complexes.[269, 265]

They display $BH_4^-$ ligands bonded to the metal by three of their four hydrogen atoms and they led to the formation of well-defined atactic PHB-diols with a conversion of 61% after 14 h for $[(DAB)Y(BH_4)_2][Li(DME)_3]$ and 91% after 24 h for $[La(BH_4)_3(THF)_3]$. Although all these exemples have open the way to the use of rare earth compounds as initiators for the rac-BBL ROP process, allowing significant advances in the comprehension of the involved mechanism, some major points remain to be adressed and improved. Polymerisation reactions under homogeneous conditions, indeed, result in polymer contamination by metal residues and in loss of catalyst. Moreover, the synthesis of organometallic complexes is usually a time-consuming and costly process. In this sense Surface Organometallic Chemistry (SOMC),[29, 60] involving the grafting of an organometallic complex directly on a surface, represents an attractive approach for the design of cleaner processes. In these systems, the surface has the role of a ligand and is involved in the coordination sphere of the metal as a “peculiar” alkoxide. Supported heterogeneous catalysts represent therefore simpler initiating systems able at the same time to i) allow an easier solid-liquid separation for cleaner processes and ii) provide well-defined active sites for the stereospecifical ring-opening polymerisation of racemic BBL. The fine tuning of the electronic and steric properties of both the surface support and the metal-coordinated ligands may also pave the way to homogeneous-like coordination sphere modifications allowing the improvement of the catalyst’s performances. The use of support effects to improve or change the regio- or stereo-chemical result of selective reactions is an emerging area of interest,[270] albeit a limited number of exemples is available for the ROP of rac-BL. With lanthanide metals, the only support used so far for the synthesis of heterogeneous compounds capable of polymerising the rac-BBL is silica. Gauvin and co-workers, indeed, demonstrated that silica ($SiO_{2-700}$) supported materials, bearing either neodymium silylamide or neodymium bis(borohydride) initiating groups, can generate stereoselective species for the ROP of rac-BL.[162, 184] In order to achieve the highest possible degree of polymerisation control, the choice of non-porous silica dehydroxylated at 700 °C ($SiO_{2-700}$) as the suitable inorganic support has proved to be critical. This specific silica surface, indeed, bears only isolated silanols which allow the formation of a single type of initiating surface species. The reaction of a $SiO_{2-700}$ surface-OH group with the $[Nd(N(SiMe_3)_2)_3]$ compound afforded, by release of $HN(SiMe_3)_2$, a mixture of the mono- and bis-grafted species $[(\equiv SiO)\text{-}Nd(N(SiMe_3)_2)_2]$ and $(\equiv SiO)_2\text{-}[Nd(N(SiMe_3)_2)]$.

These supported complexes were more active than the molecular $[Nd(N(SiMe_3)_2)_3]$ derivative in the ROP of racemic BBL and, interestingly, unlike the molecular complex which only produced atactic PHB, they were able to convert atactic rac BBL to isotactic-enriched PHB.[184] By using a similar strategy, the grafting of $[Ln(BH_4)(THF)_3]$ (Ln = La, Nd) on a $SiO_{2-700}$ surface-OH group led to the corresponding bis(borohydride) $(\equiv SiO)\text{-}[Ln(BH_4)_2(THF)_{2.2}]$ heterogeneous complexes with the release of $H_2$ and $BH_3$. Interestingly, while in the case of La, the silica supported system gave a much poorer activity than the corresponding molecular derivative, in the case of Nd, both the supported and homogeneous compounds displayed good catalytic performances. The silica grafted Nd complex, moreover, unlike the parent $[Nd(BH_4)(THF)_3]$ molecular complex which gave rise to exclusively atactic polymers, was able to convert rac-BL to isotactic-enriched PHB ($Pm = 0.85$).[162] As suggested by the authors, the better stereoselectivity of the silica-supported Nd complex is probably a consequence of the smaller ionic radius of the neodymium center: since lanthanum is larger than neodymium, the environment around the neodymium metal is more hindered, resulting in better selectivity (figure 29).[271]

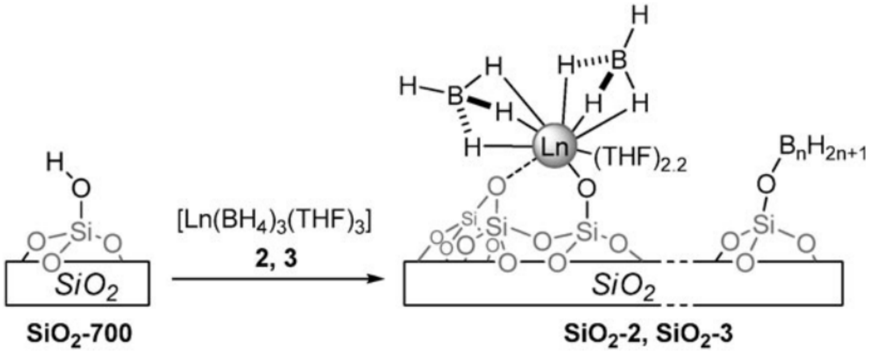

Figure 29: Synthesis of silica grafted lanthanide borohydride complexes.[162]

## 5 Summary

On the basis of what has been reported above, we have noticed that the support used in SOMC play a twofold role: i) anchor the catalyst on the surface to form well-defined active sites, in our case this correspond to the immobilisation *via* a covalent attachment occur through a direct surface-metal bond, for that purpose it requires to be thermally and mechanically stable and not generate parallel reactions, ii) act as a ligand, *i.e.* it have the function of modulating the catalytic activity of the metal which it is bound to. As we have discussed, silica is a surface that allows well-defined active sites, according to the preparation method, but has limited influence on Lewis acidity of the metallic complexes, which strongly impacts the catalytic activity of a number of reactions. In contrast, the use of alumina as a support increases the Lewis acidity of the complexes, but due to its complexity it is difficult to form well-defined and uniform active sites on the surface, and often leads to a large diversity in the metal complexes formed and thus in the produced reactions.

For this reason, in this thesis project we decided, after a description of the DFT method used in this thesis in part II, to explore potential new supports that could both i) produce well-defined active sites and ii) fine-tune the catalytic properties of the metal complex formed. Two surfaces were identified as being able to combine all these properties, each of them will be developed in a chapter dedicated to them and their reactivity: Part III: Grapene supported lanthanum systems; Part IV: Boro-nitride supported lanthanum complexes. Finally in Part V, we will explore the catalytic activity of the grafted complexes on the aformentioned support on the propene polymerisation, which represent a reaction of major concern in polymer industry.

## Part II

# Computational methods

In the present report, we have chosen the molecular approach, in order to carry out reactivity studies on these systems. Indeed, studies of the reactional mechanisms by molecular quantum chemistry provide more accurate results which allow us to elucidate these reaction mechanisms by identifying the different transition states. In the case of periodic systems, the identification of transition state is quite more complex due to the nature of the algorithms employed. All the DFT calculations were performed with Gaussian 09.[272] Calculations were carried out at the DFT level of theory using the hybrid functional B3PW91.[273, 274, 275, 276, 277, 278] Geometry optimisations were achieved without any symmetry restriction. Vibrational frequencies were systematically computed in order to characterise the nature of the stationary points. The Stuttgart effective core potential[279, 280] and their associated basis sets were used for silicon, titanium and lanthanum. For the P, Si, Ti and La atom, the basis sets were augmented by a set of polarisation function ($\zeta_d$ = 0.340 for P, $\zeta_d$ = 0.284 for Si $\zeta_d$ = 0.284 for Ti and $\zeta_f$ = 0.591 for La). [281] The H, N, C and O atoms were treated with a 6-31G(d,p) double basis sets.[282, 283] Among the various theories available to compute the chemical shielding tensors, the gauge including the atomic orbital (GIAO) method has been adopted for the numerous advantages it presents.[284, 285, 286] The same methodology was used in previous studies involving grafted systems, showing that theoretical results are fairly accurate with respect to the experimental values with an error lower than 15% for $^{29}$Si,[136] 10% for $^{31}$P[287] and $^{17}$O[117, 288, 289] and 5% for $^{1}$H[290] and $^{13}$C.[290] The electron density and partial charge distribution were examined in terms of localised electron-pair bonding units using the NBO program.[291, 292] Through this method, the input atomic orbital basis set is transformed *via* natural atomic orbitals (NAOs) and natural hybrid orbitals (NHOs) into natural bond orbitals (NBOs), which correspond to the localised one centre ("lone pair") and two-centre ("bond") elements of the Lewis structure. All the possible interactions between "filled" (donor) Lewis-type NBOs and "empty" (acceptor) non-Lewis NBOs orbitals, together with their energetic quantification (stabilisation energy), have been obtained by a second-order perturbation theory analysis of the Fock matrix.

## 1 Density Functionnal Theory

The density functional theory has its origins in the Thomas-Fermi model, developed by Llewellyn Thomas [293] and Enrico Fermi [294] in 1927. This model postulates that any electronic property of a system can be deduced from its electron density. It was in 1964 that Pierre Hohenberg and Walter Kohn [295] took up and reformulated this theory to demonstrate that there is a correspondence between the energy of a system E and its electronic density $\rho(\overrightarrow{r})$. This is called the Hohenberg - Khon theorems because this theory is based on two essential theorems.

### 1.1 Hohenberg - Kohn theorems

**First theorem :** This theorem shows that the electron density $\rho(\overrightarrow{r})$ is the only function necessary to obtain all the electronic properties of a system: for any many particle system interacting with an external potential $V_{ext}$, the external potential is only determined, up to a constant, by the density $\rho_0$ of the particle in its ground state (if it is not degenerate).

The electron density fixes the number of electrons N in the system *via* the normalisation condition:

$$N = \int \rho(\overrightarrow{r})\, d\overrightarrow{r}$$

The ground state is therefore a functional unique of the electron density whose energy is:

$$E_0\left[\rho_0\right] = T\left[\rho_0\right] + E_{ee}\left[\rho_0\right] + E_{eN}\left[\rho_0\right]$$

where $T\left[\rho_0\right]$, $E_{ee}\left[\rho_0\right]$ and $E_{eN}\left[\rho_0\right]$ respectively representing the kinetic energy, electronic repulsion and electron nucleus interaction. It is then possible to separate these terms into two parts, a first part composed by the terms whose functionals are unknown, *i.e.*, $T\left[\rho_0\right]$ and $E_{ee}\left[\rho_0\right]$. The expressions of these terms do not depend on N ( electron number), R (electron nucleus distance) and Z (atomic number). Then in a second part, the electron nucleus interaction term whose expression is known:

$$E_0\left[\rho_0\right] = F_{HK}\left[\rho_0\right] + E_{eN}\left[\rho_0\right]$$

$$E_0\left[\rho_0\right] = F_{HK}\left[\rho_0\right] + \int \rho_0(\overrightarrow{r}) V_{ext} d\overrightarrow{r}$$

where $F_{HK}\left[\rho_0\right]$ is a universal functional because the treatment of the kinetic and internal potential energies are the same for all systems. However, this first theorem it does not say anything about neither the analytic form of $F_{HK}\left[\rho_0\right]$ nor the practical ways to obtain the ground state electron densities. The second Hohenberg-Kohn theorem concerns the latter issue.

**Second theorem :** the electron density that minimises the energy of the overall functional is the true electron density corresponding to the full solutions of the Schrödinger equation. If the true functional form is known, then one can try to minimise the energy by varying the electron density, in order to find the ground state electron density. This means in our case that the functional $F_{HK}\left[\rho_0\right]$ gives the energy of the ground state if and only if the density used corresponds to that of the ground state $\rho_0$. This theorem is the application of the variational principle to the DFT, for example for a density $\rho$:

$$E_0 \leq E\left[\rho\right] = F_{HK}\left[\rho\right] + E_{eN}\left[\rho\right]$$

## 1.2 The Kohn-Sham equations

Although the first Hohenberg—Kohn theorem rigorously proves that a functional of the electron density $E_0$ exists, the theorem says nothing about the actual form of the functional. Although the Hohenberg-Kohn theorems are extremely powerful, they do not offer a way of computing the ground-state density of a system in practice. It was Walter Kohn and Lu Sham [296] who in 1965 developed a method to find $E_0$ from $\rho_0$. The Kohn-Sham formulation centres on mapping the full interacting system with the real potential, onto a fictitious "non-interacting system" whereby the electrons move within an effective potential $V_s$. The Hamiltonian of this fictitious system is

:

$$\hat{H} = -\sum_{i}^{N} \frac{\nabla_i^2}{2} + \sum_{i}^{N} V_s(\overrightarrow{r_i})$$

The kinetic energy of this non-interacting system is known exactly using spin-orbitals $\phi_i$:

$$T_s[\rho] = \sum_{i} < \phi_i| - \frac{\nabla_i^2}{2}|\phi_i >$$

By analogy with the Hartree-Fock method the $\phi_i$ spin-orbitals are determined by solving the eigenvalue equation:

$$\hat{f}_i^{KS}\phi_i = \varepsilon_i\phi_i$$

where $\hat{f}_i^{KS}$ corresponds to the monoelectronic operator of Kohn-Sham :

$$\hat{f}_i^{KS} = -\frac{\nabla_i^2}{2} + V_s(\overrightarrow{r_i})$$

The $\phi_i$ spin-orbitals are called Kohn-Sham orbitals. The connection between this fictitious system and the real system is made *via* the choice of the effective potential $V_s$ for which the electron density is equal to that of the real system:

$$\rho_s(\overrightarrow{r}) = \rho_0(\overrightarrow{r}) \tag{1}$$

The originality of this method comes from the fact that even if the kinetic energy of this system without interaction is not equal to the kinetic energy of the real system, it is possible to approach it and for that it is necessary to separate the known parts of the unknown parts which gives us the following expression of the universal functional :

$$F_{HK}[\rho(\overrightarrow{r})] = T_s[\rho(\overrightarrow{r})] + J[\rho(\overrightarrow{r})] + E_{XC}[\rho(\overrightarrow{r})]$$

in this equation, two terms are known exactly,$T_s[\rho(\overrightarrow{r})]$ the kinetic energy of the system without interaction and $J[\rho(\overrightarrow{r})]$ the Coulomb interaction between electrons, and the last term corresponding to the exchange-correlation energy, $E_{XC}[\rho(\overrightarrow{r})]$, groups together all the unknown terms :

$$E_{XC}[\rho(\overrightarrow{r})] = (T[\rho(\overrightarrow{r})] - T_s[\rho(\overrightarrow{r})]) + (E_{ee}[\rho(\overrightarrow{r})] - J[\rho(\overrightarrow{r})])$$

This term $E_{XC}[\rho(\overrightarrow{r})]$ is the difference between the exact total energy and the other known quantities. It is the energy from Pauli exclusion and many-body Coulomb interactions. It also includes the difference between the many-body and single particle kinetic energies. Through this approach, Kohn and Sham therefore transferred what is not known into only one term smaller term, $E_{XC}[\rho(\overrightarrow{r})]$. Therefore, the error made will be made on a small contribution to the total energy of the system. From there we can write the real energy of the system as follows:

$$E\left[\rho\right] = F_{HK}\left[\rho\right] + E_{eN}\left[\rho\right]$$

$$E\left[\rho\right] = T_s[\rho(\overrightarrow{r})] + J[\rho(\overrightarrow{r})] + E_{XC}[\rho(\overrightarrow{r})] + E_{eN}\left[\rho\right]$$

$$E\left[\rho\right] = \sum_{i}^{N} < \phi_i| - \frac{\nabla_i^2}{2}|\phi_i > + \frac{1}{2}\sum_{i}^{N}\sum_{j}^{N}|\phi_i(\overrightarrow{r_1})|^2\frac{1}{r_{12}}|\phi_j(\overrightarrow{r_2})|^2 + E_{XC}[\rho(\overrightarrow{r})] + \sum_{i}^{N}\int\sum_{A}^{M}\frac{Z_A}{r_{iA}}|\phi_i(\overrightarrow{r_1})|^2 d\overrightarrow{r_1}$$

The corresponding eigenvalue equation with the constraint $< \phi_i|\phi_j >= \delta_{ij}$ is :

$$[-\frac{\nabla_i^2}{2} + \int\frac{\rho(\overrightarrow{r_2})}{r_{12}}d(\overrightarrow{r_2}) + V_{XC}(\overrightarrow{r_1}) + \sum_{A}^{M}\frac{Z_A}{r_{1A}}]\phi_i = \varepsilon_i\phi_i$$

where $\int\frac{\rho(\overrightarrow{r_2})}{r_{12}}d(\overrightarrow{r_2}) + V_{XC}(\overrightarrow{r_1}) + \sum_A^M \frac{Z_A}{r_{1A}}$ being the effective potential $V_{effec}$ (or $V_s$). The exchange-correlation potential $V_{XC}$ being defined as the derivative of exchange-correlation $E_{xc}$ with respect to the electron density: $V_{xc} = \frac{\delta E_{XC}[\rho(r)]}{\delta\rho(r)}$. We can then rewrite the eigenvalue equation in the following form :

$$[-\frac{\nabla_i^2}{2} + V_{effec}]\phi_i = \varepsilon_i\phi_i \tag{2}$$

This equation is called the Kohn-Sham equation. It intrinsically depends on the spin-orbitals and the resolution must be done iteratively. From a starting electron density we obtain a value of the effective potential which allows us to solve the differential equation 2. This solution leads to a new density by the equation 1 which will give us a new effective potential ... the operation is thus repeated until convergence.

The selection of the level of approximation is made by choosing a functional of exchange and correlation that depends on the studied materials. The selectivity criterion compares the value of the theoretical result obtained, associated with the studied physico-chemical property, with the one experimentally observed. The difference between these two values must then be minimal for the functional to be used. The exchange and correlation functions are classified as follows:

- LDA local density approximation,[296] which describes locally the density,
- GGA generalised gradient approximation,[278] including a density gradient,
- meta-GGA,[297] including dependence on kinetic energy density,
- hybride,[298] including an exchange part based on occupied orbitals,
- non-local,[299, 300] including a dependency on innocent orbitals.

In this thesis we used a GGA hybrid functional: B3PW91. It has been shown by Parisel *et al.*[301] that the PW91 correlation functional leads to better results than the LYP correlation functional when a weak interaction, *i.e.* an agostic interaction. It has been also shown by Eisenstein *et al.* that the calculations with B3PW91 functional reproduce in a remarkable manner the lanthanide contraction and their geometrical parameters at all levels of calculation. The experimental value of 0.179 $\mathring{A}$ is quantatively reproduced with B3PW91 (0.180 $\mathring{A}$), whereas the values are 0.185 $\mathring{A}$ for Hartree Fock (HF) and 0.190 $\mathring{A}$ for B3LYP.[302] Moreover the results in terms of stability and activity are in aggrement with the experimental data, as reviewed by Platas-Iglesuas *et al.*.[303] In all respects, B3PW91 gives the best results and will only be considered hereafter for calculating lanthanide complexes.[302, 304]

## 1.3 Limit

The reactivity of organometallic complexes of lanthanides has been the subject of a number of theoretical studies. Theses studies validated the use of the theoretical method that will be employed in this manuscript, *i.e.* using DFT, a hybrid functional (here B3PW91) and pseudo-potentials.[157, 305, 306, 160, 307] The energy values of reactions can be calculated with an accuracy of less than 5 kcal.mol$^{-1}$ for a transition state and less than 2 kcal.mol$^{-1}$ for a stationary point.[308] For each reaction, the complete reaction path is determined, allowing the enthalpy of the reaction and the activation barrier to be calculated. These are finite differentials because these enthalpies are calculated as the difference between enthalpy of the stationary point considered and the sum of the enthalpies of the separate reagents. Finally, during the mechanistic study, it is common to use artifacts to reduce calculations times. Thus, the model usually includes the metal centre surrounded by highly simplified or idealised ligands. The latter are generally replaced by their hydrogen analogue ($PH_3$ for $PR_3$, $H_2O$, for $R_2O$, $CH_3$ for $CR_3$...). The main thing is to be able to keep the activity of the active centre and to be able to keep the electron density on the same atoms as those of the real complex.

## 1.4 Specific treatment of lanthanides

Lanthanides are chemical elements with atomic numbers between Z=57 (La) and Z=71 (Lu). The particularity of this family of elements corresponds to the gradual electronic filling of the 4f orbitals. In the case of La, the 5d underlayer is lower in energy than the 4f, explaining its electronic configuration [Xe]6s$^2$5d$^1$. The further we progress in the family, the number of protons in the nuclei increases, and the 4f orbitals contract. This makes the 4f orbitals more stable than the 5d orbitals. As shown in the figure 30, the 4f orbitals are highly contracted and cannot make significant overlaps with the ligand orbitals. Consequently, they do not participate significantly in chemical binding. As a result, the ligand field effects are very weak and the spectroscopic and magnetic properties of the lanthanides are only slightly affected by their environment. The most common ions of the family are in oxidation state III, although some lanthanides also have oxidation states II and IV. Interactions between lanthanides and ligands are mainly electrostatic, hence their attraction to ligand with high electronegativity, such as halides with low atomic numbers. Furthermore, the geometry of lanthanide complexes is not dependent on the ligand field as for transition metals, but rather on steric and electronic inter-ligand repulsion. In the lanthanide series, the atomic radius as well as the ionic radius of the Ln ions decreases as one progresses towards the largest atomic numbers. This is due to the fact that the 4f orbitals poorly shield the peripheral electrons from the nuclear charge. Thus, when the charge increases as one advances in the series, the 6s and 5d orbitals contract and the atomic radii decrease. This contraction of lanthanides is also partly due to the relativity effects.[309]

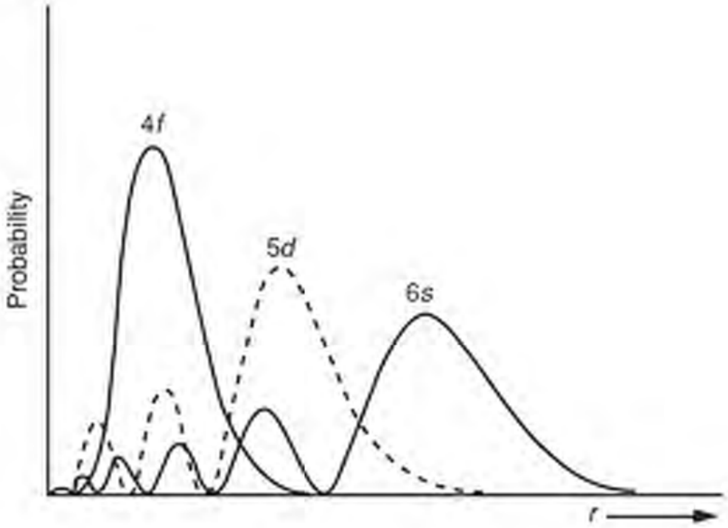

Figure 30: Radial part of the orbitals 4f, 5d, 6s of the cerium.

## 1.5 The pseudopotentials

The principle of atomic effective potentials is based on the hypothesis that core and valence can be separated energetically and spatially. The former, which are close to the nucleus and highly stabilised, contribute very little to chemical bonds. Therefore, since the scalar relativistic effects apply directly to the core electrons, it is reasonable to want to separate the valence and core electrons, either by freezing the latter, or by replacing them with an effective potential limiting the molecular calculation to the optimisation of the valence electron configuration. Thus, with this method, the effective potentials will include the scalar relativistic effects and reduce the number of explicit electrons to be processed. The calculations will therefore be lighter. In this thesis we used Energy-consistent Pseudopotentials of the Stuttgart/Cologne Group.

For this method, the real valence orbitals $\phi_V$, determined with a relativistic all-electron calculation, are replaced by pseudo-orbitals $\chi_V$ and the heart-electron interaction by an effective potential $W_{PS}$. In this case, we refer to Relativistic Electron Core Potential (RECP),[310] of the form:

$$W_{PS}(i) = -\tfrac{Z-n_c}{r_i} - \sum_{l=0}^{l=l_{max}} W^l_{PS}(i)|l><l|$$

where

$$W^l_{PS}(i) = \sum_k C_{k,l} r_i^{n_{k,l}} e^{-\alpha_{k,l} r_i^2}$$

As the relativistic effects are not the same depending on the orbitals, the projector |l><|l| assure the dependence in symmetry of the pseudo-potential.

In the ‘shape-consistent’ approach,[311, 312] the pseudo-orbitals reproduce the structure of the real orbitals in the valence region but have a polynomial shape in the core region. The pseudo-potential is then extracted by minimising with least squares the terms $<\chi_V|V_{eff}|\chi_V>$ $-\epsilon_V$, where V is the energy of the $\chi_V$.

In the 'energy-consistent' approach,[280] the orbital information is totally ignored. The pseudo-potential is extracted by reproducing observables such as the total energy of the atom, its ionisation potential, the electronic transition energies... In practice, these two methods often lead to similar results, which allows to confirm their validity.

The pseudo-potentials used in this thesis is of the 'energy-consistent' type.

# 2 Computed spectroscopy analysis

## 2.1 Frequency calculations

The vibrational Infra-Red (IR) spectrum is systematically computed after any minima or TS geometry optimisation of a molecular system so that the nature of the stationary point found can be determined. These routine verification is called frequency calculations because the frequencies of the vibrational normal modes of the molecule are computed (the vibrational IR spectrum is computed). The trick to perform such a calculation is to transform the potential and kinetic energy operators from Cartesian displacements to the so-called 'normal coordinates', doing so the Hamiltonian is re-written as a sum of independent harmonic oscillators.

## 2.2 Nuclear Magnetic Resonance (NMR)

In the context of NMR, where only the analysis of the interactions between nuclear spin and its environment is fundamental, the use of an effective Hamiltonian considering only spin variables and magnetic moments may be sufficient to report the various experimental observations. If we place in the Born-Oppenheimer approximation, the total Hamiltonian of nuclear spin $\widehat{H}_I$ can be written as the sum of two independant operators:

$$\widehat{H}_I = \widehat{H}_{int} + \widehat{H}_{ext}$$

$\hat{H}_{int}$representing the different magnetic or electrical interactions of the nucleus with its environment and $\hat{H}_{ext}$ the coupling of the magnetic moment I with $B_0$ and the radio-frequency (rf) magnetic field $B_1$.

### 2.2.1 External interactions.

To observe an NMR signal, a transition between Zeeman levels needs to be generated and then the signal is obtained during the relaxation of the spin moments. For this purpose, a $B_1$ magnetic field is applied, oscillating at the frequency corresponding to the energy between the levels. In order to have a magnetic resonance phenomenon, the polarised radio-frequency field is applied perpendicularly to $B_0$. The Hamiltonian that describes the external interactions of a single spin I is composed by one term associated to the Zeeman effect rely on $I_z$, and second term for the interaction between the nuclear spin and the radio-frequency field dependent on $I_x$ and $I_y$[313]:

$$\widehat{H}_{ext} = -\gamma\hbar B_0 I_z - \tfrac{1}{2}\gamma\hbar B_1\{cos\{\omega_{ref}t + \phi)I_x + sin(\omega_{ref}t + \phi)I_y\}$$

where $\omega_{ref}$ is the frequency and $\phi$ is the phase. Nevertheless, all the information describing the local environment of the nucleus is carried by the internal interactions.

### 2.2.2 Internal interactions

The effective Hamiltonian deriving the internal interactions can be developed on a sum of operators corresponding to each type of interaction:

$$\widehat{H}_{int} = \widehat{H}_Z + \widehat{H}_{CS} + \widehat{H}_D + \widehat{H}_J + \widehat{H}_Q$$

The different operators corresponding to the Zeeman's Hamiltonian ($\widehat{H}_Z$), chemical shielding Hamiltonian ($\widehat{H}_{CS}$), dipole coupling Hamiltonian($\widehat{H}_D$), scalar coupling Hamiltonian ($\widehat{H}_J$) and quadrupole coupling Hamiltonian ($\widehat{H}_Q$).

The goal in this thesis is to compare theoretical and experimental chemical shift values. Thus, for this thesis, we will only develop the chemical displacement interactions.

### 2.2.3 Chemical shielding interaction.

Within a molecule, the nuclei can not be considered as isolated and are electrically influenced by other neighbouring nuclei. Indeed the circulation of electrons around a nucleus i creates a secondary magnetic field $\vec{B}_{ind}$ under the effect of the main field B$_0$:

$$\overrightarrow{B}_{\text{ind}} = -\overleftrightarrow{\sigma_K}.\overrightarrow{B_0}$$

where $\overleftrightarrow{\sigma}$(r) corresponds to the chemical shielding (CS) tensor. The CS tensor describes the magnitude and orientation dependence of the CS interaction and can be represented in 3D Cartesian space using a 3x3 matrix:

$$\overleftrightarrow{\sigma_K} = \begin{bmatrix} \sigma_{xx} & \sigma_{xy} & \sigma_{xz} \\ \sigma_{yx} & \sigma_{yy} & \sigma_{yz} \\ \sigma_{zx} & \sigma_{zy} & \sigma_{zz} \end{bmatrix}$$

Each element, $\sigma_{ij}(i, j = x, y, z)$ represents the i-component of shielding when B$_0$ is applied along the j-axis. On a microscopic scale, this means that the electrons form a screen around the proton. The field received by the nucleus is no longer $\vec{B_0}$ but $\vec{B}_{effective}$ as:

$$\vec{B}_{effective} = \vec{B_0} + \vec{B}_{ind} = \vec{B_0}.(1 - \overleftrightarrow{\sigma_K})$$

If we now look at the effective Hamiltoinian nuclear spin for N nuclei K subjected to a magnetic fiald we get:

$$\widehat{H} = \sum_K^N - \hbar.\gamma_K.\vec{B}_{effective}.I_K = \sum_K^N - \hbar\gamma_K.\vec{B_0}.(1 - \overleftrightarrow{\sigma_K}).I_K$$

$$\widehat{H} = \sum_K^N - \hbar.\gamma_K.\vec{B_0}.I_K + \hbar.\gamma_K.\vec{B_0}.\overleftrightarrow{\sigma_K}.I_K$$

The Hamiltonian chemical shift would be written:

$$\widehat{H}_{CS} = \sum_K^N \hbar.\gamma_K.\vec{B_0}.\overleftrightarrow{\sigma_K}.I_K$$

where I$_K$ is the nuclear kinetic moment of the nucleus, $\gamma$ its gyromagnetic ratio. The sum is realised on all the nuclei N of the electronic structure. In this Hamiltonian, the variables associated with the electrons are explicitly absent, but implicitly present in $\overleftrightarrow{\sigma}$(r), *i.e.* $\overleftrightarrow{\sigma}$(r) contains all the information related to the electron cloud surrounding the nucleus. The CS tensor $\overleftrightarrow{\sigma}(\mathrm{r})$, can be decomposed into two parts, one symmetric and the other antisymmetric. The antisymmetric portion of the tensor, which is contained in the second-order shielding response that is perpendicular to the applied field. This antisymmetric part has negligible or no involvement in the NMR signal.[314, 315], and is omitted from subsequent discussion. The symmetric portion of the CS tensor can be diagonalised into its own principal axis system, by convention the $B_0$ field is directed along the z-axis, and can be written as follows:

$$\overleftrightarrow{\sigma}_{K_Z} = \begin{pmatrix} \sigma_{xx} & 0 & 0 \\ 0 & \sigma_{yy} & 0 \\ 0 & 0 & \sigma_{zz} \end{pmatrix}$$

We can then define three parameters to quantify the local electronic deformations. These three parameters are expressed as a function of the three main components of the tensor.

The isotropic shielding constant:

$$\sigma_{iso} = \frac{1}{3}(\sigma_{xx} + \sigma_{yy} + \sigma_{zz})$$

The shielding anisotropy:

$$\sigma_{aniso} = \sigma_{zz} - \sigma_{iso}$$

The three eigenvalues $\sigma_{11}$, $\sigma_{22}$ and $\sigma_{33}$ are represented according to the Haeberlen convention, *i.e.*:

$$|\sigma_{22} - \sigma_{iso}| \leqslant |\sigma_{11} - \sigma_{iso}| \leqslant |\sigma_{33} - \sigma_{iso}|$$

Finally, with shielding constants directly calculated in ppm, we can obtain the chemical shift value from the difference between the isotropic shielding constant of the core and the isotropic shielding constant of the identical core in a reference compound:

$$\delta_{iso} = \sigma_{ref} - \sigma_{iso}$$

### 2.2.4 Calculation of the chemical shielding (CS) tensor

The first point to perform NMR calculations will therefore be the calculation of the CS tensor. Within the framework of quantum methods applied to chemical displacement calculations, the electronic Hamiltonian must show dependence on the external magnetic field (B) and on the magnetic moment ($\mu_I$) specific to each nucleus of the system:

$$\widehat{H}_{el}(B,\mu) = \sum_{i=1}^{n} \tfrac{1}{2}(-i\nabla_i + \tfrac{1}{c}A'(r_i))^2 + \sum_{i=1}^{n}\sum_{I=1}^{N} \tfrac{Z_I}{r_{iI}} \sum_{i=1}^{n}\sum_{j>i}^{n} \tfrac{1}{|r_i - r_j|}$$

Where A'($r_i$) is the vector describing the magnetic field at the position of the electron $r_i$ for a given position of the $R_I$ nuclei. The latter is constructed in a way that its curvature reproduces the magnetic field felt by the electron j coming from B and the nuclei:

$$B(r_j) = \nabla_j.A'(r_j)$$

For an electronic system immersed in a magnetic field including the external field and the nuclear moments, the A'($r_j$) of each electron j can then be decomposed on the sum of the contributions coming from B and the magnetic moments of each atom. A'($r_j$) is then given by:

$$A'(r_j) = \tfrac{1}{2}B.r_j + \sum_{i=1}^{N} \tfrac{\mu_I.(r_j - R_I)}{|r_j - R_I|^3}$$

The energy $\varepsilon$(B,$\mu$) associated with the electronic Hamiltonian can be determined by solving Schrödinger's equation:

$$\widehat{H}_{el}(B,\mu)|\psi(B,\mu) \geqslant \varepsilon(B,\mu)|\psi(B,\mu) >$$

For low values of B and $\mu$, $\varepsilon$(B,$\mu$) can be developed in Taylor series in the vicinity of B=0 and $\mu$=0. In this way, A' is substituted by its expression developed above and the development is carried out considering the Coulomb gauge, *i.e.* ∇A=0.[316]

$$\varepsilon(B,\mu) = \epsilon^0 + \tfrac{\delta\varepsilon}{\delta B}|_0 + \sum_K \tfrac{\delta\varepsilon}{\delta\mu_K}|_0\mu_K + B^\dagger \tfrac{\delta^2\varepsilon}{\delta B^2}B|_0 + \sum_K B^\dagger \tfrac{\delta^2\varepsilon}{\delta B\delta\mu_K}\mu_K|_0 + \tfrac{1}{2}\sum_{K\neq L}\mu_K^\dagger \tfrac{\delta^2\varepsilon}{\delta\mu_K\delta\mu_L}\mu_L|_0$$

Where K designates the considered nucleus. We remind here that $B = B_0$ and $\mu_K = \gamma j I_K$

$\gamma_K$ et $I_K$ being respectively the gyromagnetic ratio and the nuclear spin moment of the considered K nucleus. By comparing the above equation with the Hamiltonian interaction equation describing the CS ($H_{CS}$), it is possible by simple identification to demonstrate that the electronic shielding tensor is equal to the second derivative of energy with respect to the external magnetic field and the spin moment:

$$\overset{\leftrightarrow}{\sigma}_K = \tfrac{\delta^2\varepsilon}{\delta\mu_K\delta B}$$

The identification can be generalised, describing the internal coupling interactions present in the nuclear spin Hamiltonian. After rearrangement, for a closed shell system (the second and third terms of this equation are null) is given by:

$$\varepsilon(B,\mu) = \varepsilon^0 + B^\dagger\overset{\leftrightarrow}{\chi}B + \sum_K B^\dagger\overset{\leftrightarrow}{\sigma}_K\mu_K + \tfrac{1}{2}\sum_{K\neq L}\mu_K^\dagger\overset{\leftrightarrow}{d}_{KL}\mu_L$$

Where $\overset{\leftrightarrow}{d}$ describes the interactions related to dipolar and scalar coupling. $\overset{\leftrightarrow}{\chi}$, which is not a property of the nuclear spin Hamiltonian, represents the diamagnetic susceptibility tensor of the system. Thus, thanks to the system energy $\varepsilon$<H(B,$\mu$)>, most of the interactions measurable by NMR are theoretically accessible. Here $\varepsilon$ can be the expression of the Hartree-Fock[317] energy, of a post-Hartree-Fock method,[316] or of the Khon-Sham approach.[318] The chemical displacement tensor is equal to the second order response of the electronic energy to a variation of the magnetic field and the nuclear spin moment. Another approach based on the evaluation of the current density j can be used for the calculation of the chemical shift tensor. The existing connections between the two approaches have been described in the literature.[319]

In reality, the calculation of chemical shielding tensor is not totally invariant to a system translation. This is mainly due to the truncated expansion of the base describing the wave function. Within the limit of a complete base, it is theoretically possible that it is gauge invariant.[320] This type of approach can only be applied to systems with only few atoms.[321] In more concrete cases, based on the use of a conventional base, the deviation between the calculated value and the ideally converged value depends on the gauge origin. A judicious choice of the gauge origin can, however, lead to a converged result more quickly.[322]

In order to preserve computing resources and to be able to process large systems, the gauge invariance problem must be explicitly solved. In order to solve the gauge invariance problem, several methods can be used. In the present case we will use the GIAO (Gauge Invariant Atomic Orbital) method used in the Gaussian 09 program.[272] This method introduced by London for the calculation of magnetic susceptibility and adapted for the calculation of chemical displacements by Ditchfield[282] allows to a certain extent to ensure the gauge invariance. The GIAO method based on the principle of gradient addition of an arbitrary function f(r) to the vector A, leaves the magnetic field $B = \nabla \times A$ unchanged. The idea proposed then by London is that each mono-electronic wave function has its own gauge origin, represented by an exponential multiplicative factor. This approach forms the basis on which the GIAO method[323, 324, 325] was developed. Therefore the mono-electronic wave function is rewritten as follows:

$$\psi_k(r, B) = exp(-\frac{i}{c}A_k.r)\psi_k(r)$$

where

$$A_k = \frac{1}{2}(B.R_k)$$

The presence of the k index emphasises that the atomic wave function $\psi_k$ is centred on the atom at the $R_k$ position. The substitution of $\psi_k$ orbitals by the GIAO $\psi(r, B)$ orbitals then makes it possible to determine the $\overleftrightarrow{\sigma}$ CS tensor, respecting the gauge invariance condition. This method is, of course, not the only existing one to fix the gauge invariance problem. Other methods proposed by Keith and Bader called CSGT (continuous se of the gauge transformation) are an alternative to the GIAO method. The CSGT methods satisfy the gauge invariance condition by performing a continuous set of gauge transformations, one for each point in real space, obtaining an accurate description of the current density from which the shielding tensors can be determined. However, Cheesemen *et al.* showed that for atoms ranging from $^{13}$C to $^{29}$Si, the isotropic electron screen components obtained with the GIAO and CSGT approaches converged to the same values dor sufficiently large atomic bases.[326] Nevertheless, the GIAO method converges more rapidly with base expansion, especially for atoms heaver than carbon.

## 2.3 Natural Bond Orbitals (NBO)

The principle of this method is to extract the partial charges from each atom of the system, as well as to quantify the influence of occupied or empty orbitals on each other, an influence they can enhance the constructive character of the bonds. NBO analysis is based on a method for optimally transforming a given wave function into localised form, corresponding to the one-centre ("lone pairs") and two-centre ("bonds") elements of the chemist's Lewis structure picture. In NBO analysis, the input atomic orbital basis set is transformed *via* natural atomic orbitals (NAOs) and natural hybrid orbitals (NHOs) into natural bond orbitals (NBOs). The NBOs obtained in this fashion correspond to the widely used Lewis picture, in which two-centre bonds and lone pairs are localised. The NBO analysis method also defines the Lewis $E_{Lewis}$ energy, corresponding to the energy of the wave function constructed from the NBOs alone. The difference E - $E_{Lewis}$ is used to evaluate the relevance of the proposed Lewis scheme. A second order perturbation calculation then allows to analyse the donor-acceptor and agostic interactions (interaction between covalent bond A-B and a vacant orbital of the metal) involved in the energitic stabilisation of the system.[292]

# Part III

# Graphene supported lanthanum systems

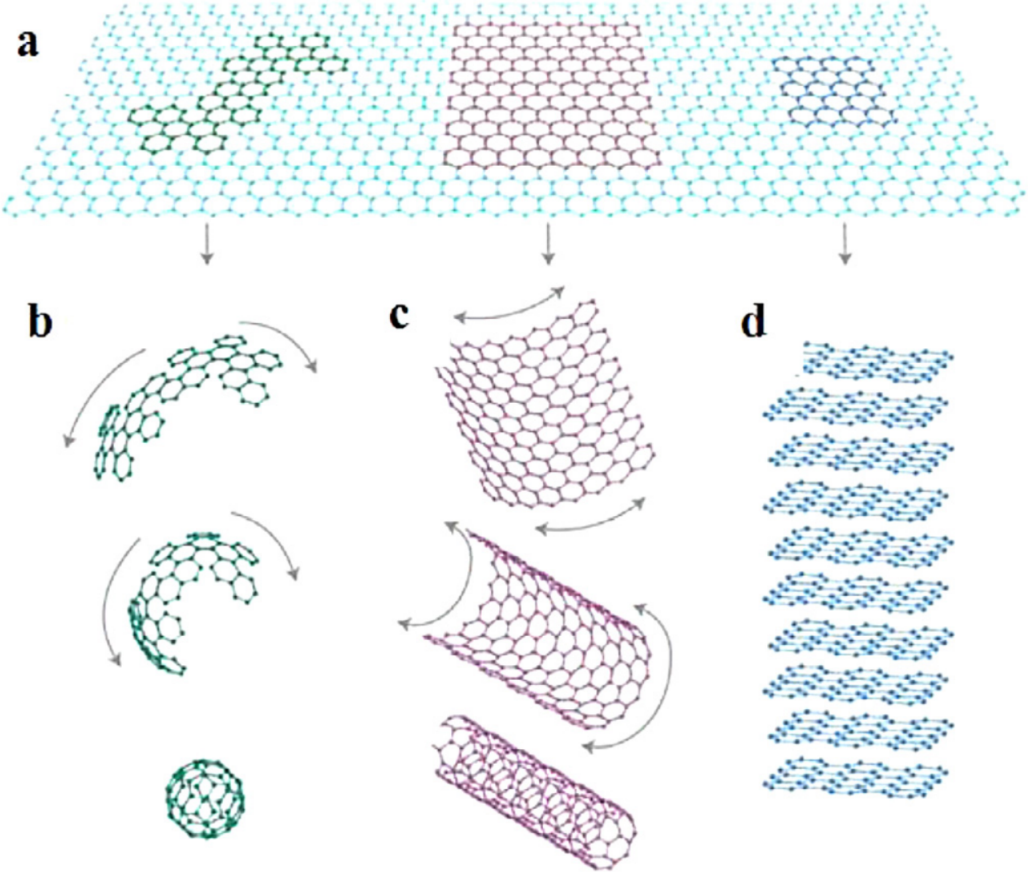

Figure 31: Allotropes of carbon: a) 2-D graphene b) 0-D fullerene, c) 1-D carbon nanotube d) 3-D graphite.[327]

Graphene is an allotrope of carbon, existing as a two-dimensional (2D) planar sheet that can be regarded as a single atomic graphite layer. Each carbon atom is bonded covalently ($sp^2$ hybridized) to three other carbon atoms in a hexagonal arrangementleaving one free electron for each atom carbon. While the $\sigma$-bonding in graphene is assumed to be a rigid honeycomb framework built out of two-centre two electron (2c-2e) C-C $\sigma$bonds, the $\pi$-bonding is delocalised. graphene represents therefore the building block for all graphitic materials. It can be wrapped into 0-dimensional fullerenes, rolled into 1-dimensional carbon nanotubes and stacked into 3-dimentional graphite, as summarised in Figure 31. Since the first experimental evidence of the electronic properties of graphene in 2004, many experimental studieshavas been devoted to the development of new synthetic routes enabling an effective production of well-defined graphene sheets.[328, 329, 330, 331, 332, 333, 334, 335, 336, 337, 338, 339, 340, 341, 342] The commonly applied synthetic methods include i) the micromechanical or chemical exfoliation of graphite,[338] ii) the chemical vapour deposition (CVD) growth,[332, 333, 334, 335, 336, 337] and iii) the chemicals, electro-chemical, thermal andphotocatalytic reduction of graphene oxide or fluorographene.[340, 341, 343, 342] The exceptional interest in graphene is not surprising given the excellent mechanical and chemical properties exhibited by graphene such as a high surface area (2630 $m^2g^{-1}$),[344] an excellent thermal conductivity (5000 $W.m^{-1}K^{-1}$),[345] a high electron mobility at room temperature (around 250 000 $cm^{-2}.V^{-1}.s^{-1}$ at electron densities of $2.10^{11}cm^{-2}$,[346] a very high Young's modulus (1 TPa),[347] a very high light transmittance (around 98%),[348] a remarkable chemical stability,[349, 350] and finally interesting electron donor and electron acceptor properties[351, 352] due to the extended conjugation of its surface.

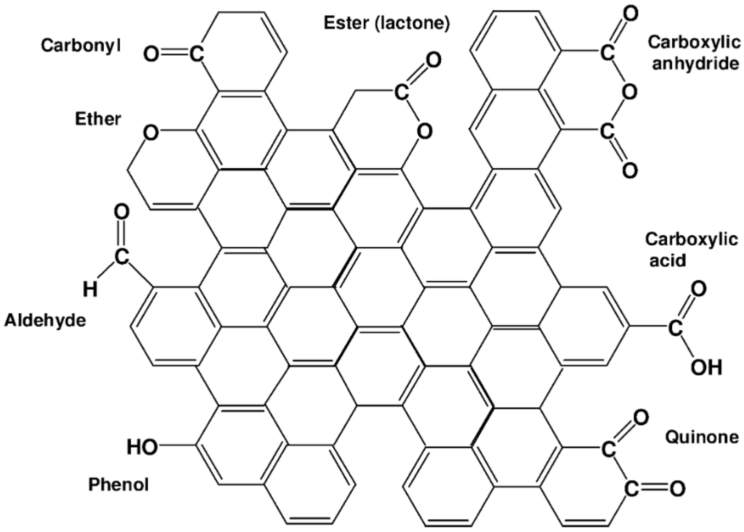

Figure 32: schematic representation of oxygen functional groups on the CNTs surface.[353]

# 1 Synthesis and characterisation of oxidised graphene surfaces

The treatment of CNTs with oxidising agents in the gas or liquid phase results in their partial oxidation, with the formation on the surface of oxygen-containing functional groups. Nitric acid or other oxidising reagents such as ozone or oxygen plasma have been reported to be highly effective for this purpose.[335, 336, 337, 338, 339] As previously described[353] the basal planes of the graphite are attacked by molecular oxygen only at their periphery or at defect sites such as edge planes and vacancies. Oxidation by nitric acid or $HNO_3/H_2SO_4$ mixtures is most frequently employed. The nitric acid treatment, indeed, allows the controlled formation of functional groups with a minimum damage of the CNT structure. Toebes *et al.*[342], moreover reported that in nitric acid the nitronium ion ($NO_2{}^+$) is able to attack aromatic compounds, this reaction probably representing the first step for the generation of the oxygen containing functional groups. The introduction of oxygen-containing groups on the surface of CNTs enhances their solubility in aqueous or organic solvents and reduces the Van der Waals interactions between different CNTs, limiting in this way the aggregation phenomenon.

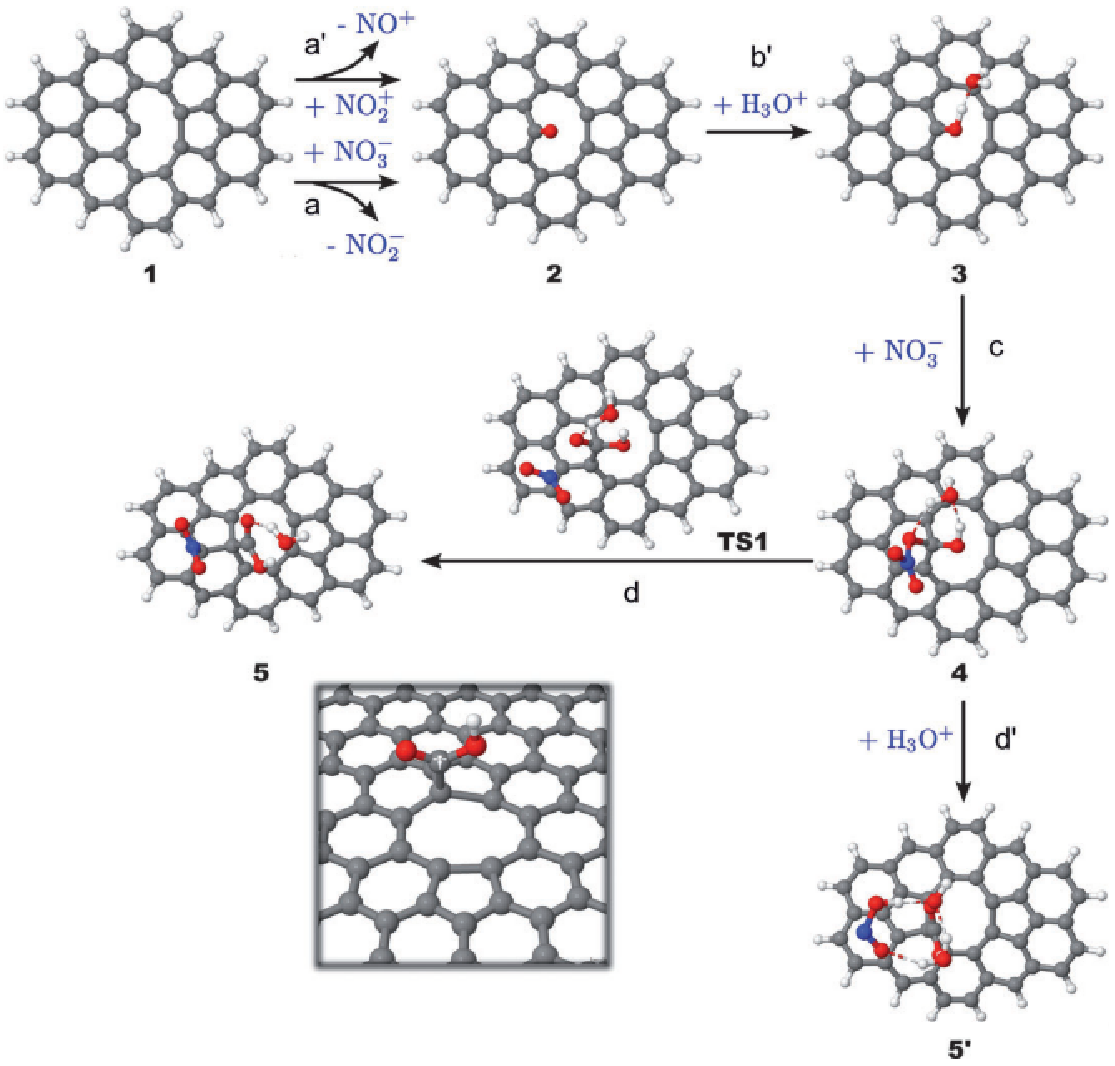

Figure 33: Scheme of the four-step mechanism proposed for the formation of a surface carbonyl function by oxidation of a mono-vacancy site 3 correspond to the -OH functional group bonded to the initial graphene mono-vacancy site and 5 and 5' correspond to the -COOH functional group bonded to the di-vacancy site obtained at the end of the reaction.

Several techniques, often in combination, such as chemical titration,[354, 355] thermal analysis/mass spectroscopy,[356, 357] X-ray photoelectron spectroscopy (XPS),[358, 359, 360] FTIR spectroscopy[359, 361] and X-ray absorption near edge structure (XANES) analysis[353] have been used to quantify these oxygenated surface functionalities and to identify their nature as mostly phenolic, lactonic, quinonic and carboxylic groups.[362, 353] Experimentally it has been observed that the nitric acid oxidation of carbon nanotubes (CNT) surfaces involves the initial rapid formation of carbonyl groups which are then transformed into mainly phenolic and carboxylic groups. Interestingly, the concentration of these surface oxygen groups evolves as a function of both reaction time and temperature. For a reaction time of 8h, the concentration of all the oxygenated groups increases with increasing temperature, their distribution above room temperature following the order: phenol $>$ carboxylic $\approx$ carbonyl $>$ anhydride $>$ lactone. The formation of these oxygenated groups is likely to occur at first on the most reactive carbon atoms, located at the CNTs structural defects.[363] They mostly concern either atomic vacancies, associated with the deficiency of surface carbon atoms, or topological defects, associated with topological deviations from the ideal hexagonal ring type structure. Single vacancies neighbouring five-membered ring defects are the simplest and the most common defect for CNT systems.[364]

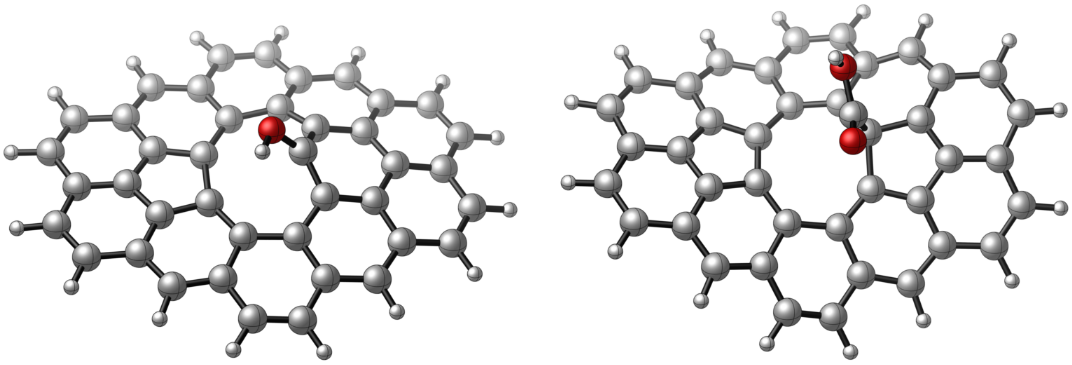

(a) gOH : $[C_{41}H_{16}\text{-}OH]^+$ (b) gOOH : $[C_{41}H_{16}\text{-}OOH]^+$

Figure 34: Graphene functionalised surface models obtained from the $C_{42}H_{16}$ polycyclic model; a) the $[C_{41}H_{16}\text{-}OH]^+$ model with a C mono-vacancy defect bonded to a hydroxo group, (gOH), as a model of the phenol function and b) the $[C_{41}H_{16}\text{-}OOH]^+$ model with a C di-vacancy defect bonded to a carboxylic group, (gOOH), as a model of the carboxylic function.

Many DFT calculations have been carried out to explain the CNT oxidation mechanism in the presence of nitric acid.[353, 364, 365, 366, 367] A recent computational study using both periodic boundary conditions (PBC), on a single graphene layer, and molecular systems, on a polycyclic aromatic hydrocarbon model ($C_{41}H_{16}$), investigated the reactivity of monovacancies characterised by carbon dangling atoms.[353] The mechanism proposed by the authors (see scheme 33) involves four-steps: i) the initial oxidation of a mono-vacancy site by either a nitrate or a nitronium ion affording a surface carbonyl function; ii) the following carbonyl to phenol protonation by an hydronium ion; iii) the formation of a nitro-hemiketal intermediate by reaction with a second nitrate ion and finally iv) the formation of a surface carboxylic group by either internal rearrangement or protonation by a second hydronium ion. Starting from mono-vacancies, therefore, the proposed mechanism ends up with the synergistic formation of dangling -COOH groups and the consequent enlargement of the vacancies, showing that the reaction of nitric acid with graphene causes damages on the CNT walls, as observed experimentally. Two molecular models for the -OH and -COOH oxygen functionalised CNT surfaces have been therefore proposed: i) the $[C_{41}H_{16}\text{-}OH]^+$ model (figure 34a), displaying a monovacancy bonded to an OH bond and ii) the $[C_{41}H_{16}\text{-}OOH]^+$ model (figure 34b), containing a di-vacancy decorated with a carboxylic function. Oxygenated protonated functionalities are of particular interest, since they can behave as coordination sites for metal complexes, thus paving the way for the preparation of grafted heterogeneous catalytic systems.

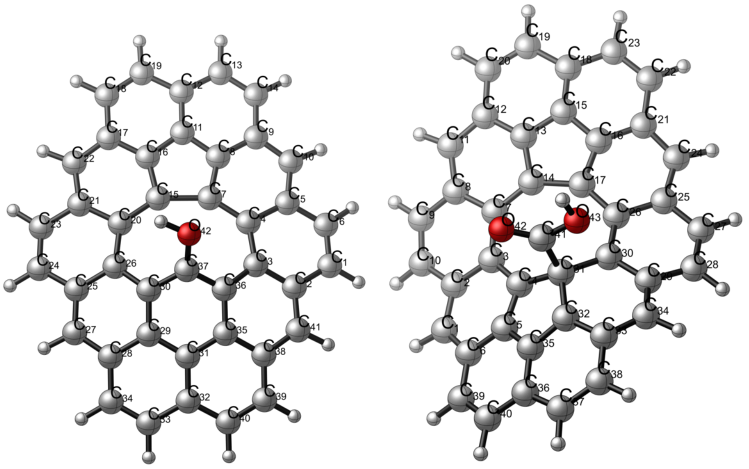

(a) gOH (b) gOOH

| Atom | Charge | Atom | Charge |
|---|---|---|---|
| C1 | -0.22 | C22 | -0.15 |
| C2 | -0.05 | C23 | -0.19 |
| C3 | 0.03 | C24 | -0.22 |
| C4 | -0.02 | C25 | -0.05 |
| C5 | -0.05 | C26 | 0.01 |
| C6 | -0.19 | C27 | -0.12 |
| C7 | 0.00 | C28 | -0.06 |
| C8 | -0.02 | C29 | 0.01 |
| C9 | -0.05 | C30 | -0.11 |
| C10 | -0.14 | C31 | -0.03 |
| C11 | -0.02 | C32 | 0.00 |
| C12 | -0.02 | C33 | -0.21 |
| C13 | -0.21 | C34 | -0.18 |
| C14 | -0.19 | C35 | 0.00 |
| C15 | -0.02 | C36 | -0.09 |
| C16 | -0.02 | C37 | 0.60 |
| C17 | -0.05 | C38 | -0.07 |
| C18 | -0.20 | C39 | -0.17 |
| C19 | -0.20 | C40 | -0.22 |
| C20 | 0.06 | C41 | -0.11 |
| C21 | -0.05 | O42 | -0.60 |

(c) gOH

| atom | Charge | atom | Charge |
|---|---|---|---|
| C1 | -0.16 | C23 | -0.18 |
| C2 | -0.03 | C24 | -0.17 |
| C3 | -0.01 | C25 | -0.02 |
| C4 | 0.04 | C26 | -0.03 |
| C5 | -0.01 | C27 | -0.19 |
| C6 | -0.07 | C28 | -0.21 |
| C7 | 0.01 | C29 | -0.09 |
| C8 | -0.05 | C30 | 0.10 |
| C9 | -0.20 | C31 | -0.19 |
| C10 | -0.22 | C32 | 0.11 |
| C11 | -0.14 | C33 | -0.10 |
| C12 | -0.06 | C34 | -0.02 |
| C13 | -0.01 | C35 | -0.03 |
| C14 | -0.03 | C36 | 0.00 |
| C15 | -0.01 | C37 | -0.21 |
| C16 | -0.02 | C38 | -0.18 |
| C17 | 0.02 | C39 | -0.15 |
| C18 | -0.03 | C40 | -0.23 |
| C19 | -0.21 | C41 | 0.87 |
| C20 | -0.19 | O42 | -0.55 |
| C21 | -0.02 | O43 | -0.71 |
| C22 | -0.21 | | |

(d) gOOH

Figure 35: Calculated Natural charges on the gOH and gOOH model

## 2 Grafting of the [La(N(SiMe$_3$)$_2$)$_3$] complex on oxidised gOH and gOOH graphene surfaces

We first investigated the grafting of the lanthanide [La(N(SiMe$_3$)$_2$)$_3$] complex onto the [C-OH] (gOH) and [C-COOH] (gOOH) aforementioned models (shown in figure 34). In the gOH model, the C-OH bond length is 1.310 Å, in accordance with the presence of a simple bond between the C and the O atoms. Interestingly, as shown in figure 35, while in the gOH model the positive charge of the surface is mainly localised on the C atom, in the gOOH model, on the other hand, the positive charge of the surface is delocalised on the surface.

## 2.1 Grafting reaction

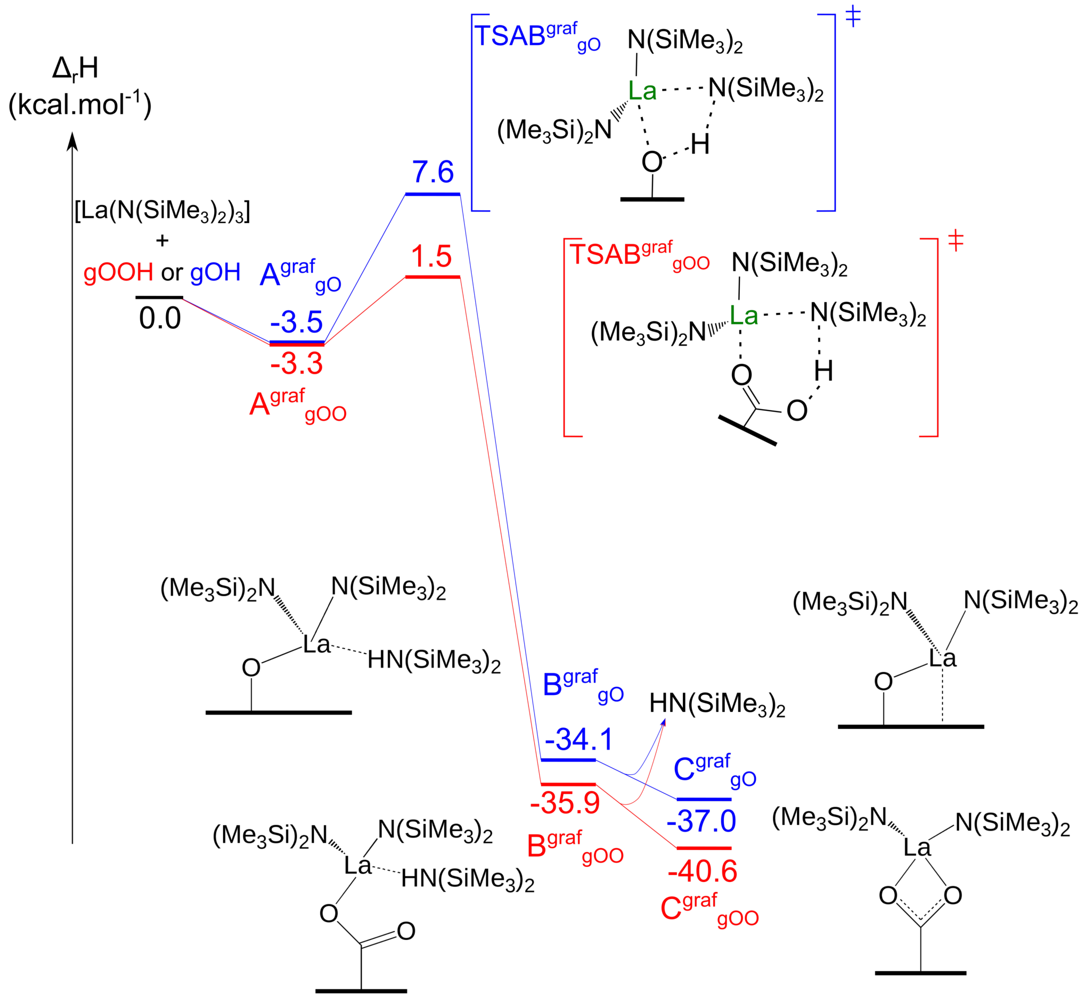

Figure 36: Calculated enthalpy-energy profile for the grafting of the [La(N(SiMe$_3$)$_2$)$_3$] complex on the gOH and gOOH graphene functionalised surfaces.

The grafting reaction occurs through a protonolysis of the La-N bond by the graphene hydroxo or carboxyl pending groups, which generates a ≡C-O-La and ≡C-COO-La bond, respectively, with the concomitant formation of a free hexamethyldisilazane molecule. The corresponding enthalpy profiles are shown in figure 36. The grafting reactions onto the gOH and gOOH graphene surfaces lead to the formation of the mono-grafted (gO)-[La(N(SiMe$_3$)$_2$)$_2$] and (gOO)-[La(N(SiMe$_3$)$_2$)$_2$] complexes, respectively, through exothermic (-37.0 and -40.6 kcal.mol$^{-1}$ for the gO and gOO surfaces, respectively, with respect to the separated reactants) and kinetically favourable processes (activation barriers : 11.1 and 4.8 kcal.mol$^{-1}$ for the gO and gOO surfaces, respectively, with respect to the corresponding hexamethyldisilylamido adducts, $A^{graf}{}_{gO}$ and $A^{graf}{}_{gOO}$). The structures of the transition states and intermediates involved in the grafting reaction are shown in figures 37 and 39. Selected bond distances are summarised in Table 1.

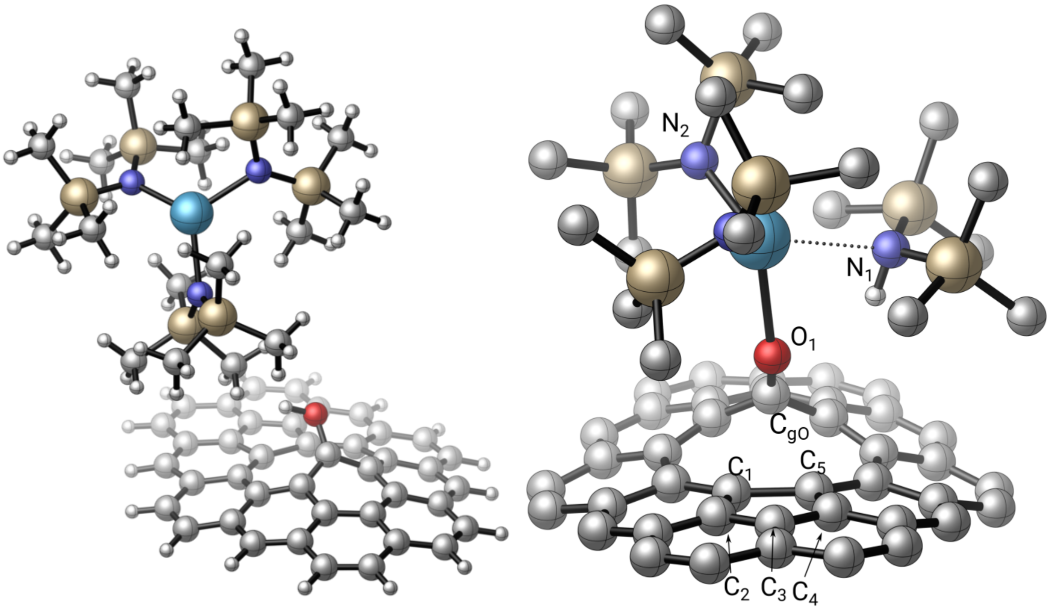

(a) $A^{graf}{}_{gO}$ (b) (gO)-[La(NR$_2$)$_2$HNR$_2$] ($B^{graf}{}_{gO}$)

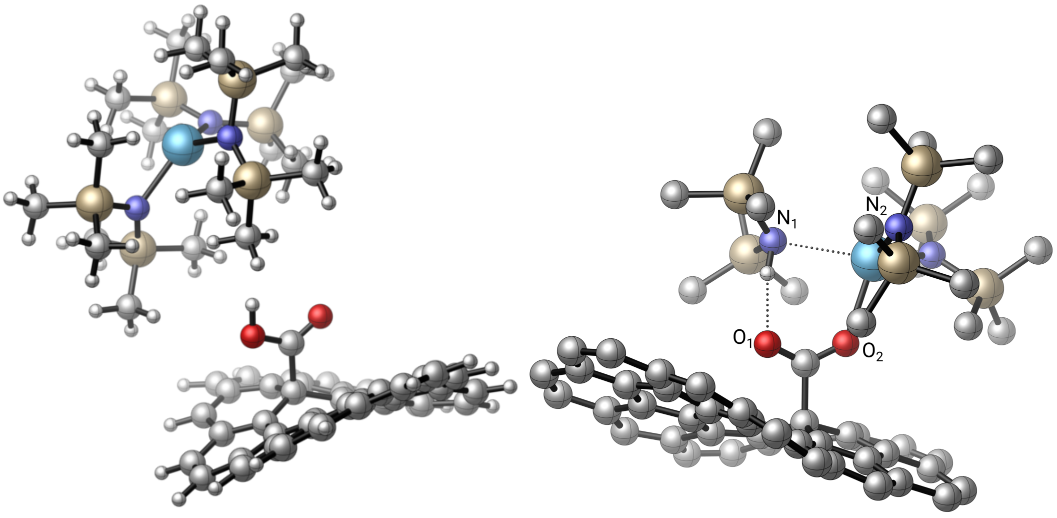

(c) $A^{graf}{}_{gOO}$ (d) (gOO)-[La(NR$_2$)$_2$HNR$_2$] ($B^{graf}{}_{gOO}$)

Figure 37: Structures of the adduct and the final product of the metathesis reaction involved in the grafting of [La(NR$_2$)$_3$] (R=SiMe$_3$) on the gOH (a,b) and gOOH (c,d) graphene functionalised surfaces. For sake of clarity, all the H of the La-grafted compounds have been omitted with the exception of the graphene-OH and graphene-COOH atoms.

Table 1: Enthalpy energies (in kcal.mol$^{-1}$) and selected bond distances ($\AA$) of the TS, the $HNR_2$ adducts and the final (gO)-[La($NR_2$)$_2$] and (gOO)-[La($NR_2$)$_2$] compounds resulting from the grafting of [Ln($NR_2$)$_3$] on the gOH and gOOH graphene functionalised surfaces (R=$SiMe_3$). The labels $O_1$, $O_2$, $N_1$, $N_2$, $C_1$, $C_2$, $C_3$, $C_4$ and $C_5$ refer to the geometries in figure 3.

| | $\Delta_R H°$ | La-$O_1$ | La-$O_2$ | La-$N_1$ | La-$N_2$ | La-$C_1$ | La-$C_2$ | La-$C_3$ | La-$C_4$ | La-$C_5$ | $O_1$-H | $N_1$-H | $C_{gO}O_1$ |
|---|---|---|---|---|---|---|---|---|---|---|---|---|---|
| TS-AB$^{graf}{}_{gO}$ | 7.6 | 4.503 | - | 2.408 | 2.349 | - | - | - | - | - | 0.975 | 3.053 | 1.308 |
| TS-AB$^{graf}{}_{gOO}$ | 1.5 | 5.638 | 6.120 | 2.396 | 2.341 | - | - | - | - | - | 0.973 | 3.314 | - |
| (gO)-[La($NR_2$)$_2$($HNR_2$)] (B$^{graf}{}_{gO}$) | -34.1 | 2.637 | - | 2.868 | 2.303 | 5.098 | 5.706 | 6.031 | 5.748 | 5.153 | 2.414 | 1.027 | 1.247 |
| (gOO)-[La($NR_2$)$_2$($HNR_2$)] (B$^{graf}{}_{gOO}$) | -35.9 | 3.788 | 2.461 | 2.865 | 2.318 | - | - | - | - | - | 2.009 | 1.034 | - |
| (gO)-[La($NR_2$)$_2$] (C$^{graf}{}_{gO}$) | -37.0 | 2.432 | - | - | 2.289 | 3.304 | 3.510 | 3.795 | 3.839 | 3.564 | - | - | 1.247 |
| (gOO)-[La($NR_2$)$_2$] (C$^{graf}{}_{gOO}$) | -40.6 | 2.556 | 2.541 | - | 2.303 | - | - | - | - | - | - | - | - |

The protonolysis transition state for the grafting reaction on the gOH surface displays a classical 4 c - 4 e$^-$ $\sigma$-bond metathesis geometry, with the graphene hydroxo oxygen atom interacting with the La centre (d(La-$O_1$)= 4.503 $\AA$) and the hexamethyldisilylamido nitrogen atom interacting with the graphene hydroxo hydrogen atom (d($N_1$-H) = 3.053 $\AA$). The height of the barrier can be rationalised by the perfect positive and negative charge alternation (+1.7, -1.7, +0.5 and -0.6 for the La, $N_1$, H and $O_1$ atoms, respectively, see figure 38a), as reported by Werkema *et al.*.[152, 157, 368] The resulting lanthanum complex is therefore mono-grafted on the gO surface (La-$O_1$ = 2.637 $\AA$), with the HN($SiMe_3$)$_2$ molecule still interacting with the lanthanum centre (La-$N_1$= 2.868 $\AA$). As shown in figure 39, the release of the amine is accompanied by the formation of a stabilising interaction between the lanthanum metal and the resulting gO graphene surface. The presence of this interaction has been confirmed by short La-C(graphene) distances (between 3.304 and 3.839 $\AA$) and by a second-order perturbation NBO analysis, which reveals a weak donation of 3.3 kcal.mol$^{-1}$ from the C=C bonds of the underlying pentagonal graphene cycle to an empty d orbital of the metal centre. The NBO analysis additionally shows a donation from the N-Si, Si-C and C-H bonds of the two hexamethyldisilylamido groups onto an empty d orbital of the metal centre, indicating the presence of two strong agostic interactions (130.8 and 170.7 kcal.mol$^{-1}$), with a La-N Wiberg bond index of 0.64. Interestingly, the $C_{gO}$-$O_1$ bond length is 1.247 $\AA$, indicating the presence of a double bond between the $C_{gO}$ and the $O_1$ atoms. This is confirmed at the second order donor-acceptor NBO analysis which indicates a strong donation from one of the $O_1$ lone pairs onto the $C_{gO}$ atom (210 kcal.mol$^{-1}$), with a $C_{gO}$-$O_1$ Wiberg bond index of 1.49. The positive charge of the graphene surface, therefore, is likely to polarise the electron density of the $O_1$ atom, which binds the La metal, recovering the formal positive charge from the surface ($O_1$-La = 2.432 $\AA$). The formation of the $O_1$-La bond is revealed by a second-order NBO analysis showing a strong donation from one of the $O_1$ lone pairs onto an empty d orbital of the La centre (177 kcal.mol$^{-1}$), with a $O_1$-La Wiberg bond index of 0.33.

The electron donation provided by the C=O$^+$ group to the Lewis acid La atom is therefore less effective than that of a pure phenolate anion, the two hexamethyldisilylamido agostic bonds and the additional interaction of the graphene surface with the metal centre balancing this electron deficiency. Interestingly, the natural charge of the La centre increases from 1.65 to 1.75 ongoing from the molecular [La(N(SiMe$_3$)$_2$)$_3$] complex to the grafted (gO)-[La(N(SiMe$_3$)$_2$)$_2$] system, indicating that the grafting of the [La(N(SiMe$_3$)$_2$)$_3$] complex on the gO surface increases the Lewis acidity of the La centre. The transition state involved in the grafting reaction on the gOOH surface, on the other hand, displays a 6 c - 4 e$^-$ $\sigma$-bond metathesis geometry (figure 39).

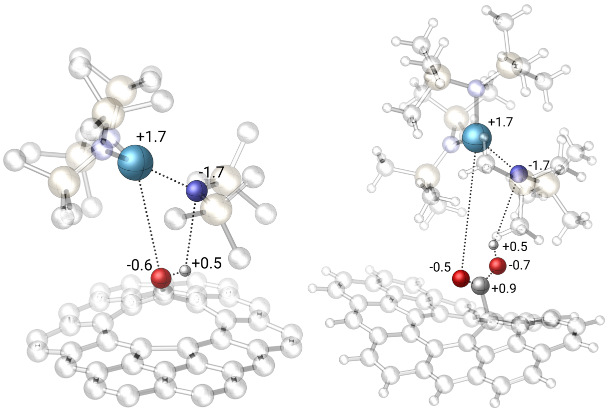

(a) TS-AB$^{graf}{}_{gO}$ (b) TS-AB$^{graf}{}_{gOO}$

Figure 38: NPA charges involved on the metathesis transition state of the grafting reaction of [La(N(SiMe$_3$)$_2$)$_3$] on the gOH (a) and gOOH (b) graphene functionalised surfaces (light blue : La, dark blue : N, white : H, red : O).

Unlike the gOH case, the La centre remains still far from the O atom (La-O$_2$ = 6.120 $\mathring{A}$), while the N atom of the leaving hexamethyldisilylamido group weakly interacts with the H atom (N$_1$-H = 3.314 $\mathring{A}$). Again, the height of the barrier fits with the perfect charge alternation (+1.7, - 1.7, +0.5, - 0.7, +0.9 and -0.5 for the La, N$_1$, H, O$_1$, C and O$_2$ atoms, respectively, see figure 38b). The transition state also evolves to an intermediate displaying the HN(SiMe$_3$)$_2$ molecule in interaction with the lanthanum centre. The removal of the amine ligand leads the lanthanum centre to interact with the second oxygen of the gOOH carboxo group (O$_1$) affording the bicoordinated monografted (gOO)-[La(N(SiMe$_3$)$_2$)$_2$] species. This bicoordinated monografted coordination mode, typical of a classical supported carboxylate group, is confirmed by the C-O and La-O bond lengths (C-O$_1$ = 1.253 $\mathring{A}$, C-O$_2$ = 1.257 $\mathring{A}$, La-O$_1$ = 2.556 $\mathring{A}$, La-O$_2$ = 2.541 $\mathring{A}$, see figure 39 and table S1) as well as by a second order NBO analysis which shows the presence of two stabilising interactions between the two oxygens of the gOO carboxylate group and the metal centre. The two hexamethyldisilylamido groups display two strong N-Si, Si-C, C-H agostic interactions with the La centre (128.0 and 138.7 kcal.mol$^{-1}$). As shown in figure 36, the (gOO)-[La(N(SiMe$_3$)$_2$)$_2$] compound is more stable than the (gO)-[La(N(SiMe$_3$)$_2$)$_2$] complex by 3.6 kcal.mol$^{-1}$, as the bicoordination of the carboxylate group strongly stabilises the gOO grafted species. In conclusion, the grafting of the [La(N(SiMe$_3$)$_2$)$_3$] complex on the gOH and gOOH surfaces is a favourable process, both kinetically and thermodynamically, affording mono-grafted complexes. The nature of the oxygenated groups at the graphene surface has a great influence on the geometry and stability of the grafted complexes, especially in determining the grafting mode of the La(N(SiMe$_3$)$_2$)$_2$ moiety. The grafting on the gOH surface leads to the formation of the (gO)-[La(N(SiMe$_3$)$_2$)$_2$] complex exhibiting a gO-La bond and a weak interaction between the La centre and the underlying pentagonal C=C groups of the graphene surface. In the presence of the gOOH surface, on the other hand, the (gOO)-[La(N(SiMe$_3$)$_2$)$_2$] compound is obtained, displaying a stabilising bicoordination of the carboxylate group to the La metal centre.

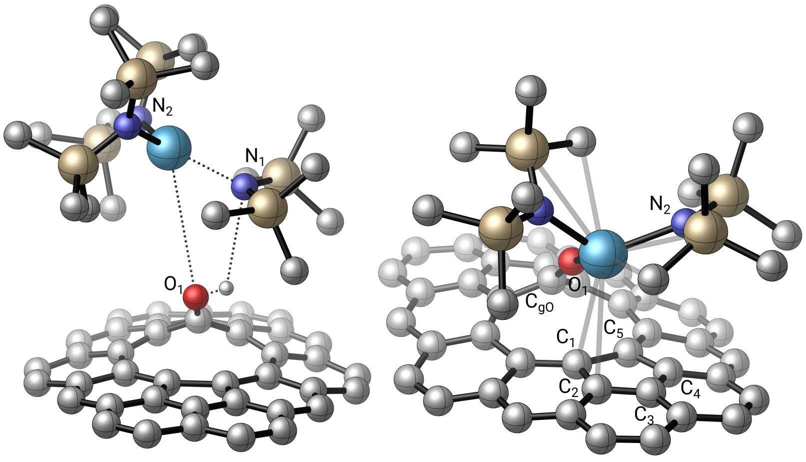

(a) TS-AB$^{graf}{}_{gO}$ (b) (gO)-[La(N(SiMe$_3$)$_2$)$_2$] (C$^{graf}{}_{gO}$)

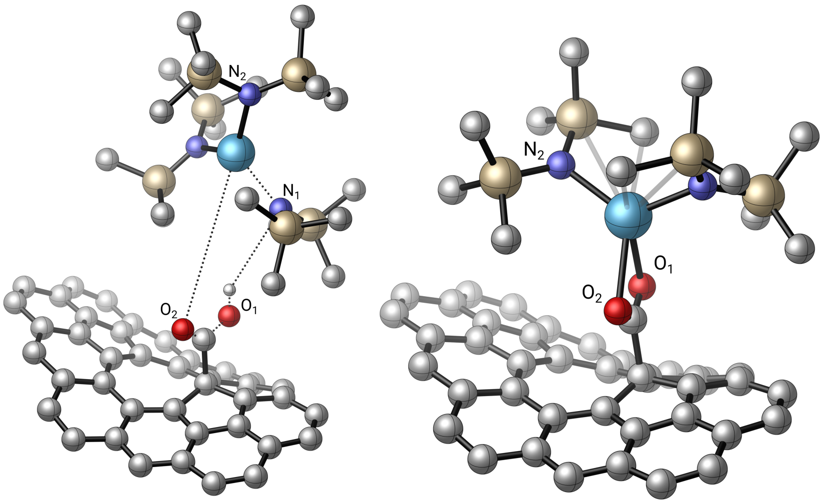

(c) TS-AB$^{graf}{}_{gOO}$ (d) (gOO)-[La(N(SiMe$_3$)$_2$)$_2$] (C$^{graf}{}_{gOO}$)

Figure 39: Structures of the transition states and final products involved in the grafting reaction of [La(N(SiMe$_3$)$_2$)$_3$] on the gOH (a,b) and gOOH (c,d) graphene functionalised surfaces (light blue : La, dark blue : N, white : H, red : O). For sake of clarity, all the H of the La-grafted compounds have been omitted with the exception of the graphene-OH and graphene-COOH atoms.

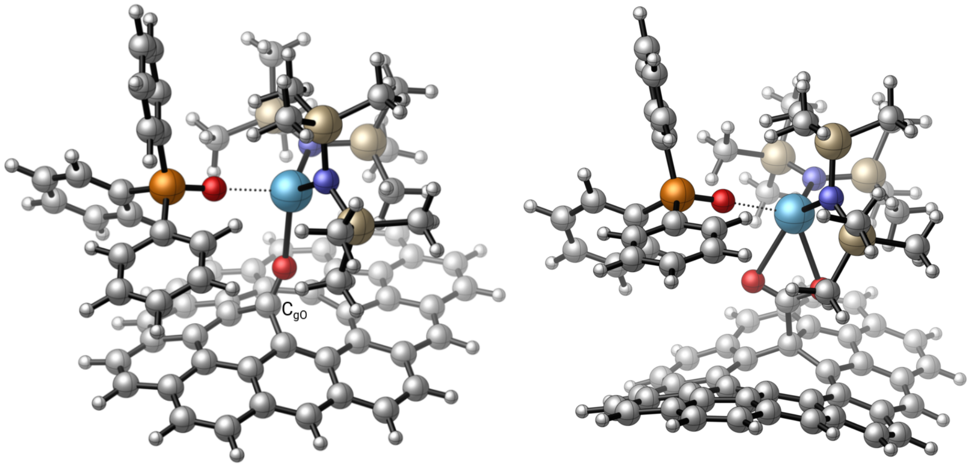

(a) (gO)-[La(N(SiMe$_3$)$_2$)$_2$(O=PPh$_3$)] (b) (gOO)-[La(N(SiMe$_3$)$_2$)$_2$(O=PPh$_3$)]

Figure 40: Structures of the OPPh$_3$ hexamethyldisilylamido La adducts grafted on a) the gO and b) the gOO graphene surface.

## 2.2 Probing the Lewis acidity of the graphene grafted lanthanum complexes

As previously reported both experimentally and theoretically, the coordination of a triphenylphosphine oxide (O=PPh$_3$) to grafted lanthanide amido complexes can be used as a probe to estimate the influence of the surface on the Lewis acidity properties of the metal centre and therefore on the reactivity of the catalyst. Experimentally it has been shown that the O=PPh$_3$ molecule re- acts with both molecular and silica-monografted lanthanide hexamethyldisilylamido compounds, affording the corresponding molecular [Ln(N(SiMe$_3$)$_2$)$_3$(O=PPh$_3$)][369] and silica-grafted (Si-O)-[Ln(N(SiMe$_3$)$_2$)$_2$ (O=PPh)$_3$] (Ln = La, Nd, Sm, Sc)[87] monoadduct species. As in the experimental approaches, some of us have recently described, from a computational point of view, the reaction of OPPh$_3$ with different silica-grafted lanthanide species, showing that the OPPh$_3$ coordination strength can be affected by the coordination sphere of the grafted complex.[136, 135] To probe the influence of the graphene surface, we have now investigated the OPPh$_3$ interaction with the graphene grafted hexamethyldisilylamido lanthanum complexes above described. The coordination of O=PPh$_3$ on both the (gO)-[La(N(SiMe$_3$)$_2$)$_2$] and gOO-[La(N(SiMe$_3$)$_2$)$_2$] grafted complexes affords the corresponding (gO)-[La(N(SiMe$_3$)$_2$)$_2$(O=PPh$_3$)] (figure 40 a) and (gOO)-[La(N(SiMe$_3$)$_2$)$_2$(O=PPh$_3$)] (figure 40 b) species through an exothermic process (-28.9 and -24.7 kcal.mol$^{-1}$, respectively). In the gO system, the coordination of the OPPh$_3$ molecule forces the La metal to move away from the surface, fully breaking the interaction La-surface. The strong donation of the OPPh$_3$ molecule to lanthanum, attested by a second order NBO stabilisation energy of 158.3 kcal.mol$^{-1}$, additionally weakens the agostic interactions of the two hexamethyldisilylamido groups which decrease from 130.8 and 170.7 kcal.mol$^{-1}$ for the (gO)-[La(N(SiMe$_3$)$_2$)$_2$] system to 47.8 and 60.4 kcal.mol$^{-1}$ for the corresponding O=PPh$_3$ adduct. In order to compare the Lewis acidity of these gO- and gOO-grafted La O=PPh$_3$ compounds with that of the SiO$_2$ grafted analogues previously reported,[136] we computed the IR and the $^1$H, $^{13}$C and $^{31}$P NMR spectra of both the (gO)-[La(N(SiMe$_3$)$_2$)$_2$(O=PPh$_3$)] and (gOO)-[La(N(SiMe$_3$)$_2$)$_2$(O=PPh$_3$)] adducts.

The C-H, aromatic C=C and O=P vibrational frequencies computed for the coordinated O=$PPh_3$ molecule are reported in Table 2. The aromatic C-H and C-C stretching vibrations are similar for both the gO and gOO grafted species (in the range 3184-3240 $cm^{-1}$ and 1471-1655 $cm^{-1}$, respectively), whereas the vibrational stretching mode corresponding to the O=P function lies at 1039 and 1047 $cm^{-1}$ for the gO and gOO systems, respectively. On silica surfaces,[135] the computed O=$PPh_3$ mono-grafted and bi-grafted silica supported systems display lower C-H and C=C vibrational frequencies (in the range 2938-3107 $cm^{-1}$ and in the range 1416-1592 $cm^{-1}$, respectively, depending on the considered silica model) and higher O=P vibrational stretching modes (in the range 1118-1152 $cm^{-1}$ depending on the considered silica model) than those of graphene grafted complexes. The comparison with the vibrational frequencies experimentally measured for the silica supported (≡Si-O)-[La(N($SiMe_3$)$_2$)$_2$(O=$PPh_3$)][55] monoadduct species reveals the same trend. While for the C-H and C-C bands, the vibrational modes of the computed graphene-grafted La silylamido systems are always higher than those of the (≡Si-O)-[La(N($SiMe_3$)$_2$)$_2$(O=$PPh_3$)] complex (CH frequencies between 3184 and 3240 $cm^{-1}$ *vs.* 3066 $cm^{-1}$; C-C frequencies in the 1471-1655 $cm^{-1}$ range *vs.* the 1440-1593 $cm^{-1}$ range), for the O=P band, it is the (≡Si-O)-[La(N($SiMe_3$)$_2$)$_2$(O=$PPh_3$)] compound which is expected to have the higher stretching frequencies (expected between 1120 and 1180 $cm^{-1}$ compared to the 1039 and 1047 $cm^{-1}$ values computed here for the gO and gOO systems, respectively). The graphene systems computed here, therefore, display a weaker O=P bond and thus a stronger La-O bond, suggesting that the La metal is a stronger Lewis acid when grafted on graphene surfaces. Another way to characterise the nature of the metal centre is to investigate the theoretical $^{1}$H, $^{13}$C and $^{31}$P NMR chemical shift of the coordinated O=$PPh_3$ molecule (Table 2). The $^{1}$H isotropic chemical shift calculated for the two gO and gOO graphene grafted species are in the range 7.3 - 7.4 ppm. While they are comparable to the experimental value measured for the (≡Si-O)-[La(N($SiMe_3$)$_2$)$_2$(O=$PPh_3$)] complex (7.4 ppm), they are slightly more shielded than those reported for the computed mono- and bi-grafted silica models (in the range 7.9-8.0 ppm). The $^{13}$C NMR values (123.5, 127.8 ppm for the (gO)-La system and 123.6, 127.8 for the (gOO)-La system) are comparable with those computed in the mono- and bi-grafted silica models (between 123.5 and 124.9 ppm for the high field $^{13}$C signal and between 128.1 and 129.2 for the high field $^{13}$C signal) as well as with those experimentally measured for the (≡Si-O)-[La(N($SiMe_3$)$_2$)$_2$(O=$PPh_3$)] compound (128.4 and 132.5 ppm). The $^{31}$P NMR signal corresponding to the O=$PPh_3$ molecule coordinated to the graphene-grafted La complex has been computed at 56.0 and 53.4 ppm, for the (gO)-La and (gOO)-La models, respectively. Interestingly both values are more deshielded than those reported for the silica-grafted systems (within the 40.3-47.6 ppm range) and for the experimentally isolated (≡Si-O)-[La(N($SiMe_3$)$_2$)$_2$(O=$PPh_3$)] complex (39.1 ppm). As evidenced by Drago *et al.*[181, 370], a positive $^{31}$P NMR chemical shift increment between free and coordinated O=$PPh_3$ indicates the coordination to a Lewis acidic site, the bigger this difference, the higher the Lewis acidic character of the metal and therefore the stronger the M-O=$PPh_3$ interaction. In agreement with the IR spectroscopy analysis, these more deshielded $^{31}$P NMR values in the La graphene-grafted systems is once again related to the stronger Lewis acidity of the graphene-supported La centre compared to silica. Following a coordination-insertion mechanism, surface- grafted lanthanide complexes are known to behave as active catalysts in many polymerization reactions.[143, 88, 162, 166, 145, 182, 184, 183] The first step of the mechanism involves the coordination of the monomer to the metal center, the higher the Lewis acidic character of the metal, the higher the activation of the monomer in the polymerization reaction. In view of their stronger Lewis acidity, therefore, we expected graphene-supported La complexes to act as active polymerization catalysts and we decided to study their catalytic activity in the homo- and co-polymerization of ethylene and 1,3-butadiene.

Table 2: Comparison between the theoretical vibrational frequencies (in cm$^{-1}$), and the $^{1}$H, $^{13}$C and $^{31}$P NMR chemical shifts (in ppm) of a free OPPh$_3$ ligand and the coordinated OPPh$_3$ molecule in different OPPh$_3$ hexamethyldisilylamido La adducts grafted on the gO and gOO graphene surfaces and on SiO$_2$ (average between all the mono- and bi-grafted species previously reported[135]). The $^{1}$H and $^{13}$C chemical shifts are given with respect to TMS (theoretical chemical shielding: 31.64 and 195.35 ppm, respectively, for $^{1}$H and $^{13}$C atoms). The $^{31}$P chemical shifts are given with respect to phosphoric acid (theoretical chemical shielding: 380.6 ppm). R = SiMe3,$^{(a)}$ x = 1 or 2$^{(b)}$ Reference [55].$^{(c)}$ Expected but not detected (see reference [55]).

| | Wavenumbers (in cm$^{-1}$) | | |
|---|---|---|---|
| | $\overline{\nu}_{C-H}$ | $\overline{\nu}_{C=C}$ | $\overline{\nu}_{O=P}$ |
| O=PPh$_3$ | [3065-3095] | [1416-1592] | 1177 |
| (gO)-[La(NR$_2$)$_2$(O=PPh$_3$)] | [3184-3240] | [1471-1655] | 1039 |
| (gOO)-[La(NR$_2$)$_2$(O=PPh$_3$)] | [3193-3230] | [1475-1655] | 1047 |
| (SiO$_2$)-[La(NR$_2$)$_2$(O=PPh$_3$)]$^{(a)}$ | [2938-3107] | [1416-1592] | [1118-1152] |
| (SiO$_2$)-[La(NR$_2$)$_2$(O=PPh$_3$)]-exp$^{(b)}$ | ca. 3066 | [1440-1593] | [1120-1180]$^{(c)}$ |

| | Chemical Shifts (in ppm) | | |
|---|---|---|---|
| | $\delta_{H_{Phenyl}}$ | $\delta_{C_{Phenyl}}$ | $\delta_{P}$ |
| O=PPh$_3$ | 7.7 | 124.7/129.9 | 25.7 |
| (gO)-[La(NR$_2$)$_2$(O=PPh$_3$)] | 7.3 | [123.5/127.8 | 56.0 |
| (gOO)-[La(NR$_2$)$_2$(O=PPh$_3$)] | 7.4 | 123.6/127.8 | 53.4 |
| (SiO$_2$)-[La(NR$_2$)$_2$(O=PPh$_3$)]$^{(a)}$ | [7.9-8.0] | 123.5/129.0 | [40.3-47.6] |
| (SiO$_2$)-[La(NR$_2$)$_2$(O=PPh$_3$)]-exp$^{(b)}$ | 7.4 | 128.4/132.5 | 39.1 |

# 3 Catalytic activity of the graphene grafted lanthanum complexes

## 3.1 Coordination insertion polymérisation.

### 3.1.1 Catalysts models.

Experimentally, as seen in 1.4.2, the formation of the active silica supported Ln alkyl species is assured by an alkylating agent, usually an alkylaluminium reagent such as the TIBA which converts the starting hexamethyldisilylamido groups into the corresponding alkyl groups. As models of the graphene supported La active species we choose the simplified (gO)-[La(CH$_3$)$_2$] (1gO) and (gOO)-[La(CH$_3$)$_2$] (1gOO) complexes, obtained by replacing both hexamethyldisilylamido groups by two methyl functions, provided that no bimetallic (La-Al) species are formed during the alkylation reaction. As shown in figure 95, 1gO displays a monografted monocoordination mode, the La metal interacting with the two methyl groups, the surface oxygen atom and

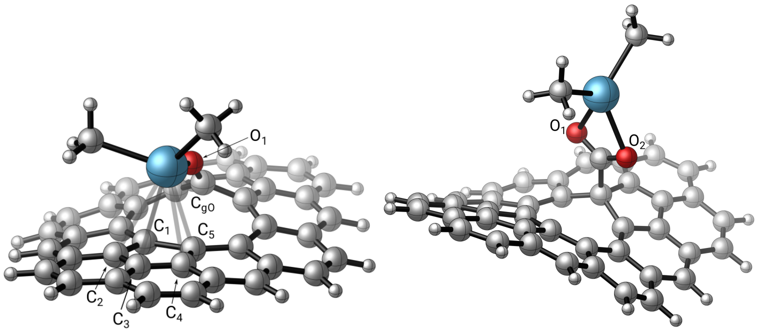

(a) (gO)-[La($CH_3$)$_2$] (1gO) (b) (gOO)-[La($CH_3$)$_2$] (1gOO)

Figure 41: Structures of the grafted (a) (gO)-[La($CH_3$)$_2$] and (b) (gOO)-[La($CH_3$)$_2$].

additionally with the pentagonal underlying graphene cycle. Also here, interestingly, the bond length of the graphene $C_{gO}$-$O_1$ group interacting with the La metal measures 1.251 $\AA$, indicating the presence of a double bond between the $C_{gO}$ and the $O_1$ atoms (confirmed by a second-order NBO analysis). The formation of the $O_1$-La bond ($O_1$-La = 2.410 $\AA$) is revealed by a second-order perturbation NBO analysis showing a strong donation from one of the $O_1$ lone pairs onto an empty d orbital of the La centre (143 kcal.mol$^{-1}$). As aforementioned, the positive charge of the graphene surface is therefore relocalised on the $O_1$ atom, the La metal strongly interacting with the surface to compensate the weak donation of the methyl ligands. The presence of this interaction has been confirmed by short La-$C_{graphene}$ distances (between 2.906 and 3.160 $\AA$) and by a second-order NBO analysis, which reveals a strong donation of the surface (51.8 kcal.mol$^{-1}$) from the C=C bonds of the underlying pentagonal graphene cycle to an empty d orbital of the La metal centre. This interaction plays a twofold role: while it stabilises the Lewis acidic La metal, providing a modular surface electronic assistance, it increases the steric hindrance around the metal, destabilising the system in the polymerisation steps that are the most sterically encumbered. The balance between these two effects will therefore influence the catalytic activity of the gO model, making it different from that of the gOO system. Interestingly, the natural charge of the La centre increases from 1.75 to 1.89 ongoing from the grafted (gO)-[La(N($SiMe_3$)$_2$)$_2$] to the grafted (gO)-[La($CH_3$)$_2$] system, showing that the less donating alkyl ligands increase the Lewis acidity of the La centre. On the other hand, 1gOO shows the monografted bicoordination mode typical of a classical supported carboxylate group ($gO_1O_2$-La = 2.491 $\AA$, $gO_2O_1$-La = 2.487 $\AA$, C-$O_1$ = 1.260 $\AA$, C-$O_2$ = 1.257 $\AA$), which forces the metal complex to rise from the surface, providing a more rigid and less sterically encumbered system.

### 3.1.2 Ethylene polymerisation.

**3.1.2.1 Reaction profiles of the 1$^{st}$ and 2$^{nd}$ insertions.** The enthalpy profile of the two first steps of the ethylene homopolymerisation is depicted in figure 42. A view of the different intermediate and transition state geometries is available in figures 43 and 44. For both 1gO and 1gOO, the reaction begins with the coordination of one ethylene molecule to the La centre. The formation of these ethylene adducts is exothermic, with a stabilising energy of -5.9

kcal.mol$^{-1}$ ($A^{Et}{}_{gO}$) and -7.1 kcal.mol$^{-1}$ ($A^{Et}{}_{gOO}$), with respect to the separated reactants. The coordination to the metal centre activates the ethylene monomers (C=C ethylene distances = 1.338 $\AA$ for both the $A^{Et}{}_{gO}$ and $A^{Et}{}_{gOO}$ compounds, compared to 1.329 $\AA$ for free ethylene), reflecting the Lewis acidity of the graphene-grafted La centre as discussed above. In the $A^{Et}{}_{gO}$ compound, interestingly, the La atom remains in interaction with the graphene surface.

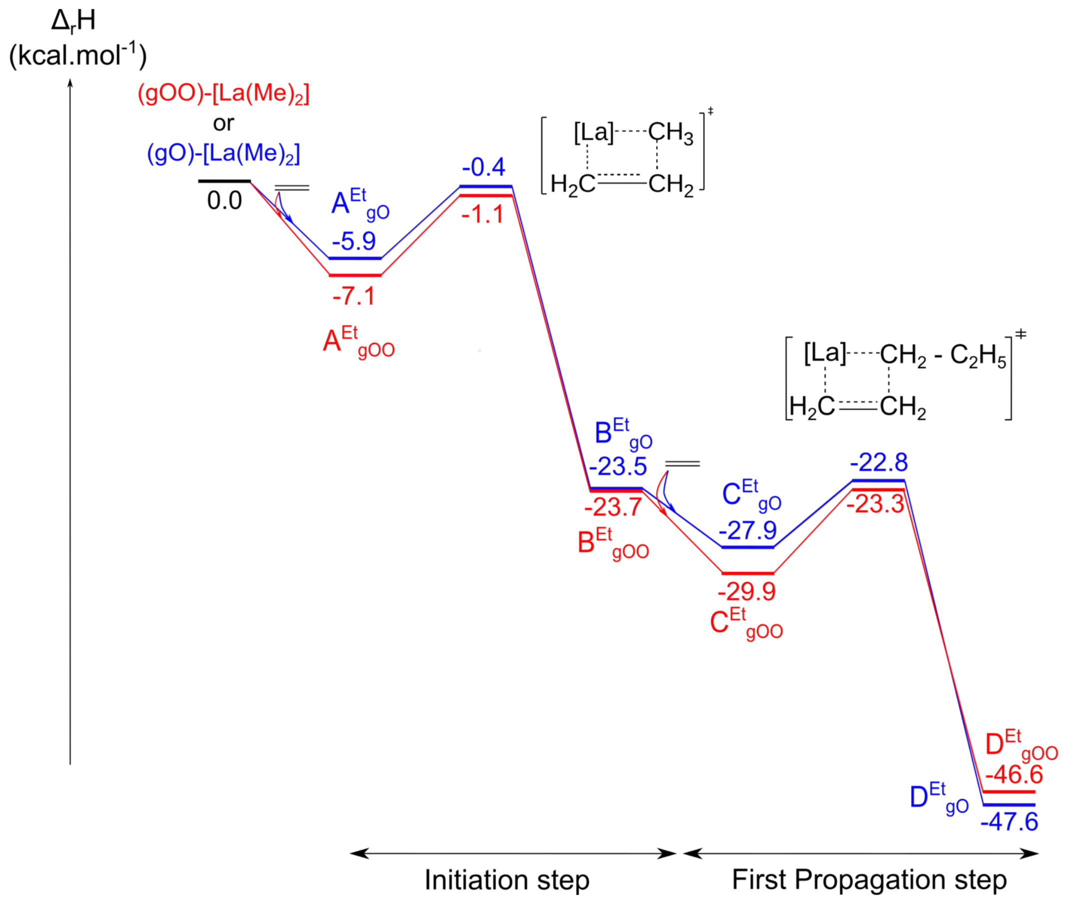

Figure 42: Reaction enthalpy profile of the initiation and first propagation step of the homopolymerisation of ethylene on the same La-Me bond.

This electronic assistance of the surface to the La centre forces the metal to stay close to the graphene surface limiting the free space around the metal and thus slightly destabilising the gO ethylene adduct for steric reasons. Starting from these adducts, the insertion of ethylene into the La-Me bond can take place *via* a four centred transition state ($2\sigma$+$2\pi$ metathesis transition state),[152, 368] with accessible enthalpy barriers of 5.5 and 6.0 kcal.mol$^{-1}$ for TS-$AB^{Et}{}_{gO}$ and TS-$AB^{Et}{}_{gOO}$, respectively, with respect to the ethylene adducts. The geometry of the corresponding transition states is quite similar in both cases and reveals a marked elongation of the La-$C_{Me}$ (La-$CH_3$ = 2.470 $\AA$ for TS-$AB^{Et}{}_{gO}$ and 2.498 $\AA$ for TS-$AB^{Et}{}_{gOO}$ *vs* 2.459 $\AA$ and 2.451 $\AA$ for 1gO and 1gOO, respectively) and of the C=C bonds (C=C = 1.384 $\AA$ for TS-$AB^{Et}{}_{gO}$ and 1.395 $\AA$ for TS-$AB^{Et}{}_{gOO}$ compared to C=C = 1.329 $\AA$ for the free ethylene). The formation of the corresponding initiation step products (propyl products) is an exothermic process, displaying an enthalpy of -23.5 and -23.7 kcal.mol$^{-1}$ for the $B^{Et}{}_{gO}$ and $B^{Et}{}_{gOO}$ species, respectively, with respect to the separated reactants. As shown in figure 43, the propyl moiety of the $B^{Et}{}_{gO}$ and $B^{Et}{}_{gOO}$ compounds interacts with the La metal through a C-H···La agostic interaction (second-order NBO stabilisation energy of 58.8 and 56.7 kcal.mol$^{-1}$ for the $B^{Et}{}_{gO}$ and $B^{Et}{}_{gOO}$ compounds, respectively).

Table 3: Enthalpy energies (in kcal.mol$^{-1}$) of the front side and the back side ethylene insertion into one of the La-Me bonds of [gO-La(CH$_3$)$_2$] and [gOO-La(CH$_3$)$_2$].

| [gO-La(CH$_3$)$_2$] | $\Delta_r$H | [gOO-La(CH$_3$)$_2$] | $\Delta_r$H |
|---|---|---|---|
| | front side | | |
| $C^{Et}{}_{gO}$ | -26.5 | $C^{Et}{}_{gOO}$ | -30.1 |
| TS-$CD^{Et}{}_{gO}$ | -23.8 | TS-$CD^{Et}{}_{gOO}$ | -23.0 |
| $D^{Et}{}_{gO}$ | -47.6 | $D^{Et}{}_{gOO}$ | -44.3 |
| | back side | | |
| $C^{Et}{}_{gO}$ | -27.9 | $C^{Et}{}_{gOO}$ | -29.9 |
| TS-$CD^{Et}{}_{gO}$ | -22.8 | TS-$CD^{Et}{}_{gOO}$ | -23.3 |
| $D^{Et}{}_{gO}$ | -46.8 | $D^{Et}{}_{gOO}$ | -46.6 |

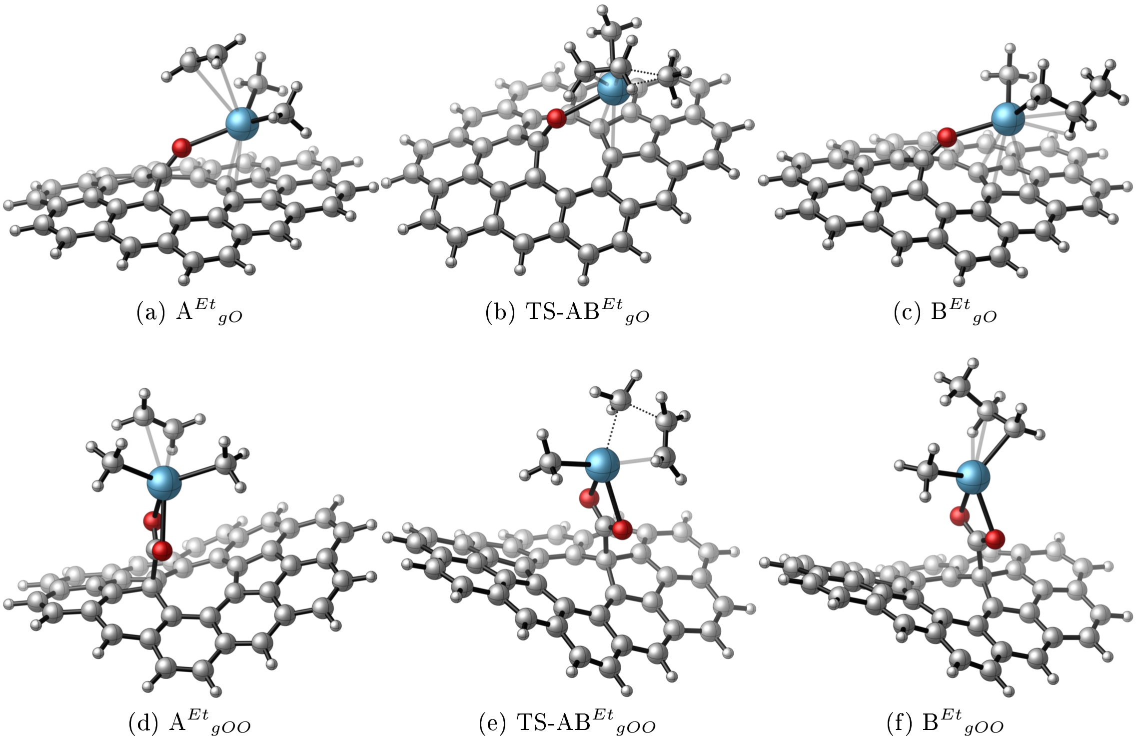
(a) $A^{Et}{}_{gO}$ (b) TS-$AB^{Et}{}_{gO}$ (c) $B^{Et}{}_{gO}$

(d) $A^{Et}{}_{gOO}$ (e) TS-$AB^{Et}{}_{gOO}$ (f) $B^{Et}{}_{gOO}$

Figure 43: Optimised structures of the complexes involved in the first ethylene insertion mediated by (gO)-[La(CH$_3$)$_2$] (1gO) and (gOO)-[La(CH$_3$)$_2$] (1gOO)

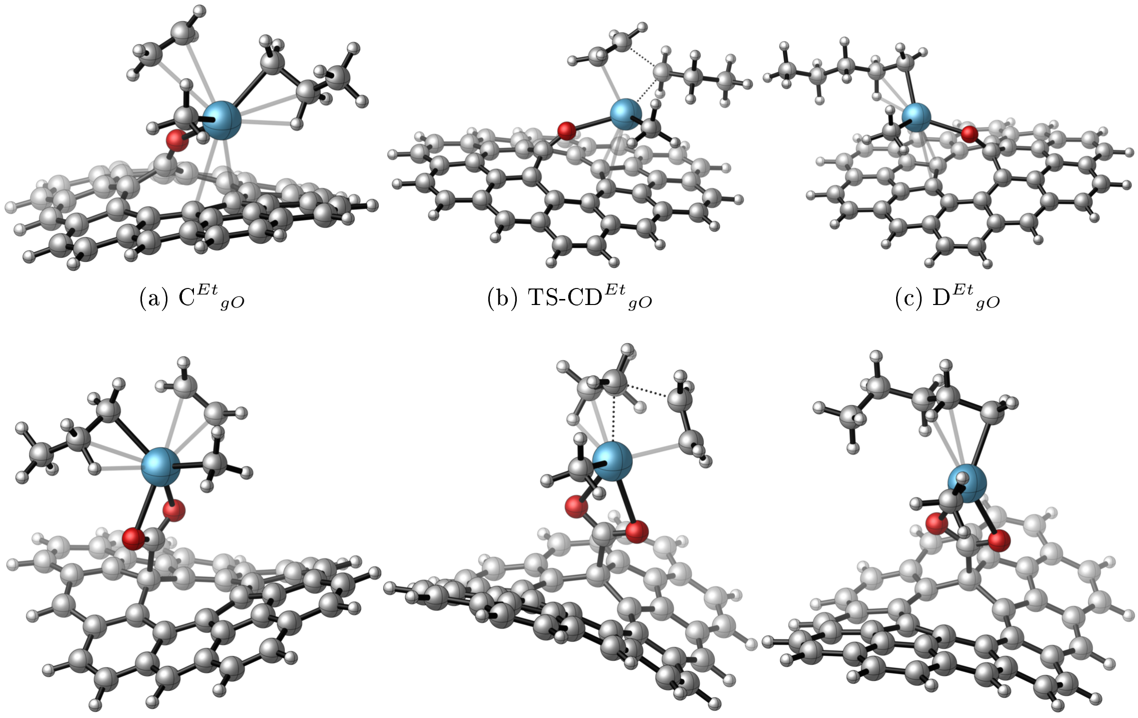

(a) $C^{Et}{}_{gO}$ (b) TS-$CD^{Et}{}_{gO}$ (c) $D^{Et}{}_{gO}$

(d) $C^{Et}{}_{gOO}$ (e) TS-$CD^{Et}{}_{gOO}$ (f) $D^{Et}{}_{gOO}$

Figure 44: Optimised structures of the complexes involved in the second ethylene insertion mediated by $B^{Et}{}_{gO}$ and $B^{Et}{}_{gOO}$.

In order to gain a deeper insight into the polymerisation process, the second ethylene insertion, corresponding to the first propagation step, has also been computed. For this second step, we considered both the front-side "migratory" and the back side "stationary" ethylene insertions, with the ethylene monomer inserting on the same side or on the opposite side of the propyl C-H $\beta$ agostic interaction, respectively (figure 45). In both cases, the formation of the final insertion products has been computed to be thermodynamically exothermic and kinetically accessible, with very similar energies for the front-side and back-side insertions (see Table 3). For sake of clarity, thus, we will limit the following discussion to the back-side insertions.

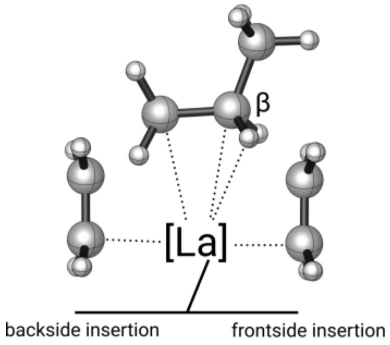

Figure 45: Schematic representation of the transition states involved in the "front side" and "back-side" second ethylene insertion, with respect to the C-H $\beta$ agostic interaction.

As described in figure 42, the first propagation step begins, as for the initiation step, by the coordination of ethylene to the metal centre, affording the thermodynamically favourable $C^{Et}{}_{gO}$ and $C^{Et}{}_{gOO}$ species (-4.4 and -6.2 kcal.mol$^{-1}$ respectively with respect to the propyl products). From these intermediates, the second insertion reaction can then take place *via* a low-energy process, displaying an activation barrier of 5.1 and 6.6 kcal.mol$^{-1}$ for the TS-$CD^{Et}{}_{gO}$ and TS-$CD^{Et}{}_{gOO}$, respectively, with respect to the previous adducts. The final $D^{Et}{}_{gO}$ and $D^{Et}{}_{gOO}$ products are obtained through a highly exothermic process (-19.7 and -16.7 kcal.mol$^{-1}$, respectively, with respect to $C^{Et}{}_{gO}$ and $C^{Et}{}_{gOO}$). The comparison of the two gO and gOO profiles from a kinetic point of view reveals that the activation barriers corresponding to the initiation and propagation steps are similar (5.5 *vs* 5.1 kcal.mol$^{-1}$ for the gO system and 6.0 *vs* 6.6 kcal.mol$^{-1}$ for the gOO system, respectively). From a thermodynamic point of view, furthermore, the exothermicity of the reaction is comparable for both the $D^{Et}{}_{gO}$ and $D^{Et}{}_{gOO}$ compounds (-47.6 *vs* -46.6 kcal.mol$^{-1}$, respectively). Therefore, both the gO- and gOO-grafted $La(CH_3)_2$ complexes are expected to efficiently catalyse the ethylene polymerisation, displaying a similar catalytic activity, from a kinetic and thermodynamic point of view.

#### 3.1.2.2 Comparaison with molecular and silica supported systems.

The enthalpy profiles in figure 42 have been compared with those reported for the molecular and silica supported analogues.[182] The molecular [$Cp_2LaMe$] and silica supported ($Si_{13}O_{20}H_{17}$)-[$La(CH_3)_2$] systems display activation barriers of 7.4 and 11.0 kcal.mol$^{-1}$, respectively, for the initiation step, and 6.1 and 4.6 kcal.mol$^{-1}$, respectively, for the first propagation step, indicating that the rate determining process is the initiation reaction. Interestingly, while the activation barriers involved in the rate determining step are comparable for the molecular and graphene grafted La systems (7.4, 6.6 and 5.5 kcal.mol$^{-1}$ for the molecular and graphene supported gOO and gO systems, respectively), they are significantly lower than those reported for the silica grafted compound (11.0 kcal.mol$^{-1}$). While behaving as the molecular compounds, the graphene grafted gO and gOO systems display a higher catalytic activity than the silica-supported analogues, underlying the important role of the graphene surface in increasing the Lewis acidity and therefore the reactivity of the grafted La systems compared to the oxygenated silica surfaces.

#### 3.1.2.3 Reaction profile on the 2$^{nd}$ arm.

From $B^{Et}{}_{gO}$ and $B^{Et}{}_{gOO}$, the insertion of a second ethylene monomer can also be achieved through the formation of a second growing chain, with the insertion of ethylene on the remaining La-Me bond. In order to gain a better insight into the propagation step, this second possibility has also been analysed. The corresponding enthalpy profile starting from $B^{Et}{}_{gO}$ and $B^{Et}{}_{gOO}$ is shown in figure 46. The optimised structure of the different intermediates and transition states are depicted in figure 47. The coordination of a second ethylene monomer to $B^{Et}{}_{gO}$ and $B^{Et}{}_{gOO}$ is an exothermic process, leading to $C'^{Et}{}_{gO}$ and $C'^{Et}{}_{gOO}$ at -4.8 and -6.3 kcal.mol$^{-1}$, respectively, with respect to $B^{Et}{}_{gO}$ and $B^{Et}{}_{gOO}$. As shown in figure 47, the propyl moiety of the $C'^{Et}{}_{gO}$ and $C'^{Et}{}_{gOO}$ compounds interacts with the La metal through a C-H···La agostic interaction with a second-order NBO stabilisation energy of 146 and 66 kcal.mol$^{-1}$, respectively. From $C'^{Et}{}_{gO}$ and $C'^{Et}{}_{gOO}$, the insertion of the ethylene monomer yields the final products $D'^{Et}{}_{gO}$ and $D'^{Et}{}_{gOO}$ through transition states TS-$C'D'^{Et}{}_{gO}$ and TS-$C'D'^{Et}{}_{gOO}$, located at 9.0 and 7.2 kcal.mol$^{-1}$, respectively, with respect to $C'^{Et}{}_{gO}$ and $C'^{Et}{}_{gOO}$.

The higher steric strain in the TS-C’D’$^{Et}{}_{gO}$ compound leads to the breaking of the agostic interaction between the propyl moiety and the La metal and to the weakening of the metal surface interaction (La-C$_{surface}$ distance in the range 3.025 – 3.280 $\AA$ for TS-C’D’$^{Et}{}_{gO}$ compared to the 2.982 – 3.149 $\AA$ range for C’$^{Et}{}_{gO}$), resulting in a more energy demanding profile. The formation of D’$^{Et}{}_{gO}$ and D’$^{Et}{}_{gOO}$ is exothermic by 23.5 and 22.6 kcal.mol$^{-1}$, respectively, with respect to B$^{Et}{}_{gO}$ and B$^{Et}{}_{gOO}$), revealing therefore an overall thermodynamically favourable and kinetically accessible process. Interestingly, while for the (gO)-[La($CH_3$)$_2$] complex, the activation barrier leading to the formation of a second growing arm is higher than that calculated for the insertion in the same arm (5.1 *vs* 9.0 kcal.mol$^{-1}$, for TS-CD$^{Et}{}_{gO}$ *vs* TS-C’D’$^{Et}{}_{gO}$, respectively), for the (gOO)-[La($CH_3$)$_2$] complex, on the other hand, the formation of a second growing arm has an activation barrier which is competitive with that of the propagation of the first growing arm (6.6 *vs* 7.2 kcal.mol$^{-1}$, for TS-CD$^{Et}{}_{gOO}$ *vs* TS-C’D’$^{Et}{}_{gOO}$, respectively). The reason of this difference has been ascribed to the different geometrical arrangement around the La metal centre in 1gO and 1gOO. While in the gOO La model the geometry of the gOO pending function forces the La metal to be raised from the surface, making the coordination sphere of the metal more accessible for bipodal polymerisation, in the gO La model, the geometrical constraints imposed by the proximity of the graphene surface cause ethylene polymerisation to take place preferentially on only one arm. A similar effect was observed on the silica ($Si_{13}O_{20}H_{17}$)-[La($CH_3$)$_2$] analogue, in which the steric hindrance imposed by the silica surface prevents the growth of two polymerisation arms.

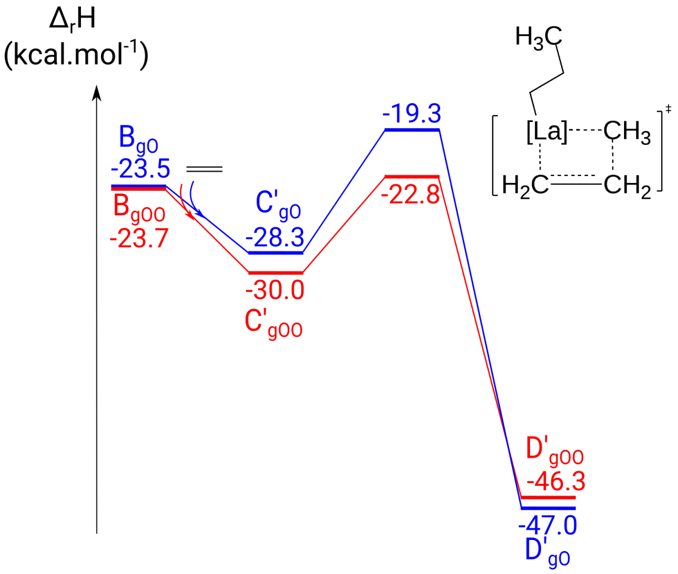

Figure 46: Calculated enthalpy profile for the insertion of a second ethylene monomer on the second La-Me bond, starting from the B$^{Et}{}_{gO}$ and B$^{Et}{}_{gOO}$ species.

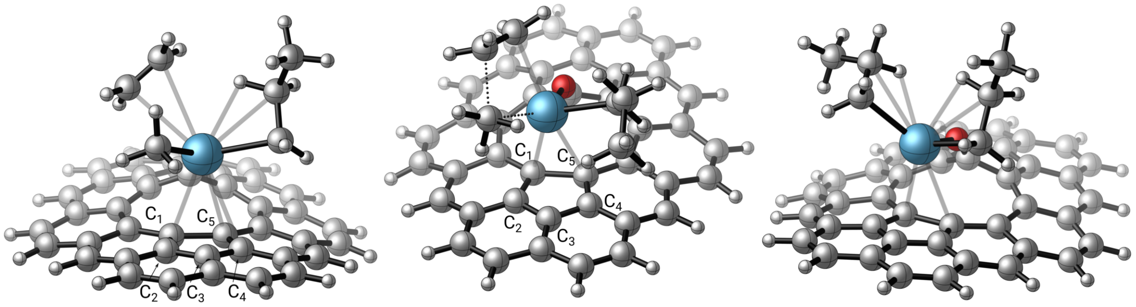

(a) C'$^{Et}{}_{gO}$ (b) TS-C'D'$^{Et}{}_{gO}$ (c) D'$^{Et}{}_{gO}$

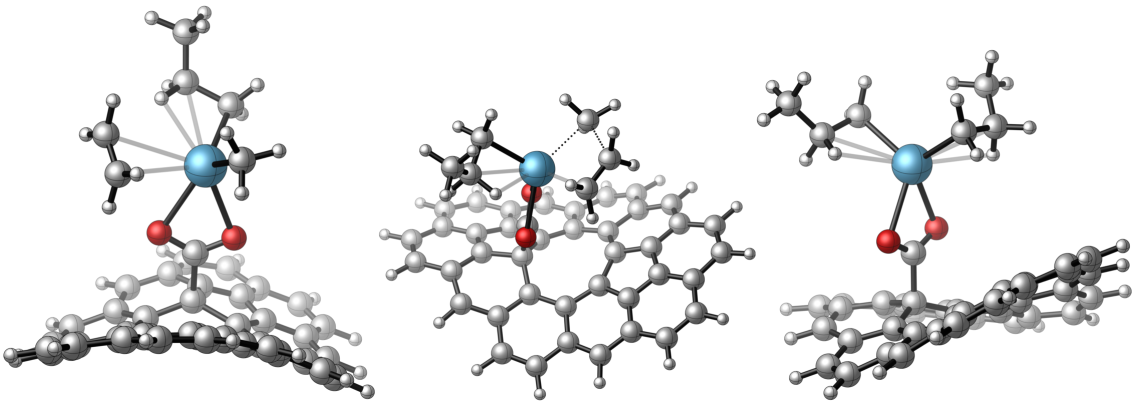

(d) C'$^{Et}{}_{gOO}$ (e) TS-C'D'$^{Et}{}_{gOO}$ (f) D'$^{Et}{}_{gOO}$

Figure 47: Optimised structures of the complexes involved in the ethylene insertion on the second La-Me bond, starting from the B$^{Et}{}_{gO}$and B$^{Et}{}_{gOO}$ species.

### 3.1.3 Butadiene homo-polymerisation.

**3.1.3.1 Reaction profiles of the 1$^{st}$ and 2$^{nd}$ insertions.** The enthalpy profile for the homopolymerisation of 1,3-butadiene, involving the 1,4-trans and 1,4-cis insertions of butadiene into the La-alkyl bond has also been computed for 1gO and 1gOO. Figure 48 shows the enthalpy profile of the first 1,4-cis and 1,4-trans 1,3-butadiene insertion. A view of the different transition states and intermediates is available in figures 49 and 50. The initiation step begins with the formation of an exothermic 1,3-butadiene adduct, corresponding to species A$^{Bu,cis}{}_{gO}$, A$^{Bu,trans}{}_{gO}$ (at -8.8 and -8.6 kcal.mol$^{-1}$) and A$^{Bu,cis}{}_{gOO}$, A$^{Bu,trans}{}_{gOO}$ (at -11.8 and -11.3 kcal.mol$^{-1}$). As shown in figure 48, the A$^{Bu}{}_{gO}$ compounds are less stable than the A$^{Bu}{}_{gOO}$ analogues by 3.0 and 2.7 kcal.mol$^{-1}$ for the cis and trans insertion respectively. This stability difference is once again ascribed to the more important steric hindrance around the metal centre in the gO model, which forces the La to move away from the surface, decreasing the electronic donation of the graphene surface to the metal (La-C$_{surface}$ distance in the range 3.028 – 3.232 Åin A$^{Bu,cis}{}_{gO}$ compared to 2.909 – 3.203 Å in (gO)-[La(CH$_3$)$_2$]). The higher is the steric hindrance, the lower is the stabilisation energy with respect to the separated reactants. Both the 1,4-trans and 1,4-cis insertions into the La-alkyl bond of the two gO and gOO grafted complexes are thermodynamically favourable, displaying enthalpy energies of -39.5 and -39.7 kcal.mol$^{-1}$ for the B$^{Bu,trans}{}_{gO}$ and B$^{Bu,trans}{}_{gOO}$ products and -42.7 and -43.3 kcal.mol$^{-1}$ for the B$^{Bu,cis}{}_{gO}$ and B$^{Bu,cis}{}_{gOO}$ products, respectively,

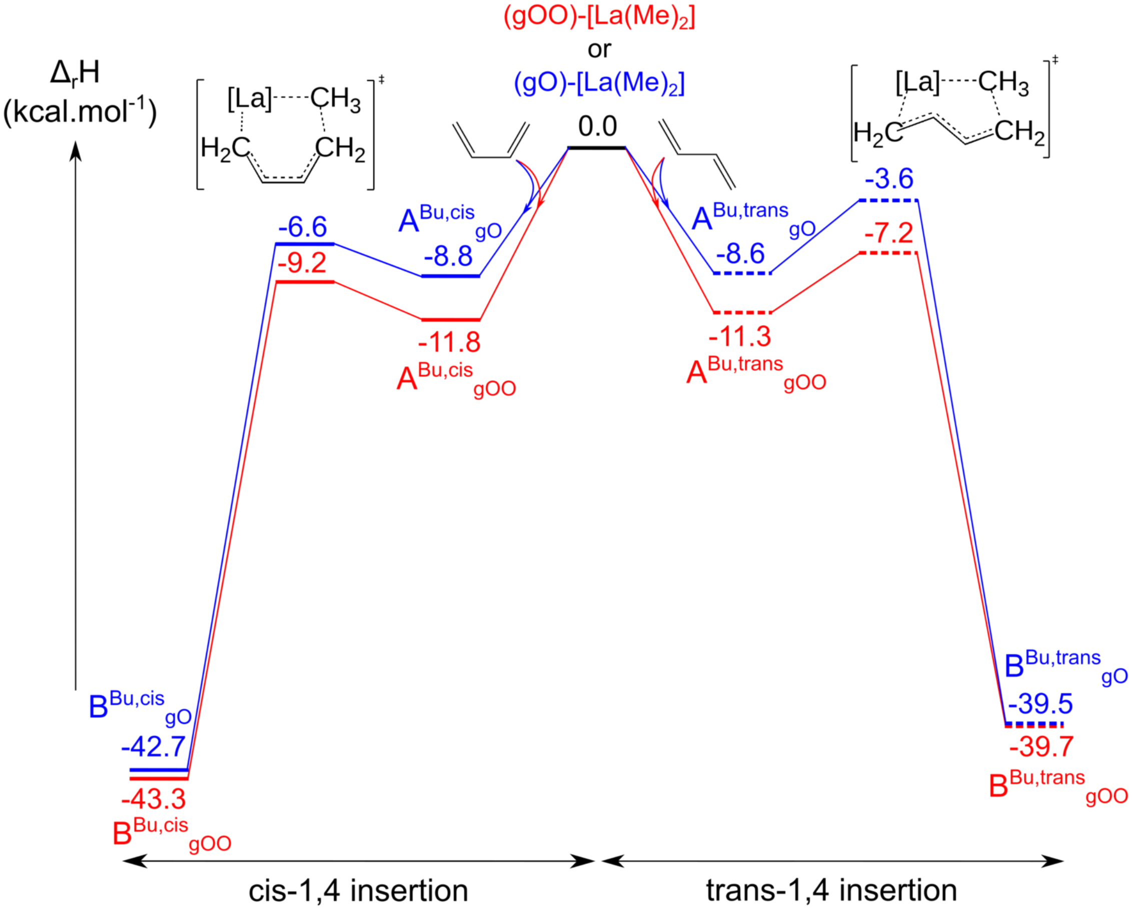

Figure 48: Calculated enthalpy profile for the first monomer insertion of the 1,3-butadiene homopolymerisation reaction mediated by (gO)-[La($CH_3$)$_2$] (1gO) and (gOO)-[La($CH_3$)$_2$] (1gOO).

with respect to the separated reagents. The strong exothermicity of these reactions is likely due to the formation of allylic La compounds which greatly differ from the alkyl products formed by ethylene insertion into the same La-alkyl bond. Both the 1,3-butadiene insertion reactions are kinetically accessible processes, displaying activation barriers for the 1,4-cis and 1,4-trans insertion of 2.2 and 5.0 kcal.mol$^{-1}$ in the gO model and 2.6 and 4.1 kcal.mol$^{-1}$ for the gOO model, respectively. For both the gOH and gOOH surfaces, therefore, the initiation profile indicates that the 1,4-cis insertion is thermodynamically and kinetically more favourable than the corresponding 1,4-trans version. This is mainly due to steric reasons as the reduced steric strain in compounds **1** and **2** allows the more sterically demanding but more electron donating 1,4-cis insertion of the 1,3-butadiene monomer.

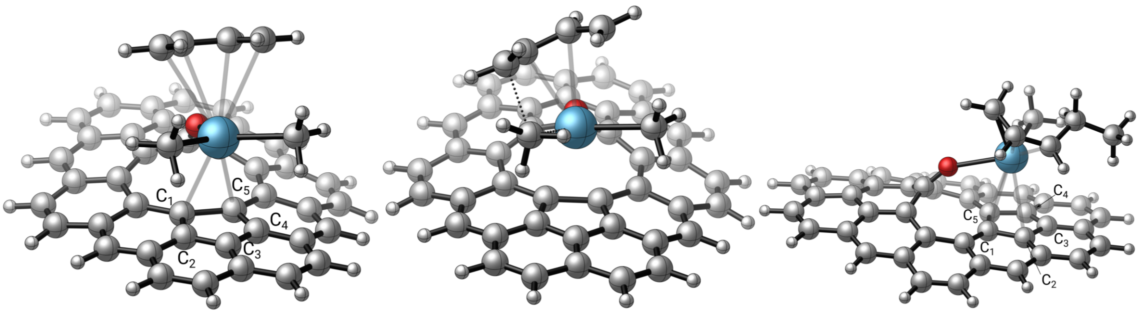

(a) $\mathrm{A}^{Bu,cis}{}_{gO}$ (b) $\mathrm{TS\text{-}AB}^{Bu,cis}{}_{gO}$ (c) $\mathrm{B}^{Bu,cis}{}_{gO}$

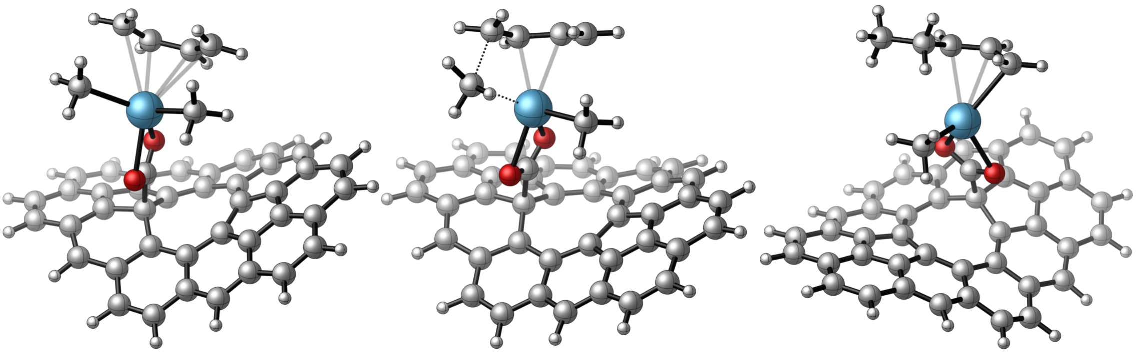

(d) $\mathrm{A}^{Bu,cis}{}_{gOO}$ (e) $\mathrm{TS\text{-}AB}^{Bu,cis}{}_{gOO}$ (f) $\mathrm{B}^{Bu,cis}{}_{gOO}$

Figure 49: Optimised structures of the complexes involved in the first 1,4-cis butadiene insertion mediated by (gO)-[La($CH_3$)$_2$] (1gO) and (gOO)-[La($CH_3$)$_2$] (1gOO)

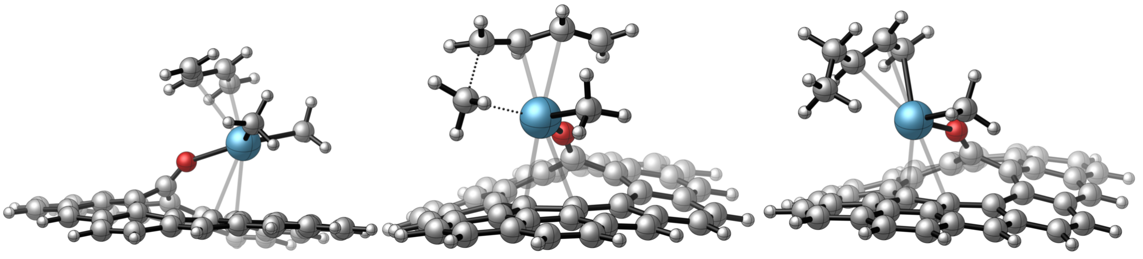

(a) $\mathrm{A}^{Bu,trans}{}_{gO}$ (b) $\mathrm{TS\text{-}AB}^{Bu,trans}{}_{gO}$ (c) $\mathrm{B}^{Bu,trans}{}_{gO}$

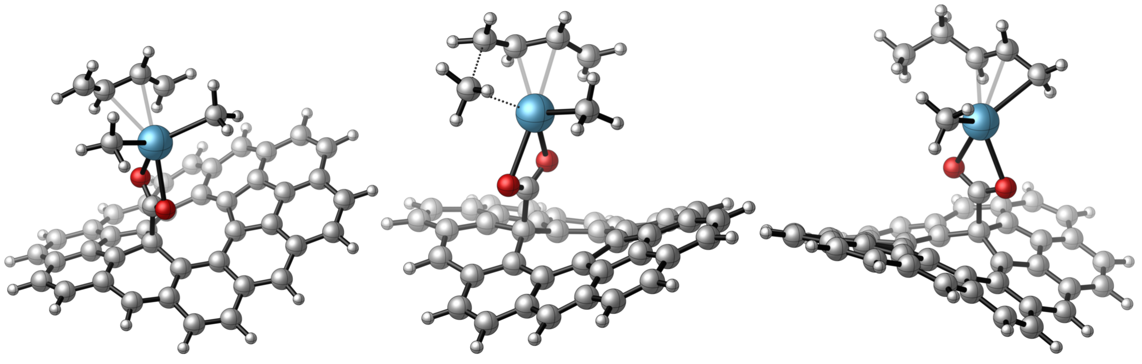

(d) $\mathrm{A}^{Bu,trans}{}_{gOO}$ (e) $\mathrm{TS\text{-}AB}^{Bu,trans}{}_{gOO}$ (f) $\mathrm{B}^{Bu,trans}{}_{gOO}$

Figure 50: Optimised structures of the complexes involved in the first 1,4-trans butadiene insertion mediated by (gO)-[La($CH_3$)$_2$] (1gO) and (gOO)-[La($CH_3$)$_2$] (1gOO)

The propagation step and the stereoselectivity of the polymerisation have been then investigated. All the possible sequences, *i.e.*, cis-cis, cis-trans, trans-cis and trans-trans, have been considered (see Table 4 and figures 54 and 55 for a view of the different transition states and intermediates). Figure 51 shows the enthalpy profile of the second 1,4-cis and 1,4-trans 1,3-butadiene insertion, starting from the most thermodynamically stable $\mathrm{B}^{Bu,cis}{}_{gO}$ and $\mathrm{B}^{Bu,cis}{}_{gOO}$ compounds. The propagation step begins with the formation of an exothermic 1,3-butadiene adduct, corresponding to species $\mathrm{C}^{Bu,cis,cis}{}_{gO}$, $\mathrm{C}^{Bu,cis,trans}{}_{gO}$ (-46.3 and -44.9 kcal.mol$^{-1}$) and $\mathrm{C}^{Bu,cis,cis}{}_{gOO}$, $\mathrm{C}^{Bu,cis,trans}{}_{gOO}$ (-52.2 and -50.1 kcal.mol$^{-1}$). As shown in figure 51, the $\mathrm{C}^{Bu}{}_{gO}$ compounds are less stable than the $\mathrm{C}^{Bu}{}_{gOO}$ analogues by 5.9 and 5.2 kcal.mol$^{-1}$ for the cis and trans insertion respectively. The increase of the steric strain during the propagation step forces the La centre of the gO model to move away from the surface, resulting in the breaking of the interaction between the gO graphene surface and the metal, as evidenced by the increase of the La – $\mathrm{C}_{surface}$ bond distances by around 1.5 $\mathring{A}$ ongoing from $\mathrm{B}^{Bu,cis}{}_{gO}$ to $\mathrm{C}^{Bu,cis,cis}{}_{gO}$ and . Interestingly, the formation of all the insertion products is exothermic (-65.3 and -64.8 kcal.mol$^{-1}$ for $\mathrm{D}^{Bu,cis,cis}{}_{gO}$ and $\mathrm{D}^{Bu,cis,trans}{}_{gO}$ and -71.0 and -67.9 kcal.mol$^{-1}$ for $\mathrm{D}^{Bu,cis,cis}{}_{gOO}$ and $\mathrm{D}^{Bu,cis,trans}{}_{gOO}$, respectively) but while for the gOO models, the 1,4-cis insertion product is more stable by 3.1 kcal.mol$^{-1}$ than the 1,4-trans insertion one, for the gO models, the 1,4-cis and 1,4-trans insertion compounds are energetically equivalent (enthalpy difference of 0.5 kcal.mol$^{-1}$). From a kinetic point of view, similarly, all the insertion processes are accessible but while for the gOO model the 1,4-cis insertion barrier is significantly lower than that of the 1,4-trans insertion (6.6 *vs* 10.9 kcal.mol$^{-1}$ for the cis-cis *vs* the cis-trans sequence), for the gO model the enthalpy difference between the TS-$\mathrm{CD}^{Bu,cis,cis}{}_{gO}$ and TS-$\mathrm{CD}^{Bu,cis,trans}{}_{gO}$ barriers (5.0 and 7.5 kcal.mol$^{-1}$) is not large enough to state the preferential formation of the cis-cis rather than the cis-trans polymer. The [gOO-La$(CH_3)_2$] grafted systems would therefore preferentially form the 1,4-cis-polybutadiene, whereas the [gO-La$(CH_3)_2$] system would afford a random 1,4-polybutadiene. The reason of this different behaviour between the gO and gOO models has been ascribed to the higher flexibility of the La coordination mode on the gO model compared to the gOO one. In the gO model, indeed, the ability of the lanthanum atom to modulate both the electronic assistance of the surface and the steric hindrance of its coordination sphere, makes the cis-cis and the cis-trans insertions energetically comparable. Experimentally, however, due to the poor regioselectivity of the graphene functionalisation reaction,[353] both types of phenolic and carboxylic OH groups co-exist on the oxygenated graphene surface. Both sites will therefore (co)-polymerise the butadiene molecule, providing the simultaneous production of both 1,4-cis and random types of polymers.

**3.1.3.2 Comparaison with molecular and silica grafted lanthanum complexes.** Silica-supported La systems also catalyse the 1,3-butadiene polymerisation, experimentally leading to the formation of 1,4-cis-polybutadiene species predominantly. A theoretical study on the

Table 4: Enthalpy energies (in kcal.mol$^{-1}$) of the first propagation step of the 1,3-butadiene polymerisation mediated by [gO-La(CH$_3$)$_2$] (1gO) and [gOO-La(CH$_3$)$_2$] (1gOO)

| [gO-La(CH$_3$)$_2$] | $\Delta_r$H | [gOO-La(CH$_3$)$_2$] | $\Delta_r$H |
|---|---|---|---|
| $C^{Bu,cis,cis}{}_{gO}$ | -46.3 | $C^{Bu,cis,cis}{}_{gOO}$ | -52.2 |
| $TS\text{-}CD^{Bu,cis,cis}{}_{gO}$ | -41.3 | $TS\text{-}CD^{Bu,cis,cis}{}_{gOO}$ | -45.6 |
| $D^{Bu,cis,cis}{}_{gO}$ | -65.3 | $D^{Bu,cis,cis}{}_{gOO}$ | -71.0 |
| $C^{Bu,cis,trans}{}_{gO}$ | -44.9 | $C^{Bu,cis,trans}{}_{gOO}$ | -50.1 |
| $TS\text{-}CD^{Bu,cis,trans}{}_{gO}$ | -37.4 | $TS\text{-}CD^{Bu,cis,trans}{}_{gOO}$ | -39.2 |
| $D^{Bu,cis,trans}{}_{gO}$ | -64.8 | $D^{Bu,cis,trans}{}_{gOO}$ | -67.9 |
| $C^{Bu,trans,cis}{}_{gO}$ | -39.9 | $C^{Bu,trans,cis}{}_{gOO}$ | -45.0 |
| $TS\text{-}CD^{Bu,trans,cis}{}_{gO}$ | -36.1 | $TS\text{-}CD^{Bu,trans,cis}{}_{gOO}$ | -39.2 |
| $D^{Bu,trans,cis}{}_{gO}$ | -57.9 | $D^{Bu,trans,cis}{}_{gOO}$ | -65.5 |
| $C^{Bu,trans,trans}{}_{gO}$ | -42.3 | $C^{Bu,trans,trans}{}_{gOO}$ | -46.5 |
| $TS\text{-}CD^{Bu,trans,trans}{}_{gO}$ | -33.9 | $TS\text{-}CD^{Bu,trans,trans}{}_{gOO}$ | -37.3 |
| $D^{Bu,trans,trans}{}_{gO}$ | -65.4 | $D^{Bu,trans,trans}{}_{gOO}$ | -66.4 |

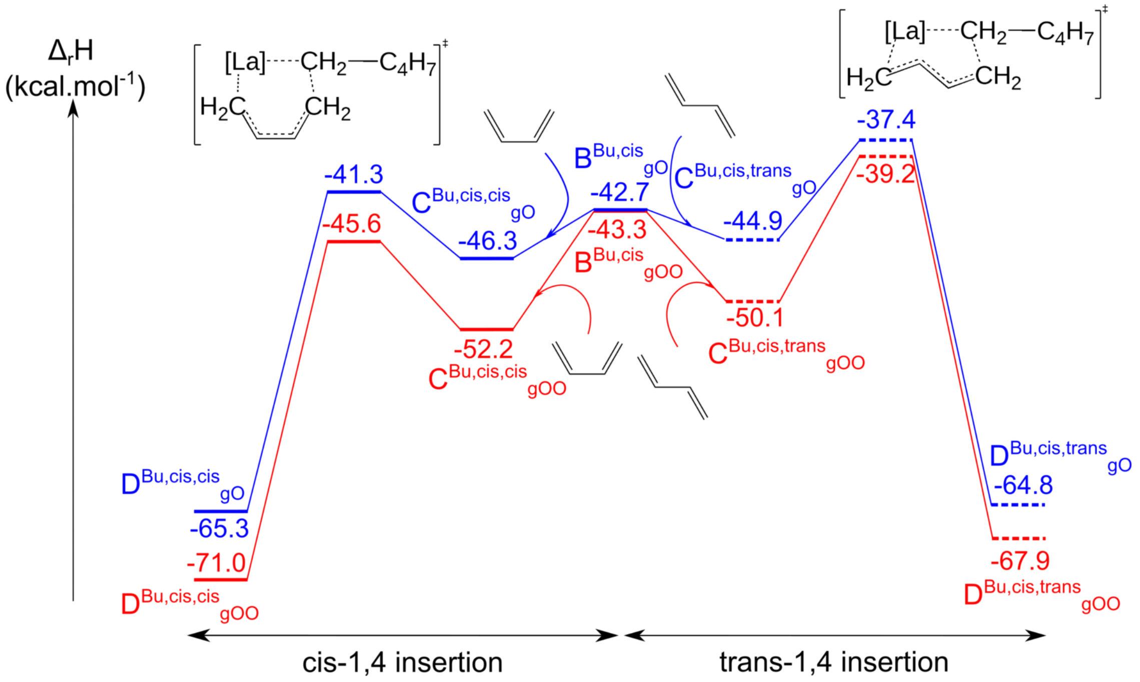

Figure 51: Calculated enthalpy profile for the second monomer insertion of the 1,3-butadiene homopolymerisation mediated by $B^{Bu,cis}{}_{gO}$ and $B^{Bu,cis}{}_{gOO}$.

silica ($Si_{13}O_{20}H_{17}$)-[$La(CH_3)_2$] model further supported this result, showing that the 1,4-cis-polybutadiene sequence corresponds to the kinetic product, whereas the 1,4-trans-polybutadiene sequence to the thermodynamic one.[182] As observed for the graphene supported systems, the initiation profile indicates the preferential insertion of the 1,4 cis monomer, with the rate limiting step corresponding to the second 1,3-butadiene insertion for both the cis-cis (barrier height 7.7 kcal.mol$^{-1}$) and cis-trans (barrier height 13.9 kcal.mol$^{-1}$) sequences. Interestingly, the formation of both the 1,4-cis- and 1,4-trans-polybutadiene products of the second insertion is more thermodynamically favourable by around 10 kcal.mol$^{-1}$ for the graphene-grafted La systems than for the silica-grafted ones, suggesting a higher catalytic activity with the graphene-grafted La compounds. Lanthanide-based molecular complexes, finally, lead to the formation of mainly 1,4-trans polybutadiene polymers, molecular catalysts showing both high activity and cis-1,4-selectivity being rather scarse.[371, 241, 372]

### 3.1.4 Ethylene butadiene copolymerisation.

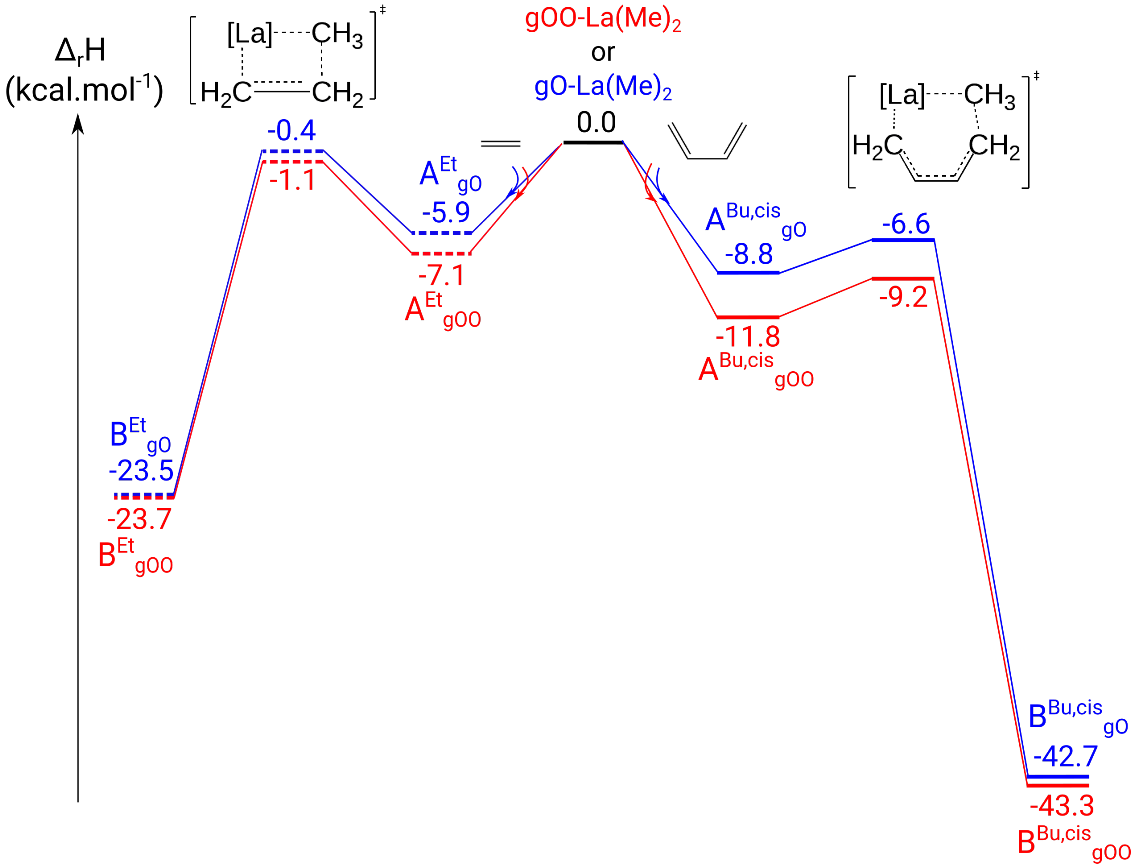

Figure 52: Calculated enthalpy profile of the first monomer insertion in the copolymerisation of ethylene and 1,3-butadiene.

In order to predict the catalytic behaviour of **1** and **2** in the ethylene-1,3-butadiene copolymerisation reaction, we compared the ethylene and 1,3-butadiene insertions for both the initiation and propagation steps. The enthalpy profile for the first insertion of the ethylene and 1,3-butadiene monomers is shown in figure 52. A view of the geometry of the involved transition states and intermediates is shown in figures 43 and 49. For sake of clarity, for the 1,3 butadiene, only the more favourable 1,4-cis insertion has been considered. As aforementioned, the reaction begins with the formation of exothermic adducts displaying a stabilisation energy of -8.8 and -11.8 kcal.mol$^{-1}$ for A$^{Bu,cis}{}_{gO}$ and A$^{Bu,cis}{}_{gOO}$ and -5.9 and -7.1 kcal.mol$^{-1}$ for A$^{Et}{}_{gO}$ and A$^{Et}{}_{gOO}$, with respect to the separated reactants. The cis 1,3-butadiene adducts are therefore more stable than the corresponding ethylene ones by 2.9 and 4.7 kcal.mol$^{-1}$ for the gO and gOO species, respectively. For both the gO and gOO systems, indeed, the 1,3-butadiene monomer is more electron donating than ethylene, better stabilising the Lewis acidic graphene-grafted La centre. The barriers for the first insertion measures 2.2 and 2.6 kcal.mol$^{-1}$ for TS-AB$^{Bu,cis}{}_{gO}$ and TS-AB$^{Bu,cis}{}_{gOO}$ and 5.5 and 6.0 kcal.mol$^{-1}$ for TS-AB$^{Et}{}_{gO}$ and TS-AB$^{Et}{}_{gOO}$, indicating that the 1,4-cis 1,3-butadiene insertion is kinetically more favourable than the ethylene one. From a thermodynamic point of view, furthermore, the 1,4-cis 1,3-butadiene insertion products are considerably more favourable than the ethylene insertion ones, by 19.2 and 19.6 kcal.mol$^{-1}$ for the gO and gOO complexes, respectively, reflecting the high stability of the B$^{Bu,cis}{}_{gO}$ and B$^{Bu,cis}{}_{gOO}$ allylic species. Starting from these kinetically and thermodynamically more favourable products, *i.e.* B$^{Bu,cis}{}_{gO}$ and B$^{Bu,cis}{}_{gOO}$, the enthalpy profile for the second insertion of the ethylene and 1,3-butadiene monomers has been computed (figure 53). A view of the different transition states and intermediates is available in figures 54, 55 and 56. As for the initiation step, the barriers involved in the second 1,4-cis 1,3 butadiene insertion are lower than those corresponding to the ethylene ones by 5.9 and 5.8 kcal.mol$^{-1}$ for the gO and gOO complexes, respectively. Thermodynamically, in the same way, the D$^{Bu,cis,cis}{}_{gO}$ and D$^{Bu,cis,cis}{}_{gOO}$ products are more favourable than the ethylene insertion ones, by 16.4 and 17.7 kcal.mol$^{-1}$ for the gO and gOO complexes, respectively, with respect to the B$^{Bu,cis}{}_{gO}$ and B$^{Bu,cis}{}_{gOO}$ species. Also in the propagation step, therefore, the higher stability of the allylic products compared to the alkyl ones drive the reaction toward the insertion of the 1,3-butadiene only, preventing the formation of alternating ethylene/ butadiene copolymers, but still allowing the formation of block copolymers. Experimentally, a similar result has been reported for silica-supported neodymium and dysprosium complexes, which copolymerise ethylene and butadiene, affording mainly block copolymers.[145]

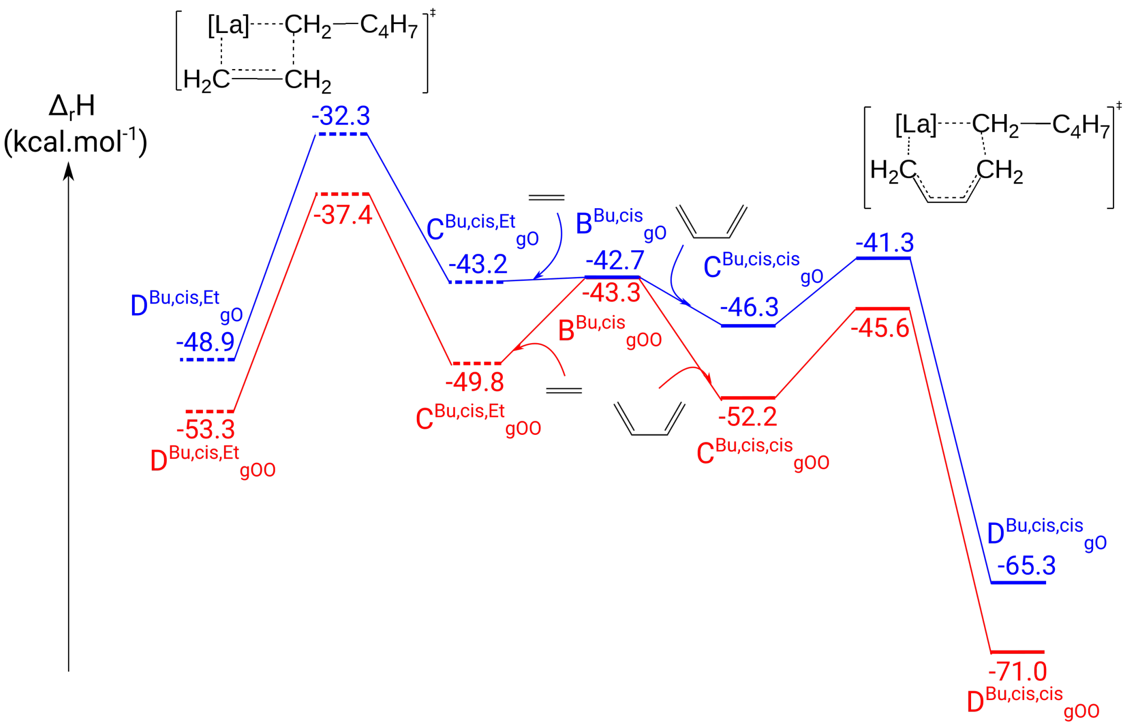

Figure 53: Calculated enthalpy profile of the second monomer insertion in the copolymerisation of ethylene and 1,3-butadiene mediated by $B^{Bu,cis}{}_{gO}$ and $B^{Bu,cis}{}_{gOO}$.

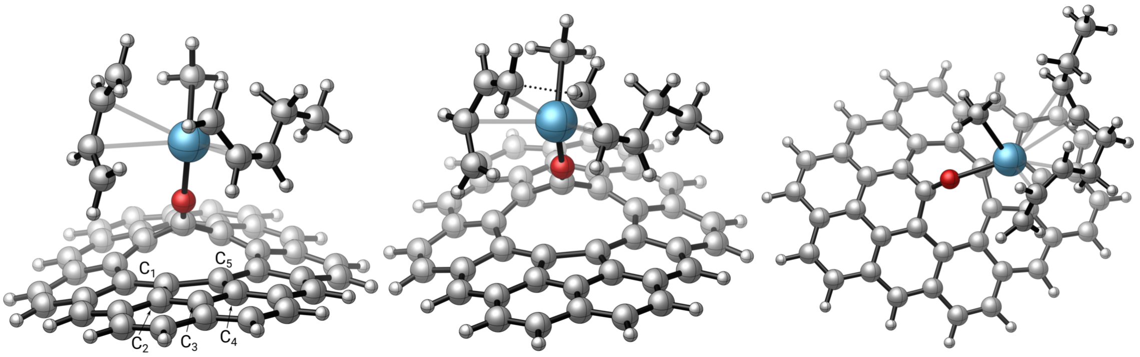

(a) $C^{Bu,cis,cis}{}_{gO}$ (b) TS-$CD^{Bu,cis,cis}{}_{gO}$ (c) $D^{Bu,cis,cis}{}_{gO}$

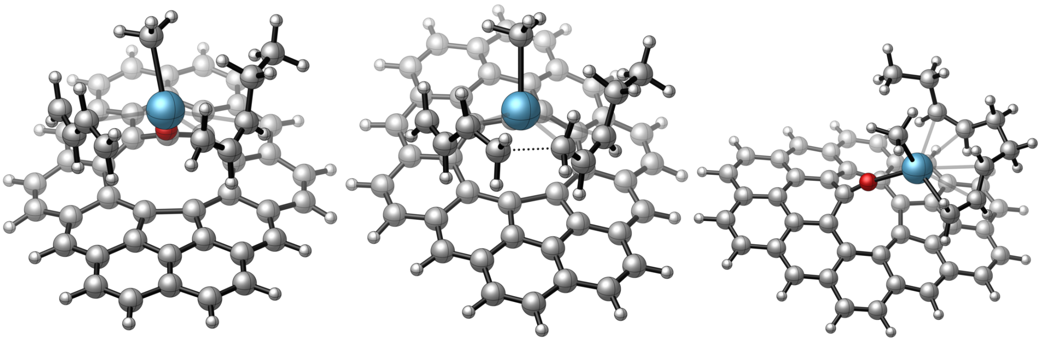

(d) $C^{Bu,cis,trans}{}_{gO}$ (e) TS-$CD^{Bu,cis,trans}{}_{gO}$ (f) $D^{Bu,cis,trans}{}_{gO}$

Figure 54: Optimised structures of the complexes involved in the second 1,3-butadiene insertion mediated by $B^{Bu,cis}{}_{gO}$.

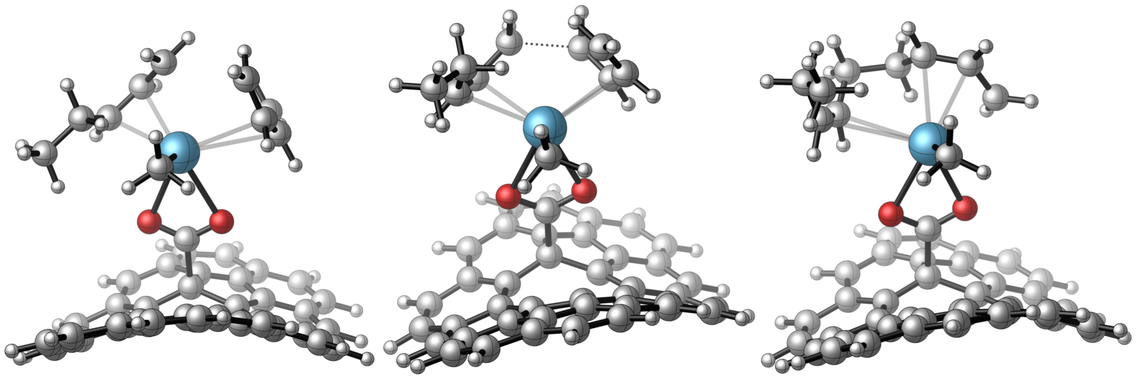

(a) $\mathrm{C}^{Bu,cis,cis}{}_{gOO}$ (b) $\mathrm{TS\text{-}CD}^{Bu,cis,cis}{}_{gOO}$ (c) $\mathrm{D}^{Bu,cis,cis}{}_{gOO}$

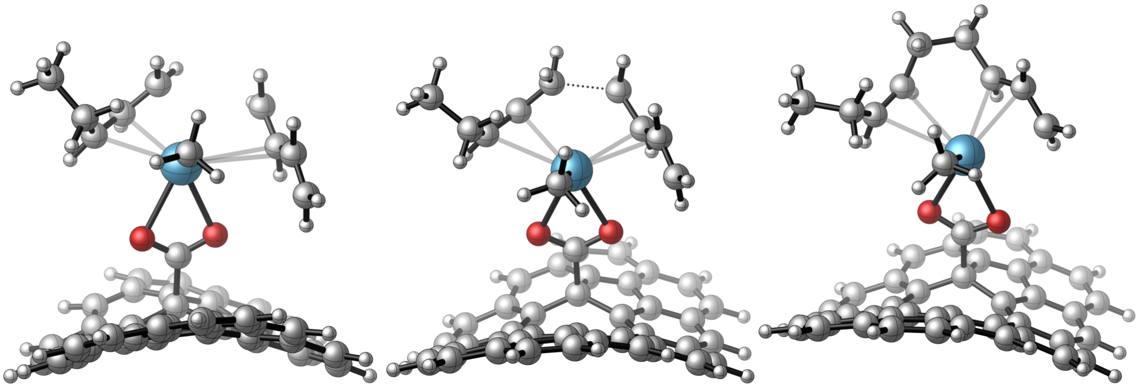

(d) $\mathrm{C}^{Bu,cis,trans}{}_{gOO}$ (e) $\mathrm{TS\text{-}CD}^{Bu,cis,trans}{}_{gOO}$ (f) $\mathrm{D}^{Bu,cis,trans}{}_{gOO}$

Figure 55: Optimised structures of the complexes involved in the second 1,3-butadiene insertion mediated by $\mathrm{B}^{Bu,cis}{}_{gOO}$.

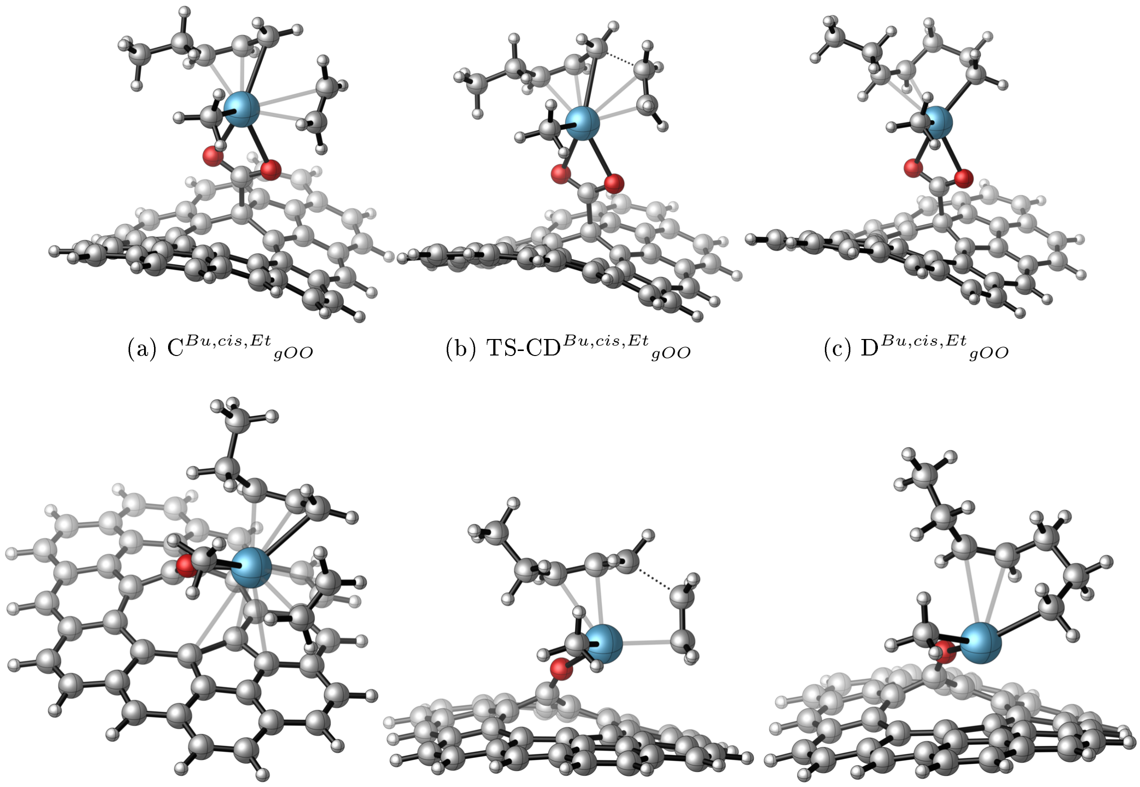

(a) $\mathrm{C}^{Bu,cis,Et}{}_{gOO}$ (b) TS-$\mathrm{CD}^{Bu,cis,Et}{}_{gOO}$ (c) $\mathrm{D}^{Bu,cis,Et}{}_{gOO}$

(d) $\mathrm{C}^{Bu,cis,Et}{}_{gO}$ (e) TS-$\mathrm{CD}^{Bu,cis,Et}{}_{gO}$ (f) $\mathrm{D}^{Bu,cis,Et}{}_{gO}$

Figure 56: Optimised structures of the complexes involved in the second ethylene insertion in the ethylene and 1,3-butadiene copolymerisation mediated by $\mathrm{B}^{Bu,cis}{}_{gO}$ and $\mathrm{B}^{Bu,cis}{}_{gOO}$.

### 3.1.5 Styrene homo-polymerisation

Syndiotactic polystyrene (sPS) is an attractive engineering plastic potentially usable for many industrial applications due to its high melting point (ca. 270 °C), high crystallinity, low permeability to gases, low dielectric constant, and good chemical and temperature resistance.[373, 374, 375] However, its brittleness is the main drawback limiting its processability. To tackle this issue, several strategies have been envisaged: i) blending or postmodification of sPS; ii) polymerisation of functionalised styrene derivatives, or iii) copolymerisation of styrene with other monomers.[376, 377] The latter approach was found effective and versatile to fine-tune the properties of sPS,[378] more particularly *via* syndioselective copolymerisation of styrene with ethylene.[379] The copolymerisation of those two monomers is quite challenging due to their strikingly different reactivity. As a result, most of the group 4 catalysts active for sPS production only provided 'ethylene-styrene co-polymers', featuring no stereoregularity and amounts of incorporated styrene below 50 mol %. Those issues were overcome by the development of group 3 catalysts, independently disclosed by Hou and co-workers.[380] Yet, the number of effective catalytic systems for sPSE synthesis remains quite limited to date.[226] In a view of the results obtained for the polymerisation of ethylene and butadiene we decided to study the catalytic activity of the graphene supported La alkyl compounds (gO)-[La($\mathrm{CH_3}$)$_2$] (1gO) and (gOO)-[La($\mathrm{CH_3}$)$_2$] (1gOO) in the homo-polymerisation of styrene and the co-polymerisation of

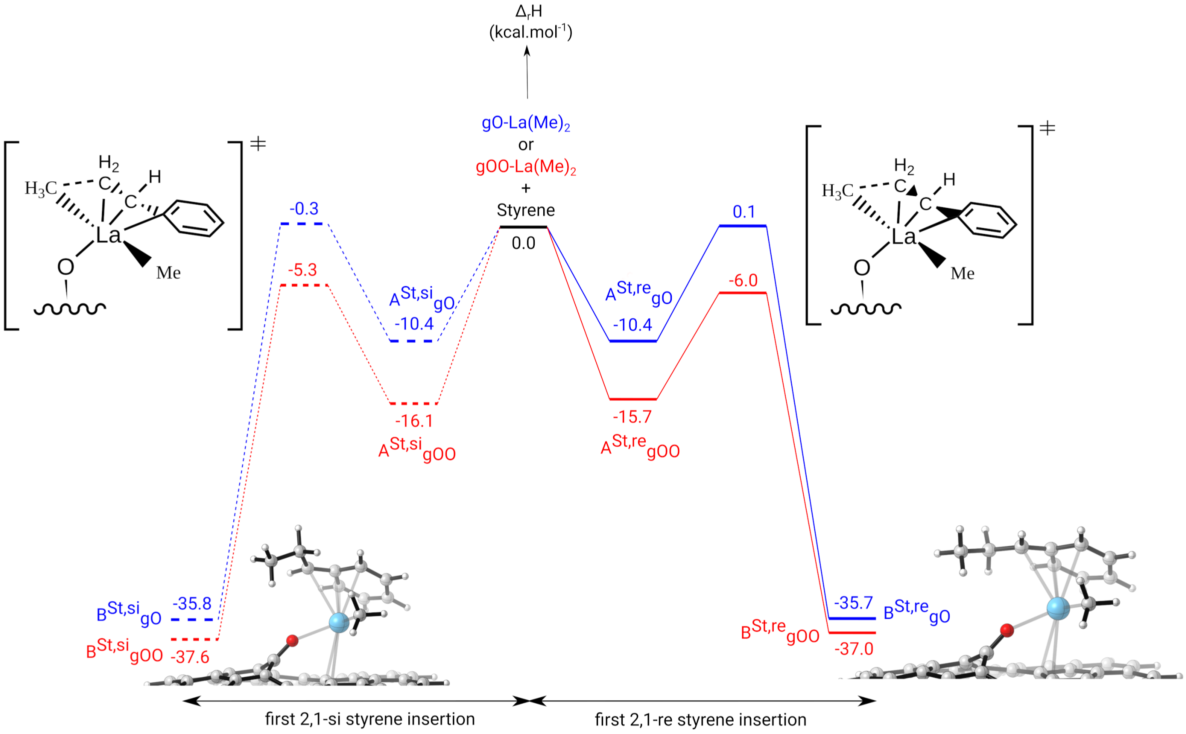

Figure 57: Computed enthalpy profile for the first 2,1-insetion of styrene onto the La-Me bond at room temperature. The blue and red pathways correspond to the gO- and gOO-grafted catalysts.

styrene with ethylene.

The first styrene insertion was computed (see Figure 57) for the two possible grafted complexes 1gO and 1gOO. A view of the different intermediate and transition state geometries is available in Appendix A, figures 157 to 162. It should be noted that only the 2,1 insertion of styrene, which is the most favourable insertion reaction,[241] was considered but the reactivity of the two styrene enantiofaces (or phenyl orientation as there is no chiral centre for the first insertion) were investigated. As expected due to the lack of stereogenic centre as well as a reduced steric congestion around the metal centre, there is no influence of the enantioface of the styrene on the energetic parameters of the first insertion. For instance, the coordination energy, insertion barrier and product energies are similar within the precision of the method for a given grafting mode. For the (gO)-[La(Me)$_2$] catalyst, the styrene coordination is exothermic by 10.4 kcal.mol$^{-1}$, indicating an acidic metal centre. From this adduct, the insertion barrier is 10.5 kcal.mol$^{-1}$ or 10.7 kcal.mol$^{-1}$, if we consider respectively the *re* or *si* enantiofaces, in line with a facile insertion to yield a very stable $\eta^3$-styryl complex (-35.7 (*re*) or 35.8 (*si*) kcal.mol$^{-1}$ with respect to the entrance channel). For (gOO)-[La(Me)$_2$], the coordination of styrene is stronger than for the (gO)-[La(Me)$_2$] catalyst (-15.7 (*re*), -16.1 (*si*) kcal.mol$^{-1}$ *vs.* -10.4 kcal.mol$^{-1}$). This difference in coordination energy is not associated to the sterics, since both metal centres seem accessible, as shown in Figure 58). The styrene, indeed, is $\eta^6$ coordinated to the lanthanide centre is both cases, as evidenced by the presence of six short La-C$_{phenyl}$ distances, in the range 3.054-3.134 $\AA$ for $A^{St,re}{}_{gO}$ and 3.077-3.125 $\AA$ for $A^{St,re}{}_{gOO}$, and by a second-order perturbation NBO analysis that reveals a donation from the styrene carbons to an empty d orbital of the La

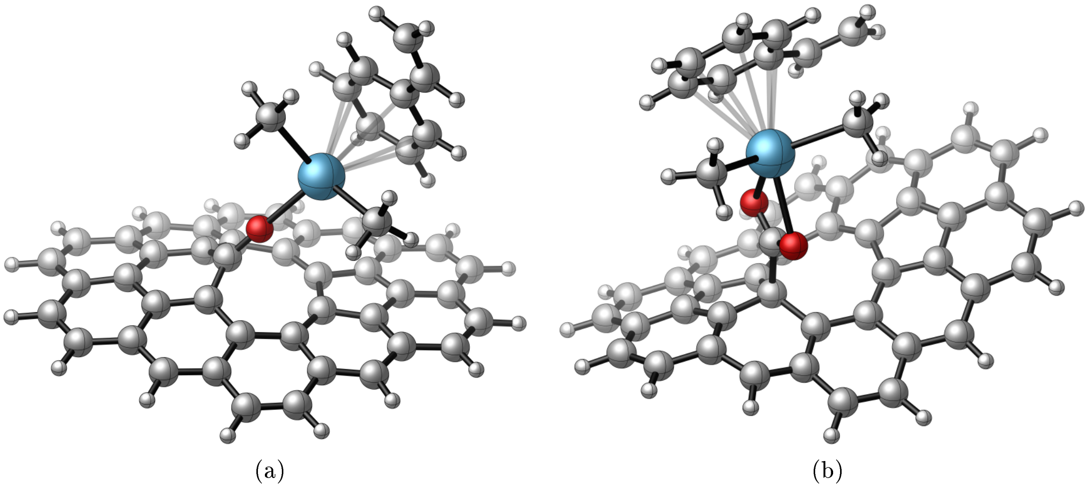
(a) (b)

Figure 58: Geometry of the styrene adducts for the two grafted complexes : a) $A^{St,re}{}_{gO}$ and $A^{St,re}{}_{gOO}$.

metal of 89.60 and 86.07 kcal.mol$^{-1}$ for gO and gOO respectively. In the gO case, however, the styrene coordination forces the metal to rise from the surface, providing the lengthening of the La-surface distance from the 2.906 - 3.160 $\AA$ range in the free catalyst to the 3.940 - 4.562 $\AA$ range for $A^{St,re}{}_{gO}$. This causes the break of the stabilising interaction between the graphene surface and the metal centre, as also confirmed by a second order NBO analysis indicating a donation of 51.8 kcal.mol$^{-1}$ for gO-La(Me)$_2$ and 0 kcal.mol$^{-1}$ for $A_{gO}$).

For the (gOO)-[La(Me)$_2$] catalyst, the insertion barrier is 9.7 or 10.8 kcal.mol$^{-1}$, if we consider respectively the *re* or *si* enantiofaces, that is quite similar to the one found for the other grafting mode. The formation of the $\eta^3$-styryl complex is also exothermic, measuring -37.6 and -37.0 kcal.mol$^{-1}$. The low barrier can be explained by the strength of the styrene coordination that has already activated the $\pi$ bond (C=C styrene distance = 1.381 and 1.391 $\AA$ for TS-$AB^{St,re}{}_{gO}$ and TS-$AB^{St,re}{}_{gOO}$, respectively, compared to 1.337 $\AA$ for free styrene). The thermodynamic of the reaction, in addition, is in line with the stability of the allylic form of the $\eta^3$-styryl complex compared to the alkyl starting material. Interestingly, the barriers obtained for the styrene insertion are very low compared to the barrier that are usually obtained for efficient styrene lanthanide based catalysts which are usually around 20 kcal.mol$^{-1}$ for neutral systems [381, 382]. These barriers are comparable to the one obtained for the highly active cationic scandium complex of Hou's group [226] making therefore this catalyst very promising in terms of activity.

In order to further investigate the activity and the stereoselectivity of the grafted catalysts, the second and third styrene insertions were computed (Figures 59 and 61). As no thermodynamic nor kinetic preference was found for the first insertion, the second insertion was only computed from the *re* insertion products of the first insertion ($B^{St,re}{}_{gO}$ and $B^{St,re}{}_{gOO}$). For the second insertion, the coordination of the styrene molecule is becoming less favourable than for

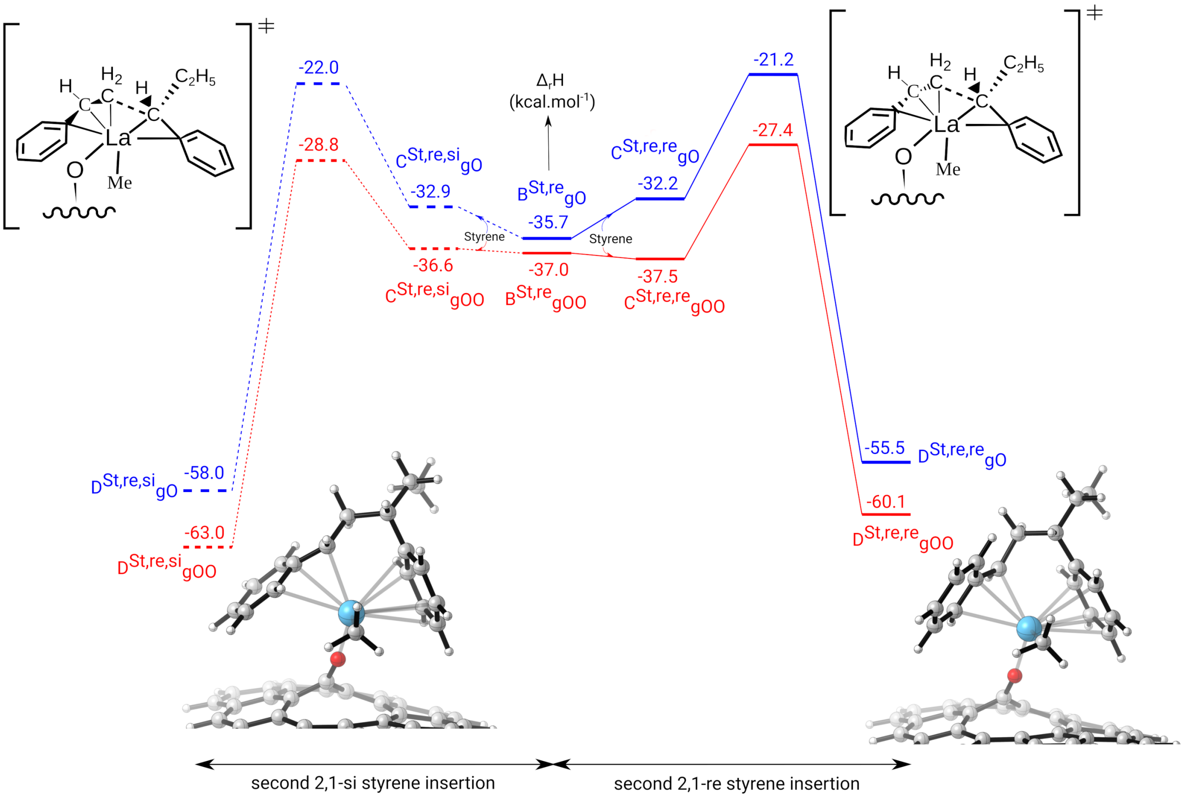

Figure 59: Computed Enthalpy profile for the second 2,1-insetion of styrene onto the La-Me bond at room temperature. The blue and red pathways correspond to the gO- and gOO-grafted compounds.

the first insertion. This is due to the fact that the styryl remains $\eta^3$ coordinated in the adduct so that the incoming styrene is only coordinated through the exocyclic double bond in a $\eta^2$-fashion (La-$C_1$ = 3.436 and 3.143 $\AA$ and La-$C_2$ = 3.160 and 3.103 $\AA$ for gO and gOO, respectively, the labels $C_1$ and $C_2$ refer to the geometries in Figure 60). This coordination induces a lower stabilisation than the $\eta^6$ found for the first insertion. For the gO-grafted complex, the insertion barrier for the two enantiofaces are similar (13.7 (*si*) and 14.5 (*re*) kcal.mol$^{-1}$) and this is 3.6 to 4 kcal.mol$^{-1}$ higher than the first insertion. The slight increase of the barrier is due to a lower activation of the styrene molecule in the adduct. In the case of the gOO-grafted complex, the insertion barrier are similar for the two enantiofaces (8.1 (*re*) kcal.mol$^{-1}$ and 9.8 (*si*) kcal.mol$^{-1}$) and are similar to the first insertion barriers. This is probably due to the higher steric hindrance around the metal centre in the gO complex compared to the gOO analogue. Differently from the $C^{St,re,si}{}_{gOO}$ compound, indeed, the geometry imposed by the $C_{surface}$-O-La angle (162.6 °) forces the metal, in the $C^{St,re,si}{}_{gO}$ complex, to be more bent on the surface, thus making the approach of the second styrene monomer more sterically difficult.

The difference is already marked at the second insertion step and seems to indicate that the gOO-grafted catalyst is more active than the gO-grafted one. On the other hand, none of them has a kinetic preference for the insertion of a peculiar enantioface. The insertion products are strongly stabilised for both catalysts whatever the enantioface that reacts. However, the products coming from the *si* insertion for both catalysts are thermodynamically preferred over the formation of the *re* insertion product (the difference of stability is greater than 2.0 kcal.mol$^{-1}$ that is the expected precision of the method here). Therefore, it seems that a preference for the formation of a syndiotactic styrene is found for both catalysts.

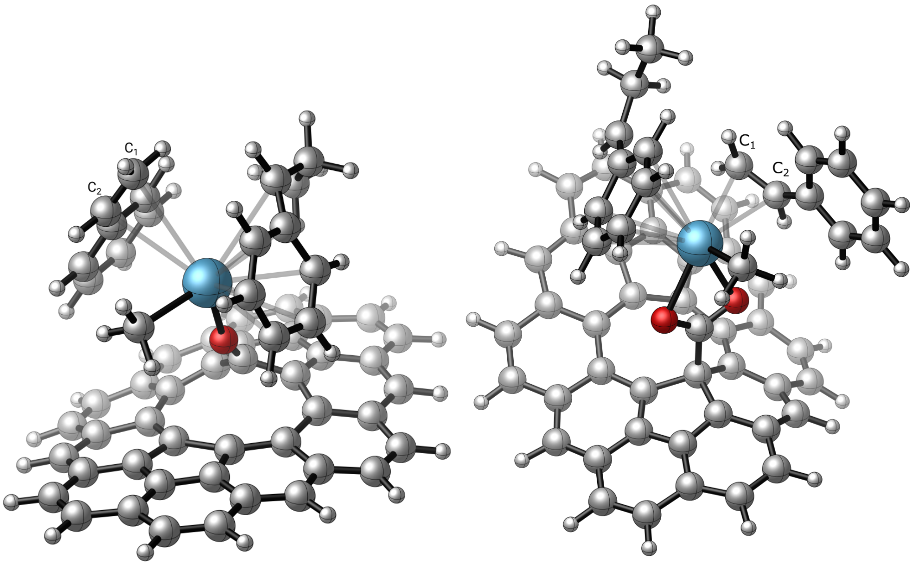

(a) (b)

Figure 60: Geometry of the styrene adducts for the two grafted complexes : a) $C^{St,re,si}{}_{gO}$ and $C^{St,re,si}{}_{gOO}$.

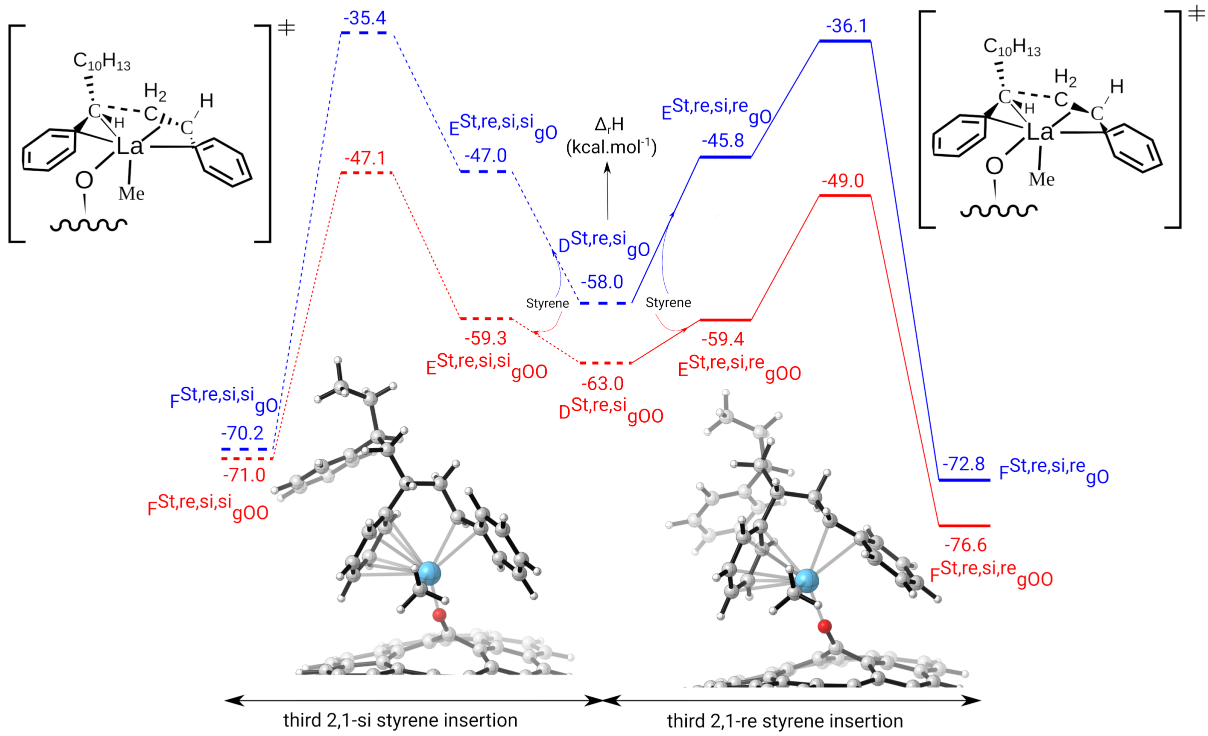

Figure 61: Computed Enthalpy profile for the third 2,1-insertion of styrene at room temperature. The blue and red pathways correspond to the go- and gOO-grafted catalysts.

To further highlight the preference for the formation of a syndiotactic polystyrene with both catalysts, the third insertion was computed (Figure 61) starting from the most stable products of the second insertion (D$^{St,re,si}{}_{g}O$ and D$^{St,re,si}{}_{g}OO$). The main features described for the second insertion hold true for the third one. Indeed, the coordination of styrene is not favourable and the gOO-grafted complex (highest barrier of 15.9 kcal.mol$^{-1}$) is more reactive than the gO-one (highest barrier of 22.6 kcal.mol$^{-1}$). Alike the first and second insertion, no kinetic preference is observed between the two enantiofaces insertion but alike the second insertion, there is a thermodynamic preference for both catalysts of the formation of a syndiotactic polystyrene. To summarise, the catalysts grafted on graphene surface favour the formation of syndiotactic polymers whose formation is thermodynamically controlled.

### 3.1.6 Ethylene styrene copolymerisation

The expected activity of these catalysts, similar to that of cationic scandium, prompted us to investigate the possibility of copolymerising ethylene and styrene since the cationic scandium complex was reported to indeed allow this copolymerisation.[226] The 1,2-ethylene insertion is compared with the 2,1-styrene insertion onto the La-Me bond for the two grafting modes (Figure 62). A view of the different intermediate and transition state geometries is available in Appendix A, figures 163 and 167. Interestingly enough, the two grafting modes, gO and gOO yields different conclusion. For the gOO, the styrene and ethylene appears to be in competition kinetically (barrier of 6.0 kcal.mol$^{-1}$ for the ethylene insertion *vs.* 9.7 kcal.mol$^{-1}$ for the styrene one). The styrene insertion is however most favourable thermodynamically (-37.0 kcal.mol$^{-1}$ *vs.* -23.7 kcal.mol$^{-1}$ for the ethylene insertion) so that one may conclude that styrene insertion

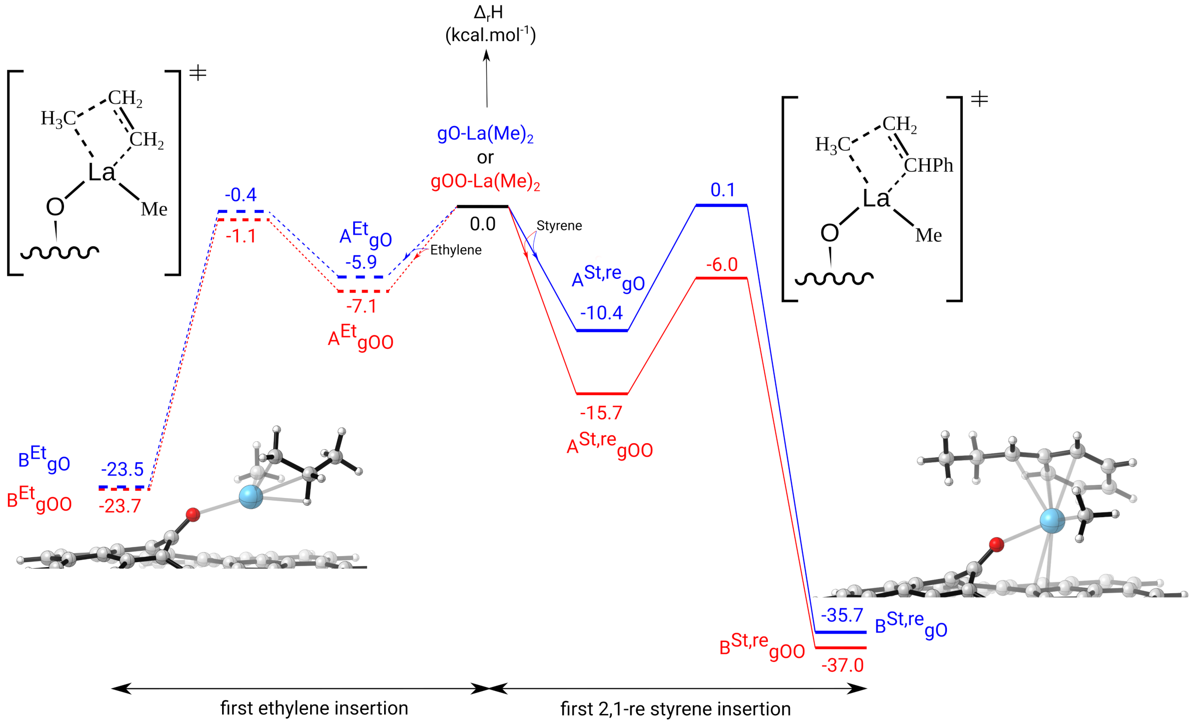

Figure 62: Computed Enthalpy profile for the 1,2 insertion of ethylene (left) and 2,1-insertion of styrene (right). The blue and red pathways correspond to the gO- and gOO-grafted catalysts.

would first occur for 1gOO. This thermodynamic preference was expected since the formation of the $\eta^3$-styryl is more favourable than the formation of an alkyl complex.

For 1gO, the situation is very different since the barrier for the ethylene insertion is 5.0 kcal.mol$^{-1}$ lower than that of styrene insertion. Therefore, there is a kinetic preference for the ethylene insertion, despite the fact that the formation of $\eta^3$-styryl is still preferred thermodynamically. Therefore, ethylene insertion is preferred for the (gO)-[La(Me)$_2$] catalyst. The second insertion was thus considered to evaluate the possibility of formation of copolymers. Indeed, the main problem of ethylene-styrene polymerisation is the difference of stability of the insertion products, $\eta^3$ styryl being more favourable than alkyl formation so that after styrene insertion ethylene incorporation is prevented thermodynamically. Therefore, both styrene or ethylene insertions on either the La-($\eta^3$-styryl) (figure 63) or La-propyl (Figure 64) were considered in order to evaluate the ability to get copolymers. The nature of the copolymer (block or statistical) will also be discussed.

Interestingly, the insertion of an ethylene moiety on the La-($\eta^3$ styryl) complex is found to be thermodynamically favourable (Figure 63) so that copolymerisation might be possible and is not controlled by the relative stability of the allyl *vs* the alkyl. However, both grafting modes favours the styrene insertion. For the gOO-grafted compound, the preference is both kinetic (difference of 5.2 kcal.mol$^{-1}$ between the styrene and ethylene insertion) and thermodynamic (7.3 kcal.mol$^{-1}$ in favour of the styryl complex). Thus, for the gOO-La catalyst, the formation

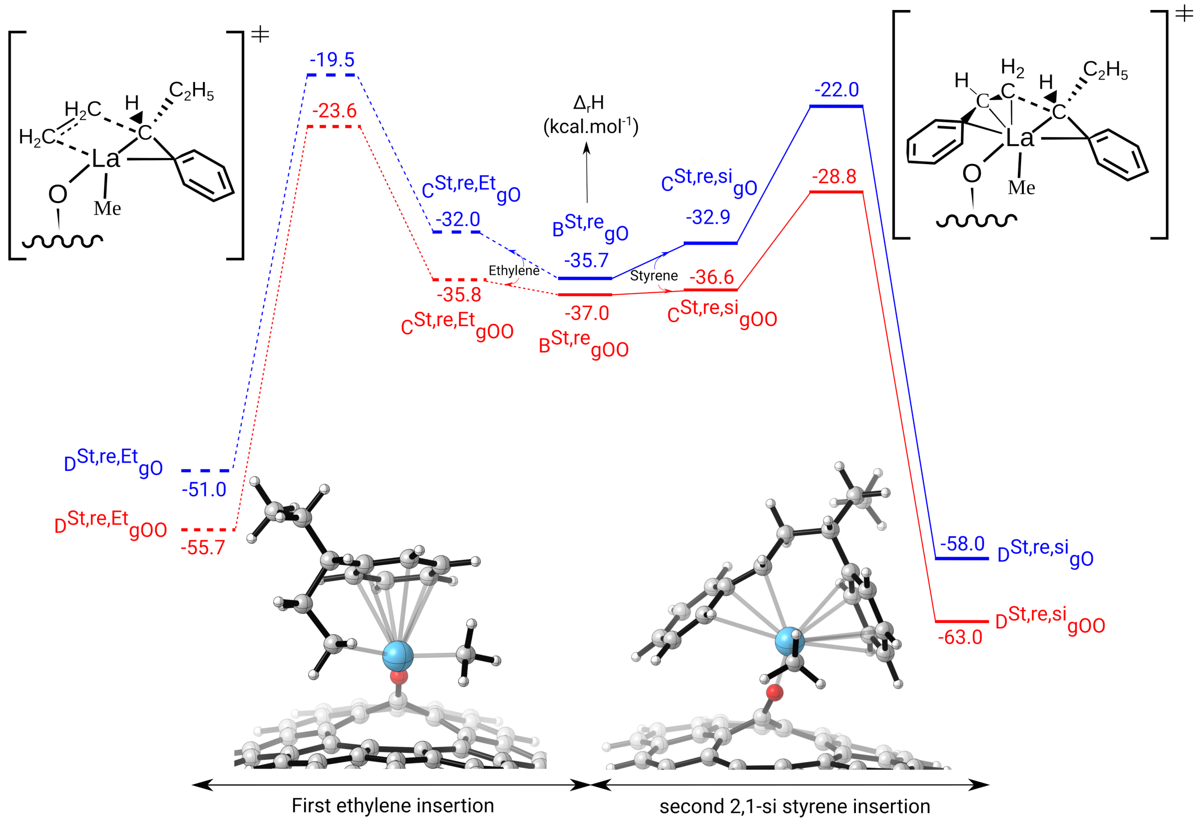

Figure 63: Computed Enthalpy profile for the 1,2 insertion of ethylene (left) and 2,1-insertion of styrene (right) on the La-($^3$-styryl) complex. The blue and red pathways correspond to the gO- and gOO-grafted catalysts

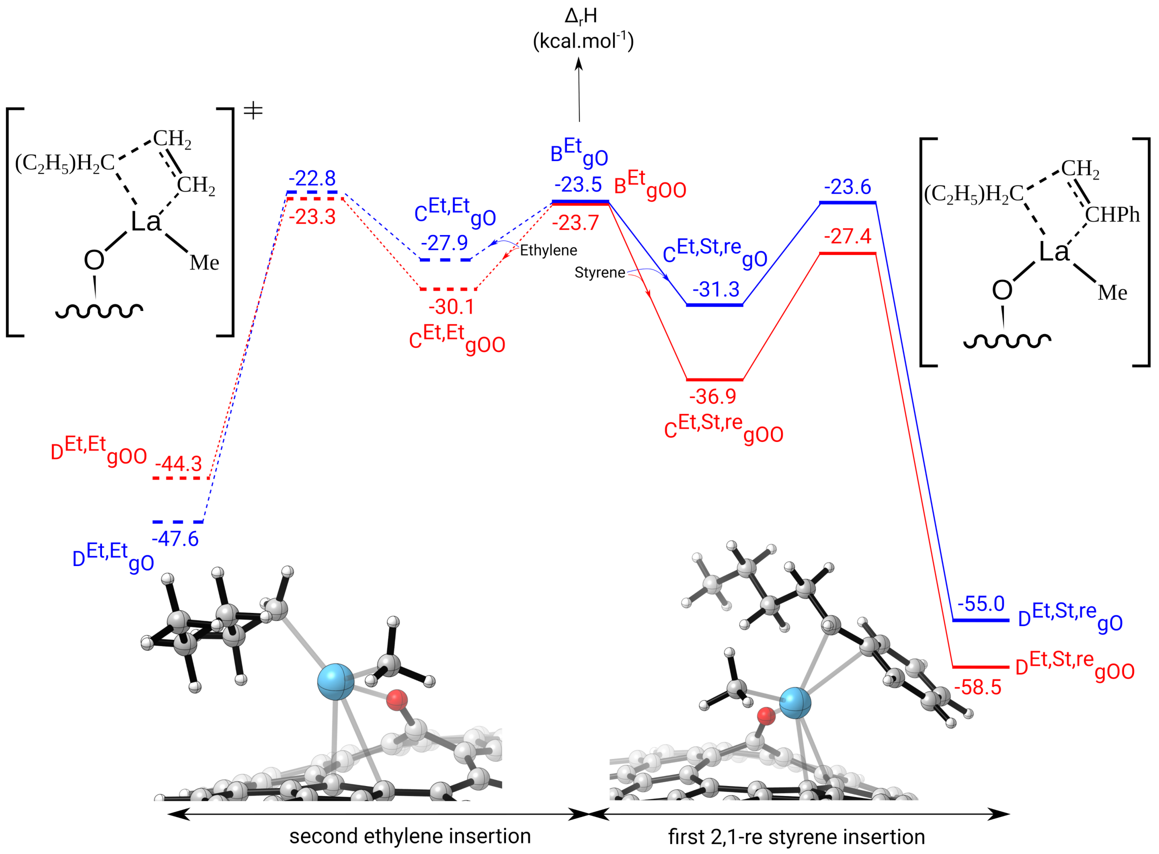

Figure 64: Computed Enthalpy profile for the 1,2 insertion of ethylene (left) and 2,1-insertion of styrene (right) on the La-propyl complex. The blue and red pathways correspond to the gO- and gOO-grafted catalyst.

of copolymer is very unlikely as styrene insertion is preferred for the two first insertions. At most a block copolymer could be obtained when all styrene would have been consumed.

For the gO- mode, there is a kinetic competition (difference of 2.5 kcal.mol$^{-1}$) but a thermodynamic preference for the styrene insertion (7.0 kcal.mol$^{-1}$ preference for the styrene insertion). Thus, for this grafting mode, the introduction of a styrene monomer in the polymer would imply subsequent styrene insertions. Since for this grafting mode, the first insertion of ethylene was preferred. Thus, the analysis of the results for the insertion onto the La-propyl is crucial (Figure 64). In this sequence, there is a kinetic competition between the ethylene and styrene insertion (2.6 kcal.mol$^{-1}$) but a thermodynamic preference for the styrene insertion (7.4 kcal.mol$^{-1}$). Thus, for the gO- grafting mode, after an ethylene insertion a styrene insertion will occur. Based on the analysis of the results of Figure 63, one would expect the formation of polystyrene with little amount of ethylene for gO, which is slightly different from the gOO- grafting mode where a pure polystyrene is expected. These results were further corroborated by the computational investigation of the third insertion.

In conclusion, therefore, both the 1gO and 1gOO compounds actively catalyse the styrene polymerization reaction, with the preferential formation of a syndiotactic polystyrene. The catalytic behaviour of these two complexes in the co-polymerisation of ethylene and styrene has

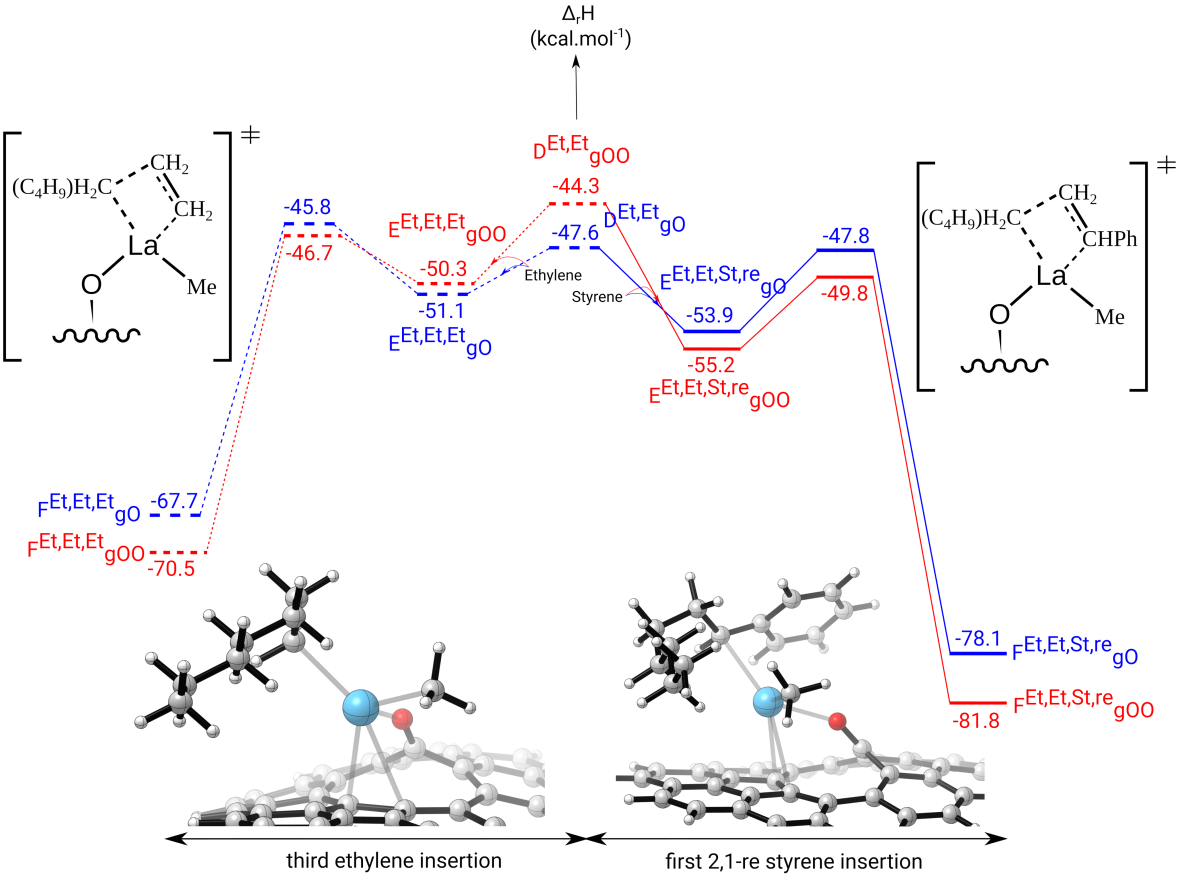

Figure 65: Computed Enthalpy profile for the third 1,2 insertion of ethylene (left) and 2,1-insertion of styrene (right) on the La-propyl complex. The blue and red pathways correspond to the gO- and gOO-grafted catalysts.

been also computationally investigated. We have shown that while the gO-grafted La compound is expected to form a polystyrene with a little amount of ethylene, the gOO-grafted catalyst, on the other hand, is expected to generate a polystyrene product, providing at most a block copolymer when all styrene has been consumed.

### 3.2 Ring opening polymerisation of the $\beta$-butyrolactone

We sought now to explore the potential applications of these graphene-supported La species to the rac-BBL ROP reaction, by using the graphene grafted (gO)-[La$(BH_4)_2(THF)_2$] and (gOO)-[La$(BH_4)_2(THF)_2$] compounds as active species. By comparing the catalytic activity of these heterogeneous graphene-grafted species with that of the previously reported molecular [La$(BH_4)_3(THF)_3$] and silica-grafted (≡SiO)-[La$(BH_4)_2(THF)_2$] analogue models, we were able to provide a better understanding of the influence of the support nature on the activity and stereoselectivity of the supported La catalysts.

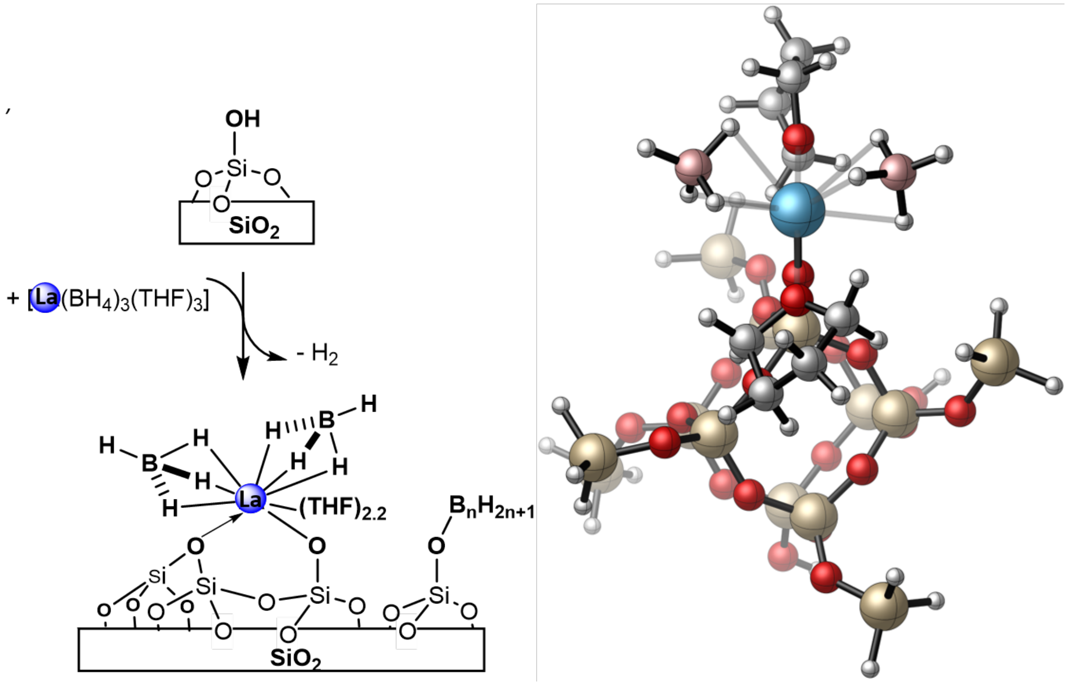

(a)

(b)

Figure 66: a) Synthesis of the silica supported bis(borohydride) (≡SiO)-[La(BH$_4$)$_2$(THF)$_{2.2}$] complex and b) Computed structure of the corresponding silica supported (≡SiO)-[La(BH$_4$)$_2$(THF)$_2$].

### 3.2.1 Rac-BBL ROP promoted by the molecular [La(BH$_4$)$_3$(THF)$_3$] and silica-supported (≡SiO)-[La(BH$_4$)$_2$(THF)$_2$] species

As previously described in the chapter I.4.3 , lanthanide trisborohydride homoleptic complexes [La(BH$_4$)$_3$(THF)$_3$] (Ln = La, Nd and Sm) efficiently initiate the ROP of rac-BL, affording, under mild operating conditions, well-defined atactic $\alpha,\omega$-hydroxy telechelic PHBs.[265] Guillaume and coworkers recently reported a DFT study on the ROP mechanism mediated by the molecular [La(BH$_4$)$_3$(THF)$_3$] complex, showing that both the initiation and propagation steps are thermodynamically and kinetically accessible processes.[265] The grafting of the homoleptic [Ln(BH$_4$)$_3$(THF)$_3$] (Ln = La, Nd) species on silica (SiO$_{2-700}$) Si-OH groups provided, after release of H$_2$, the corresponding bis(borohydride) (≡SiO)-[La(BH$_4$)$_2$(THF)$_{2.2}$] heterogeneous complexes, which have been also tested as rac-BL ROP catalysts (Figure 66a)). For the La system, interestingly, although both the molecular and supported species afforded atactic PHBs, the silica supported bis(borohydride) (≡SiO)-[La(BH$_4$)$_2$(THF)$_{2.2}$] complex displayed a much poorer activity than the corresponding molecular derivative (conversion of 9% for (≡SiO)-[La(BH$_4$)$_2$(THF)$_{2.2}$] *vs.* 91% for [La(BH$_4$)$_3$(THF)$_3$], after 24 h at 20 °C with a monomer/initiator ratio of 100).[162] In order to gain a better understanding of the ROP mechanism in silica supported heterogeneous conditions, we investigated here, by a computational DFT study, the rac-BL ROP mediated by the (≡SiO)-[La(BH$_4$)$_2$(THF)$_2$] model complex shown in Figure 66b).

Our goal was to explain the reason of the poorer catalytic activity of the heterogeneous silica supported La system compared to the molecular $[La(BH_4)_3(THF)_3]$ derivative,[162] focusing our attention on the role played by the surface in the course of the catalytic reaction. Taking into account the rigidity of the silica support, the surface density of the silanol groups at a certain temperature and the experimental IR frequencies measured for the silanol hydroxyl groups, Del Rosal and coworkers recently computed a realistic molecular model describing an isolated silanol group onto a $SiO_{2-700}$ surface.[136, 135] As shown in figure 66b, the emerged part of the silica surface is described on the top of the model by the two Si-OH and Si-O-$SiH_3$ functions, connected together by a siloxane bridge. This emerged part is surrounded by a deeper siloxane layer built around four silicon atoms, themselves connected to O–$SiH_3$ groups which mimic the continuity of the surface. The bottom layer is finally composed of two silanol units, linked each other by a siloxane bridge, which ensures the rigidity of the model. It should be kept in mind that these two silanol groups (at the bottom of the structure) are only present to saturate the fragment and are too far to be involved in any interaction with the grafted metal center. Similarly, the $SiH_3$ groups added on the upper silicon atoms allow to saturate the lateral siloxane bridges formed during the dehydroxylation reaction of the silica surface at 700 °C.[162] Following the grafting reaction in figure 66a, the theoretical model computed for the $(\equiv SiO)$-$[La(BH_4)_2(THF)_2]$ catalyst displays a monografted lanthanum complex with two borohydride ligands and two THF molecules coordinated to the metal center (figure 66b). In accordance with the experimental results, the two borohydride groups are $\eta^3$-bound to the metal center, displaying three La-($\mu$-H)-B interactions each.

In Scheme 67 we illustrate the rac-BL ROP mechanism promoted by surface-supported lanthanide complexes. It consists of three parts: i) the initiation, involving two successive BH activations; ii) the propagation, ensuring the growing of the polymeric chain; and finally iii) the termination, allowing the release of the final polymer by hydrolysis reaction. As shown in Scheme 67, the initiation step begins with the coordination of the first rac-BL monomer to the Ln metal (species i). The transfer of a $BH_4$ hydride to the adjacent carbonyl carbon may then occur, leading the resulting $BH_3$ group to interact with the exocyclic oxygen atom (species ii). The ring-opening of the BL unit, by re-formation of the carbonyl group and cleavage of the oxygen-acyl bond, may then afford the transfer of a second $BH_3$ hydride onto the same carbonyl carbon, with the formation of species iii. In the subsequent propagation step, the coordination of a second rac-BL monomer (species iv) may be followed by the nucleophilic attack of the growing alkoxoborane chain to the carbonyl carbon of the second incoming rac-BL molecule (species v). The regeneration of the carbonyl group, by the cleavage of the oxygen-acyl bond, may then afford species VI, which can carry on the propagation process, affording, upon a hydrolytic termination/deactivation reaction, the final $\alpha,\omega$-dihydroxy telechelic PHB polymer.

The substitution of one hydrogen atom by a methyl group in the BBL monomer leads to two enantiomeric BL-R and BL-S compounds. The prochirality of the C atom of the C=O group, moreover, provides two different enantiofaces, *re* and *si*, affording, after the first $BH_4$ hydride transfer, four possible diastereoisomers (specie ii in Scheme 67), labelled hereafter BL-R(R), BL-R(S), BL-S(S) and BL-S(S), respectively (Figure 68).

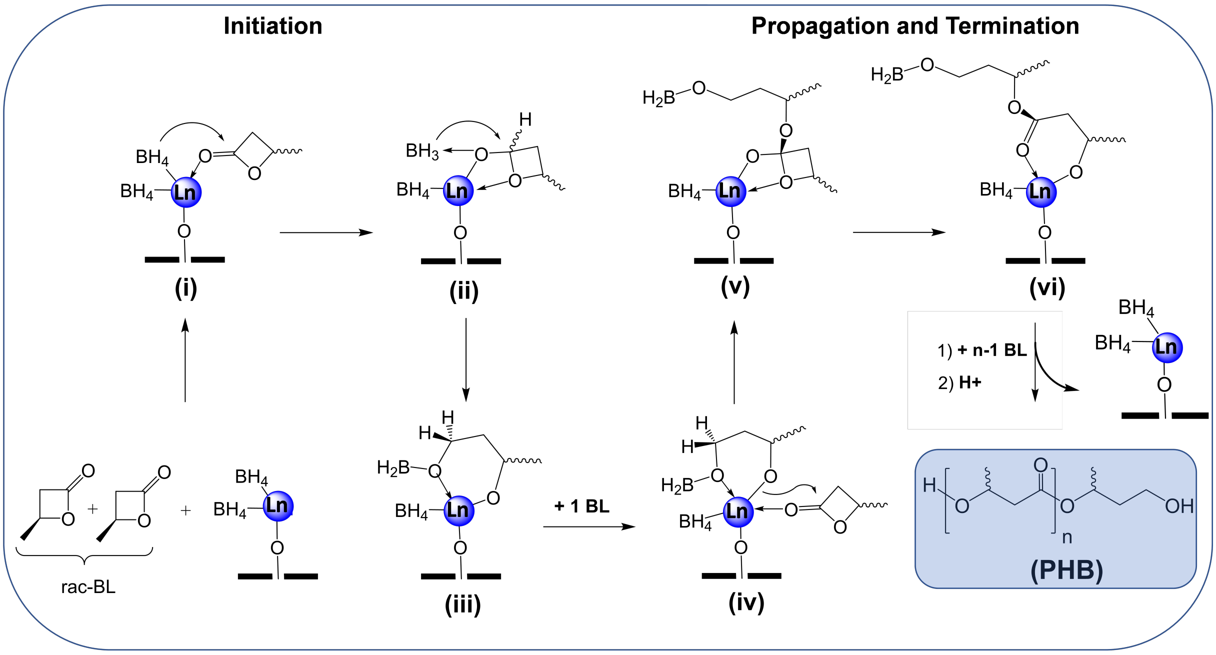

Figure 67: The rac-BL ROP mechanism catalysed by supported Ln bisborohydride complexes: synthesis of the $\alpha$,$\omega$-dihydroxy telechelic PHB polymer.

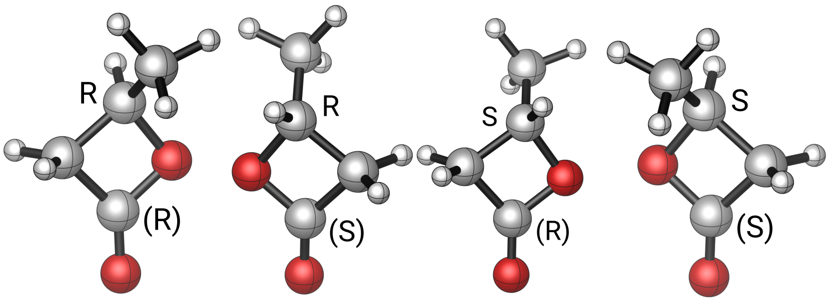

(a) BL-R(R) (b) BL-R(S) (c) BL-S(R) (d) BL-S(R)

Figure 68: Representation of the re (R) and si (S) enantiofaces of the BL-R and BL-S monomers after the first La mediated $BH_4$ hydride transfer (species ii in Scheme 67).

The initiation and propagation steps of the ROP process mediated by the silica supported ($\equiv$SiO)-[La($BH_4$)$_2$(THF)$_2$] complex have been therefore computed and compared with those obtained with the molecular [La($BH_4$)$_3$(THF)$_3$] analogue. As the rate determining step of the whole ROP process is within the initiation process, in the present study we will only discuss the rac-BL ROP initiation part, comparing in figure 69 the enthalpy-energy profiles computed for the [La($BH_4$)$_3$(THF)$_3$] and ($\equiv$SiO)-[La($BH_4$)$_2$(THF)$_2$] systems. For sake of clarity, in addition, since for the molecular [La($BH_4$)$_3$(THF)$_3$] complex the ROP enthalpy-energy profiles are identical, within the intrinsic error of the DFT methodology, regardless of the enantiomer (BL-R or BL-S) and enantioface ( *re* or *si*) considered, we will only discuss here the ROP of the BL-R enantiomer in the re enantioface (BL-R(R) case). While for the molecular [La($BH_4$)$_3$(THF)$_3$] system, the geometries of the involved species have been previously reported,[265] for the silica supported ($\equiv$SiO)-[La($BH_4$)$_2$(THF)$_2$] compound, a view of the different intermediates and transition state geometries is available in figure 70, with the key geometrical parameters summarised in table 5.

As shown in figure 69, the initiation process starts with the displacement of one THF molecule upon coordination of a BL-R monomer. For both systems this displacement is slightly exothermic (-0.8 kcal.mol$^{-1}$) affording the corresponding [La($BH_4$)$_3$(THF)$_2$(BL-R)] ($A^R$) and ($\equiv$SiO)-[La($BH_4$)$_2$(THF)(BL-R)] (${A^R}_{SiO_2}$) compounds. Starting from these adducts, the nucleophilic attack of the $BH_4$ hydride to the carbonyl carbon $C_{CO}$ of the re-enantioface of the BL-R monomer can take place with a barrier of 18.1 and 25.2 kcal.mol$^{-1}$, for the TS-$A^R B^{R(R)}$ and TS-$A^R {B^{R(R)}}_{SiO_2}$, respectively, with respect to the adducts. As shown by the transition state geometries in figure 70, interestingly, while in the molecular [La($BH_4$)$_3$(THF)$_2$(BL-R)] compound the $BH_4$ ligand completely dissociates from the La metal before transferring the hydride atom (the shortest ($H_3B$)H-La distance measures 4.090 $\AA$, with a $H_4B$-La distance of 4.663 $\AA$), in the silica-supported ($\equiv$SiO)-[La($BH_4$)$_2$(THF)(BL-R)] analogue, on the other hand, the $BH_4$ ligand remains in the metal coordination sphere while transferring the hydride atom to the BL-R $C_{CO}$ atom (the shortest ($H_3B$)H-La distance measures 2.612 $\AA$, with a $H_4B$-La distance of 3.339 $\AA$). In both compounds, the $C_{CO}$ carbon is pyramidal, with the resulting Csp$^3$ acceptor orbital pointing towards the migrating $BH_4$ hydride atom. While in the [La($BH_4$)$_3$(THF)$_2$(BL-R)] compound the boron p orbital fully overlaps with the sp$^3$ orbital of the $C_{CO}$ atom, with a B-H-$C_{CO}$ angle of 163.1°, in the ($\equiv$SiO)-[La($BH_4$)$_2$(THF)(BL-R)] analogue, on the other hand, the B-H-$C_{CO}$ angle measures 137.2°, resulting in a less efficient overlap, and therefore in a more energy demanding hydride transfer process. The resulting intermediates ($B^{R(R)}$ and ${B^{R(R)}}_{SiO_2}$) are located at 14.6 and 23.4 kcal.mol$^{-1}$ with respect to the $A^R$ and ${A^R}_{SiO_2}$ species and display the $BH_3$ group still interacting with the transferred hydride atom. In both cases, in addition, compared to the corresponding $A^R$ and ${A^R}_{SiO_2}$ adducts, the La-$O_{CO}$ distance is shortened (2.663 $\AA$ *vs.* 2.361 $\AA$ for $B^{R(R)}$ and 2.559 $\AA$ *vs.* 2.341 $\AA$ for ${B^{R(R)}}_{SiO_2}$) while the $C_{CO}$-$O_{CO}$ distance is elongated (1.209 *vs.* 1.309 for $B^{R(R)}$ and 1.218 *vs.* 1.310 $\AA$ for ${B^{R(R)}}_{SiO_2}$), which is consistent with the presence of a single bond between the $C_{CO}$ and $O_{CO}$ atoms.

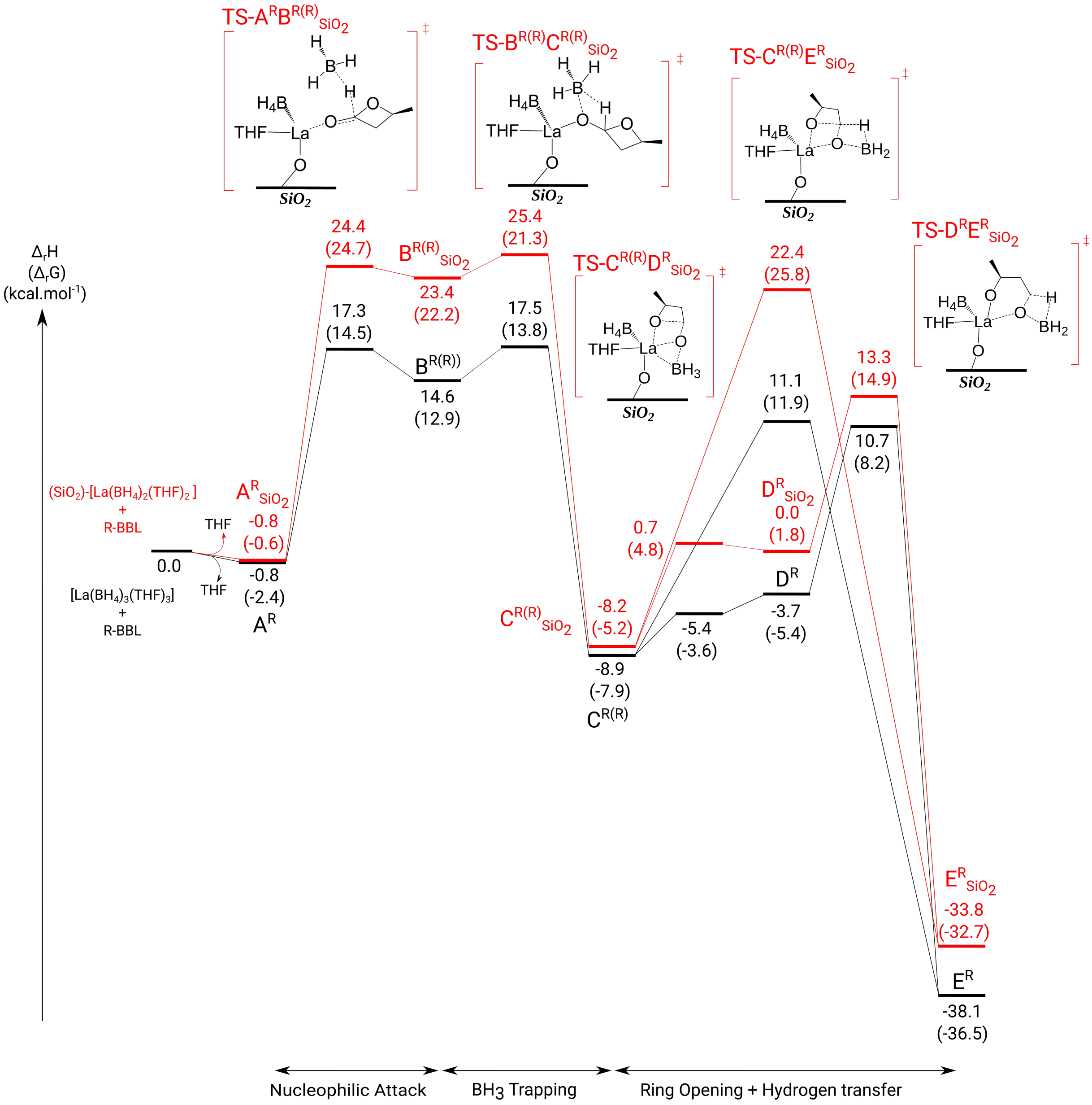

Figure 69: Enthalpy-energy profile computed for the BL-R ROP initiation step mediated by the $[La(BH_4)_3(THF)_3]$ (black) and $(\equiv SiO)\text{-}[La(BH_4)_2(THF)_2]$ (red) complexes.

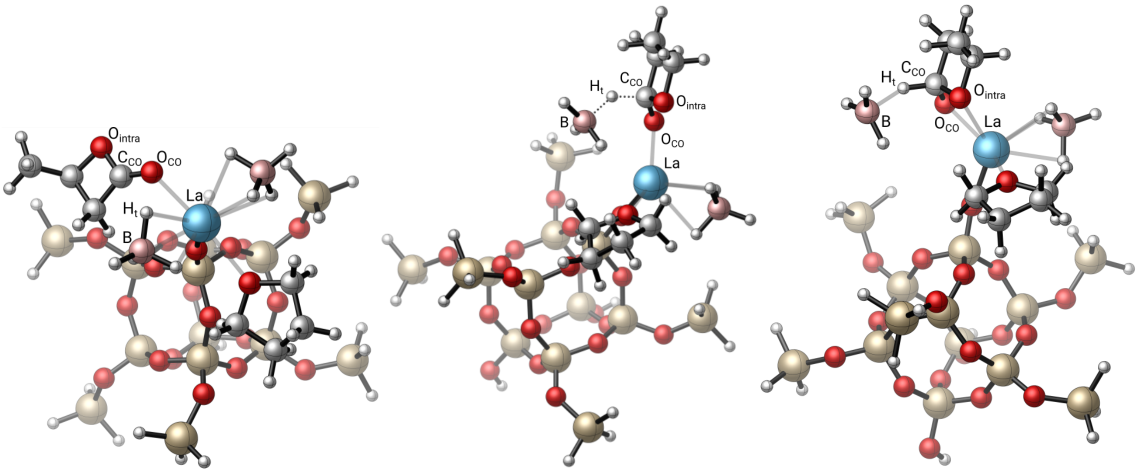

(a) $\mathrm{A}^{R}{}_{SiO_2}$ (b) TS-$\mathrm{A}^{R}\mathrm{B}^{R(R)}{}_{SiO_2}$ (c) $\mathrm{B}^{R(R)}{}_{SiO_2}$

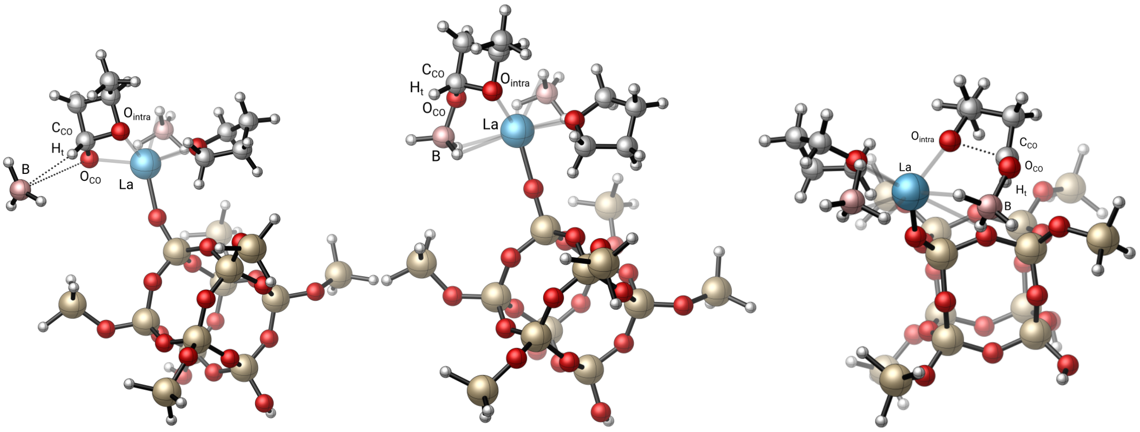

(d) TS-$\mathrm{B}^{R(R)}\mathrm{C}^{R(R)}{}_{SiO_2}$ (e) $\mathrm{C}^{R(R)}{}_{SiO_2}$ (f) TS-$\mathrm{C}^{R(R)}\mathrm{D}^{R}{}_{SiO_2}$

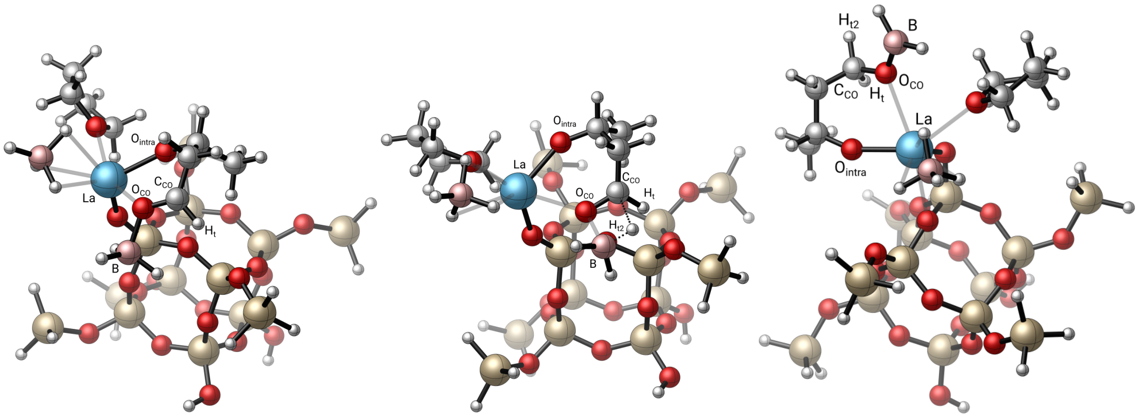

(g) $\mathrm{D}^{R}{}_{SiO_2}$ (h) TS-$\mathrm{D}^{R}\mathrm{E}^{R}{}_{SiO_2}$ (i) $\mathrm{E}^{R}{}_{SiO_2}$

Figure 70: Optimised structures of the complexes involved in the BL-R ROP initiation step mediated by the ($\equiv$SiO)-[La(BH$_4$)$_2$(THF)$_2$] catalyst.

Table 5: Selected bond lengths ($\mathring{A}$) of the stationary points calculated for the initiation step of the ROP of BL-R mediated by (≡SiO)-[La$(BH_4)_2$$(THF)_2$]. The labels refer to the intermediates and transition states depicted in Figure 70.

| | La-$O_{CO}$ | La-$O_{intra}$ | $C_{CO}$-$O_{CO}$ | $C_{CO}$-$O_{intra}$ | $C_{CO}$-$H_t$ | B-$H_t$ | $O_{CO}$-B | B-$H_{t2}$ | $C_{CO}$-$H_{t2}$ |
|---|---|---|---|---|---|---|---|---|---|
| BL-R | - | - | 1.194 | 1.369 | - | - | - | - | - |
| nucleophilic attack | | | | | | | | | |
| $A^R$ | 2.663 | - | 1.209 | 1.344 | - | 1.242 | - | - | - |
| ${A^R}_{SiO_2}$ | 2.559 | - | 1.218 | 1.333 | - | 1.242 | - | - | - |
| TS-$A^R B^{R(R)}$ | 2.275 | - | 1.315 | 1.431 | 1.174 | 1.504 | - | - | - |
| TS-$A^R {B^{R(R)}}_{SiO_2}$ | 2.355 | - | 1.291 | 1.422 | 1.270 | 1.379 | - | - | - |
| $BH_3$ trapping | | | | | | | | | |
| $B^{R(R)}$ | 2.361 | 2.623 | 1.309 | 1.500 | 1.147 | 1.609 | - | - | - |
| ${B^{R(R)}}_{SiO_2}$ | 2.341 | - | 1.310 | 1.499 | 1.150 | 1.595 | - | - | - |
| TS-$B^{R(R)} C^{R(R)}$ | 2.327 | 2.607 | 1.329 | 1.533 | 1.105 | 2.641 | 4.472 | - | - |
| TS-$B^{R(R)} {C^{R(R)}}_{SiO_2}$ | 2.317 | 4.595 | 1.326 | 1.545 | 1.106 | 2.573 | 3.936 | - | - |
| $C^{R(R)}$ | 2.577 | 2.667 | 1.366 | 1.484 | 1.097 | - | 1.532 | 1.204 | - |
| ${C^{R(R)}}_{SiO_2}$ | 2.582 | 2.633 | 1.364 | 1.492 | 1.096 | - | 1.537 | 1.202 | - |
| Ring opening + hydrogen transfer | | | | | | | | | |
| TS-$C^{R(R)} D^R$ | 3.635 | 2.387 | 1.283 | 1.824 | 1.095 | - | 1.519 | 1.241 | - |
| TS-$C^{R(R)} {D^R}_{SiO_2}$ | 3.554 | 2.284 | 1.257 | 2.066 | 1.093 | - | 1.546 | 1.264 | - |
| $D^R$ | 3.714 | 2.272 | 1.248 | 2.200 | 1.094 | - | 1.560 | 1.202 | - |
| ${D^R}_{SiO_2}$ | 2.863 | 2.239 | 1.251 | 3.054 | 1.096 | - | 1.589 | 1.207 | - |
| TS-$D^R E^R$ | 4.830 | 2.192 | 1.257 | 2.793 | 1.099 | - | 1.673 | 1.233 | 2.114 |
| TS-$D^R {E^R}_{SiO_2}$ | 2.650 | 2.222 | 1.270 | 2.850 | 1.095 | - | 1.721 | 1.226 | 2.163 |
| $E^R$ | 2.544 | 2.196 | 1.437 | 2.908 | 1.094 | - | 1.458 | - | 1.098 |
| ${E^R}_{SiO_2}$ | 2.676 | 2.177 | 1.456 | 3.197 | 1.094 | - | 1.357 | - | 1.093 |

From these adducts, the reaction progresses with the trapping of the $BH_3$ molecule by the exocyclic oxygen ($O_{CO}$) of the BL-R. The involved transition states, TS-$B^{R(R)}C^{R(R)}$ and TS-$B^{R(R)}C^{R(R)}{}_{SiO_2}$, are almost barrierless with respect to the $B^{R(R)}$ and $B^{R(R)}{}_{SiO_2}$ adducts (2.9 and 2.0 kcal.mol$^{-1}$ respectively) and display the $BH_3$ moiety interacting with the transferred hydride atom, $H_t$ (2.641 and 2.573 $\AA$ for the molecular and $SiO_2$ supported complexes, respectively).The B-$O_{CO}$ bond may then form (B-$O_{CO}$ = 1.533 and 1.543 $\AA$ for the molecular and $SiO_2$ supported complexes, respectively), providing the resulting borane complexes ($C^{R(R)}$ and $C^{R(R)}{}_{SiO_2}$), *via* an exothermic process of 8.9 and 8.2 kcal.mol$^{-1}$, respectively, with respect to the first $A^R$ and $A^R{}_{SiO_2}$ adducts. Starting from the $C^{R(R)}$ and $C^{R(R)}{}_{SiO_2}$ intermediates, two different pathways may lead to the final alkoxyborane products $E^R$ and $E^R{}_{SiO_2}$, characterised by a terminal -$CH_2OBH_2$ moiety: either a one-step concerted pathway, in which the re-formation of the carbonyl group and the cleavage of the acyl carbon-oxygen bond take place simultaneously with the transfer of the $BH_3$ hydride to the carbonyl carbon or a two-step pathway in which the cleavage of the BL ring precedes the $BH_3$ hydride transfer. Interestingly while for the molecular $[La(BH_4)_3(THF)_3]$ system, the two limiting barriers for the one- and two-step processes are comparable (TS-C $^{R(R)}E^R$ at 20.0 kcal.mol$^{-1}$ *vs.* TS-$D^RE^R$ at 19.6 kcal.mol$^{-1}$, with respect to adduct $C^{R(R)}$), for the silica supported (≡SiO)-$[La(BH_4)_2(THF)_2]$ system, on the other hand, the limiting barrier associated to the one-step pathway is higher than that corresponding to the two-step pathway (TS-$C^{R(R)}E^R{}_{SiO_2}$ at 30.6 kcal.mol$^{-1}$ *vs.* TS-$D^RE^R{}_{SiO_2}$ at 21.5 kcal.mol$^{-1}$, with respect to adduct $C^{R(R)}{}_{SiO_2}$). For comparison purposes, therefore, only the two-step mechanism will be detailed for sake of clarity. The cleavage of the acyl-oxygen bond corresponds to TS-$C^{R(R)}D^R$ and TS-$C^{R(R)}D^R{}_{SiO_2}$ which lie only 3.5 and 8.9 kcal.mol$^{-1}$ above the $C^{R(R)}$ and $C^{R(R)}{}_{SiO_2}$ adducts, respectively. The resulting $D^R$ and $D^R{}_{SiO_2}$ adducts, located at 5.2 and 8.2 kcal.mol$^{-1}$ with respect to the $C^{R(R)}$ and $C^{R(R)}{}_{SiO_2}$ adducts, display a BL-R ring already opened with a double bond between the $C_{CO}$ and $O_{CO}$ atoms ($C_{CO}$-$O_{CO}$ = 1.248 and 1.251 $\AA$ for $D^R$ and $D^R{}_{SiO_2}$, respectively, see table 5). From the $D^R$ and $D^R{}_{SiO_2}$ adducts, the transfer of the $BH_3$ hydride to the acyl $C_{CO}$ atom affords the complexes $E^R$ and $E^R{}_{SiO_2}$ *via* transition states TS-$D^RE^R$ and TS-$D^RE^R{}_{SiO_2}$, located at 19.6 and 21.5 kcal.mol$^{-1}$, respectively, relative to the $C^{R(R)}$ and $C^{R(R)}{}_{SiO_2}$ adducts. Their geometries display one B-$H_{t2}$ bond slightly elongated (1.233 and 1.226 for $\AA$ TS-$D^RE^R$ and TS-$D^RE^R{}_{SiO_2}$, respectively) with the hydrogen atom pointing toward the $C_{CO}$ atom. The $C_{CO}$-$O_{CO}$-B angle measures 92.8° and 95.4° for the molecular and silica supported models, respectively, favouring the interaction between the hydrogen and the $C_{CO}$ atoms ($H_{t2}$-$C_{CO}$ = 2.114 and 2.163 $\AA$ for TS-$D^RE^R$ and TS-$D^RE^R{}_{SiO_2}$, respectively). The formation of the resulting $E^R$ and $E^R{}_{SiO_2}$ complexes is exothermic by 38.1 and 33.8 kcal.mol$^{-1}$ with respect to the entrance channel. The $O_{intra}$-$C_{CO}$ bond distances (2.9108 and 3.197 $\AA$ for the molecular and silica supported systems, respectively) suggests a complete cleavage of the acyl-oxygen bond, with the intracyclic oxygen atom ensuring the coordination of the alkoxyborane monomer to the metal center. As shown in the $E^R$ and $E^R{}_{SiO_2}$ geometries (Figure 70), in addition, the exocyclic oxygen atom located at the terminal -$CH_2OBH_2$ moiety of the growing chain end interacts with the La center, completing its coordination sphere. This interaction is characterised by a short -$CH_2OBH_2$ O-La distance which measures 2.908 and 3.197 $\AA$ for the molecular and silica supported systems, respectively. The higher stability of the $E^R$ molecular complex compared to the silica supported analogue is probably ascribed to the coordination of one of the two THF molecules of the La coordination sphere to the -$CH_2OBH_2$ moiety, stabilising the whole metal complex. The analysis of the whole profile in figure 69, therefore, indicates that while for the silica supported (≡SiO)-[$La(BH_4)_2(THF)_2$] complex, the barriers associated to the first $BH_4$ hydride transfer and $BH_3$ trapping step (25.2 and 26.2 kcal.mol$^{-1}$) are higher than that associated to the second $BH_3$ hydride transfer (21.5 kcal.mol$^{-1}$), for the molecular [$La(BH_4)_3(THF)_3$] compound, on the other hand, the three barriers are energetically equivalent (18.1, 18.3 and 19.6 kcal.mol$^{-1}$ for the first $BH_4$ hydride transfer, the following $BH_3$ trapping and the second $BH_3$ hydride transfer, respectively). Since for the silica supported (≡SiO)-[$La(BH_4)_2(THF)_2$] system the rate-determining step of the entire ROP process clearly corresponds to the first $BH_4$ hydride transfer together with the following $BH_3$ trapping step, a careful comparison of this first part of the profile between the molecular and silica supported catalysts may rationalise the lower catalytic activity experimentally observed for the silica supported system.[162] As shown in figure 69, interestingly, while adducts A and C have similar enthalpies for the molecular and silica supported species, the rest of the profile between A and C is shifted towards higher energies for the silica supported complex. In the latter system, therefore, the enthalpy barriers associated to the $BH_4$ hydride transfer and $BH_3$ trapping are higher by 7.1 and 7.9 kcal.mol$^{-1}$ for TS-AB and TS-BC, respectively, indicating, according to the experimental results, that the silica supported (≡SiO)-[$La(BH_4)_2(THF)_2$] compound behaves as a less efficient BL ROP catalyst. In order to explain the reason of this different behaviour and thus the influence of the silica surface, we investigated the Lewis acidity of the [$La(BH_4)_3(THF)_3$] and (≡SiO)-[$La(BH_4)_2(THF)_2$] complexes, by coordination to the La center of a triphenylphosphine oxide (O=$PPh_3$). As previously reported both experimentally and theoretically,[135, 136, 87, 369] indeed, the coordination of a triphenylphosphine oxide (O=$PPh_3$) can be used as a probe to estimate the Lewis acidity of the metal center and therefore the catalytic properties of the catalyst. We therefore optimised the [$La(BH_4)_3(THF)_2(OPPh_3)$] and (≡SiO)-[$La(BH_4)_2(OPPh_3)$] complexes and we computed their corresponding IR and $^1$H, $^{13}$C and $^{31}$P NMR spectra. The C-H, aromatic C=C and O=P vibrational frequencies computed for the coordinated O=$PPh_3$ molecule are reported in Table 6. The molecular and silica-grafted species display similar vibrational stretching modes for the aromatic C-H (in the range 3196-3235 cm$^{-1}$), the aromatic C-C (in the range 1338-1655 cm$^{-1}$) and the O=P (1051 and 1050cm$^{-1}$, respectively) functions. To better characterise the nature of the metal center we also computed the theoretical $^1$H, $^{13}$C and $^{31}$P NMR chemical shift of the coordinated O=$PPh_3$ molecule (Table 6). The two complexes display similar values for the $^1$H 7.5 and 8.0 ppmand $^{13}$C [124.8/128.9] and [126.2/129.4] isotropic chemical shift for the [$La(BH_4)_3(THF)_2(OPPh_3)$] and (≡SiO)-[$La(BH_4)_2(OPPh_3)$] systems, respectively, while slightly different values were obtained for the $^{31}$P NMR signals (53.4 and 47.7 ppm for the [$La(BH_4)_3(THF)_2(OPPh_3)$] and (≡SiO)-[$La(BH_4)_2(OPPh_3)$] systems, respectively). The two $^{31}$P NMR values, interestingly, are more deshielded than that of the free O=$PPh_3$ molecule (25.7 ppm), indicating, as evidenced by Drago et al.,[181, 370] the coordination to a Lewis acidic site. The bigger the chemical shift increment between free and coordinated O=$PPh_3$, the higher the Lewis acidic character of the metal and therefore the stronger the M-O=$PPh_3$ interaction. Although both complexes can be considered as Lewis acids, due to the presence of highly ionic $BH_4$ ligands, the $^{31}$P NMR values suggest that the (≡SiO)-[$La(BH_4)_2(OPPh_3)$] complex has a stronger Lewis acid character than the molecular [$La(BH_4)_3(THF)_2(OPPh_3)$] system. Compared to the silica-grafted system in which the silica surface has replaced a $BH_4$ ligand, however, the homogeneous complex has an extra THF ligand that can stabilise the metal centre when necessary, conferring a greater flexibility to the system. In accordance to the geometries of TS-$A^RB^{R(R)}$ and TS-$A^RB^{R(R)}{}_{SiO_2}$ in figure 70, indeed, while in the molecular [La$(BH_4)_3$(THF)$_2$(BL-R)] compound the additional THF molecule may compensate the dissociation of the $BH_4$ ligand before the transfer of the hydride atom, in the silica-supported (≡SiO)-[La$(BH_4)_2$(THF)(BL-R)] analogue, on the other hand, the poorer coordination sphere of the La center prevents the complete dissociation of the $BH_4$ ligand which remains in interaction with the metal centre while transferring the hydride atom to the BL-R $C_{CO}$ atom. In the molecular TS-$A^RB^{R(R)}$ transition state, therefore, the complete dissociation of the $BH_4$ ligand makes the system much more acidic than the initial [La$(BH_4)_3$(THF)$_3$] complex, strongly activating the BBL monomer while allowing the $BH_4$ group to act as an external nucleophilic agent. In the silica TS-$A^RB^{R(R)}{}_{SiO_2}$ transition state, on the other hand, the poor electron density at the La metal center prevents the $BH_4$ group to leave the coordination sphere of the metal, activating the BBL monomer less effectively, while transferring the hydrogen atom in a more constrained and less effective way. If the molecular complex has a lower Lewis acid character than the silica supported compound, at the transition state level, the loss of the $BH_4$ ligand makes the molecular system more Lewis acid than the silica counterpart, resulting in a lower energy demanding hydrogen transfer process. This behaviour is in accordance with the geometrical parameters of the TS-$A^RB^{R(R)}$ and TS-$A^RB^{R(R)}{}_{SiO_2}$ transition states. While in the TS-$A^RB^{R(R)}$, the La-$O_{CO}$ and the $O_{CO}$=$C_{CO}$ bond distances measure 2.275 and 1.315 $\AA$, in the TS-$A^RB^{R(R)}{}_{SiO_2}$ system, on the other hand, they measure 2.355 and 1.291 $\AA$, clearly reflecting the lower BBL monomer activation in the case of the silica grafted complex. In the TS-$A^RB^{R(R)}$, in addition, the greater proximity of the BBL monomer to the La metal allows a more effective transfer of the $BH_4$ hydrogen do the $C_{CO}$ atom, with a B-H-$C_{CO}$ angle of 163.1° (compared to 132.7° in the TS-$A^RB^{R(R)}{}_{SiO_2}$ for the silica grafted complex). Thus, the higher catalytic activity of the molecular system compared to the silica supported analogue therefore, can be explained by a stronger activation of the BBL monomer, the release of the $BH_4$ group from the metal coordination sphere providing a more effective hydogen transfer process.

The insertion of a second BL-R monomer to the $E^R$ and $E^R{}_{SiO_2}$ complexes has also been then investigated. The computed enthalpy profile of this ROP propagation process is depicted in figure 71 and a view of the different transition states and intermediates is reported in figure 72. The key geometrical parameters are summarised in Table 7.

The reaction begins with the coordination of a second BL-R monomer to the La center, leading to the formation of the $F^{RR}$ and $F^{RR}{}_{SiO_2}$ intermediates *via* an exothermic process (-2.7 and -13.4 kcal.mol$^{-1}$ respectively, with respect to the entrance channel). The nucleophilic attack of the oxygen atom of the alkoxyborane group to the carbonyl carbon $C_{CO}$ of the incoming BL-R monomer can then occur through TS-$F^{RR}G^{RR(R)}$ and TS-$F^{RR}G^{RR(R)}{}_{SiO_2}$. The corresponding activation barriers measure 11.6 and 16.1 kcal.mol$^{-1}$ with respect to the $F^{RR}$ and $F^{RR}{}_{SiO_2}$ species, respectively, resulting therefore kinetically accessible.

Table 6: Comparison between the theoretical vibrational frequencies (in $cm^{-1}$), and the $^1H$, $^{13}C$ and $^{31}P$ NMR chemical shifts (in ppm) of the coordinated $OPPh_3$ molecule in different $OPPh_3$ borohydride La adducts grafted on the gO and gOO graphene and $SiO_2$ surfaces and on molecular complexes. The $^1H$ and $^{13}C$ chemical shifts are given with respect to TMS (theoretical chemical shielding: 31.64 and 195.35 ppm, respectively, for $^1H$ and $^{13}C$ atoms). The $^{31}P$ chemical shifts are given with respect to phosphoric acid (theoretical chemical shielding: 380.6 ppm).

| | Wavenumbers (in $cm^{-1}$) | | |
|---|---|---|---|
| | $\overline{\nu}_{C-H}$ | $\overline{\nu}_{C=C}$ | $\overline{\nu}_{O=P}$ |
| $[La(BH_4)_3(THF)_2(OPPh_3)]$ | [3196-3226] | [1339-1655] | 1051 |
| $(\equiv SiO)$-$[La(BH_4)_2(OPPh_3)]$ | [3199-3235] | [1338-1654] | 1050 |
| (gO)-$[La(BH_4)_2(THF)(OPPh_3)]$ | [3205-3233] | [1337-1654] | 1025 |
| (gOO)-$[La(BH_4)_2(THF)(OPPh_3)]$ | [3200-3230] | [1336-1655] | 1039 |

| | Chemical shifts (in ppm) | | |
|---|---|---|---|
| | $\delta_{H_{Phenyl}}$ | $\delta_{C_{Phenyl}}$ | $\delta_P$ |
| $[La(BH_4)_3(THF)_2(OPPh_3)]$ | 7.5 | [124.8/128.9] | 47.7 |
| $(\equiv SiO)$-$[La(BH_4)_2(OPPh_3)]$ | 8.0 | [126.2/129.4] | 53.4 |
| (gO)-$[La(BH_4)_2(THF)(OPPh_3)]$ | 7.7 | [124.7/128.7] | 60.3 |
| (gOO)-$[La(BH_4)_2(THF)(OPPh_3)]$ | 7.8 | [124.9/129.2] | 55.0 |

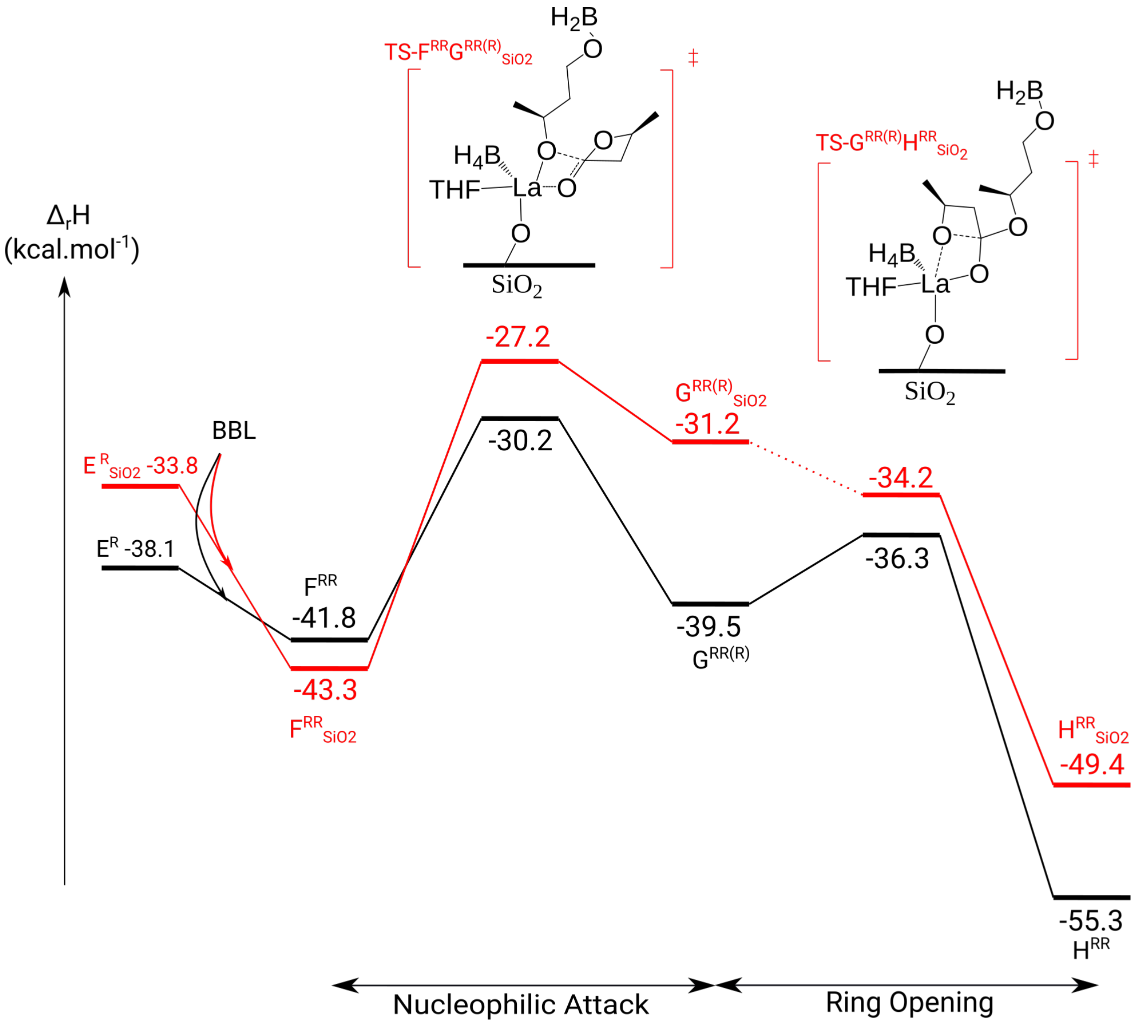

Figure 71: Enthalpy-energy profile computed for the BL-R ROP propagation step mediated by the $E^R$ (black) and $E^R{}_{SiO_2}$ (red) complexes.

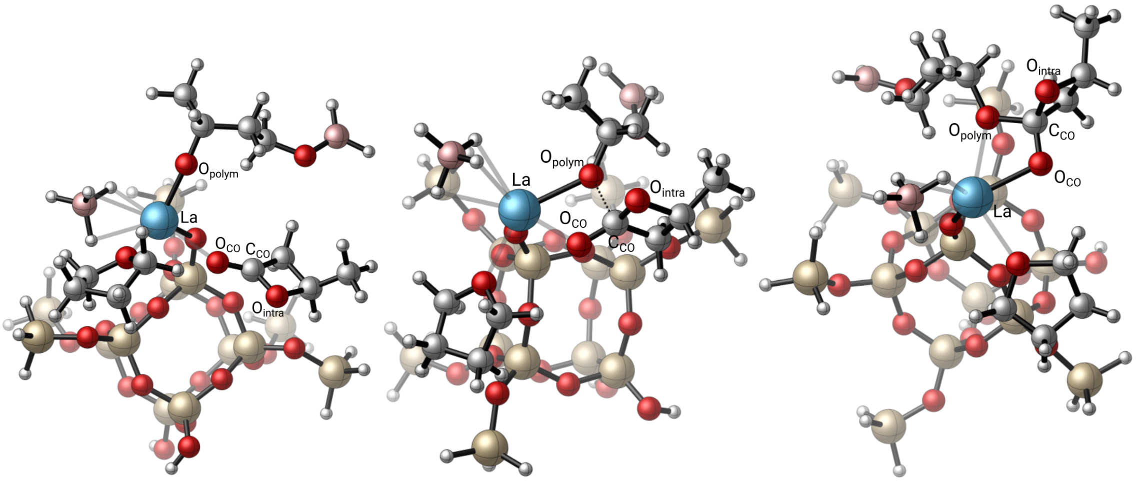

(a) $F^{RR}{}_{SiO_2}$ (b) TS-$F^{RR}G^{RR(R)}{}_{SiO_2}$ (c) $G^{RR(R)}{}_{SiO_2}$

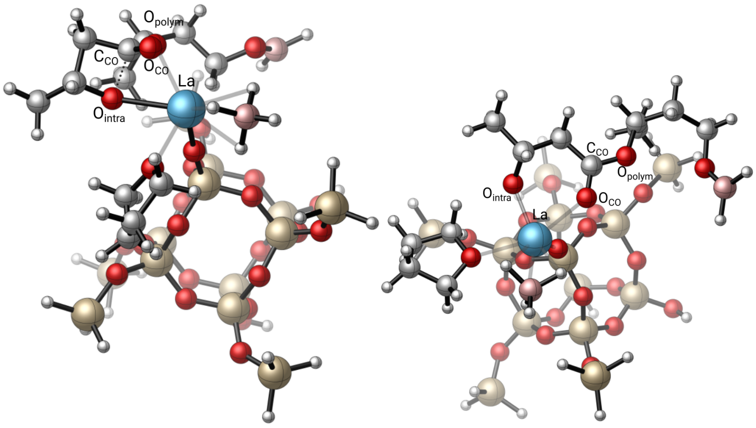

(d) TS-$G^{RR(R)}H^{RR}{}_{SiO_2}$ (e) $H^{RR}{}_{SiO_2}$

Figure 72: Optimised structures of the complexes involved in the BL-R ROP propagation step mediated by the $E^{R}{}_{SiO_2}$ catalyst.

In the following reaction, the cleavage of the acyl-$O_{intra}$ bond occurs *via* the transition states, TS-$G^{RR(R)}H^{RR}$ and TS-$G^{RR(R)}H^{RR}{}_{SiO_2}$, located at 5.5 and 9.1 kcal.mol$^{-1}$, respectively, above $F^{RR}$ and $F^{RR}{}_{SiO_2}$. As shown in Table 7, the resulting products $H^{RR}$ and $H^{RR}{}_{SiO_2}$ display a completely opened BL-R ring ($C_{CO}$-$O_{intra}$= 2.899 and 2.972 $\AA$, respectively) with the relocalisation of a double bond between the $C_{CO}$ and $O_{CO}$ atoms and the coordination of the intracyclic oxygen atom to the La center.

As described in Figure 71, the formation of the $H^{RR}$ species is more exothermic than that of the $H^{RR}{}_{SiO_2}$ analogue it displays enthalpy energies very similar to those reported above for the insertion of a second BL-R monomer. The formation of an atactic polymer has been also experimentally observed in the case of the homogeneous $[La(BH_4)_3(THF)_3]$ (3) compound.

Table 7: Selected bond lengths ($\mathring{A}$) of the stationary points calculated for the propagation step of the ROP of BL-R mediated by $E^{R}{}_{SiO_2}$. The labels refer to the intermediates and transition states depicted in Figures 72.

| | La-$O_{CO}$ | La-$O_{intra}$ | La-$O_{polym}$ | $C_{CO}$-$O_{CO}$ | $C_{CO}$-$O_{intra}$ | $C_{CO}$-$O_{polym}$ |
|---|---|---|---|---|---|---|
| | | | nucleophilic attack | | | |
| $F^{RR}$ | 2.699 | - | 2.193 | 1.210 | 1.346 | - |
| $F^{RR}{}_{SiO_2}$ | 2.629 | - | 2.169 | 1.219 | 1.335 | - |
| TS-$F^{RR}G^{RR(R)}$ | 2.470 | - | 2.401 | 1.246 | 1.376 | 1.986 |
| TS-$F^{RR}G^{RR(R)}{}_{SiO_2}$ | 2.428 | - | 2.379 | 1.261 | 1.369 | 1.925 |
| $G^{RR(R)}$ | 2.317 | - | 2.729 | 1.323 | 1.447 | 1.452 |
| $G^{RR(R)}{}_{SiO_2}$ | 2.318 | - | 2.564 | 1.325 | 1.430 | 1.479 |
| | | | Ring opening | | | |
| TS-$G^{RR(R)}H^{RR}$ | 2.390 | 2.529 | 4.158 | 1.303 | 1.663 | 1.362 |
| TS-$G^{RR(R)}H^{RR}{}_{SiO_2}$ | 2.378 | 2.478 | 3.659 | 1.301 | 1.675 | 1.364 |
| $H^{RR}$ | 2.619 | 2.223 | - | 1.234 | 2.899 | 1.323 |
| $H^{RR}{}_{SiO_2}$ | 2.574 | 2.211 | - | 1.234 | 2.972 | 1.326 |

### 3.2.2 Rac-BBL ROP promoted by the graphene grafted (gO)-[La($BH_4$)$_2$(THF)$_2$] and (gOO)-[La($BH_4$)$_2$(THF)$_2$] species

In order to investigate the influence of the support on the ROP catalytic activity of grafted borohydride La complexes, we computed the rac-BL ROP reaction, by using as catalysts the graphene grafted (gO)-[La($BH_4$)$_2$(THF)$_2$] and (gOO)-[La($BH_4$)$_2$(THF)$_2$] complexes (figures 73). The impact of using carbon supports for the La metal has been then compared to that of using silica surfaces. In order to address all the possible scenarios, we computed the ROP initiation step of both monomers (Table 10), considering the nucleophilic attack of the $BH_4$ hydride on each enantioface of each enantiomer, toward the formation of the four possible BL-R(R), BL-R(S), BL-S(S) and BL-S(S) compounds (Figure 68). As the computed profiles are identical within the accepted errors intrinsic to the DFT method, for sake of clarity we will only discuss the ROP of the BL-R enantiomer in the re enantioface (BL-R(R) case). The Figure 74 shows the enthalpy profile and the most significant transitions states for the initiation step of the BL-R ROP raction catalysed by the (gO)-[La($BH_4$)$_2$(THF)$_2$] and (gOO)-[La($BH_4$)$_2$(THF)$_2$] complexes in the re enantioface (R). A view of the different intermediates and transition state geometries is available in Figure 75 and 76 for the (gO)-[La($BH_4$)$_2$(THF)$_2$] and (gOO)-[La($BH_4$)$_2$(THF)$_2$] systems, respectively. The key geometrical parameters are summarised in Table 8.

The ROP initiation mechanism computed for the graphene supported La compounds involves the same four steps previously described for the molecular and silica supported La complexes: 1)

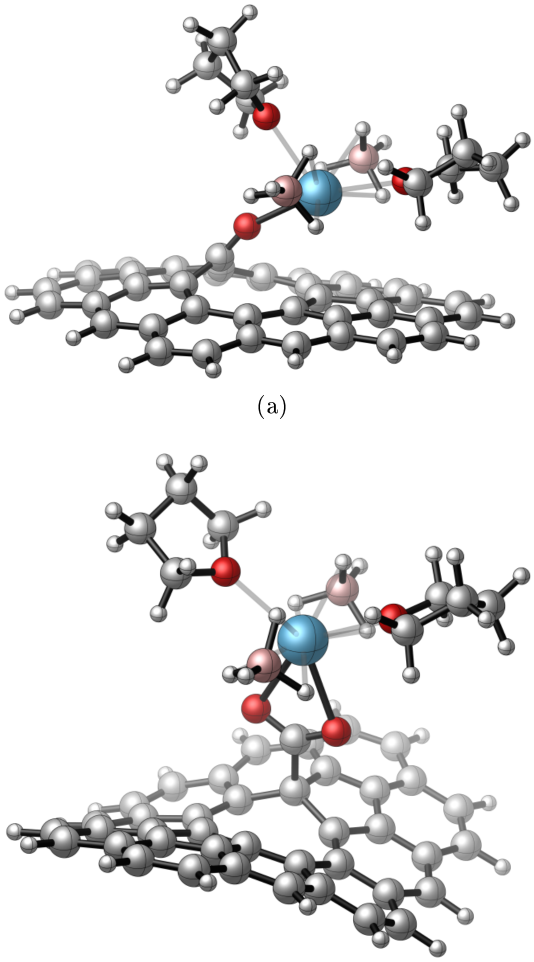

(a)

(b)

Figure 73: Structures of the grafted (a) (gO)-[La$(BH_4)_2$(THF)$_2$] and (b) (gOO)-[La$(BH_4)_2$(THF)$_2$].

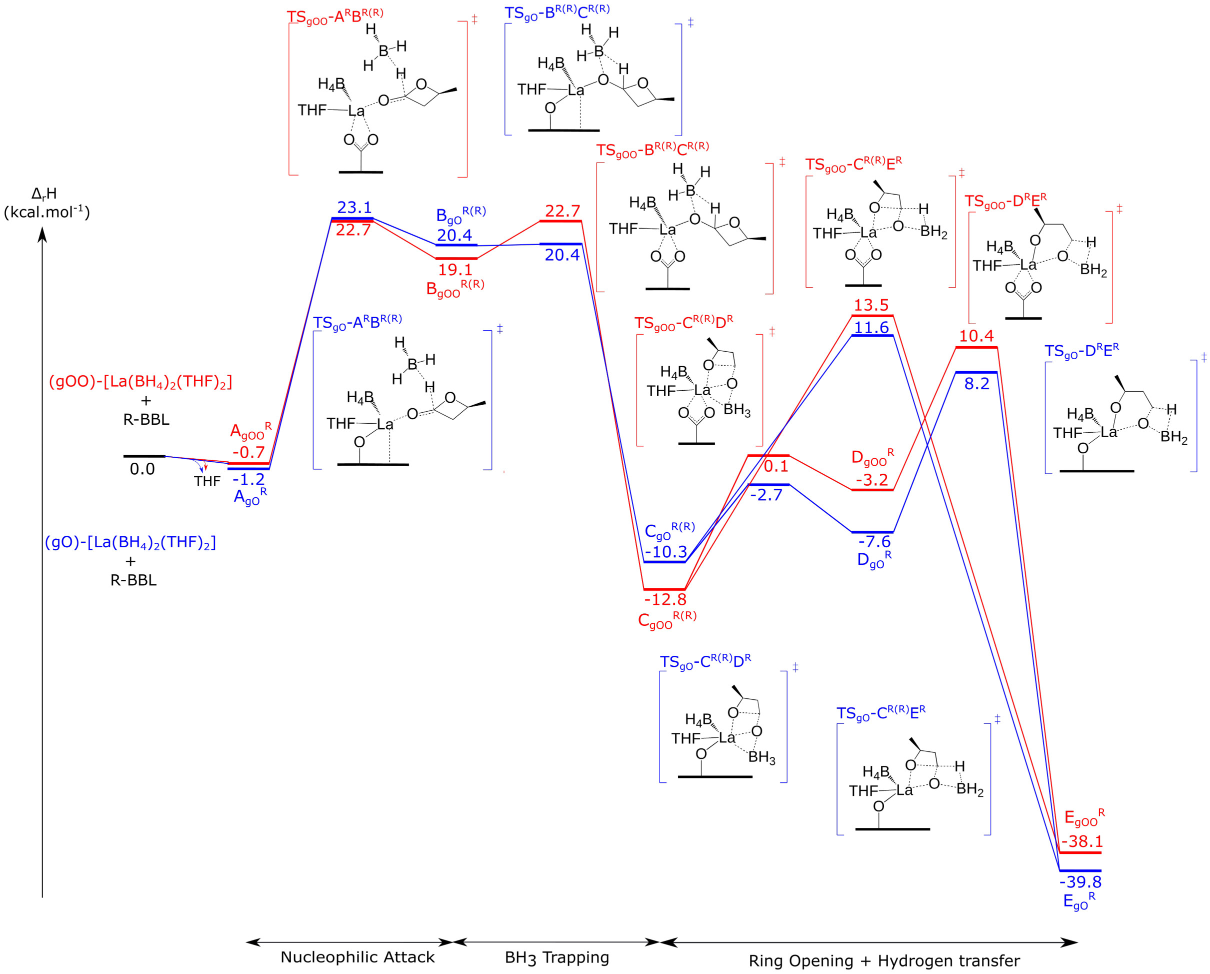

Figure 74: Enthalpy-energy profile computed for the BL-R ROP initiation step mediated by the (gO)-[La(BH$_4$)$_2$(THF)$_2$] (black) and (gOO)-[La(BH$_4$)$_2$(THF)$_2$] (red) complexes.

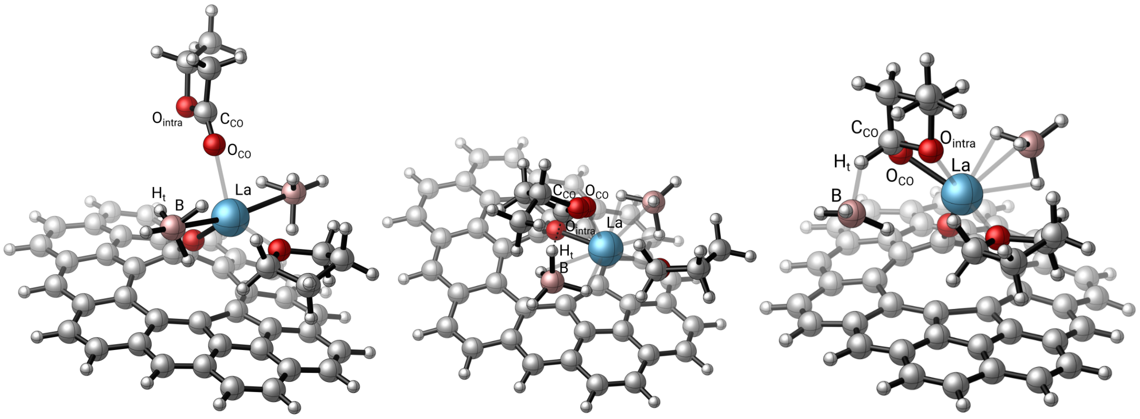

(a) $\mathrm{A}^{R}{}_{gO}$ (b) $\mathrm{TS\text{-}A}^{R}\mathrm{B}^{R(R)}{}_{gO}$ (c) $\mathrm{B}^{R(R)}{}_{gO}$

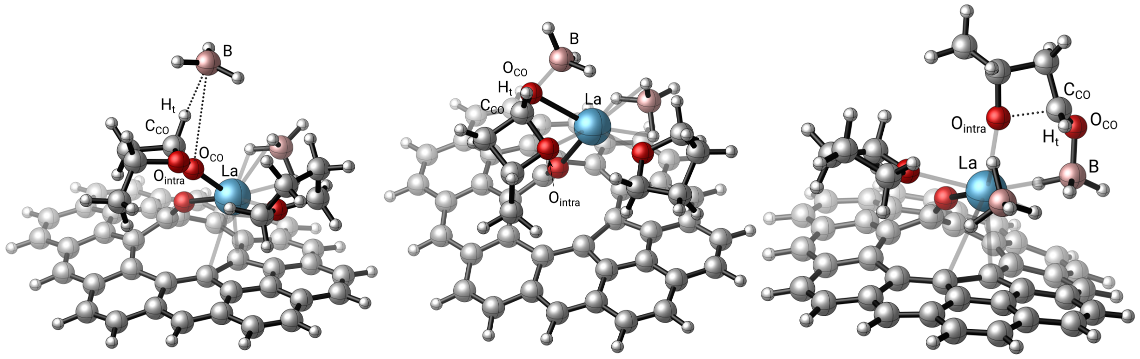

(d) $\mathrm{TS\text{-}B}^{R(R)}\mathrm{C}^{R(R)}{}_{gO}$ (e) $\mathrm{C}^{R(R)}{}_{gO}$ (f) $\mathrm{TS\text{-}C}^{R(R)}\mathrm{D}^{R}{}_{gO}$

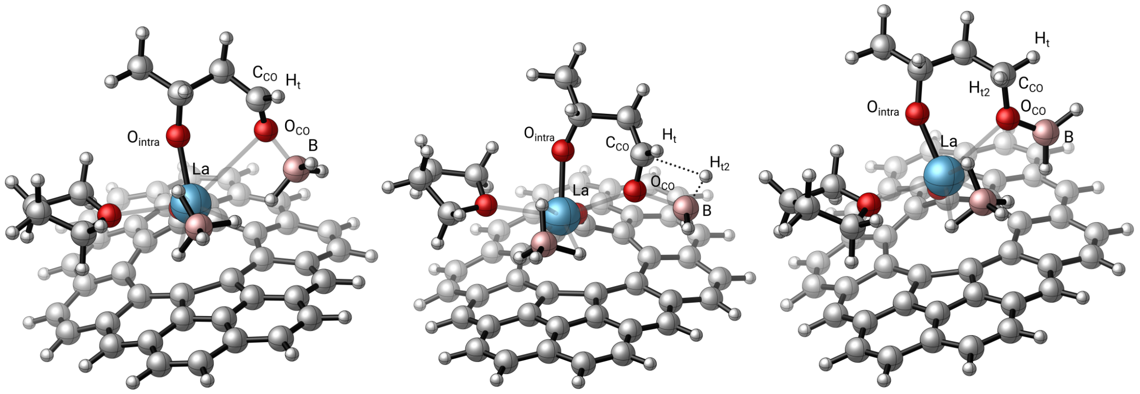

(g) $\mathrm{D}^{R}{}_{gO}$ (h) $\mathrm{TS\text{-}D}^{R}\mathrm{E}^{R}{}_{gO}$ (i) $\mathrm{E}^{R}{}_{gO}$

Figure 75: Optimised structures of the complexes involved in the BL-R ROP initiation step mediated by the (gO)-$[\mathrm{La(BH_4)_2(THF)_2}]$ catalyst.

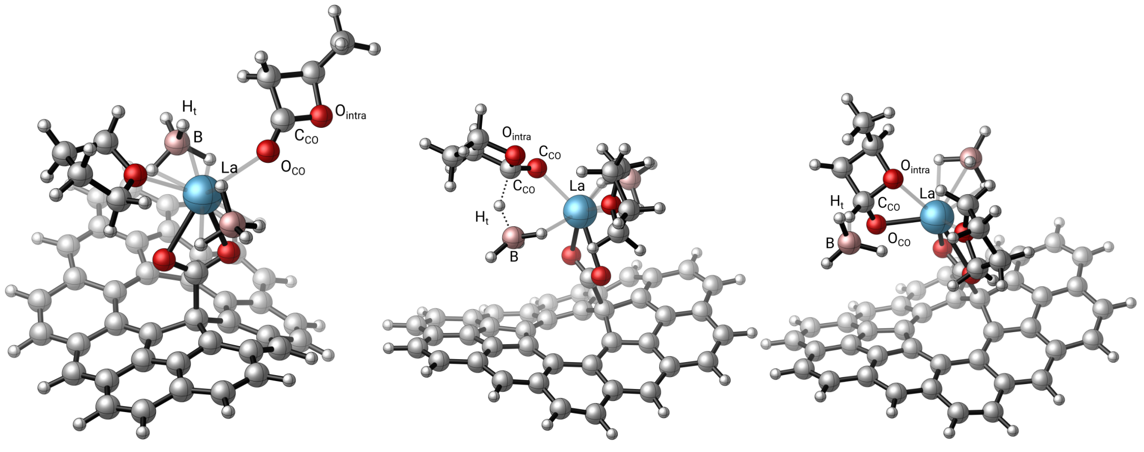

(a) $\mathrm{A}^{R}{}_{gOO}$ (b) TS-$\mathrm{A}^{R}\mathrm{B}^{R(R)}{}_{gOO}$ (c) $\mathrm{B}^{R(R)}{}_{gOO}$

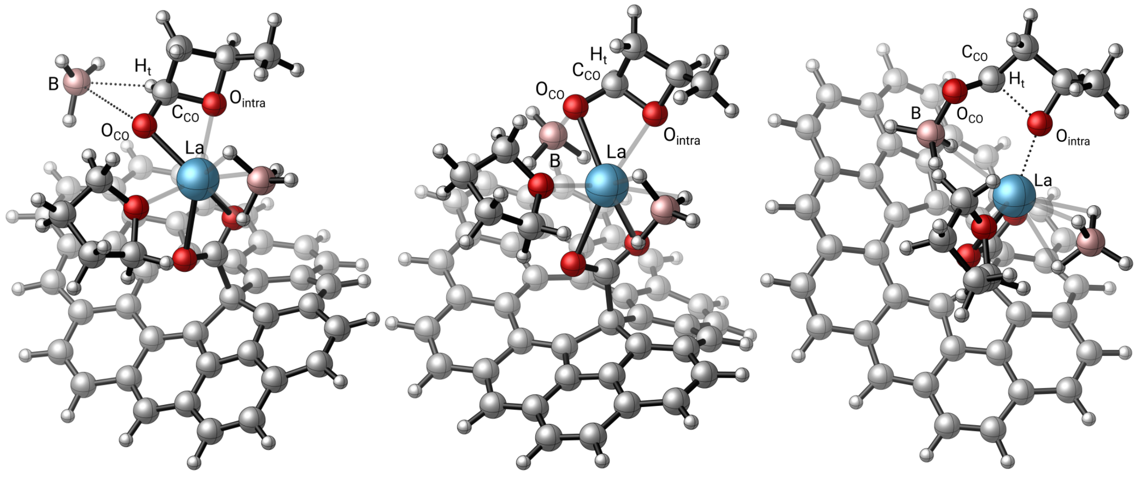

(d) TS-$\mathrm{B}^{R(R)}\mathrm{C}^{R(R)}{}_{gOO}$ (e) $\mathrm{C}^{R(R)}{}_{gOO}$ (f) TS-$\mathrm{C}^{R(R)}\mathrm{D}^{R}{}_{gOO}$

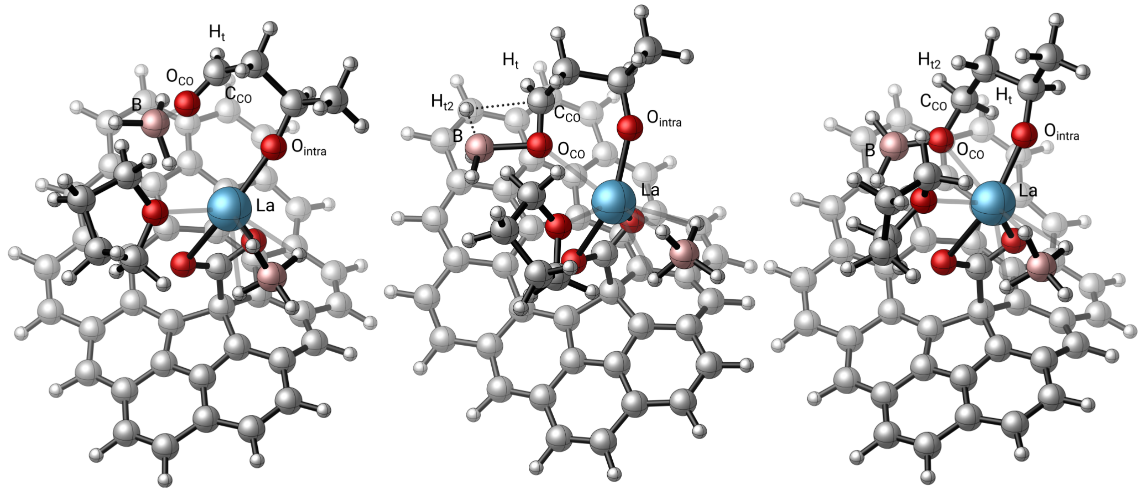

(g) $\mathrm{D}^{R}{}_{gOO}$ (h) TS-$\mathrm{D}^{R}\mathrm{E}^{R}{}_{gOO}$ (i) $\mathrm{E}^{R}{}_{gOO}$

Figure 76: Optimised structures of the complexes involved in the BL-R ROP initiation step mediated by the (gOO)-[$\mathrm{La(BH_4)_2(THF)_2}$] catalyst.

Table 8: Selected bond lengths ($\mathring{A}$) of the stationary points calculated for the initiation step of the ROP of BL-R mediated by gO-[La$(BH_4)_2(THF)_2$] (1) and gOO-[La$(BH_4)_2(THF)_2$] (2). The labels refer to the intermediates and transition states depicted in Figures 75 and 76.

| | La-$O_{CO}$ | La-$O_{intra}$ | $C_{CO}$-$O_{CO}$ | $C_{CO}$-$O_{intra}$ | $C_{CO}$-$H_t$ | B-$H_t$ | $O_{CO}$-B | B-$H_{t2}$ | $C_{CO}$-$H_{t2}$ |
|---|---|---|---|---|---|---|---|---|---|
| BL-R | - | - | 1.194 | 1.369 | - | - | - | - | - |
| nucleophilic attack | | | | | | | | | |
| $A^R{}_{gOO}$ | 2.552 | - | 1.213 | 1.334 | - | 1.238 | - | - | - |
| $A^R{}_{gO}$ | 2.487 | - | 1.217 | 1.329 | - | 1.238 | - | - | - |
| TS-$A^R B^{R(R)}{}_{gOO}$ | 2.326 | - | 1.271 | 1.373 | 1.456 | 1.287 | - | - | - |
| TS-$A^R B^{R(R)}{}_{gO}$ | 2.314 | - | 1.265 | 1.365 | 1.460 | 1.263 | - | - | - |
| $BH_3$ trapping | | | | | | | | | |
| $B^{R(R)}{}_{gOO}$ | 2.262 | 2.633 | 1.321 | 1.482 | 1.146 | 1.613 | - | - | - |
| $B^{R(R)}{}_{gO}$ | 2.248 | 2.615 | 1.317 | 1.481 | 1.163 | 1.555 | - | - | - |
| TS-$B^{R(R)} C^{R(R)}{}_{gOO}$ | 2.235 | 2.627 | 1.336 | 1.517 | 1.106 | 2.443 | 3.606 | - | - |
| TS-$B^{R(R)} C^{R(R)}{}_{gO}$ | 2.141 | 4.090 | 1.344 | 1.445 | 1.150 | 1.600 | 3.330 | - | - |
| $C^{R(R)}{}_{gOO}$ | 2.536 | 2.571 | 1.376 | 1.476 | 1.096 | - | 1.526 | 1.202 | - |
| $C^{R(R)}{}_{gO}$ | 2.470 | 2.577 | 1.374 | 1.474 | 1.094 | - | 1.540 | 1.210 | - |
| Ring opening + hydrogen transfer | | | | | | | | | |
| TS-$C^{R(R)} D^R{}_{gOO}$ | 3.442 | 2.284 | 1.261 | 1.991 | 1.094 | - | 1.543 | 1.197 | - |
| TS-$C^{R(R)} D^R{}_{gO}$ | 3.626 | 2.243 | 1.268 | 1.888 | 1.094 | - | 1.535 | 1.215 | - |
| $D^R{}_{gOO}$ | 2.962 | 2.179 | 1.248 | 2.802 | 1.097 | - | 1.578 | 1.206 | - |
| $D^R{}_{gO}$ | 3.331 | 2.128 | 1.243 | 2.701 | 1.097 | - | 1.568 | 1.210 | - |
| TS-$D^R E^R{}_{gOO}$ | 2.682 | 2.177 | 1.263 | 2.890 | 1.097 | - | 1.744 | 1.225 | 2.169 |
| TS-$D^R E^R{}_{gO}$ | 2.934 | 2.117 | 1.264 | 2.760 | 1.099 | - | 1.729 | 1.223 | 2.181 |
| $E^R{}_{gOO}$ | 2.708 | 2.128 | 1.453 | 2.910 | 1.094 | - | 1.359 | - | 1.094 |
| $E^R{}_{gO}$ | 2.734 | 2.090 | 1.456 | 2.921 | 1.094 | - | 1.356 | - | 1.093 |

the $BH_4$ hydride transfer to the carbonyl $C_{CO}$ carbon; 2) the trapping of the $BH_3$ molecule by the $O_{CO}$ atom; 3) the opening of the BL ring and 4) the reduction of the aldehyde function by the trapped $BH_3$ . After the displacement of one THF molecule upon coordination of a first rac-BL monomer, the nucleophilic attack of the $BH_4$ hydride to the carbonyl $C_{CO}$ carbon can take place with an energy barrier of 17.8 and 20.0 kcal.mol$^{-1}$ for the TS-$A^RB^{R(R)}{}_{gO}$ and TS-$A^RB^{R(R)}{}_{gOO}$, respectively, with respect to the adduct energies. The reaction progresses with the trapping of the $BH_3$ molecule by the exocyclic oxygen ($O_{CO}$) of the BL-R, the involved transition states, TS-$B^{R(R)}C^{R(R)}{}_{gO}$ and TS-$B^{R(R)}C^{R(R)}{}_{gOO}$, resulting almost barrierless with respect to the $B^{R(R)}$ adducts (0.2 and 3.6 kcal.mol$^{-1}$ respectively). Like for the molecular and silica supported systems above described, also here the resulting borane complexes ($C^{R(R)}{}_{gO}$ and $C^{R(R)}{}_{gOO}$ are computed to be exothermic by 10.3 and 12.8 kcal.mol$^{-1}$ with respect to the first $A^R$ adducts. Starting from these $C^{R(R)}$ intermediates, the two different pathways leading to the final alkoxyborane products $E^{R(R)}$ by either a one-step or a two-step mechanism have been computed. Since for both the gO and gOO systems the limiting barrier associated to the two-step pathway is lower than that corresponding to the one-step pathway (21.9 *vs.* 18.5 kcal.mol$^{-1}$ for (gO)-[$La(BH_4)_2(THF)_2$] and 26.3*vs.* 23.2 kcal.mol$^{-1}$ for (gOO)-[$La(BH_4)_2(THF)_2$], with respect to adduct $C^{R(R)}$), only the two-step mechanism will be considered for sake of clarity.

Starting from the $C^{R(R)}{}_{gO}$ and $C^{R(R)}{}_{gOO}$ adducts, the cleavage of the acyl-oxygen bond is obtained *via* TS-$C^{R(R)}D^R{}_{gO}$ and TS-$C^{R(R)}D^R{}_{gOO}$ which lie 7.6 and 12.7 kcal.mol$^{-1}$ above the $C^{R(R)}$ adducts, respectively. The resulting $D^R{}_{gO}$ and $D^R{}_{gOO}$ adducts, located at 2.7 and 9.6 kcal.mol$^{-1}$ with respect to the $C^{R(R)}{}_{gO}$ and $C^{R(R)}{}_{gOO}$ adducts, display a BL-R ring already opened with a double bond between the $C_{CO}$ and $O_{CO}$ atoms ($C_{CO}$ -$O_{CO}$ = 1.243 $\mathring{A}$ for both $D^R{}_{gO}$ and $D^R{}_{gOO}$, see table 8). From the $D^R{}_{gO}$ and $D^R{}_{gOO}$ adducts, the transfer of the second $BH_3$ hydride to the acyl $C_{CO}$ atom may then occurr, affording the complexes $E^R{}_{gO}$ and $E^R{}_{gOO}$ *via* transition states TS-$D^RE^R{}_{gO}$ and TS-$D^RE^R{}_{gOO}$, located at 18.5 and 23.2 kcal.mol$^{-1}$, respectively, relative to the $C^{R(R)}$ adducts. As previously observed for the molecular La complex, the analysis of the whole profile in figure 74 indicates that for both the (gO)-[$La(BH_4)_2(THF)_2$] and (gOO)-[$La(BH_4)_2(THF)_2$] the three barriers involved in i) the first $BH_4$ hydride transfer, ii) the following $BH_3$ trapping and iii) the second $BH_3$ hydride transfer are energetically similar (17.8, 21.6 and 18.5 kcal.mol$^{-1}$ for (gO)-[$La(BH_4)_2(THF)_2$] and 20.0, 23.4 and 23.2 kcal.mol$^{-1}$ for (gOO)-[$La(BH_4)_2(THF)_2$]). As shown in figure 74, in addition, except for the $B^{R(R)}$ and $C^{R(R)}$ adducts, in which the gO species is slightly less stable than the gOO counterpart, the whole profile of the (gOO)-[$La(BH_4)_2(THF)_2$] species is sligtly higher in energy than that of the gO analogue. The barrier heights of the (gO)-[$La(BH_4)_2(THF)_2$] complex, indeed, are slightly lower by 2.2, 1.8 and 4.7 kcal.mol$^{-1}$ than those of the (gOO)-[$La(BH_4)_2(THF)_2$] system, indicating that the gO-grafted complex is likely to behave as a more active BL ROP catalyst. Since for the silica supported (≡SiO)-[$La(BH_4)_2(THF)_2$] system the rate-determining step of the entire ROP process clearly corresponds to the first $BH_4$ hydride transfer together with the following $BH_3$ trapping step, a careful comparison of this first part of the profile between all the four catalytic species investigated here, *i.e.* the molecular, the silica- and the two graphene-supported La catalysts, may help to rationalise their computed and experimentally measured catalytic activities.[162] In order to compare the Lewis acidity of the graphene grafted systems with that previously reported for the [$La(BH_4)_3(THF)_3$] and (≡SiO)-[$La(BH_4)_2(THF)_2$] complexes, we optimised the (gO)-[La$(BH_4)_2$(THF)($OPPh_3$)] and (gOO)-[La$(BH_4)_2$(THF)($OPPh_3$)] complexes and we computed their corresponding IR and $^1$H, $^{13}$C and $^{31}$P NMR spectra. The C-H, aromatic C=C and O=P vibrational frequencies of the coordinated O=$PPh_3$ molecule are reported in Table 6. The aromatic C-H and C-C stretching vibrations are similar for both complexes (in the range 3200-3233 cm$^{-1}$ and 1336-1655 cm$^{-1}$, respectively), whereas the vibrational stretching mode corresponding to the O=P function lies at 1025 and 1039 cm$^{-1}$ for the (gO)-[La$(BH_4)_2$(THF)($OPPh_3$)] and (gOO)-[La$(BH_4)_2$(THF)($OPPh_3$)] systems, respectively. To better characterise the nature of the metal center we also computed the theoretical $^1$H, $^{13}$C and $^{31}$P NMR chemical shift of the coordinated O=$PPh_3$ molecule (Table 6). The two complexes display similar values for the $^1$H 7.7 and 7.8 ppm and $^{13}$C [124.7/128.7] and [124.9/129.2] isotropic chemical shift for the (gO)-[La$(BH_4)_2$(THF)($OPPh_3$)] and (gOO)-[La$(BH_4)_2$(THF)($OPPh_3$)] systems, respectively, whereas different values are obtained for the $^{31}$P NMR signals (60.3 and 55.0 ppm for the (gO)-[La$(BH_4)_2$(THF)($OPPh_3$)] and (gOO)-[La$(BH_4)_2$(THF)($OPPh_3$)] systems, respectively). Compared to the gOO compound, therefore, the gO system displays a lower O=P vibrational frequency (1025 *vs.* 1039 cm$^{-1}$ for the gO and gOO complexes, respectively) and a higher $^{31}$P NMR chemical shift (60.3 *vs.* 55.0 ppm the gO and gOO complexes, respectively). This reflects a weaker O=P bond and thus a stronger La-O bond for the (gO)-[La$(BH_4)_2$(THF)($OPPh_3$)] complex, which consequently behaves as a stronger Lewis acid. If we compare the graphene surfaces with the silica one, we can observe that the graphene grafted complexes display lower IR O=P vibrational frequencies (1025, 1039 and 1050 cm$^{-1}$ for the gO gOO and silica supported complexes, respectively) and more deshielded $^{31}$P NMR values (60.3, 55.0 and 53.4 ppm for the gO, gOO and silica supported complexes, respectively). This indicates that the graphene surfaces electronically deplete the metal center more than the silica surfaces, the Lewis acidic character increasing in the order (≡SiO)-[La$(BH_4)_2$(THF)($OPPh_3$)] $<$ (gOO)-[La$(BH_4)_2$(THF)($OPPh_3$)] $<$ (gO)-[La$(BH_4)_2$(THF)($OPPh_3$)]. If now we compare the first $BH_4$ hydride transfer process (TS-$A^RB^{R(R)}$) in the four complexes we can observe that the corresponding activation barrier increases from 17.8 to 18.1 to 20.0 and to 25.2 kcal.mol$^{-1}$ ongoing from the gO, to the molecular, to the gOO and to the silica system. In accordance with the Lewis acidity trend previously established, therefore, the graphene grafted systems are expected to catalyse the BL ROP reaction more efficiently than the silica supported analogue, showing similar catalytic activities to those experimentally measured for the molecular [La$(BH_4)_3(THF)_3$] complex. As previously discussed, although the starting molecular complex results the less Lewis acidic, the loss of the $BH_4$ group in the geometry of the first hydrogen transfer transition state (TS-$A^RB^{R(R)}$) causes an increase in its acidity, resulting in an activation barrier comparable to that of the graphene supported complexes. The catalytic behaviour of the four compounds is in accordance with the geometrical parameters of the corresponding TS-$A^RB^{R(R)}$ transition states. While in the TS-$A^RB^{R(R)}{}_{gO}$, the La-$O_{CO}$ and the $O_{CO}$=$C_{CO}$ bond distances measure 2.314 and 1.265 $\AA$, in the TS-$A^RB^{R(R)}{}_{gOO}$ system, on the other hand, they measure 2.326 and 1.271 $\AA$, reflecting the slightly lower BBL monomer activation in the case of the gOO grafted complex compared to the gO analogue. In the TS-$A^RB^{R(R)}{}_{gO}$ geometry, in addition, the greater proximity of the BBL monomer to the La metal allows a more effective transfer of the $BH_4$ hydrogen to the $C_{CO}$ atom, with a B-H-$C_{CO}$ angle of 144.8° (compared to 139.3° in the TS-$A^RB^{R(R)}{}_{gOO}$ complex). As a consequence of the BBL activation strength, while in the TS-$A^RB^{R(R)}{}_{gO}$ geometry the $BH_4$ ligand remains close to

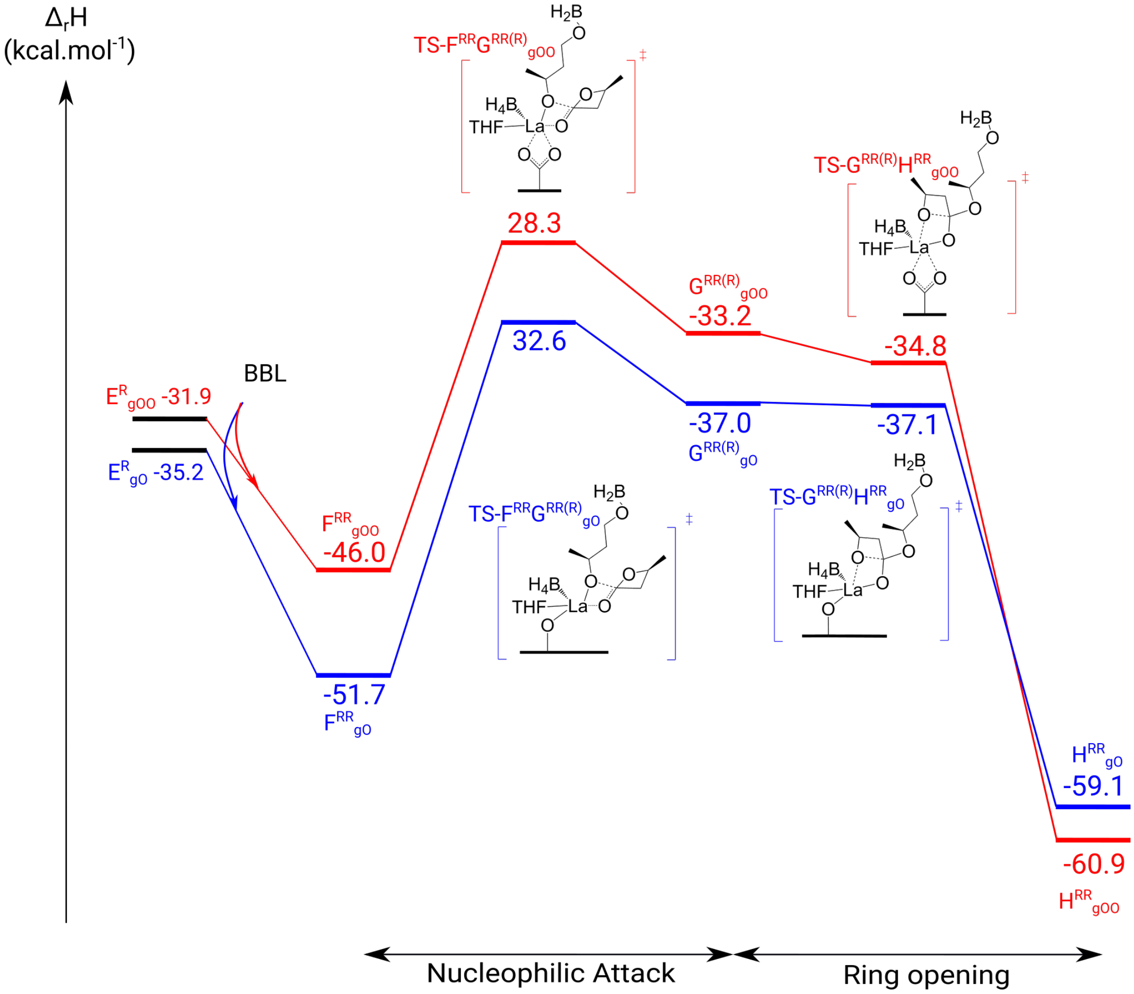

Figure 77: Enthalpy-energy profile computed for the BL-R ROP propagation step mediated by the $E^{R}{}_{gO}$ (blue) and $E^{R}{}_{gOO}$ (red) complexes.

the La metal (the shortest $(H_3B)H$-La distance measures 2.547 $\mathring{A}$, with a $H_4B$-La distance of 2.966 $\mathring{A}$), in the TS-$A^{R}B^{R(R)}{}_{gOO}$ geometry, on the other hand, the $BH_4$ ligand must move away from the metal coordination sphere to perform the hydrogen transfer (the shortest $(H_3B)H$-La distance measures 2.584 $\mathring{A}$, with a $H_4B$-La distance of 3.009 $\mathring{A}$). In the gOO complex, therefore, differently from the molecular complex in which the additional THF molecule can compensate for the loss of the $BH_4$ group, the moving away of the $BH_4$ group, due to the lower activation of the BBL monomer, destabilises the system, increasing the corresponding barrier. The silica-supported complex, as seen before, displays the same behaviour in a more accentuated form (the shortest $(H_3B)H$-La distance measures 2.612 $\mathring{A}$, with a $H_4B$-La distance of 3.339 $\mathring{A}$), providing, as a consequence, the most energy demanding $BH_4$ hydrogen transfer process.

The insertion of a second BL-R monomer to the $E^{R}$ complexes has been then investigated. The computed enthalpy profile of this ROP propagation process is depicted in figure 77 and a view of the different transition states and intermediates is reported in Figures 78 and 79. The key geometrical parameters are summarised in Table 9.

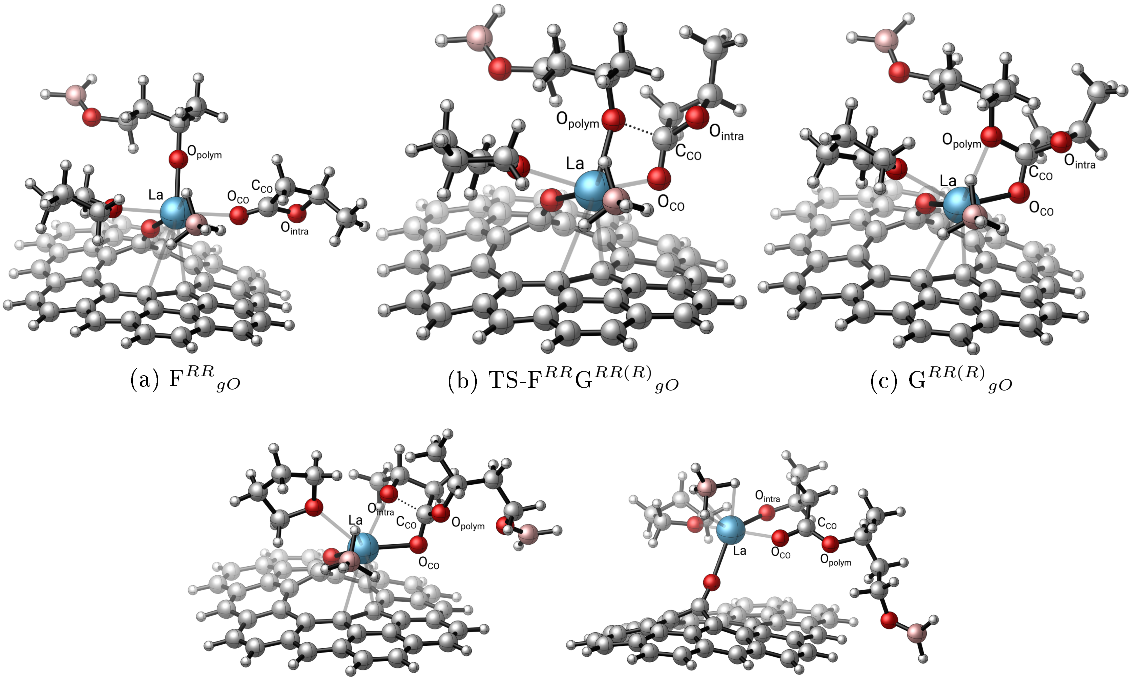

(a) $F^{RR}{}_{gO}$ (b) TS-$F^{RR}G^{RR(R)}{}_{gO}$ (c) $G^{RR(R)}{}_{gO}$

(d) TS-$G^{RR(R)}H^{RR}{}_{gO}$ (e) $H^{RR}{}_{gO}$

Figure 78: Optimised structures of the complexes involved in the BL-R ROP propagation step mediated by the $E^{R}{}_{gO}$ catalyst.

Table 9: Selected bond lengths ($\mathring{A}$) of the stationary points calculated for the propagation step of the ROP of BL-R mediated by $E^{R}{}_{gO}$ and $E^{R}{}_{gOO}$. The labels refer to the intermediates and transition states depicted in Figures 78 and 79.

| | La-$O_{CO}$ | La-$O_{intra}$ | La-$O_{polym}$ | $C_{CO}$-$O_{CO}$ | $C_{CO}$-$O_{intra}$ | $C_{CO}$-$O_{polym}$ |
|---|---|---|---|---|---|---|
| | | | nucleophilic attack | | | |
| $F^{RR}{}_{gOO}$ | 2.570 | - | 2.128 | 1.216 | 1.335 | - |
| $F^{RR}{}_{gO}$ | 2.562 | - | 2.096 | 1.215 | 1.335 | - |
| TS-$F^{RR}G^{RR(R)}{}_{gOO}$ | 2.354 | - | 2.350 | 1.273 | 1.372 | 1.819 |
| TS-$F^{RR}G^{RR(R)}{}_{gO}$ | 2.334 | - | 2.333 | 1.268 | 1.371 | 1.867 |
| $G^{RR(R)}{}_{gOO}$ | 2.268 | - | 3.985 | 1.330 | 1.550 | 1.369 |
| $G^{RR(R)}{}_{gO}$ | 2.210 | - | 2.578 | 1.337 | 1.420 | 1.464 |
| | | | Ring opening | | | |
| TS-$G^{RR(R)}H^{RR}{}_{gOO}$ | 2.301 | 2.438 | 3.943 | 1.315 | 1.358 | 1.639 |
| TS-$G^{RR(R)}H^{RR}{}_{gO}$ | 2.281 | 2.423 | 3.581 | 1.304 | 1.713 | 1.350 |
| $H^{RR}{}_{gOO}$ | 2.576 | 2.142 | - | 1.237 | 2.850 | 1.318 |
| $H^{RR}{}_{gO}$ | 2.487 | 2.148 | - | 1.236 | 2.877 | 1.320 |

The reaction begins with the coordination of a second BL-R monomer to the La center, leading to the formation of the $F^{RR}{}_{gO}$ and $F^{RR}{}_{gOO}$ intermediates *via* an exothermic process (-51.7 and-46.0 kcal.mol$^{-1}$ respectively, with respect to the entrance channel). The nucleophilic attack of

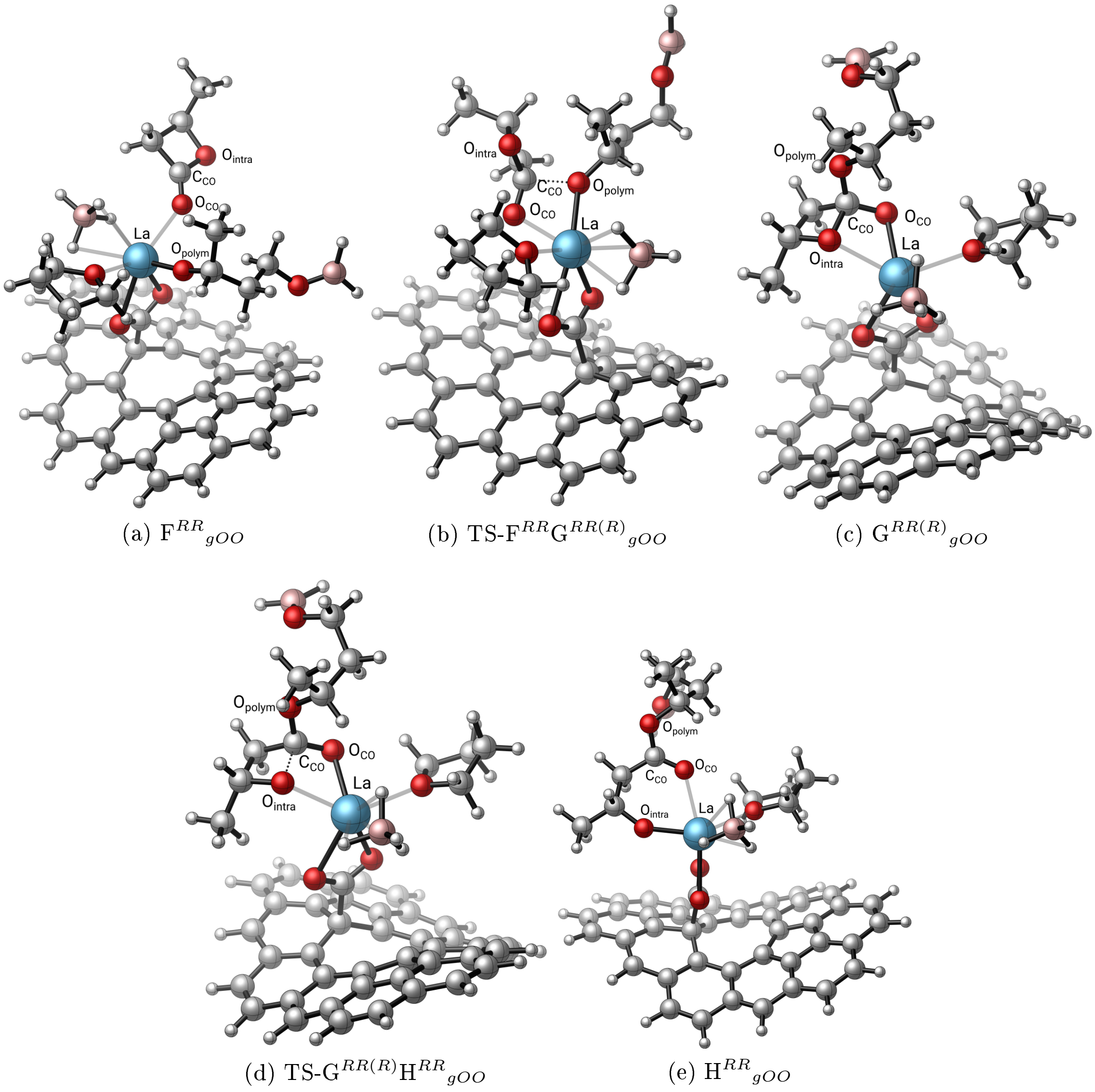

(a) $\mathrm{F}^{RR}{}_{gOO}$ (b) TS-$\mathrm{F}^{RR}\mathrm{G}^{RR(R)}{}_{gOO}$ (c) $\mathrm{G}^{RR(R)}{}_{gOO}$

(d) TS-$\mathrm{G}^{RR(R)}\mathrm{H}^{RR}{}_{gOO}$ (e) $\mathrm{H}^{RR}{}_{gOO}$

Figure 79: Optimised structures of the complexes involved in the BL-R ROP propagation step mediated by the $\mathrm{E}^{R}{}_{gOO}$ catalyst.

Table 10: Enthalpy data (kcal.mol$_{-1}$) of the initiation step of the ROP of BL mediated by gO-[La$(BH_4)_2(THF)_2$] (1) and gOO-[La$(BH_4)_2(THF)_2$] (2).

| gO-[La$(BH_4)_2THF_2$] | $\Delta_r$H | gOO-[La$(BH_4)_2THF_2$] | $\Delta_r$H |
|---|---|---|---|
| | nucleophilic attack | | |
| $A^R{}_{gO}$ | -1.2 | $A^R{}_{gOO}$ | -0.7 |
| TS-$A^RB^{R(R)}{}_{gO}$ | 16.6 | TS-$A^RB^{R(R)}{}_{gOO}$ | 19.3 |
| $A^S{}_{gO}$ | -1.1 | $A^S{}_{gOO}$ | -0.7 |
| TS-$A^SB^{S(R)}{}_{gO}$ | 22.0 | TS-$A^SB^{S(R)}{}_{gOO}$ | 21.0 |
| | $BH_3$ trapping | | |
| $B^{R(R)}{}_{gO}$ | 20.2 | $B^{R(R)}{}_{gOO}$ | 19.1 |
| TS-$B^{R(R)}C^{R(R)}{}_{gO}$ | 20.4 | TS-$B^{R(R)}C^{R(R)}{}_{gOO}$ | 22.7 |
| $C^{R(R)}{}_{gO}$ | -10.3 | $C^{R(R)}{}_{gOO}$ | -12.8 |
| $B^{S(R)}{}_{gO}$ | 20.2 | $B^{S(R)}{}_{gOO}$ | 19.2 |
| TS-$B^{S(R)}C^{S(R)}{}_{gO}$ | 22.9 | TS-$B^{S(R)}C^{S(R)}{}_{gOO}$ | 21.0 |
| $C^{S(R)}{}_{gO}$ | -12.0 | $C^{S(R)}{}_{gOO}$ | -13.0 |
| | Ring opening + hydrogen transfer | | |
| TS-$C^{R(R)}D^R{}_{gO}$ | -2.7 | TS-$C^{R(R)}D^R{}_{gOO}$ | 0.1 |
| $D^R{}_{gO}$ | -7.6 | $D^{R(R)}{}_{gOO}$ | -3.2 |
| TS-$D^RE^R{}_{gO}$ | 8.2 | TS-$D^RE^R{}_{gOO}$ | 10.4 |
| $E^R{}_{gO}$ | -39.8 | $E^R{}_{gOO}$ | -38.1 |
| TS-$C^{S(R)}D^S{}_{gO}$ | -3.2 | TS-$C^{S(R)}D^S{}_{gOO}$ | 1.7 |
| $D^{SR}{}_{gO}$ | -7.3 | $D^S{}_{gOO}$ | -6.0 |
| TS-$D^SE^S{}_{gO}$ | 6.2 | TS-$D^SE^S{}_{gOO}$ | 9.6 |
| $E^S{}_{gO}$ | -39.6 | $E^S{}_{gOO}$ | -39.2 |

the oxygen atom of the alkoxyborane group to the carbonyl carbon $C_{CO}$ of the incoming BL-R monomer can then occur through TS-$F^{RR}G^{RR(R)}{}_{gO}$ and TS-$F^{RR}G^{RR(R)}{}_{gOO}$. The corresponding activation barriers measure 19.1 and 17.7 kcal.mol$^{-1}$ with respect to the $F^{RR}{}_{gO}$ and $F^{RR}{}_{gOO}$ species, respectively, resulting therefore kinetically accessible.

In the following reaction, the cleavage of the acyl-$O_{intra}$ bond occurs *via* the transition states, TS-$G^{RR(R)}H^{RR}{}_{gO}$ and TS-$G^{RR(R)}H^{RR}{}_{gOO}$, located at 14.6 and 11.2 kcal.mol$^{-1}$, respectively, above the $F^{RR}{}_{gO}$ and $F^{RR}{}_{gOO}$ intermediates. As shown in Table 9, the resulting products $H^{RR}{}_{gO}$ and $H^{RR}{}_{gOO}$ display a completely opened BL-R ring ($C_{CO}$-$O_{intra}$= 2.877 and 2.850 $\mathring{A}$, respectively) with the relocalisation of a double bond between the $C_{CO}$ and $O_{CO}$ atoms and the coordination of the intracyclic oxygen atom to the La center. As seen above, the enthalpy profile corresponding to the insertion of a second BL-S monomer has been also computed (Table 11). It displays enthalpy energies very similar to those reported above for the insertion of a second BL-R monomer, confirming, from a theoretical point of view, the formation of an atactic polymer as previously discussed in the initiation step as well as in the polymerisation process catalysed by the molecular and silica supported systems.

In this contribution we have carry out a complete DFT study on the influence of the support on the catalytic activity of the corresponding La grafted complexes toward the rac-

Table 11: Enthalpy data (kcal.mol$^{-1}$) of the first propagation step of the ROP of BL mediated by gO-[La(BH$_4$)$_2$(THF)$_2$] (1) and gOO-[La(BH$_4$)$_2$(THF)$_2$] (2).

| gO-[La(BH$_4$)$_2$THF$_2$] | $\Delta_r$H | gOO-[La(BH$_4$)$_2$THF$_2$] | $\Delta_r$H |
|---|---|---|---|
| | | nucleophilic attack | |
| $\mathrm{F}^{RR}{}_{gO}$ | -51.7 | $\mathrm{F}^{RR}{}_{gOO}$ | -46.0 |
| $\mathrm{TS\text{-}F}^{RR}\mathrm{G}^{RR(R)}{}_{gO}$ | -32.6 | $\mathrm{TS\text{-}F}^{RR}\mathrm{G}^{RR(R)}{}_{gOO}$ | -28.3 |
| $\mathrm{G}^{RR(R)}{}_{gO}$ | -37.0 | $\mathrm{G}^{RR(R)}{}_{gOO}$ | -33.2 |
| $\mathrm{F}^{RS}{}_{gO}$ | -51.8 | $\mathrm{F}^{RS}{}_{gOO}$ | -46.6 |
| $\mathrm{TS\text{-}F}^{RS}\mathrm{G}^{RS(R)}{}_{gO}$ | -34.4 | $\mathrm{TS\text{-}F}^{RS}\mathrm{G}^{RS(R)}{}_{gOO}$ | -28.7 |
| $\mathrm{G}^{RS(R)}{}_{gO}$ | -37.8 | $\mathrm{G}^{RS(R)}{}_{gOO}$ | -37.1 |
| $\mathrm{F}^{SS}{}_{gO}$ | -50.8 | $\mathrm{F}^{SS}{}_{gOO}$ | -46.5 |
| $\mathrm{TS\text{-}F}^{SS}\mathrm{G}^{SS(R)}{}_{gO}$ | -34.9 | $\mathrm{TS\text{-}F}^{SS}\mathrm{G}^{SS(R)}{}_{gOO}$ | -31.4 |
| $\mathrm{G}^{SS(R)}{}_{gO}$ | -37.1 | $\mathrm{G}^{SS(R)}{}_{gOO}$ | –38.3 |
| $\mathrm{F}^{SR}{}_{gO}$ | -50.2 | $\mathrm{F}^{SR}{}_{gOO}$ | -47.0 |
| $\mathrm{TS\text{-}F}^{SR}\mathrm{G}^{SR(R)}{}_{gO}$ | -31.2 | $\mathrm{TS\text{-}F}^{SR}\mathrm{G}^{SR(R)}{}_{gOO}$ | -33.0 |
| $\mathrm{G}^{SR(R)}{}_{gO}$ | -36.8 | $\mathrm{G}^{SR(R)}{}_{gOO}$ | -37.3 |
| | | Ring opening | |
| $\mathrm{TS\text{-}G}^{RR(R)}\mathrm{H}^{RR}{}_{gO}$ | -37.1 | $\mathrm{TS\text{-}G}^{RR(R)}\mathrm{H}^{RR}{}_{gOO}$ | -34.8 |
| $\mathrm{H}^{RR}{}_{gO}$ | -59.1 | $\mathrm{H}^{RR}{}_{gOO}$ | -60.9 |
| $\mathrm{TS\text{-}G}^{RS(R)}\mathrm{H}^{RS}{}_{gO}$ | -32.8 | $\mathrm{TS\text{-}G}^{RS(R)}\mathrm{H}^{RS}{}_{gOO}$ | -35.9 |
| $\mathrm{H}_{OH}{}^{RS}$ | -61.5 | $\mathrm{H}^{RS}{}_{gOO}$ | -62.7 |
| $\mathrm{TS\text{-}G}^{SS(R)}\mathrm{H}^{SS}{}_{gO}$ | -37.6 | $\mathrm{TS\text{-}G}^{SS(R)}\mathrm{H}^{S}{}_{gOO}$ | -39.7 |
| $\mathrm{H}^{SS}{}_{gO}$ | -58.2 | $\mathrm{H}^{SS}{}_{gOO}$ | -62.3 |
| $\mathrm{TS\text{-}G}^{SR(R)}\mathrm{H}^{SR}{}_{gO}$ | -37.1 | $\mathrm{TS\text{-}G}^{SR(R)}\mathrm{H}^{SR}{}_{gOO}$ | -39.1 |
| $\mathrm{H}^{SR}{}_{gO}$ | -58.0 | $\mathrm{H}^{SR}{}_{gOO}$ | -62.9 |

BL ROP process. We have computed the initiation and first propagation steps of the controlled rac-BL ROP reaction by using as catalysts four different lanthanum complexes, *i.e.* the molecular [La$(BH_4)_3(THF)_3$], the silica supported (≡SiO)-[La$(BH_4)_2(THF)_2$] and the graphene-supported (gO)-[La$(BH_4)_2(THF)_2$] and (gOO)-[La$(BH_4)_2(THF)_2$] compounds. Differently from the (≡SiO)-[La$(BH_4)_2(THF)_2$] species, which poorly catalyses the BL ROP reaction, the (gO)-[La$(BH_4)_2(THF)_2$ and (gOO)-[La$(BH_4)_2(THF)_2$] systems are likely to efficiently polymerise the BL monomer, displaying the same efficiency as the homogeneous [La$(BH_4)_3(THF)_3$] (3) compound. The nature of the surface plays therefore an important role, influencing the Lewis acidity and therefore the reactivity of the grafted La compounds. According to an in-depth analysis of the enthalpy profiles, the step that differentiates the catalytic activity of the four compounds corresponds the first $BH_4$ hydride transfer to the carbonyl carbon of the BBL monomer. In accordance with the catalytic behavior observed for the four complexes, As observed in the corresponding transition states, indeed, while the molecular and graphene grafted complexes efficiently activate the BBL monomer providing an effective $BH_4$ hydride transfer, the silica grafted analogue poorly activate the BBL monomer, making the hydride transfer more constrained. In the latter system, indeed, the lower proximity of the coordinated BBL monomer forces the $BH_4$ ligand to move away from the metal coordination sphere, destabilising the complex with the consequent increase of the corresponding activation barrier. This is in accordance with the Lewis acidity trend, showing that the higher the Lewis acidic character of the metal center in the involved transition state, the stronger the BBL monomer activation and therefore the more effective the $BH_4$ hydride transfer.

Graphene supported La borohydride complexes may therefore represent interesting target compounds, combining the hight catalytic activity in the rac-BL ROP reaction with the advantages of the heterogeneous catalysis.

## 3.3 Conclusion

In this section we show that the [La$(N(SiMe_3)_2)_3$] lanthanide compound can be easily grafted on graphene-OH and -COOH functionalised surfaces, affording two stables mono-grafted compounds : the monocoordinated (gO)-[La$(N(SiMe_3)_2)_2$] system, displaying a stabilising interaction between the La metal and the underlying graphene surface and the bicoordinated (gOO)-[La$(N(SiMe_3)_2)_2$] species with both oxygens of the carboxylate group bonded to the La metal. While in the gO system, the La-surface interaction provides a modular electronic assistance of the surface, increasing however the steric hindrance around the metal, in the (gOO)-[La$(CH_3)_2$] compound, on the other hand, the bicordination of the carboxo group forces the metal complex to rise from the surface, providing a more rigid but less sterically encumbered system. Similarly to experimental approaches, the coordination of triphenylphosphine oxide ($O{=}PPh_3$) has been computed as a probe of the Lewis acidity of the metal. The spectroscopic values (IR and NMR) obtained for the corresponding (gO)-[La$(N(SiMe_3)_2)_2(O{=}PPh_3)$] and (gOO)-[La$(N(SiMe_3)_2)_2(O{=}PPh_3)$] species indicate that the graphene grafted lanthanum silylamido complexes are more Lewis acidic than the silica grafted analogues, the nature of the surface clearly playing an important role.

In order to understand the role of the support, we investigated the catalytic activity of graphene supported La compounds toward both the homo- and co-polymerisation of ethylene and 1,3-butadiene, by using the alkyl (gO)-[La$(CH_3)_2$] (1gO) and (gOO)-[La$(CH_3)_2$] (1gOO) complexes as models of the graphene supported La active species. Both compounds efficiently catalyse the ethylene homopolymerisation, displaying activation barriers which are significantly lower than those reported for silica grafted compounds. The graphene surfaces are therefore predicted to play an important role, increasing the Lewis acidity and therefore the reactivity of the grafted La systems compared to oxygenated silica surfaces. We have also shown that while in the gOO model the ethylene polymerisation may take place on both arms, in the gO model, on the other hand, only a one-growing arm polymerisation is observed, the interaction of the metal with the graphene surface increasing the steric hindrance around the metal. Concerning the 1,3-butadiene homopolymerisation, both graphene-grafted La complexes are ex- pected to behave as efficient catalysts and owing to their higher Lewis acidity they result more active than the silica-grafted La analogues. In the gOO model, the 1,4-cis 1,3-butadiene insertion is preferred over the 1,4-trans one, affording preferentially a 1,4-cis-polybutadiene polymer, as previously reported for silica-supported La compounds. Differently, the gO model inserts the 1,4-cis or 1,4-trans 1,3-butadiene without distinction, giving rise to a random 1,4-polybutadiene polymer. The stereoselectivity of the 1,3-butadiene polymerisation reaction is therefore different for the gO model compared to the gOO and silica supported systems, underlying once again the influence of the support on the polymerisation reaction outcome. The catalytic behaviour of 1gO and 1gOO has been finally investigated in the ethylene and 1,3 butadiene co-polymerisation reaction. We have shown that for both the gO and gOO complexes the insertion of the 1,4-cis 1,3-butadiene monomers is favoured over that of ethylene, due to the formation of highly stable allylic products. The higher stability of the allylic products compared to the alkyl ones, indeed, drives the reaction toward the exclusive 1,3-butadiene insertion, preventing any alternating copolymerisation reaction. In conclusion, therefore, functionalised graphene surfaces constitute efficient supports for lanthanide organometallic compounds. These graphene surfaces are likely to enhance the Lewis acidity of the La metal, playing therefore an active role in the catalytic activity of supported La complexes. Graphene supported La alkyl compounds efficiently catalyse the ethylene and 1,3-butadiene homopolymerisation, with activities and stereoselectivities depending on the nature and the coordination mode of the graphene suppport.

We subsequently explored the catalytic activity of these same alkyl complexes ((gO)-[La($CH_3$)$_2$] (1gO) and (gOO)-[La($CH_3$)$_2$] (1gOO)) on the homopolymerisation of styrene and copolymerisation of ethylene and styrene. The first three insertions reaction have been investigated, showing that both compounds efficiently catalyse the styrene homopolymerisation. The calculated barriers are comparable to the one obtained for the highly active cationic scandium complex of Hou's group[226], with a higher activity expected for the (gOO)-[La($CH_3$)$_2$] system, ascribed to the less steric congestion around the metal. As for the ethylene and butadiene polymerisation, the graphene surfaces are predicted to play an important role, increasing the Lewis acidity and therefore the reactivity of the grafted La. Concerning the stereoselectivity, a preference for the formation of a syndiotactic styrene is found for both catalysts, and whose formation is thermodynamically controlled. The catalytic behaviour of 1gO and 1gOO has been finally investigated in the ethylene and styrene co-polymerisation reaction. We have shown that while for the gOO-La catalyst, the formation of a copolymer is very unlikely as styrene insertion is preferred for the two first insertions, for the gO-La catalysts, on the other hand, the formation of polystyrene with little amount of ethylene may be envisaged.

In the last part of chapter III we have finally investigated the controlled rac-BL ROP reaction by by using as catalysts four different lanthanum complexes, *i.e.* the molecular [La($BH_4$)$_3$(THF)$_3$], the silica supported (≡SiO)-[La($BH_4$)$_2$(THF)$_2$] and the graphene-supported (gO)-[La($BH_4$)$_2$(THF)$_2$] and (gOO)-[La($BH_4$)$_2$(THF)$_2$] compounds. Differently from the (≡SiO)-[La($BH_4$)$_2$(THF)$_2$] species, which poorly catalyses the BL ROP reaction, the (gO)-[La($BH_4$)$_2$(THF)$_2$] and (gOO)-[La($BH_4$)$_2$(THF)$_2$] systems are likely to efficiently polymerise the BL monomer, displaying the same efficiency as the homogeneous [La($BH_4$)$_3$(THF)$_3$] (3) compound. Similarly to experimental approaches, the coordination of triphenylphosphine oxide (O=$PPh_3$) has been computed as a probe of the Lewis acidity of the metal. The spectroscopic values (IR and NMR) obtained for the corresponding (≡SiO)-[La($BH_4$)$_2$(THF)(O$PPh_3$)], (gO)-[La($BH_4$)$_2$(THF)(O$PPh_3$)] and (gOO)-[La($BH_4$)$_2$(THF)(O$PPh_3$)] compounds indicate that the graphene grafted lanthanide complexes are more Lewis acidic than the silica grafted analogues, the nature of the surface clearly playing an important role. According to an in-depth analysis of the enthalpy profiles, the step that differentiates the catalytic activity of the four compounds corresponds the first $BH_4$ hydride transfer to the carbonyl carbon of the BBL monomer. As observed in the corresponding transition states, indeed, while the molecular and graphene grafted complexes efficiently activate the BBL monomer providing an effective $BH_4$ hydride transfer, the silica grafted analogue poorly activate the BBL monomer, making the hydride transfer more constrained, with the consequent increase of the corresponding activation barrier. This is in accordance with the Lewis acidity trend, showing that the higher the Lewis acidic character of the metal center in the involved transition state, the stronger the BBL monomer activation and therefore the more effective the $BH_4$ hydride transfer. Concerning the stereoselectivity of the reaction, finally, the calculations suggest the formation of preferentially atactic polymers, the insertion of a BL monomer, in its either R or S configuration, providing very similar enthalpy values in both the initiation and propagation steps. In conclusion, therefore, we have shown that the graphene gOH and gOOH surfaces play an important role in enhancing the Lewis acidity and therefore the catalytic activity of the corresponding La grafted complexes. Graphene supported La borohydride complexes may therefore represent interesting target compounds, combining the hight catalytic activity in the rac-BL ROP reaction with the advantages of the heterogeneous catalysis.

## Part IV

# Boron nitride supported lanthanum complexes

## 1 Introduction

Boron nitride (BN) is a chemical compound that is isoelectronic and isostructural to carbon with equal composition of boron and nitrogen atoms. Similar to carbon, boron nitride is produced in amorphous and crystalline forms. In its crystalline form, boron nitride exists in three major allotropes: a) sphalerite boron nitride ($\beta$-BN) resembling cubic diamond (Figure 80 a), b) wurtzite boron nitride ($\gamma$-BN) resembling hexagonal diamond from (Figure 80 b) and c) hexagonal boron nitride (h-BN) resembling graphite (Figure 80 c).[383] Similar to 1D carbon nanotubes (CNTs), BN nanotubes (BNNTs) (Figure 81) also exist. They are isoelectronic to CNTs in terms of chirality (Zigzag or armchair), tube diameters and number of walls.[384]

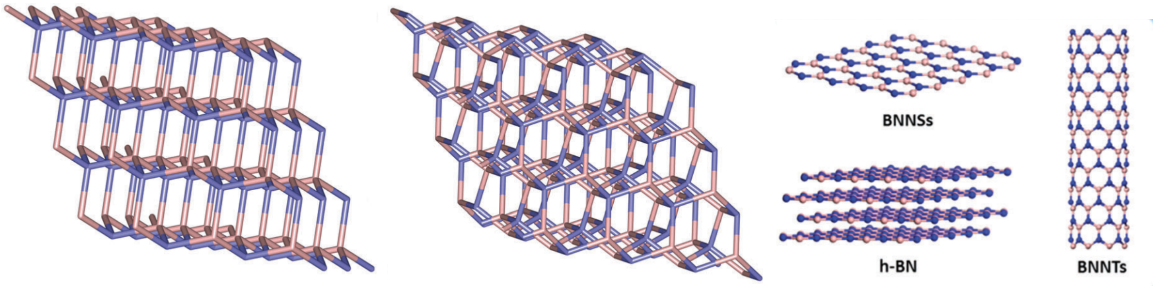

(a) sphalerite boron nitride ($\beta$-BN) (b) wurtzite boron nitride ($\gamma$-BN) (c) hexagonal boron nitride (h-BN)

Figure 80: Boron nitride crystal structures.

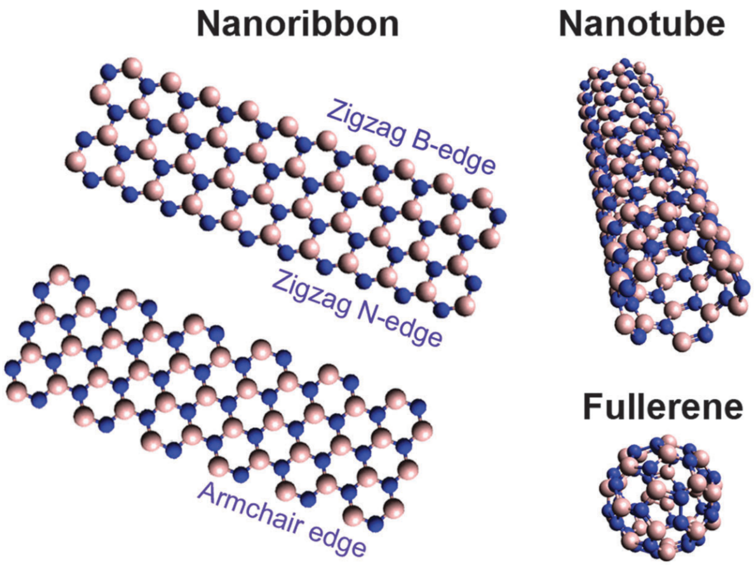

Figure 81: Structural models of 2D, 1D and 0D BN nanostructures. The edge of a BN nanosheet or a BN nanoribbon can be either zigzag (B- or N-edged) or armchair (BN pair-edged).[385, 383]

Among these different phases, h-BN is the most common stable form. After the isolation of graphene sheets in 2004,[386] h-BN has become the centre of many studies. Like graphene, indeed, h-BN has also a layered structure. Within each layer, the boron and nitrogen atoms are bound by strong in-plane covalent bonds and each layer is held together by Van der Waals forces ($\pi$ stacking). A single layer of h-BN is typically referred as a BN nanosheet or BNNS. Like graphene it is also a white/transparent material with a lower toxicity compared to their carboned counterparts.[387, 388, 389, 390] Although h-BN has a structure similar to that of graphene, it is a wide bandgap material (intrinsic band gap ($E_g$) of 5.9 eV), displaying therefore insulating properties. This makes h-BN very different from graphene, which is instead a highly conductive material. The h-BN is stable up to 1000 °C in air, 1400 °C in vacuum, and up to 2850 °C in an inert atmosphere.[391, 64] The theoretical thermal conductivity values for h-BN are comparable to those of graphene and are in the range 1700-2000 W/m.K.[392, 393] The h-BN material is chemically inert in a wide variety of acids, solvents, and oxidising agents. It is insoluble in the usual acids but is soluble in alkaline and boron nitride molten salts such as LiOH, KOH, and $Li_3BN_2$. Owing to its high chemical resistance and thermal stability, h-BN is an attractive material in view of its potential applications as a chemically inert coating in hazardous environments.[394, 395, 396] The physical form of h-BN is a white slippery powder, analogous to graphite. The flake size of commercially available h-BN ranges from hundreds of nanometres to tens of microns (information obtained from Sigma Aldrich, Alfa Aesar). A boron nitride nanosheet (BNNS) displays a honeycomb structure with alternating boron and nitrogen atoms. The B and N atoms are covalently bonded with a bond length of 1.45 $\AA$. The distance between the centres of neighbouring borazine rings is 2.5 $\AA$. A single boron nitride nanosheet can be obtained *via* top-down approaches (such as exfoliation, solvent-assisted ultrasonication, unzipping of BNNTs) or bottom-up approaches (usually chemical vapour deposition (CVD) or other deposition techniques, such as defect manipulation in h-BN using scanning tunnelling microscopy). Overall the most commonly used methods to synthesize a single boron nitride nanosheet are mechanical exfoliation,[397, 398, 399, 400, 401] chemical exfoliation,[402, 403, 404, 400, 405, 406, 407, 408, 409, 410, 411] CVD,[412, 413, 414, 415, 416, 417, 418] and the pulsed laser deposition (PLD).[419]

## 2 Experimental synthesis of BN surfaces without vacancies

The intrinsic chemical robustness of h-BN is demonstrated by its resistance to oxidation and covalent chemical functionalisation.[420, 421, 422] Much attention has been recently paid to the development of an easy process that allows the chemical functionalisation of h-BN in an extensive manner. In order to force the oxidation of h-BN, strongly oxidative conditions such as boiling aqua-regia, hot piranha solution, perchloric acid-potassium permanganate solution, or refluxing nitric acid have been attempted, without success.

As recently reported the ultrasonication assisted hydrolysis of h-BN sheets afforded the functionalisation of their edges[423] with the formation of pendant hydroxyl and proton groups on the B and N atoms respectively. Such edge functionalisation, however, imparts a negligible chemical modification with respect to the bulk properties of the h-BN crystallites. Notably, this procedure was shown to result in the destruction of extended h-BN sheets to form nanoscale fragments. In the case of boron-nitride nanotubes (BNNTs) and h-BN nanosheets, the covalent functionalisation may be achieved by the use of air-plasma of accelerated ions and particles. In an air-plasma treatment, air molecules (primarily nitrogen, oxygen, and water vapour) become excited and react with other molecules, knock off electrons, and emit photons. The excited nitrogen molecules mainly relax by emission of photons which produce the observable purple light in the plasma region. The excited oxygen molecules, on the other hand, are more stable and either react with other oxygen molecules to form ozone or break the chemical bonds of vapour water molecules to form reactive [OH], [O], and [H] species. Such reactive ions and radicals can readily react with other chemicals present in air and in the nearby BN surface, causing the breakage of existing chemical bonds with the formation of new ones. As schematically illustrated in Figure 82, thus, the functionalisation process may involve several mechanisms. The formation of covalent bonds may primarily start at the chemically active edges of the BN surfaces. The edge, indeed, contain unsaturated boron and nitrogen terminal atoms, resulting the most reactive sites in the whole BN nanostructure. The presence of reactive species, such as proton and hydroxo anions, may result in the formation of covalent bonds, *via* Lewis acid base interactions either between a hydroxo group (as the electron pair donor) and an edge boron atom (as the electron pair acceptor through its vacant p orbital) or between a proton atom (as the electron pair acceptors through its vacant s orbital) and an edge nitrogen atom (as the electron pair donor) (figure 82-1). The BN nanosheet planes and the BN nanotube walls, in addition, usually contain a certain amount of vacancies which may serve as active sites for the formation of B-OH and N-H covalent bonds (figure 82-2). The plasma components (*i.e.*, chemical species and energetic particles) may also attack the BN bonds, break them, and create new bonds. In this case, the covalent B-OH and N-H bond formation occurs with the concomitant cleavage of the involved in-plane BN bond to satisfy the valence conditions.[424] Excepts for the edge B-OH and N-H functions, interestingly, all the other B-OH and N-H groups formed on the surface rise from the planar $sp^2$ lattice, the hybridization of the involved B and N atoms passing from the $sp^2$ to the $sp^3$ tetrahedral configuration (figure 82-3).

More recently a new covalent functionalisation approach leading to the oxidation of exfoliated h-BN nanosheets (BNNSs) and the formation hydroxo-functionalised BNNSs (OH-BNNSs) has been reported.[425] As shown in Figure 83, the reaction occurs in 2 steps. In the first step the exfoliated BNNSs dispersed in the di-*tert*-butyl peroxide reagent react with the in *situ* generated *tert*-butoxy radicals, providing h-BN lattice surfaces functionalised with B-O*t*Bu and N-H dangling groups. The second step, on the other hand, involves the hydrolysis of the BNNS *tert*-butoxy bond in strongly oxidising conditions to yield B-OH and N-H functionalised h-BN surfaces (Figure 83).

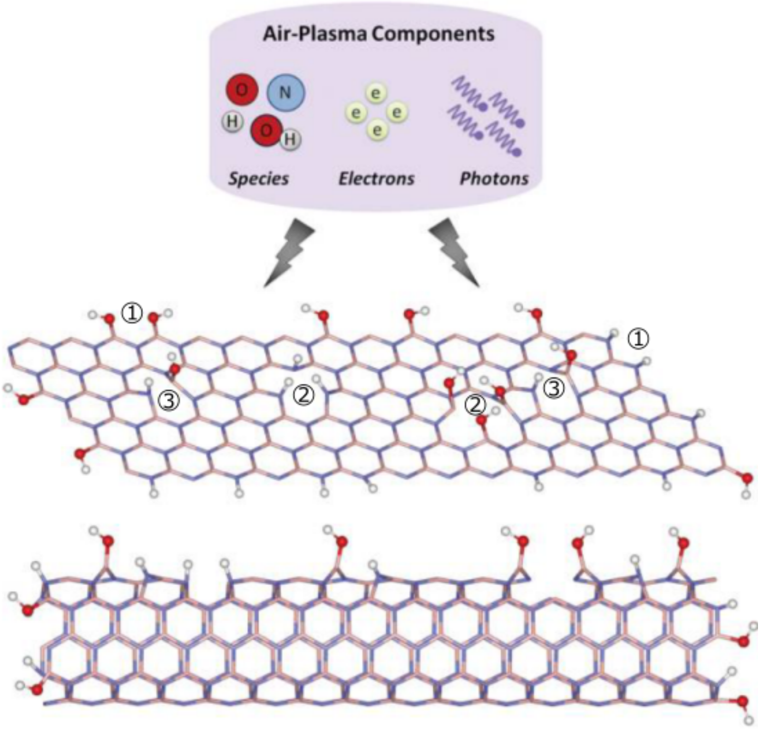

Figure 82: Schematic representation of the chemical functionalisation of BN nanostructures by air-plasma treatment. The mechanism involves the formation of B-OH and N-H bonds 1) at the edges sites; 2) at the vacancy sites and 3) at the B-N breaking sites.[424]

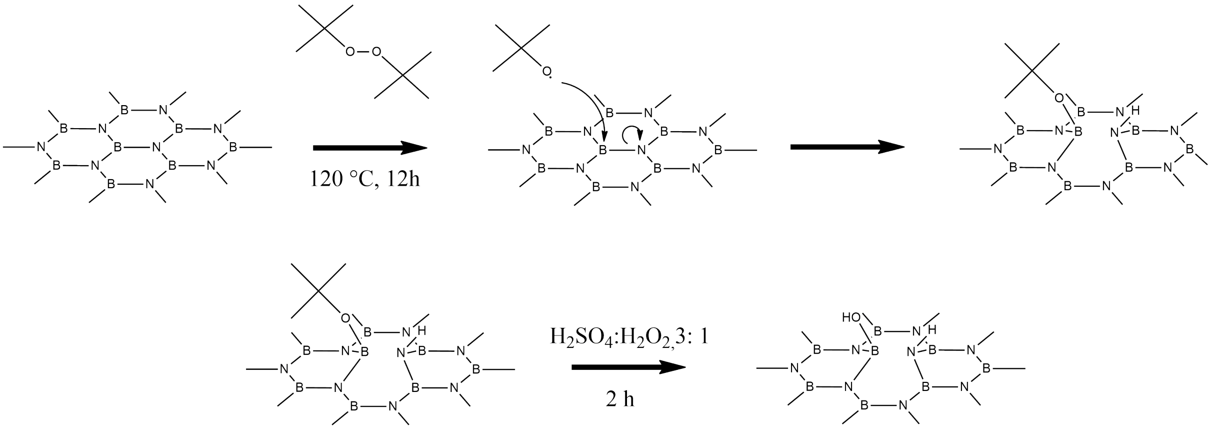

Figure 83: Functionalisation reaction of BNNSs. a) Reaction between the exfoliated BNNSs and the *tert*-butoxy radical, affording h-BN lattice surfaces functionalised by B-O*t*Bu and N-H dangling groups; b) hydrolysis of the BNNS-*tert*-butoxy bond in a strongly oxidising solution.[425]

# 3 Theoretical models previously described

# 4 The OH-functionalised h-BN model

In order to understand the surface chemistry of the BN surfaces and in particular the role they may play as supports for metal catalysts, we were interested in studying the grafting of molecular active metal complexes and the catalytic properties of the resulting BN-supported systems. In view of our interest in the field of polymerisation by coordination-insertion, we particularly focused on the grafting of lanthanide complexes, which have displayed, in their molecular form, interesting catalytic activities in many polymerisation reactions. As previously seen for the graphene supports in chapter III, the grafting of a Ln compound requires the presence of a surface-OH group. By metathesis reaction, indeed, the $La(N(SiMe_3)_2)_3]$ precursor may easily react with the surface-OH group affording the $HN(SiMe_3)_2$ amine and the corresponding (BN-O)-$[La(N(SiMe_3)_2)_2]$ supported system. The oxygen radical fonctionalisation reaction described above represents therefore a viable access route to OH-functionalised BN surfaces which may then act as starting compounds for the synthesis of BN-grafted lanthanide catalysts. To model the grafting raction, we first developed a molecular model of the OH-functionalised BN surface, using, for the BN sheet, a 72-atom model ($B_{27}N_{27}H_{18}$) previously described in the literature.[426, 427] As shown in figure 84, the hexagonal $B_{27}N_{27}H_{18}$ model contains a harmchair edge structure, displaying B-N bond distances of 1.44 $\AA$, the same as those measured for pristine hBNNs and very close to the experimental value (experimental distance of 1.45 $\AA$). According to the product of the oxygen radical functionalisation above described, we added to the $B_{27}N_{27}H_{18}$ model both one hydroxyl group, bound to a boron atom as an electron pair donor, and one proton group, bound to a nitrogen atom as an electron pair acceptor. The resulting $B_{27}N_{27}H_{20}O$ model (BNH-OH) is shown in Figure 85. The B-OH bond length measures 1.465 $\AA$ while the N-H one 1.034 $\AA$. The stretching band value computed for the O-H group, however, is higher than that measured experimentally (3719 $cm^{-1}$ vs. 3400 $cm^{-1}$).[425] This difference may be ascribed to the presence, in the experimental simple, of residual N-methylpyrrolidone solvent molecules which may interact *via* hydrogen bonds with the OH group, resulting in the decrease of the IR OH frequency and in the widening of the corresponding band. As a consequence of the functionalisation, the N-B bond interacting with the H-OH group is elongated passing from from 1.449 $\AA$ for the naked h-BN surface to 1.645 $\AA$ for the BNH-OH model. The latter value indicates that a simple bond between the nitrogen and boron atoms of the B-OH and N-H groups of the surface is maintained. The N and B atoms bonded to the H and OH groups, moreover, move out of the plane of the surface, changing their formal hybridization from a $sp^2$ to a $sp^3$ state. The natural charges computed for the naked h-BN surface show a positive charge of 1.18 on the B atom and a negative charge of -1.18 on the N atoms. Although nitrogen shares its electronic doublet with the boron atom, giving to boron a negative formal charge in the Lewis formalism, the higher electronegativity of nitrogen (3.0) compared to boron (2.0) governs the calculation of the natural charges resulting in a negatively charged nitrogen and positively charged boron. In the absence of the $\pi$ bond between boron and nitrogen, therefore, the positive charge on boron is expected to be higher, indicating that the sharing of the nitrogen doublet with boron decreases the positive charge on boron, reflecting the negative formal charge that the Lewis' formalism would indicate for the B

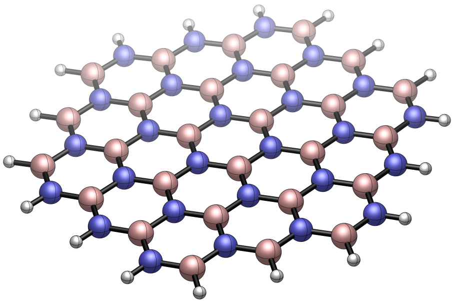

Figure 84: The hexagonal boron-nitride surface model $B_{27}N_{27}H_{19}$ (h-BN).

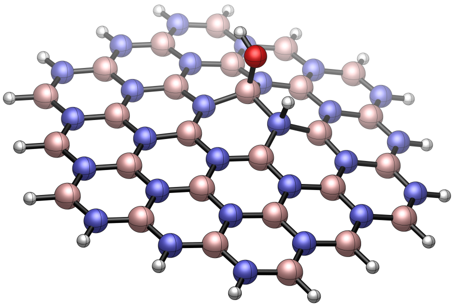

Figure 85: The OH-functionalised BN surface model $B_{27}N_{27}H_{20}O$ (BNH-OH) displaying a B atom bonded to a OH group and a N atom bonded to a H group.

atom. To evaluate the impact of the substituents on the boron and nitrogen atoms, therefore, we will then focus on the charge differences and not on the absolute value of each charge. The functionalisation of the boron and nitrogen atoms with the OH and H groups, respectively, does not modify the value of the charges which pass from 1.18 to 1.19 for boron and from -1.18 to -1.17 for N. The similar electronegative values between the N (3.0) and O (3.5) atoms and between the B (2.0) and the H (2.1) atoms may therefore explains the small charge variation observed upon replacing the double B-N bond with the two B-OH and N-H bonds.

## 4.1 Grafting reaction

In order to study the possible grafting reaction of a lanthanide complex on this OH-functionalised BN surface, we chose as starting material the $[La(N(SiMe_3)_2)_3]$ complex. Two possible grafting reaction pathways were investigated: 1) the protonolysis of the La-N bond by the BNH-OH hydroxo pending group, which generate a ≡BO-La bond and a free hexamethyldisilazane molecule and 2) the protonolysis of the La-N bond by the N-H pending group, which generates the same ≡BO-La bond with a free hexamethyldisilazane molecule after re-protonation of the surface N atom with the B-OH proton group. The corresponding enthalpy profiles are shown in Figure 86. The structures of the involved transition states and intermediates are shown in Figure 87. In the mechanism involving the B-OH hydrogen transfer, on the other hand, the reaction begins with the coordination of the $[La(N(SiMe_3)_2)_3]$ complex with the BNH-OH hydroxo group to form the $A^{graf}{}_{BNH-OH}$ adduct by an exothermic process (-18.9 kcal.mol$^{-1}$ with respect to the separated reactants). As shown in figure 87 a, the O-La distance measures 2.607 $\AA$, with the $H_{OH}$ hydrogen already pointing toward the $N_1$ atom. The following transition state displays a classical 4 c - 4e$^-$

$\sigma$-bond metathesis geometry, with the B-OH oxygen atom interacting with the La-centre (La-O = 2.423 $\mathring{A}$) and the $H_{OH}$ hydrogen atom interacting with the hexamethyldisilylamido $N_1$ atom($N_1$-$H_{OH}$ = 1.374 $\mathring{A}$). The low value of the barrier (2.1 kcal.mol$^{-1}$, with respect to the $A^{graf}{}_{BNH-OH}$ adduct) can be rationalised by the perfect positive and negative charge alternation shown in figure 88 a (+1.64, -1.72, +0.52 and -1.04 for the La, $N_1$, $H_{OH}$ and O atoms, respectively). This methathesis reaction affords, through an exothermic process (-29.2 kcal.mol$^{-1}$, with respect to the separated reactants) the $B^{graf}{}_{BNH-OH}$ complex, displaying the La amido compound monografted on the hydroxo group of the BNH-OH surface (La-O = 2.177 $\mathring{A}$), with the $HN(SiMe_3)_2$ molecule still interacting with the lanthanum centre (La-$N_1$ = 2.963 $\mathring{A}$). From the $B^{graf}{}_{BNH-OH}$ compound, the protonolysis of the $B_{BN}$-OLa bond by the $N_{BN}$-$H_{NH}$ group may then occur in TS-$BC^{graf}{}_{BNH-OH}$, leading, *via* an exothermic (-64.7 kcal.mol$^{-1}$ with respect to the separated reactant) and a kinetically accessible process (2.8 kcal.mol$^{-1}$ with respect to the $B^{graf}{}_{BNH-OH}$ adduct), to the release of the $[La(N(SiMe_3)_2)_2(OH)(HN(SiMe_3)_2]$ complex and the recovery of the aromatic BN surface.In the mechanism involving the $N_{BN}$-H hydrogen transfer, the reaction also begins with the coordination of the $[La(N(SiMe_3)_2)_3]$ complex to the BNH-OH hydroxo group, affording, this time, the $A'^{graf}{}_{BNH-OH}$ adduct (-15.6 kcal.mol$^{-1}$). Interestingly, the O-La distance measures 2.606 $\mathring{A}$, with the $H_{NH}$ hydrogen already pointing toward the $N_1$ atom. In the following transition state, the B-OH oxygen atom interacts with the La-centre (La-O = 2.411 $\mathring{A}$) and the $H_{NH}$ hydrogen atom interacts with the hexamethyldisilylamido $N_1$ nitrogen atom ($N_1$-$H_{NH}$ = 1.228 $\mathring{A}$), displaying a 6c - 4e$^-$ $\sigma$-bond metathesis geometry. The associated barrier is perfectly accessible (6.5 kcal.mol$^{-1}$, with respect to the previous adduct), reflecting the perfect positive and negative charge alternation shown in figure 88b (+1.79, -1.72, +0.50, -1.24, +1.22 and -0.98 for the La, $N_1$, $H_{NH}$, $N_{BN}$, $B_{BN}$ and O atoms, respectively), as previously reported in the literature.[368, 152, 157] This transition state (TS-$A'C^{graf}{}_{BNH-OH}$) unespectedly involves the breaking of both the $N_{BN}$-$H_{NH}$ and the B-(OH)La bonds with the concomitant formation of the $H_{NH}$-$N_1(SiMe_3)_2$, the La-OH and the $B_{BN}$=$N_{BN}$ bonds. The resulting product corresponds therefore to the same compound, $C^{graf}{}_{BNH-OH}$, obtained in the first pathway above described. The hight stability of the $[La(N(SiMe_3)_2)_2(OH)(HN(SiMe_3)_2)]$ complex, with the recovery of the aromatic h-BN surface product (-64.7 kcal.mol$^{-1}$, with respect to the separated reactant), accounts for the driving force of the reaction. The grafting reaction of the $[La(N(SiMe_3)_2)_3]$ complex on the BNH-OH surface, in conclusion, does not take place. By the two different pathways, unespectedly, the reaction leads rather to the exchange of an amido $N(SiMe_3)_2$ ligand with a hydroxo ligand, affording the release of the $[La(N(SiMe_3)_2)_2(OH)(HN(SiMe_3)_2)]$ complex and the recovery of the unfunctionalised aromatic h-BN surface. In order to strengthen the B-(OH)La bond, preventing its breakage in the final supported compound, we wondered if the use of a BN surface containing a vacancy defect could allow the grafting of a lanthanide complex. We have therefore focused on the different possible ways to experimentally obtain a BN surface containing defect vacancies, providing a BN surface functionalisation more adapted to the grafting reaction.

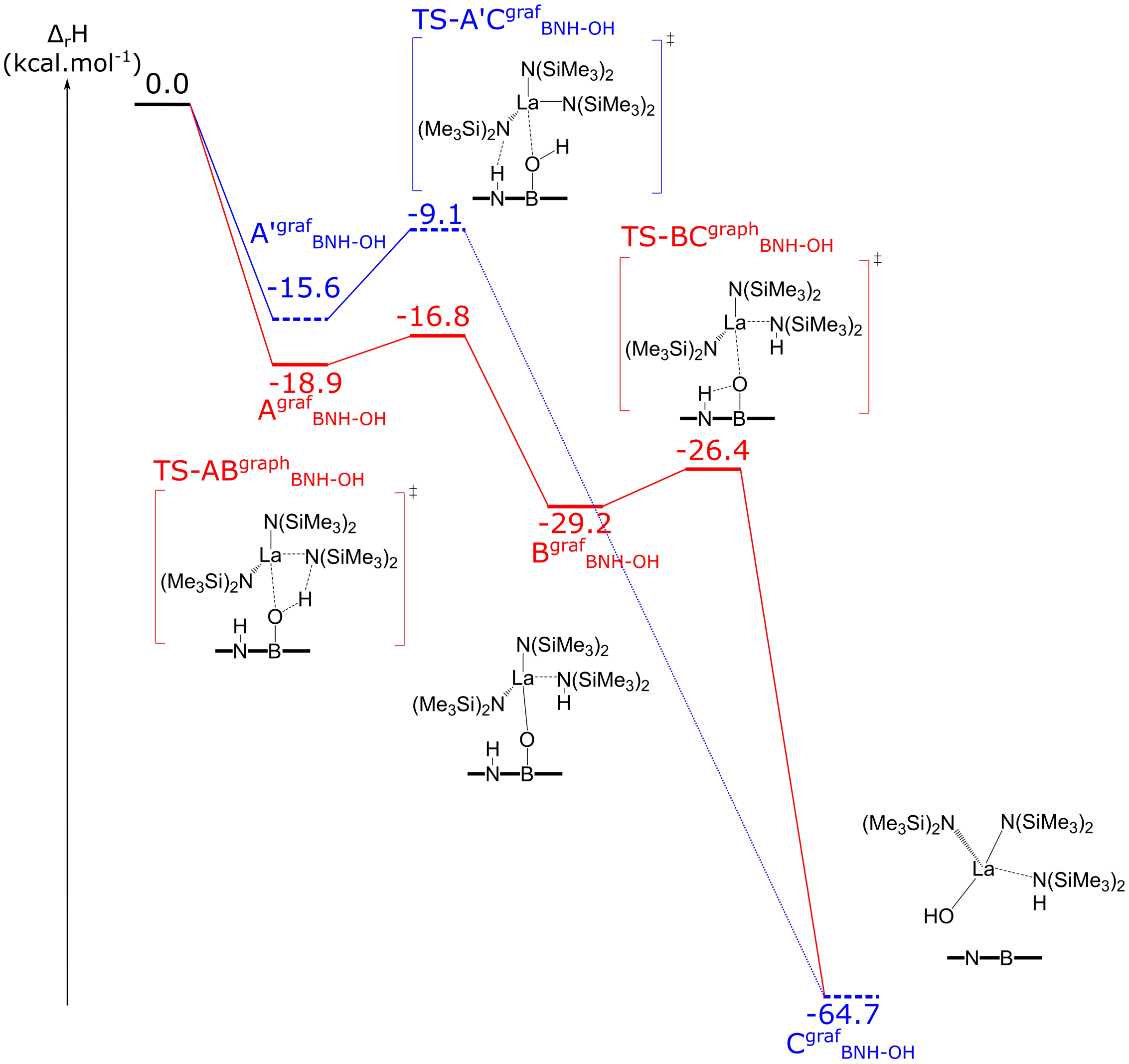

Figure 86: Computed enthalpy-energy profile of the grafting of the $[La(N(SiMe_3)_2)_3]$ complex on the BNH-OH surface.

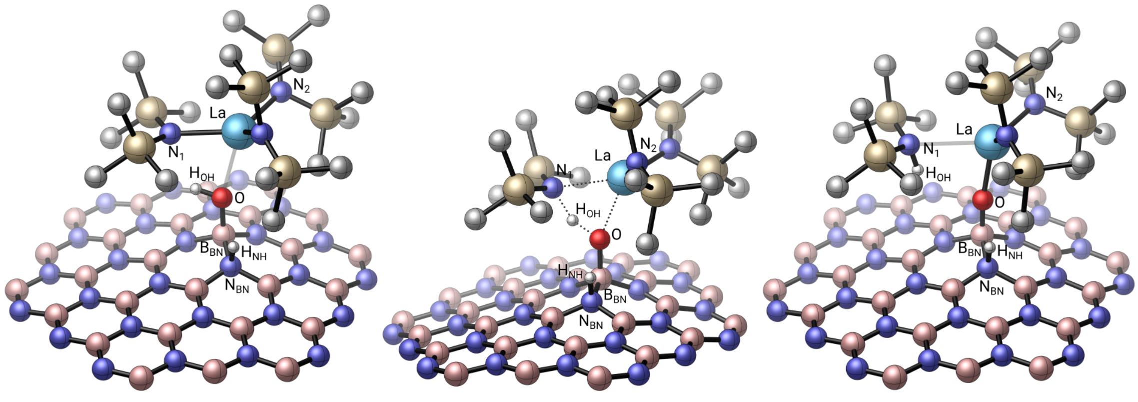

(a) A$^{graf}{}_{BNH-OH}$ (b) TS-AB$^{graf}{}_{BNH-OH}$ (c) B$^{graf}{}_{BNH-OH}$

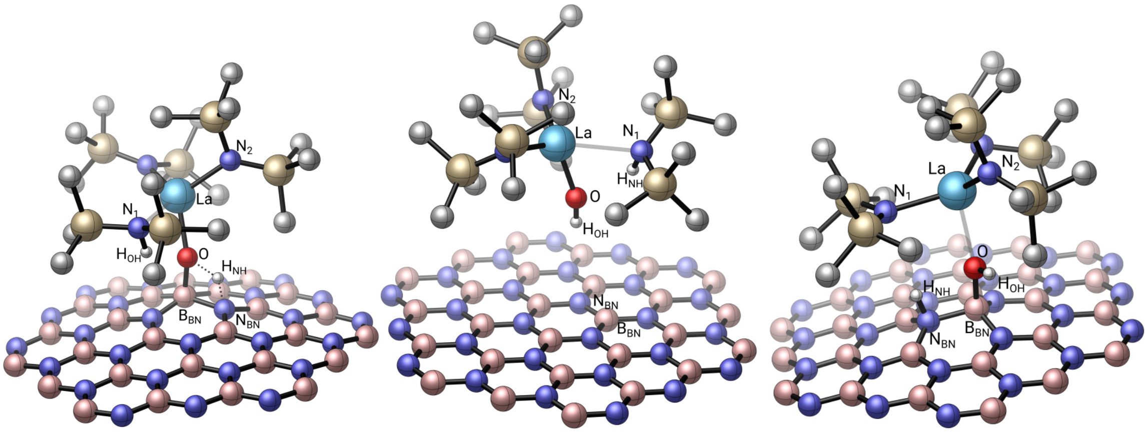

(d) TS-BC$^{graf}{}_{BNH-OH}$ (e) C$^{graf}{}_{BNH-OH}$ (f) A'$^{graf}{}_{BNH-OH}$

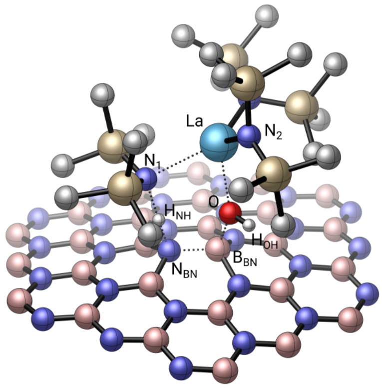

(g) TS-A'C$^{graf}{}_{BNH-OH}$

Figure 87: Geometries of the complexes involved in the grafting reaction of [La(NSiMe$_3$)$_2$)$_3$] on the BNH-OH functionalised surface (light blue : La, dark blue : N, white : H, red : O). For sake of clarity all the H of the La-grafted compounds have been omitted with the exception of the BNH-OH hydrogen atoms.

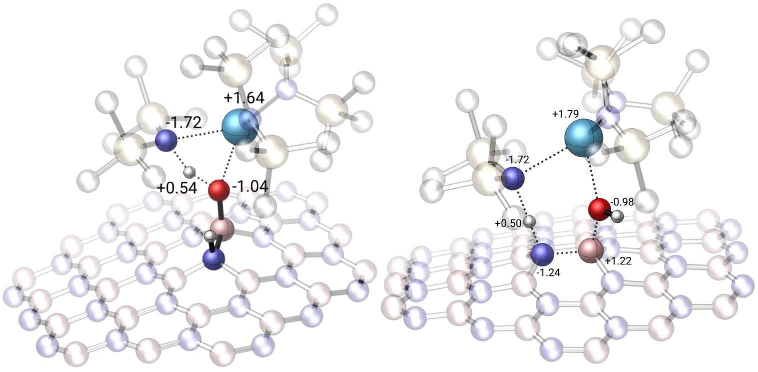

(a) (b)

Figure 88: NPA charges of the transition states involved in the grafting of $[La(N(SiMe_3)_2)_3]$ on the BNH-OH surface by a) the transfer of the $H_{OH}$ hydrogen to the $N_1$ atom and b) the transfer of the $H_{NH}$ hydrogen to the $N_1$ atom (light blue : La, dark blue : N, white : H, red : O).

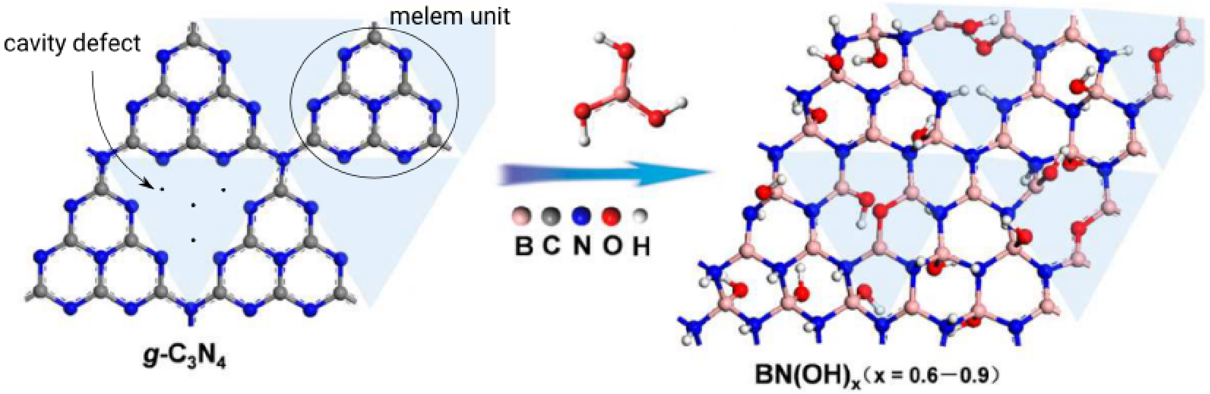

Figure 89: Schematic illustration of the thermal reaction between g-$C_3N_4$ and boric acid $B(OH)_3$. The initial g-$C_3N_4$ cavities have been filled with B-O-B and $sp^2$-hybridized $N_2$-B(OH) termination structures.

## 5 Experimental synthesis of BN surfaces containing defects

An interesting way to functionalise h-BN surfaces has been recently described by Golberg and coworkers.[428] In this recent report they reported a new synthetic procedure to directly fabricate highly water-soluble and porous BNs *via* thermal substitution of C atoms with boric acid substructures in graphitic carbon nitrides (g-$C_3N_4$). The fabricated BNs, characterised as $BN(OH)_x$ (x = 0.6-0.9), show unprecedentedly high hydroxylation degrees and can form stable and highly transparent water solutions with a concentration as high as 2.0 mg $mL^{-1}$. A mixture of g-$C_3N_4$ and aqueous boric acid are calcinated under high temperatures (between 700 and 1000 °C), with a calcination time set between 0 and 5 h. During the reaction, the authors observed the substitution of the C atoms with B(OH) atoms and the narrowing, with prolonging synthetic times, of the g-$C_3N_4$ cavities with B-O-B and $sp^2$-hybridized $N_2$-B(OH) termination structures (Figure 89). The presence of hydroxyl groups on the BN surface was demonstrated by detailed X-ray photoelectron spectroscopy (XPS), infrared spectroscopy (IR), and X-ray diffraction (XRD) analyses.

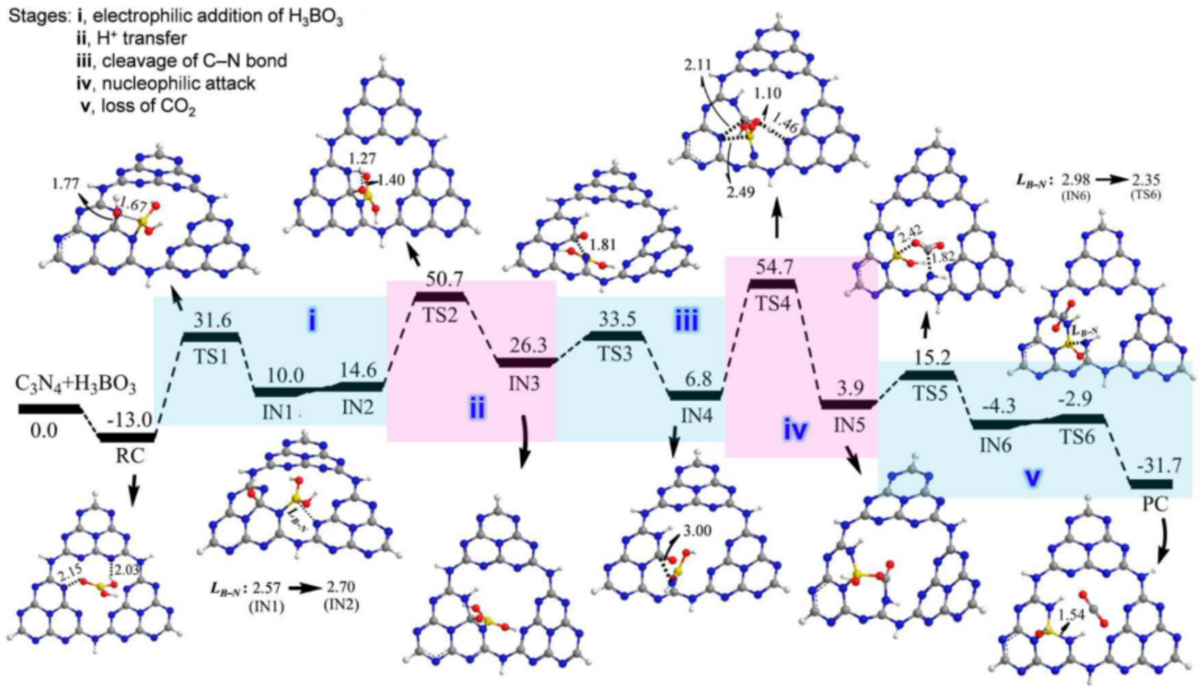

Figure 90: Calculated relative energy profiles (in kcal $mol^{-1}$) and optimized intermediate and transition state structures (lengths in $\AA$) for a typical thermal substitution of a carbon atom in graphitic carbon nitride (g-$C_3N_4$) with the boric acid substructure. The g-$C_3N_4$ model used here consists of 3 tri-s-triazine (melem) units, with the boron atoms highlighted in yellow in all structures. The total energies of g-$C_3N_4$ and boric acid are taken as the reference point of the relative energy values for the thermal substitution pathway. Generally, the whole pathway can be viewed as consisting of 5 sequent stages (i to v). With the successful substitution of a carbon atom with B(OH) in g-$C_3N_4$, carbon is released as $CO_2$, while two adjacent nitrogen sites are protonated.

The mechanism of the thermal substitution reaction between the g-$C_3N_4$ system and the $B(OH)_3$ boric acid has been carefully studied by density functional theory (DFT) calculations. The starting graphitic carbon nitride surface was modeled by using 3 tri-s-triazine (melem) units connected by planar amino groups. As shown in Figure 89, interestingly, this model results in the formation of four cavity defects in the space enclosed by the three melem units. The mechanism, showing the substitution of the C atoms of the starting g-$C_3N_4$ system with B(OH) atoms, with the concomitant protonation of the two adjacent N atoms is shown in figure 90.

The reaction begins with the addition of a $H_3BO_3$ molecule onto a C=N double bond *via*TS1 with the formation of the IN1 intermediate, displaying the-OH group attached to the carbon atom and the -$B(OH)_2$ moiety attached to the nitrogen atom. The calculated energy barrier is 31.6 kcal $mol^{-1}$ relative to the initial reactants. After a conformational isomerization from IN1 to IN2, the proton of the C-OH group transfers to an adjacent N atom *via* TS2, forming IN3. The subsequent C-N cleavage *via* TS3 leads to the formation of the IN4 adduct, displaying an energetically favourable amide structure. An O atom from the $B(OH)_2$ group may then perform a nucleophilic attack on the carbonyl carbon through TS4, providing, after a concerted proton abstraction from a N atom in the opposite melem unit, the intermediate IN5. As shown in

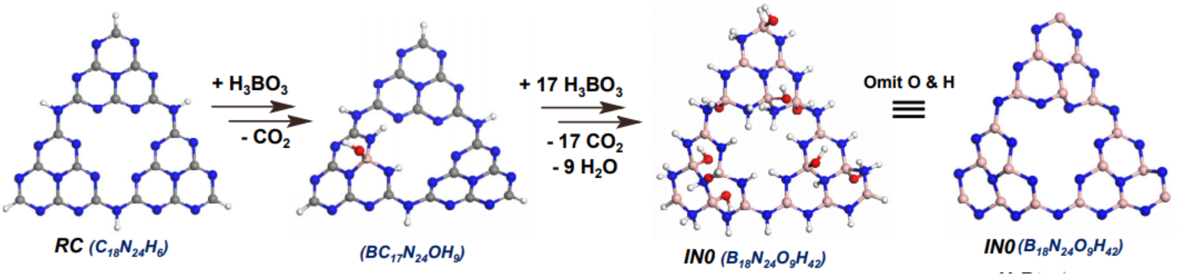

Figure 91: Stoichiometry of the thermal substitution reaction between g-$C_3N_4$ and the $B(OH)_3$ boric acid.

IN5, a new B-N bond is formed and a -$CO_2$- moiety is incorporated into an eight-membered ring. Starting from IN5, the molecular $CO_2$ can break away easily *via* TS5, yielding IN6. The formation of a second B-N bond can then occur *via* TS6, leading to the final product (PC) in which one C atom of the g-$C_3N_4$ compound has been replaced by a B(OH) group and the two adjacent N atoms have been protonated. Overall, the formation of PC is exothermic by 31.7 kcal mol$^{-1}$, suggesting that the whole process is thermodynamically favourable. As shown in Figure 91, to substitute all C atoms with B atoms, the system needs 18 $H_3BO_3$ molecules, and the dehydration of 9 $H_2O$ molecules. This process is controlled by the limited number of available protonation sites and by the steric hindrance among the hydroxyl groups.

As experimentally observed, the reaction does not stop at the IN0 intermediate in Figure 91, as the H-terminated N edges in the cavity may further react with the $H_3BO_3$ molecules and narrow the cavities after water loss. The mechanism involved in the narrowing of the g-$C_3N_4$ cavities with the formation of B-O-B and sp$^2$-hybridized B-OH terminations has been also computed by DFT calculations (Figure 92). As shown in the modeled pathway, the addition of three $B(OH)_3$ molecules, accompanied by several dehydration steps, affords the final IN3b product, with the new B-O-B and -B(OH) moieties replacing the four atom vacancies initially present in the starting g-$C_3N_4$ structure. The final IN3b compound displays therefore a highly hydroxylated surface with B-O-B and sp$^2$-hybridized B(OH) defects which may be used as anchoring functions for the grafting of lanthanide complexes.

# 6 The BNO-OH model

## 6.1 Hydroxylated BN surface containing a defect

Starting from the $B_{21}N_{24}O_{11}H_{37}$ (IN3b) model, we constructed a new model by removing 9 H2O molecules after successive dehydration reactions. The resulting $B_{21}N_{24}O_2H_{19}$ model, named hereafter BNO-OH, displays therefore, the classical sp$^2$ BN structure, with the presence of a B-O-B and $N_2$-B(OH) defect. Compared to a naked BN surface, therefore, in the BNO-OH model a N atom has been replaced by an O atom (forming the B-O-B moiety) and the in front B atom has been functionalised with a hydroxyl group (forming the sp$^2$ $N_2$B-OH moiety). The geometry

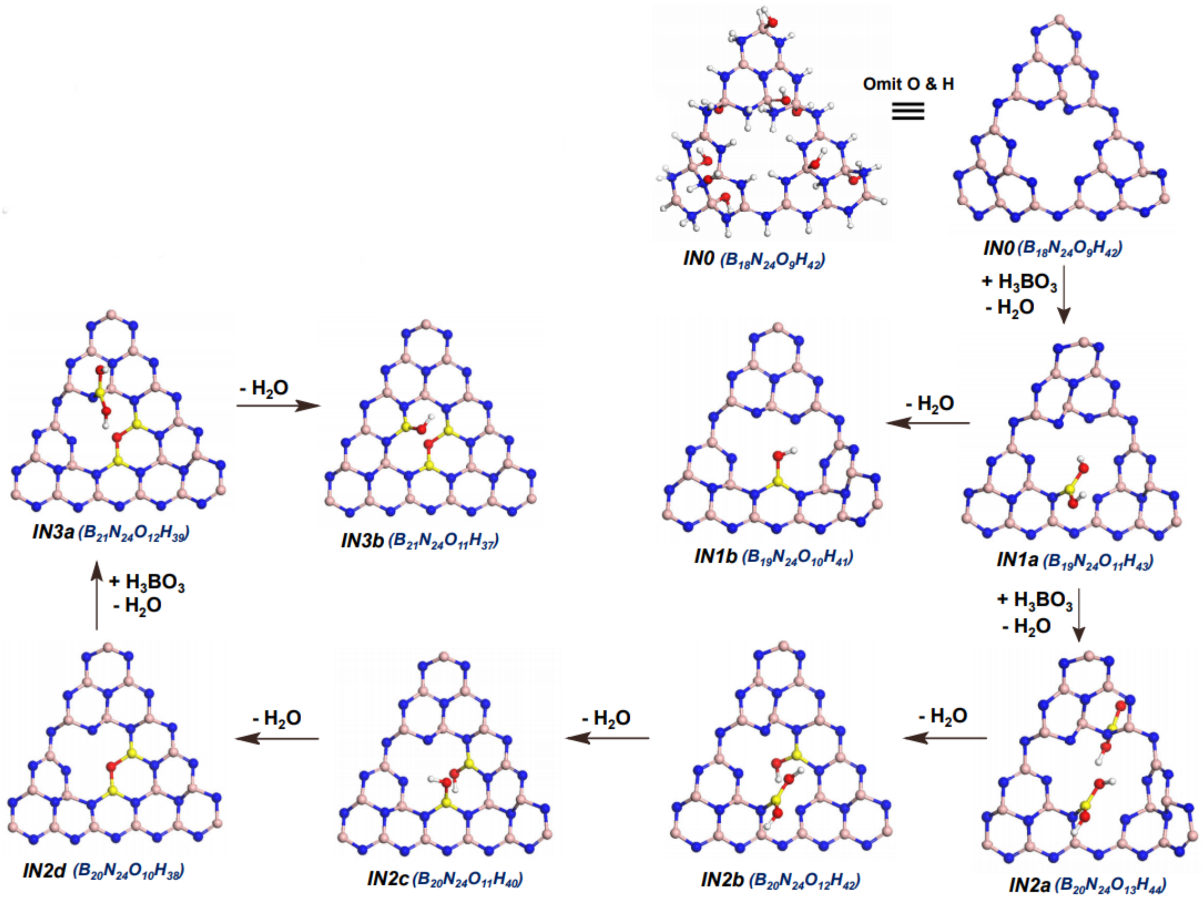

Figure 92: Proposed mechanism for the formation of the B-O-B and $N_2$-B(OH) moieties in the initial g-$C_3N_4$ cavity. For sake of clarity, in all the steps after IN0 compound, the O and H atoms are omitted and the new added B atoms are highlighted in yellow .

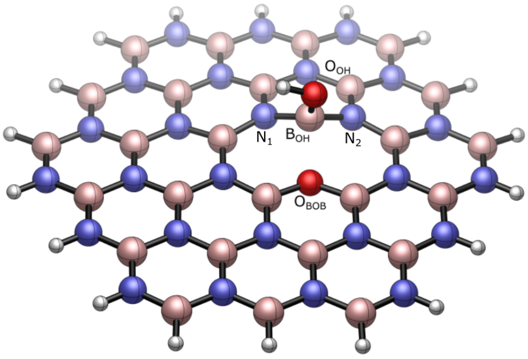

Figure 93: BNO-OH surface model obtained from the $B_{21}N_{24}O_{11}H_{37}$ (IN3b) model by removing 9 $H_2O$ molecules after successive dehydration reactions.

of the BNO-OH model is shown in Figure 93. Interestingly, while in the previous BNH-OH model the $B_{OH}$ atom presented a tetrahedral environment, in the BNO-OH model described here the $B_{OH}$ atom has a pseudo $sp^2$ hybridization, the angles $O_{OH}$-$B_{OH}$-$N_1$, $O_{OH}$-$B_{OH}$-$N_2$, and $N_1$,-$B_{OH}$-$N_2$ measuring 119.6°, 115.6° and 117.2°, respectively. This results in a stronger B-OH bond interaction for the BNO-OH system, which displays a smaller B-OH bond distance (1.391 $\AA$) compared to the 1.464 $\AA$ value of the previous BNH-OH system. As confirmed by a second-order perturbation NBO analysis, in addition, the increased strength of the B-OH bond in the BNO-OH model is also due to a donation of 66.1 kcal.mol$^{-1}$ from a lone pair of the $O_{OH}$ atom to the empty p orbital of the $B_{OH}$ centre. The second-order perturbation NBO analysis also reveals a donation of 70.3 kcal.mol$^{-1}$ from a lone pair of the $O_{BOB}$ atom to the empty p orbital of the $B_{OH}$ atom. The presence of this $O_{BOB}$-$B_{OH}$ interaction results in a $O_{BOB}$-$B_{OH}$ distance of 1.976 $\AA$. In the BNO-OH model, therefore, the p orbital of the $B_{OH}$ atom interacts simultaneously with both the lone pair on the $O_{OH}$ atom and the lone pair on the $O_{BOB}$ atom, the strength of these two interactions resulting similar. If we compare the $B_{OH}$ natural charge of the previous BNH-OH and h-BN models (1.19 and 1.18 respectively) with that of the BNO-OH model (1.28), in addition, we can observe that the $B_{OH}$ atom in the BNO-OH system is more positive, displaying therefore a more Lewis acidic character.

## 6.2 Grafting reaction

The BNO-OH surface model has been then employed to perform the grafting of the $[La(N(SiMe_3)_2)_3]$ compound. The metathesis reaction between the La-N and BO-H bonds may generate a BO-La bond, with the concomitant formation of a free hexamethyldisilazane molecule. The corresponding enthalpy profile is shown in Figure 94. The structures of the transition states and intermediates involved in the grafting reaction are shown in Figure 95. Selected bond distances are summarised in table 12. As shown in Figure 94, the grafting reaction leads to the formation of the mono-grafted (BNO-O)-$[La(N(SiMe_3)_2)_2]$ complex through an exothermic (-19.2 kcal.mol$^{-1}$ with respect to the separated reactants), and kinetically favourable (activation barrier of 1.0 kcal.mol$^{-1}$ with respect to the hexamethyldisilazane adduct $A^{graf}{}_{BNO-O}$) process.

The transition state associated to the protonolysis reaction displays a classical 4c - 4e$^-$ $\sigma$ bond metathesis geometry, with the BNO-OH hydroxo oxygen atom interacting with the La centre (La-O distance = 2.560 $\AA$) and the hexamethyldisilylamido nitrogen atom interacting with the BNO-OH hydroxo hydrogen atom (N-H distance = 1.403 $\AA$). The low value of the barrier height can be rationalised by the perfect positive and negative charge alternation (+1.65, -1.73, +0.52 and -1.00 for the La, N, H and O atoms, respectively, see figure 96). The resulting lanthanum complex $B^{graf}{}_{BNO-O}$ is therefore mono-grafted on the BNO-O surface (La-O distance = 2.257 $\AA$), with the $HN(SiMe_3)_2$ molecule still interacting with the lanthanum centre (La-N distance = 2.916 $\AA$). The release of the amine from the La coordination sphere in $C^{graf}{}_{BNO-O}$ is accompanied by a decrease of the O-La bond distance (O-La = 2.180 $\AA$ in $C^{graf}{}_{BNO-O}$ compared to 2.257 $\AA$ in $B^{graf}{}_{BNO-O}$) and by a strengthening of the $O_{BOB}\cdots B_{OH}$ interaction which increases, according to a NBO analysis, from 51.2 kcal.mol$^{-1}$ in $B^{graf}{}_{BNO-O}$ to 81.7 kcal.mol$^{-1}$ in $C^{graf}{}_{BNO-O}$.

The NBO analysis additionally shows a donation from the N-Si, Si-C and C-H bonds of the two hexamethyldisilylamido groups onto an empty d orbital of the metal centre, indicating the presence of two strong agostic interactions (116.0 and 115.7 kcal.mol$^{-1}$), with a La-N Wiberg bond index of 0.52 and 0.53. The O-La bond interaction in $C^{graf}{}_{BNO-O}$ (O-La = 2.180 $\AA$) is also revealed by a second-order NBO analysis showing a strong donation from a lone pair of the $O_{OH}$ oxygen atom onto an empty d orbital of the La centre (151.5 kcal.mol-1), with a O-La Wiberg bond index of 0.59. Interestingly, the La-O distance observed here for the (BNO-O)-$[La(N(SiMe_3)_2)_2]$-grafted system is shorter than that found in the (gO)-$[La(N(SiMe_3)_2)_2]$ analogue (La-O distance = 2.432 $\AA$). This difference is likely to reflect the different nature of the $C_{surface}$-O and $B_{surface}$-O bonds in the gOH and BNO-OH models, respectively. While in the gOH model, the positive charge of the graphene surface polarizes the electron density of the $O_{OH}$ atom, resulting in a poorly donor $C=O^+$ group, in the neutral BNO-OH surface, on the other hand, the $=B-O^-$ borate anion is a stronger donor group giving rise to a stronger B-O-La bond. Compared to the BNO-OH naked surface, interestingly, the grafting of the hexamethyldisilylamido La complex does not significantly change the pseudo sp$^2$ geometry around the $B_{OH}$ atom, the angles $O_{OH}$-$B_{OH}$-$N_1$, $O_{OH}$-$B_{OH}$-$N_2$ and $N_1$-$B_{OH}$-$N_2$ measuring 118.5°, 118.5° and 114.5°, respectively. The only small differences between the naked and La grafted BNO-OH surfaces are the shortening of the $B_{OH}$-$O_{OH}$ distance from 1.391 to 1.377 $\AA$, and the shortening of the $O_{BOB}$ - $B_{OH}$ distance from 1.976 to 1.940 $\AA$. In accordance with these values, we observe an increase of the second-order NBO donation from a lone pair of the $O_{OH}$ atom to the empty p orbital of the $B_{OH}$ atom (from 66.1 kcal.mol$^{-1}$ for the naked surface to 73.5 kcal.mol$^{-1}$ for the grafted system) and from a lone pair of the $O_{BOB}$ atom to the empty p orbital of the $B_{OH}$ atom (from 70.3 kcal.mol$^{-1}$ for the naked surface to 81.7 kcal.mol$^{-1}$ for the grafted system). Ongoing from the homogeneous $[La(N(SiMe_3)_2)_3]$ complex to the grafted (BNO-O)-$[La(N(SiMe_3)_2)_2]$ system, interestingly, the natural charge of the La centre increases from 1.65 to 1.88 , indicating that the grafting of the $[La(N(SiMe_3)_2)_3]$ complex on the BNO-OH surface increases the Lewis acidity of the La centre as we will discuss in more details in the following section.

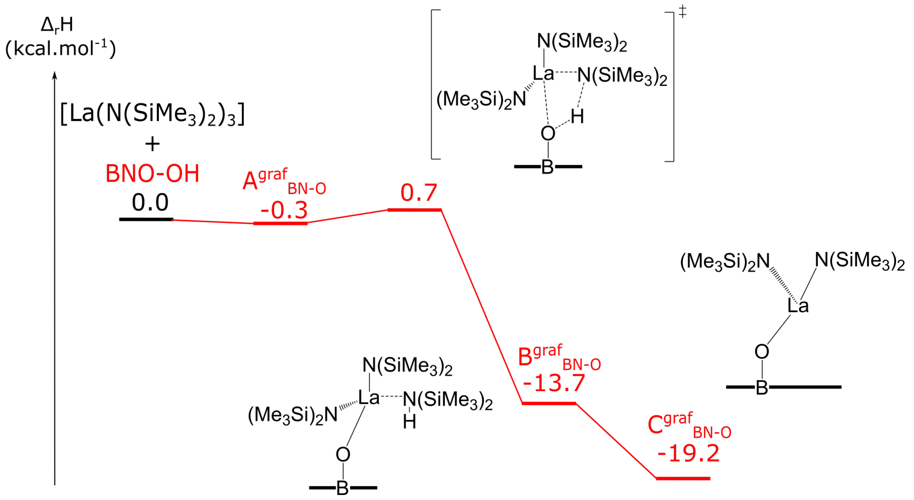

Figure 94: Calculated enthalpy-energy profile for the grafting of the [La(N(SiMe$_3$)$_2$)$_3$] complex on the BNO-OH functionalised surface.

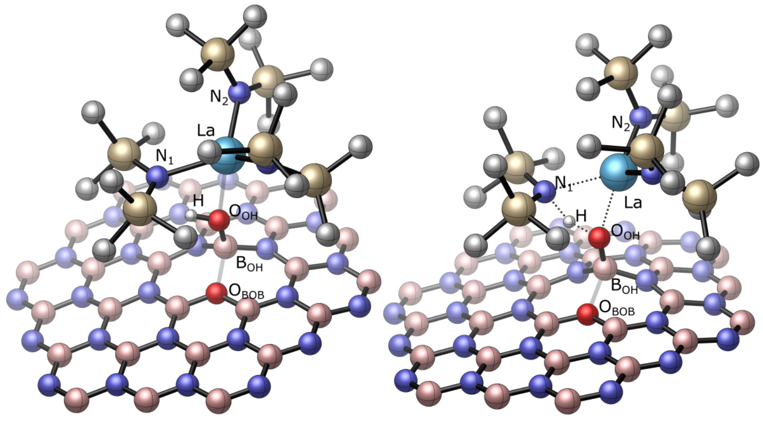

(a) $A^{graf}{}_{BNO-O}$ (b) TS-$AB^{graf}{}_{BNO-O}$

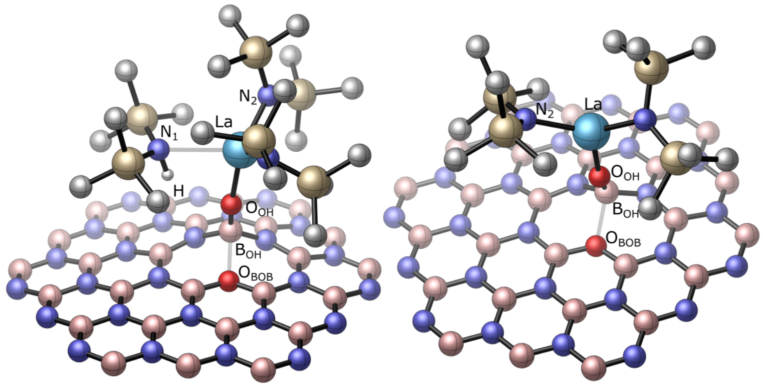

(c) $B^{graf}{}_{BNO-O}$ (d) $C^{graf}{}_{BNO-O}$

Figure 95: Structure of the complexes involved in the grafting reaction of [La(N(SiMe$_3$)$_2$)$_3$] on the BNO-OH functionalised surface (light blue : La, dark blue : N, white : H, red : O). For sake of clarity all the H of the La-grafted compounds have been omitted with the exception of the BNO-OH surface atom.

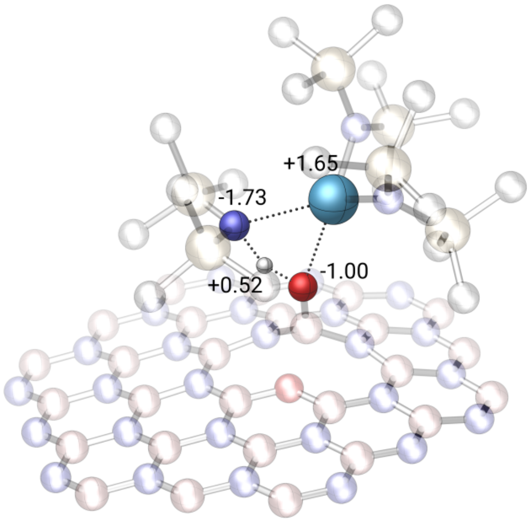

Figure 96: NPA charges involved in the metathesis transition state of the grafting reaction of [La(N(SiMe$_3$)$_2$)$_3$] on the BNO-OH functionalised surface (light blue : La, dark blue : N, white : H, red : O).

Table 12: Enthalpy data (kcal.mol$^{-1}$) and selected bond distances ($\mathring{A}$) of the TS, the HN(SiMe$_3$)$_2$ adduct and the final (BNO-O)-[La(N(SiMe$_3$)$_2$)$_2$] compounds resulting from the grafting of the [La(N(SiMe$_3$)$_2$)$_3$] complex on the BNO-OH functionalised surface. The labels La, O, O$_{BOB}$, B$_{OH}$, N$_1$, N$_2$ and H refer to the geometries in figure 95.

| | $\Delta_R$H° | La-O$_{OH}$ | La-N$_1$ | La-N$_2$ | O$_{OH}$-H | N$_1$-H | B$_{OH}$-O$_{OH}$ | B$_{OH}$-O$_{BOB}$ |
|---|---|---|---|---|---|---|---|---|
| $\text{TS-AB}^{gref}{}_{BNO-O}$ | 0.7 | 2.560 | 2.592 | 2.385 | 1.164 | 1.403 | 1.396 | 1.974 |
| $\text{B}^{gref}{}_{BNO-O}$ | -13.7 | 2.257 | 2.916 | 2.379 | - | 1.028 | 1.361 | 2.085 |
| $\text{C}^{gref}{}_{BNO-O}$ | -19.2 | 2.180 | - | 2.345 | - | - | 1.377 | 1.940 |

## 6.3 Probing the Lewis acidity of the BN grafted lanthanum complexes

As previously reported, the coordination of a triphenylphosphinoxide (O=PPh$_3$) to grafted metal complexes can be used as a probe to estimate the influence of the surface on the Lewis acidity properties of the metal centre and therefore on the reactivity of the catalyst. The O=PPh$_3$ is known to react with molecular and surface-grafted lanthanide hexamethyldisilylamido compounds, leading to the formation of the corresponding molecular [Ln(N(SiMe$_3$)$_2$)$_3$(O=PPh$_3$)] and surface-grafted [Ln(N(SiMe$_3$)$_2$)$_x$(O=PPh$_3$)] (x = 2 if mono-grafted; x = 1 if bi-grafted) complexes, respectively.[87] The coordination of O=PPh$_3$ on the (BNO-O)-[La(N(SiMe$_3$)$_2$)$_2$] grafted compound affords the corresponding (BNO-O)-[LaN(SiMe$_3$)$_2$)$_2$(O=PPh$_3$)] species (figure 97), through a highly exothermic process of 36.8 kcal.mol$^{-1}$. As attested by a second order NBO interaction of 135.1 kcal.mol$^{-1}$ between a lone pair of the O=PPh$_3$ oxygen atom to a vacant d orbital of the La, the strong donation of the O=PPh$_3$ molecule to lanthanum, weakens the agostic interactions of the two hexamethyldisilylamido groups which decrease from 116.0 and 115.7 kcal.mol$^{-1}$ to 61.9 and 78.6 kcal.mol$^{-1}$. We therefore computed the IR and the $^1$H, $^{13}$C and $^{31}$P NMR spectra of the (BNO-O)-[La(N(SiMe$_3$)$_2$)$_2$(O=PPh$_3$)] adduct, with the goal of comparing its Lewis acidity with that of the SiO$_2$-, gO- and gOO-grafted analogues previously reported. The C-H, aromatic C=C and O=P vibrational frequencies computed for the coordinated O=PPh$_3$ molecule are reported in table 13. The aromatic C-H and C=C stretching vibrations are located in the range 3199-3239 cm$^{-1}$ and 1413-1655 cm$^{-1}$, respectively, while the vibrational stretching mode corresponding to the O=P function lies at 1068 cm$^{-1}$. The O=PPh$_3$ La complexes mono-grafted and bi-grafted on silica supports, interestingly, display lower C-H and C=C vibrational frequencies (in the range 2938-3107 cm$^{-1}$ and 1416-1592 cm$^{-1}$, respectively, depending on the considered silica model) and higher O=P vibrational stretching modes (in the range 1118-1152 cm$^{-1}$ depending on the considered silica model). Compared to the silica-supported La systems, therefore, the BNO-O-supported La compound computed here displays a weaker O=P bond and thus a stronger La-O bond which reflects a stronger Lewis acid character. The O=PPh$_3$ La complexes grafted on the gOH and gOOH graphene surfaces, on the other hand, display similar C-H and C=C vibrational frequencies (in the range 3184-3240 cm$^{-1}$ and 1471-1655 cm$^{-1}$, respectively, depending on the graphene model) and slightly lower O=P vibrational stretching modes (1039 cm$^{-1}$ and 1047 cm$^{-1}$, for the gO- and gOO- supported systems, respectively), indicating that the Lewis acidity of the graphene-supported La amido complexes is slightly stronger than that of the BNO-O-supported La analogue. Another way to characterise the nature of the metal centre is to investigate the theoretical $^1$H, $^{13}$C and $^{31}$P NMR chemical shift of the coordinated O=PPh$_3$ molecule (table 13). The $^1$H isotropic chemical shift computed for the BNO-O-grafted La species is of 7.8 ppm. While this value is similar to those reported for the mono- and bi-grafted silica models (in the range 7.9 - 8.0 ppm), it results slightly more deshielded than those reported for the gO- and gOO-grafted models (in the range 7.3 - 7.4 ppm). The $^{13}$C NMR values computed for the BNO-O-supported La system (122.9 and 130.0 ppm) are comparable with those computed in the graphene-grafted (123.5 and 127.8 ppm for the (gO)-La system and 123.6 and 127.8 ppm for the (gOO)-La system) and silica-grafted models (between 123.5 and 124.9 ppm for the high field $^{13}$C signal and between 128.1 and 129.2 for the high field $^{13}$C signal). While the $^{31}$P NMR signal computed for the O=PPh$_3$ molecule

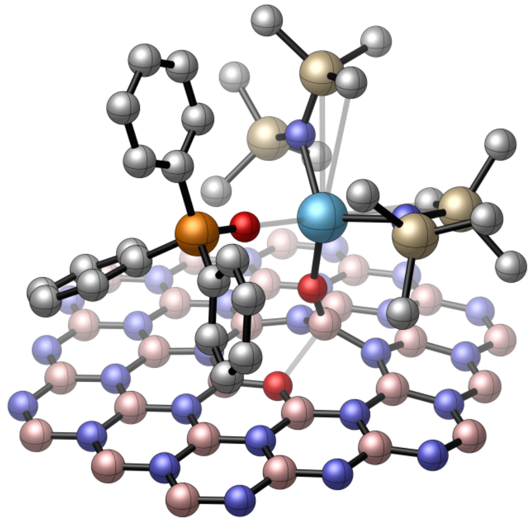

Figure 97: Geometry of the $OPPh_3$ hexamethyldisilylamido La compound, (BNO-O)-[$La(N(SiMe_3)_2)_2(O{=}PPh_3)$], grafted on the BNO-OH surface.

coordinated to the BNO-O-grafted La complex (53.8 ppm) is slightly lower than that computed for the gO La system (56.0 ppm), it is comparable with that computed for the gOO La model (53.4 ppm) and more deshielded than those obtained in the silica-grafted silica models (in the range 40.3-47.6 ppm). As evidenced by Drago,[181, 370] a positive $^{31}P$ NMR chemical shift increment between free and coordinated $O{=}PPh_3$ indicates the coordination to a Lewis acidic site, the bigger this difference, the higher the Lewis acidic character of the metal and therefore the stronger the M-$O{=}PPh_3$ interaction. The IR and $^{31}P$ NMR values, therefore, indicate that the BNO-O-grafted La system behave as the gOO-grafted La system, displaying a Lewis acidic character which is slightly lower than that of the gO-grafted analogue but considerably stronger than that of the silica-grafted analogues.

Table 13: Comparison between the theoretical vibrational frequencies (in $cm^{-1}$), and the $^1H$, $^{13}C$ and $^{31}P$ NMR chemical shifts (in ppm) of a free $OPPh_3$ ligand and the coordinated $OPPh_3$ molecule in different $OPPh_3$ hexamethyldisilylamido La adducts grafted on the BNO-OH, the graphene gOH and gOOH and the $SiO_2$ surfaces (average between all the mono- and bi-grafted species previously reported).[135] The $^1H$ and $^{13}C$ chemical shifts are given with respect to TMS (theoretical chemical shielding: 31.64 and 195.35 ppm, respectively, for the $^1H$ and $^{13}C$ atoms). The $^{31}P$ chemical shifts are given with respect to phosphoric acid (theoretical chemical shielding: 380.6 ppm). (R = $SiMe_3$).

| | vibrational frequencies | | |
|---|---|---|---|
| | $\nu_{C-H}$ | $\nu_{C=C}$ | $\nu_{O=P}$ |
| $O=PPh_3$ | [3065-3095] | [1416-1592] | 1177 |
| (BNO-O)-[$La(NR_2)_2(O=PPh_3)$] | [3199-3239] | [1413-1655] | 1068 |
| (gO)-[$La(NR_2)_2(O=PPh_3)$] | [3184-3240] | [1471-1655] | 1039 |
| (gOO)-[$La(NR_2)_2(O=PPh_3)$] | [3193-3230] | [1475-1655] | 1047 |
| ($SiO_2$)-[$La(NR_2)_2(O=PPh_3)$] | [2938-3107] | [1416-1592] | [1118-1152] |

| | NMR | | |
|---|---|---|---|
| | $\delta_{H_{Phenyl}}$ | $\delta_{C_{Phenyl}}$ | $\delta_P$ |
| $O=PPh_3$ | 7.7 | [124.7-/129.9] | 25.7 |
| (BNO-O)-[$La(NR_2)_2(O=PPh_3)$] | 7.8 | [122.9/130.0] | 53.8 |
| (gO)-[$La(NR_2)_2(O=PPh_3)$] | 7.3 | [123.5/127.8] | 56.0 |
| (gOO)-[$La(NR_2)_2(O=PPh_3)$] | 7.4 | [123.6/127.8] | 53.4 |
| ($SiO_2$)-[$La(NR_2)_2(O=PPh_3)$] | [7.9-8.0] | [123.5-124.9]/[128.1-129.0] | [40.3-47.6] |

The Lewis acidity of the BNO-O-grafted La compound is likely to be ascribed to the nature of the pseudo-$sp^2$-hybridised $B_{OH}$ atom. This atom may indeed act itself as a Lewis acid, polarising to its empty p orbital the electron density of the $O_{OH}$ atom which in turn becomes less donor toward the La metal. By comparing the IR and RMN values obtained for the (BNO-O)-[$La(N(SiMe_3)_2)_2(O=PPh_3)$] species with those computed for the analogue gO-, gOO- and $SiO_2$- supported La systems, we observe that the Lewis acidity of the metal center is likely to increase in the order $SiO_2$ < BNO-OH ≅ gOO < gO, underlying the important influence of the surface in the acidic properties of the corresponding metal complex.

## 6.4 Catalytic activity of the BN grafted lanthanum complexes

As previously described for the graphene-supported compounds, surface-grafted lanthanide complexes are known to behave as active catalysts in many polymerisation reactions.[143, 182] Following a coordination-insertion mechanism, the first step of the polymerisation process involves the coordination of the monomer to the metal centre, the higher the Lewis acidic character of the metal, the higher the activation of the monomer in the polymerisation reaction. In view of their Lewis acidity, therefore, we expected BNO-O-supported La complexes to act as active polymerisation catalysts and we decided to study their catalytic activity in the homo- and co-polymerisation of ethylene and 1,3-butadiene. Experimentally, as reported in chapter I, lanthanide alkyl complexes have been shown to behave as active polymerisation catalysts. Silica-supported alkyl species are usually synthetised by using an alkylating agent (such as the

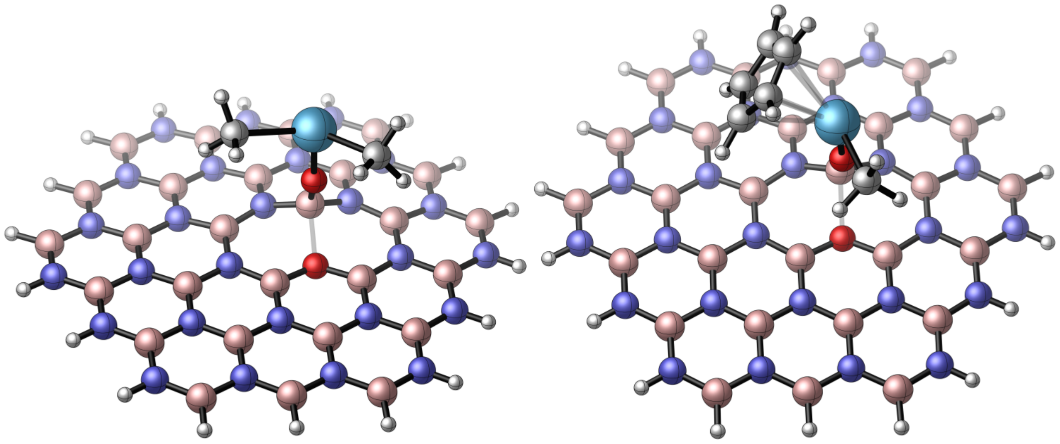

(a) (BNO-O)-[La($CH_3$)$_2$] (**1BNO-O**) (b) (BNO-O)-[La$CH_3$Cp] (**2BNO-O**)

Figure 98: Geometries of the grafted (a) (BNO-O)-[La($CH_3$)$_2$] (1BNO-O) and (b) (BNO-O)-[La(Cp)($CH_3$)] (2BNO-O) compounds.

TIBA) which converts the starting hexamethyldisilylamido groups into the corresponding alkyl groups. Following the same reactivity, we choose as the catalytically active species the (BNO-O)-[La($CH_3$)$_2$] (1BNO-O) and (BNO-O)-[La(Cp)($CH_3$)] (2BNO-O) models, obtained by replacing both hexamethyldisilylamido groups by two methyl functions in 1BNO-O and by one methyl function and one cyclopentadienyl (Cp) function in 2BNO-O. As shown in figure 98, 1BNO-O and 2BNO-O are monografted compounds, with the BNO-O oxygen atom completing the coordination sphere of lanthanum. The La-O bond decreases from 2.180 $\AA$ to 2.125 $\AA$ and 2.157 $\AA$ ongoing from the grafted (BNO-O)-[La(N(Si$Me_3$)$_2$)$_2$] to 1BNO-O and 2BNO-O, showing that the replacement of the silylamido ligands with the less donating alkyl ligands increases the Lewis acidity of the La centre, reinforcing the La-O bond strenght. In addition to the simple $B_{OH}$-$O_{OH}$ bond, a second order NBO analysis reveals a strong donation of 93.1 and 72.0 kcal.mol$^{-1}$ for 1BNO-O and 2BNO-O, respectively, from a lone pair of the $O_{OH}$ atom to an empty p orbital of the adjacent $B_{OH}$ atom. The NBO analysis also highlights a strong donation from a lone pair of the $O_{BOB}$ atom toward an empty p orbital of the $B_{OH}$ atom (93.1 and 74.5 kcal.mol$^{-1}$, in 1BNO-O and 2BNO-O respectively). The modular balance between the $LaO_{O}H$-$B_{OH}$ and $O_{BOB}$-$B_{OH}$ interactions, interestingly, may represent an adaptable electronic assistance from the surface which may stabilise, when necessary, the Lewis acidity of the La metal.

### 6.4.1 Ethylene polymerisation

**6.4.1.1 Reaction profiles of the 1$^{st}$ and 2$^{nd}$ insertions** The enthalpy profile of the first two steps of the ethylene homopolymerisation reaction is depicted in Figure 99. A view of the different intermediate and transition state geometries is available in Figures 100 and 101. For both complexes 1BNO-O and 2BNO-O, the reaction begins with the formation of an exothermic adduct with a stabilising energy of -8.1 kcal.mol$^{-1}$ ($A^{Et}{}_{1BNO-O}$) and -6.3 kcal.mol$^{-1}$ ($A^{Et}{}_{2BNO-O}$) with respect to the entrance channel, corresponding to the coordination of one ethylene molecule to the La centre. The coordination to the metal centre activates the ethylene

Table 14: Enthalpy data (kcal.mol$^{-1}$) for the first propagation step of the ethylene polymerisation mediated by (BNO-O)-[La(CH$_3$)$_2$] and (BNO-O)-[La(Cp)(CH$_3$)] for the front side and the back side insertion.

| (BNO-O)-[La(CH$_3$)$_2$] | $\Delta_r$H | (BNO-O)-[La(Cp)(CH$_3$)] | $\Delta_r$H |
|---|---|---|---|
| | front side | | |
| $C^{Et}{}_{1BNO-O}$ | -30.7 | $C^{Et}{}_{2BN-O}$ | -29.9 |
| TS-CD$^{Et}{}_{1BNO-O}$ | -22.3 | TS-CD$^{Et}{}_{2BN-O}$ | -22.5 |
| $D^{Et}{}_{1BNO-O}$ | -46.2 | $D^{Et}{}_{2BN-O}$ | -46.2 |
| | back side | | |
| $C^{Et}{}_{1BNO-O}$ | -27.5 | $C^{Et}{}_{2BN-O}$ | -28.4 |
| TS-CD$^{Et}{}_{1BNO-O}$ | -23.9 | TS-CD$^{Et}{}_{2BN-O}$ | -22.1 |
| $D^{Et}{}_{1BNO-O}$ | -47.0 | $D^{Et}{}_{2BN-O}$ | -46.3 |

monomer (C=C ethylene distances = 1.339 $\mathring{A}$ for $A^{Et}{}_{1BNO-O}$ and 1.338 $\mathring{A}$ for $A^{Et}{}_{2BNO-O}$, compared to 1.329 $\mathring{A}$ for free ethylene), reflecting the Lewis acidity of the BNO-OH-grafted La centre as discuss above. The formation of this adduct is followed by the insertion of ethylene into the La-Me bond of 1BNO-O and 2BNO-O through a 4c - 4e$^-$ $\sigma$-bond metathesis transition state,[152, 368] with accessible enthalpy barriers of 7.6 and 5.1 kcal.mol$^{-1}$ for TS-AB$^{Et}{}_{1BNO-O}$ and TS-AB$^{Et}{}_{2BNO-O}$ respectively, with respect to the corresponding $A^{Et}$ adducts. The geometry of the two transition states is quite similar in both cases and reveals a marked elongation of the La-C (La-CH$_3$ = 2.532 $\mathring{A}$ for TS-AB$^{Et}{}_{1BNO-O}$ and 2.533 $\mathring{A}$ for TS-AB$^{Et}{}_{2BNO-O}$ *vs.* 2.485 and 2.496 $\mathring{A}$ for the initial 1BNO-O and 2BNO-O complexes, respectively) and of the C=C bonds (C=C = 1.390 $\mathring{A}$ for both TS-AB$^{Et}{}_{1BNO-O}$ and TS-AB$^{Et}{}_{2BNO-O}$ compared to C=C = 1.329 $\mathring{A}$ for the free ethylene). The formation of the insertion products (propyl products) is an exothermic process, with the $B^{Et}{}_{1BNO-O}$ and $B^{Et}{}_{2BNO-O}$ adducts located at -22.6 and -20.6 kcal.mol$^{-1}$, with respect to the entrance channel. As shown in fig 100, the propyl moiety of the $B^{Et}{}_{1BNO-O}$ and $B^{Et}{}_{2BNO-O}$ compounds interacts with the La metal through a C-H···La agostic interaction, involving a second order NBO stabilisation energy of 21.9 and 40.7 kcal.mol$^{-1}$ for the $B^{Et}{}_{1BNO-O}$ and $B^{Et}{}_{2BNO-O}$ compounds, respectively.

In order to get insight into the polymerisation process, the second ethylene insertion, corresponding to the first propagation step, has also been computed. For this second step, we considered both the front side “migratory” and the back side “stationary” ethylene insertions, with the ethylene monomer inserting on the same side or on the opposite side of the propyl C-H $\beta$ agostic interaction, respectively. For both catalytic systems, the formation of the final insertion products has been computed to be a thermodynamically exothermic and a kinetically accessible process, with very similar energies for the two insertion modes (see table 14). For sake of clarity, thus, we will limit the following discussion to the back-side insertions only.

The enthalpy profiles of the back-side second ethylene insertion is shown in figure 99. A view of the different intermediate and transition state geometries is available in figure 101. The first propagation step begins, as for the initiation step, by the coordination of ethylene to the metal centre, affording the thermodynamically favourable species $C^{Et}{}_{1BNO-O}$ and $C^{Et}{}_{2BNO-O}$ located at -4.9 and -7.8 kcal.mol$^{-1}$ respectively with respect to the corresponding $B^{Et}$ adducts.

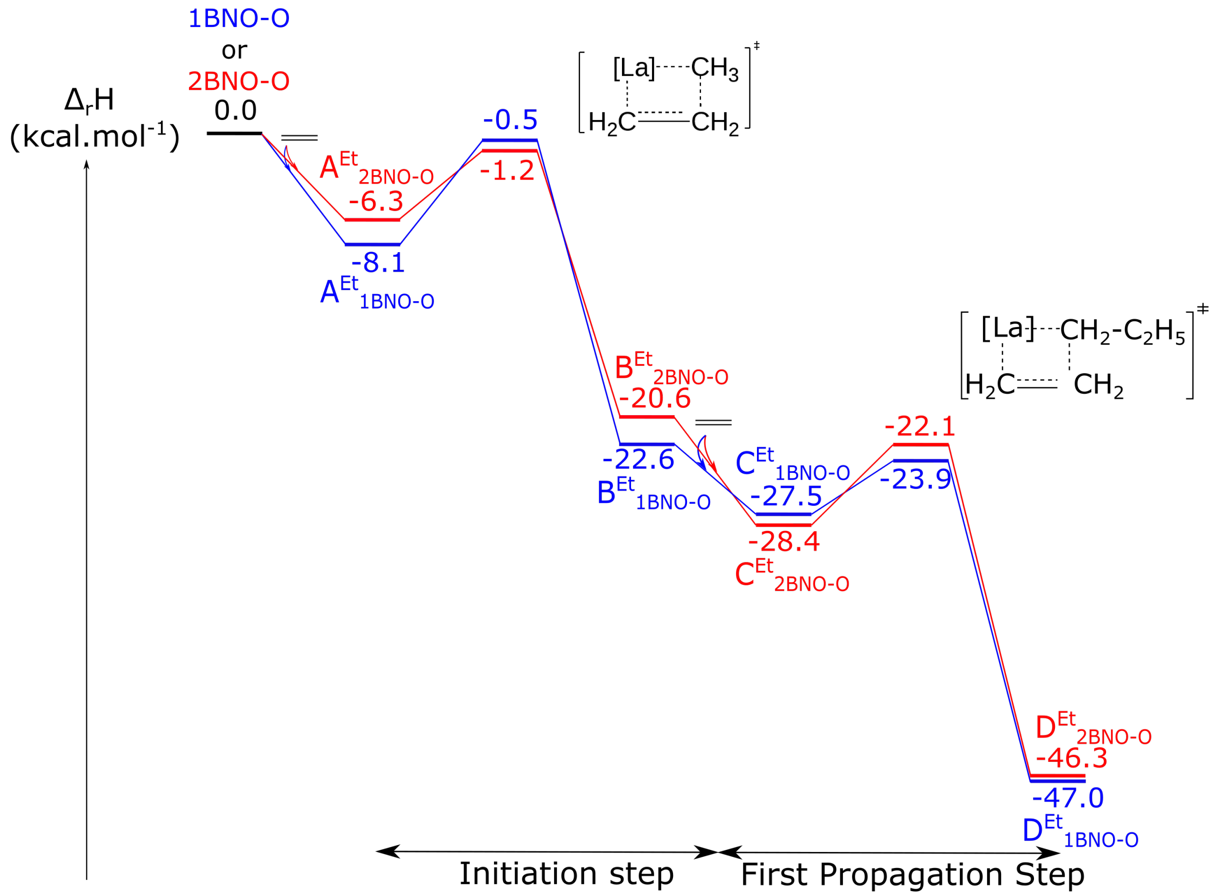

Figure 99: Enthalpy profile of the initiation and first propagation step for the homopolymerisation of ethylene.

From these intermediates, the second insertion reaction takes place *via* a low-energy process, displaying an activation barrier of 3.6 and 6.3 kcal.mol$^{-1}$ for the TS-CD$^{Et}{}_{1BNO-O}$ and TS-CD$^{Et}{}_{2BNO-O}$, respectively, with respect to the previous adducts C$^{Et}{}_{1BNO-O}$ and C$^{Et}{}_{2BNO-O}$. The final D$^{Et}{}_{1BNO-O}$ and D$^{Et}{}_{2BNO-O}$ products are obtained through a highly exothermic process (-19.5 and -17.9 kcal.mol$^{-1}$, respectively, with respect to the corresponding C$^{Et}$ adducts). From a kinetic point of view, the comparison of the two 1BNO-O and 2BNO-O profiles reveals that while for the 1BNO-O species, the activation barrier corresponding to the initiation step (7.6 kcal.mol$^{-1}$) is higher than that of the propagation one (3.6 kcal.mol$^{-1}$), for the 2BNO-O system, the barrier heights are comparable (5.1 and 6.3 kcal.mol$^{-1}$, respectively). From a thermodynamic point of view, the exothermicity of the reaction is comparable between the two compounds (-47.0 and -46.3 kcal.mol$^{-1}$ for 1BNO-O and 2BNO-O , respectively). Both the (BN-O)-[La(CH$_3$)$_2$] and (BN-O)-[La(Cp)(CH$_3$)] complexes, therefore, are expected to efficiently catalyse the ethylene polymerisation reaction, displaying a similar catalytic activity, from a kinetic and thermodynamic point of view.

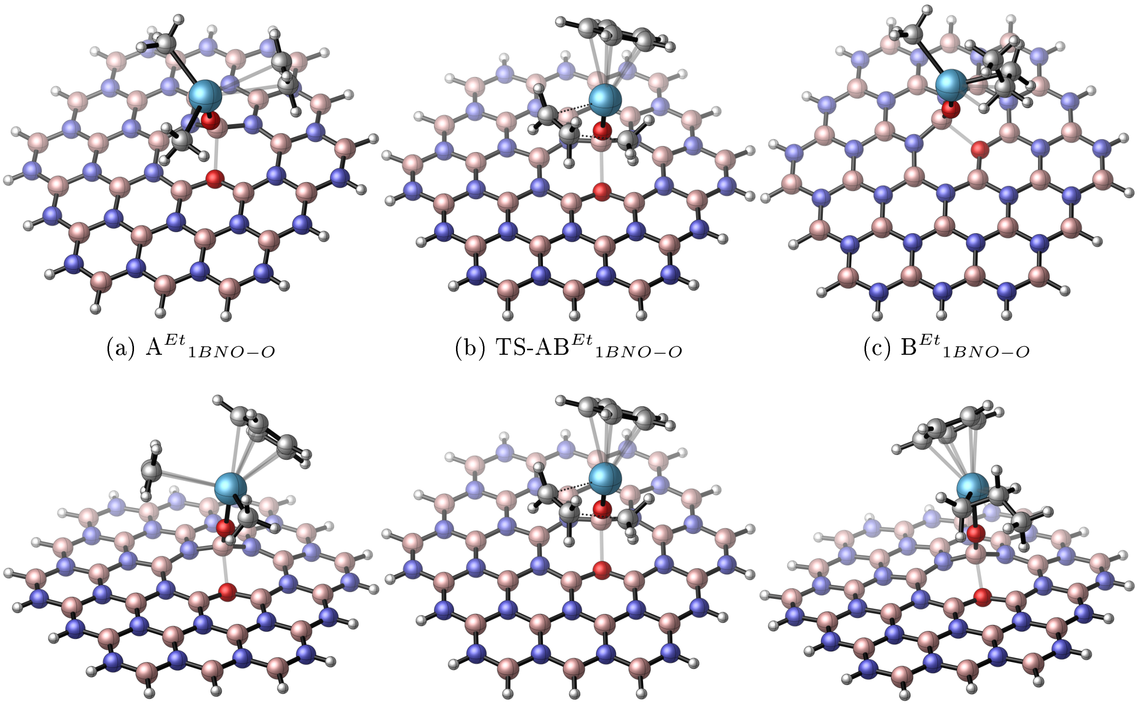

(a) $\mathrm{A}^{Et}{}_{1BNO-O}$ (b) $\mathrm{TS\text{-}AB}^{Et}{}_{1BNO-O}$ (c) $\mathrm{B}^{Et}{}_{1BNO-O}$

(d) $\mathrm{A}^{Et}{}_{2BNO-O}$ (e) $\mathrm{TS\text{-}AB}^{Et}{}_{2BNO-O}$ (f) $\mathrm{B}^{Et}{}_{2BNO-O}$

Figure 100: Optimised structures of the complexes involved in the first ethylene insertion mediated by (BNO-O)-[La($CH_3$)$_2$] (1BNO-O) and (BNO-O)-[La(Cp)($CH_3$)] (2BNO-O).

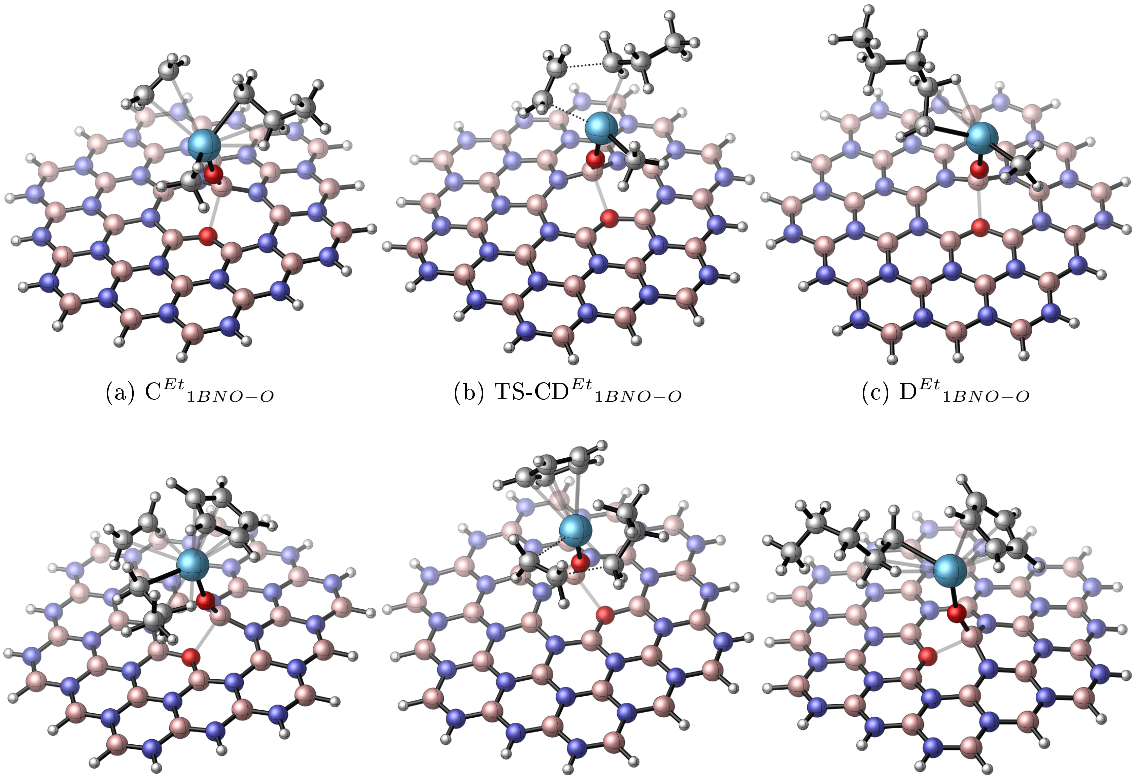

(a) $\mathrm{C}^{Et}{}_{1BNO-O}$ (b) $\mathrm{TS\text{-}CD}^{Et}{}_{1BNO-O}$ (c) $\mathrm{D}^{Et}{}_{1BNO-O}$

(d) $\mathrm{C}^{Et}{}_{2BNO-O}$ (e) $\mathrm{TS\text{-}CD}^{Et}{}_{2BNO-O}$ (f) $\mathrm{D}^{Et}{}_{2BNO-O}$

Figure 101: Optimised structures of the complexes involved in the second ethylene insertion mediated by (BNO-O)-[La($CH_3$)$_2$] (1BNO-O) and (BNO-O)-[La(Cp)($CH_3$)] (2BNO-O).

Table 15: Enthalpy data (kcal.mol$^{-1}$) for the initiation and first propagation steps of the ethylene polymerisation mediated by the (BNO-O)-[La($CH_3$)$_2$], the $Cp_2$LaMe, the ($SiO_2$)-[La($CH_3$)$_2$], the (gO)-[La($CH_3$)$_2$] and the (gOO)-[La($CH_3$)$_2$] complexes.

| | $A^{Et}$ | TS-$AB^{Et}$ | $B^{Et}$ | $C^{Et}$ | TS-$CD^{Et}$ | $D^{Et}$ |
|---|---|---|---|---|---|---|
| (BN-O)-[La($CH_3$)$_2$] | -8.1 | -0.5 | -22.6 | -27.5 | -23.9 | -47.0 |
| $Cp_2$LaMe | -7.6 | -0.2 | -21.1 | -29.5 | -23.4 | -46.4 |
| ($SiO_2$)-[La($CH_3$)$_2$] | -4.6 | 6.4 | -20.5 | -22.1 | -17.5 | -45.5 |
| gO-[La($CH_3$)$_2$] | -5.9 | -0.4 | -23.5 | -27.9 | -22.8 | -47.6 |
| gOO-[La($CH_3$)$_2$] | -7.1 | -1.1 | -23.7 | -29.9 | -23.3 | -46.6 |

**6.4.1.2 Comparison with the molecular, the silica-grafted and the graphene-grafted supported systems.** As discussed in the previous chapter, compared to the silica surfaces which mainly act as physical supports, the graphene surface is likely to actively influence the electronic properties of the supported metal complex, increasing its Lewis acidity.[429] In order to study the influence of the silica, graphene and BNO-OH supports on the catalytic properties of the grafted La compounds, we compared the ethylene polymerisation enthalpy profile computed for the (BNO-O)-[La($CH_3$)$_2$] compound with those computed for the molecular [$Cp_2$LaMe], silica-supported ($SiO_2$)-[La($CH_3$)$_2$] and graphene-supported (gO)-[La($CH_3$)$_2$] and (gOO)-[La($CH_3$)$_2$] analogues, (table 15). For the molecular, silica-supported and graphene-supported (gO and gOO) systems, the activation barrier involved in the rate determining step measures 7.4, 11.0, 5.5 and 6.6 kcal.mol$^{-1}$, respectively. From a kinetic and thermodynamic point of view, interestingly, the 1BNO-O system is comparable with the homogeneous and graphene-grafted gO and gOO systems. For these four species, indeed, the barriers involved in the rate determining step are lower than that computed for the silica-grafted system (7.6, 7.4, 5.5 and 6.6 kcal.mol$^{-1}$ *vs.* 11.0 kcal.mol$^{-1}$) underlying the similar role of the BNO-O and graphene surfaces in increasing the Lewis acidity and therefore the reactivity of the corresponding La grafted systems.

### 6.4.2 Butadiene polymerisation

**6.4.2.1 Reaction profiles of the 1$^{st}$ and 2$^{nd}$ butadiene insertions** The enthalpy profiles for the 1,3-butadiene homopolymerisation, involving the 1,4-trans and 1,4-cis insertions of butadiene into the La-alkyl bond has also been computed for 1BNO-O and 2BNO-O. Figure 102 shows the enthalpy profile of the first 1,4-cis and 1,4-trans 1,3-butadiene insertion. A view of the different transition states and intermediates is available in figures 103 and 104. As for the ethylene insertion, the initiation step begins with the formation of an exothermic adduct, corresponding to species ${A^{Bu,cis}}_{1BNO-O}$, ${A^{Bu,trans}}_{1BNO-O}$ (at -11.2 and -10.5 kcal.mol$^{-1}$, respectively) and ${A^{Bu,cis}}_{2BNO-O}$, ${A^{Bu,trans}}_{2BNO-O}$ (at -11.2 and -10.2 kcal.mol$^{-1}$, respectively). Interestingly, although the 2BNO-O system is more sterically hindered than the 1BNO-O one, due to the presence of the Cp ligand, no stability difference is observed between the ${A^{Bu}}_{1BNO-O}$ and ${A^{Bu}}_{1BNO-O}$ adducts. For both the complexes 1BNO-O and 2BNO-O, the 1,4-trans and 1,4-cis insertions into the La-alkyl bond are thermodynamically favourable processes, displaying enthalpy energies of -42.4 and -43.1 kcal.mol$^{-1}$ for the ${B^{Bu,cis}}_{1BNO-O}$ and ${B^{Bu,cis}}_{2BNO-O}$ products and -40.2 and -41.5 kcal.mol$^{-1}$ for the ${B^{Bu,trans}}_{1BNO-O}$ and ${B^{Bu,trans}}_{2BNO-O}$ products,

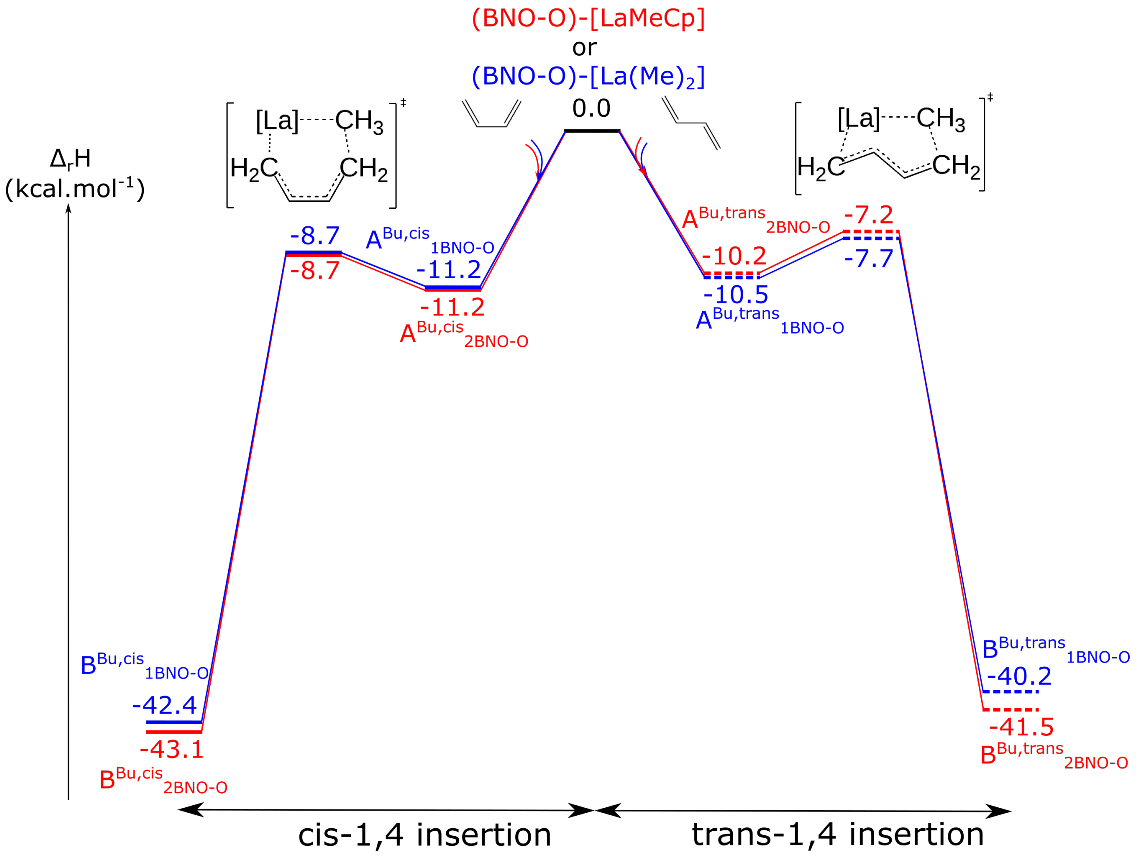

Figure 102: Enthalpy profile for the first monomer insertion of the 1,3-butadiene homopolymerisation reaction mediated by (BNO-O)-[La($CH_3$)$_2$] (1BNO-O) and (BNO-O)-[La(Cp)($CH_3$)] (2BNO-O).

respectively, with respect to the entrance channel. The strong exothermicity of these reactions is likely due to the formation of allylic groups which are considerably more stable than the alkyl products formed by ethylene insertion into the same La-alkyl bond. The activation barriers for the 1,4-cis and the 1,4-trans insertion are both accessible and they are located at 2.5 and 2.8 kcal.mol$^{-1}$ for the 1BNO-O system and 2.5 and 3.0 kcal.mol$^{-1}$ for the 2BNO-O system, respectively. In the 1BNO-O-grafted La system, interestingly, while the 1,4-cis and 1,4-trans insertion cannot be differentiated kinetically, the thermodynamics of the reaction is slightly more favourable for the 1,4-cis insertion by 2.2 kcal.mol$^{-1}$. This seems different for the 2BNO-O-grafted La system for which the 1,4-cis and the 1,4-trans insertions are equivalent from a kinetic and thermodynamic point of view (energy difference of 1.6 kcal.mol$^{-1}$ between products $B^{Bu,cis}{}_{2BNO-O}$ and $B^{Bu,trans}{}_{2BNO-O}$). Due to the small energy difference between the 1,4-cis and the 1,4-trans insertion products for both the 1BNO-O and 2BNO-O systems, in the following section, we will described the second 1,3-butadiene insertion starting from the $B^{Bu,cis}$ and the $B^{Bu,trans}$ complexes.

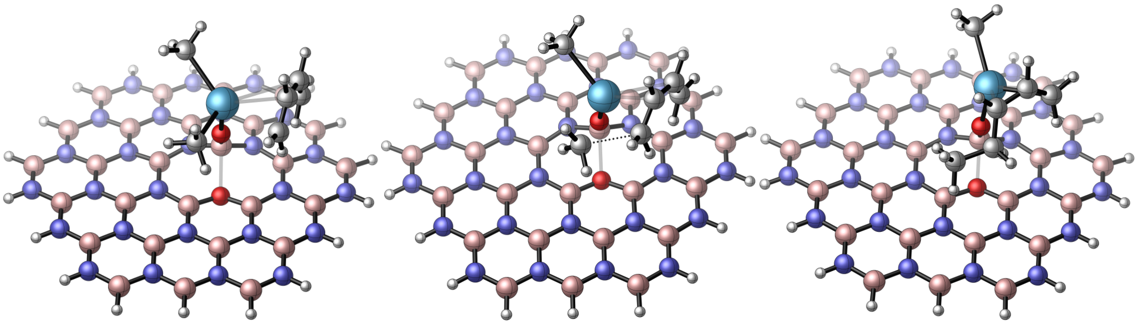

(a) $\mathrm{A}^{Bu,cis}{}_{1BNO-O}$ (b) $\text{TS-AB}^{Bu,cis}{}_{1BNO-O}$ (c) $\mathrm{B}^{Bu,cis}{}_{1BNO-O}$

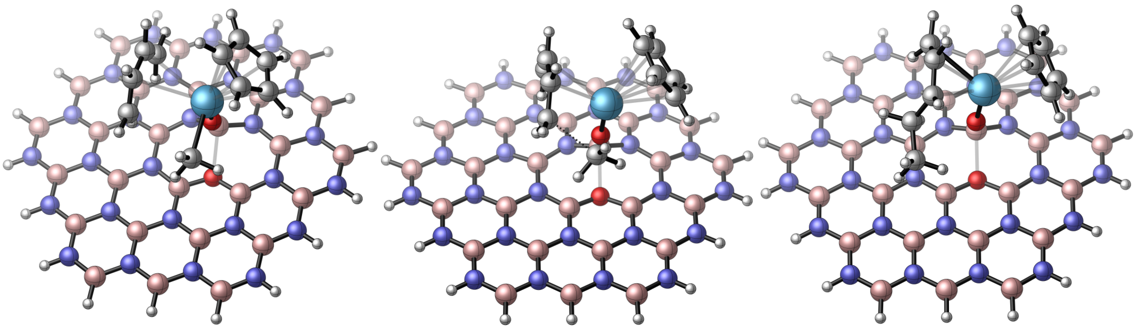

(d) $\mathrm{A}^{Bu,cis}{}_{2BNO-O}$ (e) $\text{TS-AB}^{Bu,cis}{}_{2BNO-O}$ (f) $\mathrm{B}^{Bu,cis}{}_{2BNO-O}$

Figure 103: Optimised structures of the complexes involved in the first 1,4-cis butadiene insertion mediated by (BNO-O)-[La($CH_3$)$_2$] (1BNO-O) and (BNO-O)-[La(Cp)($CH_3$)] (2BNO-O).

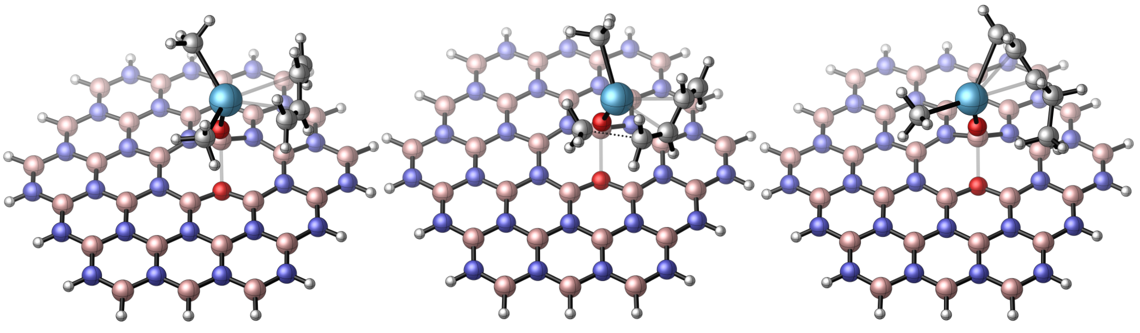

(a) $\mathrm{A}^{Bu,trans}{}_{1BNO-O}$ (b) $\text{TS-AB}^{Bu,trans}{}_{1BNO-O}$ (c) $\mathrm{B}^{Bu,trans}{}_{1BNO-O}$

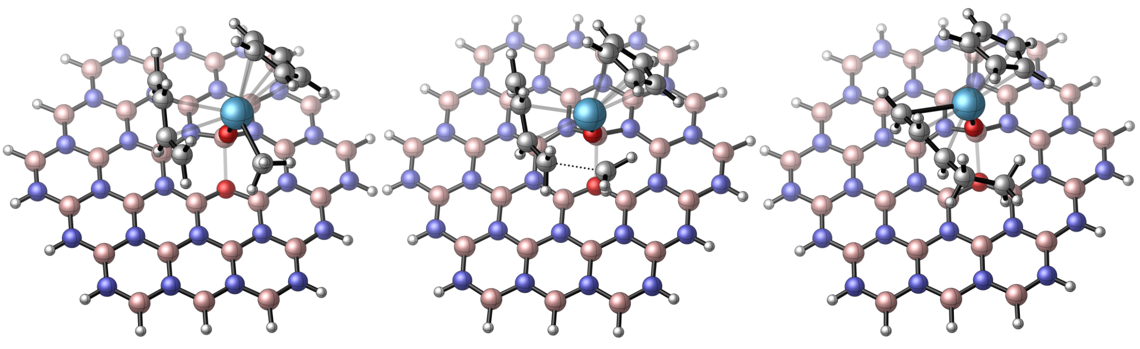

(d) $\mathrm{A}^{Bu,trans}{}_{2BNO-O}$ (e) $\text{TS-AB}^{Bu,trans}{}_{2BNO-O}$ (f) $\mathrm{B}^{Bu,trans}{}_{2BNO-O}$

Figure 104: Optimised structures of the complexes involved in the first 1,4-trans butadiene insertion mediated by (BNO-O)-[La($CH_3$)$_2$] (1BNO-O) and (BNO-O)-[La(Cp)($CH_3$)] (2BNO-O).

The propagation step and the stereoselectivity outcome of the reaction have been also investigated. All the possible sequences, *i.e.*, cis-cis, cis-trans, trans-cis and trans-trans, have been computed (see Table 16). In the following discussion, for sake of clarity, we will first describe the second 1,3-butadiene insertion starting from the $B^{Bu,cis}$ adducts of the ${B^{Bu,cis}}_{1BNO-O}$ and the ${B^{Bu,cis}}_{2BNO-O}$ complexes. Figure 105 shows the enthalpy profiles of the second 1,4-cis and 1,4-trans 1,3-butadiene insertion, starting from the ${B^{Bu,cis}}_{1BNO-O}$ and ${B^{Bu,cis}}_{2BNO-O}$ compounds. A view of the different transition states and intermediates is available in figures 106 and 107. The propagation step begins with the formation of an exothermic adduct, corresponding to species ${C^{Bu,cis,cis}}_{1BNO-O}$, ${C^{Bu,cis,trans}}_{1BNO-O}$ (-52.2 and -53.7 kcal.mol$^{-1}$) and ${C^{Bu,cis,cis}}_{2BNO-O}$, ${C^{Bu,cis,trans}}_{2BNO-O}$ (-48.2 and -47.5 kcal.mol$^{-1}$). The ${C^{Bu}}_{1BNO-O}$ La compounds are more stable than the ${C^{Bu}}_{2BNO-O}$ analogues by 4.0 and 6.2 kcal.mol$^{-1}$ for the cis and trans insertions respectively. Interestingly, the formation of all the insertion products is exothermic (-72.0 and -71.7 kcal.mol$^{-1}$ for ${D^{Bu,cis,cis}}_{1BNO-O}$ and ${D^{Bu,cis,trans}}_{1BNO-O}$ and -71.1 and -68.1 kcal.mol$^{-1}$ for ${D^{Bu,cis,cis}}_{2BNO-O}$ and ${D^{Bu,cis,trans}}_{2BNO-O}$, respectively) but while for the 2BNO-O La complex, the 1,4-cis insertion product is more stable by 3.0 kcal.mol$^{-1}$ than the 1,4-trans insertion analogue, for the 1BNO-O La complexes the 1,4-cis and 1,4-trans insertion products are energetically equivalent (enthalpy difference of 0.3 kcal.mol$^{-1}$). From a kinetic point of view, although all the insertion processes are accessible, the 1,4-cis insertion barrier is significantly lower than the 1,4-trans insertion by 4.2 and 5.0 kcal.mol$^{-1}$ for both the 1BNO-O and 2BNO-O systems, respectively.

Since for both the 1BNO-O and the 2BNO-O system, the 1,4-cis and 1,4-trans 1,3-butadiene insertion products are very close thermodynamically, we completed our study by computing the enthalpy profile of the second 1,3-butadiene insertion, starting this time from the ${B^{Bu,trans}}_{1BNO-O}$ and ${B^{Bu,trans}}_{2BNO-O}$ compounds (Figure 108). In the presence of the 1,4-cis and 1,4-trans 1,3-butadiene monomers, the formation of the corresponding $C^{Bu,trans,cis}$ and $C^{Bu,trans,trans}$ adducts is exothermic (-49.0 and -44.7 kcal.mol$^{-1}$ for $C^{Bu,trans,cis}$ and -47.4 and -46.0 kcal.mol$^{-1}$ for $C^{Bu,trans,trans}$, for the 1BNO-O and 2BNO-O systems, respectively). As shown in Figure 108, interestingly, in the 1BNO-O case the insertion barrier are similar (6.8 kcal.mol$^{-1}$ for the cis-1,4 insertion *vs.* 8.5 kcal.mol$^{-1}$ for the trans-1,4 insertion, with an enthalpy difference of 2.3 kcal.mol$^{-1}$) whereas the enthalpy of the 1,4-cis insertion product ${D^{Bu,trans,cis}}_{1BNO-O}$ (-69.1 kcal.mol$^{-1}$) is lower than that of the 1,4-trans insertion one (-66.4 kcal.mol$^{-1}$) by 2.7 kcal.mol$^{-1}$. In the 2BNO-O system, on the other hand, while the enthalpies of the 1,4-cis and 1,4-trans insertion products, ${D^{Bu,trans,cis}}_{2BNO-O}$ and ${D^{Bu,trans,trans}}_{2BNO-O}$, are identical (-65.6 kcal.mol$^{-1}$), the 1,4-cis insertion barrier (5.5 kcal.mol$^{-1}$) is significantly lower than the 1,4-trans one (14.2 kcal.mol$^{-1}$). According to these profiles, therefore, both the 1BNO-O and 2BNO-O La systems are likely to polymerize the 1,3 butadiene efficiently, providing in a stereoselective way the 1,4-cis-polybutadiene polymer.

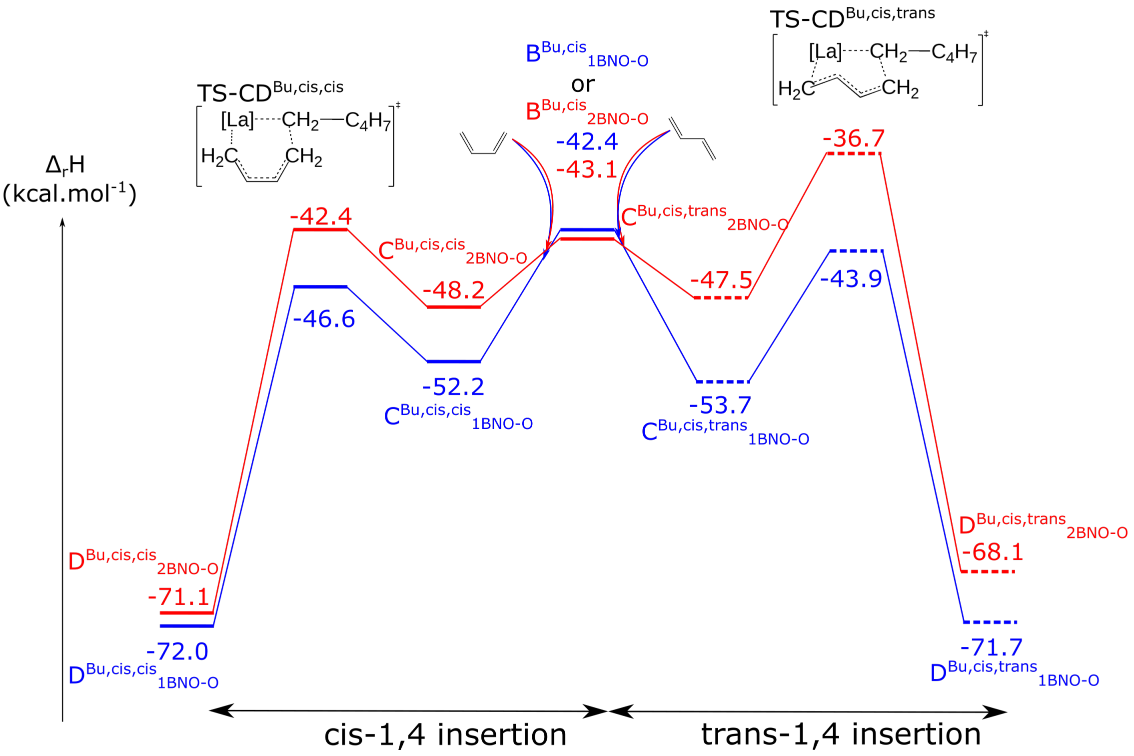

Figure 105: Enthalpy profiles for the second monomer insertion of the 1,3-butadiene homopolymerisation reaction mediated by the $B^{Bu,cis}{}_{1BNO-O}$ and $B^{Bu,cis}{}_{2BNO-O}$ compounds.

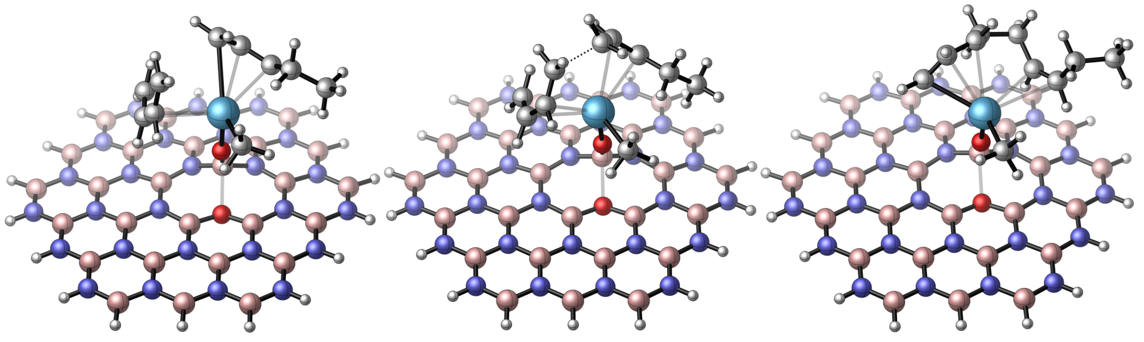

(a) $C^{Bu,cis,cis}{}_{1BNO-O}$ (b) TS-CD$^{Bu,cis,cis}{}_{1BNO-O}$ (c) $D^{Bu,cis,cis}{}_{1BNO-O}$

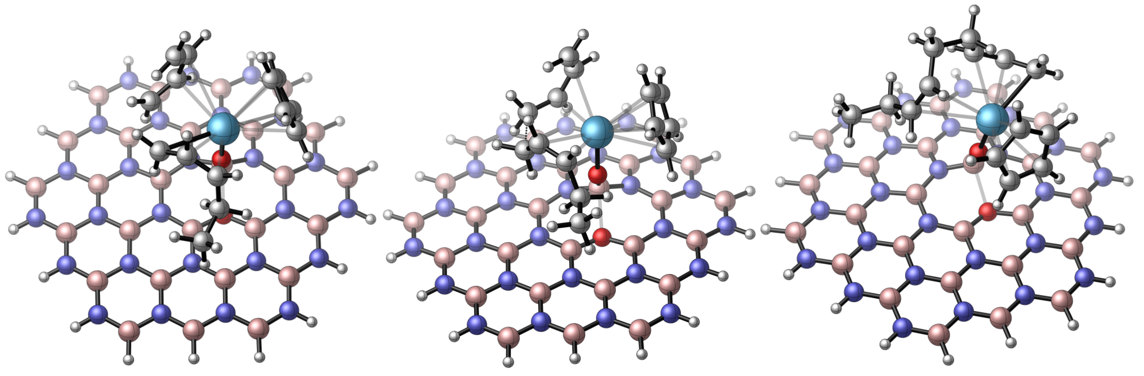

(d) $C^{Bu,cis,cis}{}_{2BNO-O}$ (e) TS-CD$^{Bu,cis,cis}{}_{2BNO-O}$ (f) $D^{Bu,cis,cis}{}_{2BNO-O}$

Figure 106: Optimised structures of the complexes involved in the second 1,4-cis butadiene insertion mediated by the $B^{Bu,cis}{}_{1BNO-O}$ and $B^{Bu,cis}{}_{2BNO-O}$ compounds.

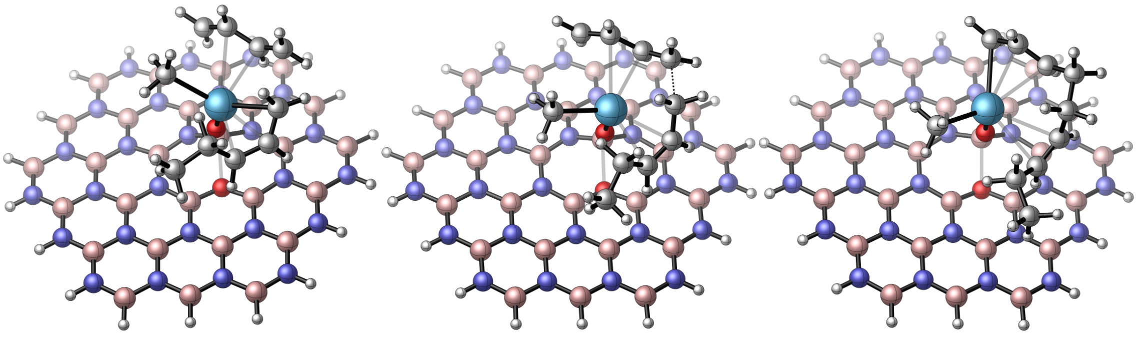

(a) $C^{Bu,cis,trans}{}_{1BNO-O}$ (b) TS-$CD^{Bu,cis,trans}{}_{1BNO-O}$ (c) $D^{Bu,cis,trans}{}_{1BNO-O}$

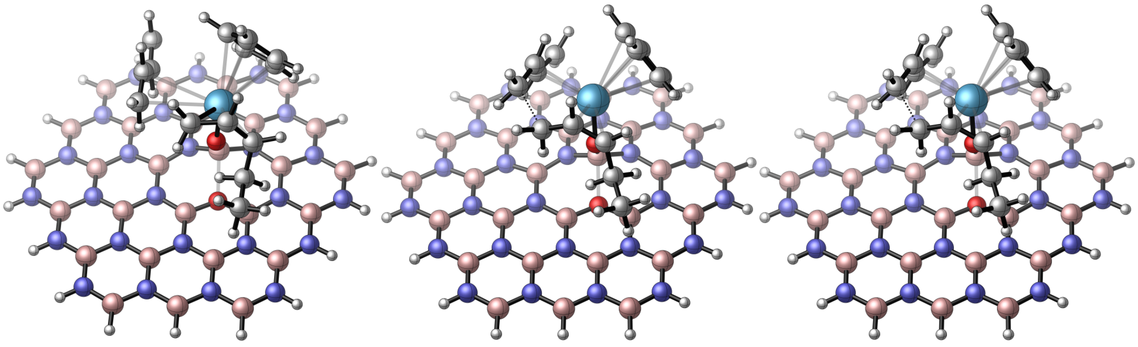

(d) $C^{Bu,cis,trans}{}_{2BNO-O}$ (e) TS-$CD^{Bu,cis,trans}{}_{2BNO-O}$ (f) $D^{Bu,cis,trans}{}_{2BNO-O}$

Figure 107: Optimised structures of the complexes involved in the second 1,4-trans butadiene insertion mediated by the $B^{Bu,cis}{}_{1BNO-O}$ and $B^{Bu,cis}{}_{2BNO-O}$ compounds.

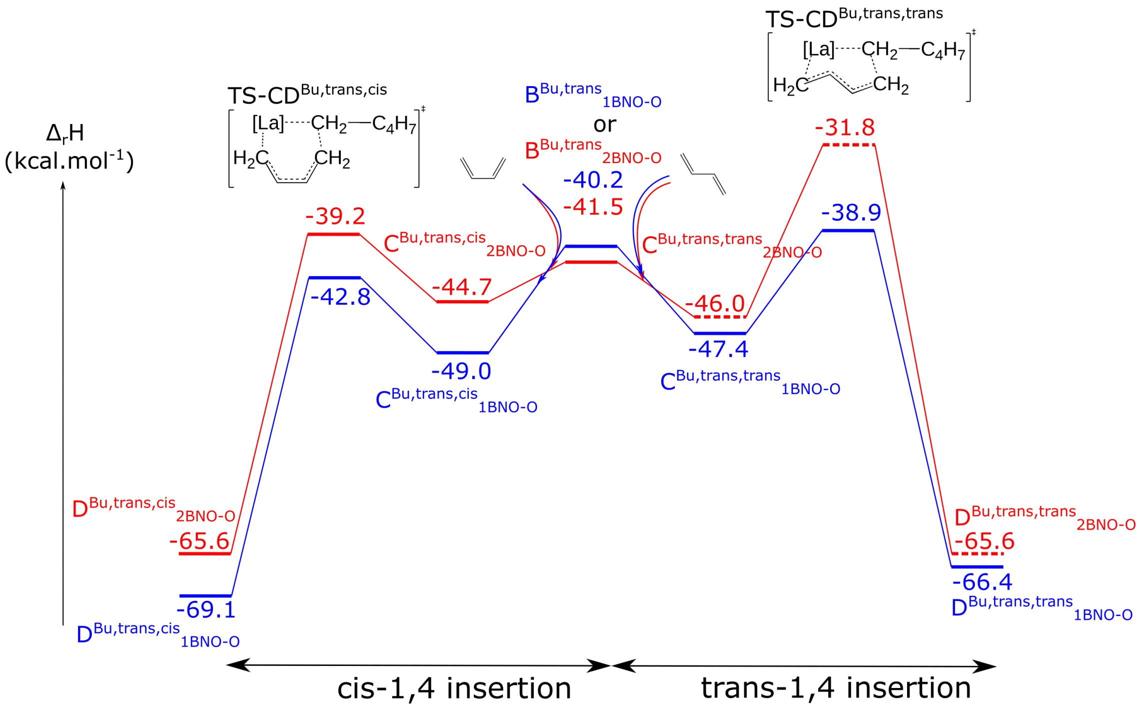

Figure 108: Enthalpy profile for the second monomer insertion, of the 1,3-butadiene homopolymerisation reaction mediated by the $B^{Bu,trans}{}_{1BNO-O}$ and $B^{Bu,trans}{}_{2BNO-O}$ compound.

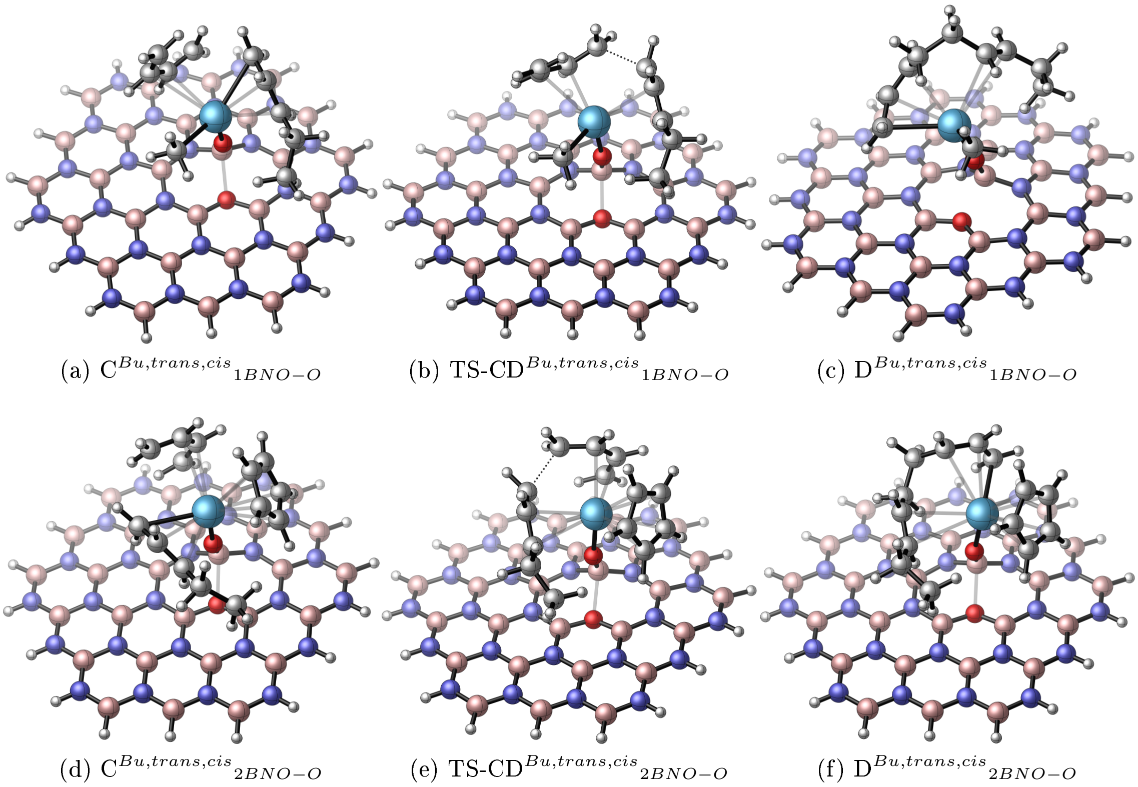

(a) $C^{Bu,trans,cis}{}_{1BNO-O}$ (b) TS-$CD^{Bu,trans,cis}{}_{1BNO-O}$ (c) $D^{Bu,trans,cis}{}_{1BNO-O}$

(d) $C^{Bu,trans,cis}{}_{2BNO-O}$ (e) TS-$CD^{Bu,trans,cis}{}_{2BNO-O}$ (f) $D^{Bu,trans,cis}{}_{2BNO-O}$

Figure 109: Optimised structures of the complexes involved in the second 1,4-cis butadiene insertion mediated by the $B^{Bu,trans}{}_{1BNO-O}$ and $B^{Bu,trans}{}_{2BNO-O}$ compounds.

#### 6.4.2.2 Comparison with the molecular, the silica-grafted and the graphene-grafted La systems

As discussed above, the silica-supported La systems afford predominantly the 1,4-cis-polybutadiene polymer. A theoretical study on the silica-supported La systems further supported this result, showing that the 1,4-cis-polybutadiene compound corresponds to the kinetic product. Concerning the graphene-supported La systems, on the other hand, we showed that while the (gOO)-[La($CH_3$)$_2$] system would preferentially form the 1,4-cis-polybutadiene, the (gO)-[La($CH_3$)$_2$] system would preferentially afford a random 1,4-polybutadiene. This difference between the gO and gOO models has been ascribed to the higher flexibility of the La coordination mode on the gO model compared to the gOO one. In the gO model, indeed, the ability of the lanthanum atom to modulate both the electronic assistance of the surface and the steric hindrance of its coordination sphere, would make the cis-cis and the cis-trans insertions energetically comparable. In the case of the BNO-O- supported systems, finally, the study of the first two insertions indicates the preferential formation of the 1,4-cis-polybutadiene polymer for both the 1BNO-O and 2BNO-O compounds. The rate determining step of both systems corresponds to the second 1,3-butadiene insertion in the cis-cis sequences, with a barrier height of 5.6 and 5.8 kcal.mol$^{-1}$ for 1BNO-O and 2BNO-O, respectively. Interestingly, the enthalpy profile

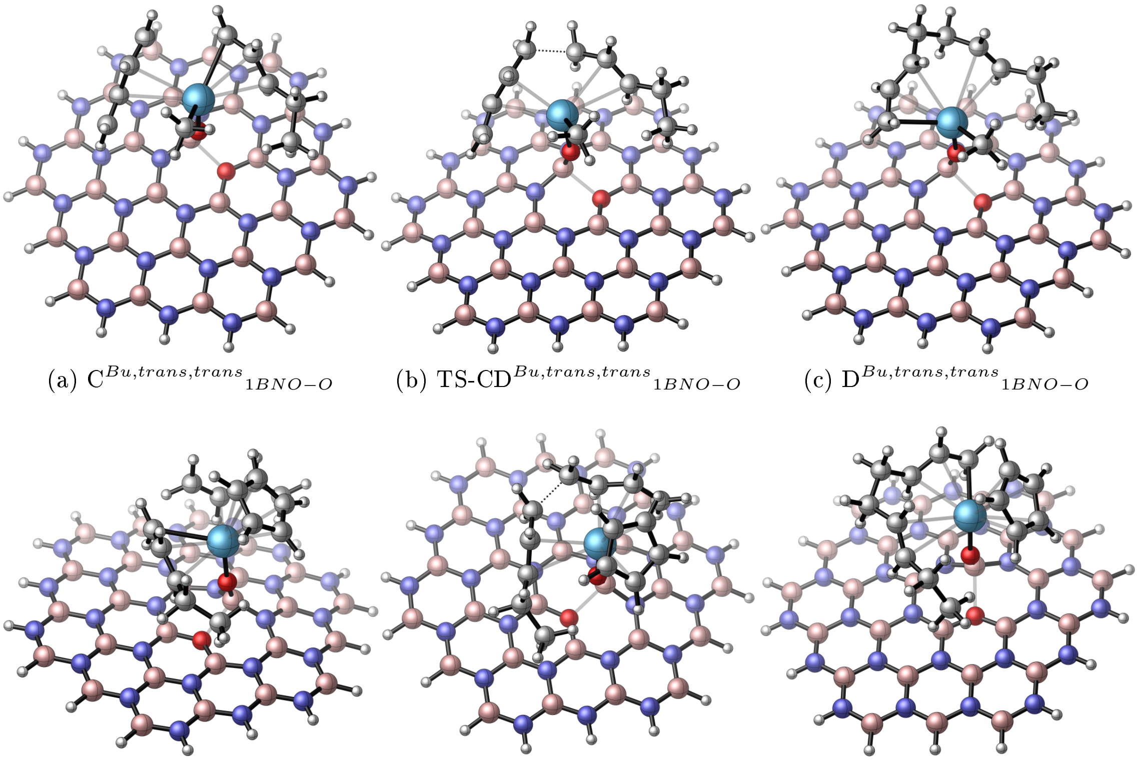

(a) $\mathrm{C}^{Bu,trans,trans}{}_{1BNO-O}$ (b) $\mathrm{TS\text{-}CD}^{Bu,trans,trans}{}_{1BNO-O}$ (c) $\mathrm{D}^{Bu,trans,trans}{}_{1BNO-O}$

(d) $\mathrm{C}^{Bu,trans,trans}{}_{2BNO-O}$ (e) $\mathrm{TS\text{-}CD}^{Bu,trans,trans}{}_{2BNO-O}$ (f) $\mathrm{D}^{Bu,trans,trans}{}_{2BNO-O}$

Figure 110: Optimised structures of the complexes involved in the second 1,4-trans butadiene insertion mediated by the $\mathrm{B}^{Bu,trans}{}_{1BNO-O}$ and $\mathrm{B}^{Bu,trans}{}_{2BNO-O}$ compounds.

Table 16: Enthalpy data (kcal.mol$^{-1}$) of the first propagation step of the 1,3-butadiene polymerisation mediated by (BN-O)-[La($CH_3$)$_2$] and (BN-O)-[La(Cp)($CH_3$)].

| (BNO-O)-[La($CH_3$)$_2$] (1) | $\Delta_r$H | (BNO-O)-[La($CH_3$)(Cp)] (2) | $\Delta_r$H |
|---|---|---|---|
| $\mathrm{C}^{Bu,cis,cis}{}_{1BNO-O}$ | -52.2 | $\mathrm{C}^{Bu,cis,cis}{}_{2BNO-O}$ | -48.2 |
| $\mathrm{TS\text{-}CD}^{Bu,cis,cis}{}_{1BNO-O}$ | -46.6 | $\mathrm{TS\text{-}CD}^{Bu,cis,cis}{}_{2BNO-O}$ | -42.4 |
| $\mathrm{D}^{Bu,cis,cis}{}_{1BNO-O}$ | -72.0 | $\mathrm{D}^{Bu,cis,cis}{}_{2BNO-O}$ | -71.1 |
| $\mathrm{C}^{Bu,cis,trans}{}_{1BNO-O}$ | -53.7 | $\mathrm{C}^{Bu,cis,trans}{}_{2BNO-O}$ | -47.5 |
| $\mathrm{TS\text{-}CD}^{Bu,cis,trans}{}_{1BNO-O}$ | -43.9 | $\mathrm{TS\text{-}CD}^{Bu,cis,trans}{}_{2BNO-O}$ | -36.7 |
| $\mathrm{D}^{Bu,cis,trans}{}_{1BNO-O}$ | -71.7 | $\mathrm{D}^{Bu,cis,trans}{}_{2BNO-O}$ | -66.6 |
| $\mathrm{C}^{Bu,trans,cis}{}_{1BNO-O}$ | -49.0 | $\mathrm{C}^{Bu,trans,cis}{}_{2BNO-O}$ | -44.7 |
| $\mathrm{TS\text{-}CD}^{Bu,trans,cis}{}_{1BNO-O}$ | -42.8 | $\mathrm{TS\text{-}CD}^{Bu,trans,cis}{}_{2BNO-O}$ | -39.2 |
| $\mathrm{D}^{Bu,trans,cis}{}_{1BNO-O}$ | -69.1 | $\mathrm{D}^{Bu,trans,cis}{}_{2BNO-O}$ | -65.6 |
| $\mathrm{C}^{Bu,trans,trans}{}_{1BNO-O}$ | -47.4 | $\mathrm{C}^{Bu,trans,trans}{}_{2BNO-O}$ | -46.0 |
| $\mathrm{TS\text{-}CD}^{Bu,trans,trans}{}_{1BNO-O}$ | -38.9 | $\mathrm{TS\text{-}CD}^{Bu,trans,trans}{}_{2BNO-O}$ | -31.8 |
| $\mathrm{D}^{Bu,trans,trans}{}_{1BNO-O}$ | -66.4 | $\mathrm{D}^{Bu,trans,trans}{}_{2BNO-O}$ | -65.6 |

computed for the formation of the 1,4-cis-polybutadiene product in the presence of the 1BNO-O and 2BNO-O catalysts is thermodynamically and kinetically comparable to that obtained with the graphene-grafted (gOO)-[La($CH_3$)$_2$] system, which shows a barrier height of 6.6 kcal.mol$^{-1}$ and a 1,4-cis-polybutadiene product at -71.0 kcal.mol$^{-1}$. This suggests a similar catalatic activity for the 1BNO-O, the 2BNO-O and the (gOO)-[La($CH_3$)$_2$] complexes.

# 7 Conclusion

In this chapter we have shown that the grafting of the [La(N($SiMe_3$)$_2$)$_3$] complex on the hydroxy-functionalised BN surface (BNH-OH) leads to the exchange of an amido N(SiMe)$_3$ ligand by a hydroxo ligand, with the release of the [La(N($SiMe_3$)$_2$)$_2$(OH)(HN($SiMe_3$)$_2$)] compound and the recovery of the unfunctionalised aromatic h-BN surface. We have then shown a second BN surface containing a vacancy defect, *i.e.*, a B-O-B and $N_2$-B(OH) functional groups. The [La(N($SiMe_3$)$_2$)$_3$] compound can be easily grafted on this BNO-OH functionalised surface, affording a stable mono-grafted compound. Similarly to experimental approaches, the coordination of triphenylphosphinoxide (O=$PPh_3$) has been computed as a probe of the Lewis acidity of the metal. The spectroscopic values (IR and NMR) obtained for the corresponding (BNO-O)-[La(N($SiMe_3$)$_2$)$_2$(O=$PPh_3$)] species indicate that the Lewis acidity of the BNO-O-grafted complex is very similar to that of the gOO-grafted analogue. The influence of the surface on the Lewis acidity of the metal centre, therefore, is likely to follow the order: gO $>$ gOO $\cong$ BNO-O $>$ silica.

In order to understand the role of the support, we then investigated the catalytic activity of BNO-OH supported La compounds toward both the homopolymerisation of ethylene and 1,3-butadiene, by using the alkyl (BNO-O)-[La($CH_3$)$_2$] (1BNO-O) and (gOO)-[LaCp$CH_3$] (2BNO-O) complexes as the active species. Both compounds efficiently catalyse the ethylene homopolymerisation reaction, displaying activation barriers which lie between those of the graphene-grafted and silica-grafted compounds. The BNO-OH surfaces are therefore predicted to play an important role, increasing the Lewis acidity and therefore the reactivity of the grafted La systems, like the graphene surfaces. Concerning the 1,3-butadiene homopolymerisation reaction, on the other hand, both species are likely to behave as efficient catalytic species, displaying like the graphene-supported species, a higher activity than the silica grafted La analogues. In both the 1BNO-O and the 2BNO-O models, interestingly, the 1,4-cis 1,3-butadiene insertion is preferred over the 1,4-trans one, affording preferentially a 1,4-cis-polybutadiene polymer, as previously reported for the silica-supported La compounds. In conclusion, therefore, the functionalised BNO-OH surfaces constitute efficient supports for lanthanide organometallic compounds. These BNO-OH surfaces are likely to enhance the Lewis acidity of the La metal, playing therefore an active role in the catalytic activity of the supported La complexes. The BNO-O supported La alkyl compounds, finally, efficiently catalyse the ethylene and 1,3-butadiene homopolymerisation reaction, with activities and stereoselectivities similar to those found for the graphene grafted gOO complex.

## Part V

# Propene polymerisation

## 1 Introduction

As mentioned in the paragraph 1.4.2 homogeneous rare-earth complexes display a low activity in propylene polymerisation, the deactivation of the catalyst and the control of the stereoselectivity still representing a difficult issues. From a theoretical point of view, moreover, very few reports concerning the use of lanthanide complexes as propylene polymerisation catalysts have been reported in the literature.[182, 430, 431] The propylene insertion is a complex process, involving, in principle, four different paths: i) the primary 1,2 insertion; ii) the secondary 2,1 insertion; iii) the allylic C-H activation and iv) the vinylic C-H activation (Figure 111). Propylene, moreover, is a prochiral olefin which may coordinate and insert into a La−C carbon bond *via* either the *re* or *si* enantioface, increasing considerably the complexity of the system.

In a DFT computational study on the catalytic hydrosilysation of propene in the presence of $SiH_4$, Eisenstein, Maron and coworkers[431, 430] showed that the insertion of propene on either the [$Cp_2SmH$] or [$Cp_2SmSiH_3$] complex is less kinetically and thermodynamically favoured than the allylic activation process. The predominance of the allylic H transfer reaction leads therefore to the deactivation of the catalysts, with the formation, in agreement with the experiments, of a very stable $\pi$-allylic complex.

In order to study the catalytic activity of different lanthanum complexes supported on a silica surface dehydroxylated either at 200 °C ($SiO_{2-200}$) or at 700 °C ($SiO2-700$), Del Rosal, Maron and coworkers [182] described from a theoretical point of view the formation of three silica grafted La compounds: a (≡Si-O)-[$LaMe_2$] compound, monografted on a silica surface dehydroxylated at 700 °C, a bigrafted (=$SiO_2$)-[La(Me)] compound, obtained after breaking a Si-O-Si bridge on a silica surface dehydroxylated at 700 °C and finally a (=$SiO_2$)-[La(Me)($NH_3$)] compound, bigrafted on a silica surface dehydroxylated at 200 °C (Figure 112). In the presence of the three catalysts, the allylic activation leads to the more thermodynamically stable products, displaying a $\eta^3$ allylic complex. From a kinetic point of view, while for the (≡Si-O)-[$LaMe_2$] and (=$SiO_2$)-[La(Me)] compounds, monografted and bigrafted respectively on a silica surface dehydroxylated at 700 °C, the activation barrier of the allylic C-H bond activation is comparable to that of the 1,2-insertion reaction, for the (=$SiO_2$)-[La(Me)($NH_3$)] compound, bigrafted on a silica surface dehydroxylated at 200 °C, on the other hand, the activation barrier of the allylic C-H bond activation is higher than that found for the 1,2-insertion. Thus, the first two compounds are likely to behave as poor catalysts for the homopolymerisation of propene as a consequence of their deactivation by the allylic C-H bond activation. However, the third compound is expected to polymerise the propene monomer. The particular grafting mode of the (=$SiO_2$)-[La(Me)($NH_3$)] compound, indeed, leads the La metal to partially insert into the silica surface, increasing the steric hindrance around the metal. The active site is therefore less accessible, inducing a decrease of the allyl-metal interaction strengh and, consequently, a destabilisation of the corresponding transition state.

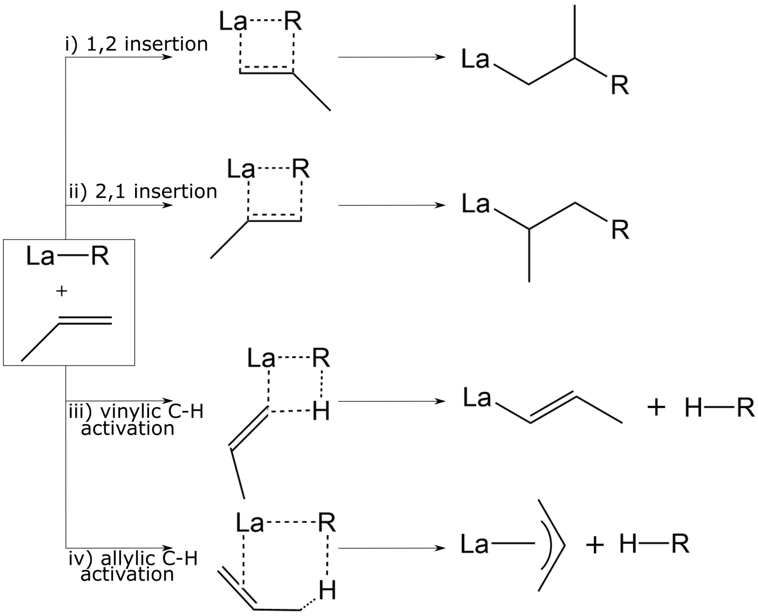

Figure 111: Elementary steps explored in the homopolymerisation of propene mediated by lanthanide-grafted complexes.

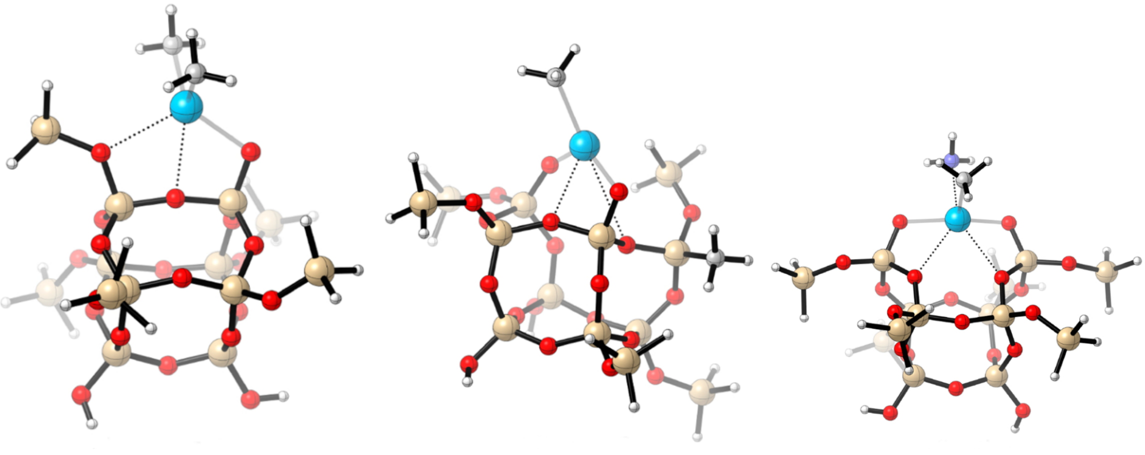

(a) (≡Si-O)-[LaMe$_2$] (b) (=SiO$_2$)-[La(Me)] (c) (=SiO$_2$)-[La(Me)(NH$_3$)]

Figure 112: Optimised structures of the La complexes monografted (a) and bigrafted (b) on a silica surface dehydroxylated at 700 °C and bigrafted (c) on a silica surface dehydroxylated at 200 °C, for the study of the propylene polymerisation.

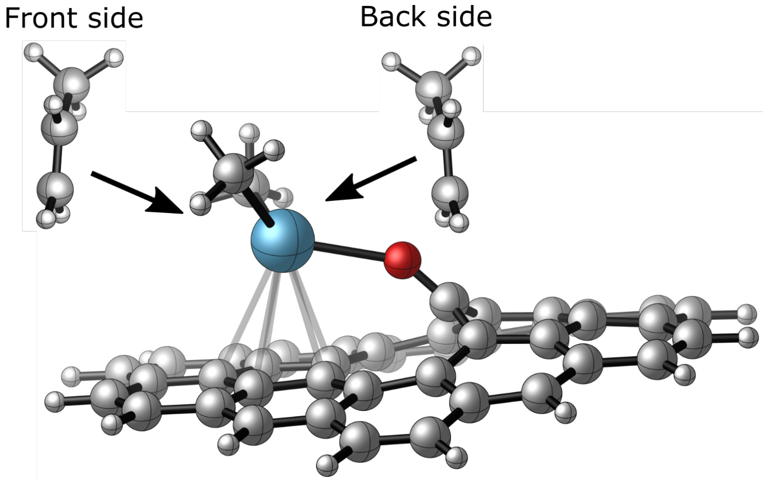

Figure 113: Schematic representation of the ‘front side’ and ’back side’ propene insertions approaches.

Based on this work we wondered whether the replacement of the silica surface by the gO graphene support might have an influence in the catalytic activity of the corresponding lanthanum-grafted complexes toward the propylene homopolymerisation reaction. As shwon in chapter 3, indeed, the (gO)-[La($CH_3$)$_2$] (1gO) compound displays a strong interaction between the metal centre and the graphene surface, which might disfavour the allylic activation, by increasing the steric hindrance around the metal and thus by limiting the $\eta^3$ approach of propene. We therefore computed the initiation and first propagation steps of the homopolymerisation of propene by using the (gO)-[La($CH_3$)$_2$] (1gO) as the active catalyst. As shown in figure 113, two possible approaching ways have to be considered for propene. Taking as a reference the metal-grahene interaction, indeed, the propene monomer can reach the metal centre either from the same side or from the opposite side of the metal-graphene interaction. When the propene will be inserted on the same side, we will named it ‘front side’ insertion, and when the propene will be inserted in the opposite side, we will named it ’back side’ insertion respectively.

## 2 Propene polymerisation catalysed by the (gO)-[La($CH_3$)$_2$] (1gO) compound

Based on the promising results obtained with grahene-grafted lanthanum complexes on the ethylene, butadiene and styrene polymerisation, we realised that graphene may represent a suitable metal support in the propene homopolymerisation reaction. The graphene surface may indeed play two important functions: while it increases the Lewis acidity of the metal enhancing the reactivity of the corresponding graphene grafted La catalyst, it also increases the steric hindrance around the metal, destabilising the system in the polymerisation steps that are the most sterically encumbered such as the $\pi$-allylic H transfer reaction. Figure 114 shows the geometries of the optimised transition states of the 1,2 insertion and C-H allylic activation reactions. By

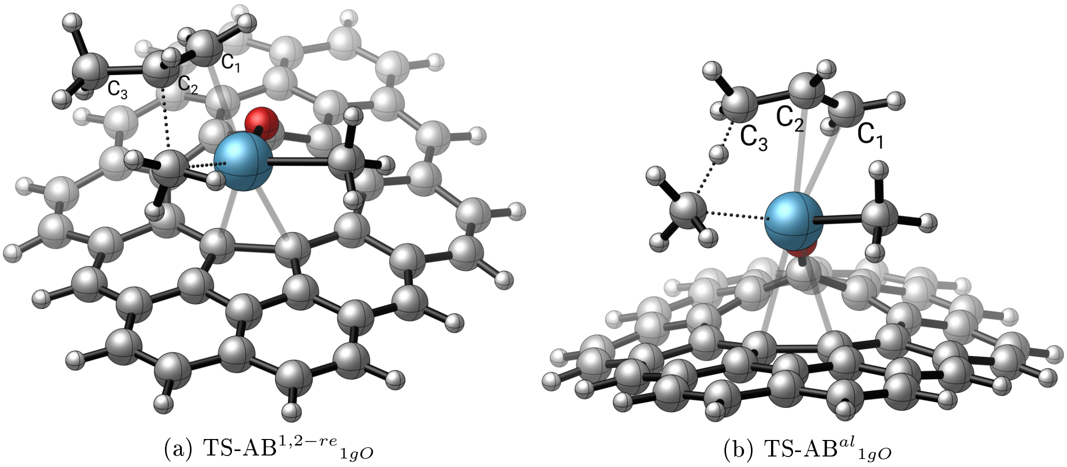

(a) TS-AB$^{1,2-re}{}_{1gO}$ (b) TS-AB$^{al}{}_{1gO}$

Figure 114: Examples of a) the 1,2-insertion mode and b) the allylic insertion mediated by (gO)-[La($CH_3$)$_2$].

comparing the two geometries, we can notice that while in the 1,2-insertion the propene interacts with the metal through only two carbons (Figure 114 a), in the allylic hydrogen transfer, on the other hand, the propene must approach the metal with all three carbons in order to transfer its hydrogen to the La-bound methyl group (Figure 114 b). This is evidenced by the distances observed on the two transition states: La-$C_1$ = 2.561 $\mathring{A}$, La-$C_2$ = 2.918 $\mathring{A}$, La-$C_3$ = 3.858 $\mathring{A}$ for TS-AB$^{1,2-re}{}_{1gO}$, whereas La-$C_1$ = 2.895 $\mathring{A}$, La-$C_2$ = 2.814 $\mathring{A}$, La-$C_3$ = 2.755 $\mathring{A}$ for TS-AB$^{al}{}_{1gO}$.

## 2.1 Reaction profiles of the 1st and 2nd insertions.

In this chapter three catalysts will be used for the polymerisation of propene. The first one will be the (gO)-[La($CH_3$)$_2$] complex (1gO) obtained, as shown in chapter 3, by replacing both hexamethyldisilylamido groups by two methyl functions in the presence of an alkylating agent, such as the TIBA. As shown in figure 115, the (gO)-[La($CH_3$)$_2$] complex displays a monografted monocoordination mode, with the La metal interacting with the two methyl groups (La-C = 2.459 $\mathring{A}$, La-C = 2.441 $\mathring{A}$), with the surface oxygen atom (La-O = 2.410 $\mathring{A}$) and additionally with the pentagonal underlying graphene cycle. The presence of this interaction has been confirmed by the short La-$C_{graphene}$ distances and by a second-order NBO analysis, which reveals a strong donation of 51.8 kcal.mol$^{-1}$ from the C=C bonds of the underlying pentagonal graphene cycle to an empty d orbital of the La metal.

The enthalpy reaction profiles for the initiation step of the homopolymerisation of propene mediated by the gO-[La($CH_3$)$_2$] complex (1gO) are depicted in figures 116 and 117, for the front side and the back side approach of the propene monomer to the La centre, respectively. A view of the different transition states and intermediates is available in Figures from 118 to 123. Concerning the insertion reactions, in all cases, the reaction begins by the formation of an exothermic $\pi$ adduct in which the propene is coordinated either with the *si* or the *re* enantioface to the metal centre. It is worth noting that a stability difference is observed between 'front side'

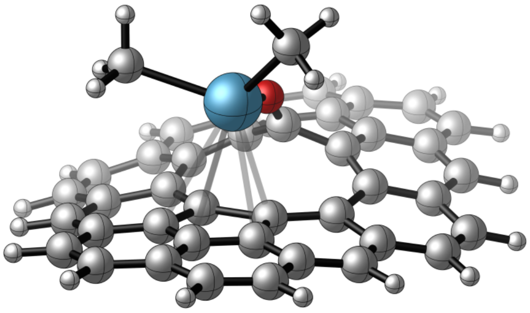

Figure 115: Structures of the grafted (gO)-[La($CH_3$)$_2$] complex (1gO).

and 'back side' insertion mode. While in the front side insertion, the propene approaches on the side of the La-graphene surface interaction, forcing the metal to slightly raise from the surface and to reduce the metal surface interaction, in the back side insertion, on the other hand, the propene approaches on the opposite side of the La-graphene surface interaction, without altering the metal surface interaction. As shown in Figures 118a and 121a, indeed, while in the front side approach, the distances between the metal and the pentagonal underlying graphene cycle in the $A_{1gO}$ adducts lie in the range 3.046-3.475 $\AA$, in the back side approach, on the other hand, they lie in the range 2.990-3.159 $\AA$. For the rest, the geometry of the initial complex is poorly affected by the coordination of propene to the metal centre. The La-$CH_3$ bond is not elongated and the C-C double bond of the coordinated propene is the same as in the free propene (1.343 $\AA$ for $A_{1gO}$ *vs.* 1.332 $\AA$ for the free propene) with both carbon atoms keeping their sp$^2$ hybridization.

In the profile of the front side approach, the insertion barrier height from the $A_{1gO}$ adduct is 7.9 kcal.mol$^{-1}$ for both the *re* and *si* 1,2 insertion and 10.0 and 11.9 kcal.mol$^{-1}$ for the 2,1 insertion in the *re* and *si* enantiofaces, respectively. Both reactions are exothermic, with the corresponding insertion products located at -21.6 and -21.7 kcal.mol$^{-1}$ for the *re* and *si* 1,2 insertion and -17.4 and -17.6 kcal.mol$^{-1}$ for the *re* and *si* 2,1 insertion, respectively. This indicates that for both the front side 1,2 and 2,1 insertion processes, the two *re* and *si* enantiofaces behave identically both thermodynamically and kinetically. The comparison between the 1,2 and 2,1 insertion reaction (respectively in blue and red in Figure 121) shows that, while from a kinetic point of view the enthalpy difference between the 1,2 and 2,1 insertion modes is not large enough to state the preferential formation of one over the other (enthalpy difference of 2.1 and 4.0 kcal.mol$^{-1}$ in favour of the 1,2 insertion for the *re* and *si* approach, respectively), from a thermodynamic point of view the 1,2 product is more stable than the 2,1 one by 4.2 and 4.1 kcal.mol$^{-1}$ for the *re* and *si* enantiofaces, respectively. The lower 1,2 insertion barrier can be ascribed to the higher steric repulsion between the methyl group and the graphene surface in the 2,1 insertion as well as to the lower stability of the secondary alkyl anion with respect to the primary one.[182] As shown in Figures 117 and 119 c) and f), the higher stability of the 1,2 insertion products is due to the formation of a stabilising $\beta$C-H···La-agostic interaction, with a H-La distance of 2.429 $\AA$. This is also confirmed by a second order perturbation NBO analysis, displaying a slight delocalisation of 55.8 kcal.mol$^{-1}$ of the C-H $\sigma$ bond to an empty d orbitals of the metal centre. Like in the front side approach, also in the back side approach, there is no preference for a specific enantioface for both the 1,2 and 2,1 insertion, neither thermodynamically nor kinetically. According to the profiles in figure 117 additionally, while the 1,2 and 2,1 insertion mechanisms do not differ kinetically (enthalpy difference of 2.2 and 1.4 kcal.mol$^{-1}$ in favour of the 1,2 insertion for the *re* and *si* enantiofaces), they differ thermodynamically, with the 1,2 insertion products resulting more stable than the 2,1 ones by 4.4 and 3.8 kcal.mol$^{-1}$ for the *re* and *si* enantiofaces, respectively. As shown in Figures 121 and 122 c) and f), the higher stability of the 1,2 insertion products is due, as for the front side approach, to the formation of a stabilising $\beta$C-H···La-agostic interaction, with a H-La distance of 2.496 $\AA$. Also here, the presence of the agostic interaction is confirmed by a second order perturbation NBO analysis, displaying a slight delocalisation of 48.3 kcal.mol$^{-1}$ of the C-H $\sigma$ bond to an empty d orbital of the metal centre. By comparing the front side and the back side insertion we observe no significant difference between the two profiles from both a kinetic and thermodynamic point of view. This similarity can be explained by the fact that, in both approaches, the low steric hindrance around the metal centre allows the growing chain polymer to form a strong $\beta$C-H agostic interaction with the lanthanum centre (H-La distance of 2.429 and 2.496 $\AA$ in the $\mathrm{D^{1,2}}_{2gO}$ front and back side approach, respectively). We subsequently investigated two common processes leading to the catalyst deactivation: (i) the vinylic C-H bond activation in which an H atom from the $CH_2$ group of the incoming propene is transferred to the coordinated alkyl group ($CH_3$), affording the corresponding vinyl complex with the concomitant release of a methane molecule and (ii) the allylic C-H bond activation in which a H atom from the $CH_3$ group of the incoming propene is transferred to the coordinated alkyl group ($CH_3$), affording the corresponding allylic complex with the concomitant release of a methane molecule. As for the insertion reactions, for the front side and the back side approach, these transfer reactions begin with the formation of an exothermic $\pi$ adduct located at -5.7 and -5.8 kcal.mol$^{-1}$ for the vinylic and allylic insertion, respectively, in the front side profile, and at -7.3 and -7.9 kcal.mol$^{-1}$ for the vinylic and allylic insertion, respectively, in the back side profile. The lower stability of the front side $\mathrm{A^{vyn}}_{1gO}$ and $\mathrm{A^{al}}_{1gO}$ is also here ascribed to the decrease of the metal surface interaction as a result of the propene approach from the surface side, as evidenced by the elongation of the C-La bonds in the 3.049-3.475 $\AA$ range for the front side insertion and in the 2.991-3.159 $\AA$ range for the back side insertion. From these adducts, while the vinylic transfer affords a slightly favourable product (-5.3 and -3.4 kcal.mol$^{-1}$ for the front side and the back side approach, respectively) through an activation barrier of 16.0 (front side) and 18.0 (back side) kcal.mol$^{-1}$, the allylic transfer, on the other hand, affords a more stable product (-24.0 and -24.1 kcal.mol$^{-1}$ for the front side and back side approaches, respectively), through a more accessible barrier of 9.2 (front side) and 11.6 (back side) kcal.mol$^{-1}$. Compared to the two insertion reactions and the allylic C-H bond activation, therefore, the vinylic C-H bond activation is not competitive exhibiting higher activation barriers and yielding less stable products. This is probably due to the high strength of the vinylic Csp$^2$-H bond which must be broken to allow the transfer of the vinyl proton to La the coordinated methyl group. The comparison between the allylic C-H bond activation and the 1,2 and 2,1 insertions reactions shows that while from a kinetic point of view the three processes are equivalent, with an activation barrier of 9.2 and 11.6 kcal.mol$^{-1}$ for the allylic C-H bond activation and in the range 7.9-11.9 kcal.mol$^{-1}$ for the two insertion reactions, from a thermodynamic point of view, on the other hand, the allylic products (-24.0 and -24.1 kcal.mol$^{-1}$ for the front side and back side insertion approach, respectively) are significantly more stable than those of the insertion reactions (in the range between -16.8 and -21.7 kcal.mol$^{-1}$). The high stability of the allylic

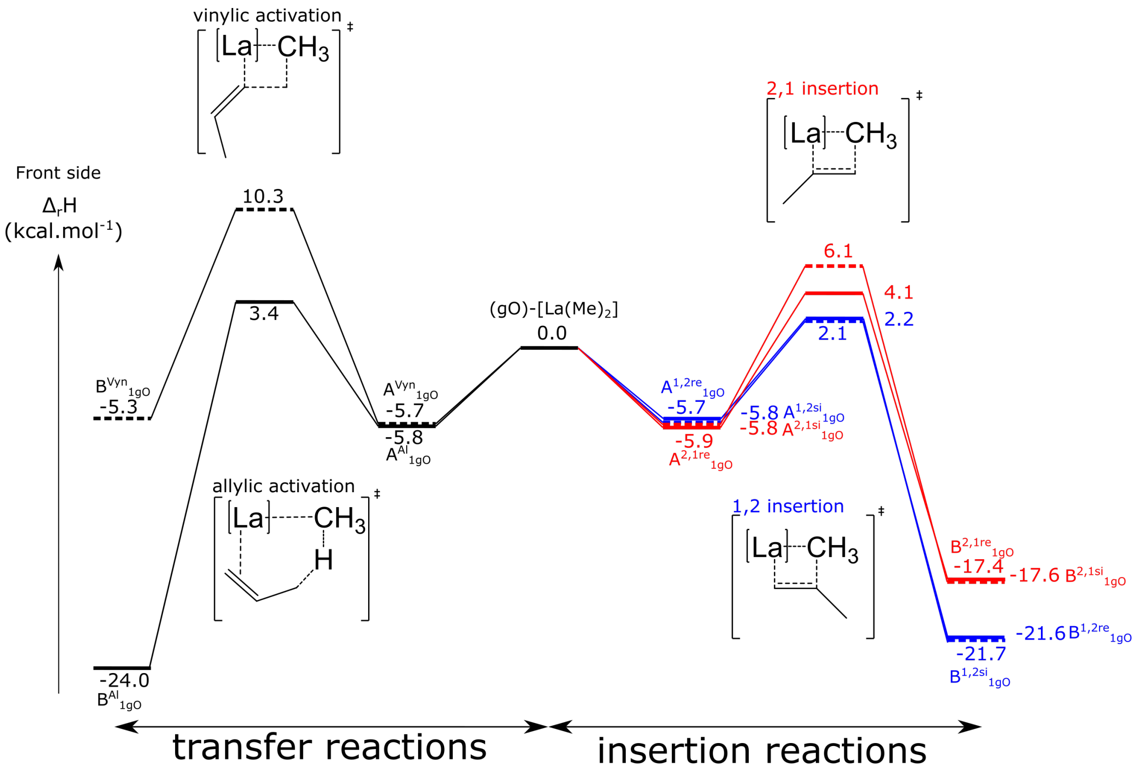

Figure 116: Calculated enthalpy profile for the first 1,2 and 2,1 front side propene insertion (on the right) and for the front side allylic and vinylic C-H activation (on the left) mediated by (gO)-[La(CH$_3$)$_2$] (1gO ).

deactivation products can be explained by the formation of a highly stable allylic interaction between the CH$_2$CHCH$_2$ group and the La metal centre. In conclusion, therefore, the computed profiles for the first propene insertion catalysed by the (gO)-[La(CH$_3$)$_2$] complex reveals that while from a kinetic point of view the allylic transfer reaction is kinetically comparable with the 1,2 and 2,1 insertion processes, from a thermodynamic point of view, the allylic insertion product is preferred over the insertion ones. The (gO)-[La(CH$_3$)$_2$] complex, therefore, does not seem to catalyse the propene polymerisation, leading instead to the formation of a highly stable allylic La complex.

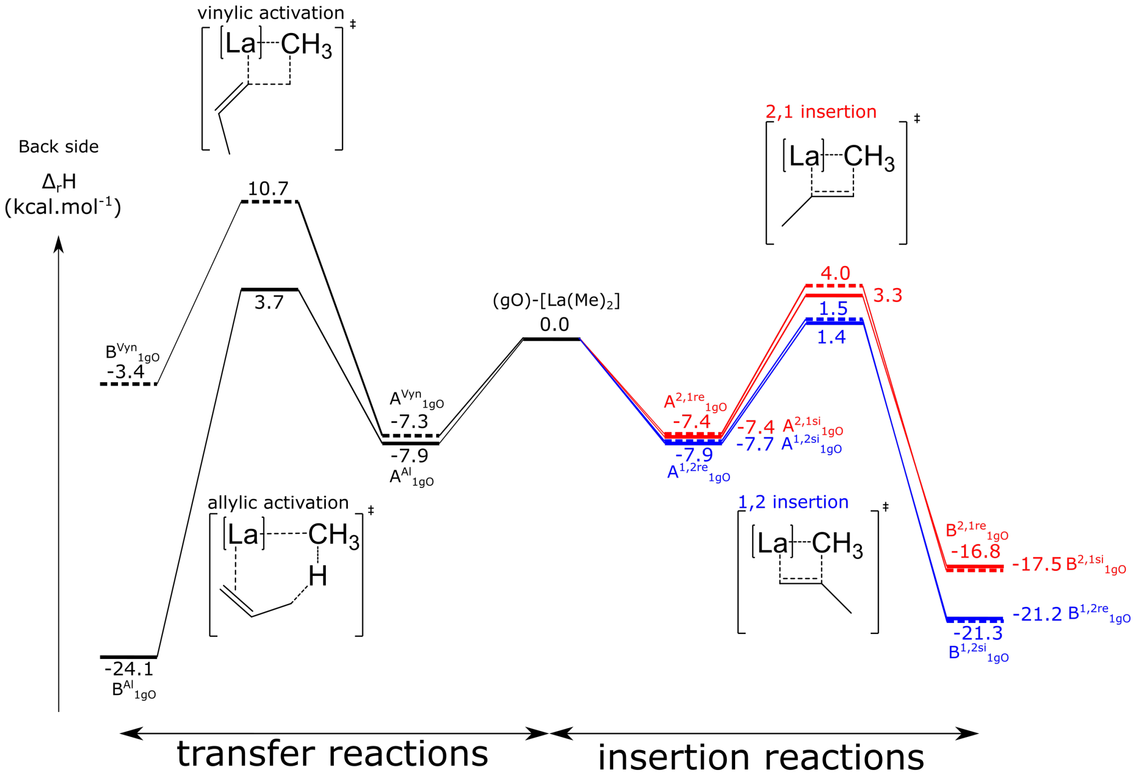

Figure 117: Calculated enthalpy profile for the first 1,2 and 2,1 back side propene insertion (on the right) and for the back side allylic and vinylic C-H activation (on the left) mediated by (gO)-[La($CH_3$)$_2$].

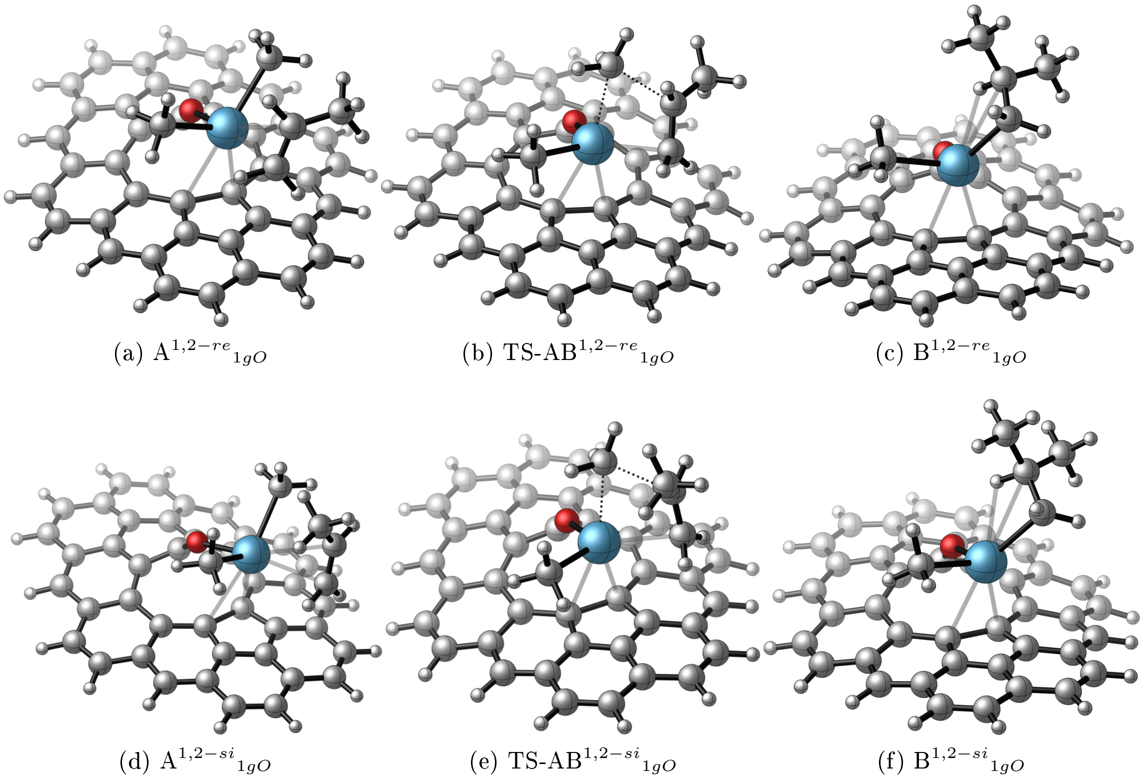

(a) $A^{1,2-re}{}_{1gO}$ (b) TS-$AB^{1,2-re}{}_{1gO}$ (c) $B^{1,2-re}{}_{1gO}$

(d) $A^{1,2-si}{}_{1gO}$ (e) TS-$AB^{1,2-si}{}_{1gO}$ (f) $B^{1,2-si}{}_{1gO}$

Figure 118: Geometries of the complexes involved in the first 1,2 front side propene insertion mediated by (gO)-[La($CH_3$)$_2$].

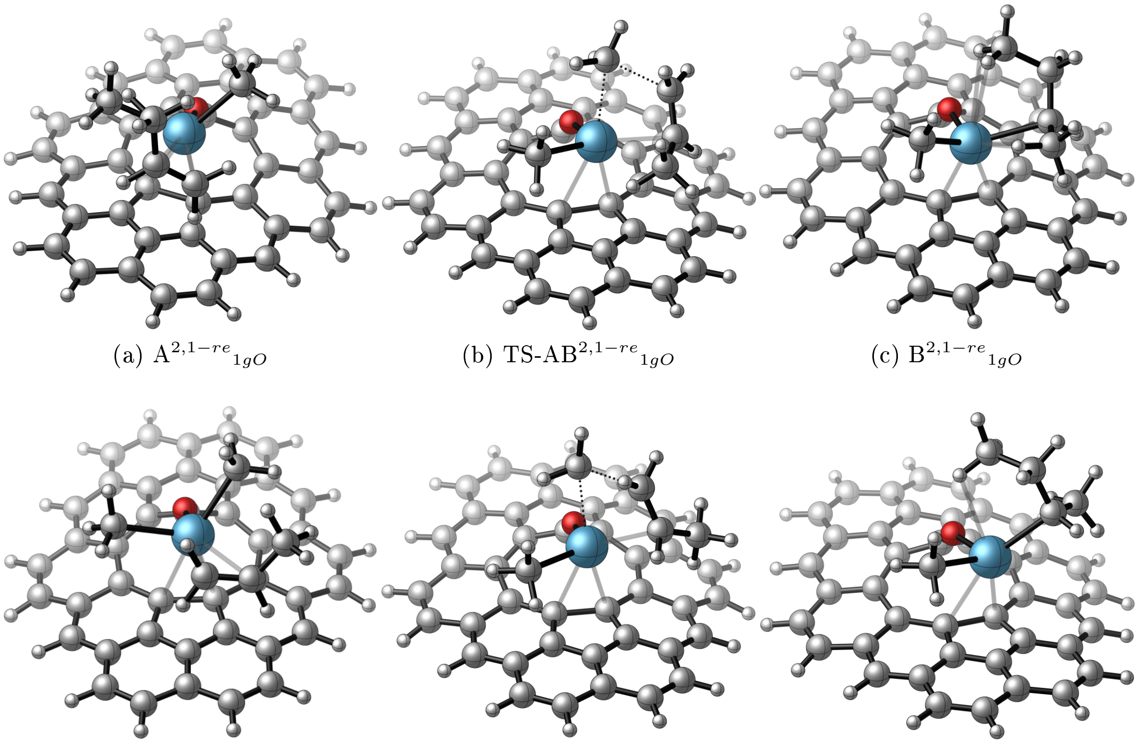

(a) $\mathrm{A}^{2,1-re}{}_{1gO}$ (b) $\text{TS-AB}^{2,1-re}{}_{1gO}$ (c) $\mathrm{B}^{2,1-re}{}_{1gO}$

(d) $\mathrm{A}^{2,1-si}{}_{1gO}$ (e) $\text{TS-AB}^{2,1-si}{}_{1gO}$ (f) $\mathrm{B}^{2,1-si}{}_{1gO}$

Figure 119: Geometries of the complexes involved in the first 2,1 front side propene insertion mediated by (gO)-[La$(CH_3)_2$].

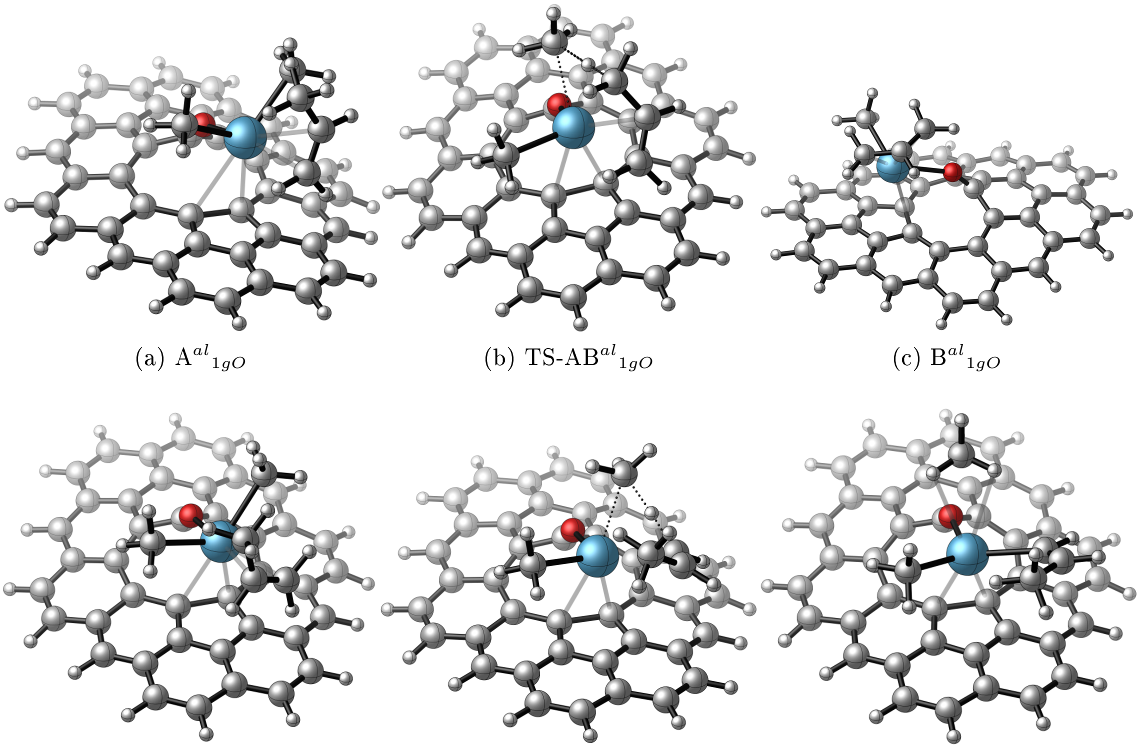

(a) $\mathrm{A}^{al}{}_{1gO}$ (b) $\text{TS-AB}^{al}{}_{1gO}$ (c) $\mathrm{B}^{al}{}_{1gO}$

(d) $\mathrm{A}^{vyn}{}_{1gO}$ (e) $\text{TS-AB}^{vyn}{}_{1gO}$ (f) $\mathrm{B}^{vyn}{}_{1gO}$

Figure 120: Geometries of the complexes involved in the front side allylic and vinylic C-H activation mediated by (gO)-[La$(CH_3)_2$].

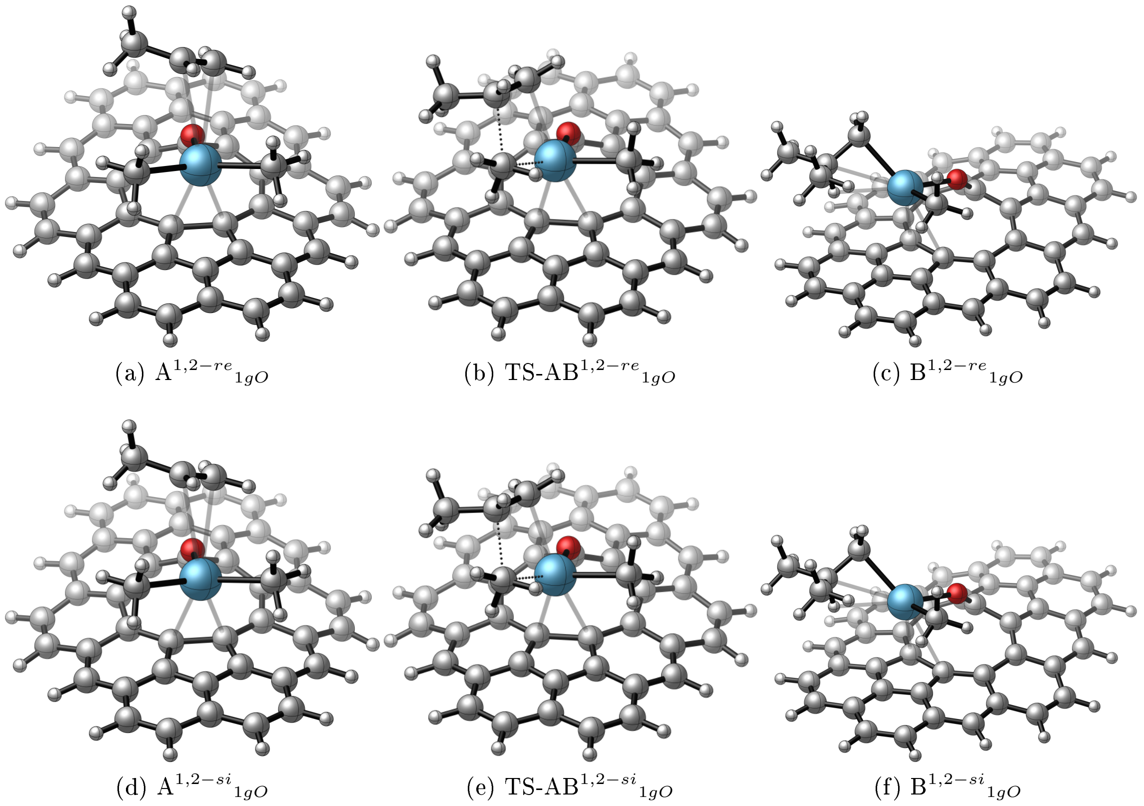

(a) $A^{1,2-re}{}_{1gO}$ (b) $TS\text{-}AB^{1,2-re}{}_{1gO}$ (c) $B^{1,2-re}{}_{1gO}$

(d) $A^{1,2-si}{}_{1gO}$ (e) $TS\text{-}AB^{1,2-si}{}_{1gO}$ (f) $B^{1,2-si}{}_{1gO}$

Figure 121: Geometries of the complexes involved in the first 1,2 back side propene insertion mediated by (gO)-[La($CH_3$)$_2$].

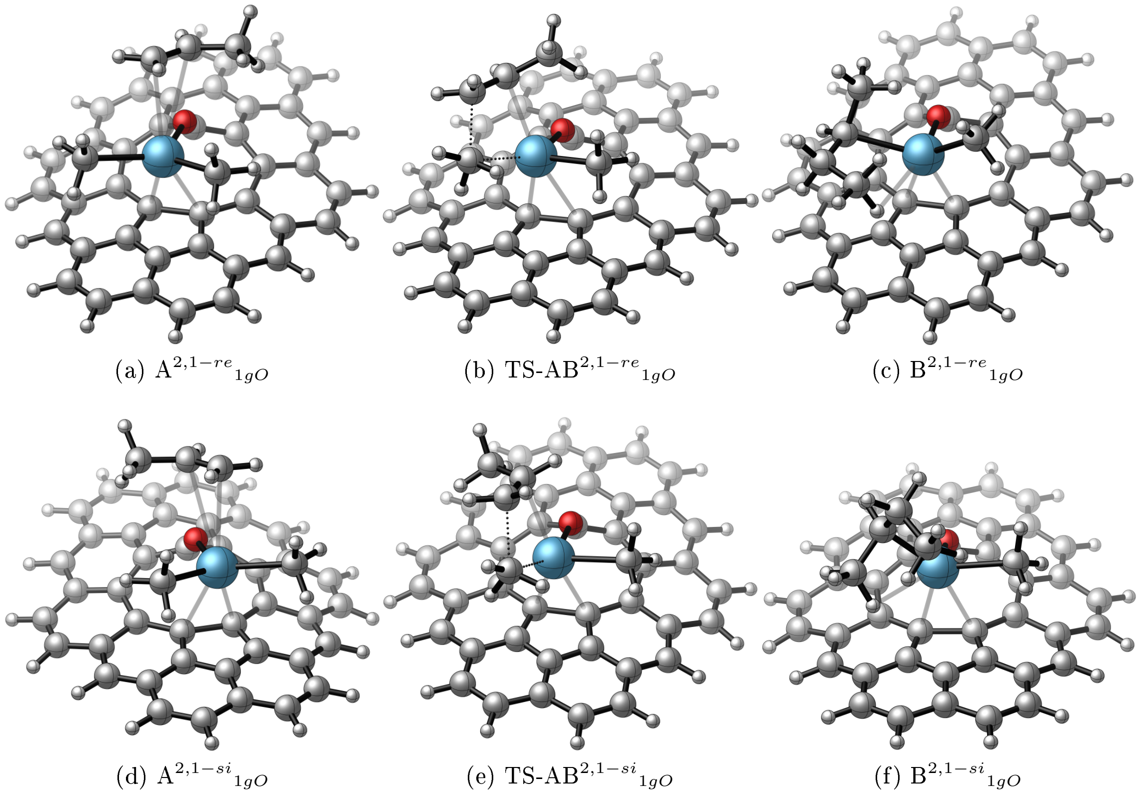

(a) $A^{2,1-re}{}_{1gO}$ (b) $TS\text{-}AB^{2,1-re}{}_{1gO}$ (c) $B^{2,1-re}{}_{1gO}$

(d) $A^{2,1-si}{}_{1gO}$ (e) $TS\text{-}AB^{2,1-si}{}_{1gO}$ (f) $B^{2,1-si}{}_{1gO}$

Figure 122: Geometries of the complexes involved in the first 2,1 back side propene insertion mediated by (gO)-[La($CH_3$)$_2$].

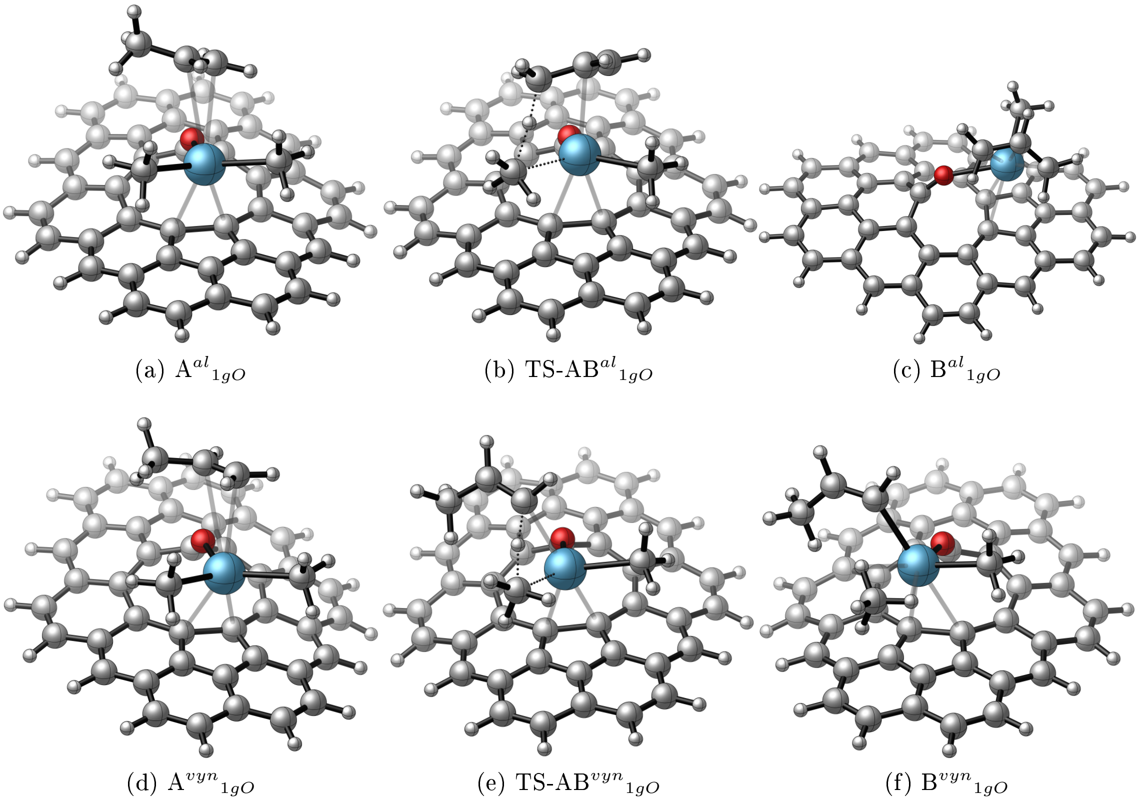

(a) $\mathrm{A}^{al}{}_{1gO}$ (b) TS-$\mathrm{AB}^{al}{}_{1gO}$ (c) $\mathrm{B}^{al}{}_{1gO}$

(d) $\mathrm{A}^{vyn}{}_{1gO}$ (e) TS-$\mathrm{AB}^{vyn}{}_{1gO}$ (f) $\mathrm{B}^{vyn}{}_{1gO}$

Figure 123: Geometries of the complexes involved in the front side allylic and vinylic C-H activation mediated by (gO)-[La($CH_3$)$_2$].

In order to verify if the thermodynamic preference for the allylic product is maintained during the second propene insertion, we also computed the first propagation step, considering both the front side and the back side propene approaches. As a starting complex, we chose the most stable insertion product corresponding to the La propyl compound: $\mathrm{B}^{1,2si}{}_{1gO}$. For the first propagation step, as for the initiation step, six reactions have been considered: the 1,2- and 2,1-propene insertions, with either the *si* or *re* enantioface, and the allylic and vinylic C-H bond activation reactions. All these reactions have been computed considering both the ‘front side’ and 'back side' approach, representing a total of twelve possible reactions pathways. Moreover, as for the initiation step, the vinylic C-H bond activation is not competitive because it exhibits higher activation barriers and affords less stable products than the allylic C-H bond activation. The enthalpy profiles for the second propene insertion mediated by the propyl $\mathrm{B}^{1,2si}{}_{1gO}$ complex are depicted in figures 124 and 125. A view of the different transition state and intermediates geometries is available in figures 126 to 131. It is worth noting that the first propagation step follows the same trend observed in the initiation step. Starting from the propyl $\mathrm{B}^{1,2si}{}_{1gO}$ complex, the approach of a second propene monomer affords the corresponding $\mathrm{C}_{1gO}$ adducts, which differ depending on the insertion path (1,2 or 2,1) and the propene enantiofaces (*re* and *si*). The coordination of a second propene monomer shows a lower stabilisation energy compared to that computed in the initiation step. The stabilisation energies of the $\mathrm{C}_{1gO}$ adducts, indeed, range from -1.6 to -3.8 kcal.mol$^{-1}$ for the front side insertion, compared to the -5.7/-5.9 kcal.mol$^{-1}$ range value in the first propene insertion, and from -1.0 to -2.1 kcal.mol$^{-1}$ for the back side insertion, compared to the -7.3/-7.9 range value for the first propene insertion. For the front side approach, the insertion barrier from the $C_{1gO}$ adducts measure 7.4 and 6.4 kcal.mol$^{-1}$ for the *re* and *si* 1,2 insertion and 10.8 and 10.3 kcal.mol$^{-1}$ for the *re* and *si* 2,1 insertion, respectively. Both reactions are exothermic, with the corresponding insertion products located at -37.0 and -35.0 kcal.mol$^{-1}$ for the *re* and *si* 1,2 inserton, and at -37.1 and -36.8 kcal.mol$^{-1}$ for the *re* and *si* 2,1 insertion, respectively. This indicates therefore that the two *re* and *si* enantiofaces behave identically from a thermodynamic as well as kinetic point of view, for the front side 1,2 and 2,1 insertion processes. The comparison between the 1,2 and 2,1 insertion reactions shows that, while from a kinetic point of view the 1,2 insertion mode is preferred over the 2,1 insertion one (the two corresponding barriers differing by 3.4 and 3.9 kcal.mol$^{-1}$ in favour of the 1,2 insertion for the *re* and *si* approach, respectively), from a thermodynamic point of view, on the other hand, the two insertion products are equally stable, displaying an enthalpy difference of 0.1 and 1.5 kcal.mol$^{-1}$ for the *re* and *si* enantiofaces, respectively. Like in the front side approach, the profile of the back side approach shows that, while the 1,2 insertion activation barrier is lower than the 2,1 one by 3.5 and 4.3 kcal.mol$^{-1}$, for the *re* and *si* approach, respectively, the corresponding insertion products, on the other hand, results thermodynamically equivalent, differing by 1.0 and 2.2 kcal.mol$^{-1}$ in favour of the 1,2-insertion for the *re* and *si* approach. Interestingly, unlike the front side approach in which the two enantiofaces behave identically, in the back side mechanism we observe a thermodynamic preference for the products of the *si* enantioface, in particular for the 1,2 insertion products located at -38.2 (*re*) and -41.6 (*si*) kcal.mol$^{-1}$. The comparison between the front and back side approaches, interestingly, shows that while in both approaches the 1,2 insertion mechanism is always kinetically preferred over the 2,1 one, the back side insertion mode provides thermodynamically more stable products. This might be explained by the different direction of growth of the polymer chain in the two front and back side approaches: while in the front side insertion, indeed, the growing polymer extends towards the surface, raising the metal from the surface, in the back side insertion the polymer grows at the opposite side of the surface, maintaining the stabilising La-surface interaction. This is confirmed by the distances measured between the metal and the pentagonal underlying graphene cycle which fall in the range 3.002-3.252 $\AA$ for the front side insertion compared to the 2.929-3.122 $\AA$ one for the back side insertion. As for the initiation step, we subsequently investigated the two deactivation processes involving either the vinylic or the allylic C-H bond activation. As for the initiation step, the vinylic C-H bond activation is not competitive exhibiting high activation barriers and yielding less stable products than the two insertion reactions and the allylic C-H bond activation. Concerning the allylic C-H bond activation, while the allylic activation barrier is comparable with those reported above for the preferred 1,2-insertion reactions, the allylic transfer products are more stable than the insertion ones (-44.1 and -42.0 kcal.mol$^{-1}$ for the front and the back side approach, respectively). Like for the initiation step, therefore, also in the propagation step the allylic deactivation of the catalyst is likely to represent the dominant reaction, precluding the use of the (gO)-[La($CH_3$)$_2$] complex as a propene polymerisation catalyst.

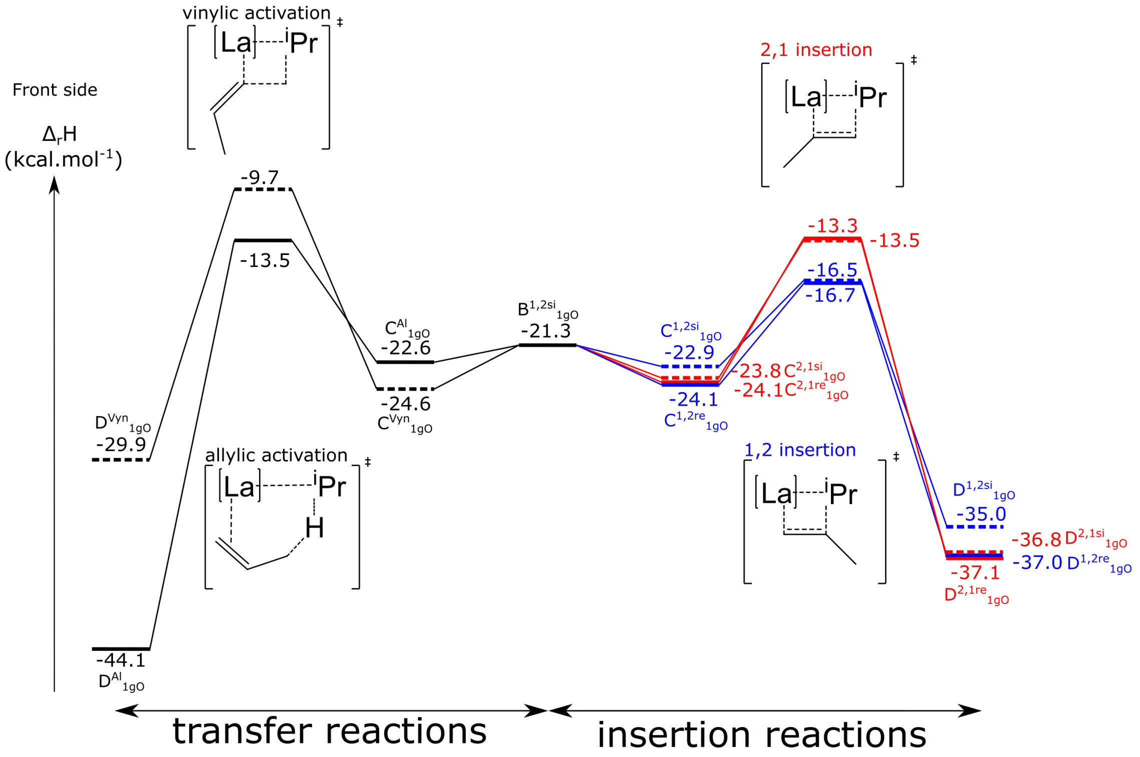

Figure 124: Calculated enthalpy profile for the second 1,2 and 2,1 front side propene insertion (on the right) and for the front side allylic and vinylic C-H activation (on the left) mediated by the $B^{1,2si}{}_{1gO}$ complex.

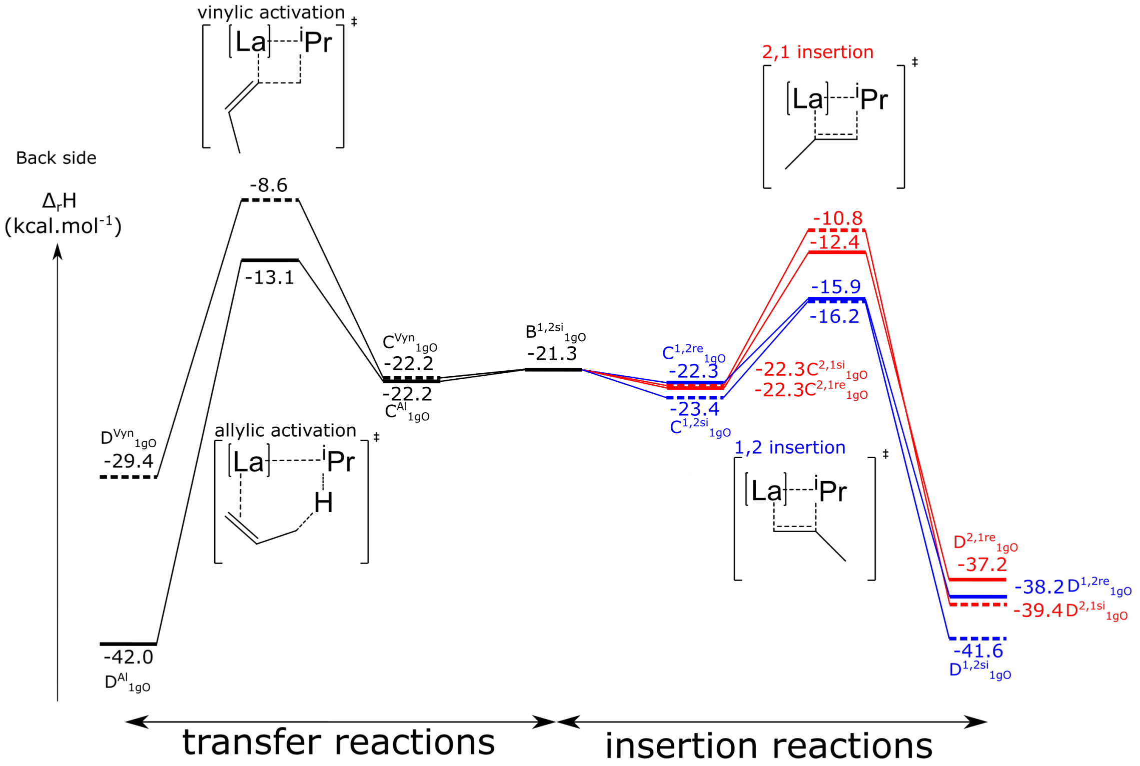

Figure 125: Calculated enthalpy profile for the second 1,2 and 2,1 back side propene insertion (on the right) and for the back side allylic and vinylic C-H activation (on the left) mediated by the $B^{1,2si}{}_{1gO}$ complex.

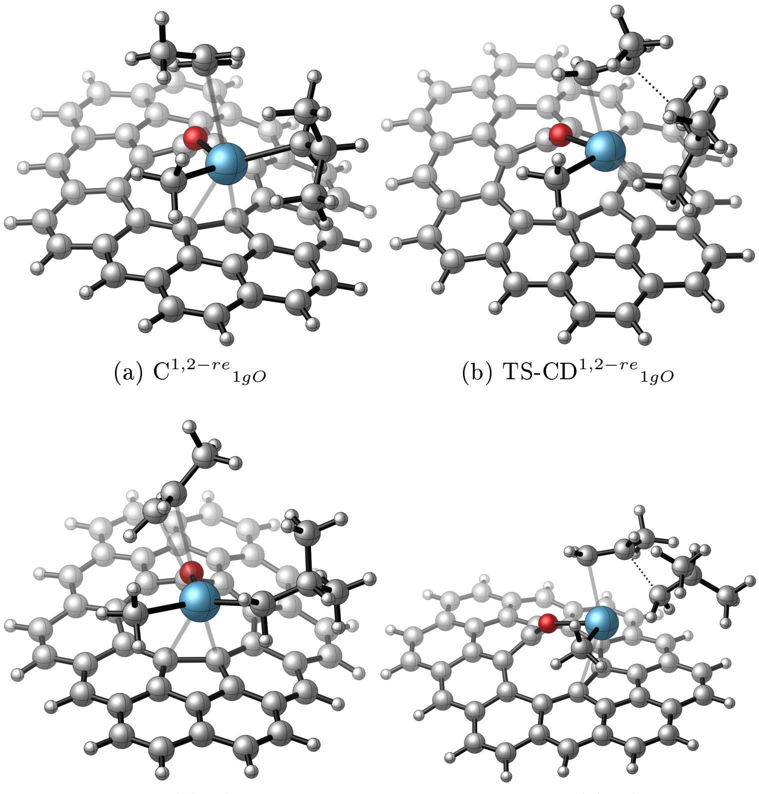

(a) $C^{1,2-re}{}_{1gO}$ (b) TS-$CD^{1,2-re}{}_{1gO}$ (c) $D^{1,2-re}{}_{1gO}$

(d) $C^{1,2-si}{}_{1gO}$ (e) TS-$CD^{1,2-si}{}_{1gO}$ (f) $D^{1,2-si}{}_{1gO}$

Figure 126: Geometries of the complexes involved in the second 1,2 front side propene insertion mediated by the $B^{1,2si}{}_{1gO}$ complex.

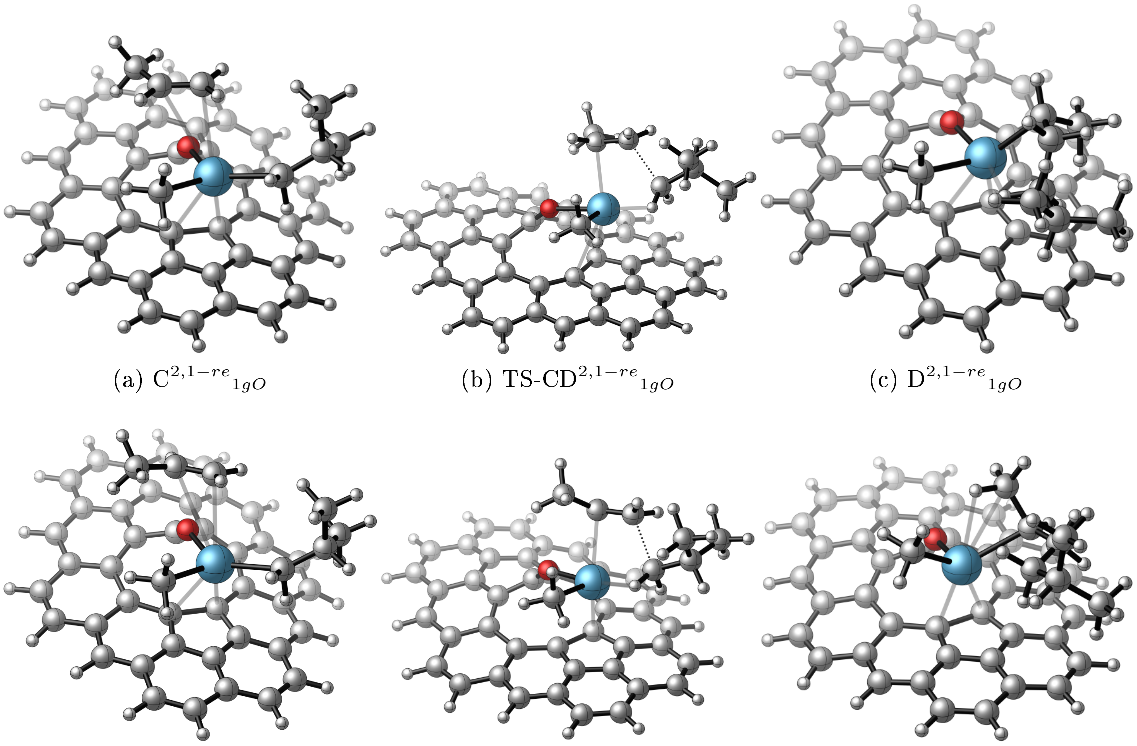

(a) $C^{2,1-re}{}_{1gO}$ (b) $TS\text{-}CD^{2,1-re}{}_{1gO}$ (c) $D^{2,1-re}{}_{1gO}$

(d) $C^{2,1-si}{}_{1gO}$ (e) $TS\text{-}CD^{2,1-si}{}_{1gO}$ (f) $D^{2,1-si}{}_{1gO}$

Figure 127: Geometries of the complexes involved in the second 2,1 front side propene insertion mediated by the $B^{1,2si}{}_{1gO}$ complex.

## 2.2 Reaction profiles of the 1st and 2nd insertions on gO-[La(Cp)($CH_3$)] (2gO) and gO-[La(Cp*)($CH_3$)] (3gO).

In the previous section, we have shown that gO-[La($CH_3$)$_2$] poorly catalyses the propene homopolymerisation reaction due to the formation of a very stable $\pi$-allylic La deactivation compound. In order to prevent the formation of the $\pi$-allylic complex, we decided to modify the initial catalytic complex by substituting one of the alkyl ligands by more hindered cyclopentadienyl ligands. The steric repulsion between these more sterically encumbered ligands and the approaching propene could indeed raise the activation energy barriers of the allylic transfer reaction and destabilise the corresponding $\pi$-allylic products. To verify this point, we therefore considered the two (gO)-[La(Cp)($CH_3$)] (2gO) and (gO)-[La(Cp*)($CH_3$)] (3gO) more hindered systems (see figure 132), obtained by replacing one of the two alkyls ligands of the 1gO complex by a cyclopentadienyl (Cp) or a pentamethylcyclopentadienyl (Cp*) ligand, respectively. As

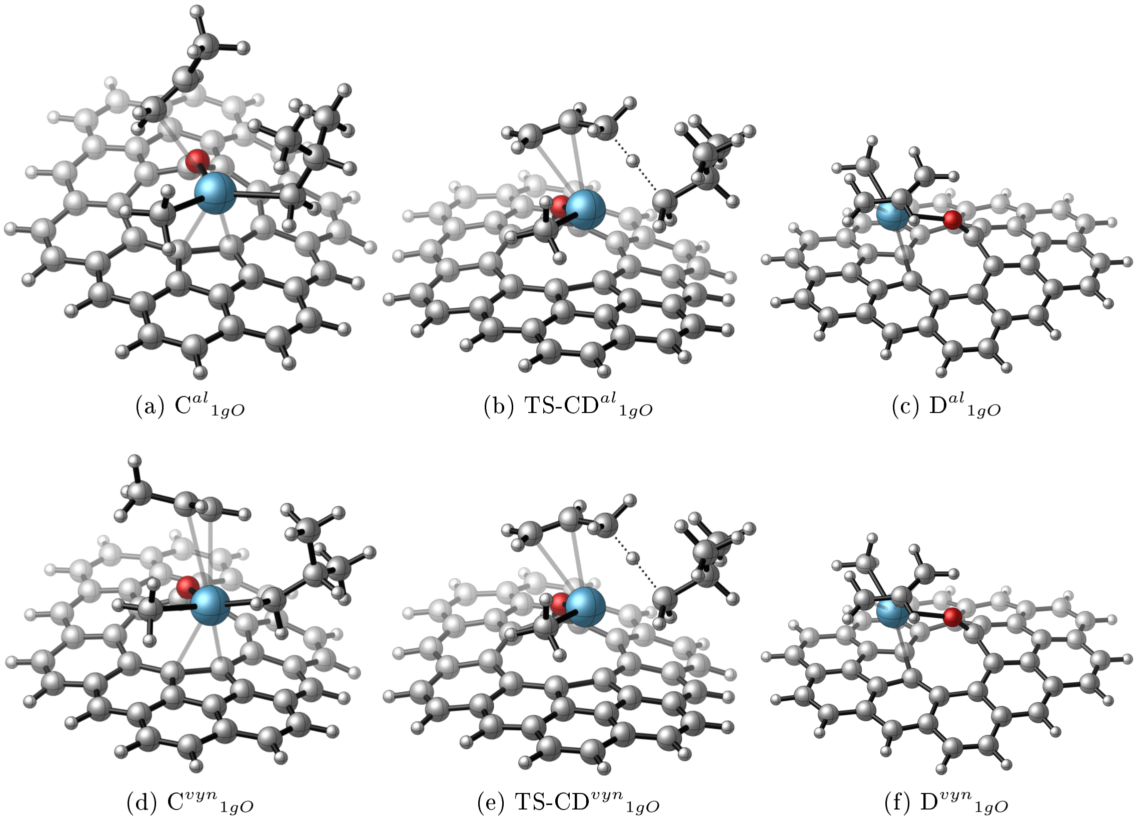
(a) $C^{al}{}_{1gO}$ (b) TS-$CD^{al}{}_{1gO}$ (c) $D^{al}{}_{1gO}$

(d) $C^{vyn}{}_{1gO}$ (e) TS-$CD^{vyn}{}_{1gO}$ (f) $D^{vyn}{}_{1gO}$

Figure 128: Geometries of the complexes involved in the front side allylic and vinylic C-H activation mediated by the $B^{1,2si}{}_{1gO}$ complex.

shown in Figure 132, while the presence of the Cp ligand does not modify significantly the La-$C_{graphene}$ distances (in the range 2.985-3.147 $\mathring{A}$ for 2gO compared to the 2.990-3.159 $\mathring{A}$ range for 1gO), the presence of the Cp* ligand forces the metal to slightly rise from the surface providing La-$C_{graphene}$ distances ranging from 3.018 to 3.210 $\mathring{A}$. Ongoing from 1gO to 2gO and 3gO, interestingly, the La-O bond slightly increase from 2.410 to 2.448 and 2.438 $\mathring{A}$, respectively, showing the weakening of the La-O bond, thus the more donating character of the Cp and Cp* ligands compared to the methyl one. The natural charge of the La centre, additionaly, decreases from 1.89 to 1.56 and 1.59 ongoing from the 1gO to the 2gO and 3gO complexes, the more donating properties of the Cp and Cp* ligands decreasing the Lewis acidity of the La centre. The replacement of the methyl by the Cp and Cp* ligands has therefore two main consequences: while it enhances the steric hindrance around the metal, it is likely to reduce the metal Lewis acidity character.

We therefore computed the allylic C-H bond activation catalysed by the 2gO and 3gO complexes and we compared the obtained $\pi$-allylic products with those previously reported for the 1gO compound. The geometries of the allylic products resulting from the 1gO, 2gO and 3gO complexes ($B^{Al}{}_{1gO}$, $B^{Al}{}_{2gO}$ and $B^{Al}{}_{3gO}$, respectively) are shown in Figure 133. As shown in in Table 17, interestingly, the bond distances between the La metal and the $C_1$, $C_2$ and $C_3$ carbon atoms of the allylic moiety increase ongoing from the $B^{Al}{}_{1gO}$ (La-$C_1$ = 2.669 $\mathring{A}$, La-$C_2$ = 2.748 $\mathring{A}$ and La-$C_3$ = 2.696 $\mathring{A}$) to the $B^{Al}{}_{2gO}$ (La-$C_1$ = 2.702 $\mathring{A}$, La-$C_2$ = 2.758 $\mathring{A}$ and La-$C_3$ = 2.732 $\mathring{A}$) and $B^{Al}{}_{3gO}$ (La-$C_1$ = 2.707 $\mathring{A}$, La-$C_2$ = 2.761 $\mathring{A}$ and La-$C_3$ = 2.732 $\mathring{A}$) compounds. The augmented steric strain around the metal, indeed, disfavour the interaction of the allylic group

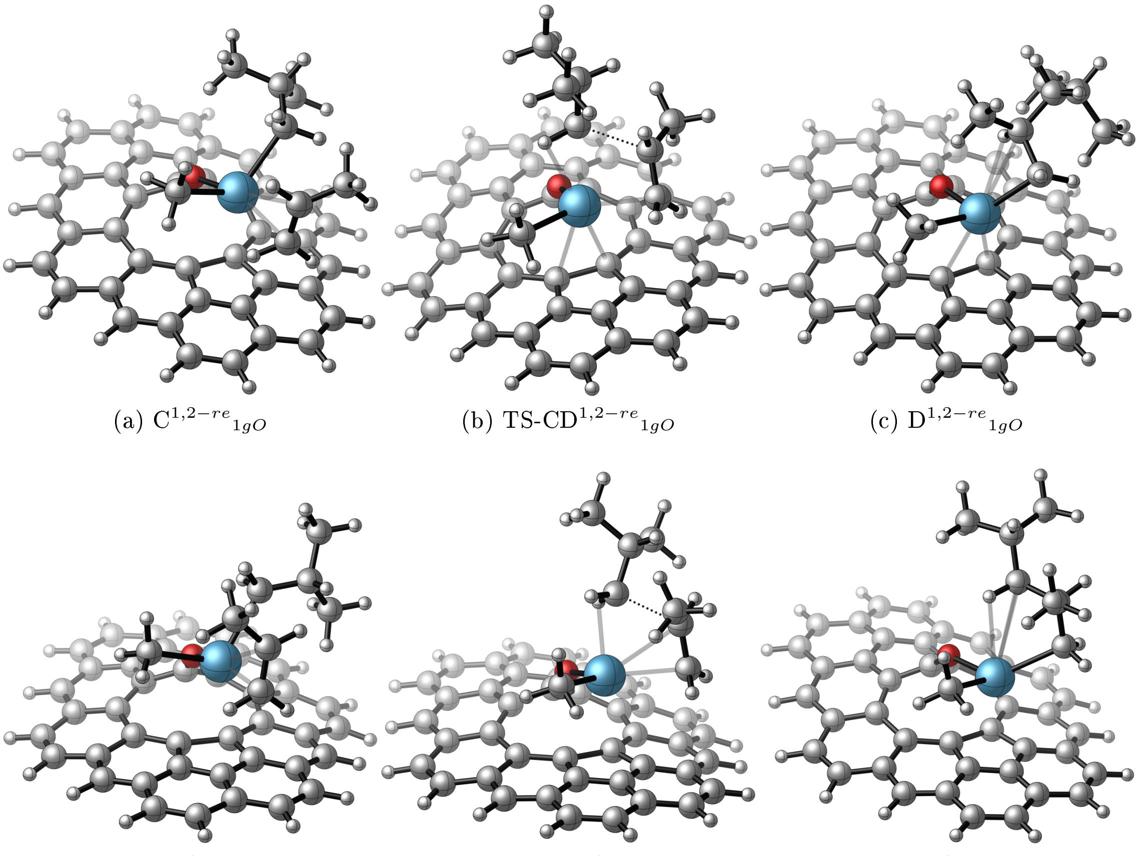

(a) $\mathrm{C}^{1,2-re}{}_{1gO}$ (b) TS-$\mathrm{CD}^{1,2-re}{}_{1gO}$ (c) $\mathrm{D}^{1,2-re}{}_{1gO}$

(d) $\mathrm{C}^{1,2-si}{}_{1gO}$ (e) TS-$\mathrm{CD}^{1,2-si}{}_{1gO}$ (f) $\mathrm{D}^{1,2-si}{}_{1gO}$

Figure 129: Geometries of the complexes involved in the second 1,2 back side propene insertion mediated by the $\mathrm{B}^{1,2si}{}_{1gO}$ complex.

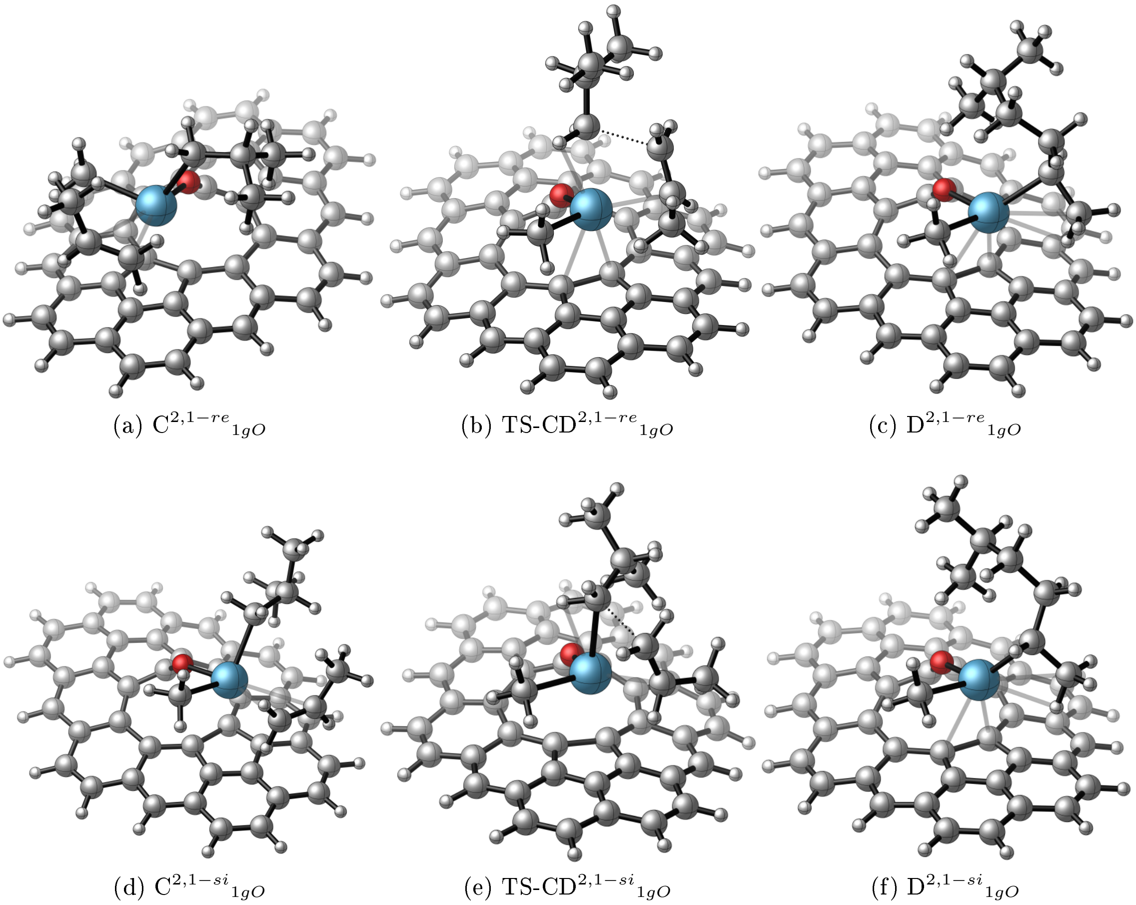

(a) $\mathrm{C}^{2,1-re}{}_{1gO}$ (b) TS-$\mathrm{CD}^{2,1-re}{}_{1gO}$ (c) $\mathrm{D}^{2,1-re}{}_{1gO}$

(d) $\mathrm{C}^{2,1-si}{}_{1gO}$ (e) TS-$\mathrm{CD}^{2,1-si}{}_{1gO}$ (f) $\mathrm{D}^{2,1-si}{}_{1gO}$

Figure 130: Geometries of the complexes involved in the second 2,1 back side propene insertion mediated by the $\mathrm{B}^{1,2si}{}_{1gO}$ complex.

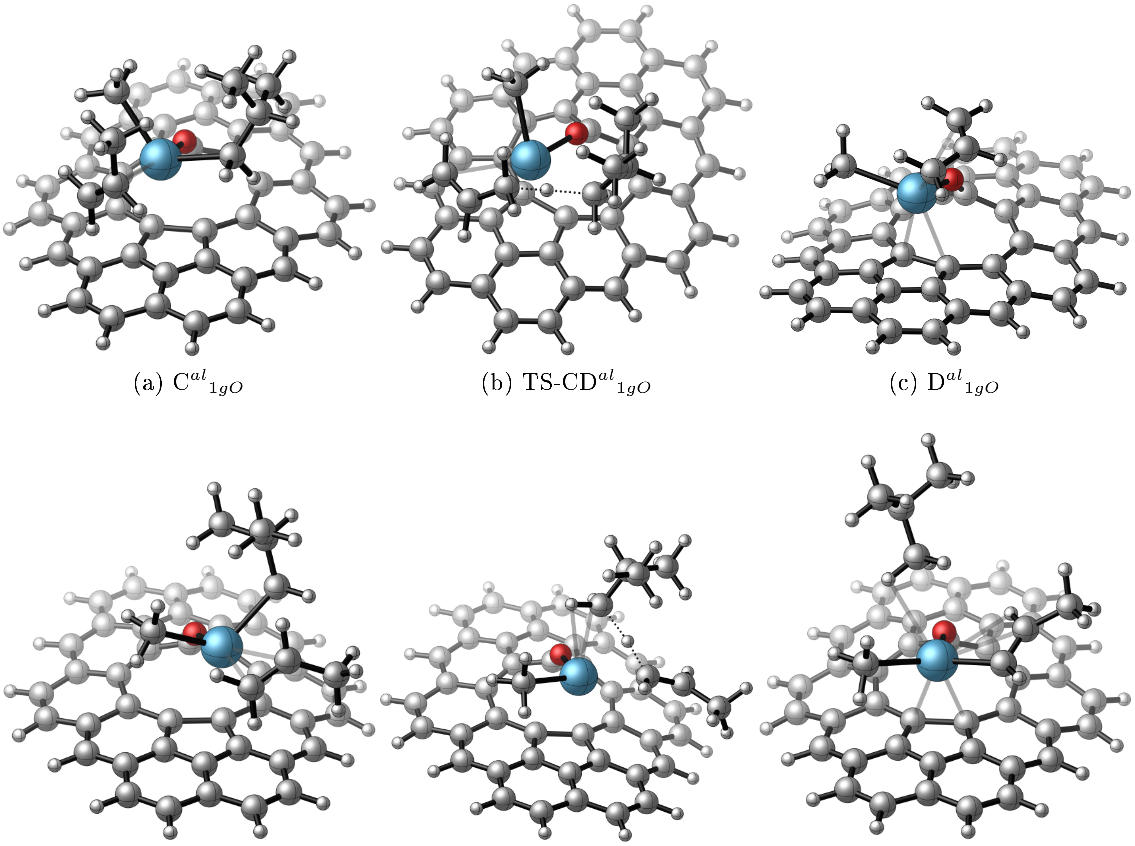

(a) $C^{al}{}_{1gO}$ (b) TS-$CD^{al}{}_{1gO}$ (c) $D^{al}{}_{1gO}$

(d) $C^{vyn}{}_{1gO}$ (e) TS-$CD^{vyn}{}_{1gO}$ (f) $D^{vyn}{}_{1gO}$

Figure 131: Geometries of the complexes involved in the back side allylic and vinylic C-H activation mediated by the $B^{1,2si}{}_{1gO}$ complex.

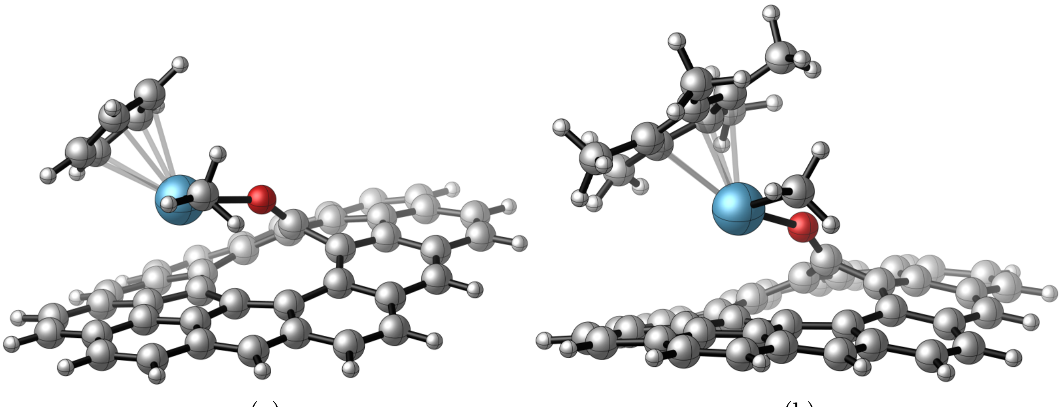
(a) (b)

Figure 132: Geometries of the grafted (a) (gO)-[La(Cp)($CH_3$)Cp] (2gO) and (b) (gO)-[La(Cp*)($CH_3$)] (3gO) complexes.

with the La metal. Following the same trend, in addition, ongoing from the $B^{Al}{}_{1gO}$ to the $B^{Al}{}_{2gO}$ and $B^{Al}{}_{3gO}$ compounds, the La metal moves away from the surface, the La-$C_{graphene}$ distances increasing from the 2.936-3.153 $\AA$ range for $B^{Al}{}_{1gO}$ to the 3.007-3.163 $\AA$ and 3.072-3.241 $\AA$ range for $B^{Al}{}_{2gO}$ and $B^{Al}{}_{3gO}$, respectively. We then computed the 1,2 insertion reaction catalysed by the 2gO and 3gO complexes and we compared the obtained 1,2 insertion products with those previously reported for the 1gO compound. The geometries of the 1,2 insertion products resulting from the 1gO, 2gO and 3gO complexes ($B^{1,2}{}_{1gO}$, $B^{1,2}{}_{2gO}$ and $B^{1,2}{}_{3gO}$, respectively) are shown in Figure133. As shown in Table 17, interestingly, while the La-$C_{graphene}$ distances increase ongoing from the $B^{1,2}{}_{1gO}$ (2.909-3.137 $\AA$) to the $B^{1,2}{}_{2gO}$ (2.988-3.159 $\AA$) and $B^{1,2}{}_{3gO}$ (3.048-3.236 $\AA$) compounds, the bond distances between the La metal and the propene $C_1$ and $C_2$ carbon atoms do not change significantly between the three complexes (La-$C_1$ in the range 2.461 - 2.466 $\AA$, and La-$C_2$ in the range 2.931-2.959 $\AA$). We can therefore observe that the geometry variations due to the replacement of the methyl ligand by the cyclopentadienyl groups, are much less pronounced for the 1,2 insertion products than for the allylic deactivation ones, suggesting that the augmented steric hindrance disfavours predominantly the allylic C-H bond activation pathway.

For the two 2gO and 3gO catalysts, the initiation and first propagation steps of the propene polymerisation process have been computed and compared with the concomitant allylic C-H activation bond reactions (Figure 135 for complex 2gO and Figure 136 for complex 3gO). The geometries of the corresponding intermediates and transition states are shown in the Appendix B (from Figures 168 to 199). For sake of clarity, only the *re* 1,2 and 2,1 insertion and the allylic transfer mechanisms, involving the back side approach of propene will be discussed in the following section. As shown in Figures 135 and 136, for both the 2gO and 3gO compounds, the 1,2

Table 17: Selected bond distances ($\mathring{A}$) and angles (°) of the products resulting from the 1,2 propene insertion and allylic C-H activation reactions mediated by 1gO, 2gO and 3gO. The labels $C_1$, $C_2$, $C_3$ and H refer to the geometries in Figures 133 and 134. R = Me, $Cp_{centroid}$ and $Cp*_{centroid}$ in 1gO, 2gO and 3gO, respectively.

| | $C_1$-La | $C_2$-La | $C_3$-La | H-La | $C_1$-La-R | $C_2$-La-R | Cgraphene-La | $C_{centroid-graphene}$-La-$C_1$ | $C_{centroid-graphene}$-La-$C_2$ |
|---|---|---|---|---|---|---|---|---|---|
| ${B^{Al}}_{1gO}$ | 2.669 | 2.748 | 2.696 | - | - | 113.9 | 2.936-3.153 | - | 139.9 |
| ${B^{Al}}_{2gO}$ | 2.702 | 2.758 | 2.732 | - | - | 121.8 | 3.007-3.163 | - | 105.9 |
| ${B^{Al}}_{3gO}$ | 2.707 | 2.761 | 2.732 | - | - | 119.7 | 3.072-3.241 | - | 98.6 |
| ${B^{1,2}}_{1gO}$ | 2.464 | 2.931 | - | 2.428 | 104.6 | 105.9 | 2.909-3.137 | 135.7 | 153.1 |
| ${B^{1,2}}_{2gO}$ | 2.461 | 2.932 | - | 2.437 | 106.5 | 102.6 | 2.988-3.159 | 110.3 | 128.6 |
| ${B^{1,2}}_{3gO}$ | 2.466 | 2.959 | - | 2.533 | 107.0 | 105.3 | 3.048-3.236 | 103.4 | 115.4 |

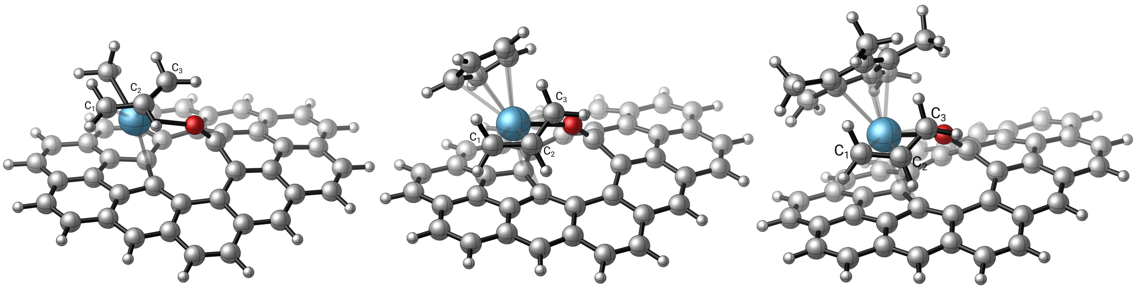

(a) $\mathrm{B}^{al}{}_{1gO}$ (b) $\mathrm{B}^{al}{}_{2gO}$ (c) $\mathrm{B}^{al}{}_{3gO}$

Figure 133: Geometries of the allylic products resulting from the allylic C-H bond activation reaction mediated by a) 1gO, b) 2gO and c) 3gO.

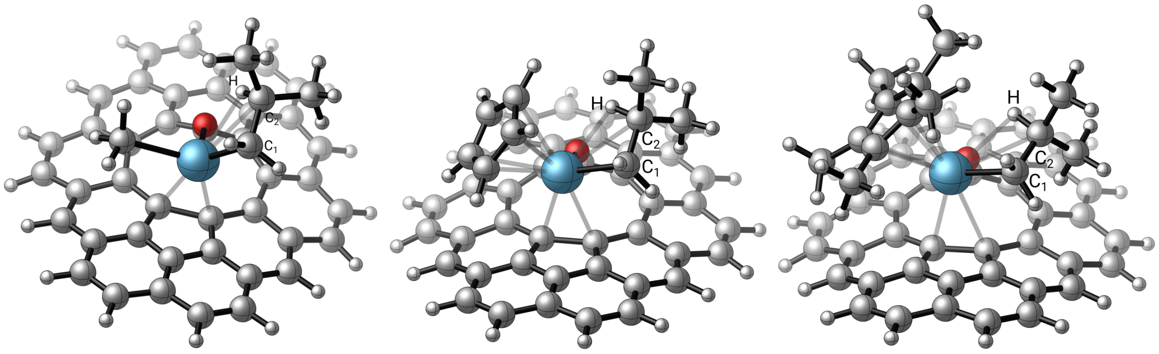

(a) $\mathrm{B}^{1,2}{}_{1gO}$ (b) $\mathrm{B}^{1,2}{}_{2gO}$ (c) $\mathrm{B}^{1,2}{}_{3gO}$

Figure 134: Geometries structures of the 1,2 insertion products resulting from the first propene insertion mediated by a) 1gO, b) 2gO and c) 3gO.

and 2,1 insertion reactions begin with the formation of the corresponding propene $A^{1,2}$ and $A^{2,1}$ adducts located at -3.6 kcal.mol$^{-1}$ for the 2gO compound and at 0.6 and 1.3 kcal.mol$^{-1}$ for the 3gO compound. Interestingly, we can observe that the less stabilised ${A^{1,2}}_{3gO}$ and ${A^{2,1}}_{3gO}$ adducts correspond to the more hindered (gO)-[La(Cp*)($CH_3$)] complex (3gO). These adducts connect to a 4c-4e$^-$ transition state where the double bond of propene is elongated (1.406 and 1.399 $\AA$ for TS-${AB^{1,2}}_{2gO}$ and TS-${AB^{2,1}}_{2gO}$ and 1.403 and 1.397 $\AA$ for TS-${AB^{1,2}}_{3gO}$ and TS-${AB^{2,1}}_{3gO}$, respectively, compared to 1.332 $\AA$ for free propene) and where the carbon atoms interacting with either the La or the $C_{Me}$ centres are pyramidilised. As shown by the profiles in Figures 135 and 136, while the 1,2-insertion barriers computed for the 2gO and 3gO complexes do not significantly change from those of the 1gO compound (9.3 kcal.mol$^{-1}$ for 1gO to 10.0 kcal.mol$^{-1}$ and 9.5 kcal.mol$^{-1}$) the 2,1 insertion barriers computed for the 2gO and 3gO complexes, on the other hand, increase, passing from 10.7 kcal.mol$^{-1}$ for 1gO to 14.1 kcal.mol$^{-1}$ for both 2gO and 3gO. The analysis of the corresponding 1,2 and 2,1 insertion products $B_{2gO}$ and $B_{3gO}$, interestingly, shows that the ${B^{1,2}}_{2gO}$ and ${B^{2,1}}_{2gO}$ compounds are considerably more stable than the corresponding ${B^{1,2}}_{3gO}$ and ${B^{2,1}}_{3gO}$ analogues (-20.0 and -17.9 kcal.mol$^{-1}$ *vs* -15.7 and -13.6 kcal.mol$^{-1}$). The insertion products of the 2gO compounds, indeed, are energetically equivalent to those compound for the 1gO complex (-21.2 and -16.8 kcal.mol$^{-1}$), whereas those corresponding to the 3gO complex are less thermodynamically favourable, probably due to the influence of the more sterically hindered Cp* ligand. If now we analyse the allylic deactivation process, we observe that the corresponding activation barriers measure 12.2 kcal.mol$^{-1}$ for 2gO and 11.3 kcal.mol$^{-1}$ for 3gO, resulting therefore comparable with the 1,2 activation barriers for 2gO (10.0 kcal.mol$^{-1}$) and for 3gO (8.9 kcal.mol$^{-1}$) as well as with the allylic C-H bond activation barrier computed for 1gO (11.6 kcal.mol$^{-1}$). Like for the 1gO complex, therefore, also for the 2gO and 3gO complexes the allylic C—H bond activation competes, from a kinetic point of view, with the 1,2 insertion reaction. From a thermodynamic point of view, the stabilisation energies of the allylic products (-21.5 kcal.mol$^{-1}$ for ${B^{Al}}_{2gO}$ and -17.9 kcal.mol$^{-1}$ for ${B^{Al}}_{3gO}$) are slightly higher than those computed for the corresponding 1,2 insertion products (-20.0 kcal.mol$^{-1}$ for ${B^{1,2}}_{2gO}$ and -15.7 kcal.mol$^{-1}$ for ${B^{1,2}}_{3gO}$). Like the 1gO complex, therefore, the allylic deactivation products computed for the 2gO and 3gO complexes are slightly more stable than to those of the 1,2-insertion reaction showing that the increased steric hindrance of the cyclopentadienyl ligands is not sufficient to effectively disfavour the allylic deactivation process over the insertion reactions.

The results obtained for the first propagation step are similar to those described above for the initiation one. Indeed, while from a kinetic point of view the allylic deactivation barriers remain competitive with the activation ones, from a thermodynamic point of view the stability of the allylic deactivation products increases with respect to that of the insertion ones (-42.1 and -38.1 kcal.mol$^{-1}$ for ${D^{Al}}_{2gO}$ and ${D^{Al}}_{3gO}$, compared to -39.6 and -35.3 kcal.mol$^{-1}$ for ${D^{1,2}}_{2gO}$ and ${D^{1,2}}_{3gO}$, respectively).

In conclusion, therefore, although the Cp and Cp* ligands increase the steric hindrance around the metal centre, these effects are not large enough to avoid the allylic transfer pathway which remains competitive with the 1,2 insertion process, deactivating the catalyst.

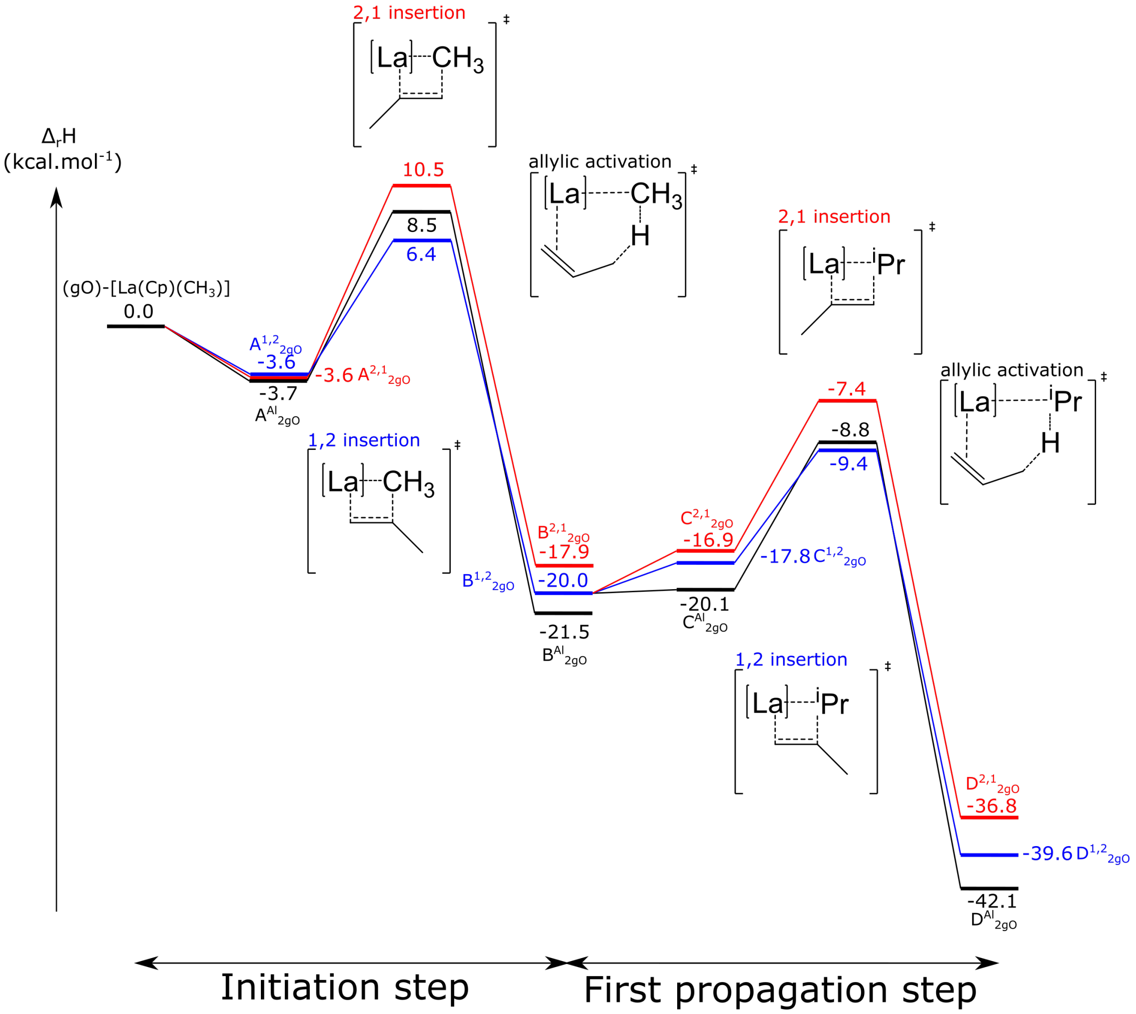

Figure 135: Reaction enthalpy profile of the initiation and first propagation step of the homopolymerisation of propene mediated by 2gO.

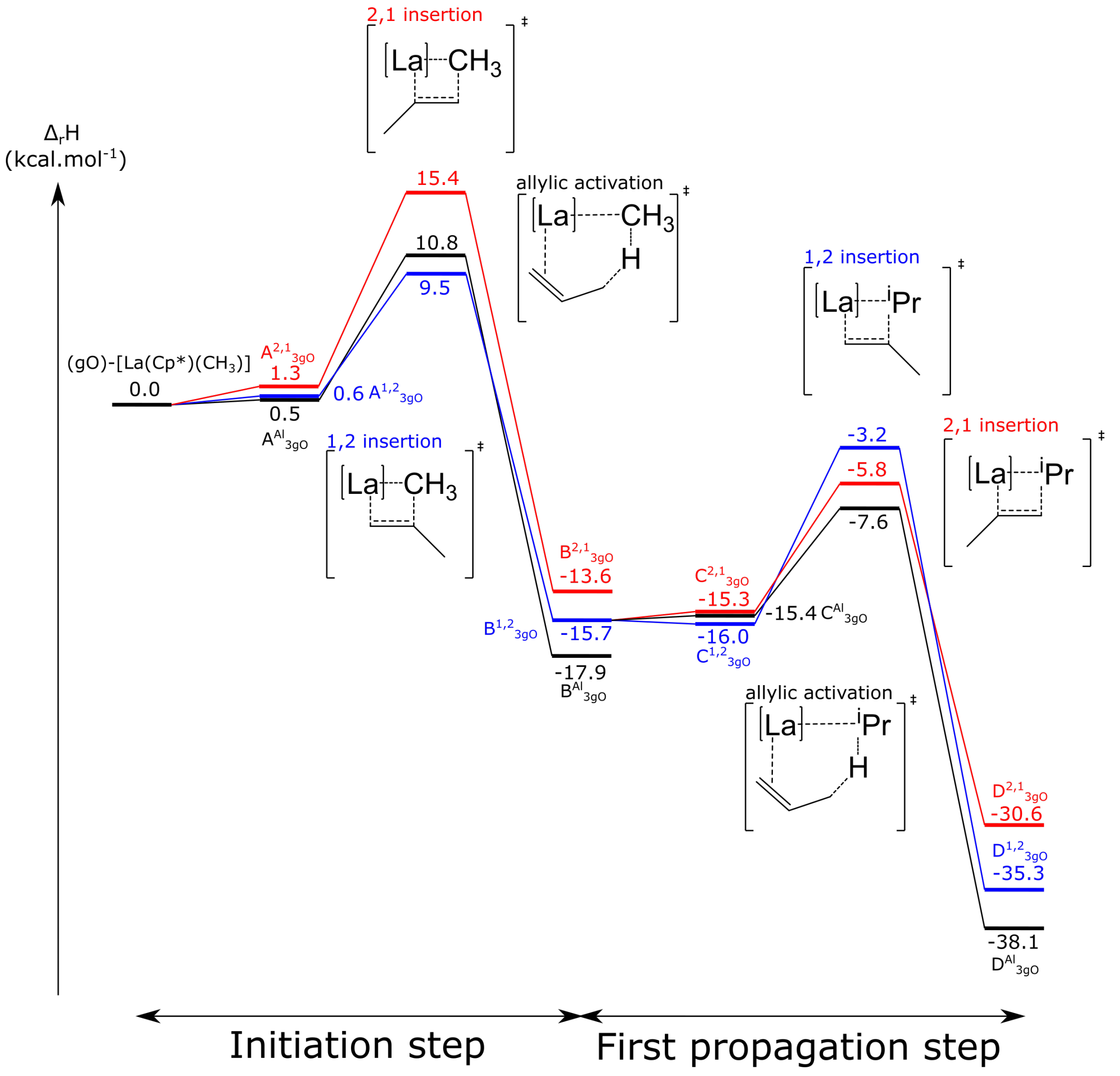

Figure 136: Reaction enthalpy profile of the initiation and first propagation step of the homopolymerisation of propene mediated by 3gO.

# 3 Conclusion

In the present chapter we have investigated the propene polymerisation reaction catalysed by the three graphene-grafted lanthanum complexes (gO)-[La($CH_3$)$_2$] (1gO), (gO)-[La(Cp)($CH_3$)] (2gO) and (gO)-[La(Cp*)($CH_3$)] (3gO). In the (gO)-[La($CH_3$)$_2$] system, while from a kinetic point of view the 1,2 and 2,1 insertion barriers are comparable with that of the allylic transfer process, from a thermodynamic point of view the allylic product is more stable that the 1,2 and 2,1 insertion ones. In order to disfavour the allylic transfer reaction we decided to increase the steric hindrance around the metal centre, by replacing one methyl with the more hindered Cp and Cp* ligands affording the (gO)-[La(Cp)($CH_3$)] and (gO)-[La(Cp*)($CH_3$)] complexes. The energy profiles computed for the latters indicate that, although the energy of the allylic deactivation products decreases passing from -24.1 to -21.5 and -17.9 kcal.mol$^{-1}$ for the 1gO, 2gO and 3gO, respectively, this energy decrease is not large enough to disfavour the allylic deactivation with regard to the 1,2-insertion process. In a perspective way, we plan to further increase the steric hindrance around the metal by either employing bulkier ligands or changing the nature of the metal toward a smaller element.

# Part VI

# Overview and final conclusion

The objective of this thesis was to explore and rationalise the effects that a potential surface may have when employed as a support for La molecular complexes.

After an introduction, in chapter I, of the different polymerisation catalysts reported in the literature, and after a description, in chapter II, of the computational methods employed in this work, we investigated, in Chapter III, through a computational DFT study, the grafting of the amido $[La(N(SiMe_3)_2)_3]$ complex on two functionalised graphene surfaces: the gOH and the gOOH surfaces. These graphene supports contain either an hydroxo (gOH) or a carboxylic group (gOOH), which allow the grafting of a lanthanide complex, as previously reported for silica and alumina. The grafting of a lanthanum complex on these surfaces, ineterstingly, has shown that the nature of the functional group on the surface (OH or COOH), has an influence on the geometry and therefore on the stability of the corresponding grafted complexes. In all cases the grafting reaction is shown to be a favourable process, both kinetically and thermodynamically, affording mono-grafted complexes. The grafting of the $[La(N(SiMe_3)_2)_3]$ precursor on the gOH surface leads to the formation of the corresponding (gO)-$[La(N(SiMe_3)_2)_2]$ complex, exhibiting a gO-La bond and a weak interaction between the La centre and the underlying pentagonal C=C groups of the graphene surface. In the presence of the gOOH surface, on the other hand, we obtain the corresponding (gOO)-$[La(N(SiMe_3)_2)_2]$ compound, displaying the monografted La metal bicoordinated to the surface through the carboxylate function.

In order to estimate the influence of the surface on the Lewis acidity properties of the metal centre and therefore on the reactivity of the catalyst, we used the $O{=}PPh_3$ molecule as a probe, by computing the corresponding $OPPh_3$ adducts, *i.e.* the (gO)-$[La(N(SiMe_3)_2)_2(OPPh_3)]$ and (gOO)-$[La(N(SiMe_3)_2)_2(OPPh_3)]$ complexes. The $^{31}P$ NMR and O=P IR spectroscopy analyses have shown that the graphene gOH and gOOH surfaces increase the Lewis acidity of the corresponding graphene grafted La complexes which display a Lewis acidic character more pronounced than the silica grafted analogues.

The influence of the surface on the catalytic properties of the supported lanthanum complexes has been then evaluated by studying the catalytic activity toward both the homo- and co-polymerisation of ethylene and 1,3-butadiene, of the corresponding graphene supported La alkyl compounds (gO)-$[La(CH_3)_2]$ and (gOO)-$[La(CH_3)_2]$. Both compounds efficiently catalyse the ethylene homopolymerisation reaction, displaying activation barriers which are significantly lower than those reported for the silica-grafted compounds. The graphene surfaces are therefore predicted to play an important role in the catalytic process, increasing the Lewis acidity and therefore the reactivity of the grafted La systems compared to oxygenated silica surfaces. Concerning the 1,3-butadiene homo-polymerisation, both the (gO)-$[La(CH_3)_2]$ and (gOO)-$[La(CH_3)_2]$ species are likely to behave as efficient catalysts, resulting more active than the silica grafted La analogues. In the gOO model, the 1,4-cis 1,3-butadiene insertion is preferred over the 1,4-trans one, affording preferentially a 1,4-cis-polybutadiene polymer, as previously reported for the silica-supported La compounds. Differently, the gO model inserts the 1,4-cis or 1,4-trans 1,3-butadiene without distinction, giving rise to a random 1,4-polybutadiene polymer. The stereoselectivity of the 1,3-butadiene polymerisation reaction is therefore different for the gO model compared to the gOO and silica supported systems, underlying once again the influence of the support on the polymerisation reaction outcome. The catalytic behaviour of these graphene grafted systems has been then investigated in the ethylene and 1,3 butadiene co-polymerisation reaction. We have shown that for both the gO and gOO complexes the insertion of the 1,4-cis 1,3-butadiene monomers is favoured over that of ethylene, with the formation of a highly stable allylic product. The higher stability of the allylic products compared to the alkyl ones, indeed, drives the reaction toward the exclusive 1,3-butadiene insertion, preventing any alternating co-polymerisation reaction.

The graphene-grafted (gO)-[La($CH_3$)$_2$] and (gOO)-[La($CH_3$)$_2$] alkyl complexes have been also tested as catalysts in the homo-polymerisation of styrene and in the co-polymerisation of ethylene and styrene. The study of the first three insertion reactions shows that both compounds efficiently catalyse the styrene homopolymerisation. The calculated barriers are comparable to those obtained for the highly active cationic scandium complex of Hou's group, with a higher activity expected for the (gOO)-[La($CH_3$)$_2$] system, due to the less steric congestion around the metal. As for the ethylene and butadiene polymerisation, the increase of the Lewis acidic character of the metal centre enhances the reactivity of the grafted La complexes. Concerning the stereoselectivity, a preference for the formation of a syndiotactic polystyrene is found for both catalysts, this type of polymer resulting thermodynamically controlled. The catalytic behavior of the graphene-grafted La alkyl complexes ((gO)-[La($CH_3$)$_2$] and (gOO)-[La($CH_3$)$_2$]) has been finally investigated in the ethylene and styrene co-polymerisation reaction. We have shown that while for the gO-La catalyst, the formation of a polystyrene with a little amount of ethylene is expected for the gOO-La catalyst, on the other hand, the formation of a copolymer is very unlikely, as styrene insertion is preferred for the two first insertions. For the latter system, therefore, at most a block copolymer may be obtained when all styrene has been consumed.

In the last part of chapter 3 we have then computed the initiation and first propagation steps of the controlled rac-BL ROP reaction by using as catalysts four different lanthanum borohydride complexes, *i.e.* the molecular [La($BH_4$)$_3$(THF)$_3$], the silica supported (≡SiO)-[La($BH_4$)$_2$(THF)$_2$] and the graphene-supported (gO)-[La($BH_4$)$_2$(THF)$_2$] and (gOO)-[La($BH_4$)$_2$(THF)$_2$] compounds. Differently from the (≡SiO)-[La($BH_4$)$_2$(THF)$_2$] species, which poorly catalyses the BL ROP reaction, the (gO)-[La($BH_4$)$_2$(THF)$_2$] and (gOO)-[La($BH_4$)$_2$(THF)$_2$] systems are likely to efficiently polymerise the BL monomer, displaying the same efficiency as the homogeneous [La($BH_4$)$_3$(THF)$_3$] compound. The nature of the surface, therefore, plays, also in this case, an important role, influencing the Lewis acidity and therefore the reactivity of the grafted La compounds.

In chapter IV, we focused on the boron nitride surfaces, employing as model support, a boron nitride surface functionalised with either an hydroxyl group (BNH-OH) or an hydroxyl group joined to a defect vacancy site (BNO-OH). Also here, the grafting of the [La(N($SiMe_3$)$_2$)$_3$] precursor on both surfaces has been computed, showing that a vacancy defect is necessary to graft a lanthanide metal complex onto the surface. In the absence of a vacancy defect, indeed, the grafting on the BNH-OH surface leads to a ligand exchange between the hydroxyl group of the surface and one of the amido ligands of the metal complex, affording the release of the final [La(N($SiMe_3$)$_2$)$_2$(OH)](HN($SiMe_3$)$_2$) complex. The grafting on the BNO-OH surface, on the other hand, leads to the formation of the (BNO-O)-[La(N($SiMe_3$)$_2$)$_2$] grafted complex, which, in opposition to the gO analogue, is raised from the surface. The $^{31}P$ NMR and O=P IR spectroscopy analyses of the corresponding (BNO-O)-[La(N(SiMe$_3$)$_2$)$_2$(OPPh$_3$)] adduct have been computed and compared with those obtained for the graphene grafted analogues. Interestingly, while the BNO-O grafted lanthanide silylamide complex has a Lewis acidic character comparable with that of the gOO counterpart, it results more Lewis acidic than the silica grafted analogues. The nature of the surface, therefore, is likely to play an important role, increasing the Lewis acidity of the grafted complexes in the order: $SiO_2 <$ BNO-OH $\cong$ gOOH $<$ gOH.

In order to study the influence of these boron nitride surfaces on the catalytic properties of the supported lanthanum complexes, we then evaluated the catalytic activity toward the homopolymerisation of ethylene and 1,3-butadiene, by using as catalysts the (BNO-O)-[La(CH$_3$)$_2$] (1BNO-O) and the (BNO-O)-[La(Cp)(CH$_3$)] (2BNO-O) complexes. Both compounds efficiently catalyse the ethylene homopolymerisation, displaying activation barriers which lie between those of the graphene-grafted and silica-grafted compounds. The Lewis acidity trend before established for the four grafted La compounds is therefore reflected in their catalytic activities which also increase in the order $SiO_2 <$ BNO-OH $\cong$ gOOH $<$ gOH. Concerning the 1,3-butadiene homopolymerisation reaction, similarly, both the 1BNO-O and 2BNO-O species are expected to behave as efficient catalysts, resulting as active as the graphene supported La systems, but more active than the silica grafted La analogues. Interestingly, the 1,4-cis 1,3-butadiene insertion is preferred over the 1,4-trans one, affording the 1,4-cis-polybutadiene polymer which results the only expected product, as previously reported for the gOO- and silica-supported La compounds.

In chapter 5, finally, considering the promising results obtained for the different polymerisations reactions catalysed by graphene-supported La compounds, we focused on the propene polymerisation by using as catalysts the three graphene-grafted lanthanum complexes (gO)-[La(CH$_3$)$_2$], (gO)-[La(Cp)(CH$_3$)] and (gO)-[La(Cp*)(CH$_3$)]. The study of the propene polymerisation reaction is a challenging topic, since the molecular lanthanide complexes usually afford, in the presence of propene, the allylic deactivation products instead of the polypropypene polymer. In the (gO)-[La(CH$_3$)$_2$] system, while from a kinetic point of view, the 1,2 and 2,1 insertion barriers are comparable with that of the allylic transfer process, from a thermodynamic point of view, the allylic product is more stable than the 1,2 and 2,1 insertion ones. In order to disfavour the allylic transfer reaction we decided to increase the steric hindrance around the metal centre. The (gO)-[La(Cp)(CH$_3$)] and (gO)-[La(Cp*)(CH$_3$)] complexes have been therefore considered by replacing one methyl with the more hindered Cp and Cp* ligands. The energy profiles computed with these more sterically hindered systems indicate that, although the energy of the allylic deactivation products decreases ongoing from the 1gO to the 2gO and 3gO compounds, this energy reduction is not large enough to disfavour the allylic deactivation with regard to the 1,2-insertion process.

In conclusion, this thesis work clearly demonstrates, by a DFT study, that functionalised graphene (gOH and gOOH) and boron nitride (BNO-OH) surfaces behave as good supports for the grafting of lanthanum complexes. As shown along the manuscript, these supports play two main roles: while they increase the Lewis acidity and therefore the reactivity of the grafted La systems compared to the oxygenated silica surfaces, they also act as bulky ligands, increasing the congestion around the metal centre. Graphene- and boron nitride-supported La complexes, therefore, may represent interesting target compounds, combining a high catalytic activity with the advantages of the supported catalysis.

## Septième partie

# Résumé de thèse

Les enjeux de la chimie auxquels la planète est confrontée en termes d'énergie et d'environnement augmentent la pression sur la communauté scientifique pour trouver des solutions catalytiques alternatives. Dans ce contexte changeant, la catalyse reste essentielle car, en principe, elle peut améliorer l'efficacité, la vitesse et la sélectivité de toute réaction chimique. La catalyse hétérogène est une branche importante de la catalyse et est considérée comme le choix idéal pour l'industrie chimique. En effet, les catalyseurs hétérogènes permettent la transformation efficace d'une large gamme de matières premières et de produits de base en raison de leur robustesse, de leur praticabilité opérationnelle et de leur recyclabilité. Les catalyseurs hétérogènes peuvent être divisés en plusieurs catégories : matériaux massif, oxydes métalliques tels que $CrO_x$, x = 1-3, $GaO_x$, x = 3/2, 3, $VO_x$, x = 3/2-5/2, etc[3] ou sulfures métalliques tels que $FeS_2$, ZnS, etc[4], zéolites ou aluminosilicates, tels que $Na_2Al_2Si_3O_{10}{\cdot}2H_2O$, *etc*) [5, 6], les nanoparticules métalliques supportées (*eg.* Au nanoparticules supportées sur $TiO_2$(111), ...),[7] et systèmes isolés sur des sites bien défini *i.e.* ions isolés, atomes, complexe moléculaire ou amas bimétalliques ancrés sur des supports de grande surface. Le point commun à tous les catalyseurs industriels hétérogènes est la difficulté de comprendre au niveau moléculaire la structure des sites actifs et les étapes élémentaires des processus catalytiques [9, 10], ce qui est principalement dû à la complexité intrinsèque de ces catalyseurs, due à la grande distribution et à la grande diversité des sites actifs. En outre, la caractérisation de ces catalyseurs peut s'avérer très complexe dans certains cas, nécessitant l'utilisation de nombreuses techniques de caractérisation. La catalyse hétérogène classique, principalement basée sur une approche par 'essais et erreurs', pourrait être considérée comme plus facile en termes d'avantages pratiques. Un des premiers exemples de catalyse hétérogène est la synthèse d'ammoniac à partir de $H_2$ et $N_2$, dans le procédé Haber Bosch, dont le développement a nécessité le test systématique d'environ 20 000 matériaux comme catalyseur.[15] Son mécanisme et la nature du site actif ont été élucidés plus tard, après des décennies de recherche par Ertl et ses collaborateurs, grâce au développement important de la science des surfaces [16].

La force des approches par structure-activité au niveau moléculaire a été reconnue très tôt dans le développement des catalyseurs hétérogènes [30, 31, 6, 32, 33]. Suite au développement rapide de la catalyse homogène, il y a environ 50 ans, les tentatives d'appliquer les mêmes approches à la catalyse hétérogène ont finalement abouti au domaine connu sous le nom de chimie organométallique de surface (SOMC).[29, 34, 35, 36, 37, 38, 39, 8, 40, 41] La recherche dans ce nouveau domaine a suscité beaucoup d'intérêt au cours des 25 dernières années, stimulée par la nécessité d'améliorer les catalyseurs existants et les progrès des méthodes spectroscopiques et informatiques, qui permettent une caractérisation structurelle très détaillée, étape essentielle pour le développement des catalyseurs. L'essence des SOMC est de traiter la surface d'un support, typiquement un oxyde métallique, comme un ligand rigide volumineux sur lequel des précurseurs moléculaires, tels que des complexes organométalliques, peuvent être greffés de manière covalente *via* une ou plusieurs liaisons M-O, afin de limiter leur mobilité et agglomération de surface. Les complexes moléculaires greffés peuvent être utilisés directement en catalyse ou : (i) transformés après greffage par un post-traitement thermique sous vide, sous gaz inertes ; (ii) modifiés par un traitement post-réaction pour incorporer de nouveaux ligands auxiliaires. Le traitement de la surface avant greffage peut en outre réguler la densité des fonctions OH par lesquelles les complexes seront greffés, contrôlant la densité de site des complexes greffés et empêchant ainsi des réactions indésirables telles que les processus de désactivation impliquant la dimérisation des intermédiaires réactifs [48] La liaison du complexe métallique aux groupes OH d'oxyde de surface du support peut modifier à la fois l'électrophilie du centre métallique et sa sphère de coordination. Chacun de ces effets a un impact sur l'activité, la sélectivité et la stabilité de ces catalyseurs bien définis, ce qui entraîne des activités et des stabilités différentes par rapport à celles observées dans des analogues homogènes étroitement liés.[49, 50] De la même manière, cette approche permet de préparer des espèces bien définies greffées en surface qui peuvent être entièrement caractérisées par des techniques modernes de caractérisation des solides/surfaces (analyse élémentaire, IR, UV, RMN, EXAFS, etc) [51, 52, 53, 54, 55, 57].

Différentes voies ont été développées ces dernières années pour le greffage de complexes inorganiques sur ce type de support : ici nous nous concentrerons uniquement sur le greffage direct. Le greffage direct d'un complexe $LnMX_x$ (X = R, $NR_2$, OR, Cl) sur un support partiellement déshydroxylé se fait par protonolyse d'au moins une liaison M-X par des groupes hydroxyles de surface (Surface-OH). Cette réaction conduit à la formation d'une espèce Surface-O-M-$LnX_{x-1}$ et à la libération d'une molécule HX. En fonction de la température de déshydroxylation, des espèces bipodales $(\text{Surface-O})_2$-M-$LnX_{x-2}$ ou tripodales $(\text{Surface-O})_3$-M-$LnX_{x-3}$ peuvent également être formées [121, 122, 123, 124, 125, 126]. Ces espèces greffées sont souvent désignées comme des sites bien définis ou uniques. Le greffage d'un précurseur métallique sur des supports d'oxyde nécessite des conditions anhydres et anaérobies strictes. Ceci est dû à la sensibilité générale de nombreux complexes métalliques à l'air et à l'eau en solution, les espèces de surface supportées sur une surface élevée présentant une sensibilité accrue.[127, 128, 129] Plusieurs complexes métalliques supportés, contenant i) des métaux de la gauche du tableau périodique (Zr, V, Ti, Hf, Ta, W, Cr, Mo),[37, 432, 130, 44, 131] ii) des métauc de la droite du tableau périodique (Ru, Rh, Ir, Pt)[20, 132, 121, 118, 133, 134, 49] et iii) des terres rares (Y, Sc, La-Lu) [135, 136] ont été décrits dans la littérature.

Parmi les métaux utilisés en catalyse, les complexes de terres rares ont fait l'objet d'un intérêt constant en raison de leur forte activité dans plusieurs domaines, tels que la polymérisation [88, 143, 144, 145] et la chimie fine,[146, 87, 148, 147] ainsi que de leur faible toxicité et de leur coût modéré. La série des lanthanides comprend les 15 éléments chimiques métalliques portant les numéros atomiques 57-71, du lanthane au lutécium. Ces éléments, ainsi que les éléments chimiquement similaires que sont le scandium et l'yttrium, sont souvent connus sous le nom d'éléments des terres rares, bien que les lanthanides et les éléments du groupe III diffèrent par leurs rayons ioniques et leur électronégativité. Tous les lanthanides sont des éléments du bloc f, correspondant au remplissage de la couche électronique 4f. Dans l'ensemble, leur configuration électronique peut s'écrire comme suit $[\text{Xe}]_{54}4\text{f}^n5\text{d}^16\text{s}^2$, avec n allant de 0 à 14. En solution, les lanthanides sont fortement oxopliles, formant des complexes stables avec des ligands fortement donneurs d'électrons contenant des atomes d'oxygène ou de fluor. Les ions les plus courants de la famille des lanthanides se trouvent au degré d'oxydation +III, bien que certains lanthanides aux degrés d'oxydation +II et +IV aient été décrits.[149] Dans ce travail, nous nous concentrerons sur les lanthanides au degré d'oxydation +III. En raison de leur degré d'oxydation +III,

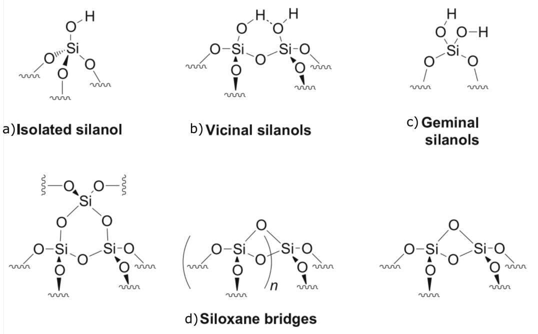

FIGURE 137: Schéma des différents types de groupes hydroxyles de surface et de ponts siloxanes présents à la surface de la silice avec a) les silanols isolés, b) les silanols vicinaux, c) les silanols géminés, et d) les ponts siloxanes.

les complexes considérés dans le manuscrit peuvent être assimilés à des composés $d^0$. Au degré d'oxydation +III, le centre métallique du lanthanide ne dispose pas d'électrons pour réaliser les mécanismes d'activation nécessitant la modification de son état d'oxydation, comme par exemple les réactions d'addition oxydative. Cela leur permet de réagir efficacement par des mécanismes qui fonctionnent sans modifier l'état d'oxydation, comme les processus de métathèse des liaisons. La réaction expérimentale de greffage de dérivés homoleptiques du type $[Ln(N(SiMe_3)_2)_3]$ (Ln = Y, La, Nd, Sm) a déjà été décrite par Anwander et ses collaborateurs en 1997[180]. Ces composés réagissent avec les groupes hydroxyles de la silice, conduisant à la formation d'une liaison covalente lanthanide-siloxyde avec la protonolyse concomitante de la liaison lanthanide-amino. La nature du mode de greffage de ces composés greffés de silice a été caractérisée par la thermogravimétrie, la spectroscopie IR et RMN. Leur réactivité vis-à-vis de l'oxyde de triphénylphosphine ($O{=}PPh_3$), utilisé comme sonde pour mesurer l'acidité du centre du métal, a été signalée par Gauvin *et al.*.[87] Comme l'ont montré Drago et ses collaborateurs, une différence positive de déplacement chimique par RMN de $^{31}P$ ($\Delta\delta$) entre l'$OPR_3$ physisorbé et chimisorbé indique une coordination vers un site acide, la force de l'interaction étant en corrélation avec l'ampleur de la différence. Sur la base de ces rapports expérimentaux, différents modes de coordination du composé $(SiO_2)$-$[Ln(N(SiMe_3)_2)_3]$, avec $SiO_2$ prétraité à 200 °C et 700 °C, ont donc été calculés et comparés aux résultats expérimentaux.[135, 136] Ces études théoriques ont montré que la formation d'une liaison covalente SiO-Ln nécessite la présence de groupes hydroxyle à la surface, la nature des groupes silanol à la surface de la silice influençant la géométrie et la stabilité des complexes greffés. Différentes espèces de La greffées sur la silice ont été calculées : (i) des complexes mono-greffés en présence de groupes silanol isolés et géminés, (ii) des complexes bi-greffés en présence de deux silanols vicinaux interagissant par liaison H et (iii) des complexes tri-greffés obtenus par ouverture d'un ou deux ponts siloxanes adjacents *via* le transfert d'un ligand au niveau du complexe métallique à la surface de la silice (voir figure 137). Les fréquences vibratoires IR et les deplacements chimiques de RMN $^{31}P$ calculés pour les adduits $OPPh_3$ correspondants affichent des valeurs similaires, indiquant un petit effet du mode de greffage sur l'acidité de Lewis du centre du métal.

Les propriétés catalytiques des complexes de lanthanides greffés sur la silice ont également été étudiées, à la fois théoriquement et expérimentalement, en considérant différentes réactions telles que la dimérisation des alcynes, l'hydrosilylation des alcènes, l'hydroamination/cyclisation intramoléculaire des aminoalcènes et les réactions de polymérisation de l'éthylène, de la caprolactone, de l'isoprène, du méthacrylate de méthyle et du butadiène.[182, 144, 183, 184, 166] Ces études ont révélé que le greffage d'un complexe moléculaire sur des surfaces de silice apporte une modification significative de ses propriétés catalytiques, par rapport à son analogue moléculaire.[135, 136, 185] La polymérisation du métacrylate de méthyle par un catalyseur au néodyme supporté par la silice conduit en effet à la formation d'un polymère modérément isotactique alors que le précurseur moléculaire génère un polymère modérément syndiotactique.[161, 184] Selon une étude DFT, réalisée sur le même système, la préférence expérimentale pour un polymère modérément isotactique s'explique par les conformations préférées des produits d'addition énolate-monomère métallique par rapport aux premières insertions[166].

Le développement de catalyseurs de polymérisation hautement efficaces et sélectifs, pour la synthèse d'homo- ou de copolymères de haute performance avec des structures contrôlées avec précision et les propriétés désirées, est encore aujourd'hui un sujet de première importance.[186, 187, 188, 189, 190] Parmi les différents types de polymérisation (croissance par étapes, croissance en chaîne, photopolymérisation, *etc*), dans ce travail de doctorat, nous nous concentrerons uniquement sur les réactions de polymérisation par croissance en chaîne. La polymérisation par croissance en chaîne est une technique de polymérisation dans laquelle des molécules de monomères insaturés s'ajoutent au site actif d'une chaîne de polymère en croissance, une à la suite de l'autre. En général, la polymérisation par croissance en chaîne implique trois étapes importantes : i) l'initiation, conduisant, par activation du premier monomère, à la formation du centre actif ou des espèces de propagation, ii) la propagation, impliquant l'insertion successive des monomères, avec l'augmentation de la chaîne de polymère et iii) la terminaison, arrêtant le processus de croissance du polymère. Il existe plusieurs façons d'initier la polymérisation en chaîne qui dépendent non seulement de la nature du monomère mais aussi de la nature du centre actif. Sur ce travail, deux processus de polymérisation majeurs seront étudiés : la polymérisation par coordination-insertion et la polymérisation par ouverture de cycle. L'étape de terminaison peut être spontanée (selon la nature des centres actifs et le mode de polymérisation considéré). Par définition, un polymère est une substance ou un matériau composé d'un grand nombre d'unités similaires liées entre elles tout en formant une chaîne.

La réactivité des complexes lanthanides cationiques dans les réactions catalytiques et stoechiométriques a souvent conduit à une amélioration de l'activité par rapport à leurs analogues neutres, permettant dans certains cas, le développement de voies de synthèse totalement nouvelles.

L'utilisation des effets de support pour améliorer ou modifier le résultat régio- ou stéréochimique des réactions sélectives apparaît actuellement comme un domaine d'intérêt, même si le nombre d'exemples disponibles est limité. Pour n'en citer que quelques-uns, Bochmann et ses collaborateurs en 2005.[145] et Gauvin et ses collaborateurs en 2006[88] ont rapporté l'activité catalytique de complexes de $Ln[N(SiMe_3)_2]_3$ (Ln=Sc, Y, La, Nd, Sm, Dg, Dy) greffés sur de la silice déshydroxylée à 250, 500 ou 700 °C (figure 138). Ces études ont montré que, en mélangeant le catalyseur à base de silice et l'activateur alkylaluminium $Al(^iBu)_3$ (TIBA), tous les différents composés lanthanides se sont avérés actifs dans l'homopolymérisation de l'éthylène et du 1,3-

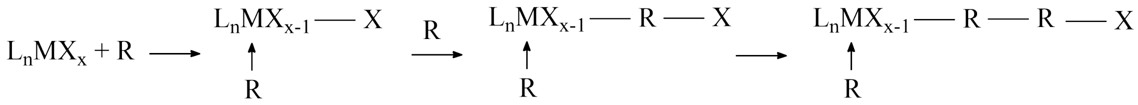

Figure 138: Représentation schématique d'un mécanisme de polymérisation par coordination-insertion.

butadiène.

Sur la base de ce qui a été rapporté ci-dessus, nous avons remarqué que les supports utilisés dans les SOMC jouent un double rôle : i) ancrer le catalyseur à la surface pour former des sites actifs bien définis, dans notre cas cela correspond à l'immobilisation *via* une fixation covalente se produit par une liaison directe surface-métal, pour cela il faut être thermiquement et mécaniquement stable et ne pas générer de réactions parallèles, ii) agir comme un ligand, *i.e.* il a pour fonction de moduler l'activité catalytique du métal auquel il est lié. Comme nous l'avons vu, la silice est une surface qui permet de former des sites actifs bien définis, selon la méthode de préparation, mais qui a une influence limitée sur l'acidité de Lewis des complexes métalliques, ce qui a un impact important sur l'activité catalytique d'un certain nombre de réactions. En revanche, l'utilisation de l'alumine comme support augmente l'acidité de Lewis des complexes, mais en raison de sa complexité, il est difficile de former des sites actifs bien définis et uniformes sur la surface, et entraîne souvent une grande diversité dans les complexes métalliques formés et donc dans les réactions produites. C'est pourquoi, dans ce projet de thèse, nous avons décidé, après une description de la méthode DFT dans la partie II, d'explorer de nouveaux supports potentiels qui pourraient à la fois i) produire des sites actifs bien définis et ii) régler avec précision les propriétés catalytiques du complexe métallique formé. Deux surfaces ont été identifiées comme étant capables de combiner toutes ces propriétés, chacune d'entre elles sera développée dans un chapitre qui leur sera consacré ainsi qu'à leur réactivité : Partie III : systèmes de lanthane sur support de graphène ; Partie IV : complexes de lanthane sur support de nitrure de bore. Enfin, dans la partie V, nous explorerons l'activité catalytique des complexes greffés sur le support mentionné ci-dessus sur la polymérisation du propène, qui représentent une réaction de très grande importance dans l'industrie des polymères.

Dans ce rapport, nous avons choisi l'approche moléculaire, afin de réaliser des études de réactivité sur ces systèmes. En effet, l'étude des mécanismes réactionnels par la chimie quantique fournit des résultats plus précis qui nous permettent d'élucider ces mécanismes réactionnels en identifiant les différents états de transition. Dans le cas des systèmes périodiques, l'identification de l'état de transition est beaucoup plus complexe en raison de la nature des algorithmes utilisés. Tous les calculs de DFT ont été effectués avec Gaussian 09 [272] Les calculs ont été effectués au niveau de la théorie DFT en utilisant la fonction hybride B3PW91. [278, 276, 275, 274, 277, 273] Les optimisations de géométriques ont été réalisées sans aucune restriction de symétrie. Les fréquences vibratoires ont été systématiquement calculées afin de caractériser la nature des points stationnaires. Le potentiel effectif de coeur de Stuttgart [279, 280] et les ensembles de base associés ont été utilisés pour le silicium, le titane et le lanthane. Pour l'atome de P, Si, Ti et La, les ensembles de base ont été augmentés par un ensemble de fonctions de polarisation

($\zeta_d$ = 0,340 pour P, $\zeta_d$ = 0,284 pour Si $\zeta_d$ = 0,284 pour Ti et $\zeta_f$ = 0,591 pour La). [281] Les atomes H, N, C et O ont été traités avec un double jeu de bases 6-31G(d,p).[282, 283] Parmi les différentes théories disponibles pour calculer les tenseurs de blindage chimique, la jauge incluant la méthode de l'orbite atomique (GIAO) a été adoptée pour les nombreux avantages qu'elle présente.[284, 285, 286] La même méthodologie a été utilisée dans des études précédentes impliquant des systèmes greffés, montrant que les résultats théoriques sont assez précis par rapport aux valeurs expérimentales avec une erreur inférieure à 15% pour $^{29}$Si,[136] 10% pour $^{31}$P[287] et $^{17}$O [288, 117, 289] et 5% pour $^{1}$H[290] et $^{13}$C. [290] La densité d'électrons et la distribution des charges partielles ont été examinées en termes d'unités de liaison de paires d'électrons localisées à l'aide du programme NBO. Par cette méthode, l'ensemble de base des orbitales atomiques d'entrée est transformé via les orbitales atomiques naturelles (NAO) et les orbitales hybrides naturelles (NHO) en orbitales de liaison naturelles (NBO), qui correspondent aux éléments localisés à un centre ("paire unique") et à deux centres ("liaison") de la structure de Lewis. Toutes les interactions possibles entre les NBO de type Lewis "remplies" (donneuses) et les NBO non Lewis "vides" (acceptrices), ainsi que leur quantification énergétique (énergie de stabilisation), ont été obtenues par une analyse de la théorie des perturbations du second ordre de la matrice de Fock.

Dans la partie III, nous montrons que le composé de lanthanide [La(N(SiMe$_3$)$_2$)$_3$] peut être facilement greffé sur des surfaces fonctionnalisées au graphène-OH et -COOH (figures 139 et 141), ce qui permet d'obtenir deux composés stables monogreffés : le système monocoordonné (gO)-[La(N(SiMe$_3$)$_2$)$_2$], présentant une interaction stabilisante entre le métal La et la surface de graphène sous-jacente et l'espèce bicoordonnée (gOO)-[La(N(SiMe$_3$)$_2$)$_2$] avec les deux oxygènes du groupe carboxylate liés au métal La. Alors que dans le système gO, l'interaction La-surface fournit une assistance électronique modulaire de la surface, augmentant cependant l'encombrement stérique autour du métal, dans le composé (gOO)-[La(CH$_3$)$_2$], en revanche, la bicordination du groupe carboxo force le complexe métallique à s'élever de la surface, fournissant un système plus rigide mais moins encombré stériquement (voir figure 140).

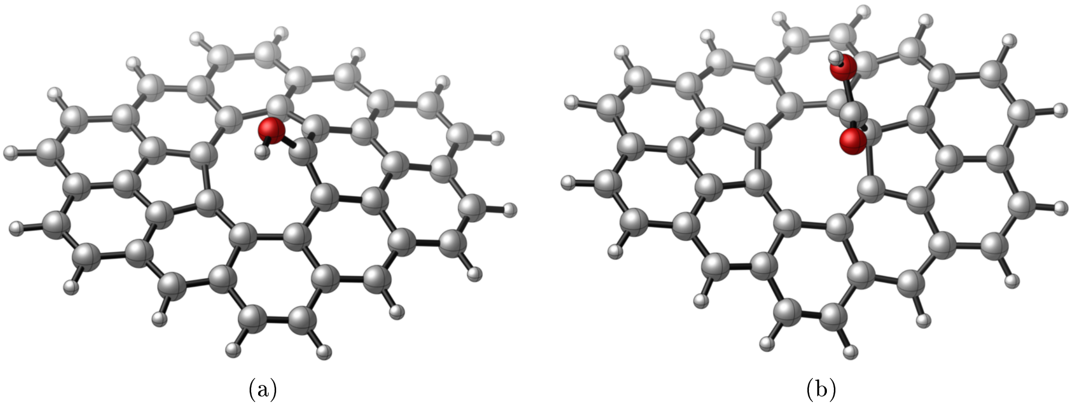
(a)

(b)

Figure 139: Modèles de surface fonctionnalisés de graphène obtenus à partir du modèle polycyclique $C_{42}H_{16}$; a) le modèle $[C_{41}H_{16}\text{-}OH]^+$ avec une lacune C lié à un groupe hydroxy, (gOH), comme modèle de la fonction phénol et b) le modèle $[C_{41}H_{16}\text{-}OOH]^+$ avec deux lacunes C lié à un groupe carboxylique, (gOOH), comme modèle de la fonction carboxylique.

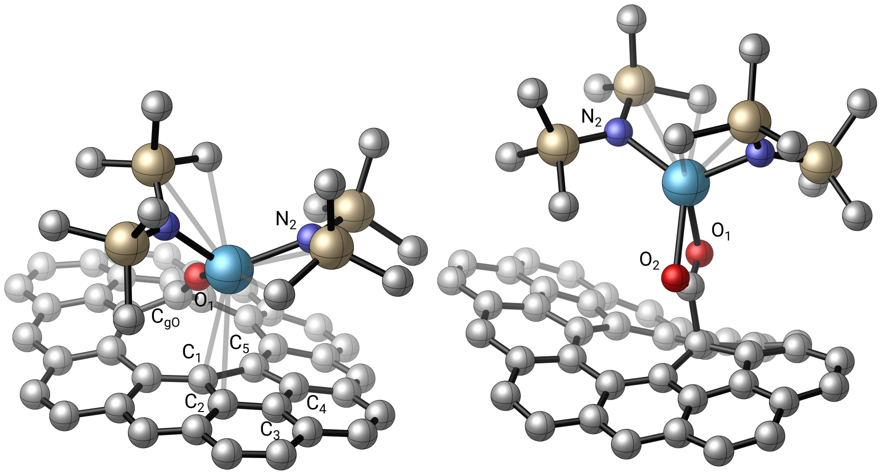

(a) (gO)-[La(N(SiMe$_3$)$_2$)$_2$] (C$^{graf}{}_{gO}$) (b) (gOO)-[La(N(SiMe$_3$)$_2$)$_2$] (C$^{graf}{}_{gOO}$)

FIGURE 140: Structures des produits finaux impliqués dans la réaction de greffage de [La(N(SiMe$_3$)$_2$)$_3$] sur les surfaces fonctionnalisées au graphène de gOH et de gOOH (bleu clair : La, bleu foncé : N, blanc : H, rouge : O). Par souci de clarté, tous les H des composés greffés en La ont été omis, à l'exception des atomes de graphène-OH et de graphène-COOH.

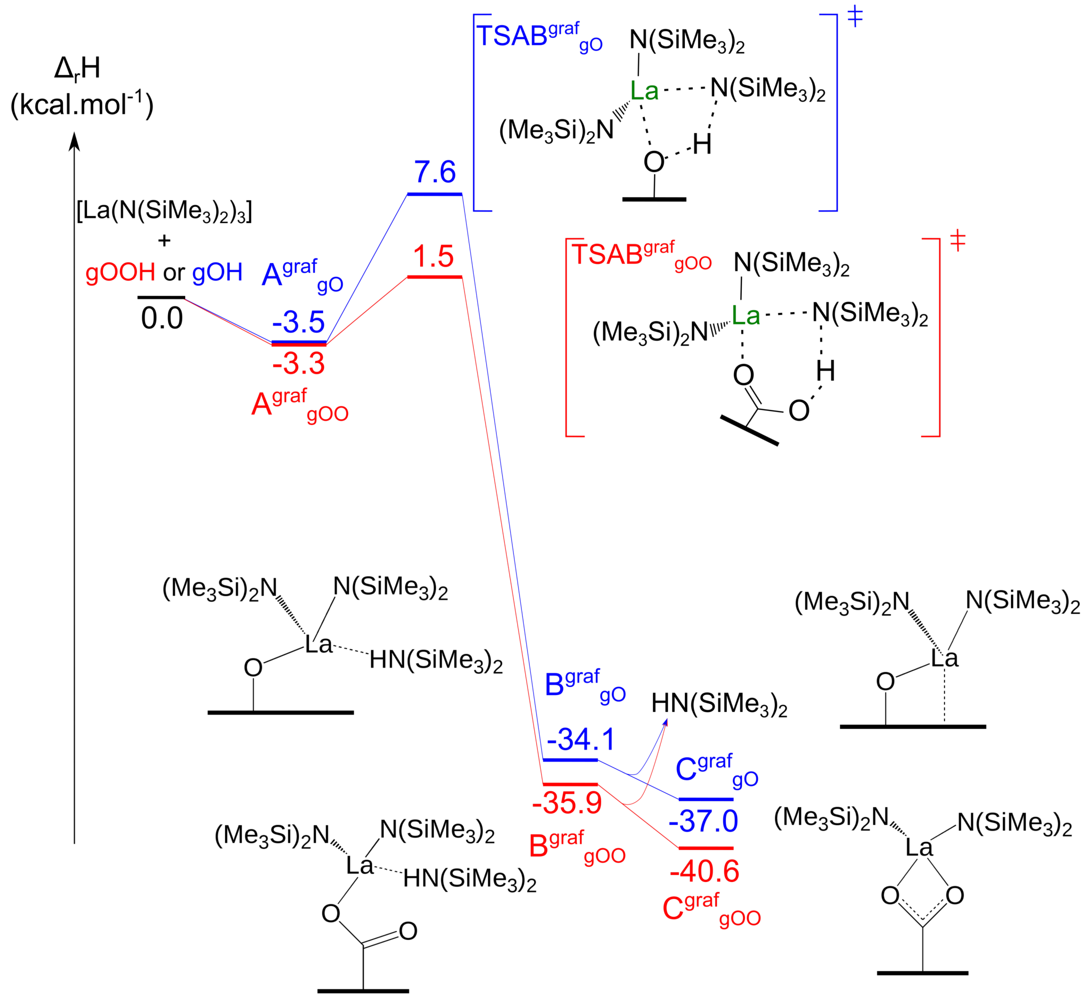

Figure 141: Profil énergétique calculé pour la greffe du complexe [La(N(SiMe$_3$)$_2$)$_3$] sur les surfaces fonctionnalisées de gOH et de graphène gOOH.

Comme pour les approches expérimentales, la coordination de l'oxyde de triphénylphosphine (O=PPh$_3$) (figure 142) a été calculée comme une sonde de l'acidité de Lewis du métal. Les valeurs spectroscopiques (IR et RMN tableau 18) obtenues pour les espèces (gO)-[La(N(SiMe$_3$)$_2$)$_2$(O=PPh$_3$)] et (gOO)-[La(N(SiMe$_3$)$_2$)$_2$(O=PPh$_3$)] correspondantes indiquent que les complexes silylamido de lanthane greffés au graphène sont plus acides selon Lewis que les analogues greffés à la silice, la nature de la surface jouant manifestement un rôle important.

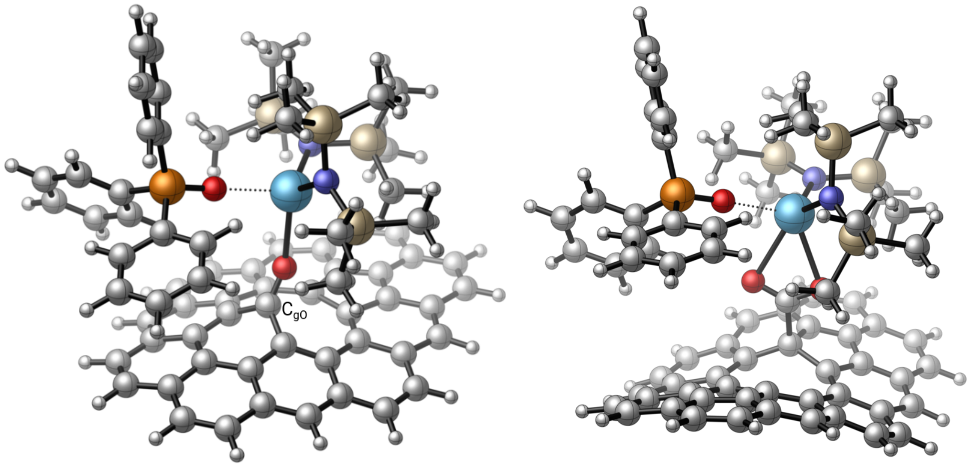

(a) (gO)-[La(N(SiMe$_3$)$_2$)$_2$(O=PPh$_3$)] (b) (gOO)-[La(N(SiMe$_3$)$_2$)$_2$(O=PPh$_3$)]

Figure 142: Structures des adduits OPPh$_3$ hexaméthyldisilylamido La greffés sur a) le gO et b) la surface de graphène gOO.

Table 18: Comparaison entre les fréquences vibratoires théoriques (en cm$^{-1}$), et les $^1$H, $^{13}$C and $^{31}$P deplacements chimiques RMN (en ppm) d'un ligand libre OPPh$_3$ et de la molécule coordonnée OPPh$_3$ dans différents produits d'addition OPPh$_3$ hexaméthyldisilylamido La greffés sur les surfaces de graphène gO et gOO et sur SiO$_2$ (moyenne entre toutes les espèces mono- et bi-greffées précédemment signalées[135]). Les deplacements chimiques $^1$H et $^{13}$C sont donnés par rapport au TMS (blindage chimique théorique: 31.64 et 195.35 ppm, respectivement, pour les atomes de $^1$H and $^{13}$C. Les déplacements chimiques $^{31}$P sont donnés par rapport à l'acide phosphorique (déplacement chimique théorique: 380.6 ppm). R = SiMe$_3$,(a) x = 1 or 2(b) Reference [55].(c) Attendu mais non détecté (voir reference [55]).

| | Nombres d'onde (en cm$^{-1}$) | | |
|---|---|---|---|
| | $\overline{\nu}_{C-H}$ | $\overline{\nu}_{C=C}$ | $\overline{\nu}_{O=P}$ |
| O=PPh$_3$ | [3065-3095] | [1416-1592] | 1177 |
| (gO)-[La(NR$_2$)$_2$(O=PPh$_3$)] | [3184-3240] | [1471-1655] | 1039 |
| (gOO)-[La(NR$_2$)$_2$(O=PPh$_3$)] | [3193-3230] | [1475-1655] | 1047 |
| (SiO$_2$)-[La(NR$_2$)$_2$(O=PPh$_3$)](a) | [2938-3107] | [1416-1592] | [1118-1152] |
| (SiO$_2$)-[La(NR$_2$)$_2$(O=PPh$_3$)]-exp(b) | ca. 3066 | [1440-1593] | [1120-1180](c) |

| | Déplacement chimique (en ppm) | | |
|---|---|---|---|
| | $\delta_{H_{Phenyl}}$ | $\delta_{C_{Phenyl}}$ | $\delta_P$ |
| O=PPh$_3$ | 7.7 | 124.7/129.9 | 25.7 |
| (gO)-[La(NR$_2$)$_2$(O=PPh$_3$)] | 7.3 | [123.5/127.8 | 56.0 |
| (gOO)-[La(NR$_2$)$_2$(O=PPh$_3$)] | 7.4 | 123.6/127.8 | 53.4 |
| (SiO$_2$)-[La(NR$_2$)$_2$(O=PPh$_3$)](a) | [7.9-8.0] | 123.5/129.0 | [40.3-47.6] |
| (SiO$_2$)-[La(NR$_2$)$_2$(O=PPh$_3$)]-exp(b) | 7.4 | 128.4/132.5 | 39.1 |

Afin de comprendre le rôle du support, nous avons étudié l'activité catalytique des composés La supportés par le graphène vers l'homo- et la co-polymérisation de l'éthylène et du 1,3-butadiène, en utilisant les complexes alkyles (gO)-[La(CH$_3$)$_2$] (1gO) et (gOO)-[La(CH$_3$)$_2$] (1gOO) (figure 143) comme modèles des espèces actives La supportées par le graphène. Les

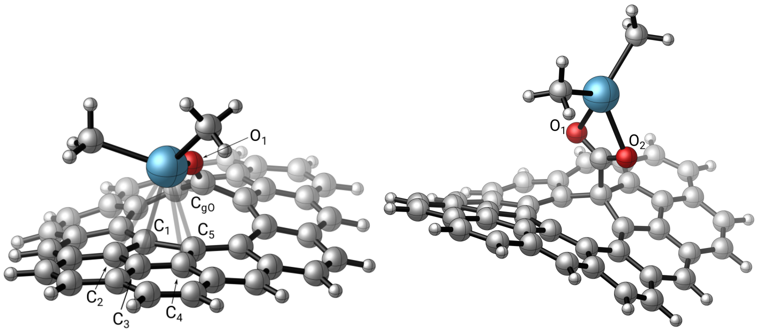

(a) (gO)-[La($CH_3$)$_2$] (1gO) (b) (gOO)-[La($CH_3$)$_2$] (1gOO)

Figure 143: Structures des composés (a) (gO)-[La($CH_3$)$_2$] et (b) (gOO)-[La($CH_3$)$_2$].

deux composés catalysent efficacement l'homopolymérisation de l'éthylène, présentant des barrières d'activation qui sont nettement inférieures à celles signalées pour les composés greffés à la silice. On prévoit donc que les surfaces de graphène jouent un rôle important, augmentant l'acidité de Lewis et donc la réactivité des systèmes La greffés par rapport aux surfaces de silice oxygénée.

Nous avons également montré que si dans le modèle gOO la polymérisation de l'éthylène peut avoir lieu sur les deux bras, dans le modèle gO, en revanche, on n'observe qu'une polymérisation sur un seul bras, l'interaction du métal avec la surface de graphène augmentant l'encombrement stérique autour du métal (figure 144). En ce qui concerne l'homopolymérisation du 1,3-butadiène, les deux complexes de La greffés au graphène sont censés être efficace dans ça polymérisation (figure 145) et, en raison de leur acidité de Lewis plus élevée, ils sont plus actifs que les analogues de La greffés à la silice. Dans le modèle gOO, l'insertion de 1,4-cis 1,3-butadiène est préférée à celle de 1,4-trans, ce qui donne de préférence un polymère 1,4-cis-polybutadiène, comme indiqué précédemment pour les composés La à base de silice. Differemment, le modèle gO insère le 1,4-cis ou le 1,4-trans 1,3-butadiène sans distinction, donnant lieu à un polymère de 1,4-polybutadiène aléatoire. La stéréosélectivité de la réaction de polymérisation du 1,3-butadiène est donc différente pour le modèle gO par rapport aux systèmes à support de gOO et de silice, ce qui souligne une fois de plus l'influence du support sur le résultat de la réaction de polymérisation. Le comportement catalytique du 1gO et du 1gOO a finalement été étudié dans la réaction de copolymérisation de l'éthylène et du 1,3-butadiène. Nous avons montré que pour les complexes gO et gOO, l'insertion des monomères 1,4-cis 1,3-butadiène est favorisée par rapport à celle de l'éthylène, en raison de la formation de produits allyliques très stables. En effet, la stabilité supérieure des produits allyliques par rapport aux produits alkyles conduit la réaction vers l'insertion exclusive de 1,3-butadiène, empêchant toute réaction de copolymérisation alternée. En conclusion, les surfaces de graphène fonctionnalisées constituent donc des supports efficaces pour les composés organométalliques lanthanides. Ces surfaces de graphène sont susceptibles d'augmenter l'acidité de Lewis du métal La, jouant ainsi un rôle actif dans l'activité catalytique des complexes La supportés. Les composés alkyles de La supportés par le graphène catalysent efficacement l'homopolymérisation de l'éthylène et du 1,3-butadiène, avec des activités et des stéréosélectivités qui dépendent de la nature et du mode de coordination du support du graphène.

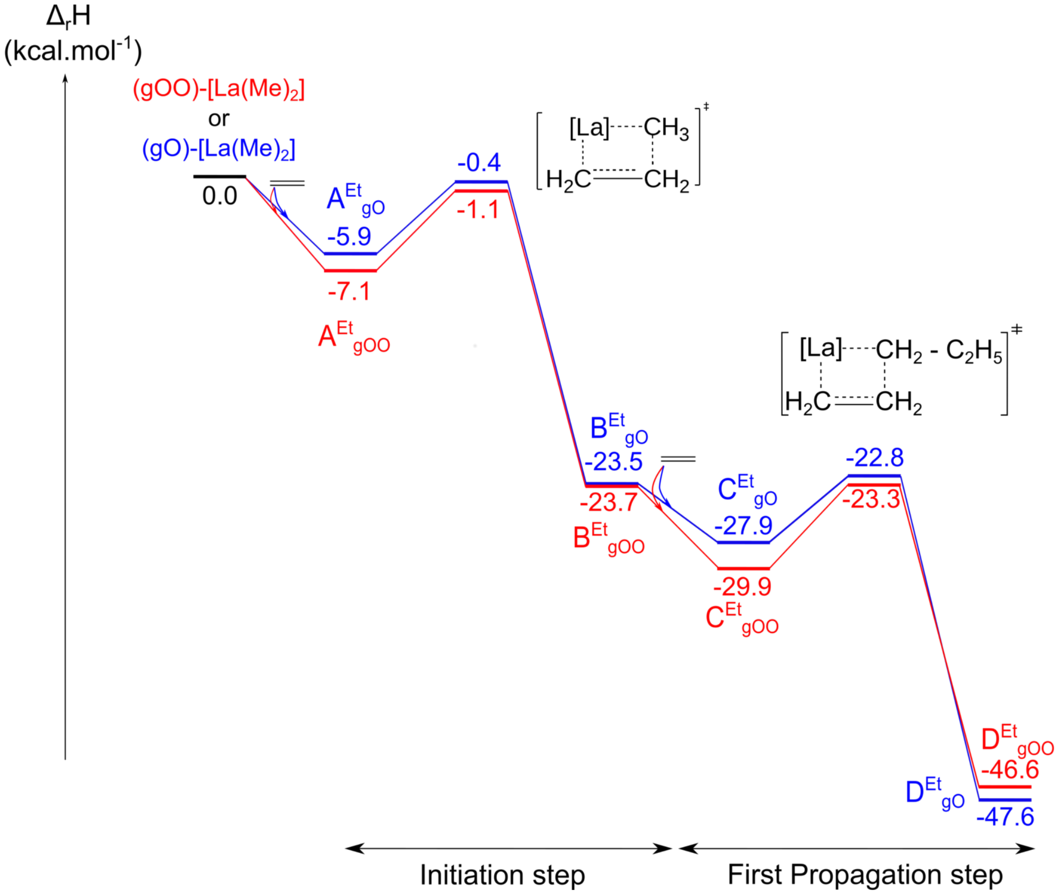

Figure 144: Profil d'enthalpie de réaction de l'initiation et de la première étape de propagation de l'homopolymérisation de l'éthylène sur la même liaison La-Me.

Nous avons ensuite exploré l'activité catalytique de ces mêmes complexes alkyles ((gO)-[La($CH_3$)$_2$] (1gO) et (gOO)-[La($CH_3$)$_2$] (1gOO)) sur l'homopolymérisation du styrène (figure 146) et la copolymérisation de l'éthylène et du styrène. Les trois premières réactions d'insertion ont été étudiées, montrant que les deux composés catalysent efficacement l'homopolymérisation du styrène. Les barrières calculées sont comparables à celles obtenues pour le complexe de scandium cationique hautement actif du groupe de Hou[226], une activité plus élevée étant attendue pour le système (gOO)-[La($CH_3$)$_2$], attribuée à la congestion moins forte autour du métal. Quant à la polymérisation de l'éthylène et du butadiène, les surfaces de graphène devraient jouer un rôle important, en augmentant l'acidité de Lewis et donc la réactivité du La greffé. En ce qui concerne la stéréosélectivité, on constate une préférence pour la formation d'un styrène syndiotactique pour les deux catalyseurs, et dont la formation est contrôlée thermodynamiquement. Le comportement catalytique de 1gO et 1gOO a finalement été étudié dans la réaction de copolymérisation de l'éthylène et du styrène. Nous avons montré que si pour le catalyseur gOO-La, la formation d'un

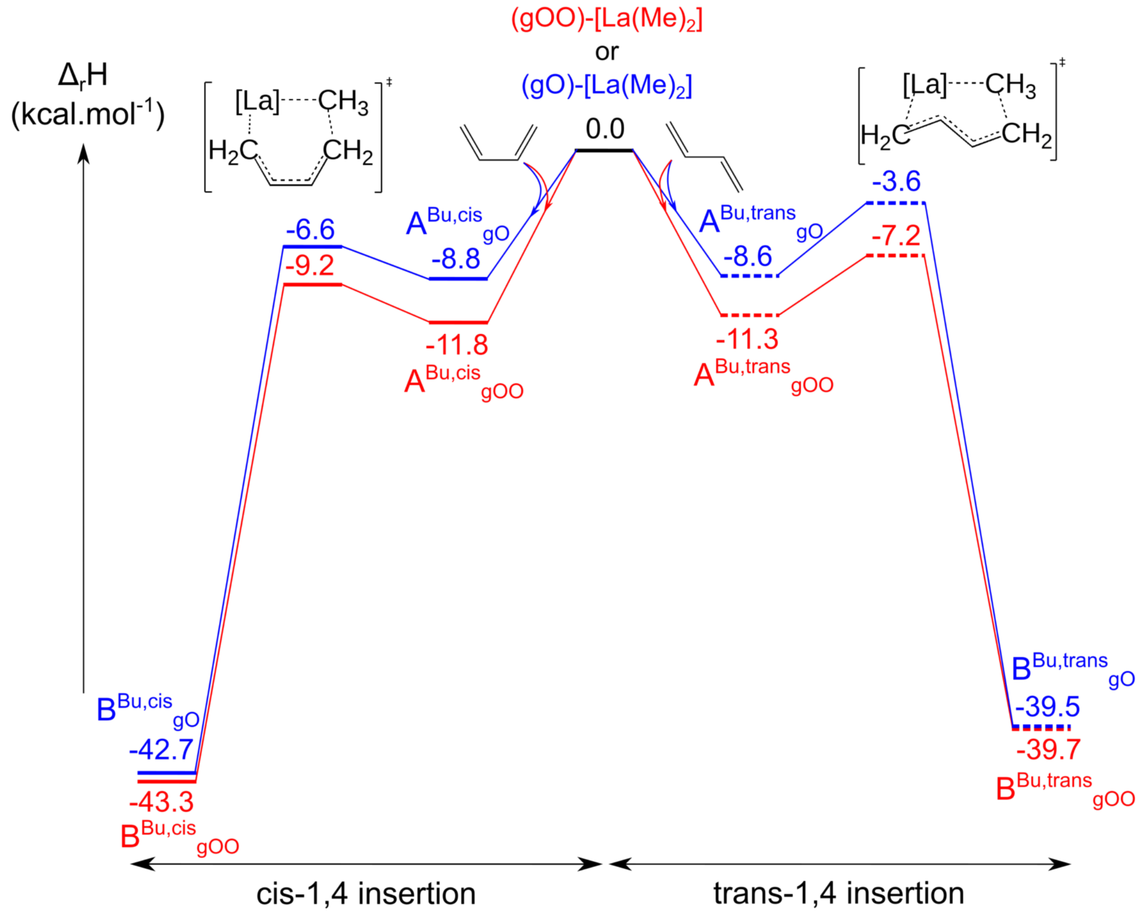

Figure 145: Profil d'enthalpie calculé pour la première insertion de monomère de la réaction d'homopolymérisation du 1,3-butadiène médiée par (gO)-[La(CH$_3$)$_2$] (1gO) et (gOO)-[La(CH$_3$)$_2$] (1gOO).

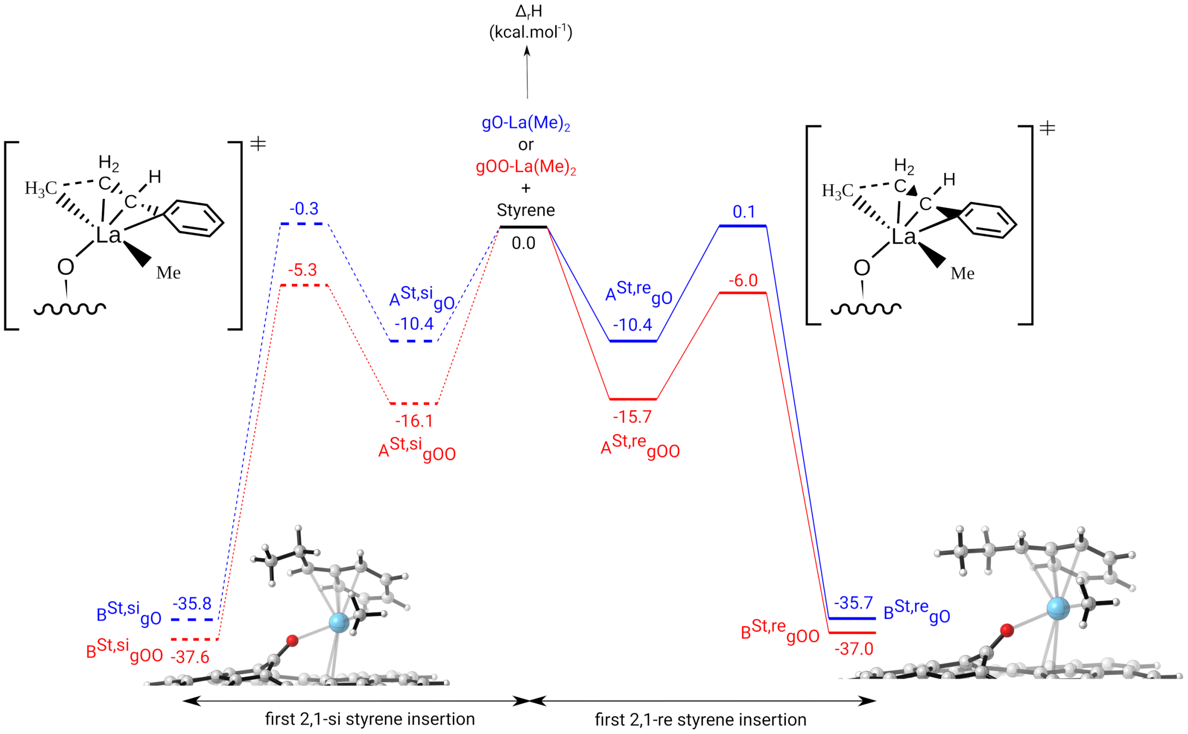

Figure 146: Profil d'enthalpie calculé pour la première injection de 2,1 de styrène sur la liaison La-Me à température ambiante. La voie bleue correspond au catalyseur greffé sur l'alkoxy alors que la voie rouge correspond au carboxy greffé.

copolymère est très peu probable car l'insertion de styrène est préférée pour les deux premières insertions, pour les catalyseurs gO-La, en revanche, la formation de polystyrène avec une faible quantité d'éthylène peut être envisagée.

Dans la dernière partie du chapitre III, nous avons enfin étudié la réaction contrôlée rac-BL ROP en utilisant comme catalyseurs quatre complexes de lanthane différents, c'est-à-dire la molécule $[La(BH_4)_3(THF)_3]$, le composé supportée sur silice $(\equiv SiO)$-$[La(BH_4)_2(THF)_2]$ et les composés supportés par le graphène (gO)-$[La(BH_4)_2(THF)_2]$ et (gOO)-$[La(BH_4)_2(THF)_2]$ (figure 147).

Différemment de l'espèce $(\equiv SiO)$-$[La(BH_4)_2(THF)_2]$, qui catalyse mal la réaction BL ROP, les systèmes (gO)-$[La(BH_4)_2(THF)_2]$ et (gOO)-$[La(BH_4)_2(THF)_2]$ (figure 148) sont susceptibles de polymériser efficacement le monomère BL, affichant la même efficacité que le composé homogène $[La(BH_4)_3(THF)_3]$ (3). Comme pour les approches expérimentales, la coordination de l'oxyde de triphénylphosphine ($O{=}PPh_3$) a été calculée comme une sonde de l'acidité de Lewis du métal. Les valeurs spectroscopiques (IR et RMN) obtenues pour le composé correspondant $(\equiv SiO)$-$[La(BH_4)_2(THF)(OPPh_3)]$, Les composés (gO)-$[La(BH_4)_2(THF)(OPPh_3)]$ et (gOO)-$[La(BH_4)_2(THF)(OPPh_3)]$ indiquent que les complexes de lanthanides greffés au graphène sont plus acides de Lewis que les analogues greffés à la silice, la nature de la surface jouant clairement un rôle important. Selon une analyse approfondie des profils enthalpiques, l'étape qui différencie

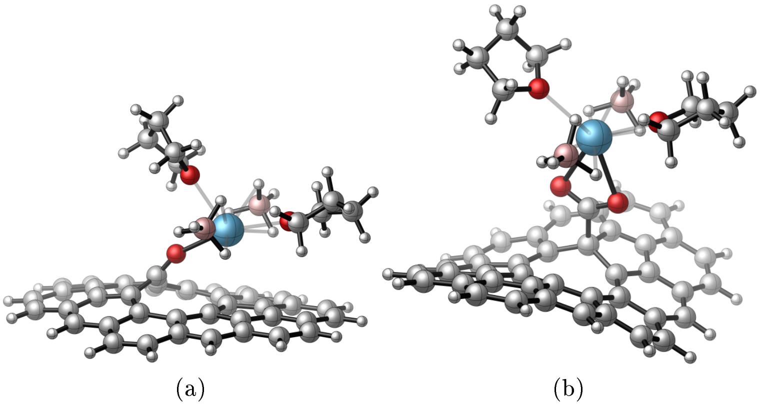

Figure 147: Structures des composés greffés (a) (gO)-$[La(BH_4)_2(THF)_2$ et (b) (gOO)-$[La(BH_4)_2(THF)_2]$.

l'activité catalytique des quatre composés correspond au premier transfert d'hydrure $BH_4$ vers le carbone carbonyle du monomère BL. Comme observé dans les états de transition correspondants, en effet, alors que les complexes moléculaires et greffés au graphène activent efficacement le monomère BL en fournissant un transfert d'hydrure $BH_4$ efficace, l'analogue greffé à la silice active mal le monomère BL, rendant le transfert d'hydrure plus contraint, avec l'augmentation conséquente de la barrière d'activation correspondante. Ceci est conforme à la tendance de Lewis en matière d'acidité, qui montre que plus le caractère acide de Lewis du centre métallique est élevé dans l'état de transition concerné, plus l'activation du monomère BL est forte et donc plus le transfert d'hydrure $BH_4$ est efficace. Concernant la stéréosélectivité de la réaction, enfin, les calculs suggèrent la formation de polymères préférentiellement atactiques, l'insertion d'un monomère BL, dans sa configuration R ou S, fournissant des valeurs d'enthalpie très similaires dans les étapes d'initiation et de propagation. En conclusion, nous avons donc montré que les surfaces gOH et gOOH du graphène jouent un rôle important dans l'amélioration de l'acidité de Lewis et donc de l'activité catalytique des complexes greffés de La correspondants. Les complexes de borohydrure de La supportés par du graphène peuvent donc représenter des composés cibles intéressants, combinant la forte activité catalytique de la réaction rac-BL ROP avec les avantages de la catalyse hétérogène.

Dans le chapitre IV, nous avons montré que le greffage du complexe $[La(N(SiMe_3)_2)_3]$ sur la surface BN à fonction hydroxy (BNH-OH) entraîne l'échange d'un ligand amido $N(SiMe)_3$ par un ligand hydroxy, avec la libération du composé $[La(N(SiMe_3)_2)_2(OH)(HN(SiMe_3)_2)]$ et la réaromatisation de la surface non fonctionnalisée du h-BN (figure 149 et 150). Nous avons ensuite montré une deuxième surface BN contenant un défaut de vacance sur la surface BN, *i.e.*, un groupe fonctionnel B-O-B et $N_2$-B(OH). Le composé lanthanide $[La(N(SiMe_3)_2)_3]$ peut être facilement greffé sur cette surface fonctionnalisée BNO-OH, ce qui permet d'obtenir des composés monogreffés stables (figure 151). Comme pour les approches expérimentales, la coordination de l'oxyde de triphénylphosphine ($O{=}PPh_3$) a été calculée comme une sonde de l'acidité de Lewis du métal. Les valeurs spectroscopiques (IR et RMN figure 19) obtenues pour les espèces correspondantes (BNO-O)-$[La(N(SiMe_3)_2)_2(O{=}PPh_3)]$ (figure 152) indiquent que l'acidité de

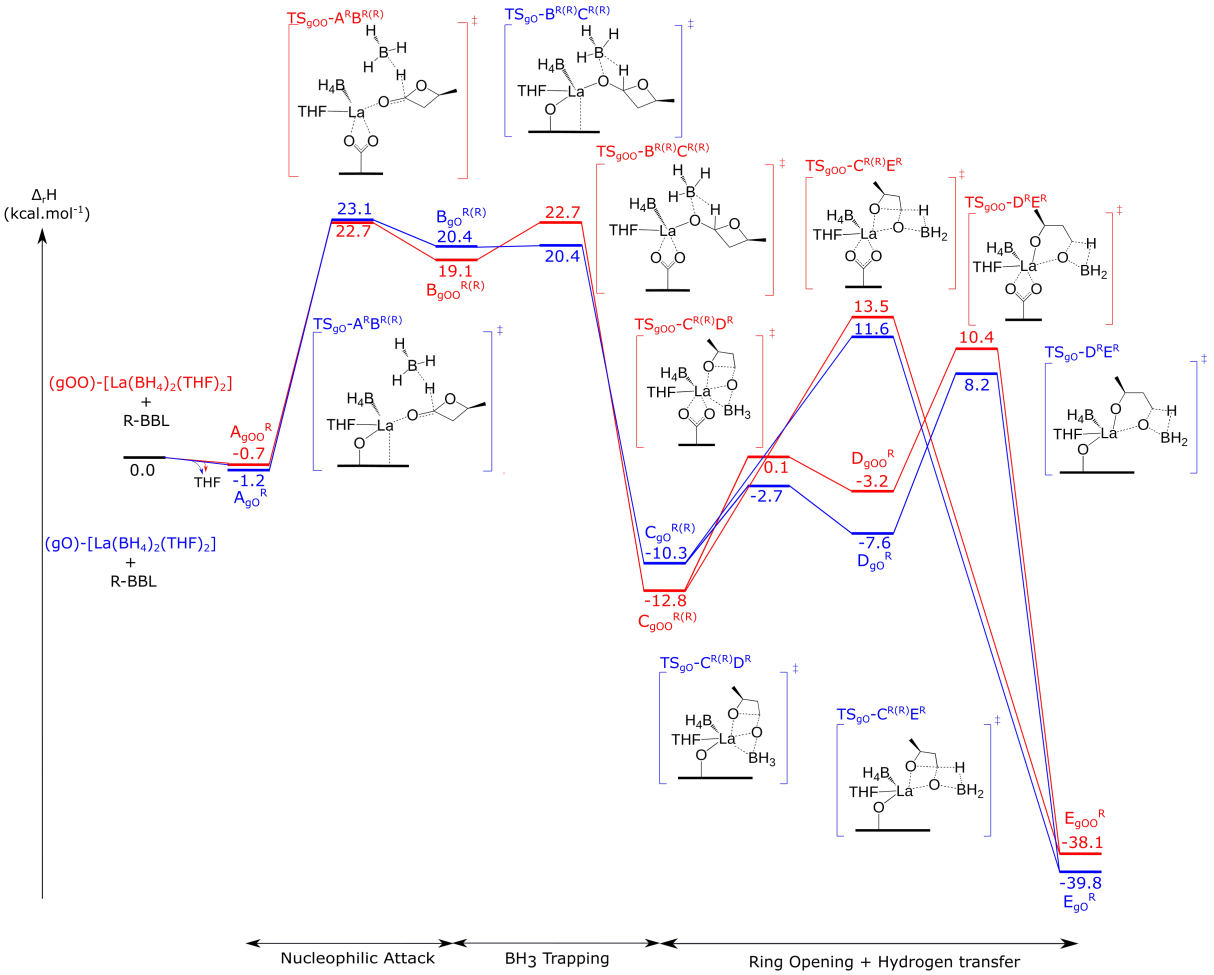

Figure 148: Profil d'enthalpie-énergie calculé pour l'étape d'initiation du ROP BL-R par les complexes (gO)-[La$(BH_4)_2$(THF)$_2$] (bleue) et (gOO)-[La$(BH_4)_2$(THF)$_2$] (rouge).

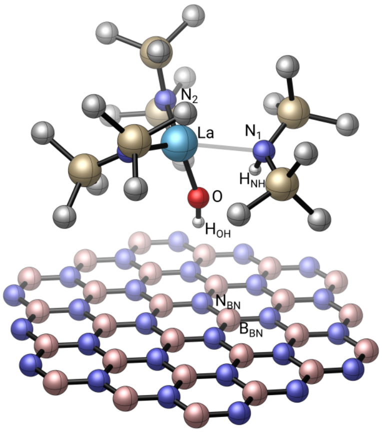

Figure 149: Géométries des complexes impliqués dans la réaction de greffage de [La(NSiMe$_3$)$_3$] sur la surface fonctionnalisée de BNH-OH (bleu clair : La, bleu foncé : N, blanc : H, rouge : O). Par souci de clarté, tous les H des composés greffés en La ont été omis, à l'exception des atomes d'hydrogène du BNH-OH.

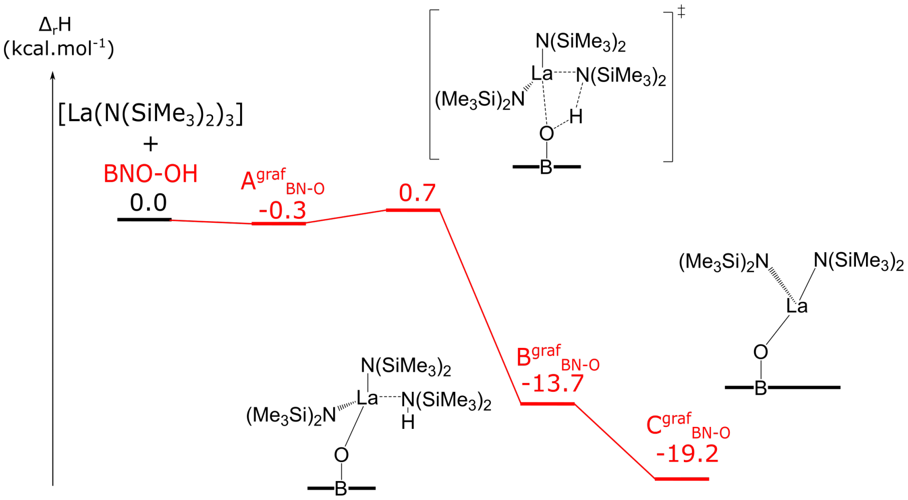

Figure 150: Profil énergétique calculé pour la greffe du complexe [La(N(SiMe$_3$)$_2$)$_3$] sur la surface fonctionnalisée de BNO-OH.

Lewis du complexe greffé au BNO-O est très similaire à celle de l'analogue greffé au gOO. L'influence de la surface sur l'acidité de Lewis du centre métallique est donc susceptible de suivre l'ordre suivant : entre celle du gO-supporté, il existe une tendance sur les différents complexes lanthanides-silylamides supportés sur l'acidité de Lewis du centre métallique, allant du plus acide au moins acide : gO > gOO ≅ BNO-O > silice.

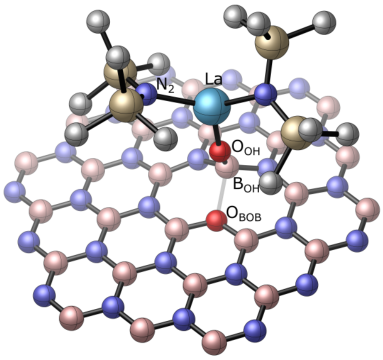

Figure 151: Structure des complexes impliqués dans la réaction de greffage de $[La(N(SiMe_3)_2)_3]$ sur la surface fonctionnalisée de BNO-OH (bleu clair : La, bleu foncé : N, blanc : H, rouge : O). Par souci de clarté, tous les H des composés greffés en La ont été omis, à l'exception de l'atome de surface BNO-OH.

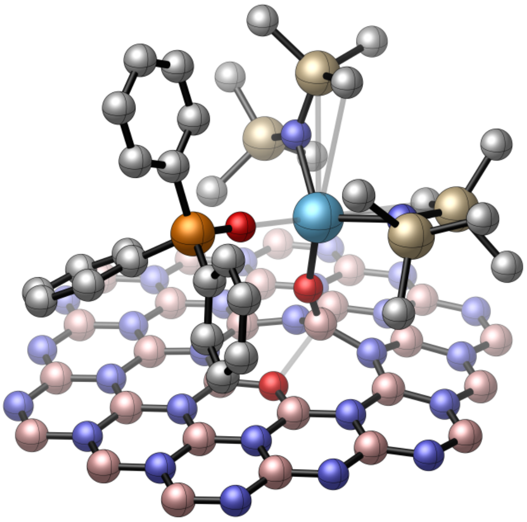

Figure 152: Géométrie du composé $OPPh_3$ hexaméthyldisilylamido La, (BNO-O)-$[LaN(SiMe_3)_2)_2(O{=}PPh_3)]$, greffé sur la surface de BNO-OH.

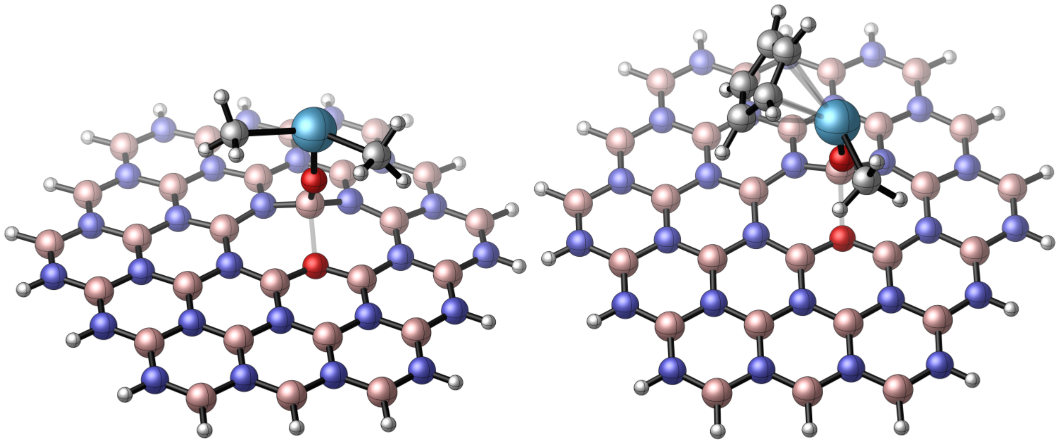

(a) (b)

Figure 153: Géométries des composés greffés (a) (BNO-O)-[La$(CH_3)_2$] (1BNO-O) and (b) (BNO-O)-[La(Cp)$(CH_3)$] (2BNO-O).

Table 19: Comparaison entre les fréquences vibratoires théoriques (en cm$^{-1}$), et les $^{1}$H, $^{13}$C and $^{31}$P deplacements chimiques RMN (en ppm) d'un ligand libre $OPPh_3$ et de la molécule coordonnée $OPPh_3$ dans différents produits d'addition $OPPh_3$ hexaméthyldisilylamido La greffés sur les surfaces de graphène gO et gOO et sur $SiO_2$ (moyenne entre toutes les espèces mono- et bi-greffées précédemment signalées[135]). Les deplacements chimiques $^{1}$H et $^{13}$C sont donnés par rapport au TMS (blindage chimique théorique: 31.64 et 195.35 ppm, respectivement, pour les atomes de $^{1}$H and $^{13}$C. Les déplacements chimiques $^{31}$P sont donnés par rapport à l'acide phosphorique (blindage chimique théorique: 380.6 ppm). R = SiMe3,$^{(a)}$ x = 1 or 2$^{(b)}$ Reference [55].$^{(c)}$ Attendu mais non détecté (voir reference [55]).

| | fréquences vibrationnelle | | |
|---|---|---|---|
| | $\nu_{C-H}$ | $\nu_{C=C}$ | $\nu_{O=P}$ |
| O=$PPh_3$ | [3065-3095] | [1416-1592] | 1177 |
| (BNO-O)-[La$(NR_2)_2$(O=$PPh_3$)] | [3199-3239] | [1413-1655] | 1068 |
| (gO)-[La$(NR_2)_2$(O=$PPh_3$)] | [3184-3240] | [1471-1655] | 1039 |
| (gOO)-[La$(NR_2)_2$(O=$PPh_3$)] | [3193-3230] | [1475-1655] | 1047 |
| ($SiO_2$)-[La$(NR_2)_2$(O=$PPh_3$)] | [2938-3107] | [1416-1592] | [1118-1152] |

| | RMN | | |
|---|---|---|---|
| | $\delta_{H_{Phenyl}}$ | $\delta_{C_{Phenyl}}$ | $\delta_P$ |
| O=$PPh_3$ | 7.7 | [124.7-/129.9] | 25.7 |
| (BNO-O)-[La$(NR_2)_2$(O=$PPh_3$)] | 7.8 | [122.9/130.0] | 53.8 |
| (gO)-[La$(NR_2)_2$(O=$PPh_3$)] | 7.3 | [123.5/127.8] | 56.0 |
| (gOO)-[La$(NR_2)_2$(O=$PPh_3$)] | 7.4 | [123.6/127.8] | 53.4 |
| ($SiO_2$)-[La$(NR_2)_2$(O=$PPh_3$)] | [7.9-8.0] | [123.5-124.9]/[128.1-129.0] | [40.3-47.6] |

Afin de comprendre le rôle du support, nous avons ensuite étudié l'activité catalytique des composés La supportés par BNO-OH envers l'homopolymérisation de l'éthylène et du 1,3-butadiène, en utilisant les complexes alkyles (BNO-O)-[La$(CH_3)_2$] (1BNO-O) et (gOO)-[LaCp$CH_3$] (2BNO-O) comme espèces actives (figure 153).

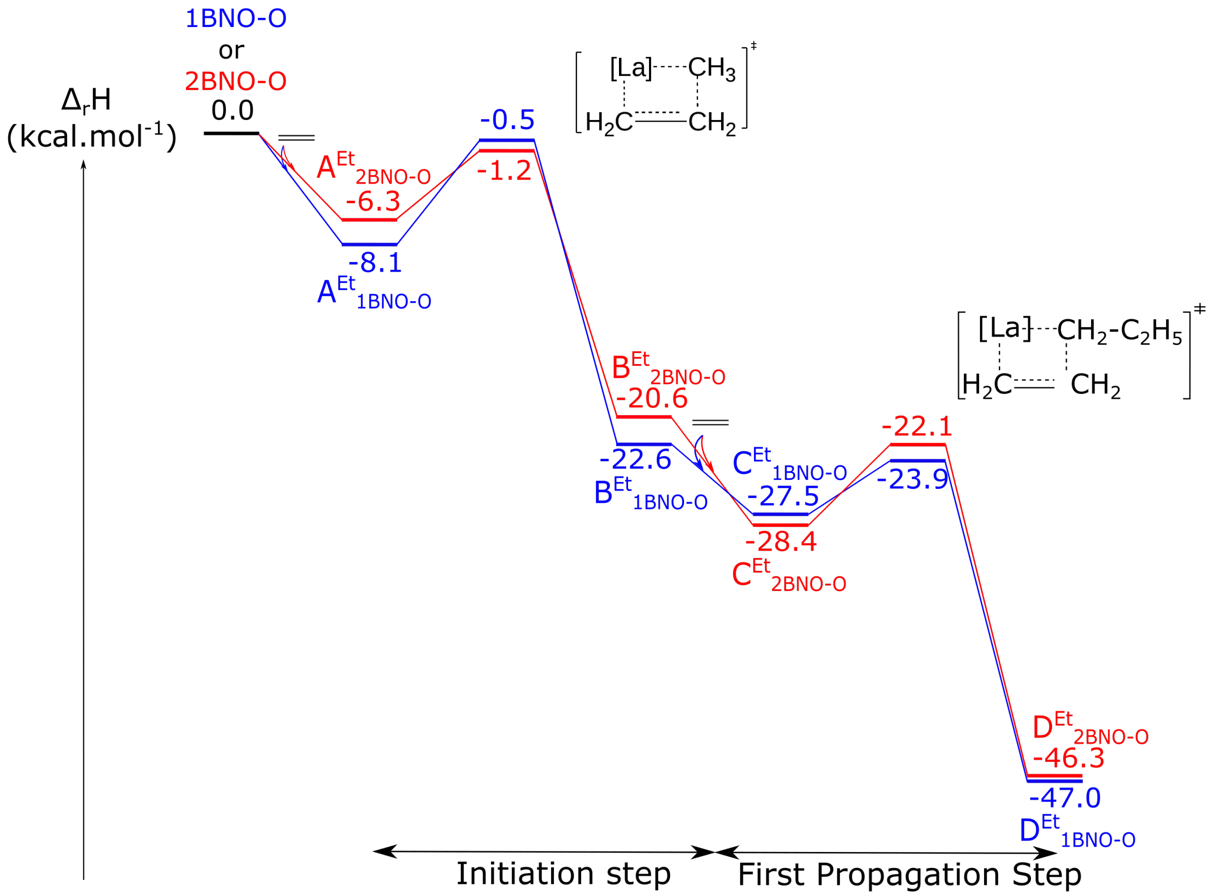

Figure 154: Profil enthalpique de l'initiation et de la première étape de propagation pour l'homopolymérisation de l'éthylène.

Les deux composés catalysent efficacement la réaction d'homopolymérisation de l'éthylène (figure 154), présentant des barrières d'activation qui se situent entre celles des composés greffés au graphène et des composés greffés à la silice. On prévoit donc que les surfaces de BNO-OH jouent un rôle important, en augmentant l'acidité de Lewis et donc la réactivité des systèmes La greffés, comme les surfaces de graphène. En ce qui concerne la réaction d'homopolymérisation du 1,3-butadiène (figure 155), d'autre part, les deux espèces sont susceptibles de se comporter comme des espèces catalytiques efficaces, présentant, comme les supports de graphène, une activité plus élevée que les analogues de La greffés sur la silice. Dans les modèles 1BNO-O et 2BNO-O, il est intéressant de noter que l'insertion de 1,4-cis 1,3-butadiène est préférée à celle de 1,4-trans, ce qui donne un polymère 1,4-cis-polybutadiène, comme indiqué précédemment pour les composés La à base de silice. En conclusion, les surfaces BNO-OH fonctionnalisées constituent donc des supports efficaces pour les composés organométalliques lanthanides. Ces surfaces BNO-OH sont susceptibles d'augmenter l'acidité de Lewis du métal La, jouant ainsi un rôle actif dans l'activité catalytique des complexes La supportés. Enfin, les BNO-O supportent les composés alkyles de La et catalysent efficacement la réaction d'homopolymérisation de l'éthylène et du 1,3-butadiène, avec des activités et des stéréosélectivités similaires à celles du complexe gOO greffé au graphène (tableau 20).

Table 20: Données sur l'enthalpie (kcal.mol$^{-1}$) pour l'initiation et les premières étapes de propagation de la polymérisation de l'éthylène par les complexes (BNO-O)-[La($CH_3$)$_2$], $Cp_2$LaMe, ($SiO_2$)-[La($CH_3$)$_2$], (gO)-[La($CH_3$)$_2$] et (gOO)-[La($CH_3$)$_2$].

| | $A^{Et}$ | TS-$AB^{Et}$ | $B^{Et}$ | $C^{Et}$ | TS-$CD^{Et}$ | $D^{Et}$ |
|---|---|---|---|---|---|---|
| (BN-O)-[La($CH_3$)$_2$] | -8.1 | -0.5 | -22.6 | -27.5 | -23.9 | -47.0 |
| $Cp_2$LaMe | -7.6 | -0.2 | -21.1 | -29.5 | -23.4 | -46.4 |
| ($SiO_2$)-[La($CH_3$)$_2$] | -4.6 | 6.4 | -20.5 | -22.1 | -17.5 | -45.5 |
| gO-[La($CH_3$)$_2$] | -5.9 | -0.4 | -23.5 | -27.9 | -22.8 | -47.6 |
| gOO-[La($CH_3$)$_2$] | -7.1 | -1.1 | -23.7 | -29.9 | -23.3 | -46.6 |

Dans le chapitre V, nous avons étudié la réaction de polymérisation du propène catalysée par les trois complexes de lanthane greffés au graphène (gO)-[La($CH_3$)$_2$] (1gO) (figure 156), (gO)-[La(Cp)($CH_3$)] (2gO) et (gO)-[La(Cp*)($CH_3$)] (3gO). Dans le système (gO)-[La($CH_3$)$_2$], alors que d'un point de vue cinétique les barrières d'insertion 1,2 et 2,1 sont comparables à celles du processus de transfert allylique, d'un point de vue thermodynamique le produit allylique est plus stable que les barrières d'insertion 1,2 et 2,1. Afin de défavoriser la réaction de transfert allylique, nous avons décidé d'augmenter l'encombrement stérique autour du centre métallique, en remplaçant un méthyle par les ligands Cp et Cp* plus encombrés, ce qui permet d'obtenir les complexes (gO)-[La(Cp)($CH_3$)] et (gO)-[La(Cp*)($CH_3$)]. Les profils énergétiques calculés pour ces derniers indiquent que, bien que l'énergie des produits de désactivation allyliques diminue en passant de -24,1 à -21,5 et -17,9 kcal.mol$^{-1}$ pour les 1gO, 2gO et 3gO, respectivement, cette diminution d'énergie n'est pas assez importante pour défavoriser la désactivation allylique par rapport au processus d'insertion 1,2. En perspective, nous prévoyons d'augmenter encore la gêne stérique autour du métal en employant des ligands plus volumineux ou en changeant la nature du métal vers un élément plus petit.

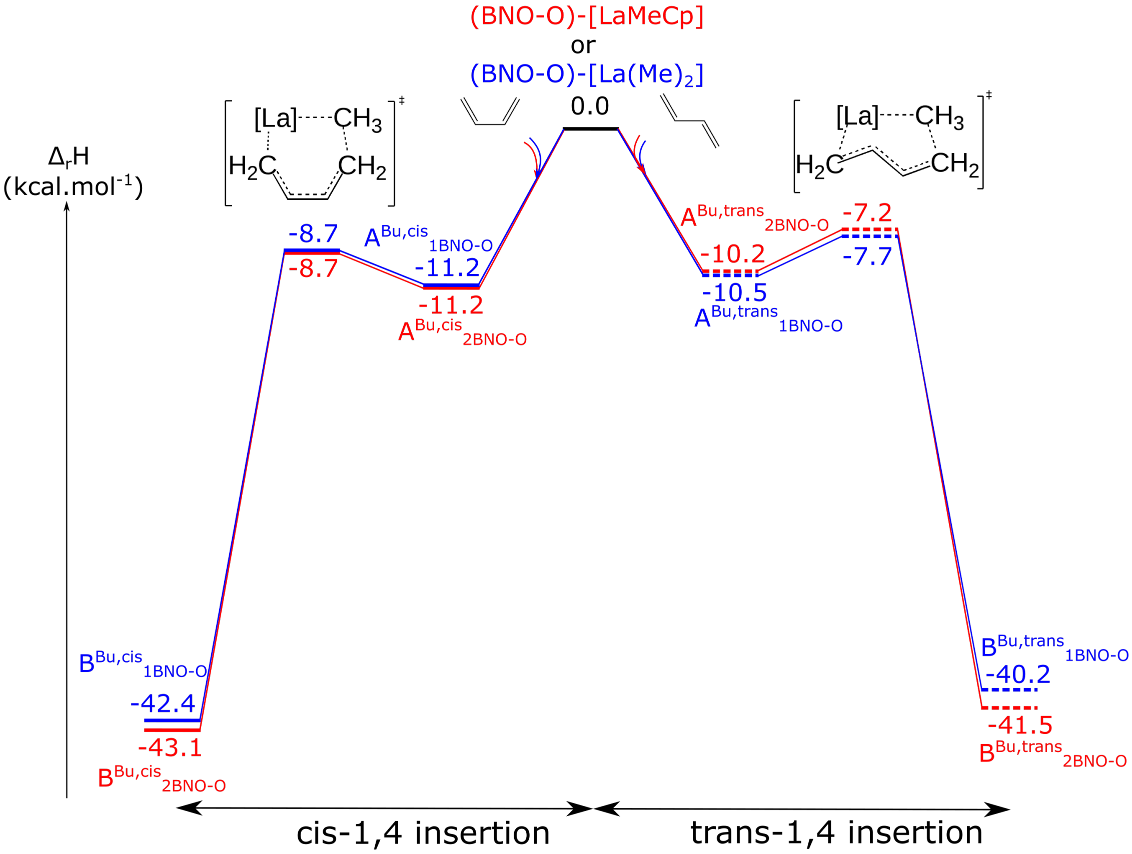

Figure 155: Profil d'enthalpie pour la première insertion de monomère de la réaction d'homopolymérisation du 1,3-butadiène médiée par (BNO-O)-[La($CH_3$)$_2$] (1BNO-O) and (BNO-O)-[La(Cp)($CH_3$)] (2BNO-O).

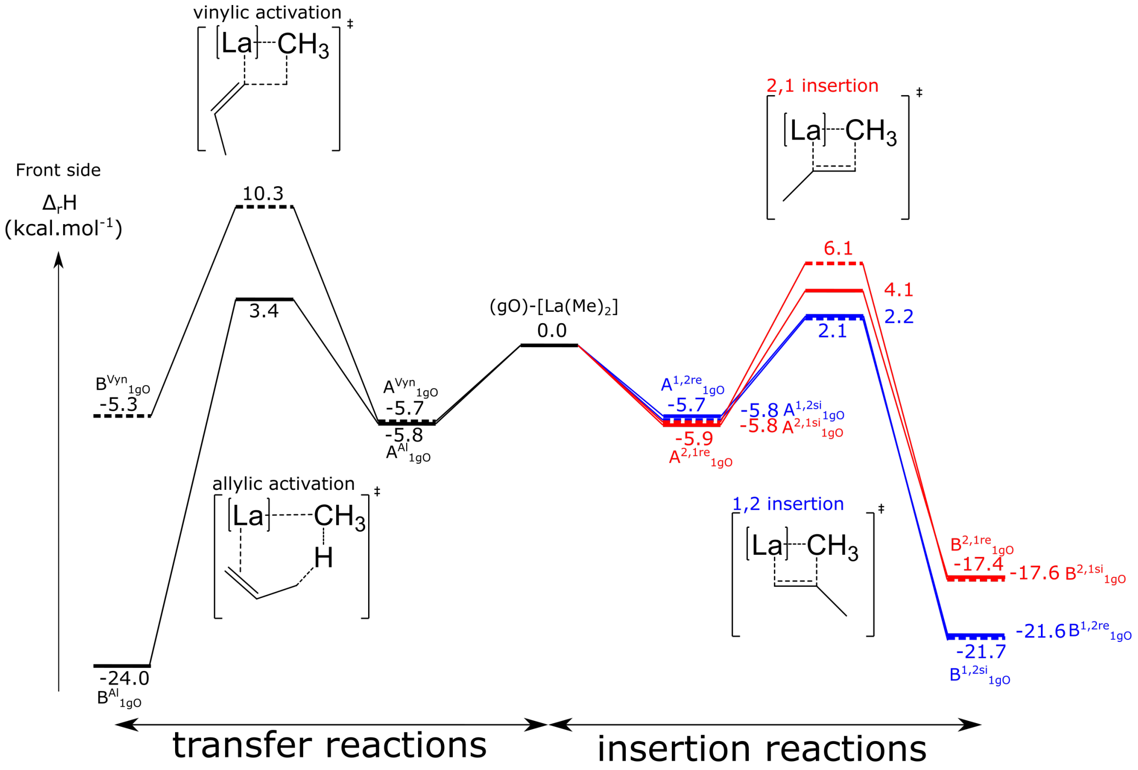

Figure 156: Profil d'enthalpie calculé pour la première insertion de propène monomère 1,2 et 2,1 sur la face avant (à droite) et pour l'insertion d'activation C-H allylique et vinylique sur la face avant (à gauche) de la voie arrière de la réaction d'homopolymérisation du propylène médiée par (gO)-$[La(CH_3)_2]$ (1gO ).

# Appendix A : Part III Graphene supported lanthanum systems

## Styrene homopolymerisation

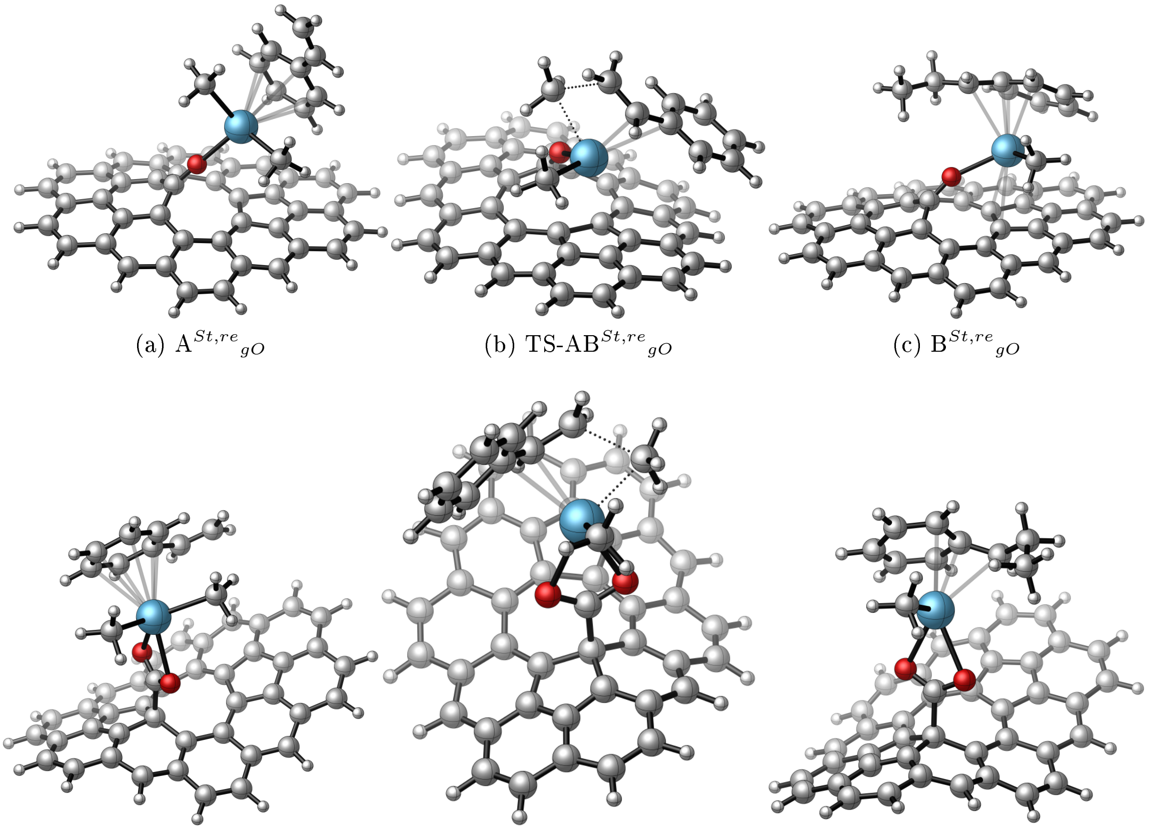

(a) $A^{St,re}{}_{gO}$ (b) TS-$AB^{St,re}{}_{gO}$ (c) $B^{St,re}{}_{gO}$

(d) $A^{St,re}{}_{gOO}$ (e) TS-$AB^{St,re}{}_{gOO}$ (f) $B^{St,re}{}_{gOO}$

FIGURE 157: Optimised structures of the complexes involved in the first styrene insertion of the '*re*' eniantoface mediated by the (gO)-[La$(CH_3)_2$] and (gOO)-[La$(CH_3)_2$] compounds.

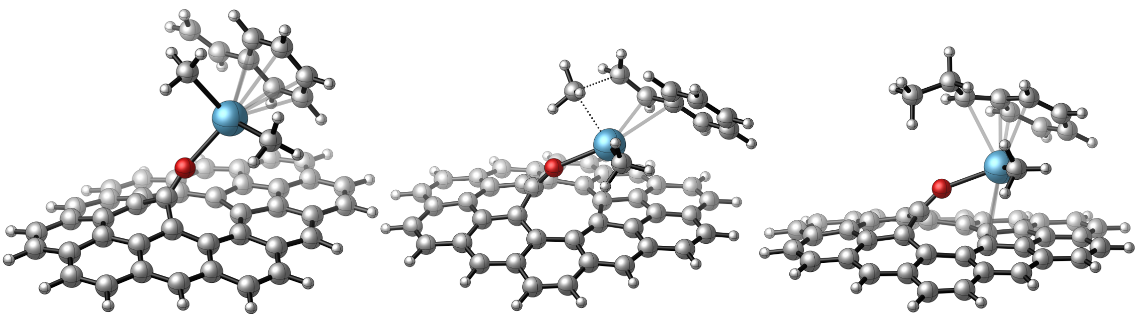

(a) $\mathrm{A}^{St,si}{}_{gO}$ (b) $\mathrm{TS\text{-}AB}^{St,si}{}_{gO}$ (c) $\mathrm{B}^{St,si}{}_{gO}$

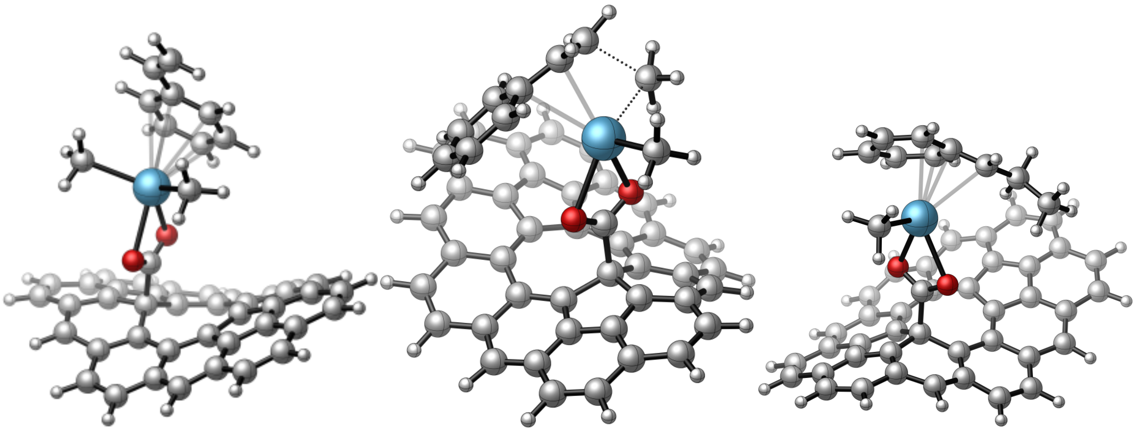

(d) $\mathrm{A}^{St,si}{}_{gOO}$ (e) $\mathrm{TS\text{-}AB}^{St,si}{}_{gOO}$ (f) $\mathrm{B}^{St,si}{}_{gOO}$

FIGURE 158: Optimised structures of the complexes involved in the first styrene insertion of the '*si*' eniantoface mediated by the (gO)-[La$(CH_3)_2$] and (gOO)-[La$(CH_3)_2$] compounds.

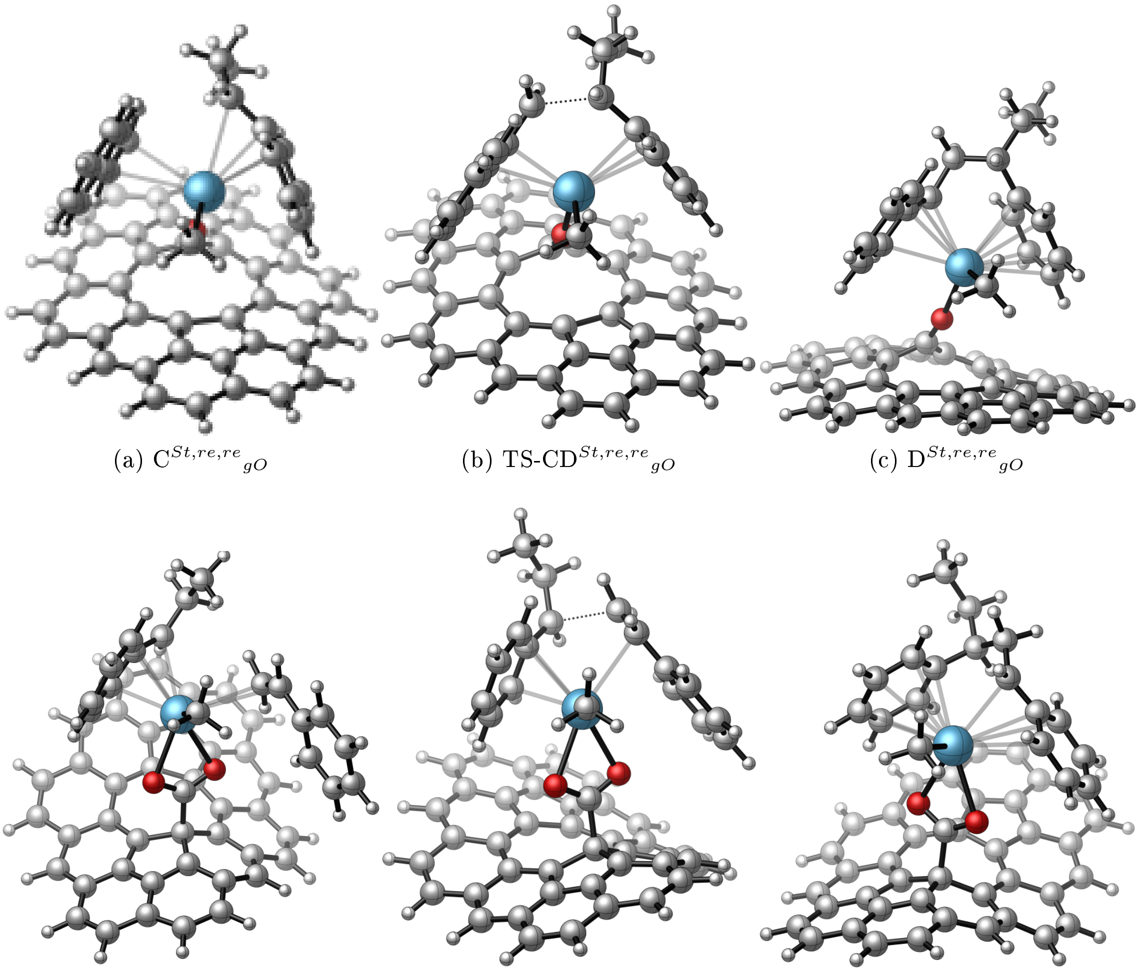

(a) $\mathrm{C}^{St,re,re}{}_{gO}$ (b) $\mathrm{TS\text{-}CD}^{St,re,re}{}_{gO}$ (c) $\mathrm{D}^{St,re,re}{}_{gO}$

(d) $\mathrm{C}^{St,re,re}{}_{gOO}$ (e) $\mathrm{TS\text{-}CD}^{St,re,re}{}_{gOO}$ (f) $\mathrm{D}^{St,re,re}{}_{gOO}$

FIGURE 159: Optimised structures of the complexes involved in the second styrene insertion of the '*re*' eniantoface mediated by the (gO)-[La$(CH_3)_2$] and (gOO)-[La$(CH_3)_2$] compounds.

## Ethylene styrene copolymerisation

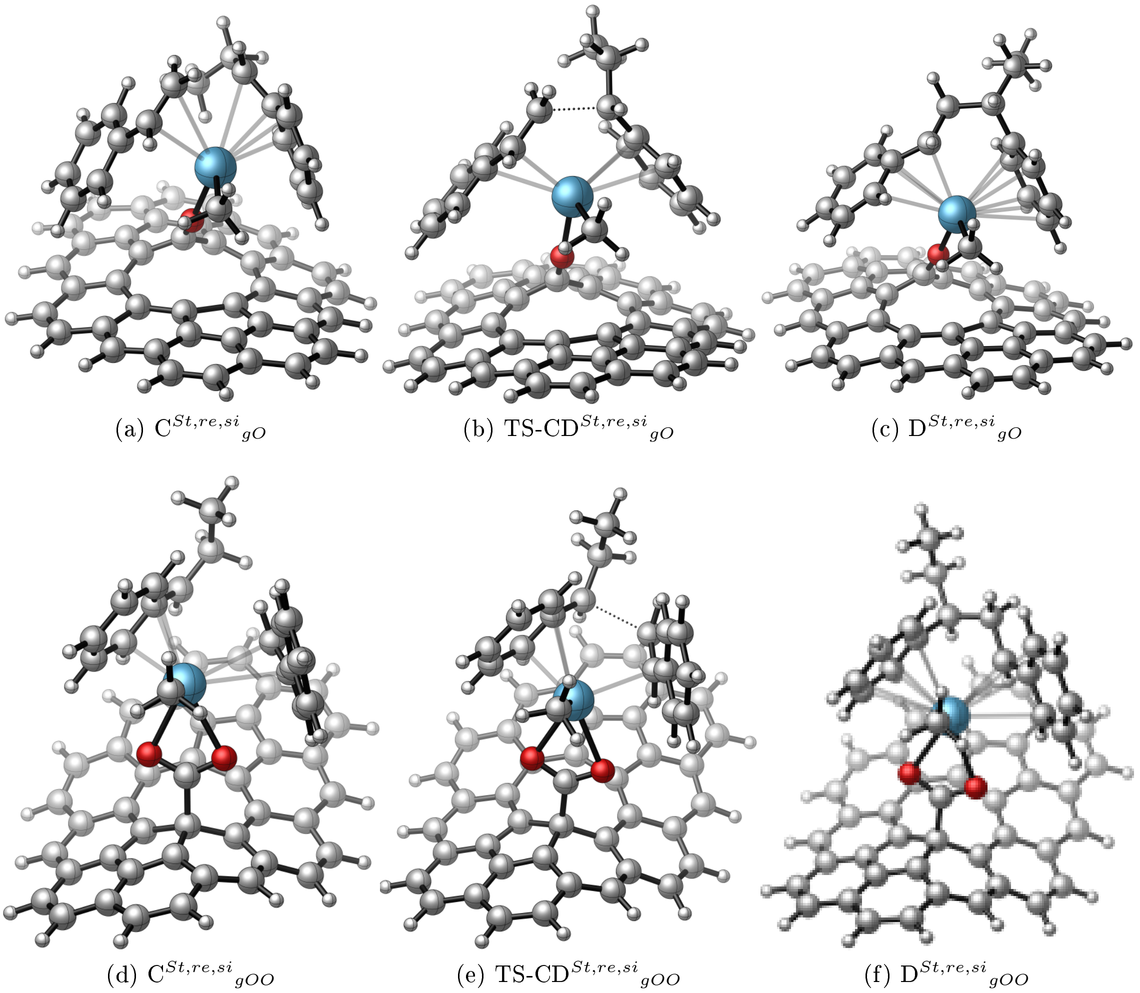

(a) $\mathrm{C}^{St,re,si}{}_{gO}$ (b) TS-$\mathrm{CD}^{St,re,si}{}_{gO}$ (c) $\mathrm{D}^{St,re,si}{}_{gO}$

(d) $\mathrm{C}^{St,re,si}{}_{gOO}$ (e) TS-$\mathrm{CD}^{St,re,si}{}_{gOO}$ (f) $\mathrm{D}^{St,re,si}{}_{gOO}$

FIGURE 160: Optimised structures of the complexes involved in the second styrene insertion of the '*si*' eniantoface mediated by the (gO)-[La$(CH_3)_2$] and (gOO)- [La$(CH_3)_2$] compounds.

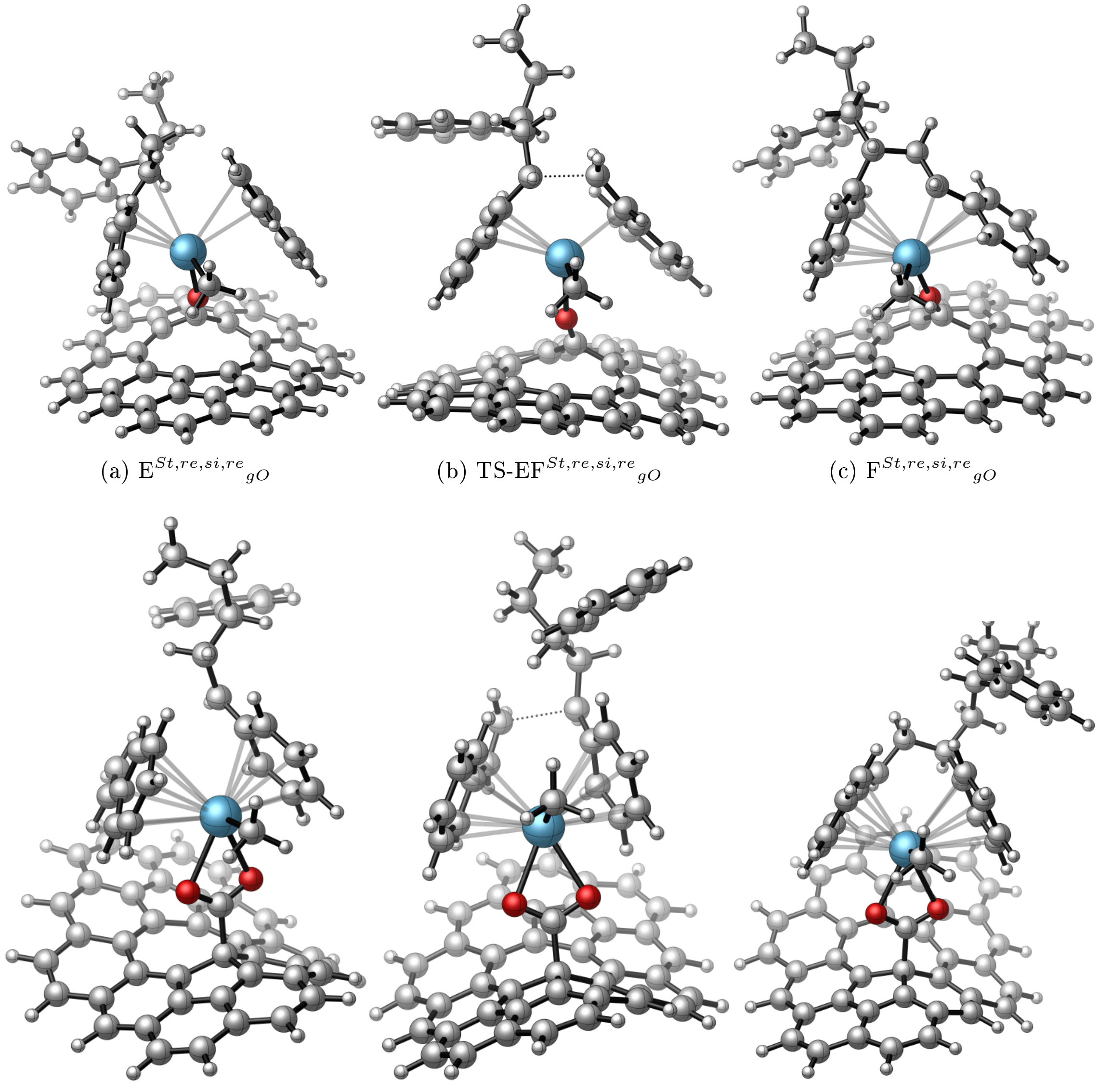

(a) $E^{St,re,si,re}{}_{gO}$ (b) TS-$EF^{St,re,si,re}{}_{gO}$ (c) $F^{St,re,si,re}{}_{gO}$

(d) $E^{St,re,si,re}{}_{gOO}$ (e) TS-$EF^{St,re,si,re}{}_{gOO}$ (f) $F^{St,re,si,re}{}_{gOO}$

FIGURE 161: Optimised structures of the complexes involved in the third styrene insertion of the '*re*' eniantoface mediated by the (gO)-[La($CH_3$)$_2$] and (gOO)-[La($CH_3$)$_2$] compounds.

# Appendix B: Part V Propene polymerisation

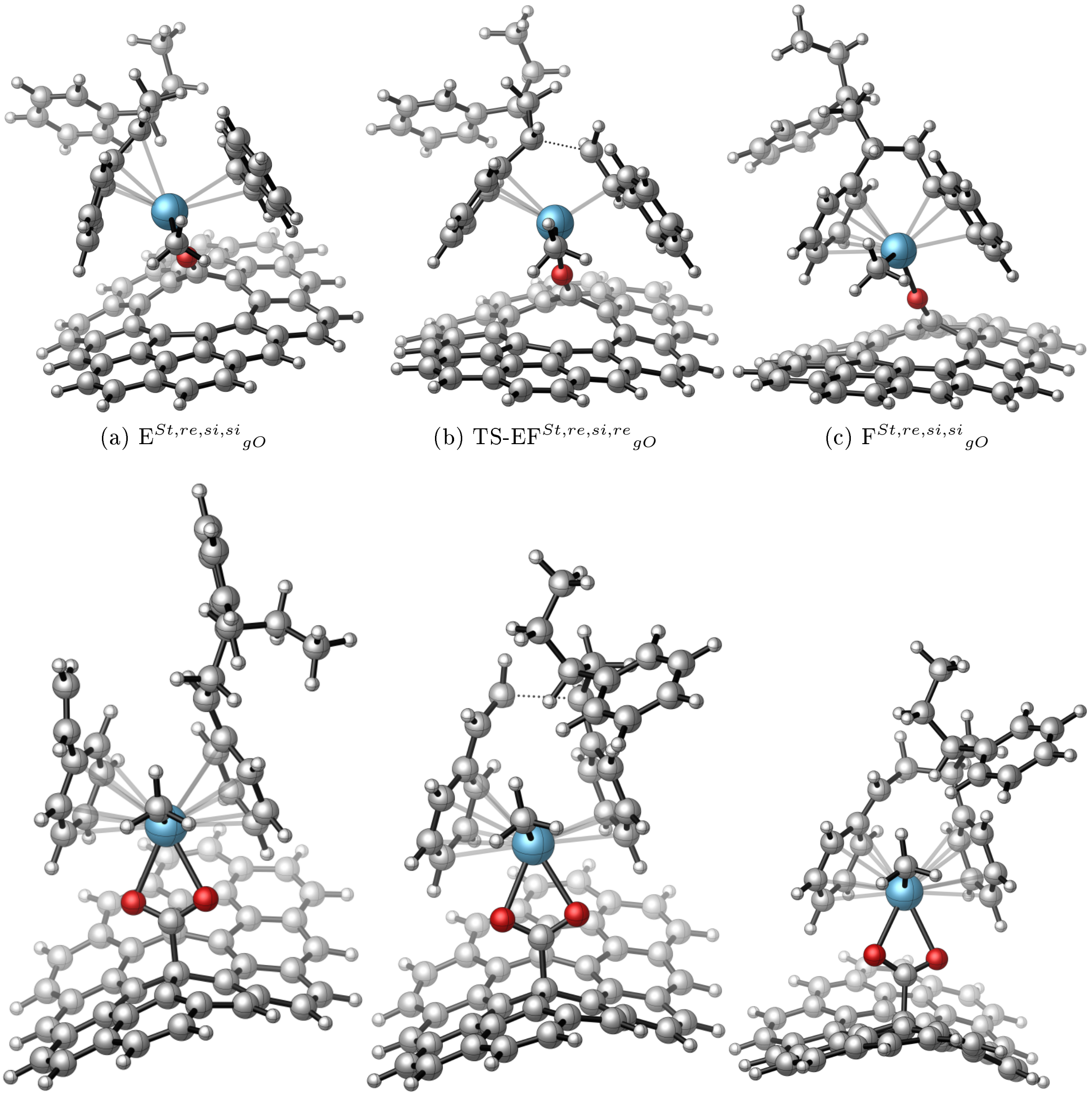

(a) $\mathrm{E}^{St,re,si,si}{}_{gO}$ (b) $\mathrm{TS\text{-}EF}^{St,re,si,re}{}_{gO}$ (c) $\mathrm{F}^{St,re,si,si}{}_{gO}$

(d) $\mathrm{E}^{St,re,si,si}{}_{gOO}$ (e) $\mathrm{TS\text{-}EF}^{St,re,si,si}{}_{gOO}$ (f) $\mathrm{F}^{St,re,si,si}{}_{gOO}$

FIGURE 162: Optimised structures of the complexes involved in the third styrene insertion of the '*si*' eniantoface mediated by the (gO)-[La($CH_3$)$_2$] and (gOO)-[La($CH_3$)$_2$] compounds.

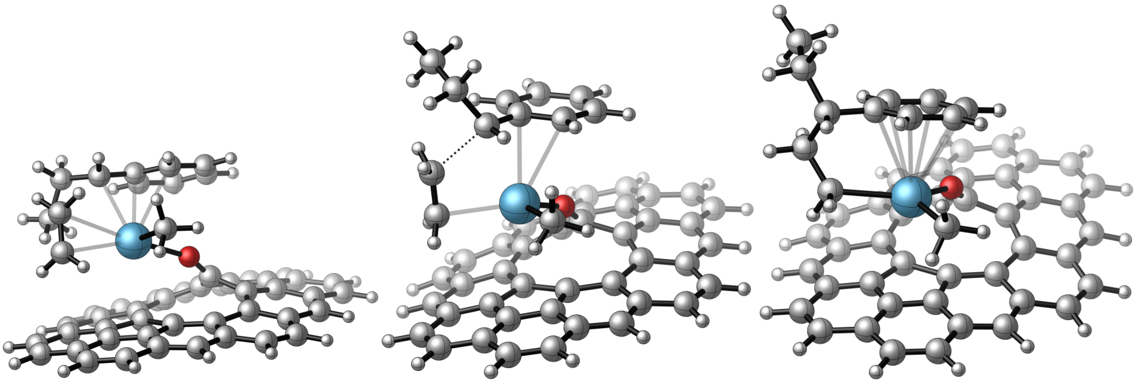

(a) $C^{St,re,Et}{}_{gO}$ (b) TS-$CD^{St,re,Et}{}_{gO}$ (c) $D^{St,re,Et}{}_{gO}$

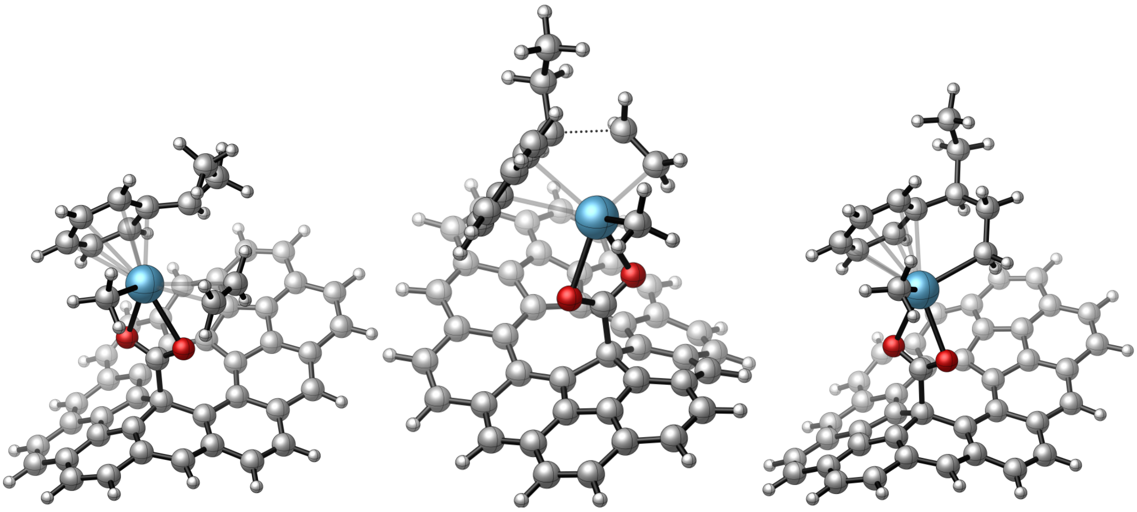

(d) $C^{St,re,Et}{}_{gOO}$ (e) TS-$CD^{St,re,Et}{}_{gOO}$ (f) $D^{St,re,Et}{}_{gOO}$

FIGURE 163: Optimised structures of the complexes involved in the second ethylene insertion in the ethylene and styrene copolymerisation mediated by the $B^{St,re}{}_{gO}$ and $B^{St,re}{}_{gOO}$ compounds.

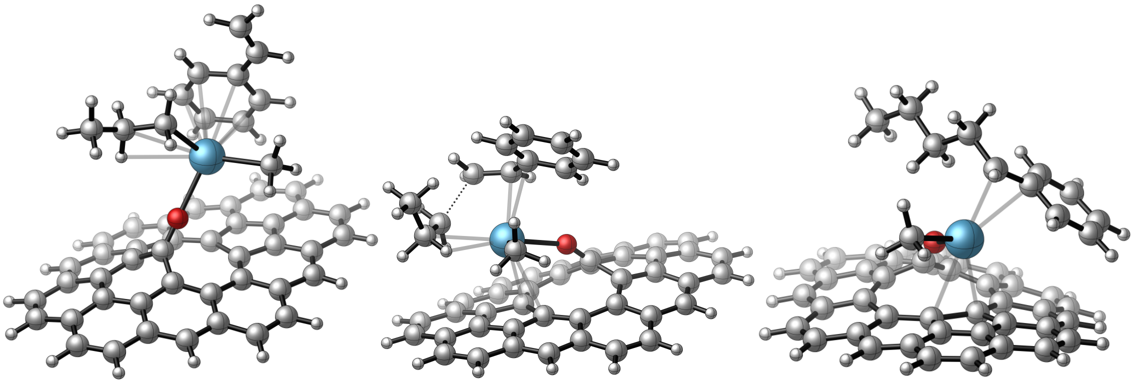

(a) $\mathrm{C}^{Et,St,re}{}_{gO}$ (b) TS-$\mathrm{CD}^{Et,St,re}{}_{gO}$ (c) $\mathrm{D}^{Et,St,re}{}_{gO}$

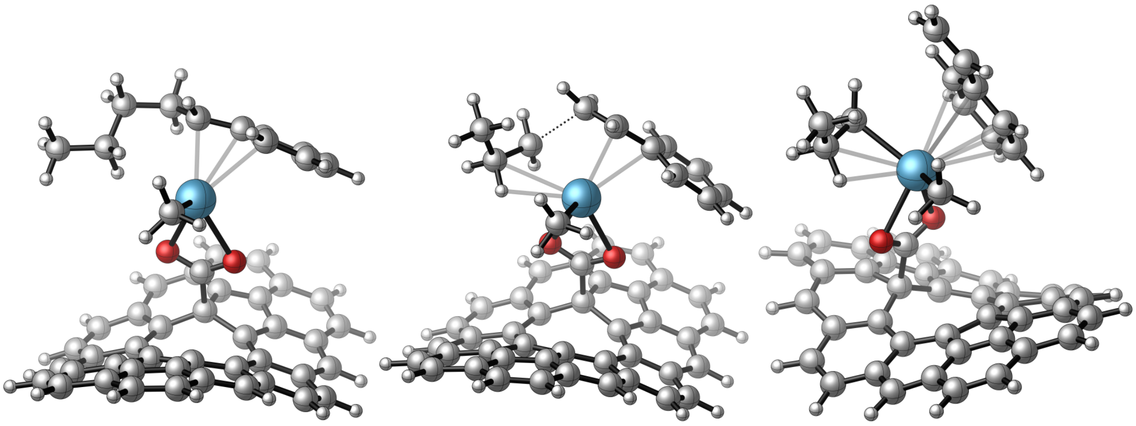

(d) $\mathrm{C}^{Et,St,re}{}_{gOO}$ (e) TS-$\mathrm{CD}^{Et,St,re}{}_{gO}$ (f) $\mathrm{D}^{Et,St,re}{}_{gO}$

FIGURE 164: Optimised structures of the complexes involved in the second styrene insertion in the ethylene and styrene copolymerisation mediated by the $\mathrm{B}^{Et}{}_{gO}$ and $\mathrm{B}^{Et}{}_{gOO}$ compounds.

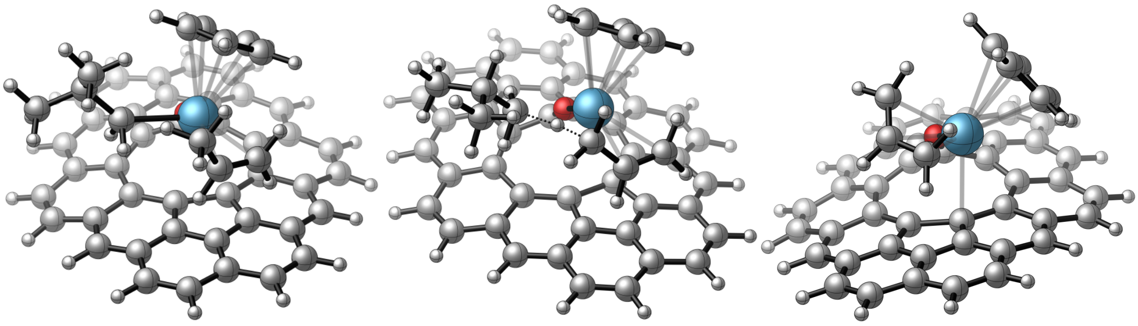

(a) $\mathrm{C}^{al}{}_{2gO}$ (b) TS-$\mathrm{CD}^{al}{}_{2gO}$ (c) $\mathrm{D}^{al}{}_{2gO}$

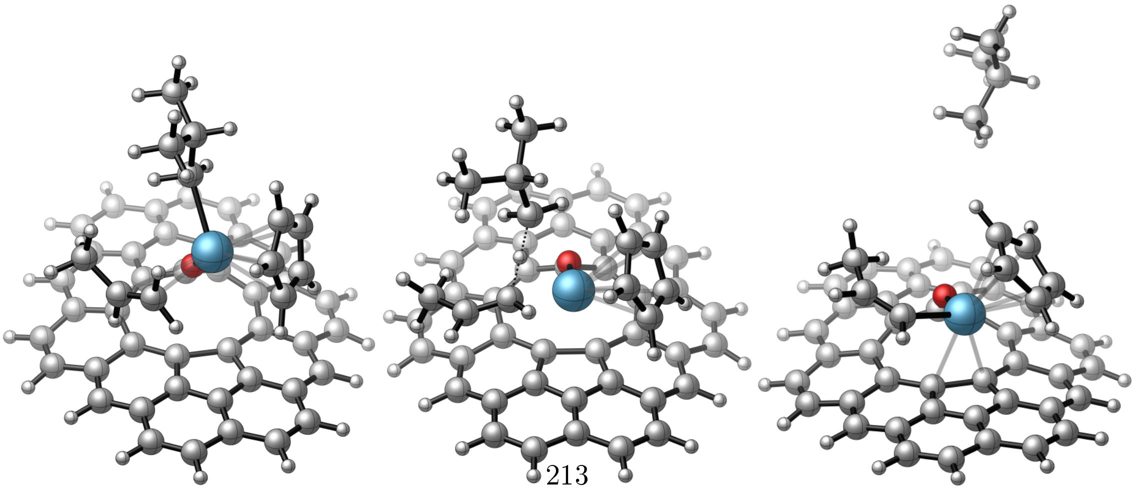

(d) $\mathrm{C}^{vyn}{}_{2gO}$ (e) TS-$\mathrm{CD}^{vyn}{}_{2gO}$ (f) $\mathrm{D}^{vyn}{}_{2gO}$

Figure 191: Geometries of the complexes involved in the back side allylic and vinylic C-H activ-

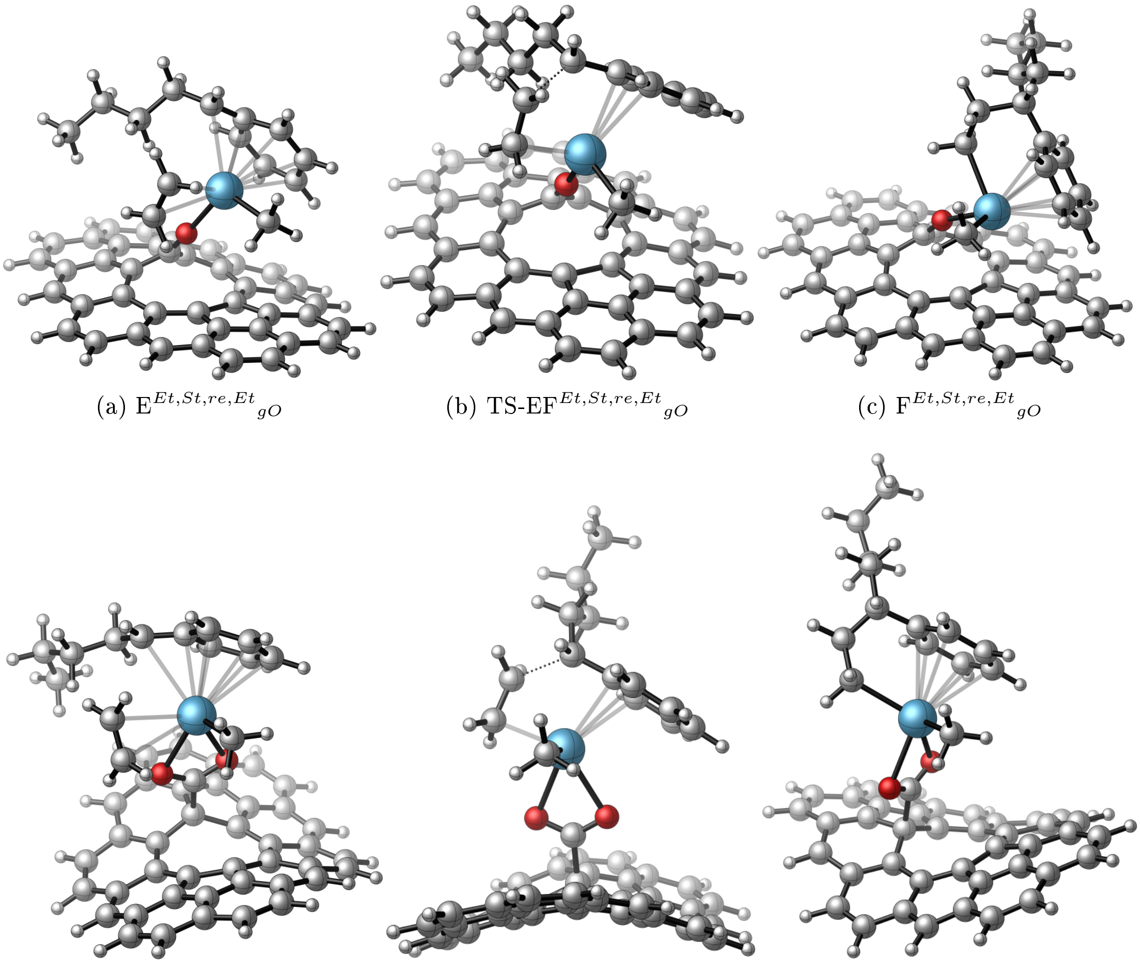

(a) $\mathrm{E}^{Et,St,re,Et}{}_{gO}$ (b) TS-$\mathrm{EF}^{Et,St,re,Et}{}_{gO}$ (c) $\mathrm{F}^{Et,St,re,Et}{}_{gO}$

(d) $\mathrm{E}^{Et,St,re,Et}{}_{gOO}$ (e) TS-$\mathrm{EF}^{Et,St,re,Et}{}_{gOO}$ (f) $\mathrm{F}^{Et,St,re,Et}{}_{gOO}$

FIGURE 165: Optimised structures of the complexes involved in the third ethylene insertion in the ethylene and styrene copolymerisation mediated by the $\mathrm{D}^{Et,St,re}{}_{gO}$ and $\mathrm{D}^{Et,St,re}{}_{gOO}$ compounds.

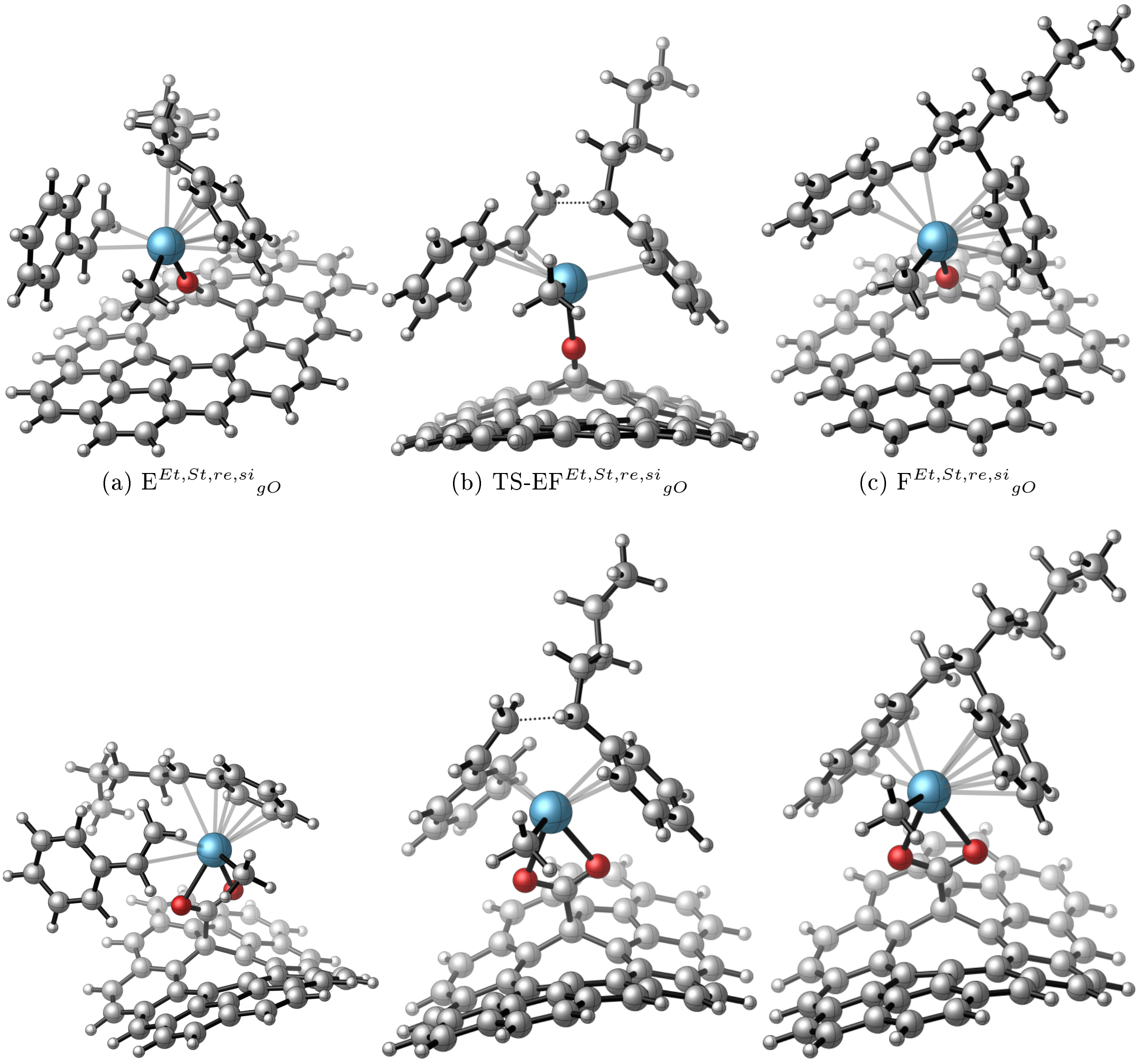

(a) $\mathrm{E}^{Et,St,re,si}{}_{gO}$ (b) $\text{TS-EF}^{Et,St,re,si}{}_{gO}$ (c) $\mathrm{F}^{Et,St,re,si}{}_{gO}$

(d) $\mathrm{E}^{Et,St,re,si}{}_{gOO}$ (e) $\text{TS-EF}^{Et,St,re,si}{}_{gOO}$ (f) $\mathrm{F}^{Et,St,re,si}{}_{gOO}$

FIGURE 166: Optimised structures of the complexes involved in the third styrene insertion in the ethylene and styrene copolymerisation mediated by the $\mathrm{D}^{Et,St,re}{}_{gO}$ and $\mathrm{D}^{Et,St,re}{}_{gOO}$ compounds.

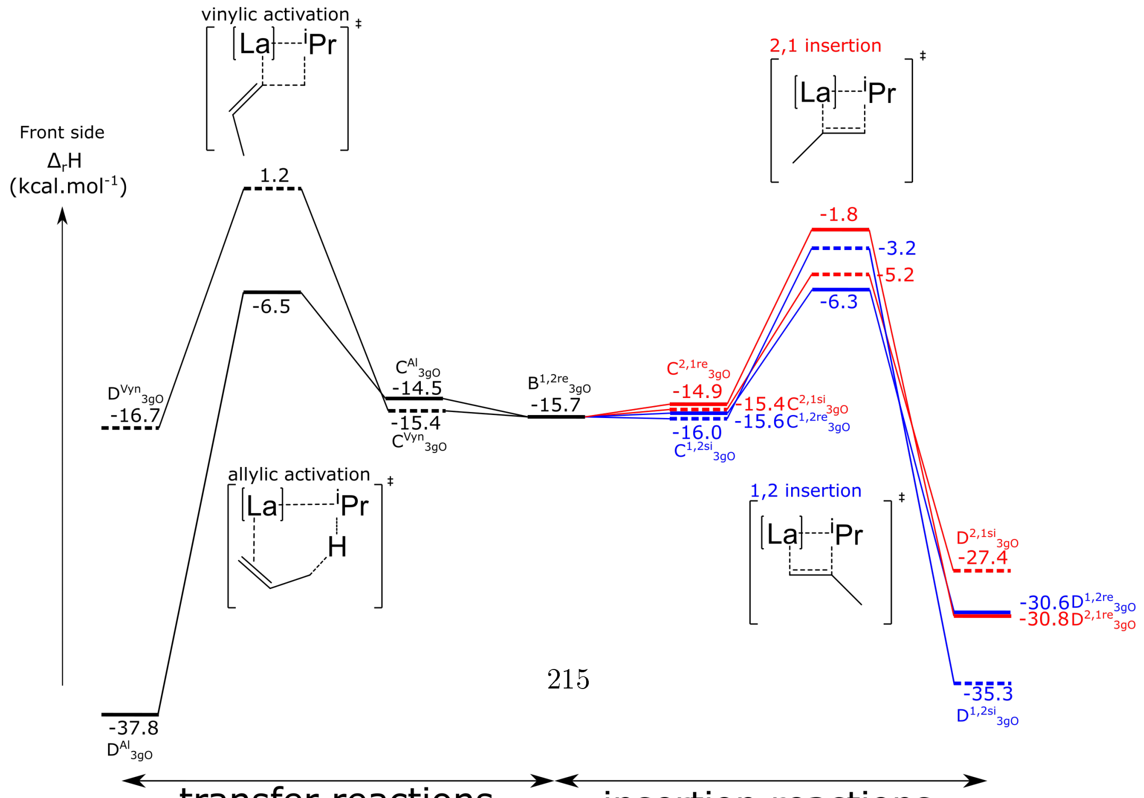

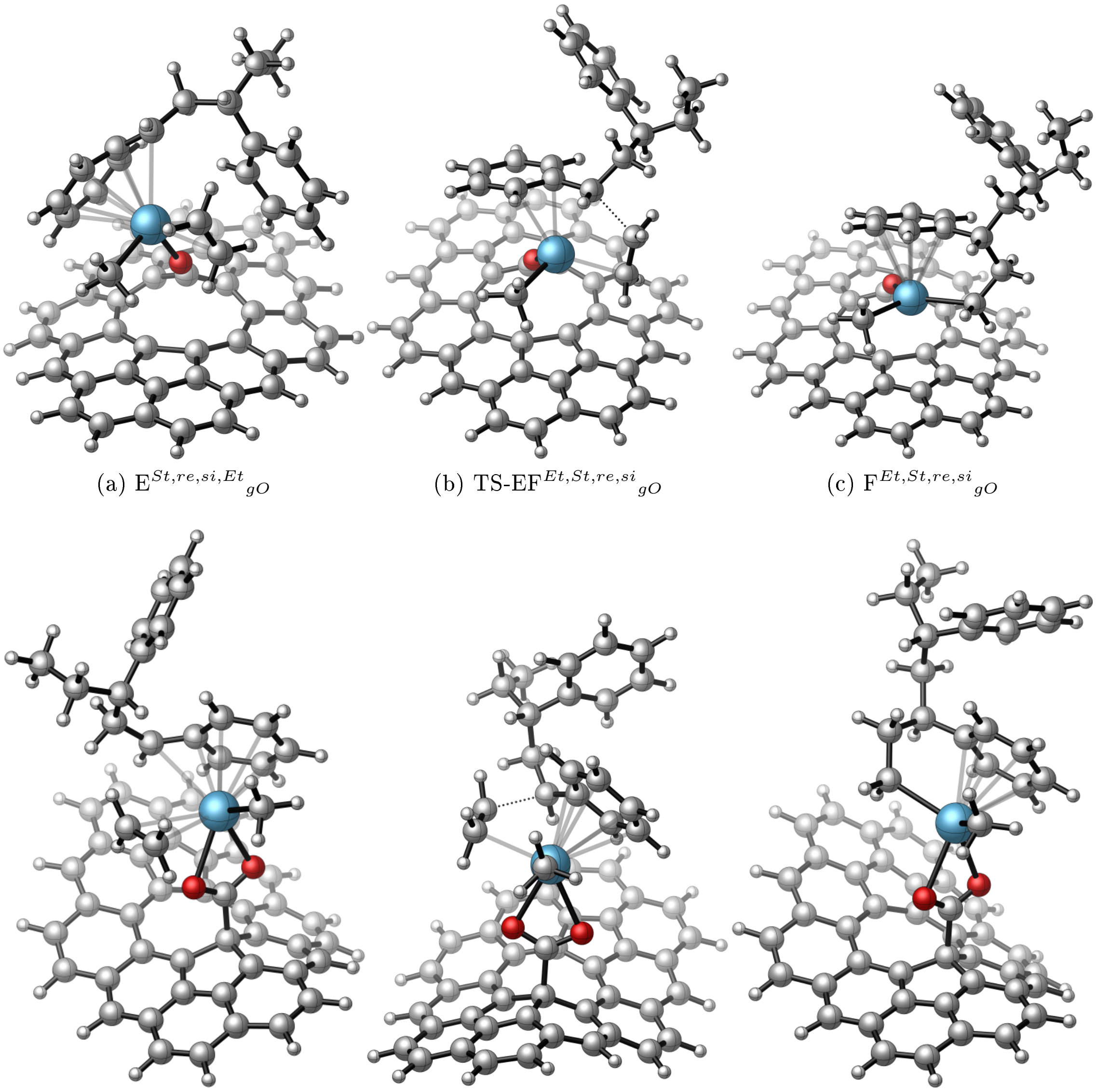

(a) $\mathrm{E}^{St,re,si,Et}{}_{gO}$

(b) $\mathrm{TS\text{-}EF}^{Et,St,re,si}{}_{gO}$

(c) $\mathrm{F}^{Et,St,re,si}{}_{gO}$

(d) $\mathrm{E}^{St,re,si,Et}{}_{gOO}$

(e) $\mathrm{TS\text{-}EF}^{St,re,si,Et}{}_{gOO}$

(f) $\mathrm{F}^{St,re,si,Et}{}_{gOO}$

FIGURE 167: Optimised structures of the complexes involved in the third ethylene insertion in the ethylene and styrene copolymerisation mediated by the $\mathrm{D}^{St,re,si}{}_{gO}$ and $\mathrm{D}^{St,re,si}{}_{gOO}$ compounds.

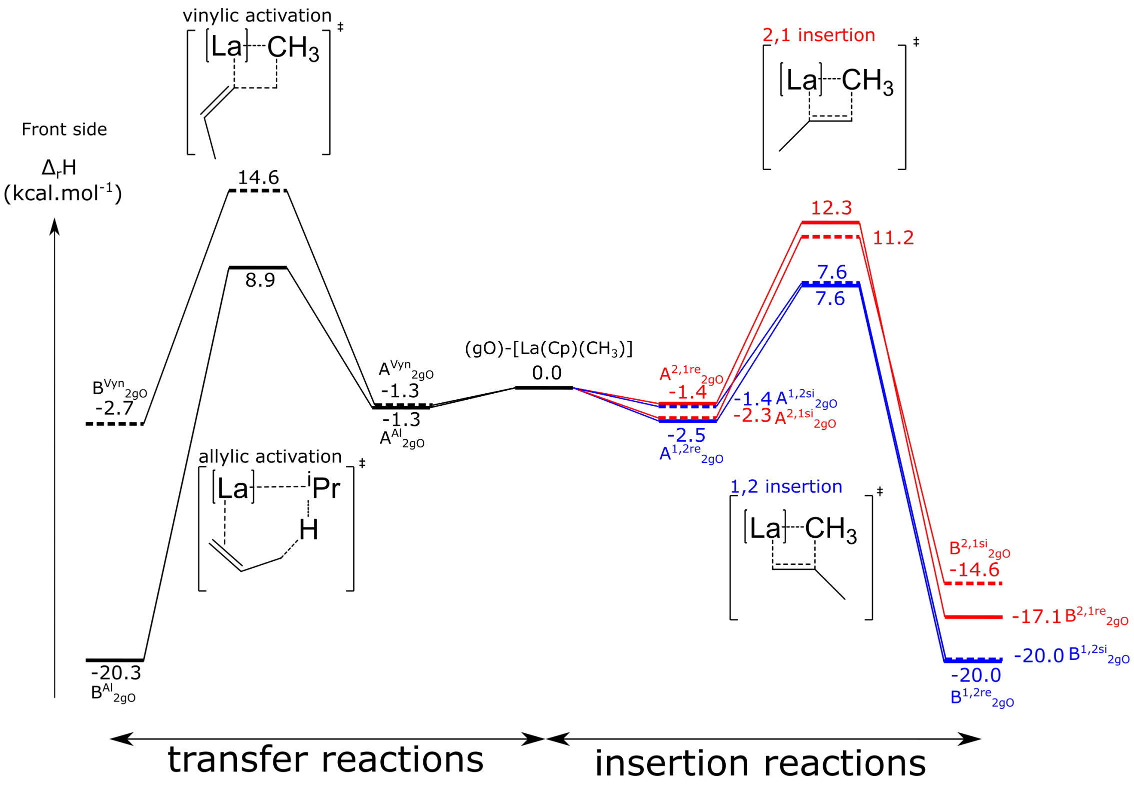

Figure 168: Calculated enthalpy profile for the first 1,2 and 2,1 front side monomer propene insertion (on the right) and for the front side allylic and vinylic C-H activation insertion (on the left) of the front side path of the propylene homopolymerisation reaction mediated by (gO)-[La(Cp)($CH_3$)] (2gO).

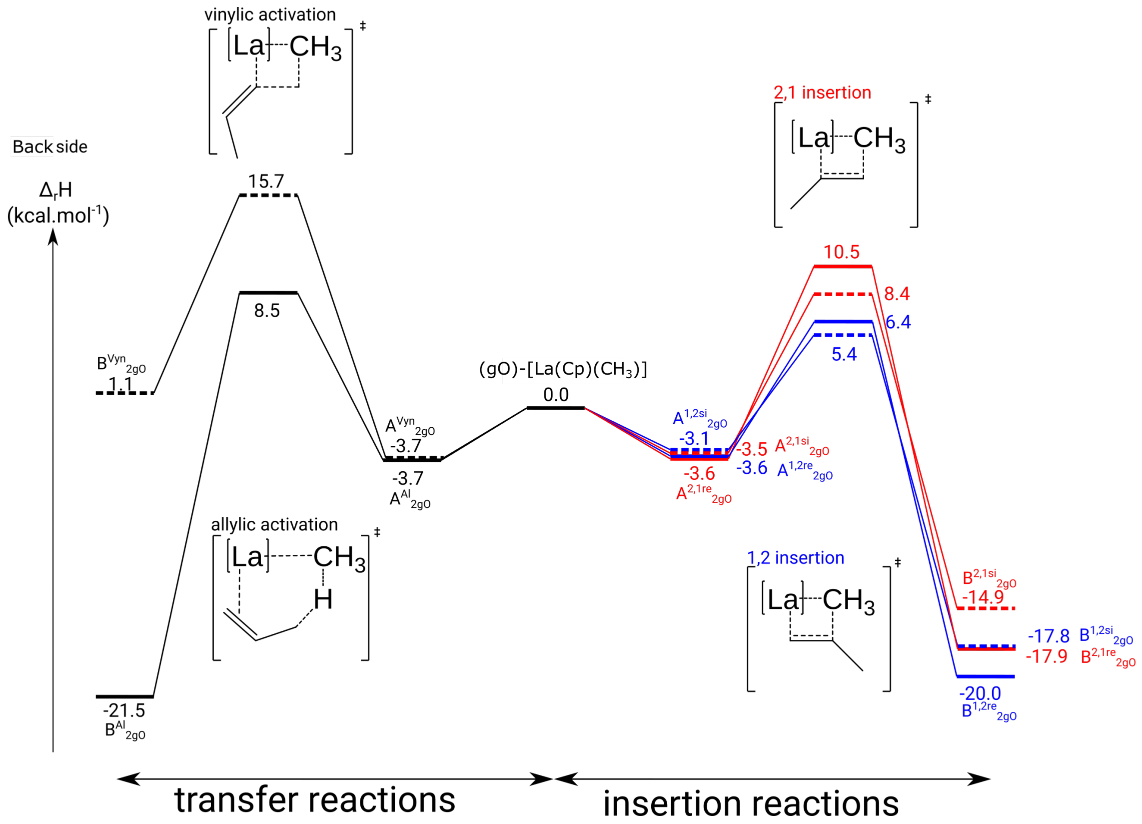

Figure 169: Calculated enthalpy profile for the first 1,2 and 2,1 front side monomer propene insertion (on the right) and for the front side allylic and vinylic C-H activation insertion (on the left) of the back side path of the propylene homopolymerisation reaction mediated by (gO)-[La(Cp)($CH_3$)] (2gO).

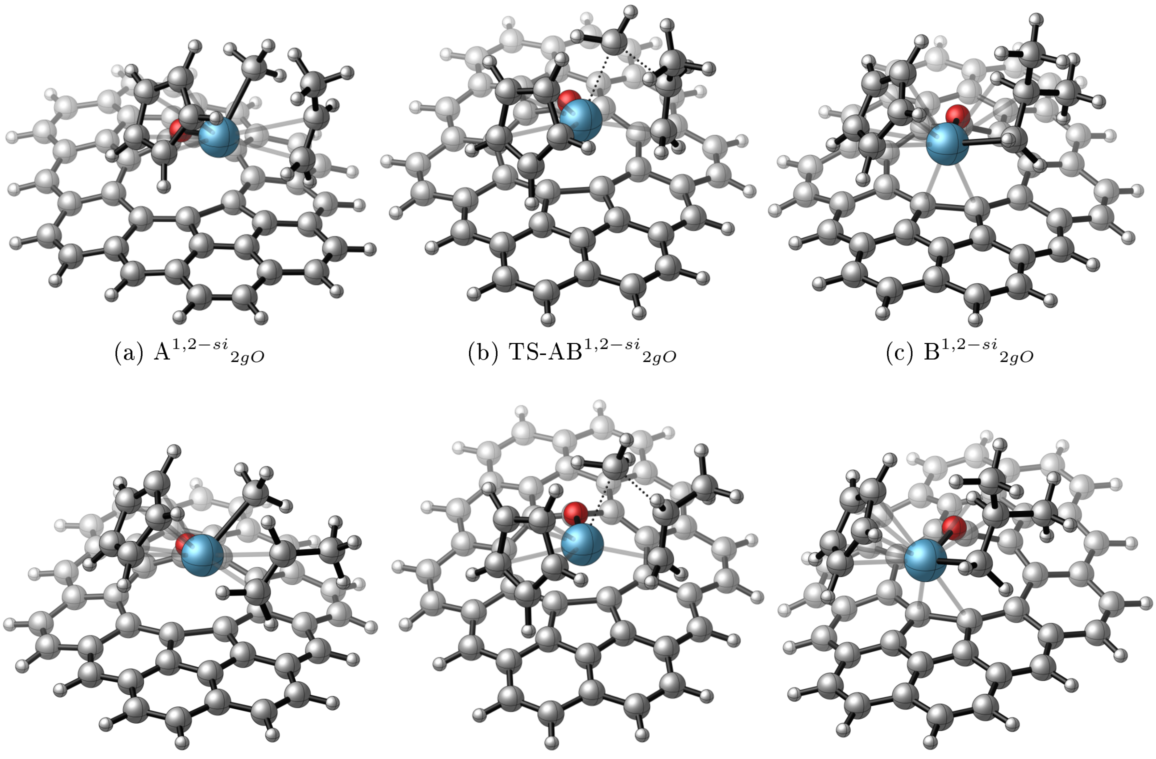

(a) $\mathrm{A}^{1,2-si}{}_{2gO}$ (b) $\mathrm{TS\text{-}AB}^{1,2-si}{}_{2gO}$ (c) $\mathrm{B}^{1,2-si}{}_{2gO}$

(d) $\mathrm{A}^{1,2-re}{}_{2gO}$ (e) $\mathrm{TS\text{-}AB}^{1,2-re}{}_{2gO}$ (f) $\mathrm{B}^{1,2-re}{}_{2gO}$

Figure 170: Geometries of the complexes involved in the first 1,2 front side propene insertion mediated by (gO)-[La(Cp)($CH_3$)] (2gO).

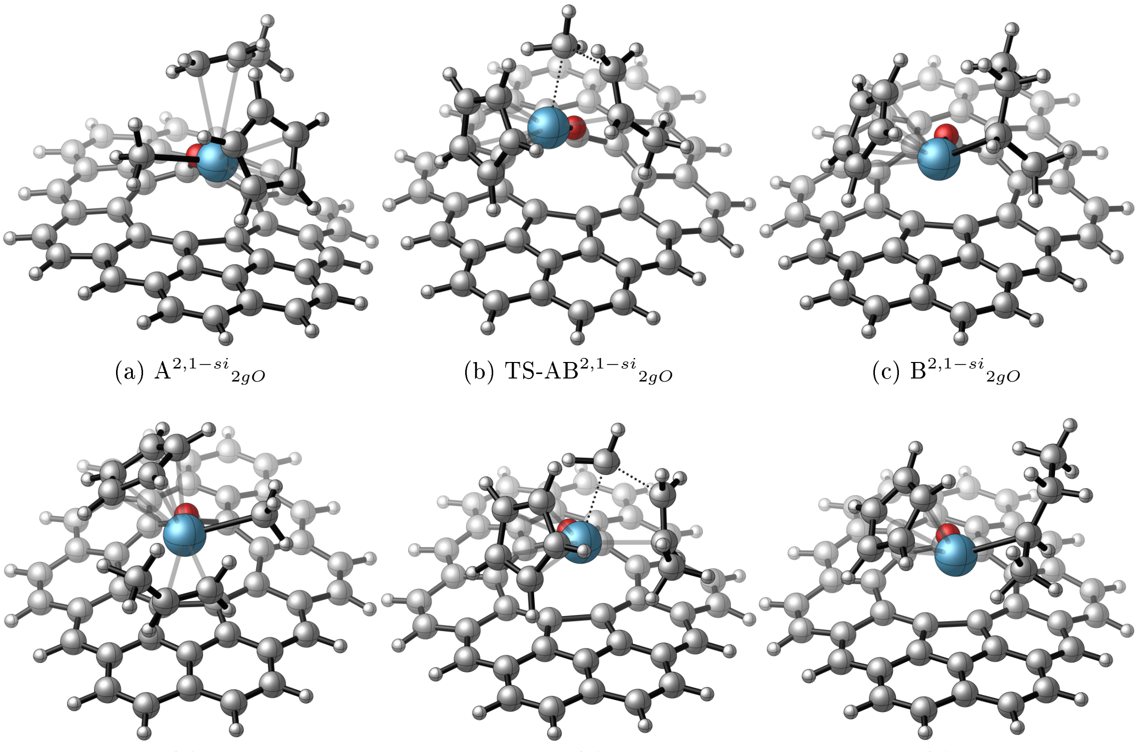

(a) $\mathrm{A}^{2,1-si}{}_{2gO}$ (b) $\mathrm{TS\text{-}AB}^{2,1-si}{}_{2gO}$ (c) $\mathrm{B}^{2,1-si}{}_{2gO}$

(d) $\mathrm{A}^{2,1-re}{}_{2gO}$ (e) $\mathrm{TS\text{-}AB}^{2,1-re}{}_{2gO}$ (f) $\mathrm{B}^{2,1-re}{}_{2gO}$

Figure 171: Geometries of the complexes involved in the first 2,1 front side propene insertion mediated by (gO)-[La(Cp)($CH_3$)] (2gO).

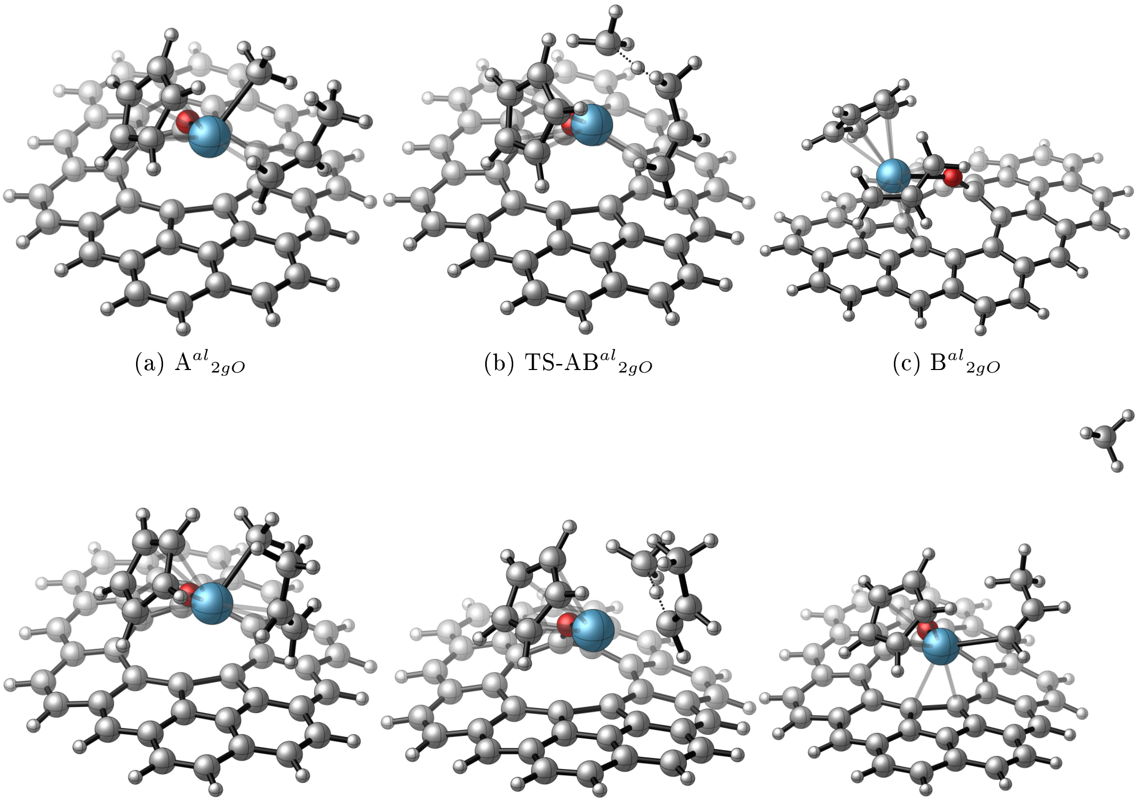

(a) A$^{al}{}_{2gO}$ (b) TS-AB$^{al}{}_{2gO}$ (c) B$^{al}{}_{2gO}$

(d) A$^{vyn}{}_{2gO}$ (e) TS-AB$^{vyn}{}_{2gO}$ (f) B$^{al}{}_{2gO}$

Figure 172: Geometries of the complexes involved in the front side allylic and vinylic C-H activation by (gO)-[La($CH_3$)Cp] (2gO).

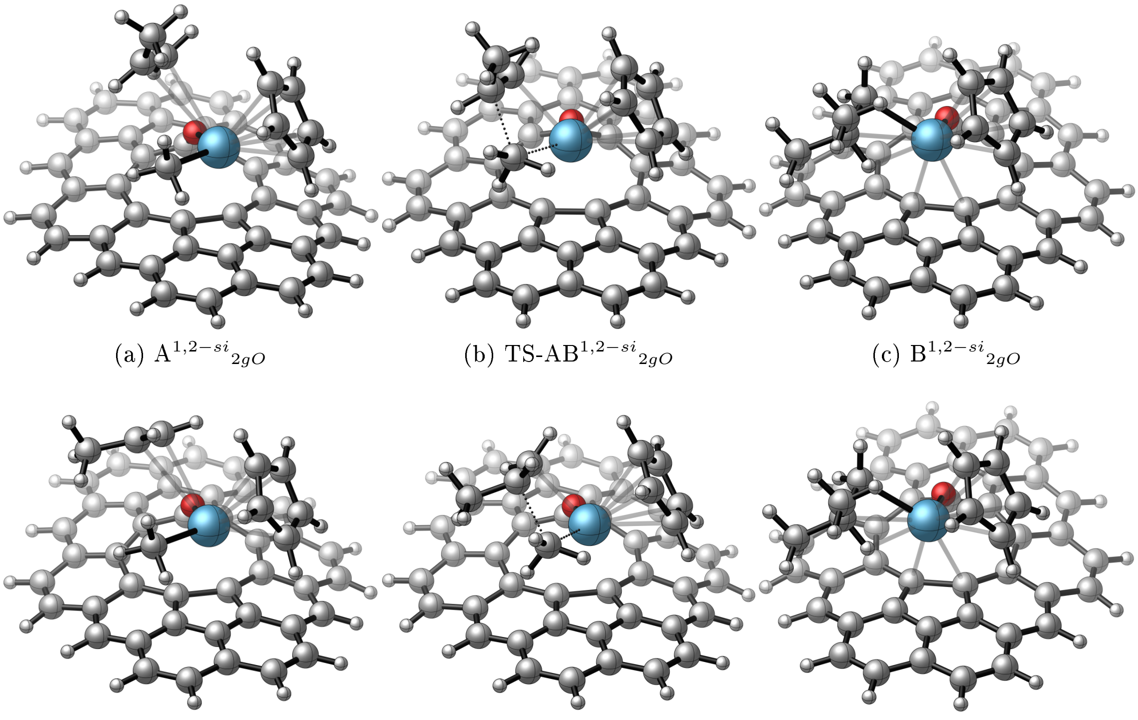

(a) A$^{1,2-si}{}_{2gO}$ (b) TS-AB$^{1,2-si}{}_{2gO}$ (c) B$^{1,2-si}{}_{2gO}$

(d) A$^{1,2-re}{}_{2gO}$ (e) TS-AB$^{1,2-re}{}_{2gO}$ (f) B$^{1,2-re}{}_{2gO}$

Figure 173: Geometries of the complexes involved in the first 1,2 back side propene insertion mediated by (gO)-[La(Cp)($CH_3$)] (2gO).

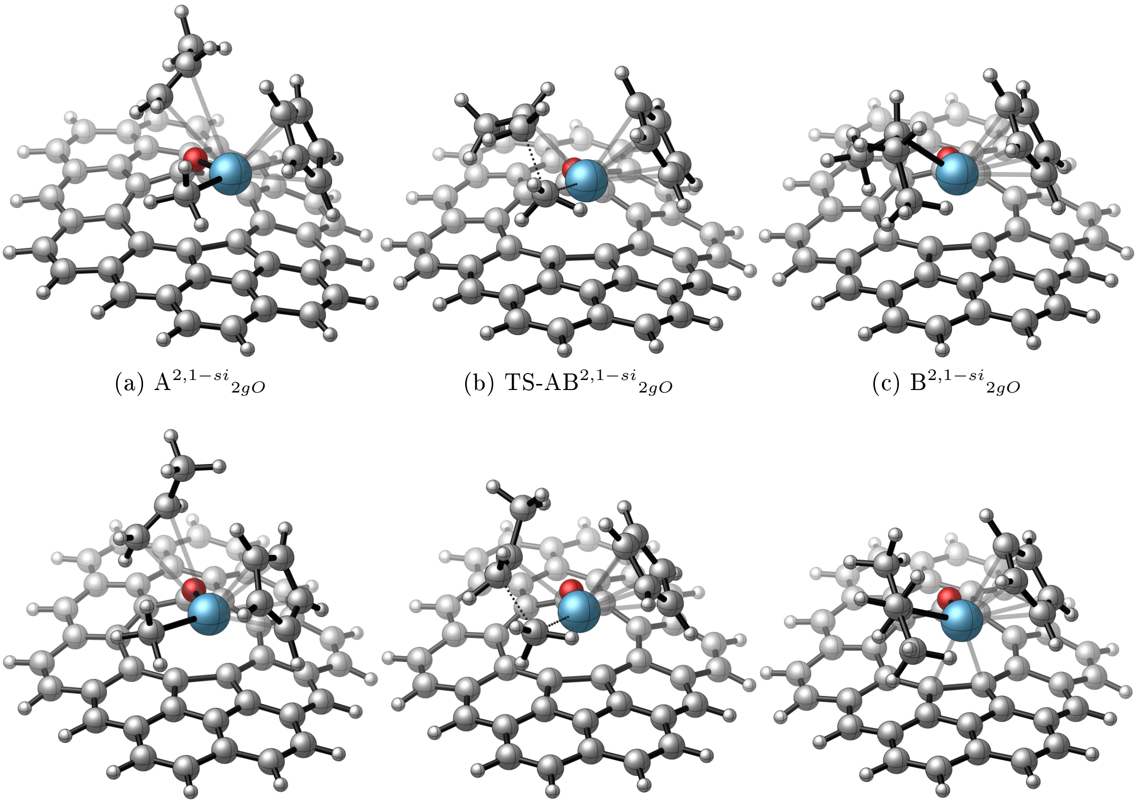

(a) $A^{2,1-si}{}_{2gO}$ (b) TS-$AB^{2,1-si}{}_{2gO}$ (c) $B^{2,1-si}{}_{2gO}$

(d) $A^{2,1-re}{}_{2gO}$ (e) TS-$AB^{2,1-re}{}_{2gO}$ (f) $B^{2,1-re}{}_{2gO}$

Figure 174: Geometries of the complexes involved in the first 2,1 back side propene insertion mediated by (gO)-[La(Cp)($CH_3$)] (2gO).

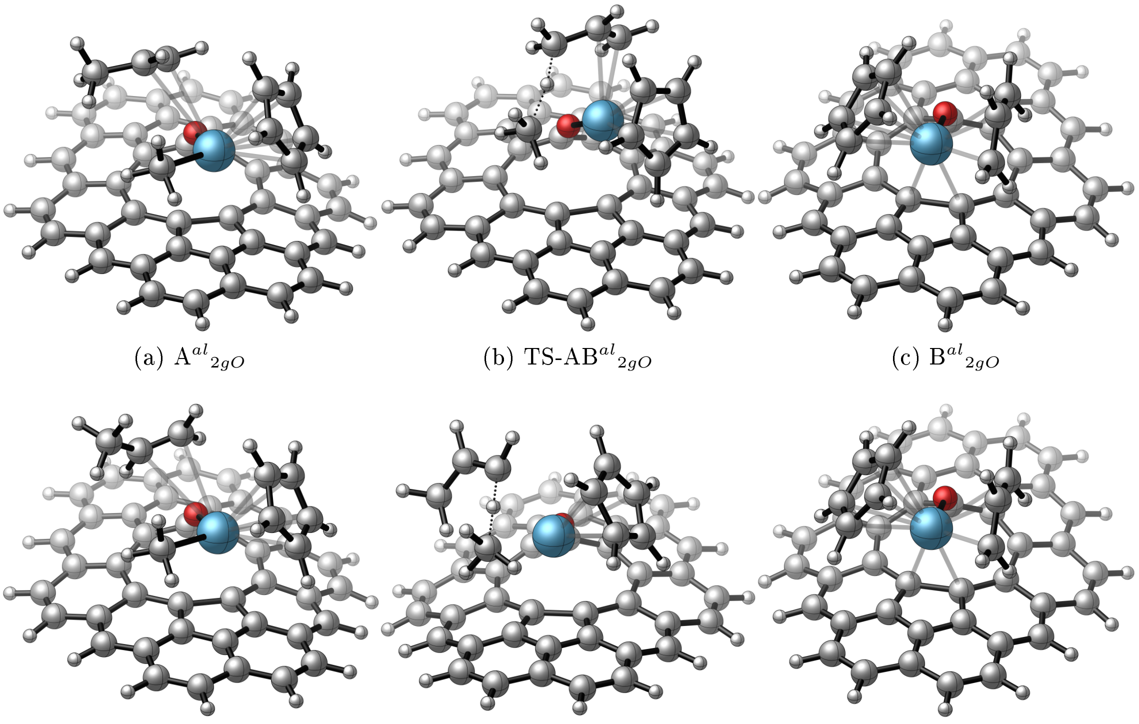

(a) $A^{al}{}_{2gO}$ (b) TS-$AB^{al}{}_{2gO}$ (c) $B^{al}{}_{2gO}$

(d) $A^{vyn}{}_{2gO}$ (e) TS-$AB^{vyn}{}_{2gO}$ (f) $B^{vyn}{}_{2gO}$

Figure 175: Geometries of the complexes involved in the back side allylic and vinylic C-H activation by (gO)-[La(Cp)($CH_3$)] (2gO).

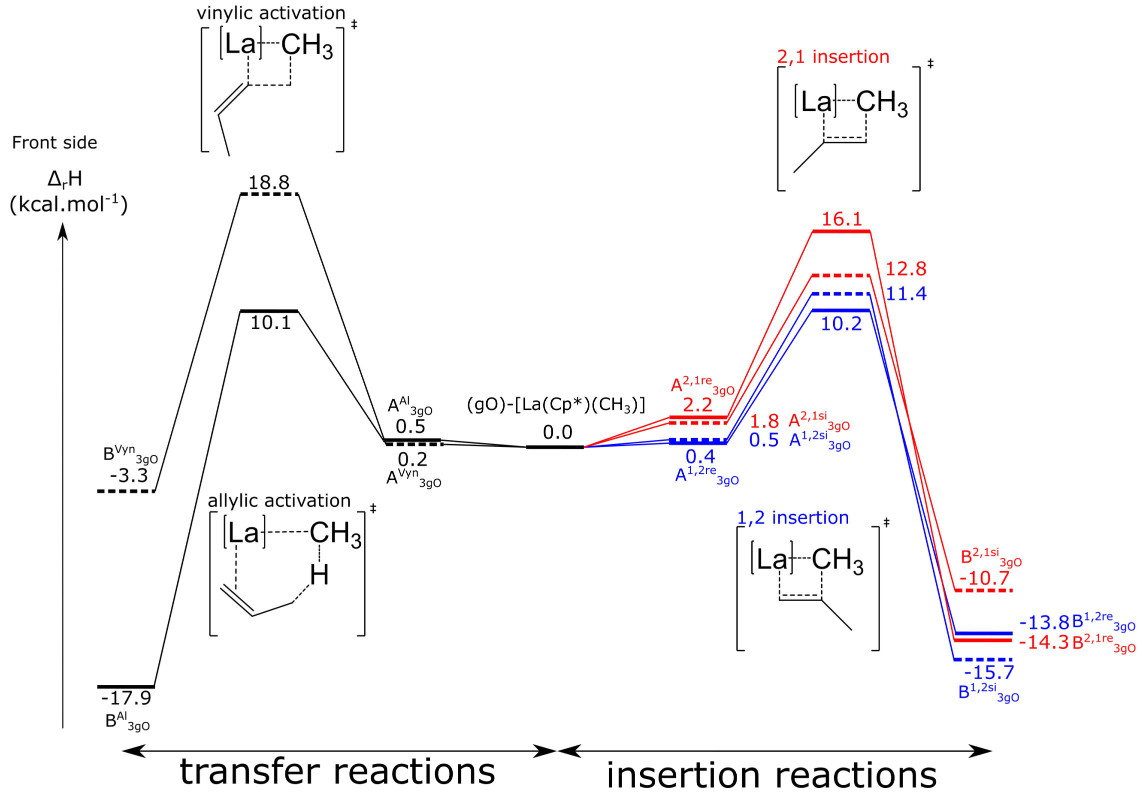

Figure 176: Calculated enthalpy profile for the first 1,2 and 2,1 front side monomer propene insertion (on the right) and for the front side allylic and vinylic C-H activation insertion (on the left) of the front side path of the propylene homopolymerisation reaction mediated by (gO)-[La(Cp*)($CH_3$)] (3gO).

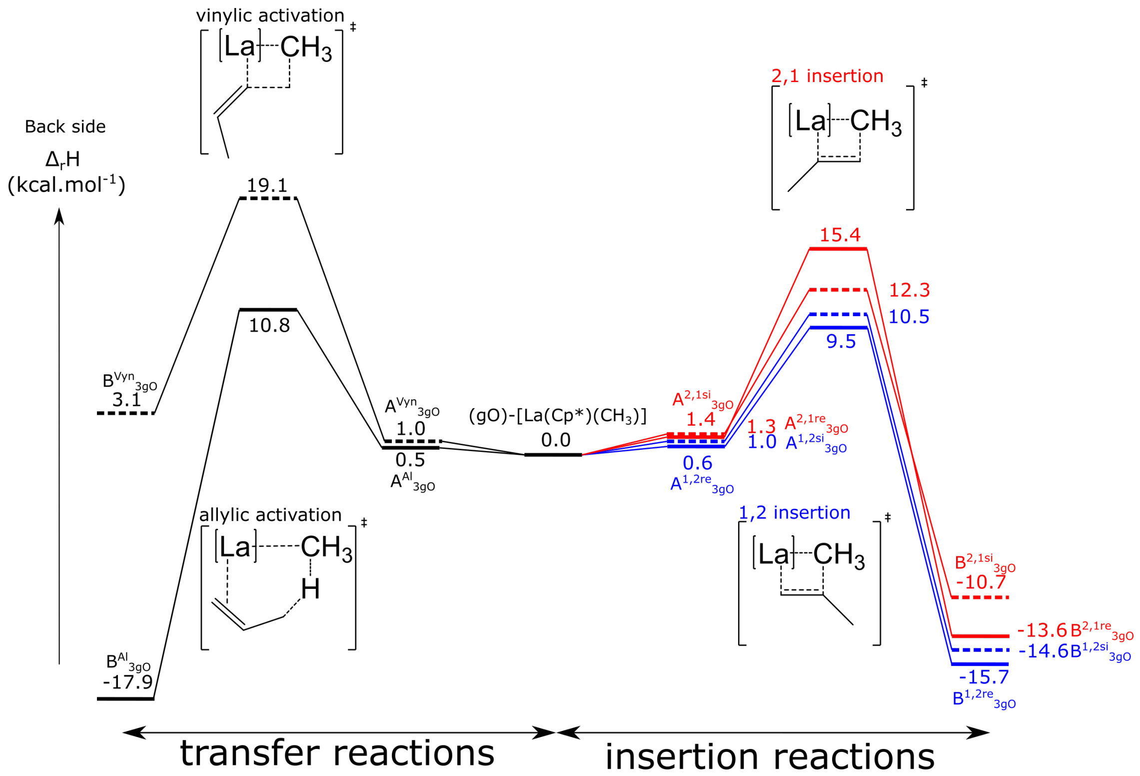

Figure 177: Calculated enthalpy profile for the first 1,2 and 2,1 back side monomer propene insertion (on the right) and for the front side allylic and vinylic C-H activation insertion (on the left) of the front side path of the propylene homopolymerisation reaction mediated by (gO)-[La(Cp*)(CH$_3$)] (3gO).

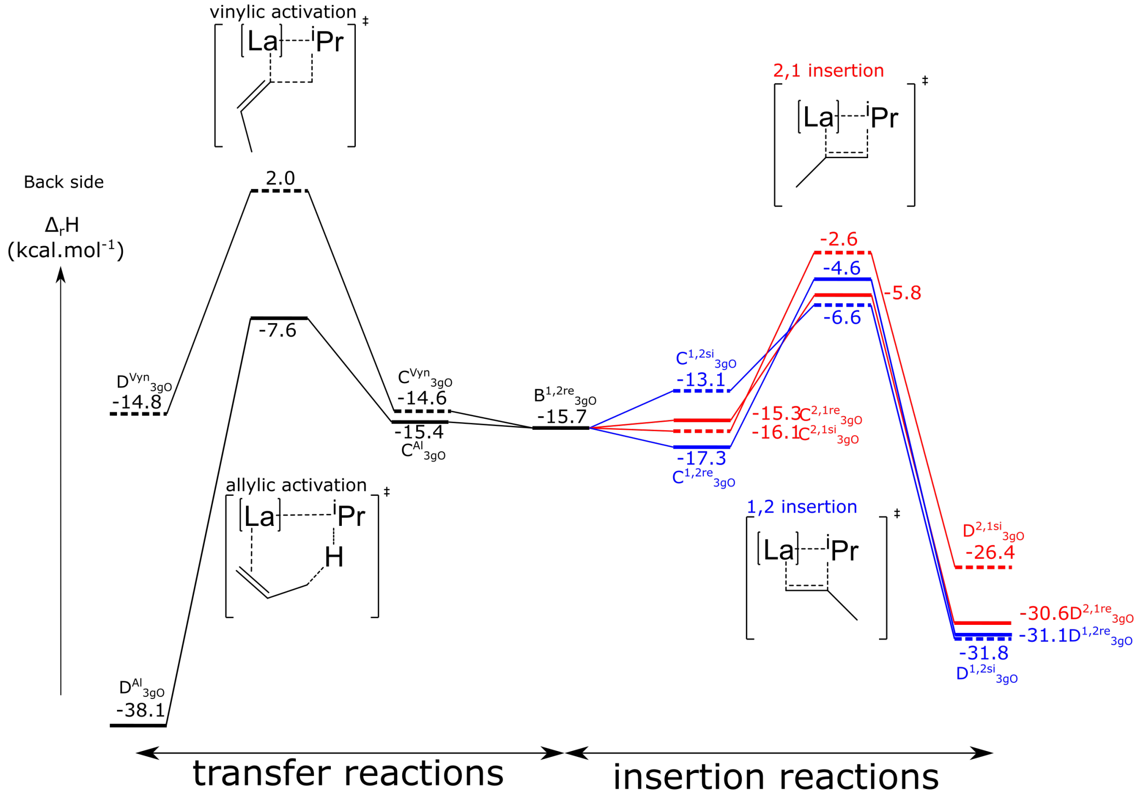

Figure 193: Calculated enthalpy profile for the second 1,2 and 2,1 back side propene insertion (on the right) and for the back side allylic and vinylic C-H activation (on the left) mediated by the $B^{1,2re}{}_{3gO}$ complex.

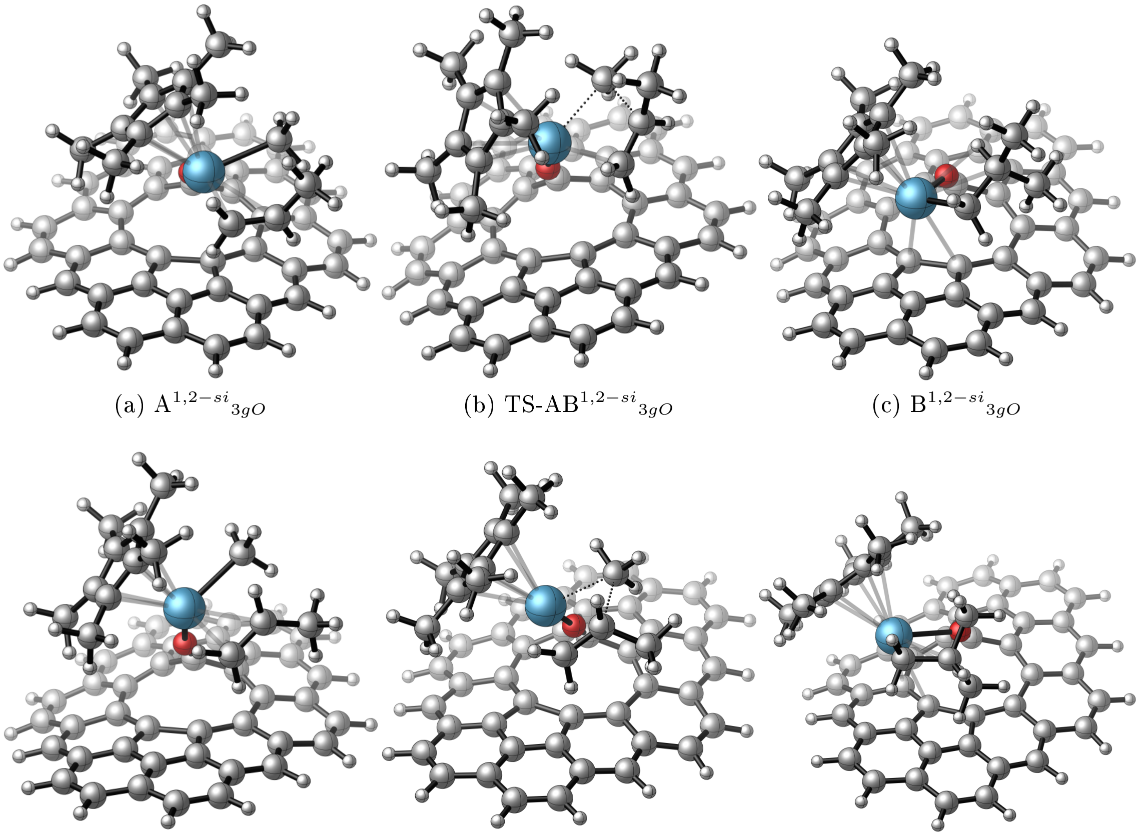

(a) $\mathrm{A}^{1,2-si}{}_{3gO}$

(b) TS-$\mathrm{AB}^{1,2-si}{}_{3gO}$

(c) $\mathrm{B}^{1,2-si}{}_{3gO}$

(d) $\mathrm{A}^{1,2-re}{}_{3gO}$

(e) TS-$\mathrm{AB}^{1,2-re}{}_{3gO}$

(f) $\mathrm{B}^{1,2-re}{}_{3gO}$

Figure 178: Geometries of the complexes involved in the first 1,2 front side propene insertion mediated by (gO)-[La(Cp*)($CH_3$)] (3gO).

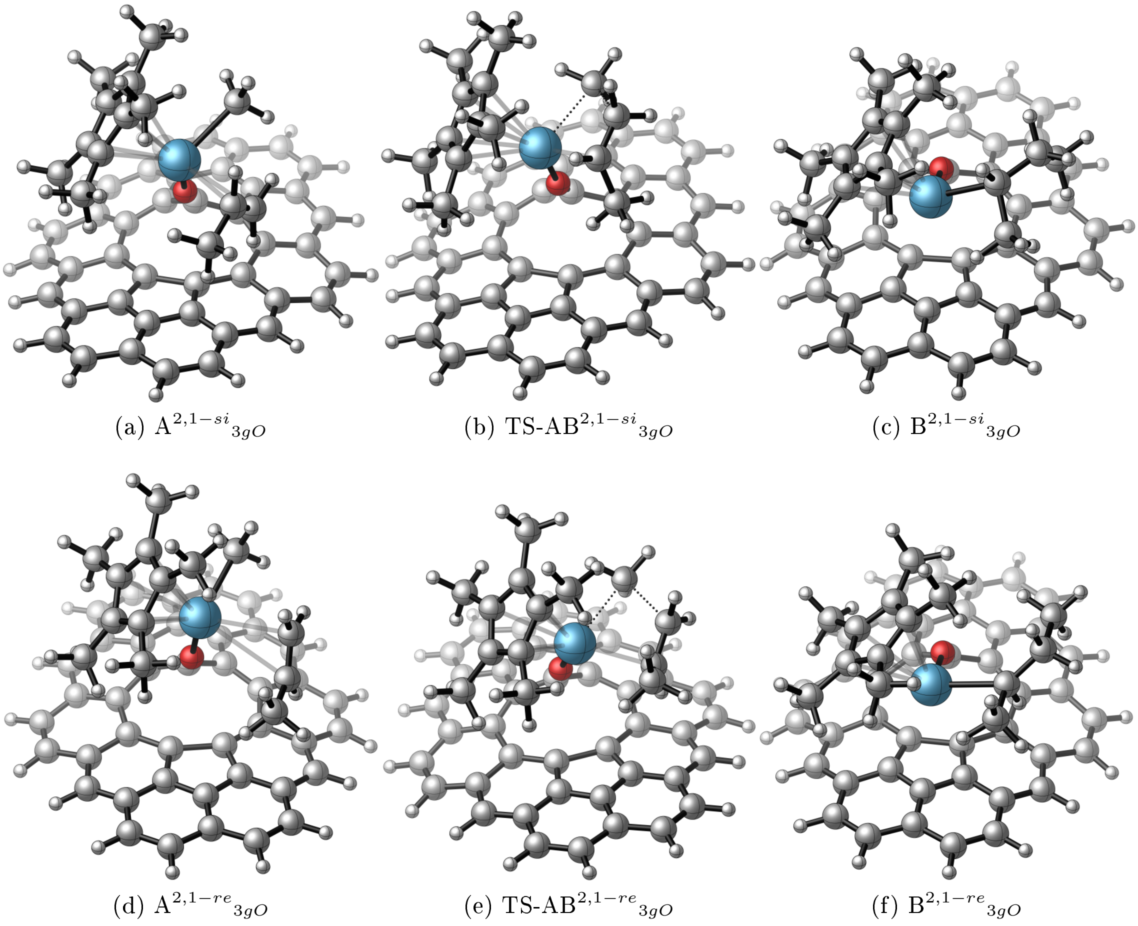

(a) $A^{2,1-si}{}_{3gO}$ (b) TS-$AB^{2,1-si}{}_{3gO}$ (c) $B^{2,1-si}{}_{3gO}$

(d) $A^{2,1-re}{}_{3gO}$ (e) TS-$AB^{2,1-re}{}_{3gO}$ (f) $B^{2,1-re}{}_{3gO}$

Figure 179: Geometries of the complexes involved in the first 2,1 front side propene insertion mediated by (gO)-[La(Cp*)($CH_3$)] (3gO).

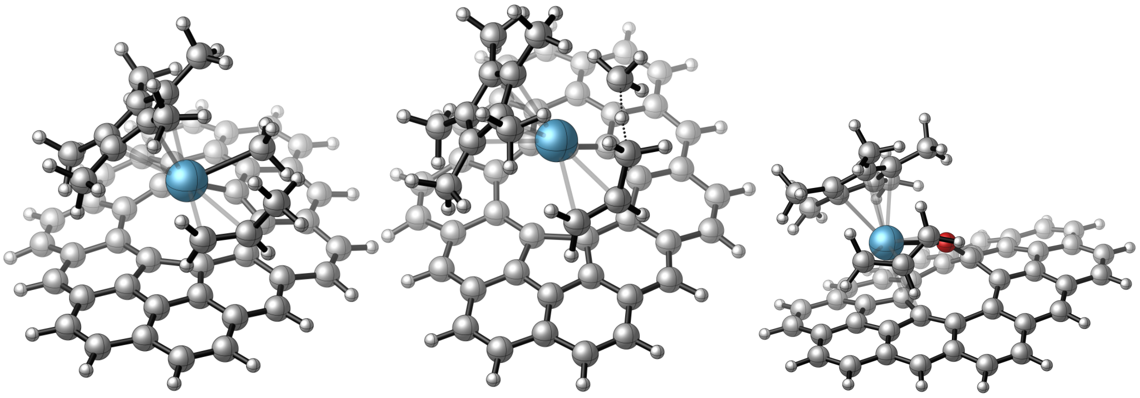

(a) $A^{al}{}_{3gO}$ (b) TS-$AB^{al}{}_{3gO}$ (c) $B^{al}{}_{3gO}$

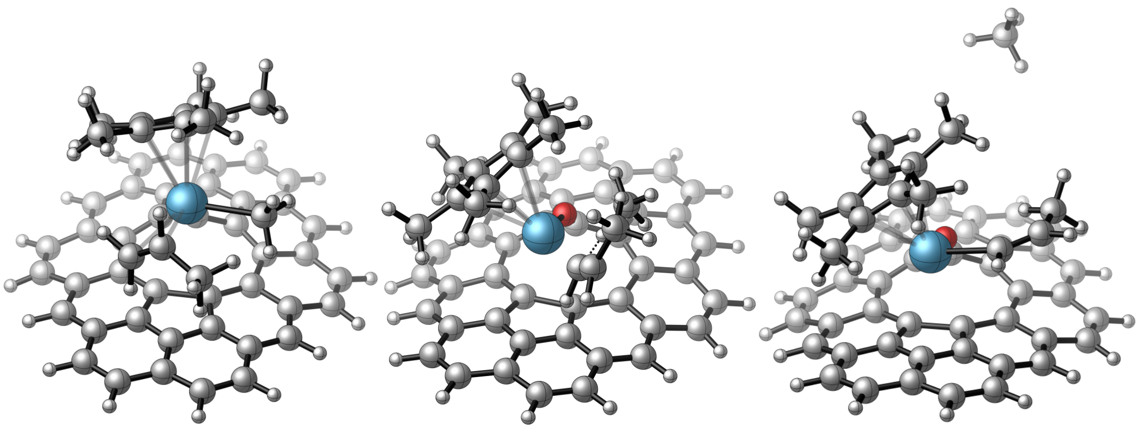

(d) $A^{vyn}{}_{3gO}$ (e) TS-$AB^{vyn}{}_{3gO}$ (f) $B^{vyn}{}_{3gO}$

Figure 180: Geometries of the complexes involved in the front side allylic and vinylic C-H activation by (gO)-[La($CH_3$)Cp*] (3gO).

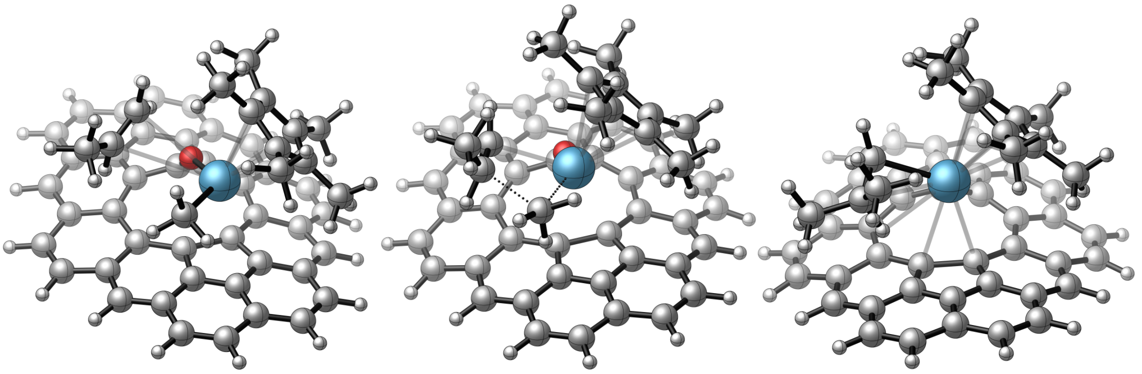

(a) $\mathrm{A}^{1,2-si}{}_{3gO}$ (b) TS-$\mathrm{AB}^{1,2-si}{}_{3gO}$ (c) $\mathrm{B}^{1,2-si}{}_{3gO}$

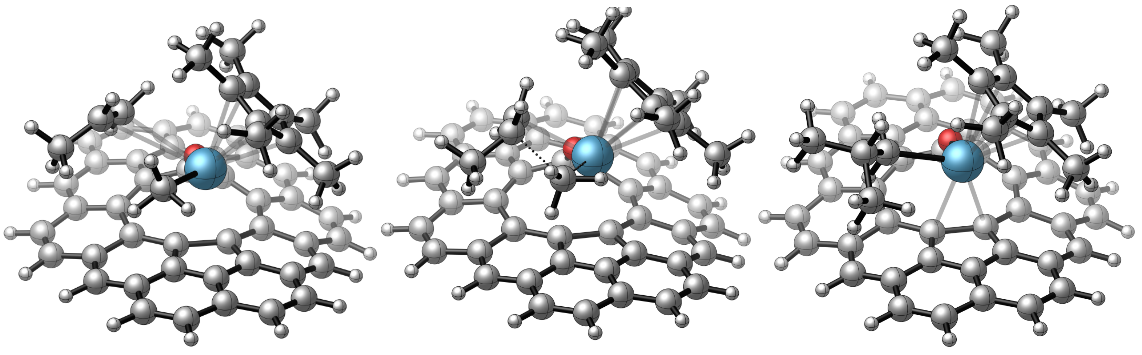

(d) $\mathrm{A}^{1,2-re}{}_{3gO}$ (e) TS-$\mathrm{AB}^{1,2-re}{}_{3gO}$ (f) $\mathrm{B}^{1,2-re}{}_{3gO}$

Figure 181: Geometries of the complexes involved in the first 1,2 back side propene insertion mediated by (gO)-[La($CH_3$)Cp*] (3gO).

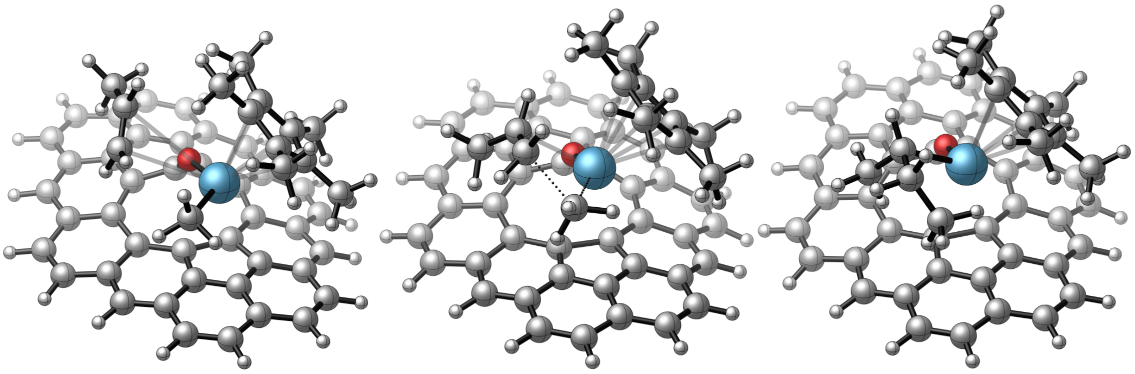

(a) A$^{2,1-si}{}_{3gO}$ (b) TS-AB$^{2,1-si}{}_{3gO}$ (c) B$^{2,1-si}{}_{3gO}$

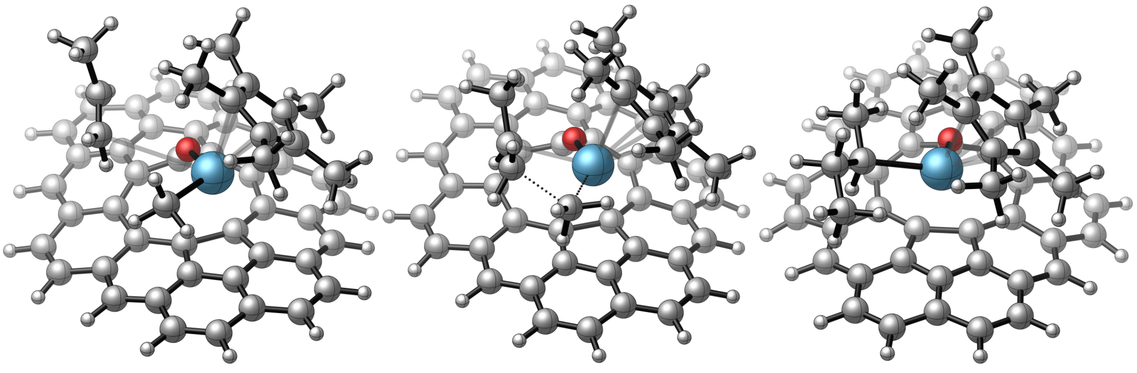

(d) A$^{2,1-re}{}_{3gO}$ (e) TS-AB$^{2,1-re}{}_{3gO}$ (f) B$^{2,1-re}{}_{3gO}$

Figure 182: Geometries of the complexes involved in the first 2,1 back side propene insertion mediated by (gO)-[La(CH$_3$)Cp*] (3gO).

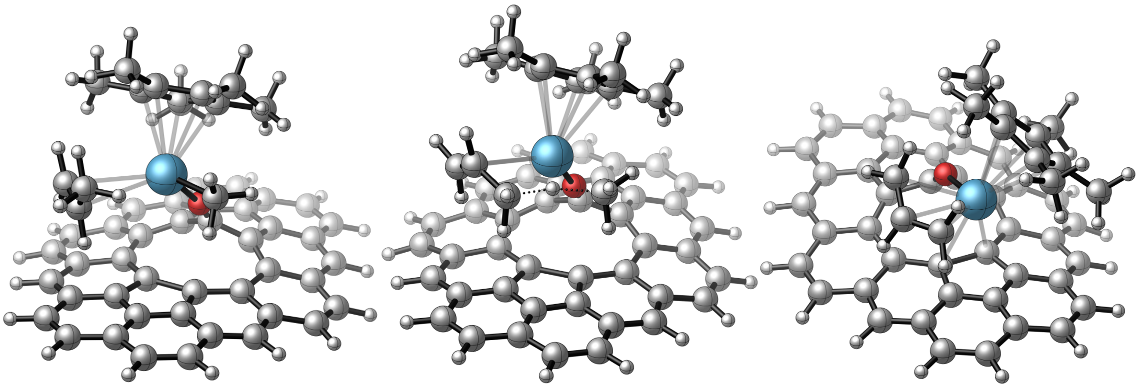

(a) $\mathrm{A}^{al}{}_{3gO}$ (b) $\mathrm{TS\text{-}AB}^{al}{}_{3gO}$ (c) $\mathrm{B}^{al}{}_{3gO}$

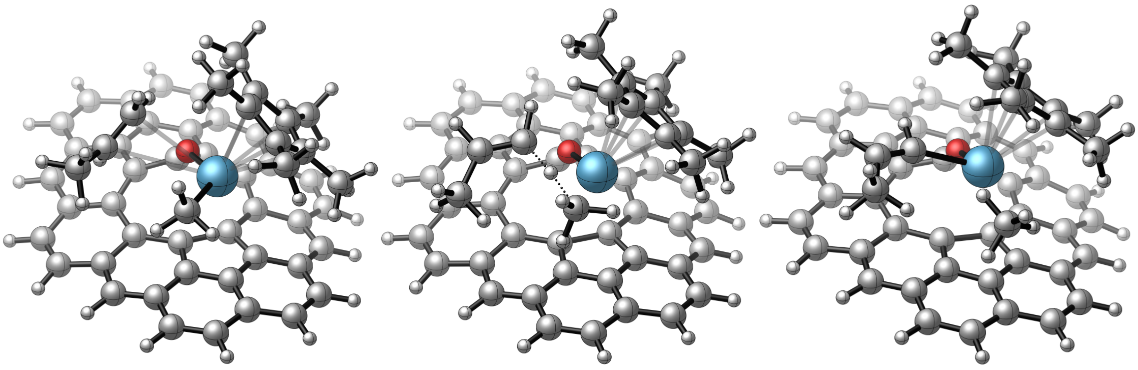

(d) $\mathrm{A}^{vyn}{}_{3gO}$ (e) $\mathrm{TS\text{-}AB}^{vyn}{}_{3gO}$ (f) $\mathrm{B}^{vyn}{}_{3gO}$

Figure 183: Geometries of the complexes involved in the back side allylic and vinylic C-H activation by (gO)-[La($CH_3$)Cp*] (3gO).

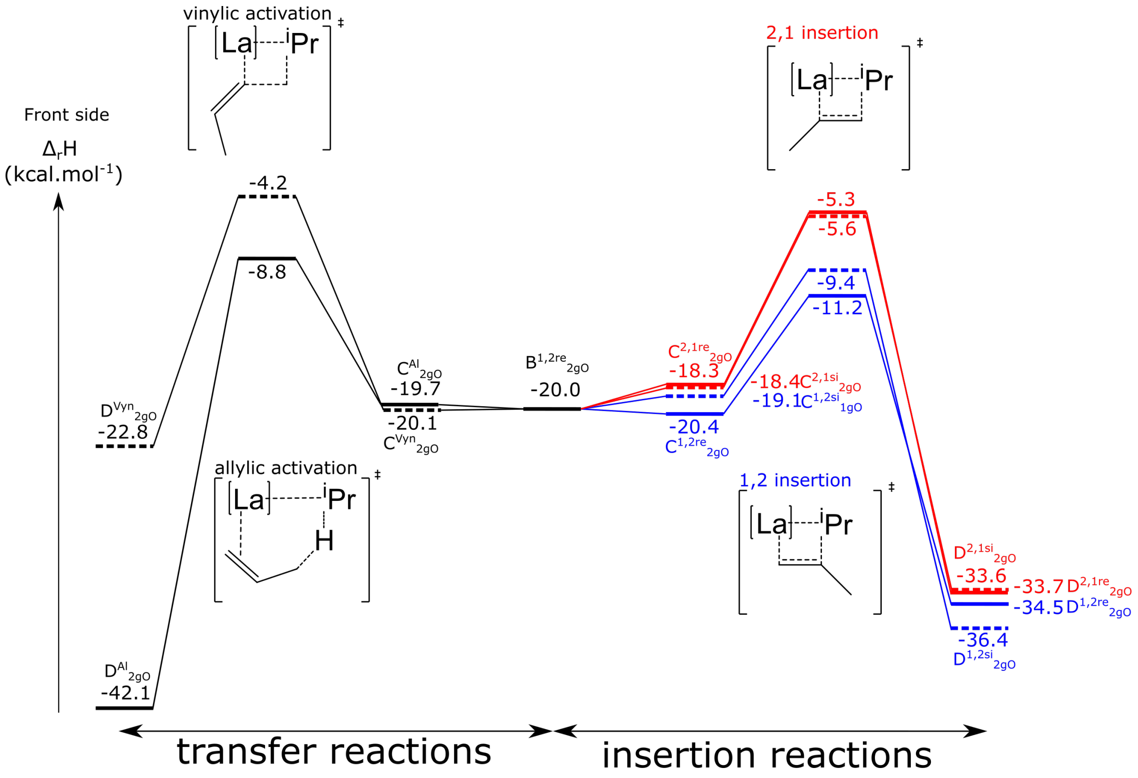

Figure 184: Calculated enthalpy profile for the second 1,2 and 2,1 front side propene insertion (on the right) and for the front side allylic and vinylic C-H activation (on the left) mediated by the $B^{1,2re}_{2gO}$ complex.

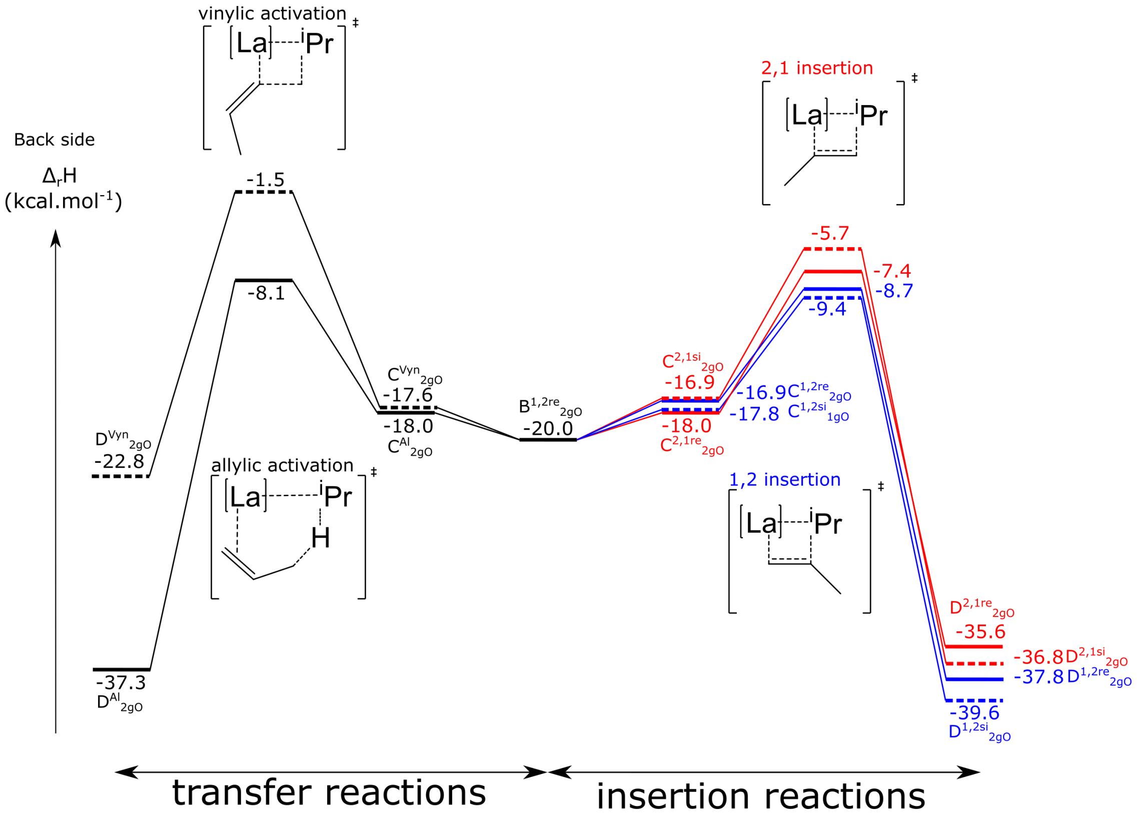

Figure 185: Calculated enthalpy profile for the second 1,2 and 2,1 back side propene insertion (on the right) and for the back side allylic and vinylic C-H activation (on the left) mediated by the $B^{1,2re}_{2gO}$ complex.

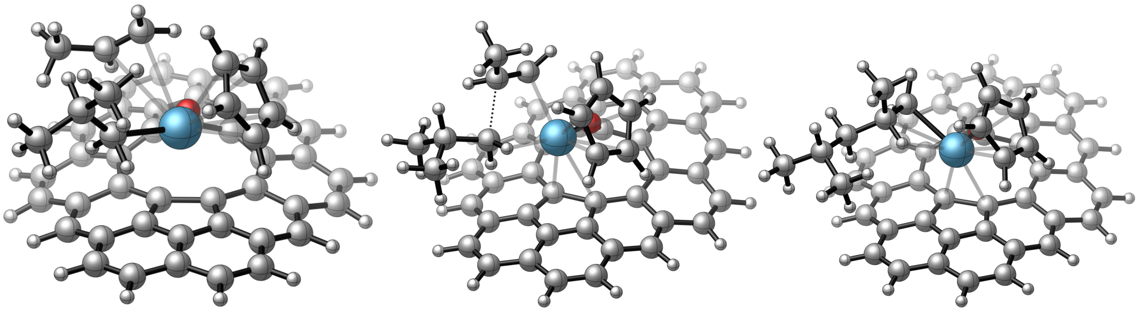

(a) $\mathrm{C}^{1,2-si}{}_{2gO}$ (b) TS-$\mathrm{CD}^{1,2-si}{}_{2gO}$ (c) $\mathrm{D}^{1,2-si}{}_{2gO}$

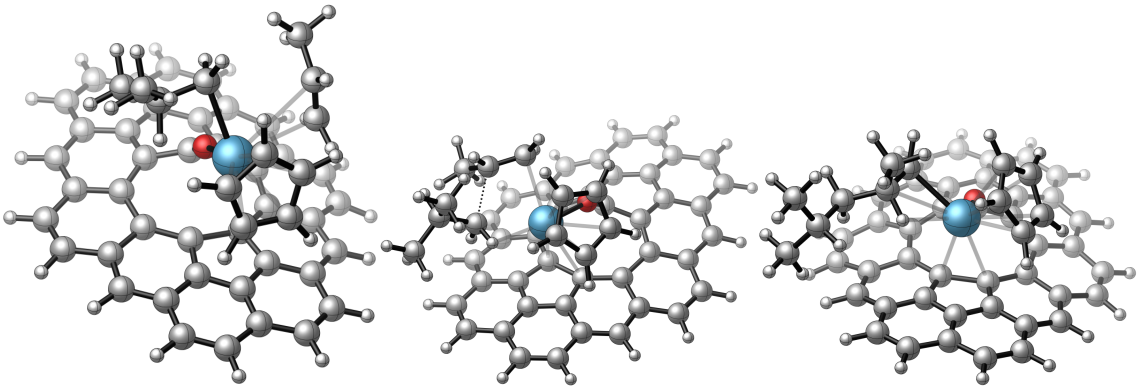

(d) $\mathrm{C}^{1,2-re}{}_{2gO}$ (e) TS-$\mathrm{CD}^{1,2-re}{}_{2gO}$ (f) $\mathrm{D}^{1,2-re}{}_{2gO}$

Figure 186: Geometries of the complexes involved in the second 1,2 front side propene insertion mediated by the $\mathrm{B}^{1,2re}{}_{2gO}$ complex.

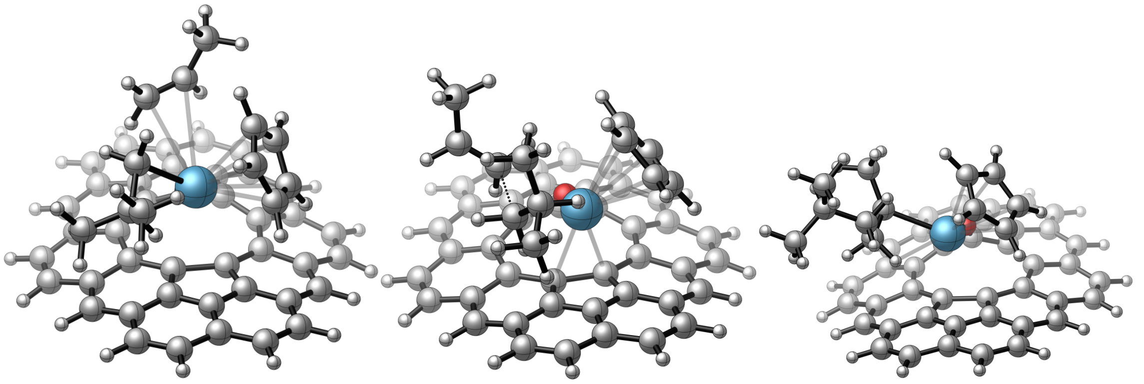

(a) $\mathrm{C}^{2,1-si}{}_{2gO}$ (b) $\mathrm{TS\text{-}CD}^{2,1-si}{}_{2gO}$ (c) $\mathrm{D}^{2,1-si}{}_{2gO}$

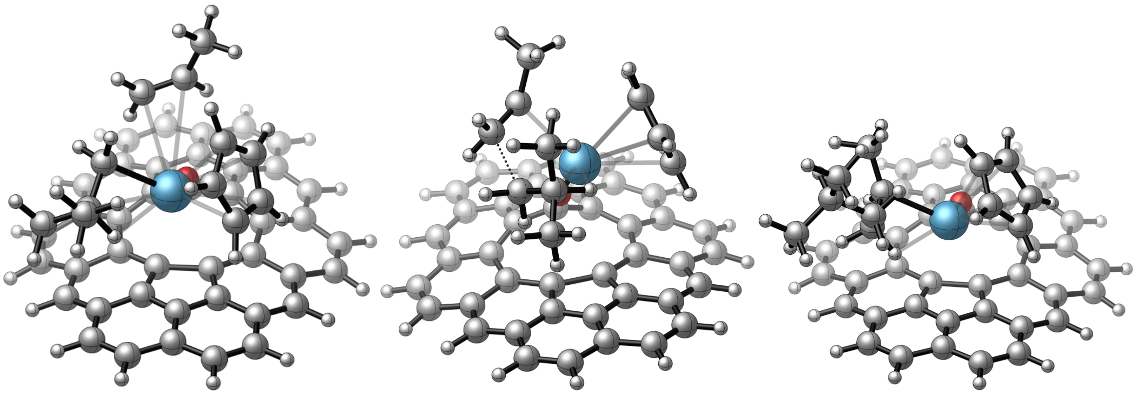

(d) $\mathrm{C}^{2,1-re}{}_{2gO}$ (e) $\mathrm{TS\text{-}CD}^{2,1-re}{}_{2gO}$ (f) $\mathrm{D}^{2,1-re}{}_{2gO}$

Figure 187: Geometries of the complexes involved in the second 2,1 front side propene insertion mediated by the $\mathrm{B}^{1,2re}{}_{2gO}$ complex.

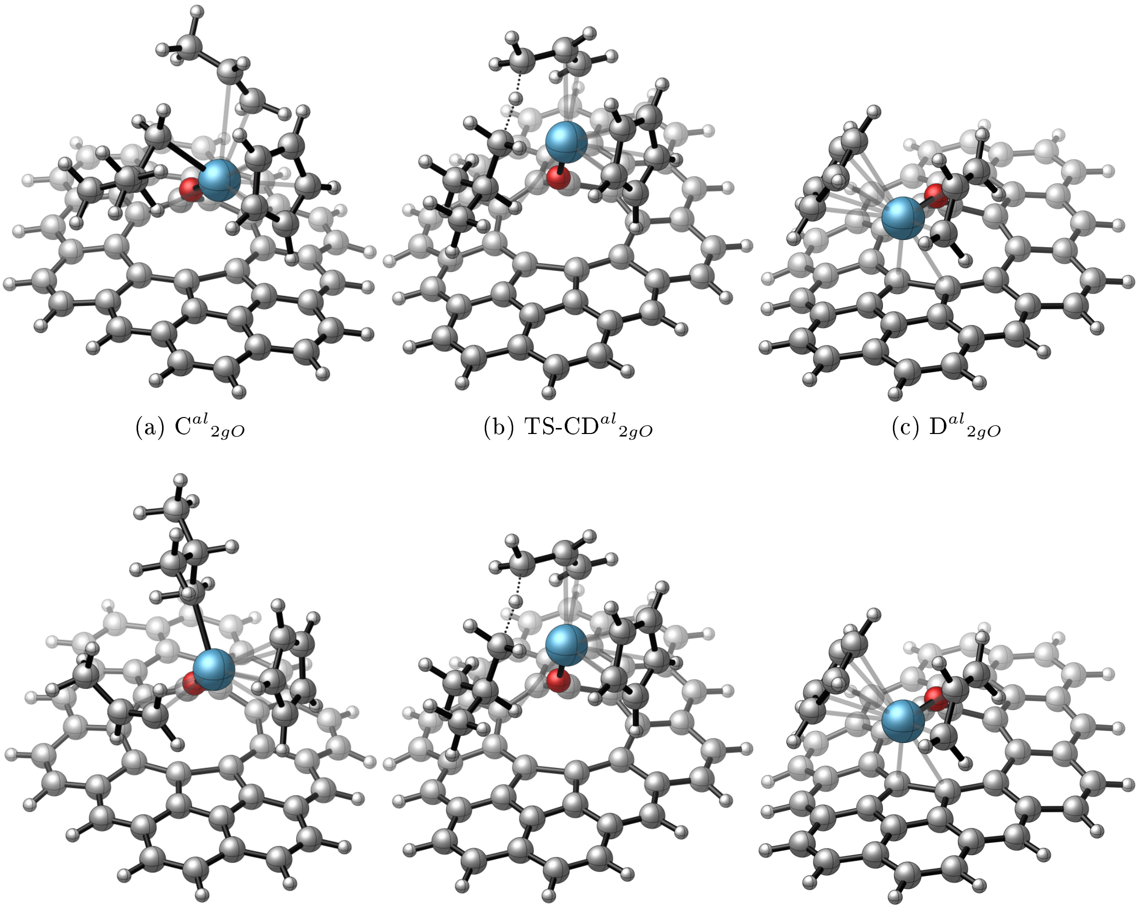

(a) $\mathrm{C}^{al}{}_{2gO}$ (b) $\mathrm{TS\text{-}CD}^{al}{}_{2gO}$ (c) $\mathrm{D}^{al}{}_{2gO}$

(d) $\mathrm{C}^{vyn}{}_{2gO}$ (e) $\mathrm{TS\text{-}CD}^{vyn}{}_{2gO}$ (f) $\mathrm{D}^{vyn}{}_{2gO}$

Figure 188: Geometries of the complexes involved in the front side allylic and vinylic C-H activation by the $\mathrm{B}^{1,2re}{}_{2gO}$ complex.

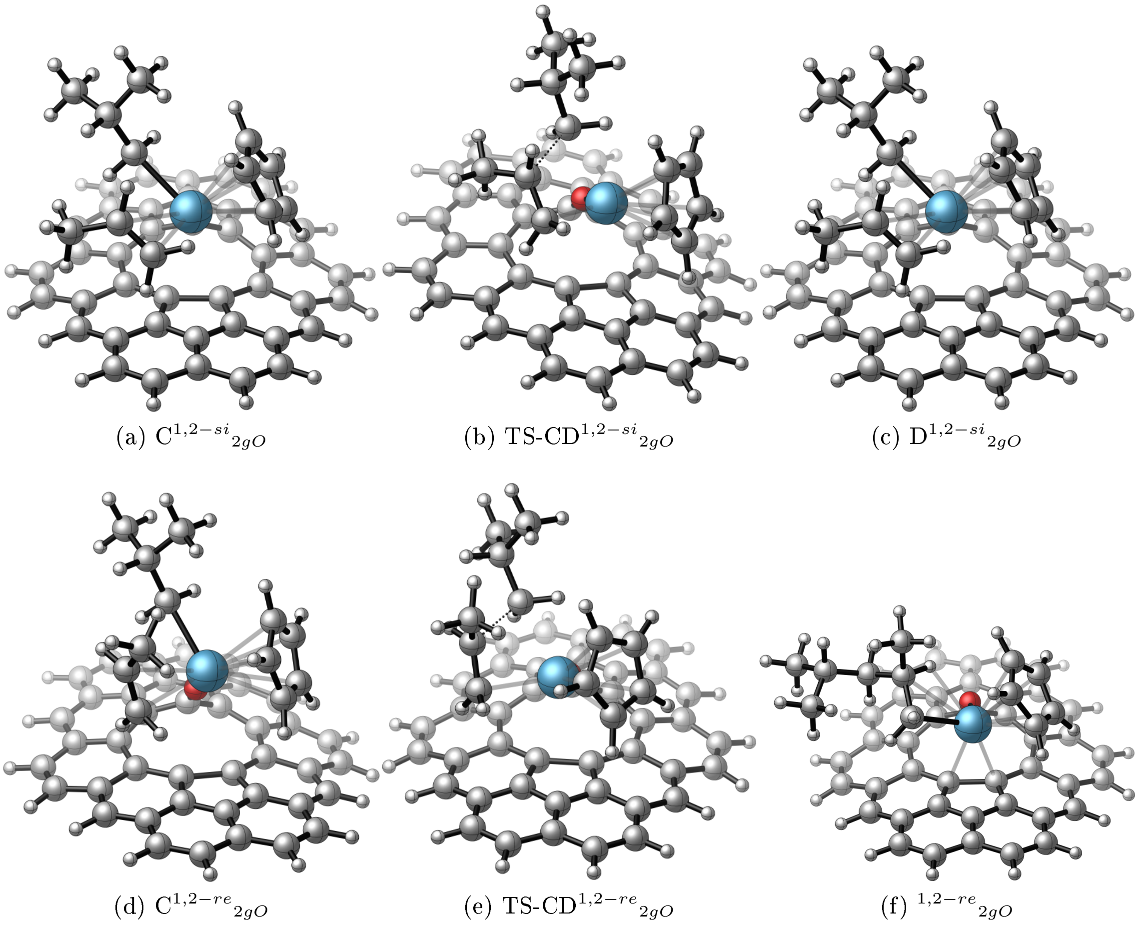

(a) $\mathrm{C}^{1,2-si}{}_{2gO}$

(b) TS-$\mathrm{CD}^{1,2-si}{}_{2gO}$

(c) $\mathrm{D}^{1,2-si}{}_{2gO}$

(d) $\mathrm{C}^{1,2-re}{}_{2gO}$

(e) TS-$\mathrm{CD}^{1,2-re}{}_{2gO}$

(f) ${}^{1,2-re}{}_{2gO}$

Figure 189: Geometries of the complexes involved in the second 1,2 back side propene insertion mediated by the $\mathrm{B}^{1,2re}{}_{2gO}$ complex.

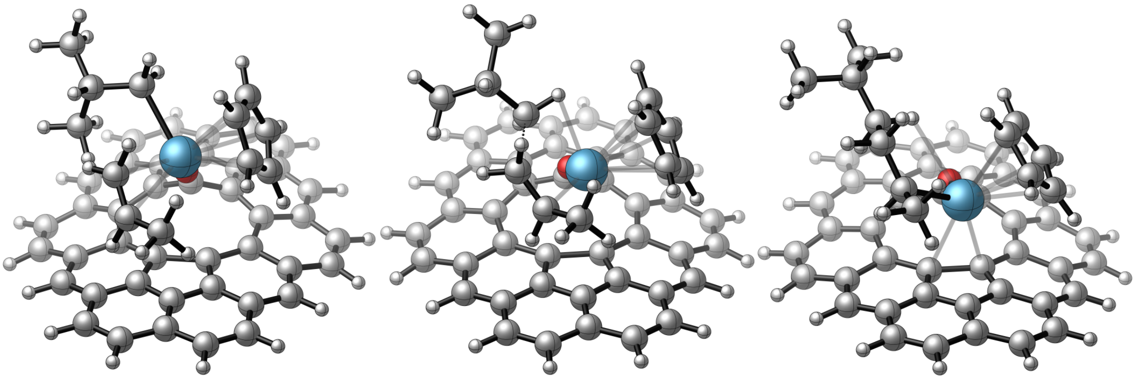

(a) $\mathrm{C}^{2,1-si}{}_{2gO}$ (b) $\mathrm{TS\text{-}CD}^{2,1-si}{}_{2gO}$ (c) $\mathrm{D}^{2,1-si}{}_{2gO}$

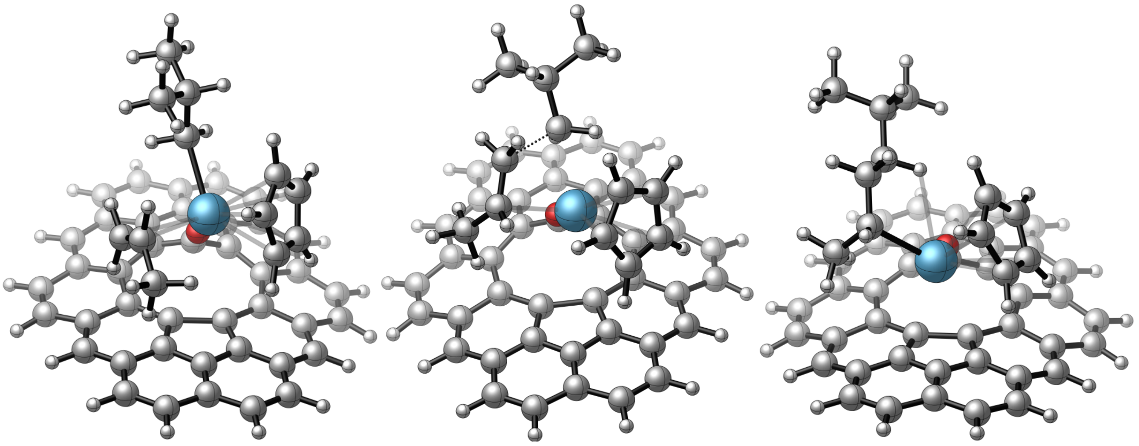

(d) $\mathrm{C}^{2,1-re}{}_{2gO}$ (e) $\mathrm{TS\text{-}CD}^{2,1-re}{}_{2gO}$ (f) $\mathrm{D}^{2,1-re}{}_{2gO}$

Figure 190: Geometries of the complexes involved in the second 2,1 back side propene insertion mediated by the $\mathrm{B}^{1,2re}{}_{2gO}$ complex.

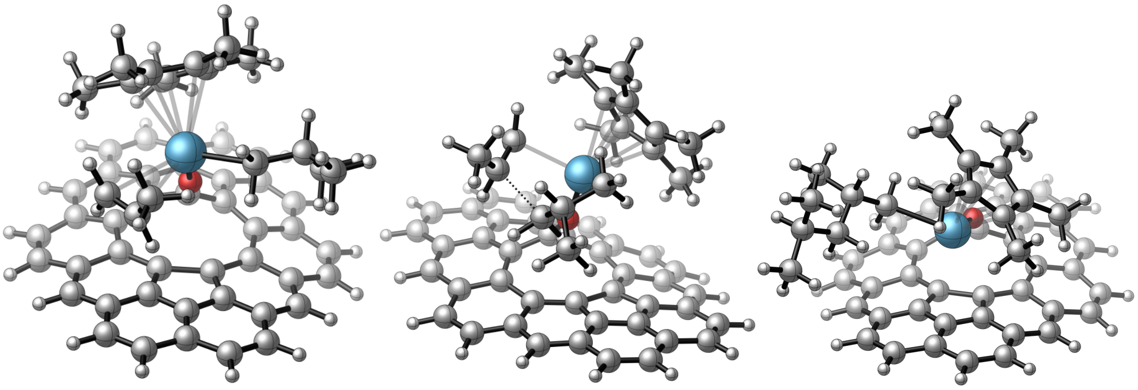

(a) $\mathrm{C}^{1,2-si}{}_{3gO}$ (b) TS-$\mathrm{CD}^{1,2-si}{}_{3gO}$ (c) $\mathrm{D}^{1,2-si}{}_{3gO}$

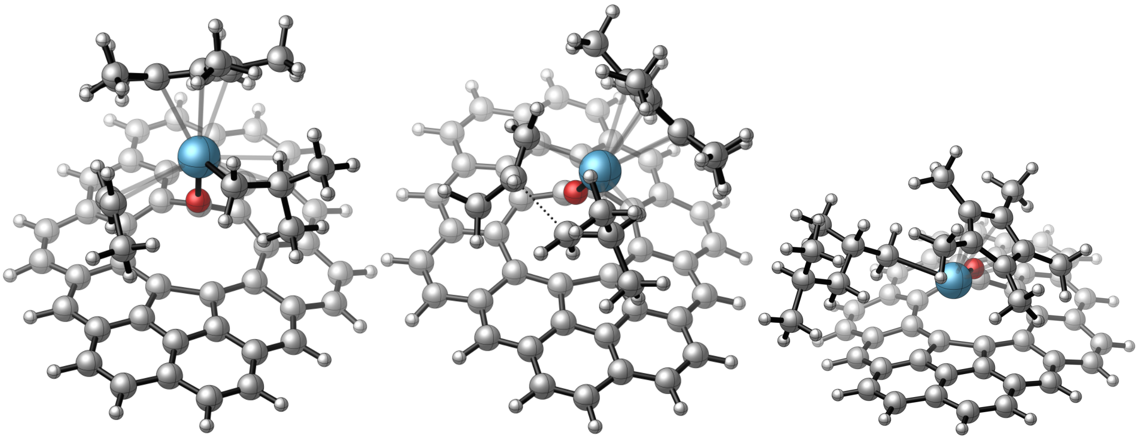

(d) $\mathrm{C}^{1,2-re}{}_{3gO}$ (e) TS-$\mathrm{CD}^{1,2-re}{}_{3gO}$ (f) $\mathrm{D}^{1,2-re}{}_{3gO}$

Figure 194: Geometries of the complexes involved in the second 1,2 front side propene insertion mediated by the $\mathrm{B}^{1,2re}{}_{3gO}$ complex.

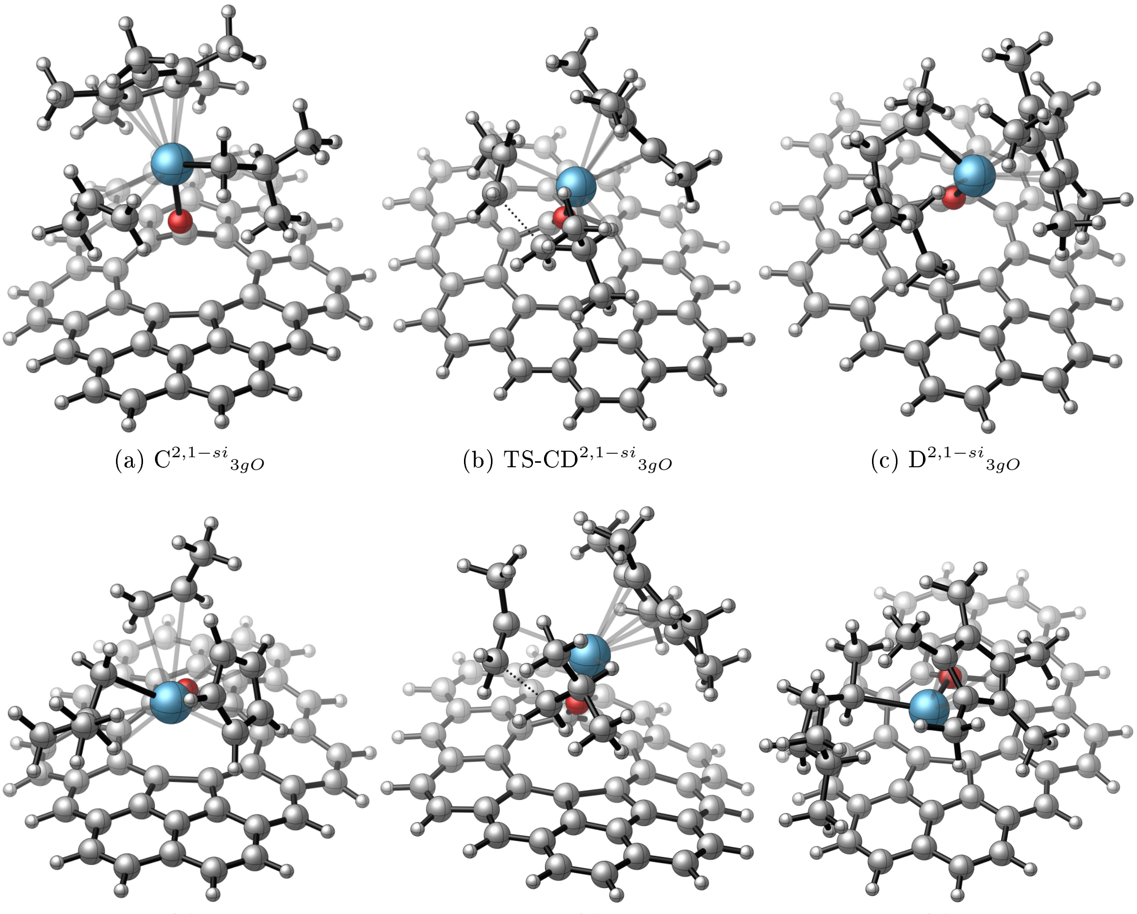

(a) $\mathrm{C}^{2,1-si}{}_{3gO}$ (b) TS-$\mathrm{CD}^{2,1-si}{}_{3gO}$ (c) $\mathrm{D}^{2,1-si}{}_{3gO}$

(d) $\mathrm{C}^{2,1-re}{}_{3gO}$ (e) TS-$\mathrm{CD}^{2,1-re}{}_{3gO}$ (f) $\mathrm{D}^{2,1-re}{}_{3gO}$

Figure 195: Geometries of the complexes involved in the second 2,1 front side propene insertion mediated by the $\mathrm{B}^{1,2re}{}_{3gO}$ complex.

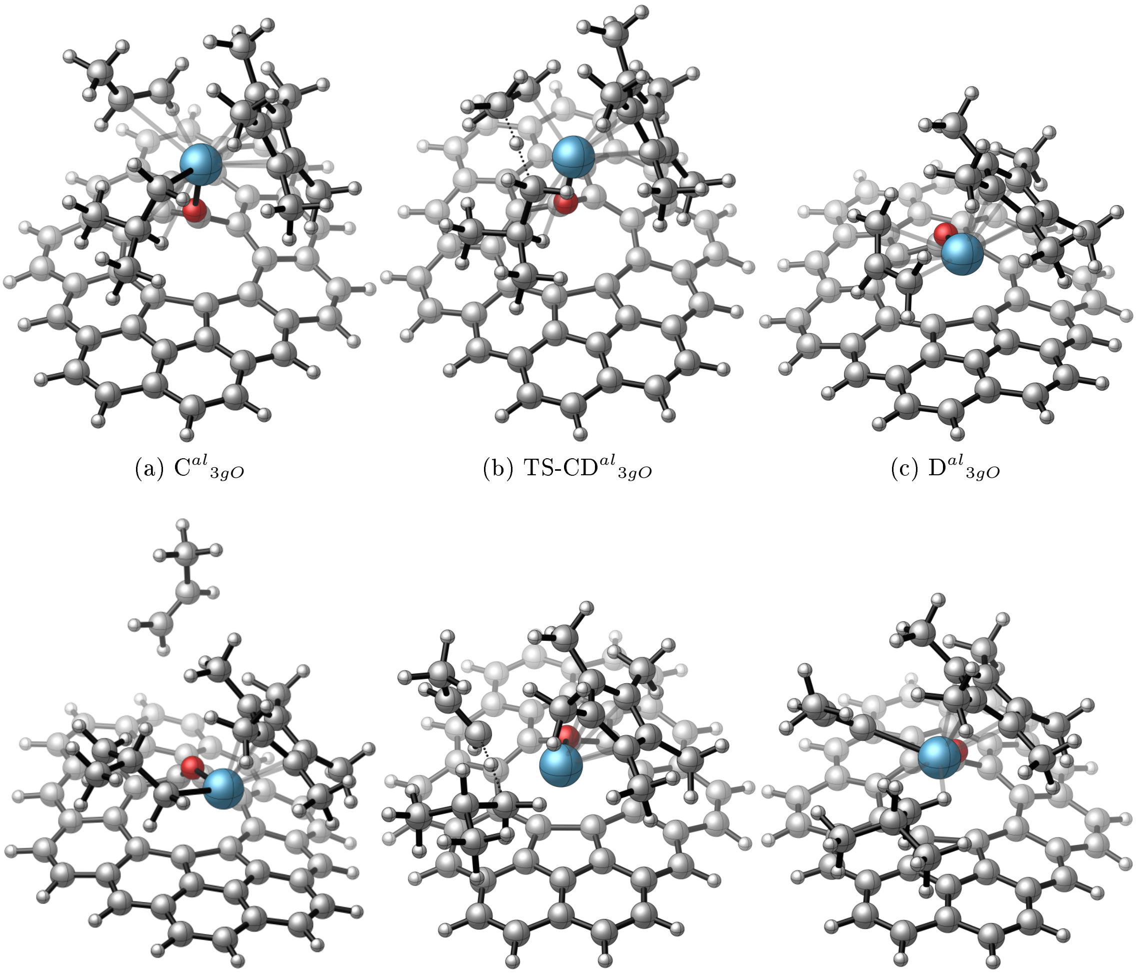

(a) $\mathrm{C}^{al}{}_{3gO}$ (b) $\mathrm{TS\text{-}CD}^{al}{}_{3gO}$ (c) $\mathrm{D}^{al}{}_{3gO}$

(d) $\mathrm{C}^{vyn}{}_{3gO}$ (e) $\mathrm{TS\text{-}CD}^{vyn}{}_{3gO}$ (f) $\mathrm{D}^{vyn}{}_{3gO}$

Figure 196: Geometries of the complexes involved in the front side allylic and vinylic C-H activation by the $\mathrm{B}^{1,2re}{}_{3gO}$ complex.

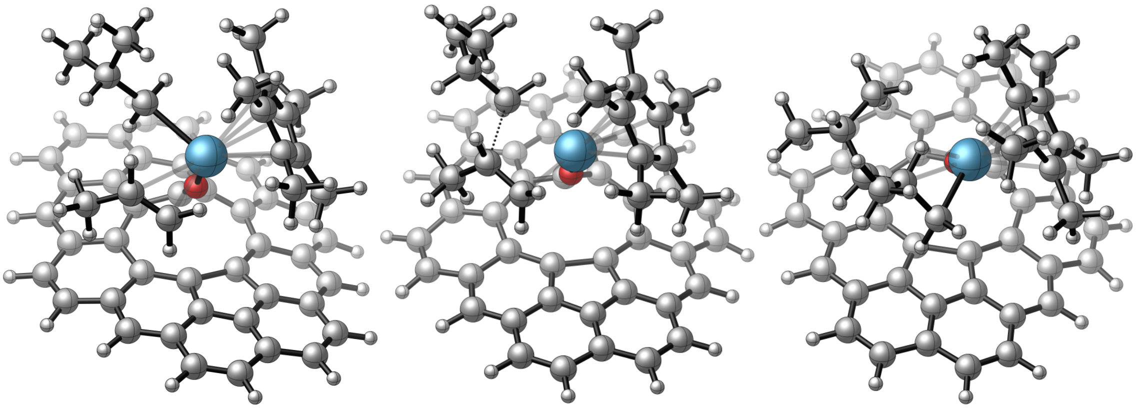

(a) $\mathrm{C}^{1,2-si}{}_{3gO}$ (b) $\mathrm{TS\text{-}CD}^{1,2-si}{}_{3gO}$ (c) $\mathrm{D}^{1,2-si}{}_{3gO}$

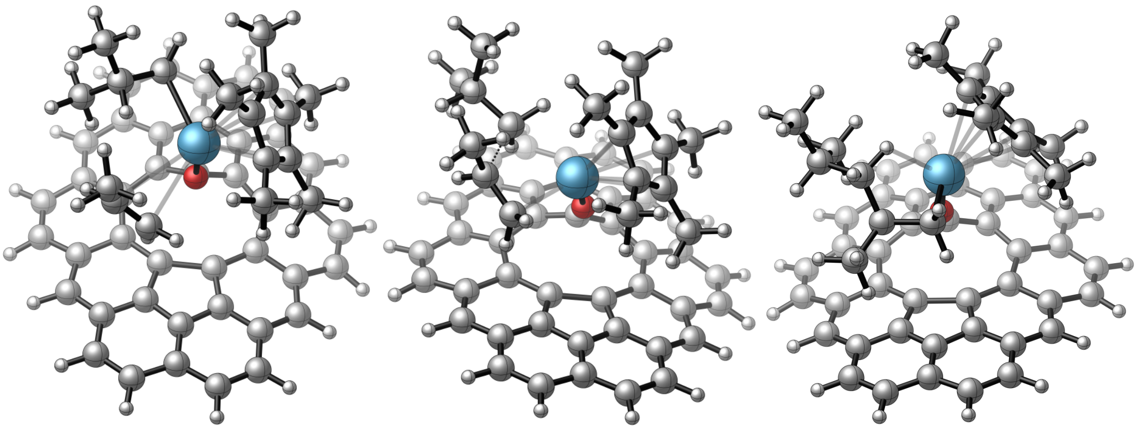

(d) $\mathrm{C}^{1,2-re}{}_{3gO}$ (e) $\mathrm{TS\text{-}CD}^{1,2-re}{}_{3gO}$ (f) $\mathrm{D}^{1,2-re}{}_{3gO}$

Figure 197: Geometries of the complexes involved in the second 1,2 back side propene insertion mediated by the $\mathrm{B}^{1,2re}{}_{3gO}$ complex.

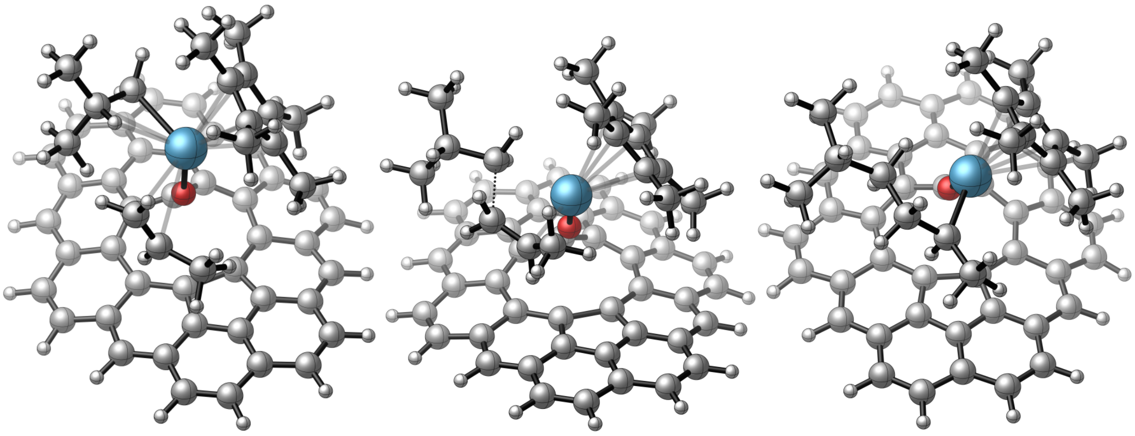

(a) $\mathrm{C}^{2,1-si}{}_{3gO}$ (b) TS-$\mathrm{CD}^{2,1-si}{}_{3gO}$ (c) $\mathrm{D}^{2,1-si}{}_{3gO}$

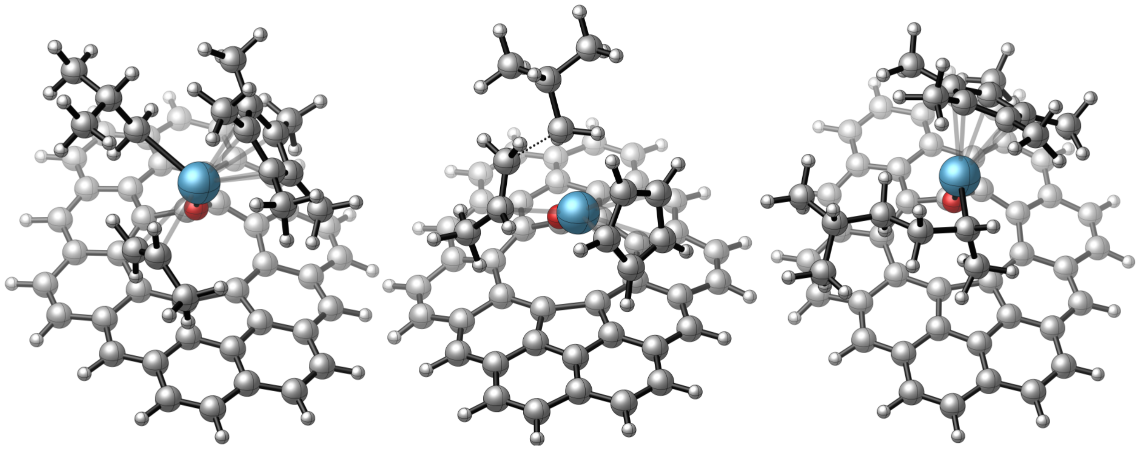

(d) $\mathrm{C}^{2,1-re}{}_{3gO}$ (e) TS-$\mathrm{CD}^{2,1-re}{}_{3gO}$ (f) $\mathrm{D}^{2,1-re}{}_{3gO}$

Figure 198: Geometries of the complexes involved in the second 2,1 back side propene insertion mediated by the $\mathrm{B}^{1,2re}{}_{3gO}$ complex.

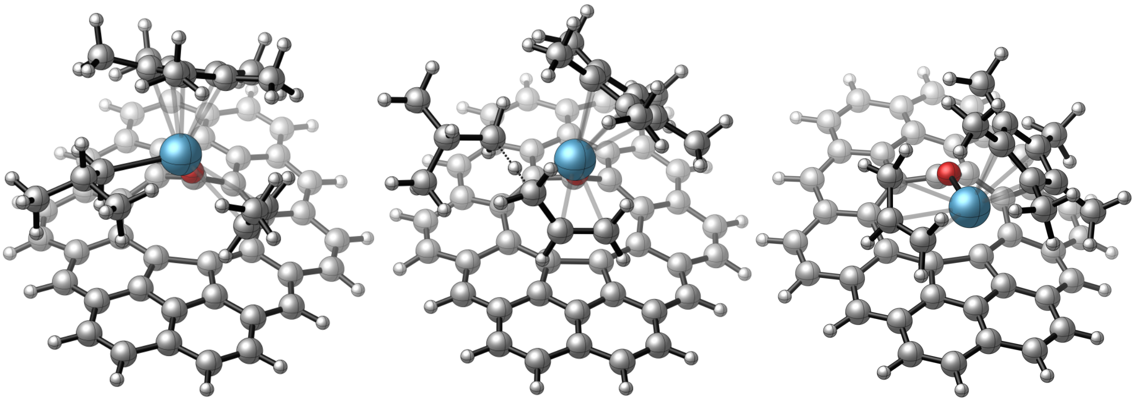

(a) $\mathrm{C}^{al}{}_{3gO}$ (b) $\mathrm{TS\text{-}CD}^{al}{}_{3gO}$ (c) $\mathrm{D}^{al}{}_{3gO}$

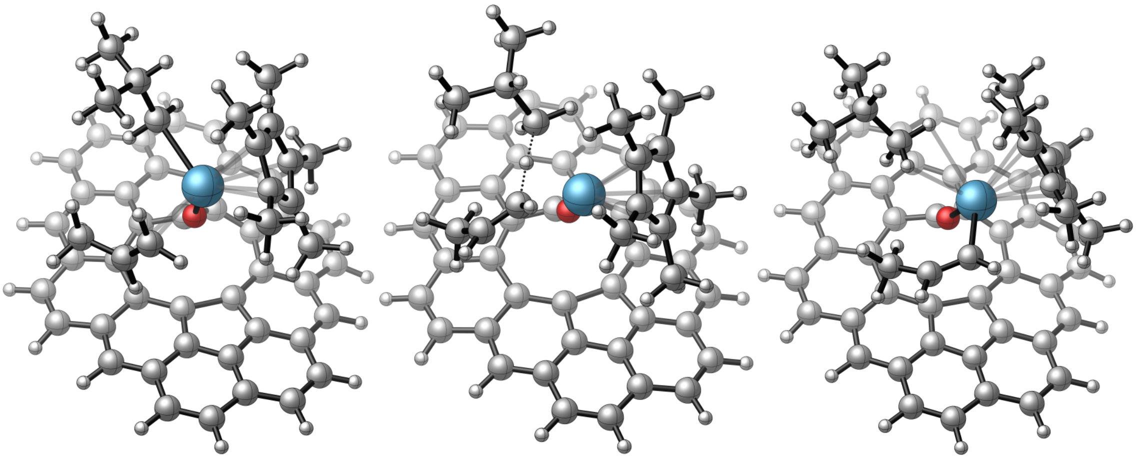

(d) $\mathrm{C}^{vyn}{}_{3gO}$ (e) $\mathrm{TS\text{-}CD}^{vyn}{}_{3gO}$ (f) $\mathrm{D}^{vyn}{}_{3gO}$

Figure 199: Geometries of the complexes involved in the back side allylic and vinylic C-H activation by the $\mathrm{B}^{1,2re}{}_{3gO}$ complex.

# References

[1] R. A. Sheldon and H. van Bekkum. *Fine chemicals through heterogeneous catalysis.* John Wiley & Sons, 1980.

[2] G. Ertl, H. Knozinger, F Schuth, and J. Weitkamp, editors. *Handbook of heterogeneous catalysis.* 2008.

[3] J. J.H.B. Sattler, J. Ruiz-Martinez, E. Santillan-Jimenez, and B. M. Weckhuysen, *Chemical Reviews*, 2014, **114**(20),10613–10653.

[4] N M Harrison, J Muscat, and A Wander, *Chemical Physics Letters*, 2001, **342**(July),397–401.

[5] J. Guzman and B. C. Gates, *Journal of the Chemical Society. Dalton Transactions*, 2003, **3**(17),3303–3318.

[6] B. C. Gates and H. H. Lamb, *Journal of Molecular Catalysis*, 1989, **52**(1),1–18.

[7] Ton V.W. Janssens, Bjerne S. Clausen, Britt Hvolbæk, Hanne Falsig, Claus H. Christensen, Thomas Bligaard, and Jens K. Nørskov, *Topics in Catalysis*, 2007, **44**(1-2),15–26.

[8] J. M. Thomas, R. Raja, and D.W. Lewis, *Angewandte Chemie - International Edition*, 2005, **44**(40),6456–6482.

[9] G. Ertl. *Reactions at solid surfaces.* John Wiley & Sons, 2010.

[10] G. A. Somorjai and Y. Li. *Introduction to Surface Chemistry and Catalysis.* John Wiley & Sons, 1994.

[11] R. R. Schrock, R. T. DePue, J. Feldman, K. B. Yap, D. C. Yang, W. M. Davis, L. Park, M. Dimare, M. Schofield, J. Anhaus, E. Walborsky, E. Evitt, C. Krüger, and P. Betz, *Organometallics*, 1990, **9**(8),2262–2275.

[12] L. P. H. Lopez and R. R. Schrock, *Journal of the American Chemical Society*, 2004, **126**(31),9526–9527.

[13] S. Arndt, R. R. Schrock, and P. Müller, *Organometallics*, 2007, **26**(5),1279–1290.

[14] L. P. H. Lopez, R. R. Schrock, and P. Müller, *Organometallics*, 2008, **27**(15),3857–3865.

[15] C Bosch. PATENT US990191A - Process of producing ammonia, 1911.

[16] G Ertl, 1990, **37**,213–277.

[17] B. Cornils and W. A. Herrmann. *Applied Homogeneous Catalysis with Organometallic Compounds: Applications; Volume 2. Developments; Volume 3. Developments.* Wiley-VCH, 2002.

[18] S. Bhaduri and D. Mukesh. *Homogeneous catalysis: mechanisms and industrial applications.* John Wiley & Sons, 2014.

[19] R. G. Wilkins. *Kinetics and mechanisms of reactions of transition metal complexes.* VCH, 1991.

[20] J. Joubert, F. Delbecq, C. Copéret, J. M. Basset, and P. Sautet, *Topics in Catalysis*, 2008, **48**(1-4),114–119.

[21] J. P. Candy, C. Copéret, and J. M. Basset, 2005, (September),151–210.

[22] F. Calderazzo, D. Carmona, M. Catellani, H. Brintzinger, M. G. Clerici, C. Dwyer, G. Fink, J. Fraile, A. Haynes, and P. Howard. *Metal-catalysis in industrial organic processes.* Royal Society of Chemistry, 2006.

[23] A Wang, J Li, and T Zhang, *Nature Reviews Chemistry*, 2018, **2**(6),65–81.

[24] X Cui, W Li, P Ryabchuk, K Junge, and M Beller, *Nature Catalysis*, 2018, **1**(6),385–397.

[25] C. Rivera-Cárcamo and P. Serp, *ChemCatChem*, 2018, **10**(22),5058–5091.

[26] L Liu and A Corma, *Chemical reviews*, 2018, **118**(10),4981–5079.

[27] G Malta, S A Kondrat, S J Freakley, C J Davies, L Lu, S Dawson, A Thetford, E K Gibson, D J Morgan, W Jones, et al., *Science*, 2017, **355**(6332),1399–1403.

[28] P Johnston, N Carthey, and G J Hutchings, *Journal of the American Chemical Society*, 2015, **137**(46),14548–14557.

[29] J. M. Basset, R. Psaro, D. Roberto, and R. Ugo. *Modern surface organometallic chemistry.* John Wiley & Sons, 2009.

[30] J. M. Basset and A. Choplin, *Journal of Molecular Catalysis*, 1983, **21**(1-3),95–108.

[31] Y. Iwasawa, *Advances in Catalysis*, 1987, **35**(C),187–264.

[32] I. Yu. Yermakov, *Catalysis Reviews - Science and Engineering*, 2006, (December 2012),37–41.

[33] J. P. Candlin and H. Thomas, *Adv Chem Ser*, 1974, (13),212–239.

[34] T. J. Marks, *Accounts of Chemical Research*, 1992, **25**(2),57–65.

[35] S. L. Wegener and T. J. Marks, *Accounts of Chemical Research*, 2012, **45**(2).

[36] P. Serna and B. C. Gates, 2014, (Table 1).

[37] C. Copéret, M. Chabanas, R. Petroff Saint-Arroman, and J. M. Basset, *Angewandte Chemie - International Edition*, 2003, **42**(2),156–181.

[38] M. Tada and Y. Iwasawa, *Coordination Chemistry Reviews*, 2007, **251**(21-24),2702–2716.

[39] R. Anwander, *Chemistry of Materials*, 2001, **13**(12),4419–4438.

[40] V. Dal Santo, F. Liguori, C. Pirovano, and M. Guidotti, *Molecules*, 2010, **15**(6),3829–3856.

[41] Y. Liang and R. Anwander, *Dalton Transactions*, 2013, **42**(35),12521–12545.

[42] C. Copéret, W. C. Liao, C. P. Gordon, and T. C. Ong, *Journal of the American Chemical Society*, 2017, **139**(31),10588–10596.

[43] M. Rimoldi and A. Mezzetti, *Catalysis Science and Technology*, 2014, **4**(9),2724–2740.

[44] D. Gajan and C. Copéret, *New Journal of Chemistry*, 2011, **35**(11),2403–2408.

[45] F. Rascón, R. Wischert, and C. Copéret, *Chemical Science*, 2011, **2**(8),1449–1456.

[46] M. M. Stalzer, M. Delferro, and T. J. Marks, *Catalysis Letters*, 2015, **145**(1),3–14.

[47] M. P. Conley and C. Copéret, *Topics in Catalysis*, 2014, **57**(10-13),843–851.

[48] F. Blanc, C. Copéret, J. Thivolle-Cazat, J. M. Basset, A. Lesage, L. Emsley, A. Sinha, and R. R. Schrock, *Angewandte Chemie - International Edition*, 2006, **45**(8),1216–1220.

[49] C. Coperet, A. Comas-Vives, M. P. Conley, D. P. Estes, A. Fedorov, V. Mougel, H. Nagae, F. Nunez-Zarur, and P. A. Zhizhko, *Chemical Reviews*, 2016, **116**(2),323–421.

[50] M. Jezequel, V. Dufaud, M. J. Ruiz-Garcia, F. Carrillo-Hermosilla, U. Neugebauer, G. P. Niccolai, F. Lefebvre, F. Bayard, J. Corker, S. Fiddy, J. Evans, J. P. Broyer, J. Malinge, and J. M. Basset, *Journal of the American Chemical Society*, 2001, **123**(15),3520–3540.

[51] D. D. Laws, H.L. Bitter, and A. Jerschow, *Angewandte Chemie (International ed. in English)*, 2002, **41**,3096–3129.

[52] M. A. Newton and W. Van Beek, *Chemical Society Reviews*, 2010, **39**(12),4845–4863.

[53] A. J. Rossini, A. Zagdoun, M. Lelli, A. Lesage, C. Copéret, and L. Emsley, *Accounts of Chemical Research*, 2013, **46**(9),1942–1951.

[54] A. I. Frenkel, J. A. Rodriguez, and J. G. Chen, *ACS Catalysis*, 2012, **2**(11),2269–2280.

[55] R. P. Saint-Arroman, M. Chabanas, A. Baudouin, C. Copéret, J. M. Basset, A. Lesage, and L. Emsley, *Journal of the American Chemical Society*, 2001, **123**(16),3820–3821.

[56] S. E. Ashbrook and S. Sneddon, 2014.

[57] D. Grekov, T. Vancompernolle, M. Taoufik, L. Delevoye, and R. M. Gauvin, *Chemical Society Reviews*, 2018, **47**(8),2572–2590.

[58] J. D.A. Pelletier and J. M. Basset, *Accounts of Chemical Research*, 2016, **49**(4),664–677.

[59] J. Jarupatrakorn and T. D. Tilley, *Journal of the American Chemical Society*, 2002, **124**(28),8380–8388.

[60] C. Copéret, *Dalton Transactions*, 2007, (47),5546–5548.

[61] N. Popoff, E. Mazoyer, J. Pelletier, R. M. Gauvin, and M. Taoufik, *Chemical Society Reviews*, 2013, **42**(23),9035–9054.

[62] D. A. Ruddy and T. D. Tilley, *Chemical Communications*, 2007, **1**(32),3350–3352.

[63] N.E. Thornburg, A. B. Thompson, and J. M. Notestein, *ACS Catalysis*, 2015, **5**(9),5077–5088.

[64] P. E. Sinclair, G. Sankar, C. R. A. Catlow, J. M. Thomas, and T. Maschmeyer, *Journal of Physical Chemistry B*, 1997, **101**(21),4232–4237.

[65] K. L. Fujdala and T. D. Tilley, *Journal of Catalysis*, 2003, **216**(1-2),265–275.

[66] L. T. Zhuravlev, *Colloids and Surfaces A: Physicochemical and Engineering Aspects*, 2000, **173**(1-3),1–38.

[67] A. P. Legrand. *The surface properties of silicas.* John Wiley & Sons, 1998.

[68] J. R. HARRIS and D. R. ROSSINGTON, *Journal of the American Ceramic Society*, 1968, **51**(9),511–518.

[69] Y Wan and D Zhao, *Chemical reviews*, 2007, **107**(7),2821–2860.

[70] C.T. Kresge, M.E. Leonowicz, W. J. Roth, J.C. Vartuli, and J.S. Beck, *nature*, 1992, **359**(6397),710–712.

[71] A. Monnier, F. Schüth, Q. Huo, D. Kumar, D. Margolese, R.S. Maxwell, G.D. Stucky, M. Krishnamurty, P. Petroff, A. Firouzi, et al., *Science*, 1993, **261**(5126),1299–1303.

[72] S. P Naik, A. ST Chiang, and RW Thompson, *The Journal of Physical Chemistry B*, 2003, **107**(29),7006–7014.

[73] P. Behrens and G. D. Stucky, *Angewandte Chemie*, 1993, **105**(5),729–732.

[74] M. A Karakassides, A. Bourlinos, D. Petridis, L. Coche-Guerènte, and P. Labbè, *Journal of Materials Chemistry*, 2000, **10**(2),403–408.

[75] B. G. Trewyn, I. I. Slowing, S. Giri, H.T. Chen, and V. S-Y Lin, *Accounts of chemical research*, 2007, **40**(9),846–853.

[76] M Ichikawa. Metal cluster compounds as molecular precursors for tailored metal catalysts. In *Advances in catalysis*, volume 38, pages 283–400. Elsevier, 1992.

[77] W MH Sachtler, *Accounts of chemical research*, 1993, **26**(7),383–387.

[78] G A Ozin, *Advanced Materials*, 1994, **6**(1),71–76.

[79] F Lefebvre, A de Mallmann, and J-M Basset, *European journal of inorganic chemistry*, 1999, **1999**(3),361–371.

[80] A Gil, L M Gandia, and M A Vicente, *Catalysis Reviews*, 2000, **42**(1-2),145–212.

[81] S Soignier, M Taoufik, E Le Roux, G Saggio, C Dablemont, A Baudouin, F Lefebvre, A de Mallmann, J Thivolle-Cazat, J-M Basset, et al., *Organometallics*, 2006, **25**(7),1569–1577.

[82] M Ide, M El-Roz, E De Canck, A Vicente, T Planckaert, T Bogaerts, I Van Driessche, F Lynen, V Van Speybroeck, F Thybault-Starzyk, et al., *Physical Chemistry Chemical Physics*, 2013, **15**(2),642–650.

[83] YU. Yermakov and V Zakharov, *Advances in Catalysis*, 1975, **24**(173).

[84] D. G.H. Ballard, *J Polym Sci Polym Chem Ed*, 1975, **13**(10),2191–2212.

[85] P. Hoffmann, *Surface Science*, 1987, **188**,1–11.

[86] C. C. Liu and G. E. Maciel, *Journal of the American Chemical Society*, 1996, **118**(21),5103–5119.

[87] R. M. Gauvin, L. Delevoye, R. A. Hassan, J. Keldenich, and A. Mortreux, *Inorganic Chemistry*, 2007, **46**,1062–1070.

[88] R. M. Gauvin, T. Chenal, R. A. Hassan, A. Addadb, and A. Mortreux, *Journal of Molecular Catalysis A: Chemical*, 2006, **257**(1-2),31–40.

[89] E. Groppo, C. Lamberti, S. Bordiga, G. Spoto, and A. Zecchina, *Chemical Reviews*, 2005, **105**(1),115–183.

[90] VY DAVYDOV, LT ZHURAVLEV, and AV KISELEV, *ZHURNAL FIZICHESKOI KHIMII*, 1964, **38**(8),2047–2054.

[91] V Ya Davydov, AV Kiselev, and LT Zhuravlev, *Transactions of the Faraday Society*, 1964, **60**,2254–2264.

[92] LT Zhuravlev, *Langmuir*, 1987, **3**(3),316–318.

[93] BA Morrow and AJ McFarlan. Infrared study of chemical and h-d exchange probes for silica surfaces. ACS Publications, 1994.

[94] BA Morrow and AJ McFarlan, *The Journal of Physical Chemistry*, 1992, **96**(3),1395–1400.

[95] BA Morrow and AJ McFarlan, *Langmuir*, 1991, **7**(8),1695–1701.

[96] BA Morrow and AJ McFarlan, *Journal of non-crystalline solids*, 1990, **120**(1-3),61–71.

[97] AJ McFarlan and BA Morrow, *The Journal of Physical Chemistry*, 1991, **95**(14),5388–5390.

[98] E Le Roux. *New generation of tantalum and tungsten based catalysts supported on oxides for alkane metathesis.* PhD thesis, 10 2004.

[99] K L Fujdala and T D Tilley, *Journal of the American Chemical Society*, 2001, **123**(41),10133–10134.

[100] N Merle, M Taoufik, M Nayer, A Baudouin, E Le Roux, R M Gauvin, F Lefebvre, J Thivolle-Cazat, and J-M Basset, *Journal of Organometallic Chemistry*, 2008, **693**(10),1733–1737.

[101] R Anwander, I Nagl, M Widenmeyer, G Engelhardt, O Groeger, C Palm, and T Röser, *The Journal of Physical Chemistry B*, 2000, **104**(15),3532–3544.

[102] A. Zecchina, D. Scarano, S. Bordiga, G. Spoto, and C. Lamberti. *Surface structures of oxides and halides and their relationships to catalytic properties.* Advances in catalysis, 2001.

[103] G. Busca, *Catalysis Today*, 2014, **226**,2–13.

[104] X. Krokidis, P. Raybaud, A. E. Gobichon, B. Rebours, P. Euzen, and H. Toulhoat, *Journal of Physical Chemistry B*, 2001, **105**(22),5121–5130.

[105] C. S. John, N. C.M. Alma, and G. R. Hays, *Applied Catalysis*, 1983, **6**(3),341–346.

[106] C. Pecharroman, I. Sobrados, J. E. Iglesias, T. Gonzalez-Carreno, and J. Sanz, *Journal of Physical Chemistry B*, 1999, **103**(30),6160–6170.

[107] L. Kovarik, M. Bowden, A. Genc, J. Szanyi, C. H.F. Peden, and J. H. Kwak, *Journal of Physical Chemistry C*, 2014, **118**(31),18051–18058.

[108] R. S Zhou and R. L. Snyder, *Acta Crystallographica Section B*, 1991, **47**(5),617–630.

[109] H. S. Kim, S. A. Zygmunt, P. C. Stair, P. Zapol, and L.A. Curtiss, *Journal of Physical Chemistry C*, 2009, **113**(20),8836–8843.

[110] C. K. Narula and G. M. Stocks, *Journal of Physical Chemistry C*, 2012, **116**(9),5628–5636.

[111] R. Wischert, P. Laurent, C. Coperet, F. Delbecq, and P. Sautet, *Sites. J. Am. Chem. Soc.*, 2012, **134**,14430.

[112] D. Martin and D. Duprez, *Journal of Physical Chemistry*, 1996, **100**(22),9429–9438.

[113] M. Corno, A. Rimola, V. Bolis, and P. Ugliengo, *Physical Chemistry Chemical Physics*, 2010, **12**(24),6309–6329.

[114] J. Joubert, A. Salameh, V. Krakoviack, F. Delbecq, P. Sautet, C. Copéret, and J. M. Basset, *Journal of Physical Chemistry B*, 2006, **110**(47),23944–23950.

[115] M DIGNE, P SAUTET, P RAYBAUD, P EUZEN, and H TOULHOAT, *Journal of Catalysis*, 2002, **211**(1),1–5.

[116] M. Digne, P. Sautet, P. Raybaud, P. Euzen, and H. Toulhoat, *Journal of Catalysis*, 2004, **226**(1),54–68.

[117] N. Merle, G. Girard, N. Popoff, A. De Mallmann, Y. Bouhoute, J. Trebosc, E. Berrier, J.F. Paul, C. P Nicholas, I. Del Rosal, L. Maron, R. M Gauvin, L. Delevoye, and M. Taoufik, *Inorg. Chem.*, 2013, **52**(17),10119–10130.

[118] E. Le Roux, M. Taoufik, A. Baudouin, C. Copéret, J. Thivolle-Cazat, J. M. Basset, B. M. Maunders, and G. J. Sunley, *Advanced Synthesis and Catalysis*, 2007, **349**(1-2),231–237.

[119] D. G.H. Ballard, E. Jones, R. J. Wyatt, R. T. Murray, and P. A. Robinson, *Polymers*, 1974, **15**(3),169–174.

[120] R. L. Burwell, *Journal of Catalysis*, 1984, **86**(2),301–314.

[121] G. Tosin, C. C. Santini, A. Baudouin, A. De Mailman, S. Fiddy, C. Dablemont, and J. M. Basset, *Organometallics*, 2007, **26**(17),4118–4127.

[122] C Vallantin-Rosier. *Surface Organometallic Chemistry of Titanium. Toward the Synthesis of New Epoxidation Catalysts.* PhD thesis, 10 1999.

[123] C Rosier, G P Niccolai, and J-M Basset, *Journal of the American Chemical Society*, 1997, **119**(50),12408–12409.

[124] L d'Ornelas, S Reyes, F Quignard, A Choplin, and J-M Basset, *Chemistry letters*, 1993, **22**(11),1931–1934.

[125] J Corker, F Lefebvre, C Lécuyer, V Dufaud, F Quignard, A Choplin, J Evans, and J-M Basset, *Science*, 1996, **271**(5251),966–969.

[126] F Quignard, A Choplin, and J-M Basset, *Journal of the Chemical Society, Chemical Communications*, 1991, (22),1589–1590.

[127] G. Lapadula, A. Bourdolle, F. Allouche, M. P Conley, I. del Rosal, L. Maron, W. W Lukens, Y. Guyot, C. Andraud, S. Brasselet, C. Copéret, O. Maury, and R. A Andersen, *Chem. Mater*, 2014, **26**,1062–1073.

[128] G. Lapadula, D. Trummer, M. P. Conley, M. Steinmann, Y. F. Ran, S. Brasselet, Y. Guyot, O. Maury, S. Decurtins, S.X. Liu, and C. Copéret, *Chemistry of Materials*, 2015, **27**(6),2033–2039.

[129] F. Allouche, G. Lapadula, G. Siddiqi, W. W. Lukens, O. Maury, B. Le Guennic, F. Pointillart, J. Dreiser, V. Mougel, O. Cador, and C. Copéret, *ACS Central Science*, 2017, **3**(3),244–249.

[130] C. Copéret, *New Journal of Chemistry*, 2004, **28**(1),1–10.

[131] G. Jeske, H. Lauke, H. Mauermann, H. Schumann, and T. J. Marks, *Journal of the American Chemical Society*, 1985, **107**(26),8111–8118.

[132] F. Rataboul, A. Baudouin, C. Thieuleux, L. Veyre, C. Copéret, J. Thivolle-Cazat, J. M. Basset, A; Lesage, and L. Emsley, *Journal of the American Chemical Society*, 2004, **126**(39),12541–12550.

[133] G. Tosin, M. Delgado, A. Baudouin, C. C. Santini, F. Bayard, and J. M. Basset, *Organometallics*, 2010, **29**(6),1312–1322.

[134] M. Delgado, C. C. Santini, F. Delbecq, A. Baudouin, A. De Mallmann, C. Prestipino, S. Norsic, P. Sautet, and J. M. Basset, *Journal of Physical Chemistry C*, 2011, **115**(14),6757–6763.

[135] I. Del Rosal, I. C. Gerber, R. Poteau, and L. Maron, *New Journal of Chemistry*, 2015, **39**(10),7703–7715.

[136] I. Del Rosal, I. C. Gerber, R. Poteau, and L. Maron, *Journal of Physical Chemistry A*, 2010, **114**(21),6322–6330.

[137] M. Fadhli, I. Khedher, and J. M. Fraile, *Journal of Molecular Catalysis A: Chemical*, 2016, **420**,282–289.

[138] P. A. Zhizhko, A. A. Zhizhin, D. N. Zarubin, N. A. Ustynyuk, D. A. Lemenovskii, B. N. Shelimov, L. M. Kustov, O.P. Tkachenko, and G. A. Kirakosyan, *Journal of Catalysis*, 2011, **283**(1),108–118.

[139] P. A. Zhizhko, A. A. Zhizhin, D. N. Zarubin, and N. A. Ustynyuk, *Mendeleev Communications*, 2012, **22**(2),64–66.

[140] P. A. Zhizhko, A. A. Zhizhin, O. A. Belyakova, Y. V. Zubavichus, Y. G. Kolyagin, D. N. Zarubin, and N. A. Ustynyuk, *Organometallics*, 2013, **32**(13),3611–3617.

[141] M. K Samantaray, J. Alauzun, D. Gajan, S. Kavitake, A. Mehdi, L. Veyre, M. Lelli, A. Lesage, L. Emsley, and C. Coperet, *journal of american chemical society*, 2013, (135),3193–3199.

[142] F. Blanc, J. Thivolle-Cazat, J. M. Basset, and C. Copéret, *Chemistry - A European Journal*, 2008, **14**(29),9030–9037.

[143] R. M. Gauvin and A. Mortreux, *Chemical Communications*, 2005, (9),1146–1148.

[144] K. Tortosa, T. Hamaide, C. Boisson, and R. Spitz, *Macromol. Chem. Phys*, 2001.

[145] T. J. Woodman, Y. Sarazin, G. Fink, K. Hauschild, and M. Bochmann, *Macromolecules*, 2005, **38**,3060–3067.

[146] E. Le Roux, Y. Liang, M. P. Storz, and R. Anwander, *Journal of the American Chemical Society*, 2010, **132**(46),16368–16371.

[147] G. Gerstberger, C. Palm, and R. Anwander, *Chemistry - A European Journal*, 2002, **5**(3),997–1005.

[148] G. Gerstberger and R. Anwander, *Microporous and Mesoporous Materials*, 2001, **44-45**,303–310.

[149] M. R. MacDonald, J. E. Bates, J. W. Ziller, and W. J. Evans, *journal of american chemical society*, 2013, **135**(26),9857–9868.

[150] L Watson and W Parshall, *Acc.Chem.Res*, 1985, **18**(5),51–56.

[151] M. L. Steigerwald and W. A. Goddard, *Journal of the American Chemical Society*, 1984, **106**(2),308–311.

[152] R. Waterman, *Organometallics*, 2013.

[153] P. Watson and C. D. Roe, *journal of american chemical society*, 1982, **104**,6471–6473.

[154] P. L Watson, *Journal of the American Chemical Society*, 1982, **104**,337–339.

[155] A. D. Sadow and T. D. Tilley, *Journal of the American Chemical Society*, 2003, **125**(31),9462–9475.

[156] S. Bajo, M. A Esteruelas, A. M Lopez, and E. Onate, 2014.

[157] L. Maron, E. L Werkema, L. Perrin, O. Eisenstein, and R. A Andersen, *Journal of the American Chemical Society*, 2005, **127**(1),279–292.

[158] A. Motta, I. L. Fragala, and T. J. Marks, *Organometallics*, 2005, **24**(21),4995–5003.

[159] P. L. Watson and G. W. Parshall, *Accounts of Chemical Research*, 1985, **18**(2),51–56.

[160] L. Maron and O. Eisenstein, 2001, (14),1036–1039.

[161] E. Le Roux, O. Michel, H. M. Sommerfeldt, Y. Liang, C. Maichle-Mossmer, K. W. Tornroos, and R. Anwander, *Dalton Transactions*, 2010, **39**(36),8552–8559.

[162] N. Ajellal, G. Durieux, L. Delevoye, G. Tricot, C. Dujardin, C. M. Thomas, and R. M. Gauvin, *Chemical Communications*, 2010, **46**(7),1032–1034.

[163] A. Fischbach, M. G. Klimpel, M. Widenmeyer, E. Herdtweck, W. Scherer, and R. Anwander, *Angew. Chem.*, 2004, **43**(17),2234–2239.

[164] M. J. Vitorino, T. Devic, M. Tromp, G. Férey, and M. Visseaux, *Macromol. Chem. Phys.*, 2009, **210**(22),1923–1932.

[165] F. Yang and X. Li, *Journal of Polymer Science, Part A: Polymer Chemistry*, 2017, **55**(14),2271–2280.

[166] I. Del Rosal, M. J.L. Tschan, R. M. Gauvin, L. Maron, and C. M. Thomas, *Polymer Chemistry*, 2012, **3**(7),1730–1739.

[167] D. C. Bradley, J. S. Ghotra, and F. A. Hart, *J. Chem. Soc., Chem. Commun.*, 1972, pages 349–350.

[168] D. C. Bradley, J. S. Ghotra, and F. A. Hart, *J.C.S Dalton*, 1973, pages 1021–1023.

[169] P. W. Roesky, *Zeitschrift fur Anorganische und Allgemeine Chemie*, 2003, **629**(11),1881–1894.

[170] H. Berberich and P. W Roesky, *Communications*, 1998, pages 1569–1571.

[171] Y.K. Kim, T. Livinghouse, and J. E. Bercaw, *Tetrahedron Letters*, 2001, **42**(16),2933–2935.

[172] Y.K. Kim and T. Livinghouse, *Angewandte Chemie - International Edition*, 2002, **41**(19),3645–3647.

[173] D. V. Gribkov, K. C. Hultzsch, and F. Hampel, *Chemistry - A European Journal*, 2003, **9**(19),4796–4810.

[174] A. M. Kawaoka, M. R. Douglass, and T. J. Marks, *Organometallics*, 2003, **22**(23),4630–4632.

[175] M. Suzuki, N. Kato, M. Kanaki, and M. Shibasaki, *Organic Letters*, 2005, **7**(13),2527–2530.

[176] I. Nagl, M. Widenmeyer, E. Herdtweck, G. Raudaschl-Sieber, and R. Anwander, *Microporous and Mesoporous Materials*, 2001, **44-45**,311–319.

[177] R. Anwander. *Routes to monomeric lanthanide alkoxides*, volume 179. Springer, Berlin, 2005.

[178] J. Eppinger, M. Spiegler, W. Hieringer, W. A. Herrmann, and R. Anwander, *Journal of the American Chemical Society*, 2000, **122**(13),3080–3096.

[179] A. K. Dash, A. Razavi, A. Mortreux, C. W. Lehmann, and J. F. Carpentier, *Organometallics*, 2002, **21**(15),3238–3249.

[180] R. Anwander and R. Roesky, *J. Chem. Soc., Dalton Trans*, 1997, **2**,137–138.

[181] J. P. Osegovic and R. S. Drago, 1999, **4**,1–4.

[182] I. Del Rosal, A. Yahia, and L. Maron, *Inorganic Chemistry*, 2016, **55**(20),10024–10033.

[183] I. Del Rosal, R. Poteau, and L. Maron, *The Royal Society of Chemistry*, 2011, **40**,11211–11227.

[184] M. Terrier, E. Brulé, M. J. Vitorino, N. Ajellal, C. Robert, R. M. Gauvin, and C. M. Thomas, *Macromolecular Rapid Communications*, 2011, **32**(2),215–219.

[185] T. Vancompernolle, A. Valente, T. Chenal, P. Zinck, I. Del Rosal, L. Maron, M. Taou, and S. Harder, 2017.

[186] T. Li, J. Jenter, and P. W. Roesky. *Rare-Earth Metal Postmetallocene Catalysts with Chelating Amido Ligands.* Berlin, 2010.

[187] W. E. Piers and D.J.H. Emslie, *Coordination Chemistry Reviews*, 2002, **233-234**(2002),131–155.

[188] E. Kirillov, J. Y. Saillard, and J. F. Carpentier, *Coordination Chemistry Reviews*, 2005, **249**(11-12),1221–1248.

[189] P. M. Zeimentz, S. Arndt, B. R. Elvidge, and J. Okuda, *Chemical Reviews*, 2006, **106**(6),2404–2433.

[190] F. T. Edelmann, *Chemical Society Reviews*, 2012, **41**(23),7657–7672.

[191] E Y-X Chen, *Chemical reviews*, 2009, **109**(11),5157–5214.

[192] R.J. Young and P.A. Lovell. *Introduction to polymers.* CRC press, 2011.

[193] R. O. Ebewele. *Polymer science and technology.* CRC press, 2000.

[194] L. J. Kuzma. Polybutadiene and Polyisoprene Rubbers. In Maurice Morton, editor, *Rubber Technology*, pages 235–259. Springer US, Boston, MA, 1987.

[195] W. Kuran. *Principles of Coordination Polymerisation*, volume 9. John Wiley & Sons, 2002.

[196] J. Thuilliez, L. Ricard, F. Nief, F. Boisson, and C. Boisson, *Macromolecules*, 2009, **42**(11),3774–3779.

[197] V. Monteil, R. Spitz, F. Barbotin, and C. Boisson, *Macromolecular Chemistry and Physics*, 2004, **205**(6),737–742.

[198] H. Nsiri, I. Belaid, P. Larini, J. Thuilliez, C. Boisson, and L. Perrin, *ACS Catalysis*, 2016, **6**(2),1028–1036.

[199] J. Gromada, J. F. Carpentier, and A. Mortreux, *Coordination Chemistry Reviews*, 2004, **248**(3-4),397–410.

[200] P.V. Danckwerts, *Chemical Engineering Science*, 1962, **17**(11),955.

[201] G Natta, 1996, **XVI**(1955),321–332.

[202] K. Ziegler, H. G. Gellert, H. Lehmkuhl, W. Pfohl, and K. Zosel, *Liebigs Ann. Chem. Bd.*, 1959, **91**(1954),1–13.

[203] G. Natta, P. Pino, P. Corradini, F. Danusso, G. Moraglio, E. Mantica, and G. Mazzanti, *Journal of the American Chemical Society*, 1955, **77**(6),1708–1710.

[204] P Cossee, *The stereochemistry of macromolecules*, 1967, **1**,145–175.

[205] D. Liu and D. Cui, *Dalton Transactions*, 2011, **40**(30),7666–7682.

[206] S. Agarwal, C. Mast, K. Dehnicke, and A. Greiner, *Macromolecular Rapid Communications*, 2000, **21**(5),195–212.

[207] E. Ihara, M. Nodono, H. Yasuda, N. Kanehisa, and Y. Kai, 1996, **7**,1909–1917.

[208] H. Yasuda, *Progress in Polymer Science*, 2000, **25**(5),573–626.

[209] L. Watson and W. Parshall, *Acc.Chem.Res*, 1985, **18**(5),51–56.

[210] D. G.H. Ballard, A. Courtis, J. Holton, J. McMeeking, and R. Pearce, *Journal of the Chemical Society, Chemical Communications*, 1978, (22),994–995.

[211] P. L. Watson and T. Herskovitz, *American Chemical Society*, 1983.

[212] C. P. Casey, J. A. Tunge, T.Y. Lee, and M. A. Fagan, *Journal of the American Chemical Society*, 2003, **125**(9),2641–2651.

[213] C. P. Casey, J. A. Tunge, T. Y. Lee, and D. W. Carpenetti, *Organometallics*, 2002, **21**(2),389–396.

[214] M. E. Thompson and J. E. Bercaw, *Pure and Applied Chemistry*, 1984, **56**(1),1–11.

[215] H. Wiesenfeldt, A. Reinmuth, E. Barsties, K. Evertz, and H.H. Brintzinger, *Journal of Organometallic Chemistry*, 1989, **369**(3),359–370.

[216] W. Röll, H.H. Brintzinger, B. Rieger, and R. Zolk, *Angewandte Chemie International Edition in English*, 1990, **29**(3),279–280.

[217] E. Ihara, M. Nodono, K. Katsura, Y. Adachi, H. Yasuda, M. Yamagashira, H. Hashimoto, N. Kanehisa, and Y. Kai, *Organometallics*, 1998, **17**(18),3945–3956.

[218] H. Yasuda, *Journal of Polymer Science, Part A: Polymer Chemistry*, 2001, **39**(12),1955–1959.

[219] Y. Chen, Y. Zhang, Z. Shen, R. Kou, and L. Chen, *European Polymer Journal*, 2001, **37**(6),1181–1184.

[220] Z. Hou, Y. Luo, and X. Li, *Journal of Organometallic Chemistry*, 2006, **691**(14),3114–3121.

[221] Z. Hou and Y. Wakatsuki, *Journal of Organometalic Chemistry*, 2002, **647**(1-2),61–70.

[222] O. Tardif, M. Nishiura, and Z. Hou, *Tetrahedron*, 2003, **59**(52),10525–10539.

[223] Z. Hou and Y. Wakatsuki, *Coordination Chemistry Reviews*, 2002, **231**,1–22.

[224] Z. Hou, M. Nishiura, and T. Shima, *European Journal of Inorganic Chemistry*, 2007, (18),2535–2545.

[225] X. Li and Z. Hou, *Coordination Chemistry Reviews*, 2008, **252**(15-17),1842–1869.

[226] X. Li, X. Wang, X. Tong, H. Zhang, Y. Chen, Y. Liu, H. Liu, X. Wang, M. Nishiura, H. He, Z. Lin, S. Zhang, and Z. Hou, *Organometallics*, 2013, **32**(5),1445–1458.

[227] J. Hitzbleck, K. Beckerle, J. Okuda, T. Halbach, and R. Mülhaupt, *Macromolecular Symposia*, 2006, **236**,23–29.

[228] H. Yasuda and I. Eiji, *the chemical society of japon*, 1997, **70**(8),1745–1767.

[229] E. Ihara, S. Yoshioka, M. Furo, K. Katsura, H. Yasuda, S. Mohri, N. Kanehisa, and Y. Kai, *Organometallics*, 2001, **20**(9),1752–1761.

[230] S. Kaita, Y. Takeguchi, Z. Hou, and M. Nishiura, *Macromolecules*, 2003, pages 7923–7926.

[231] S. Kaita, M. Yamanaka, A. C. Horiuchi, and Y. Wakatsuki, *Macromolecules*, 2006, **39**(4),1359–1363.

[232] A. Fischbach, F. Perdih, P. Sirsch, W. Scherer, and R. Anwander, *Organometallics*, 2002, **4**(22),2001–2003.

[233] A. Fischbach, F. Perdih, E. Herdtweck, and R. Anwander, *Organometallics*, 2006, **25**(7),1626–1642.

[234] S. Kaita, Z. Hou, and Y. Wakatsuki, *Macromolecules*, 1999, pages 9078–9079.

[235] S. Kaita, Z. Hou, and Y. Wakatsuki, *Macromolecules*, 2001, pages 1539–1541.

[236] S. Kaita, Y. Doi, K. Kaneko, A. C. Horiuchi, and Y. Wakatsuki, *Macromolecules*, 2004, **37**(16),5860–5862.

[237] Y. F. Zhang, W. Lin, Y. Li, K. N. Ding, and J. Q. Li, *Journal of Physical Chemistry B*, 2005, **109**(41),19270–19277.

[238] D. P. Long and P. A. Bianconi, *Journal of the American Chemical Society*, 1996, **118**(49),12453–12454.

[239] R. Duchateau, C.T. Van Wee, and J.H. Teuben, *Organometallics*, 1996, **15**(95),2291–2302.

[240] E. C. Yang, H. K. Zhao, B. Ding, X. G. Wang, and X.J. Zhao, *Crystal Growth and Design*, 2007, **7**(10),2009–2015.

[241] L. Perrin, F. Bonnet, T. Chenal, M. Visseaux, and L. Maron, *Chemistry - A European Journal*, 2010, **16**(37),11376–11385.

[242] O Nuyken and S D Pask, *Polymers*, 2013, **5**(2),361–403.

[243] H.M. Müller and D. Seebach, *Angewandte Chemie International Edition in English*, 1993, **32**(4),477–502.

[244] R. W. Lenz and R. H. Marchessault, *Biomacromolecules*, 2005, **6**(1),1–8.

[245] W McDonough, M Braungart, P T Anastas, and J B Zimmerman. Peer reviewed: Applying the principles of green engineering to cradle-to-cradle design, 2003.

[246] G. Q. Chen, *Chemical Society Reviews*, 2009, **38**(8),2434–2446.

[247] E. Bugnicourt, P. Cinelli, A. Lazzeri, and V. Alvarez, *Express Polymer Letters*, 2014, **8**(11),791–808.

[248] M. Winnacker, *European Journal of Lipid Science and Technology*, 2019, **121**(11),1–9.

[249] D. Kai, Low Z.W., Liow S. S., A. A. Karim, H. Ye, G. Jin, K. Li, and X.J. Loh, *sustainable chemistry and engineering*, 2010, **5**(2),1–23.

[250] A. Steinbuchel, M. H. Madkour, D. Heinrich, A. M. Alghamdi, and I. I. Shabbaj, *Biomacromolecules*, 2013.

[251] B Rieger, A Künkel, G W Coates, R Reichardt, E Dinjus, and T A Zevaco. *Synthetic biodegradable polymers*, volume 245. Springer Science & Business Media, 2012.

[252] A. El-Hadi, R. Schnabel, E. Straube, G. Müller, and S. Henning, *Polymer Testing*, 2002, **21**(6),665–674.

[253] Y. Doi, K. Mukai, K. Kasuya, and K. Yamada. *Biodegradation of Biosynthetic and Chemosynthetic Polyhydroxyalkanoates*, volume 12. Elsevier B.V., 1994.

[254] N. Grassie, E. J. Murray, and P. A. Holmes, *Polymer Degradation and Stability*, 1984, **6**(2),95–103.

[255] J. C. Middleton and A. J. Tipton, *Biomaterials*, 2000, **21**(23),2335–2346.

[256] R. A. Jain, *Biomaterials*, 2000, **21**(23),2475–2490.

[257] N. Tanahashi and Y. Doi, *Macromolecules*, 1991, **24**(20),5732–5733.

[258] H. R. Kricheldorf and S. Eggerstedt, *Macromolecules*, 1997, **30**(19),5693–5697.

[259] A. Amgoune, C. M. Thomas, S. Ilinca, T. Roisnel, and J. F. Carpentier, *Angewandte Chemie - International Edition*, 2006, **45**(17),2782–2784.

[260] N. Ajellal, M. Bouyahyi, A. Amgoune, C. M. Thomas, A. Bondon, I. Pillin, Y. Grohens, and J.F. Carpentier, *Macromolecules*, 2009, **42**(4),987–993.

[261] C. M. Thomas, 2010, pages 165–173.

[262] A. Le Borgne, C. Pluta, and N. Spassky, *Macromolecular Rapid Communications*, 1994, **15**(12),955–960.

[263] E. Grunova, E. Kirillov, T. Roisnel, and J. F. Carpentier, *Dalton Transactions*, 2010, **39**(29),6576–6588.

[264] J. Fang, M.J.L. Tschan, T. Roisnel, X. Trivelli, R. M. Gauvin, C. M. Thomas, and L. Maron, *Polymer Chemistry*, 2013, **4**(2),360–367.

[265] S. M. Guillaume, L. Annunziata, I. Del Rosal, C. Iftner, L. Maron, P. W. Roesky, and M. Schmid, *Polymer Chemistry*, 2013, **4**(10),3077–3087.

[266] J-F Carpentier, *Macromolecular rapid communications*, 2010, **31**(19),1696–1705.

[267] T Zeng, Q Qian, B Zhao, D Yuan, Y Yao, and Q Shen, *RSC Advances*, 2015, **5**(65),53161–53171.

[268] N Ajellal, D M Lyubov, M A Sinenkov, G K Fukin, A V Cherkasov, C M Thomas, J-F Carpentier, and A A Trifonov, *Chemistry–A European Journal*, 2008, **14**(18),5440–5448.

[269] M. Visseaux and F. Bonnet, *Coordination Chemistry Reviews*, 2011, **255**(3-4),374–420.

[270] J M Fraile, J I García, C I Herrerías, J A Mayoral, and E Pires, *Chemical Society Reviews*, 2009, **38**(3),695–706.

[271] R Anwander. Principles in organolanthanide chemistry. In *Lanthanides: Chemistry and Use in Organic Synthesis*, pages 1–61. Springer, 1999.

[272] M J Frisch, G W Trucks, H B Schlegel, G E Scuseria, M A Robb, J R Cheeseman, G Scalmani, V Barone, G A Petersson, H Nakatsuji, X Li, M Caricato, A Marenich, J Bloino, B G Janesko, R Gomperts, B Mennucci, H P Hratchian, J V Ort, and D J Fox. *Gaussian 09, Revision A. 02.* Wallingford CT, 2016.

[273] J.P. Perdew, K. Burke, and Y. Wang, *Physical Review B*, 1996.

[274] J P Perdew, J A Chevary, S H Vosko, K A Jackson, M R Pederson, D J Singh, and C Fiolhais, *Physical Review B*, 1993, **48**(7),4978.

[275] J P Perdew, K Burke, and Y Wang, *Phys. Rev. B*, 1998, **57**,14999–15033.

[276] C Perdew, J. P.; Chevary, J. A.; Vosko, S. H.; Jackson, K. A.; Pederson, M. R.; Singh, D. J.; Fiolhais, *Phys. Rev. B: Condens. Matter Mater. Phys.*, 1992, **46**(11),6671–6687.

[277] J P Perdew. *Unified theory of exchange and correlation beyond the local density approximation.*, volume 11. Akademie Verlag, Berlin, 1991.

[278] J. P. Perdew, K Burke, and M. Ernzerhof, *Physical Review Letters*, 1996, **77**(18),3865–3868.

[279] X Cao and M Dolg, *J. Mol. Struct.*, 2002, **581**(1–3),139–147.

[280] M. Dolg, U. Wedig, H. Stoll, and H. Preuss, *J. Chem. Phys.*, 1987, **86**(2),866–872.

[281] A. W. Ehlers, M. Böhme, S. Dapprich, A. Gobbi, A. Höllwarth, V. Jonas, K. F. Köhler, R. Stegmann, A. Veldkamp, and G. Frenking, *Chemical Physics Letters*, 1993, **208**(3-4),111–114.

[282] R. Ditchfield, *Molecular Physics*, 1974, **27**(4),789–807.

[283] P C Pople and J A Hariharan, *Theo. Chim. Acta*, 1973, **28**(3),213–222.

[284] R. McWeeny, *PHYSICAL REVIEW*, 1962, **126**(1931).

[285] J. L. Dodds, R. McWeeny, and A.J. Sadlej, *Molecular Physics*, 1977, **34**(6),1779–1791.

[286] F London. *Théorie quantique des courants interatomiques dans les combinaisons aromatiques.* PhD thesis, 1937.

[287] H. Staub, I. Del Rosal, L. Maron, F. Kleitz, and F. G. Fontaine, *Journal of Physical Chemistry C*, 2012, **116**(49),25919–25927.

[288] N. Merle, J. Trébosc, A. Baudouin, I. Del Rosal, L. Maron, K. Szeto, M. Genelot, A. Mortreux, M. Taoufik, L. Delevoye, and R. M. Gauvin, *Journal of the American Chemical Society*, 2012, **134**(22),9263–9275.

[289] Y. Bouhoute, A. Garron, D. Grekov, N. Merle, K. C. Szeto, A. De Mallmann, I. Del Rosal, L. Maron, G. Girard, R. M. Gauvin, et al., *ACS Catalysis*, 2014, **4**(11),4232–4241.

[290] N. Popoff, J. Espinas, J. Pelletier, K. C. Szeto, B. Macqueron, O. Boyron, C. Boisson, I. Del Rosal, L. Maron, A. De Mallmann, R. M. Gauvin, and M. Taoufik, *Chem. Eur. J.*, 2013, **19**,964–973.

[291] A. E. Reed and F. Weinhold, *The Journal of Chemical Physics*, 1983, **78**(6),4066–4073.

[292] A. E. Reed, L. A. Curtiss, and F. Weinhold, *Chemical Reviews*, 1988, **88**(6),899–926.

[293] L. H. Thomas. The calculation of atomic fields. In *Mathematical Proceedings of the Cambridge Philosophical Society*, volume 23, pages 542–548. Cambridge University Press, 1927.

[294] E. Fermi, *Rend. Accad. Naz. Lincei*, 1927, **6**(602-607),5.

[295] P. Hohenberg and W. Kohn, *PHYSICAL REVIEW*, 1964, **136**(3),864–871.

[296] W Kohn and J. Sham, *PHYSICAL REVIEW*, 1965, **140**(4),1133–1138.

[297] J. Tao, J. P. Perdew, V. N. Staroverov, and G. E. Scuseria, *Physical Review Letters*, 2003, **91**(14),3–6.

[298] A. D. Becke, *The Journal of Chemical Physics*, 1993, **98**(2),1372–1377.

[299] M. Dion, H. Rydberg, E. Schröder, D. C. Langreth, and B. I. Lundqvist, *Physical Review Letters*, 2004, **92**(24),22–25.

[300] J. Klime, D. R. Bowler, and A. Michaelides, *Physical Review B - Condensed Matter and Materials Physics*, 2011, **83**(19),1–13.

[301] T. A. Wesolowski, O. Parisel, Y. Ellinger, and J. Weber, *The Journal of Physical Chemistry A*, 1997, **101**(42),7818–7825.

[302] L. Maron and O. Eisenstein, *The Journal of Physical Chemistry A*, 2000, **104**(30),7140–7143.

[303] J. A. Peters, K. Djanashvili, C. FGC Geraldes, and C. Platas-Iglesias, *Coordination Chemistry Reviews*, 2020, **406**,213146.

[304] A Roca-Sabio, M Regueiro-Figueroa, D Esteban-Gómez, A de Blas, T Rodríguez-Blas, and C Platas-Iglesias, *Computational and Theoretical Chemistry*, 2012, **999**,93–104.

[305] N. Barros, P. Mountford, S. M. Guillaume, and L. Maron, *Chemistry - A European Journal*, 2008, **14**(18),5507–5518.

[306] N. Barros, M. Schappacher, P. Dessuge, L. Maron, and S. M. Guillaume, *Chemistry - A European Journal*, 2008, **14**(6),1881–1890.

[307] L. Maron and O. Eisenstein, *The Journal of Physical Chemistry A*, 2002, **104**(30),7140–7143.

[308] Y. Zhao and D. G. Truhlar, *ACCOUNTS OF CHEMICAL RESEARCH*, 2008, **41**(2),157–167.

[309] P. Pyykko and J. P. Desclaux, *Accounts of Chemical Research*, 1979, **12**(8),276–281.

[310] L. Kleinman and J. C. Phillips, *Physical Review*, 1959, **116**(4),880–884.

[311] P. Durand and J. C. Barthelat, *Theoretica Chimica Acta*, 1975, **38**(4),283–302.

[312] L. R. Kahn, P. Baybutt, and D. G. Truhlar, *The Journal of Chemical Physics*, 1976, **65**(10),3826–3853.

[313] M.H. Levitt. *Spin dynamics: basics of nuclear magnetic resonance*, volume 40. John Wiley & Sons, 2002.

[314] H. Haeberlen. *High-Resolution NMR in Solids. slective averaging.* ACADEMIC PRESS INC., 1976.

[315] M. J. Duer. *Solid-State NMR Spectroscopy Principles and Applications.* blackwell science, 2002.

[316] T. Helgaker, M. Jaszuński, and K. Ruud, *Chemical Reviews*, 1999, **99**(1),293–352.

[317] K. Wolinski, J. F. Hinton, and P. Pulay, *Journal of the American Chemical Society*, 1990, **112**(23),8251–8260.

[318] V. G. Malkin, O. L. Malkina, and D. R. Salahub, *Chemical Physics Letters*, 1993, **204**(1-2),80–86.

[319] J. I. Musher. *Theory of the Chemical Shift*, volume 2. ACADEMIC PRESS INC., 1966.

[320] W. N. Lipscomb. *The Chemical Shift and Other Second-Order Magnetic and Electric Properties of Small Molecules*, volume 2. ACADEMIC PRESS INC., 1966.

[321] P. Lazzeretti and R. Zanasi, *The Journal of Chemical Physics*, 1978, **68**(3),832–839.

[322] T. A. Keith and R. F.W. Bader, *Chemical Physics Letters*, 1992, **194**(1-2),1–8.

[323] J. A. Pople, *Molecular Physics*, 1964, **7**(4),301–306.

[324] J. A. Pople, *The Journal of Chemical Physics*, 1962, **37**.

[325] J. A. Pople, *Discussions of the Faraday Society*, 1962, **34**(I),7–14.

[326] J. R. Cheeseman, *Journal of Chemical Physics*, 1996, **104**(14),5497–5509.

[327] J Phiri, P Gane, and T C Maloney, *Materials Science and Engineering: B*, 2017, **215**,9–28.

[328] C. Berger, Z. Song, X. Li, X. Wu, N. Brown, C. Naud, D. Mayou, T. Li, J. Hass, A. N Marchenkov, E. H. Conrad, P. N. First, and W. a. De Heer, *Science*, 2006, **312**(May),1191–1196.

[329] S. Stankovich, D. A. Dikin, G. H.B. Dommett, K. M. Kohlhaas, E. J. Zimney, E. A. Stach, R. D. Piner, S. B. T. Nguyen, and R. S. Ruoff, *Nature*, 2006, **442**(7100),282–286.

[330] D. Li, M. B. Müller, S. Gilje, R. B. Kaner, and G. G. Wallace, *Nature Nanotechnology*, 2008, **3**(2),101–105.

[331] Y. Hernandez, V. Nicolosi, M. Lotya, F. M. Blighe, Z. Sun, S. De, I. T. McGovern, B. Holland, M. Byrne, Y. K. Gun'ko, J. J. Boland, P. Niraj, G. Duesberg, S. Krishnamurthy, R. Goodhue, J. Hutchison, V. Scardaci, A. C. Ferrari, and J. N. Coleman, *Nature Nanotechnology*, 2008, **3**(9),563–568.

[332] K. S. Kim, Y. Zhao, H. Jang, S. Y. Lee, J. M. Kim, K. S. Kim, J. H. Ahn, P. Kim, J. Y. Choi, and B. H. Hong, *Nature*, 2009, **457**(7230),706–710.

[333] X. Li, W. Cai, J. An, S. Kim, J. Nah, D. Yang, R. Piner, A. Velamakanni, I. Jung, E. Tutuc, S. K. Banerjee, L. Colombo, and R. S. Ruoff, *Science*, 2009, **324**(5932),1312–1314.

[334] A. Reina, X. Jia, J. Ho, D. Nezich, H. Son, V. Bulovic, M. S Dresselhaus, and J. Kong, 2008, pages 1–6.

[335] Z. Sun, Z. Yan, J. Yao, E. Beitler, Y. Zhu, and J. M. Tour, *Nature*, 2010, **468**(7323),549–552.

[336] P. W. Sutter, J. I. Flege, and E. A. Sutter, *Nature Materials*, 2008, **7**(5),406–411.

[337] A. N. Obraztsov, *Nature Nanotechnology*, 2009, **4**(4),212–213.

[338] M. Lotya, Y. Hernandez, P. J. King, R. J. Smith, V. Nicolosi, L. S. Karlsson, F. M. Blighe, S. De, W. Zhiming, I. T. McGovern, G. S. Duesberg, and J. N. Coleman, *Journal of the American Chemical Society*, 2009, **131**(10),3611–3620.

[339] D. Guo, Y. Nakagawa, H. Ariga, S. Suzuki, K. Kinoshita, T. Miyamoto, S. Takakusagi, K. Asakura, S. Otani, and S. T. Oyama, *Surface Science*, 2010, **604**(17-18),1347–1352.

[340] S. Park and R. S. Ruoff, *Nature Nanotechnology*, 2009, **4**(4),217–224.

[341] Y. Shao, J. Wang, M. Engelhard, C. Wang, and Y. Lin, *Journal of Materials Chemistry*, 2010, **20**(4),743–748.

[342] G Williams, B Seger, and P V Kamat, *ACS Nano*, 2008, **2**(7),1487–1491.

[343] G. Zhu, H. Yin, C. Yang, H. Cui, Z. Wang, J. Xu, T. Lin, and F. Huang, *ChemCatChem*, 2015, **7**(17),2614–2619.

[344] Y Zhu, S Murali, W Cai, X Li, Ji W Suk, J R Potts, and R S Ruoff, *Advanced materials*, 2010, **22**(35),3906–3924.

[345] A. A. Balandin, S. Ghosh, W. Bao, I. Calizo, D. Teweldebrhan, F. Miao, and C.N. Lau, *Nano Letters*, 2008, **8**(3),902–907.

[346] K I Bolotin, K J Sikes, Z Jiang, M Klima, G Fudenberg, J Hone, Ph Kim, and HL Stormer, *Solid state communications*, 2008, **146**(9-10),351–355.

[347] C Lee, X Wei, J W Kysar, and J Hone, *science*, 2008, **321**(5887),385–388.

[348] R. R. Nair, P. Blake, A. N. Grigorenko, K. S. Novoselov, T. J. Booth, T. Stauber, N. M.R. Peres, and A. K. Geim, *Science*, 2008, **320**(5881),1308.

[349] N. Komatsu, *Japanese Journal of Applied Physics*, 2010, **49**(2 PART 2).

[350] M. A. Bissett, S. Konabe, S. Okada, M. Tsuji, and H. Ago, *ACS Nano*, 2013, **7**(11),10335–10343.

[351] D. Akinwande, C. J. Brennan, J. S. Bunch, P. Egberts, J. R. Felts, H. Gao, R. Huang, J. S. Kim, T. Li, Y. Li, K. M. Liechti, N. Lu, H. S. Park, E. J. Reed, P. Wang, B. I. Yakobson, T. Zhang, Y. W. Zhang, Y. Zhou, and Y. Zhu, *Extreme Mechanics Letters*, 2017, **13**,42–77.

[352] F. Gaspari. *Semiconductors*, volume 2-5. Springer International Publishing, 2018.

[353] I. Gerber, M. Oubenali, R. Bacsa, J. Durand, A. Gonçalves, M. F. R. Pereira, F. Jolibois, L. Perrin, R. Poteau, and P. Serp, *Chemistry - A European Journal*, 2011, **17**(41),11467–11477.

[354] S. Kundu, Y. Wang, W. Xia, and M. Muhler, *The Journal of Physical Chemistry C*, 2008, **112**(43),16869–16878.

[355] B. Scheibe, Borowiak-Palen E., and R. J. Kalenczuk, *Journal of Alloys and Compounds*, 2010, **500**(1),117–124.

[356] H. F Gorgulho, J. P Mesquita, F. Gonçalves, M. F. R Pereira, and J. L Figueiredo, *Carbon*, 2008, **46**(12),1544–1555.

[357] R. R. N. Marques, B. F. Machado, J. L. Faria, and A. M. T. Silva, *Carbon*, 2010, **48**(5),1515–1523.

[358] Y. Tian, Z. Hu, Y. Yang, X. Chen, W. Ji, and Y. Chen, *Chemical Physics Letters*, 2004, **388**(4-6),259–262.

[359] L. Stobinski, B. Lesiak, L. Kövér, J. Tóth, S. Biniak, G. Trykowski, and J. Judek, *Journal of Alloys and Compounds*, 2010, **501**(1),77–84.

[360] Zs. Ötvös, Gy. Onyestyák, A. Hancz, I. Kiricsi, and L. V. C. Rees, *Carbon*, 2006, **44**(9),1665–1672.

[361] H. Kitamura, M. Sekido, H. Takeuchi, and M. Ohno, *Carbon*, 2011, **49**(12),3851–3856.

[362] B. Scheibe, E. Borowiak-Palen, and R. J. Kalenczuk, *Materials Characterization*, 2010, **61**(2),185–191.

[363] M. T. Martínez, M. A. Callejas, A. M. Benito, M. Cochet, T. Seeger, A. Ansón, J. Schreiber, C. Gordon, C. Marhic, O. Chauvet, J. L. G. Fierro, and W. K. Maser, *Carbon*, 2003, **41**(12),2247–2256.

[364] S. Berber and A. Oshiyama, *Physica B: Condensed Matter*, 2006, **376-377**(1),272–275.

[365] A. Rodríguez-Fortea, M. Iannuzzi, and M. Parrinello, *Journal of Physical Chemistry B*, 2006, **110**(8),3477–3484.

[366] A. Rodríguez-Fortea, M. Iannuzzi, and M. Parrinello, *Journal of Physical Chemistry C*, 2007, **111**(5),2251–2258.

[367] G. Ghigo, A. Maranzana, G. Tonachini, C. M. Zicovich-Wilson, and M. Causà, *The Journal of Physical Chemistry B*, 2004, **108**(10),3215–3223.

[368] C. E. Kefalidis, L. Castro, L. Perrin, I. Del Rosal, and L. Maron, *Chemical Society Reviews*, 2016, **45**(9),2516–2543.

[369] H. C. Aspinall, S. R. Moore, and A. K. Smith, *Journal of the Chemical Society, Dalton Transactions*, 1992, (1),153–156.

[370] J. P. Osegovic, R. S. Drago, V. Uni, P. O. Box, and V. Gaines, 2000, pages 147–154.

[371] A. Ventura, T. Chenal, M. Bria, F. Bonnet, P. Zinck, Y. Ngono-Ravache, E. Balanzat, and M. Visseaux, *European Polymer Journal*, 2013, **49**(12),4130–4140.

[372] Dongtao Liu and Dongmei Cui, *Dalton Transactions*, 2011, **40**(30),7755–7761.

[373] N Ishihara, M Kuramoto, and M Uoi, *Macromolecules*, 1988, **21**(12),3356–3360.

[374] M Malanga, *Advanced Materials*, 2000, **12**(23),1869–1872.

[375] J Schellenberg and H-J Leder, *Advances in Polymer Technology: Journal of the Polymer Processing Institute*, 2006, **25**(3),141–151.

[376] P Zinck, F Bonnet, A Mortreux, and M Visseaux, *Progress in polymer science*, 2009, **34**(4),369–392.

[377] M Jaymand, *Polymer Chemistry*, 2014, **5**(8),2663–2690.

[378] E Laur, E Kirillov, and J-F Carpentier, *Molecules*, 2017, **22**(4),594.

[379] A-S Rodrigues and J-F Carpentier, *Coordination Chemistry Reviews*, 2008, **252**(18-20),2137–2154.

[380] Y Luo, J Baldamus, and Z Hou, *Journal of the American Chemical Society*, 2004, **126**(43),13910–13911.

[381] E. Laur, E. Louyriac, V. Dorcet, A. Welle, A. Vantomme, O. Miserque, J.M. Brusson, L. Maron, J.F. Carpentier, and E. Kirillov, *Macromolecules*, 2017, **50**(17),6539–6551.

[382] E. Louyriac, E. Laur, A. Welle, A. Vantomme, O. Miserque, J.M. Brusson, L. Maron, J.F. Carpentier, and E. Kirillov, *Macromolecules*, 2017, **50**(24),9577–9588.

[383] A. Pakdel, Y. Bando, and D. Golberg, *Chemical Society Reviews*, 2014, **43**(3),934–959.

[384] G. R. Bhimanapati, N. R. Glavin, and J. A. Robinson. *2D Boron Nitride: Synthesis and Applications*, volume 95. Elsevier Inc., 1 edition, 2016.

[385] Q. Weng, X. Wang, X. Wang, Y. Bando, and D. Golberg, *Chemical Society Reviews*, 2016, **45**(14),3989–4012.

[386] G. R. Bhimanapati, Z. Lin, V. Meunier, Y. Jung, J. Cha, S. Das, D. Xiao, Y. Son, M. S. Strano, V. R. Cooper, L. Liang, S. G. Louie, E. Ringe, W. Zhou, S. S. Kim, R. R. Naik, B. G. Sumpter, H. Terrones, F. Xia, Y. Wang, J. Zhu, D. Akinwande, N. Alem, J. A. Schuller, R. E. Schaak, M. Terrones, and J.A. Robinson, *ACS Nano*, 2015, **9**(12),11509–11539.

[387] G. Ciofani, S. Danti, G. G. Genchi, B. Mazzolai, and V. Mattoli, *Small*, 2013, **9**(9-10),1672–1685.

[388] G. Ciofani, V. Raffa, A. Menciassi, and A. Cuschieri, *Biotechnology and Bioengineering*, 2008, **101**(4),850–858.

[389] X. Chen, P. Wu, M. Rousseas, D. Okawa, Z. Gartner, A. Zettl, and C.R. Bertozzi, *Journal of the American Chemical Society*, 2009, **131**(3),890–891.

[390] D. Lahiri, F. Rouzaud, T. Richard, A. K. Keshri, S. R. Bakshi, L. Kos, and A. Agarwal, *Acta Biomaterialia*, 2010, **6**(9),3524–3533.

[391] R. T. Paine and C. K. Narula, *Chemical Reviews*, 1990, **90**(1),73–91.

[392] J. W. Jiang, J. S. Wang, and B. Li, *Physical Review B - Condensed Matter and Materials Physics*, 2009, **79**(20),1–6.

[393] J. Lan, J. S. Wang, C. K. Gan, and S.K. Chin, *Physical Review B - Condensed Matter and Materials Physics*, 2009, **79**(11),2–6.

[394] Z. Liu, Y. Gong, W. Zhou, L. Ma, J. Yu, J. C. Idrobo, J. Jung, A. H. Macdonald, R. Vajtai, J. Lou, and P. M. Ajayan, *Nature Communications*, 2013, **4**(May),1–8.

[395] C. Zhi, Y. Bando, C. Tang, H. Kuwahara, and D. Golberg, *Advanced Materials*, 2009, **21**(28),2889–2893.

[396] M. A. Rafiee, T. N. Narayanan, D. P. Hashim, N. Sakhavand, R. Shahsavari, R. Vajtai, and P. M. Ajayan, *Advanced Functional Materials*, 2013, **23**(45),5624–5630.

[397] X. Chen, J. F. Dobson, and C. L. Raston, *Chemical Communications*, 2012, **48**(31),3703–3705.

[398] J. Ghosh, S. Mazumdar, M. Das, S. Ghatak, and A. K. Basu, *Materials Research Bulletin*, 2008, **43**(4),1023–1031.

[399] L. Hua Li, Y. Chen, B. M. Cheng, M.Y. Lin, S. L. Chou, and Y. C. Peng, *Applied Physics Letters*, 2012, **100**(26),26–30.

[400] D. Lee, B. Lee, K. H. Park, H.J. Ryu, S. Jeon, and S. H. Hong, *Nano Letters*, 2015, **15**(2),1238–1244.

[401] L. H. Li, Y. Chen, G. Behan, H. Zhang, M. Petravic, and A. M. Glushenkov, *Journal of Materials Chemistry*, 2011, **21**(32),11862–11866.

[402] E. C. Anota, Y. Tlapale, M. S. Villanueva, and J. A.R. Márquez, *Journal of Molecular Modeling*, 2015, **21**(8).

[403] G. R. Bhimanapati, D. Kozuch, and J. A. Robinson, *Nanoscale*, 2014, **6**(20),11671–11675.

[404] Z. Cui, A. J. Oyer, A. J. Glover, H. C. Schniepp, and D. H. Adamson, *Small*, 2014, **10**(12),2352–2355.

[405] X. Li, X. Hao, M. Zhao, Y. Wu, J. Yang, Y. Tian, and G. Qian, *Advanced Materials*, 2013, **25**(15),2200–2204.

[406] Y. Lin, T. V. Williams, and J. W. Connell, *Journal of Physical Chemistry Letters*, 2010, **1**(1),277–283.

[407] A. K. Roy, B. Park, K. S. Lee, S. Y. Park, and I. In, *Nanotechnology*, 2014, **25**(44).

[408] T. Sainsbury, A. Satti, P. May, A. O'Neill, V. Nicolosi, Y. K. Gun'Ko, and J. N. Coleman, *Chemistry - A European Journal*, 2012, **18**(35),10808–10812.

[409] T. Sainsbury, A. O'Neill, M. K. Passarelli, M. Seraffon, D. Gohil, S. Gnaniah, S. J. Spencer, A. Rae, and J. N. Coleman, *Chemistry of Materials*, 2014, **26**(24),7039–7050.

[410] Y. Wang, Z. Shi, and J. Yin, *Journal of Materials Chemistry*, 2011, **21**(30),11371–11377.

[411] J. H. Warner, M. H. Rümmeli, A. Bachmatiuk, and B. Büchner, *ACS Nano*, 2010, **4**(3),1299–1304.

[412] M. S. Bresnehan, G. R. Bhimanapati, K. Wang, D. W. Snyder, and J. A. Robinson, *ACS Applied Materials and Interfaces*, 2014, **6**(19),16755–16762.

[413] K. K. Kim, A. Hsu, X. Jia, S. M. Kim, Y. Shi, M. Hofmann, D. Nezich, J. F Rodriguez-nieva, M. Dresselhaus, T. Palacios, and J. Kong, *Nano Letters*, 2012.

[414] K. K. Kim, A. Hsu, X. Jia, S. M. Kim, Y. Shi, M. Dresselhaus, T. Palacios, and J. Kong, *ACS Nano*, 2012, **6**(10),8583–8590.

[415] G. Kim, A. R. Jang, H. Y. Jeong, Z. Lee, D. J. Kang, and H. S. Shin, *Nano Letters*, 2013, **13**(4),1834–1839.

[416] K. H. Lee, H.-j. Shin, J. Lee, I.-y. Lee, G.h. Kim, J.-y. Choi, and S.w. Kim, *Nano Letters*, 2012.

[417] Y. H. Lee, K. K. Liu, A. Y. Lu, C. Y. Wu, C.T. Lin, W. Zhang, C. Y. Su, C. L. Hsu, T.W. Lin, K. H. Wei, Y. Shi, and L. J. Li, *RSC Advances*, 2012, **2**(1),111–115.

[418] L. Song, L. Ci, H. Lu, P. B. Sorokin, C. Jin, J. Ni, A. G. Kvashnin, D. G. Kvashnin, J. Lou, B. I. Yakobson, and P.M. Ajayan, *Nano Letters*, 2010, **10**(8),3209–3215.

[419] N. R. Glavin, M. L. Jespersen, M. H. Check, J. Hu, A.M. Hilton, T. S. Fisher, and A. A. Voevodin, *Thin Solid Films*, 2014, **572**,245–250.

[420] D. Golberg, B. Yoshio, Y. Huang, T. Terao, M. Mitome, C. Tang, and C. Zhi, *ACS Nano*, 2010, **4**(6),2979–2993.

[421] C. Li, Y. Bando, C. Zhi, Y. Huang, and D. Golberg, *Nanotechnology*, 2009, **20**(38).

[422] W.Q. Han, W. Mickelson, J. Cumings, and A. Zettl, *Applied Physics Letters*, 2002, **81**(6),1110–1112.

[423] Y. Lin, T. V. Williams, T. B. Xu, W. Cao, H. E. Elsayed-Ali, and J. W. Connell, *Journal of Physical Chemistry C*, 2011, **115**(6),2679–2685.

[424] A. Pakdel, Y. Bando, and D. Golberg, *ACS Nano*, 2014, **8**(10),10631–10639.

[425] T. Sainsbury, A. Satti, P. May, Z. Wang, I. McGovern, Y. K. Gun'ko, and J. Coleman, *Journal of the American Chemical Society*, 2012, **134**(45),18758–18771.

[426] E. Chigo Anota, H. Hernández Cocoletzi, and E. Rubio Rosas, *European Physical Journal D*, 2011, **63**(2),271–273.

[427] M. Castro and E. Chigo-Anota, *Mex. J. Mat. Sci. Eng.*, 2014, **1**,21–29.

[428] X. Jiang, Q. Weng, X. Wang, X. Wang, N. Hanagata, D. Golberg, D. Liu, B. Wang, X. Li, and Y. Bando, *ACS Nano*, 2014, **8**(6),6123–6130.

[429] A. Bathellier, D. Moreno, L. Maron, C. Dinoi, and I. Del Rosal, *Chemistry–A European Journal*, 2020.

[430] Noémi Barros, Odile Eisenstein, and Laurent Maron, *Dalton Transactions*, 2010, **39**(44),10757–10767.

[431] Noémi Barros, Odile Eisenstein, and Laurent Maron, *Dalton Transactions*, 2010, **39**(44),10749–10756.

[432] C. Copéret, D. P. Estes, K. Larmier, and K. Searles, *Chemical Reviews*, 2016, **116**(15),8463–8505.